

UCLA

UCLA Electronic Theses and Dissertations

Title

A Crosslink Between Mitochondrial Architecture and Metabolism

Permalink

<https://escholarship.org/uc/item/9zh0f60f>

Author

Ngo, Jennifer

Publication Date

2022

Peer reviewed|Thesis/dissertation

UNIVERSITY OF CALIFORNIA

Los Angeles

A Crosslink Between Mitochondrial Architecture and Metabolism

A dissertation submitted in partial satisfaction of the requirements for the degree

Doctor of Philosophy in Biochemistry, Molecular and Structural Biology

by

Jennifer Ngo

2022

© Copyright by

Jennifer Ngo

2022

ABSTRACT OF THE DISSERTATION

A Crosslink Between Mitochondrial Architecture and Metabolism

by

Jennifer Ngo

Doctor of Philosophy in Biochemistry, Molecular and Structural Biology

University of California, Los Angeles, 2022

Professor Orian Shirihai, Co-Chair

Professor Catherine F. Clarke, Co-Chair

Mitochondrial architecture has long been associated with metabolic flexibility, although the precise causalities and the underlying mechanisms are still enigmatic. We showed that mitochondrial fragmentation is highly associated with fatty acid oxidation (FAO) rates. Furthermore, forced mitochondrial elongation using Mfn2 over-expression or Drp1 depletion significantly decreased FAO rates, while Mfn2 knockout lead to enhanced FAO rates, suggesting that mitochondrial fragmentation is functionally coupled with fatty acid utilization. Notably, the increased FAO rates upon mitochondrial fragmentation is attributed to decreased CPT1 sensitivity to malonyl-CoA, the endogenous CPT1 inhibitor, consistent with the observation that mitochondrial fragmentation specifically facilitates long chain-fatty acid oxidation (LCFAO), but not short

chain fatty acid oxidation. Furthermore, we show pharmacological activators of CPT1 enhance FAO of elongate mitochondria but not in the presence of malonyl-CoA binding. Suggesting mitochondrial morphology influences CPT1's binding to a CoA moiety. Taken together, our study provides a biochemical and mechanistic explanation of how mitochondrial architecture links cellular metabolic needs to differential fuel utilization, such as LCFAO, which may be implicated in a myriad of human physiologies and pathologies.

In non-alcoholic steatohepatitis (NASH), increased Drp1 mediated mitochondrial fragmentation has been observed in hepatocytes. NASH is characterized by liver inflammation, increased hepatocyte swelling, and some degree of fibrosis. Hepatic steatosis can occur when glucose and fatty acid availability exceeds the energy demand of the liver. This presents the question, is increased fission in NASH a compensatory or a pathogenic mechanism? To address this question, we decreased Drp1 function in liver from adult mice with established NASH (26 week-GAN diet) using GalNAc-siRNA mediated delivery. While NASH alone only elevated circulating AST and ALT levels, markers of hepatic injury, Drp1KD in the NASH liver engaged the mitochondrial integrated stress response (ISR) by OMA1 activation and ER stress. The fibrosis and hepatocyte necrosis observed only in Drp1KD of NASH mice can be explained by reduced metabolic adaptability as a result of inhibiting fission-mediated fragmentation, reducing FAO capacity, and enhancing accumulation of NEFA. Overall, our data suggests Drp1-mediated mitochondrial fragmentation is an adaptive mechanism in NASH that prevents lipotoxicity, overactivation of the integrated stress response, and ER stress to limit fibrosis, inflammation, and necrosis.

The dissertation of Jennifer Ngo is approved.

Linsey Stiles

Ajit S. Divakaruni

Marc Liesa-Roig

Joseph Ambrose Loo

Catherine F. Clarke, Committee Co-Chair

Orian Shirihai, Committee Co-Chair

University of California, Los Angeles

2022

DEDICATION

This work is dedicated to my loving family, my parents Toan Nguyen Ngo and Linh Vien Ngo, and my brother Henry Can Ngo, for all they have sacrificed so that I may succeed.

TABLE OF CONTENTS

ABSTRACT OF THE DISSERTATION.....	ii
DEDICATION	v
TABLE OF CONTENTS	vi
LIST OF FIGURES AND TABLES	ix
LIST OF ABBREVIATIONS.....	x
ACKNOWLEDGMENTS.....	xiii
CURRICULUM VITAE.....	xx
CHAPTER 1	22
INTRODUCTION.....	23
1. Overview of intracellular heterogeneity	23
1.1. What is mitochondrial heterogeneity and why should we care?	23
1.2. Nongenetic contributors to mitochondrial homogeneity and heterogeneity	25
2. Mitochondrial heterogeneity increases under pathological states	27
2.1. Brief overview of mediators in mitochondrial fusion and fission	27
2.2. Architectural variance under pathological states introduces metabolic defects	28
3. Overview of mitochondrial fatty acid oxidation.	34
3.1 . Regulation of CPT1.....	35
3.2 . Contribution of CPT1 to pathology.	36
4. The role of mitochondrial oxidative function in liver in health and NAFLD.	37
5. Overview whereby decreased mitochondrial oxidative function contributes to NAFLD.....	40
5.1. The role of mitochondrial fragmentation in the decrease in mitochondrial oxidative function observed in simple steatosis and NASH	41
5.2. JNK can induce mitochondrial fragmentation, decrease fat oxidation and elevate mitochondrial ROS in simple steatosis and NASH	43
5.3. Defects in mitophagy contribute to reduced oxidative capacity in NAFLD	45
6. Overview whereby mitochondrial oxidative function is not impaired in NAFLD	47
FIGURES.....	54
REFERENCES	64

CHAPTER 2	85
Mitochondrial architecture controls fatty acid utilization by regulating CPT1 sensitivity to Malonyl-CoA.....	85
ABSTRACT.....	87
INTRODUCTION	88
EXPERIMENTAL PROCEDURES	91
RESULTS	107
DISCUSSION & FUTURE DIRECTIONS.....	123
FIGURES.....	131
REFERENCES	149
CHAPTER 3	155
Decreasing DRP1 expression in liver activates the mitochondrial integrated stress response and exacerbates NASH	155
ABSTRACT.....	157
INTRODUCTION	159
EXPERIMENTAL PROCEDURES	161
RESULTS	174
DISCUSSION & FUTURE DIRECTIONS.....	182
FIGURES.....	189
SUPPLEMENTAL FIGURES	199
REFERENCES	202
CHAPTER 4	209
Discussion & Future Directions	209
1. A second job for the mitochondrial life cycle	210
2. Investigation of inhibiting fission as a therapeutic revealed novel role for mitochondrial morphology in FFA metabolism	211
3. Potential for mitochondrial heterogeneity to influence Malonyl-CoA sensitivity and FAO	212
4. Mitochondrial subpopulations influence cellular function	213
5. Three distinct mitochondrial sub-populations could regulate hepatic steatosis in opposite ways in NAFLD.....	215
6. Challenges and considerations to be made when studying intracellular heterogeneity	217
7. Current and hypothetical therapies targeting liver mitochondria to treat NAFLD and hyperglycemia.....	219
8. Remaining questions in the field	223
9. Conclusion	224
Figures.....	226
References	232
Appendix I	243

Isolation and Functional Analysis of Mitochondria Bound to Lipid Droplets from Murine Brown Adipose Tissue.....	243
Appendix II	264
Measuring mitochondrial respiration in previously frozen biological samples.....	264
Appendix III	283
Parkin Regulates Adiposity by Coordinating Mitophagy with Mitochondrial Biogenesis in White Adipocytes.....	283
Appendix IV	320
ABCB10 exports mitochondrial biliverdin, driving metabolic maladaptation in obesity.	320
Appendix V	366
COQ11 deletion mitigates respiratory deficiency caused by mutations in the gene encoding the coenzyme Q chaperone protein Coq10.	366
Appendix VI.....	395
Atomic structure of a toxic, oligomeric segment of SOD1 linked to amyotrophic lateral sclerosis (ALS).	395

LIST OF FIGURES AND TABLES

Figure 1- 1. The role of mitochondrial dynamics in mitochondrial heterogeneity.....	54
Figure 1- 2. Pathogenesis of the pancreatic beta-cell and renal proximal tubule cell induced by increased mitochondrial heterogeneity.	56
Figure 1- 3. Mitochondria as a compromised friend in NAFLD.....	58
Figure 1- 4. Mitochondria as a foe in NAFLD.	61
Figure 1- 5. Mitochondrial states throughout the progression of NAFLD.....	62
Figure 2- 1. Hepatic mitochondrial fatty acid utilization and glucose production is associated with mitochondrial morphology.	132
Figure 2- 2. Mitochondrial fragmentation induced by Mfn2 in beta-cells increases fatty acid sensitivity	134
Figure 2- 3. Mitochondrial elongation reduces OxPHOS-DLBCL FAO and impairs cell survival.....	137
Figure 2- 4. Mitochondrial architecture specifically alters CPT1-dependent FAO	139
Figure 2- 5. Mitochondrial architecture specifically alters the interaction between CPT1 and Malonyl-CoA.....	141
Expanded View Figure 2- 1. Drp1 reduction verification in hepatocytes.....	143
Expanded View Figure 2- 2. Beta cell specific Mfn2KO islet verification.....	144
Expanded View Figure 2- 3. Mfn2-TAT peptide validation	147
Expanded View Figure 2- 4. CPT1 sensitivity in INS1 cells.....	148
Figure 3- 1. Hepatocyte specific knockdown of Drp1 causes liver damage, inflammation, fibrosis and bodyweight loss due to Gdf15 mediated reduced food intake.....	189
Figure 3- 2. Drp1 ablation reduces mitochondrial respiration and activates the ATF4 mediated ISR	191
Figure 3- 3. Improved plasma metabolic profile in mice on GAN diet by Drp1 knockdown	193
Figure 3- 4. Reduced respiratory capacity and accumulation of FFA upon Drp1 knockdown activates the ISR in mice on GAN diet	195
Figure 3- 5. Hepatocyte specific Drp1 knockdown worsens fibrosis and inflammation in GAN mice.....	198
Expanded View Figure 3- 1	199
Expanded View Figure 3- 2.....	200
Expanded View Figure 3- 3.....	201
Figure 4- 1. Mitochondrial subpopulations reveal unique mitochondrial traits.	226
Figure 4- 2. Proposed model of three distinct mitochondrial populations in hepatocytes.	228
Table 1. Proposed models of modulating fission as a therapeutic approach to NASH & NAFLD.	231

LIST OF ABBREVIATIONS

ADP	adenosine diphosphate
AKI	acute kidney injury
ALT	alanine aminotransferase
AMPK	AMP-activated protein kinase
AR	aspect ratio
AST	aspartate aminotransferase
ATF4	Activating Transcription Factor 4
ATP	adenosine triphosphate
BAT	brown adipose tissue
BCR-DLBCLs	B cell receptor subset- diffuse large B cell lymphoma
Cer	ceramide
CI	Complex I
CII	Complex II
CIII	Complex III
CIV	Complex IV
CKD	chronic kidney disease
CPT1	carnitine palmitoyltransferase 1
DLBCL	Diffuse large B cell lymphoma
dnDrp1	dominant negative-Drp1; Drp1 K38A
Drp1	Dynamin-related protein 1
EIF2alpha	eukaryotic initiation factor-2 α
EM	Electron microscopy
ER	endoplasmic reticulum
ETC	Electron Transport Chain
Eto	etomoxir
FA	fatty acid
FAO	Fatty Acid Oxidation
FCCP	Carbonyl cyanide-p-trifluoromethoxyphenylhydrazone
FFA	Free fatty acid
FGF21	Fibroblast growth factor 21
Fis1	Mitochondrial fission 1 protein
GalNAc	N-acetylgalactosamine
GAN	Gubra-Amylin NASH
GC/MS	Gas chromatography–mass spectrometry
GCGR	glucagon receptor
GDF15	Growth Differentiation Factor 15
GEP	gene expression profile
GFP	green fluorescent protein
GFRAL	GDNF Family Receptor Alpha Like
GLP1R	glucagon-like peptide 1 receptor
GLT	glucolipotoxicity
GNG	gluconeogenesis

GPR40	G-protein-coupled receptor 40
GRP75	G Protein-Coupled Receptor 75
GSIS	glucose-stimulated insulin secretion
H&E	hematoxylin and eosin
H ₂ O ₂	hydrogen peroxide
HFD	high fat diet
HGP	hepatic glucose production
HSC	hepatic stellate cell
IR	insulin resistance
ISR	Integrated stress response
JNK	c-Jun-N terminal kinase
KD	Knockdown
KO	Knockout
LCFAO	long chain-fatty acid oxidation
MAG	monoacylglycerol
Mal-CoA	malonyl-CoA
MAM	mitochondria-associated membranes
MCFAO	Medium chain fatty acid oxidation
MCU	mitochondrial calcium uniporter
Mff	mitochondrial fission factor
Mfn2	Mitofusin 2
MPC1	mitochondrial pyruvate importer
mPTP	mitochondrial permeability transition pore
mtDNA	mitochondrial DNA
MTG	MitoTracker Green
NAD	Nicotinamide adenine dinucleotide
NADH	nicotinamide adenine dinucleotide (NAD) + hydrogen (H)
NADPH	nicotinamide adenine dinucleotide phosphate
NAFLD	non-alcoholic fatty liver disease
NASH	non-alcoholic steatohepatitis
NEFA	non-esterified fatty acid
OE	overexpression
Oligo	oligomycin
OMA1	OMA1 zinc metallopeptidase
OPA1	Optic Atrophy 1
OXPHOS	Oxidative phosphorylation
OxPhos-DLBCLs	Oxidative phosphorylation subset-diffuse large B cell lymphoma
PAGFPmt	photoactivatable-mitochondrially-targeted GFP
PBS	Phosphate-buffered saline
PERK	PKR-like ER kinase
PFO	Perfringolysin O
PKA	protein kinase A
PPAR α	Peroxisome Proliferator Activated Receptor Alpha

PSR	picrosirius red
qPCR	quantitative polymerase chain reaction
qRT-PCR	Real-Time Quantitative Reverse Transcription PCR
RC	regular CHOW
RIP-Cre	Rat insulin promoter-mediate Cre
ROS	reactive oxygen species
SAB	spectrin-actin binding
SCFAO	short chain fatty acid oxidation
siRNA	small interfering RNA
T2D	type 2 diabetes
T2DM	Type 2 diabetes mellitus
TCA	tricarboxylic acid cycle
TG	triglycerides
TMRE	Tetramethylrhodamine, ethyl ester
UPR	Unfolded protein response
VLDL	very low density lipoprotein
WT	wildtype
ZD	Zucker diabetic
ZDF	Zucker diabetic fatty rats
ZDL	Zucker diabetic lean
ZF	Zucker fatty
ZL	Zucker Lean
β Mfn2KO	beta-cell specific Mfn2 Knockout
$\Delta\Psi$	mitochondrial membrane potential

ACKNOWLEDGMENTS

I would like to thank my mentor, Orian Shirihai and co-mentor, Marc Liesa. Orian Shirihai for his phenomenal guidance and support. His “one in a million” mentoring style made my development as a scientist a really fun experience. My favorite quotes that changed my perspective on research, “Our job is not to generate positive data but to move forward,” and “research is like going into a dark closet you always come out with something you didn’t intend to find.” I am especially grateful to him for putting emphasis on creative thinking and making science communication fun. I also want to thank him for creating a wondrous lab environment. I would like to thank Marc Liesa for his invaluable advice on data interpretation, storytelling, and writing. He taught me the importance of critically analyzing data that may be discarded. I am incredibly grateful for his humbleness and down-to-earth personality, which made training, under such a great mind, less daunting.

This dissertation contains significant contributions from a group of talented researchers. I am grateful to my thesis committee, Dr. Catherine Clarke, Dr. Joseph Loo, Dr. Ajit Divakaruni, and Dr. Linsey Stiles. They have given me instrumental advice regarding research projects and career development. Science is the process of building upon previous findings, I want to thank Dr. Marck Prentki and Dr. Barbara Corkey for their critical discussions and for all that they have contributed to the field of metabolism and islet physiology.

Chapter one of this dissertation is adapted from Shum et al. Mitochondrial oxidative function in NAFLD: friend or foe? *Molecular Metabolism*. 2020. doi: 10.1016/j.molmet.2020.101134 and Ngo et al. Mitochondrial heterogeneity in health and

disease. MDPI Biology. 2021. 10(9), 927. doi: 10.3390/biology10090927.

Chapter two of this dissertation is a version of the manuscript in preparation titled: Mitochondrial architecture controls fatty acid utilization by regulating CPT1 sensitivity to Malonyl-CoA. Jennifer Ngo*, Dong Wook Choi*, Anthony Molina, Linsey Stiles, Nate Miller, Siyouneh Baghdasarian, Brett Roach, Karel Erion, Anthony Jones, Kristen Kim, Sam B. Sereda, Jakob D. Wikstrom, Evan Taddeo, Ajit Divakaruni, David Chan, Barbara E. Corkey, Marc Liesa, Orian Shirihai, and Nika Danial. I would like to thank Dr. Dong Wook Choi and Dr. Nika Danial for their collaboration on this project. I am grateful to all of my co-authors who worked tirelessly towards this project, including Dr. Dong Wook for performing thorough biochemical studies on primary mouse hepatocytes and DLBCLs; Dr. Nate Miller who excluded numerous hypothesis; Siyouneh Baghdasarian who performed insulin secretions from islets isolated from HFD mice; Brett Roach who optimized the Mfn2-TAT peptides; and Sam Sereda as well as Drs. Anthony Molina, Linsey Stiles, Jakob Wikstrom, and Marc Liesa for establishing the basis of the islet study in Mfn2KO mice. For INS1 insulin secretions, I would like to thank Siyouneh Baghdasarian for her utmost patience and guidance in teaching me how to assess insulin secretion thoroughly. For all images and image analysis, I would like to thank Dr. Nate Miller who spent numerous hours teaching me how to use the LSM880, how to design and write image analysis macros, and how to apply this knowledge across several software. For metabolite tracing experiments, I would like to thank the Ajit Divakaruni lab for their collaborative efforts. I am especially appreciative of Anthony Jones and Kristen Kim for aiding me in the optimization process and thoroughly mentoring me in performing tracing experiments. I would also like to thank Dr. David Chan and Dr. Gerald Dorn for provision

of key reagents. A huge thank you to Dr. Barbara Corkey, Dr. Karel Erion, and Dr. Evan Taddeo for critical discussion and project mentorship.

Chapter three of this dissertation is a version of the manuscript in preparation titled: Decreasing DRP1 expression in liver activates the mitochondrial integrated stress response and exacerbates NASH. Janos Steffen, Sheng-Ping Wang, Kevin Williams, Fritz Kramer, George Ho, Carlos Rodriguez, Krishna Yekkala, Chidozie Amuzie, Russell Bialecki, Lisa Norquay, Andrea Nawrocki, Mark Erion, Alessandro Pocai, Orian Shirihai, and Marc Liesa. I would like to thank Dr. Alessandro Pocai, Dr. Lisa Norquay, Dr. Mark Erion, Dr. Janos Steffen, Dr. Sheng Ping Wang and the team at Janssen for their collaboration on this project. I would like to thank Dr. Janos Steffen for western blot and quantitative PCR analysis of integrated stress response genes; Dr. Sheng Ping Wang for all animal work; and Dr. Kevin Williams for performing lipidomic analysis. I would like to thank Dr. Marc Liesa for critical discussions. I would also like to thank Dr. Mark Erion, Dr. Lisa Norquay, and Dr. Alessandro Pocai for provision of key reagents and making this collaboration possible.

Parts of discussion and conclusions are adapted from Ngo et al. Mitochondrial heterogeneity in health and disease. *MDPI Biology*. 2021. 10(9), 927. doi: 10.3390/biology10090927 and Shum et al. Mitochondrial oxidative function in NAFLD: friend or foe? *Molecular Metabolism*. 2020. doi: 10.1016/j.molmet.2020.101134.

Appendix I is a reprint of an article in *STAR Protocols* (2020) 2, 100243; I would like to thank Cell Press and all of the Shirihai and Liesa laboratory co-authors who have contributed, for permission to use this copyrighted material. Appendix II is a reprint of an article from *Current Protocols in Cell Biology* (2020) 89, e116. I would like to thank Wiley

Online Library and the primary author for permission to use this copyrighted material. Appendix III is a reprint of an article under review in *Nature Metabolism* (2021); I would like to thank primary authors, Drs. Timothy Moore and Lijing Cheng, for permission to use this material. Appendix IV is a reprint of an article in *Science Translational Medicine* (2021) 13, eabd1869; I would like to thank the American Association for the Advancement of Science and primary author Dr. Michael Shum for permission to use this copyrighted material. Appendix V is a reprint of an article in *Journal of Biological Chemistry* (2020) 295(18) 6023-6042; I would like to thank the American Society for Biochemistry and Molecular Biology and primary author Michelle Bradley for permission to use this copyrighted material. Appendix VI is a reprint of an article in *Proceedings of the National Academy of Sciences* (2017) 114; 33; 8770-8775; I would like to thank The National Academy of Sciences and primary author Dr. Smriti Sangwan for permission to use this copyrighted material. All work is supported by funding from the NIH and ADA to Dr. Orian Shirihai, the Cota V. Robles Fellowship to Jennifer Ngo, and the Gates Millennium Fellowship to Jennifer Ngo.

The journey has been challenging but rewarding, I am extremely grateful to my previous mentors Dr. Barry L. Taylor, Dr. Kylie J. Watts, Dr. Xian Luo-Owen, Dr. Peter J. Bradley, and Dr. Carla M. Koehler for teaching me and giving me an excellent foundation in molecular biology and biochemistry lab techniques. As a high schooler, Dr. Barry L. Taylor, Dr. Kylie J. Watts, and Dr. Xian Luo-Owen mentored me with my own research project and encouraged me to ask questions, improve upon techniques, and explore different projects in their labs, which showed me the endless approaches to tackling a question. Dr. Peter J. Bradley for mentoring me one-on-one throughout my entire 4 years

of undergraduate. Dr. Bradley patiently taught me the rationale behind each and every step of a process, gave me the opportunity to work with animals, and emphasized the importance of delivering a clear message with an audible voice. My ability to speak loudly and project is largely attributed to Dr. Bradley's training. Dr. Carla M. Koehler saw all my faults and weaknesses but empowered me and constantly challenged me when no one else would to become better. Through her guidance I became a better speaker and fell in love with mitochondrial metabolism.

I also want to recognize and extend thanks to my colleagues in the UCLA Department of Chemistry and Biochemistry. Dr. Hui Tsui, Dr. Agape Awad, and Dr. Michelle Bradley provided invaluable guidance, mentorship, and friendship. Also, a huge thank to my cohort, and cohort mates, Fay Lin and Callie Glynn, for always keeping each other on track of our graduate timeline and making time to take a stroll through Target.

I would like to recognize the amazing mentorship and collaboration under Dr. Yijun Chen. For performing bariatric surgery on many of our mice cohorts, provision of key reagents, post-surgery guidance, and critical discussions on clinical relevance.

I would like to thank all the past and present members of the Shirihai Lab, Liesa Lab, and Divakaruni Lab, for all their support, great collaborations, friendships, and for making my time in the lab the happiest time I could imagine. So happy I don't want to leave. The hours we have spent working in the laboratory together will always hold a distinct place in my heart. I would also like to thank Dr. Linsey Stiles for her mentorship and kind support. I am very grateful for all her advice on troubleshooting experiments and for keeping me on track while preparing my manuscripts. Even though she has endless core projects, I appreciate her company with Scott Wilde to all of our Disney trips.

I particularly want to thank Dr. Karel Erion, for being a great mentor, collaborator, and friend. Karel has helped me with multiple projects and given excellent advice. His amazing ability to recite numerous publications as well as refusal to help me directly (and rather force me to seek help from others) has contributed to not only my personal growth but also my growth as a scientist. I extremely appreciate his time and dedication to my professional development. May we never have another GTT competition with blue Gatorades.

Finally, I want to thank my friends and family, who are some of the most important people in my life. Who have given me the gift of unwavering companionship. I greatly appreciate that during stressful times. I want to express my deepest thanks to Jesmine Cheung, Ramsay Macdonald, Eric Torres, and Vivian Zhang for their perfect combination of mentorship and friendship. For keeping me grounded when the tides of graduate school went to my head and for taking me to new hiking spots. My college misfits (Not Study Game) Melissa Barcelona, Anthony Padilla, Lorianne Esturas, Hieu Jason Tang, Thomas Kwak, and Jessica Nyon. For keeping me company in the lab and at the analysis computer while I did experiments late into the night. I greatly appreciate their kindness and camaraderie. For always being a call away and for allowing me to always practice my talks to them. I would like to give thanks to my oldest friends Michelyne Chavez, Samia Chowdhury, and Michelle Nelson for always supporting my scientific endeavors. Their friendship has made navigating higher education as a first-generation college student more enjoyable.

To my brother, Henry Ngo, for being my main motivator and competitor throughout most of my life. You have motivated me to prove people wrong without falling into despair.

My mom and dad, Linh Vien Ngo and Toan Nguyen Ngo, have inspired me in all aspects of my life. Thank you for giving me everything I could need and more. I am not able to express in words how grateful I am to have such giving parents.

Lastly, to EXO and EXO-Ls, for the fantastic music that turned every undesirable experimental outcome or 12-hour imaging session into a party.

CURRICULUM VITAE

Education:

- 05/ 2017 Master of Science in Biochemistry, Molecular & Structural Biology, University of California-Los Angeles.
- 05/ 2015 Bachelor of Science in Microbiology, Immunology, and Molecular Genetics, University of California-Los Angeles.
- 05/ 2020 Public Health & Food Studies Certification, University of California-Los Angeles

Positions and Employments:

- 06/19 – 09/19 **Teaching Assistant** for the Image Analysis Workshop, Metabolism Theme Imaging Core Facility, University of California, Los Angeles
- 2017 - 2019 **Teaching Assistant** for Introductory/ Physical Biochemistry, Department of Chemistry & Biochemistry, University of California, Los Angeles
- 2017 - 2019 **Lab Teaching Assistant I/II** for the Biomedical Sciences Enrichment Program (BISEP), Undergraduate Research Center, University of California, Los Angeles
- 03/15 – 06/16 **Research Assistant/Lab Manager** with Dr. Carla M. Koehler, Department of Chemistry & Biochemistry, University of California-Los Angeles

Other Experience and Professional Memberships:

- 2022 Co-Founder, Mitochondria and Metabolism Collective
- 2020 Reviewer, EMBO Reports – EMBO Press; Redox Biology - FEBS Open Bio; STAR Protocols – Cell Press
- 2016 Co-Founder/ Outreach Chair, Graduate Biochemistry Student Association (gBSA)

Publications

Ngo J*, Choi DW*, Molina A, Stiles L, Miller N, Cerqueira F, Bagdasharian S, Roach B, Erion K, Jones A, Kim K, Sereda SB, Wikstrom JD, Taddeo E, Divakaruni A, Chan D, Corkey BE, Liesa M, Shirihai O**, Danial N.** Mitochondrial architecture controls fatty acid utilization by regulating CPT1 sensitivity to Malonyl-CoA. Manuscript submitted.

Steffen J*, **Ngo J***, Wang SP*, Kramer F, Ho G, Rodriguez C, Pocai A, Shirihai O, Liesa M. Drp1KD by GalNAc siRNA on liver enzymes, body weight in WT and GFRAL KO mice and its NASH efficacy in GAN mice. Decreasing DNM1L expression in liver activates the mitochondrial integrated stress response and exacerbates NASH. Manuscript in submitted to Hepatology 2022.

Torres E, Douglas C, Damoiseaux R, **Ngo J**, Frank K, Wohlschlegel J, van der Blik A, Koehler CM. A New Role for the Mitochondrial Processing Peptidase in Protein Translocation into Mitochondria. Submitted to Journal of Molecular Biology. 2022.

Moore T*, Cheng L*, Wolf D, **Ngo J**, Segawa M, Zhu X, Strumwasser A, Cao Y, Clifford B, Ma A, Scumpia P, Shirihai O, Vallim TDA, Laakso M, Lusis A, Hevener A, Zhou Z. Parkin Regulates Adiposity by Coordinating Mitophagy with Mitochondrial Biogenesis in White Adipocytes. Submitted to Nature Metabolism. 2021.

Ngo J, Osto C, Villalobos F, Shirihai OS. Mitochondrial heterogeneity in health and disease. MDPI Biology. 2021. 10(9), 927. doi: 10.3390/biology10090927.

Shum M, Shintre C, Althoff T, Gutierrez V, Segawa M, Saxberg AD, Martinez M, Adamson R, Young MR, Faust B, Gharakhanian R, Su S, Krishnan K, Mahdaviani K, Veliova M, Wolf D, **Ngo J**, Nocito L, Stiles L, Abramson J, Lusis A, Hevener A, Zoghbi ME, Carpenter EP, Liesa M. ABCB10 exports mitochondrial biliverdin, driving metabolic maladaptation in obesity. Science Translational Medicine. 2021. doi: 10.1126/scitranslmed.abd1869.

Ngo J, Benador IY, Brownstein A, Vergnes L, Veliova M, Shum M, Acín-Pérez R, Reue K, Shirihai OS, Liesa M. Isolation and Functional Analysis of Mitochondria Bound to Lipid Droplets from Murine Brown Adipose Tissue. STAR Protocols. 2020. doi: 10.1016/j.xpro.2020.100243.

Shum M, **Ngo J**, Shirihai OS, Liesa M. Mitochondrial oxidative function in NAFLD: friend or foe? Molecular Metabolism. 2020. doi: 10.1016/j.molmet.2020.101134.

Osto C, Benador IY, **Ngo J**, Liesa M, Stiles L, Acin-Perez R, Shirihai O. Measuring mitochondrial respiration in previously frozen biological samples. Currents Protocols in Cell Biology. 2020. 89, e116. doi: 10.1002/cpcb.116.

Bradley MC, Yang K, Fernandez-del-Rio L, **Ngo J**, Ayer A, Tsui HS, Stocker R, Shirihai OS, Barros MH, Clarke CF. COQ11 deletion mitigates respiratory deficiency caused by mutations in the gene encoding the coenzyme Q chaperone protein Coq10. J. Biol. Chem. 2020. doi: 10.1074/jbc.RA119.012420.

Sangwan S, Zhao A, Adams KL, Jayson CK, Sawaya MK, Guenther E, Pan AC, **Ngo J**, Moore D, Soriaga AB, Panchal A, Do TD, Goldschmidt L, Nelson R, Bowers MT, Geisberg M, Koehler CM, Shaw DE, Novitsch BG, Eisenberg DS. Atomic structure of a toxic, oligomeric segment of SOD1 linked to amyotrophic lateral sclerosis (ALS). PNAS. 2017. 114 (33) 8770-8775. doi.org/10.1073/pnas.1705091114.

CHAPTER 1

Introduction: Mitochondrial Heterogeneity and Connections to Liver Health and NAFLD

INTRODUCTION

1. Overview of intracellular heterogeneity

Cellular heterogeneity represents the observation that in an organ, neighboring cells of the same type may show structural and functional differences that evolve from their different stages of differentiation, maturation, or exposure to environmental challenges. Whichever is the trigger, the outcome is structural diversity that results in varying functionality. Similar to cellular heterogeneity, the pool of mitochondria within a singular cell may also represent mitochondria at different stages of their development as well as the consequences of their response to the cellular environment (Aryaman *et al*, 2019). This section will focus on the subcellular heterogeneity of the mitochondria within the same cell, the mechanisms generating subcellular heterogeneity, and the functional consequences thereof (Kuznetsov *et al*, 2006; Wikstrom *et al*, 2009; Collins *et al*, 2002; Aryaman *et al*, 2019).

Metabolic diseases can be inherited, known as inborn errors of metabolism, or they can be acquired. We will focus on heterogeneity of mitochondrial morphology reported in metabolic diseases resulting from excess nutrient exposure, focusing section 2 on their effects in the pancreatic beta-cell and the renal proximal tubule cells, section 3 on the effects of mitochondrial morphology on FAO, and then section 4 – 6 on hepatocytes.

1.1. What is mitochondrial heterogeneity and why should we care?

We define mitochondrial heterogeneity as the variation in a mitochondrial feature of a singular mitochondrion inside one cell. Amongst what has previously been considered as

homogenous groups of mitochondria, higher-resolution technology continues to further the discovery of variation in ultrastructural, biophysical, and electrochemical features (Kuznetsov *et al*, 2006; Wikstrom *et al*, 2007; Zorova *et al*, 2018; Chen *et al*, 2005; Duchen *et al*, 2003). The observation that every biological structure will always show some level of diversity raises the question, when should we care? We suggest two considerations to determine if a variation in some parameter is of interest: either the heterogeneity yields functional consequences or the heterogeneity is an association with a phenomenon of interest. For example, mitochondria deficient in cristae heterogeneity carry the functional consequences of reduced respiratory capacity (Chen *et al*, 2005; Wolf *et al*, 2019; Zorzano *et al*, 2010). Mitochondrial fragmentation has been associated with stress, yet direct functional consequences of the heterogeneity introduced by fragmentation have not been fully determined. We will describe the observed variations and functional consequences in mitochondrial ultrastructure and dynamics associated with metabolic diseases, T2D and chronic kidney diseases. It is not to say heterogeneity only occurs under pathological states; rather, heterogeneity is heightened. Indeed, some level of heterogeneity is physiological. Mitochondrial variance at the physiological state provides functional fitness to specific groups of mitochondria within the cell; yet, upon chronic stress, physiological levels of heterogeneity begin to shift towards pathological levels (Twig *et al*, 2008a). For instance, a small percentage of mitochondria undergo depolarization as they prepare to be removed by mitophagy; however, under the pathological impairment of mitophagy, the percentage of depolarized mitochondria increases (Chen *et al*, 2005; Twig *et al*, 2008c). Impaired clearance and accumulation of depolarized and damaged mitochondria lead to the release of apoptogenic factors and

cellular apoptosis. Whether changes to mitochondrial features are small or large, mitochondrial heterogeneity matters when changes yield functional consequences or are associated with a phenomenon of interest.

1.2. Nongenetic contributors to mitochondrial homogeneity and heterogeneity

Mitochondrial heterogeneity can be caused by genetic and non-genetic mechanisms. Variation in mitochondrial DNA (mtDNA) sequences provides genetic sources of intracellular heterogeneity, influencing factors such as reactive oxygen species (ROS) production, protein structure conformation, and electron transport chain capacity (Palmer *et al*, 1985). However, structural and functional variation is also controlled by post-translational mechanisms such as phosphorylation and ubiquitination of mitochondrial proteins. Further, mitochondrial heterogeneity can be established by the molecular machinery determining the mitochondrial life cycle: biogenesis, mitochondrial motility, fusion and fission, and clearance of damaged mitochondria. Sustained activity of fission, fusion, and mitophagy events of the mitochondrial life cycle serve to decrease mitochondrial heterogeneity (**Figure 1A**). However, blockades at different points of the mitochondrial life cycle may induce heterogeneity by expanding a specific stage of the life cycle disproportionately (**Figure 1B**).

A higher number of fusion events promote homogeneity by increasing the rate by which different mitochondria within a cell mix and equilibrate mitochondrial content (Twig *et al*, 2008c). Impaired fusion reduces the rate of mitochondrial content mixing and increases heterogeneity. Depolarization of an individual mitochondrion induces the recruitment of fission mechanisms. The impaired portion of a mitochondrion can be removed through

fission into two daughter mitochondria. One of the daughter mitochondria will come out of the fission event with reduced membrane potential. If membrane potential does not recover, the mitochondrion will sustain depolarization and remain solitary until it is removed by mitophagy. During this period, this mitochondrion remains depolarized and fusion-less, two characteristics of the mitochondrial pre-autophagic pool. Autophagic clearance of mitochondria reduces heterogeneity by removing depolarized mitochondria and promotes homogeneity by maintaining a pool of similarly polarized mitochondria. Thus, the progression at the fission and mitophagy stages influences mitochondrial heterogeneity (**Figure 1**). Mitochondrial heterogeneity in this sense may seem to be detrimental to cellular function; however, observations have shown mitochondrial heterogeneity to be beneficial and to play an important role in cellular fitness (Chen *et al*, 2005; Herms *et al*, 2013). Additionally, the long-term consequences of declining heterogeneity lead to disease onset (Gottlieb & Stotland; Georgiadou *et al*, 2020). Through the use of MitoTimer, it was revealed that the age of mitochondrial protein is homogenous across the cell. Yet, inhibition of mitochondrial fusion resulted in the appearance of two mitochondrial populations, mitochondria primarily containing old protein and mitochondria containing primarily young protein. Such heterogeneity based on protein age demonstrated the role of mitochondrial fusion in homogenizing the distribution of newly synthesized proteins (Gottlieb & Stotland).

In section 2, we focus on literature concerning mitochondrial heterogeneity in pancreatic beta-cells and proximal tubules. Specifically, how mitochondrial heterogeneity fluctuates in response to nutrient excess and affects cellular behavior at the pathological state.

2. Mitochondrial heterogeneity increases under pathological states

Mitochondria are highly dynamic organelles that respond to changes in their immediate environment through diverse structural and functional adaptation, resulting in intracellular heterogeneity. When subcellular heterogeneity is induced by metabolic stress, we define this occurrence as the pathological state, under which mitochondria display an increase in functional diversity. In pancreatic beta-cells and renal proximal tubule cells, metabolic stress via high levels of glucose and free fatty acids increase heterogeneity by disrupting the mitochondrial fusion. Depending on the degree and duration of metabolic stress, increased heterogeneity affects cellular behavior and can contribute to the pathogenesis of T2D and chronic kidney disease (Georgiadou *et al*, 2020; Brooks *et al*, 2009; Zhan *et al*, 2013).

2.1. Brief overview of mediators in mitochondrial fusion and fission

Mitochondrial architecture is determined by motility, fusion, and fission events. Although some disorders of mitochondrial dynamics result from monogenic mutation, most reflect changes in the function of fission and fusion mediators due to changes in the cellular environment. Fission and fusion influence cellular processes such as ATP production, ROS generation, and calcium homeostasis and consequently impact bioenergetics and mitophagy (Liesa *et al*, 2009).

Fusion in mammals is mediated by the outer mitochondrial membrane proteins Mitofusin 1 and 2 (Mfn1 and Mfn2) and the inner mitochondrial membrane protein, optic atrophy gene 1 (Opa1). Mitofusins are targeted to the mitochondria by sequences in their transmembrane and C-terminal domains. Through the C-terminal, Mfn1/2 initiate fusion

by creating homodimeric or heterodimeric, antiparallel, coiled-coil linkages between mitochondria. Mfn2 is also located in the endoplasmic reticulum (ER) and promotes ER-mitochondria tethering. Calcium storage is one of the functions commonly attributed to the ER; hence, mitochondria–ER tethering enhances mitochondrial calcium uptake and alters morphology. In the case of Opal, fusion activity is mediated by proteolytic processing. Opal also controls cristae remodeling independent of fusion (Liesa *et al*, 2009; Ishihara *et al*, 2006; Frezza *et al*, 2006). OPA1 has eight splice variants, each with differential fusion activity and mitochondrial protease susceptibility. The fusion mediators also regulate mitochondrial metabolism, and when they are downregulated or dysfunctional, there is generally a reduction in mitochondrial oxidative capacity (Zorzano *et al*, 2010).

On the other hand, mitochondrial fission is mediated by the outer mitochondrial membrane proteins, fission 1 protein (Fis1) and mitochondrial fission factor (Mff), and the cytosolic dynamin-related protein 1 (Drp1). GTP hydrolysis and recruitment of Drp1 to the outer mitochondrial membrane are required for Drp1-mediated fission (Liesa & Shirihai, 2013a). Furthermore, Drp1 activity is regulated by the phosphorylation of serine 616 and serine 637. Phosphorylation of serine 616 increases DRP1 activity, whereas phosphorylation of serine 637 decreases it. Mff and Fis1 have been shown to mediate fission by recruiting Drp1 to the mitochondria (van der Bliek *et al*, 2013; Gandre-Babbe & Bliek, 2008; Zorzano *et al*, 2010).

2.2. Architectural variance under pathological states introduces metabolic defects

Mitochondrial function and morphology are closely linked; the mitochondria life cycle

involves changes to morphology to preserve mtDNA integrity and mitochondrial bioenergetic efficiency. Increases in intracellular mtDNA heterogeneity (i.e., accumulation of damaged mtDNA) and declines in fusion/fission regulation result in tissue dysfunction (Srinivasan *et al*, 2017).

Increased intracellular heterogeneity in mitochondrial membrane potential (MMP) and morphology has been observed under various metabolic states, such as glucotoxicity, oxidative stress, and starvation (**Figure 2**). Under glucotoxicity-induced ROS, enhances in mtDNA oxidation and mitochondrial fragmentation result in an increased pool of fragmented mitochondria. Skeletal muscles under oxidative stress yield increased architectural heterogeneity due to a 30% reduction in mitochondrial velocity. Additionally, reductions in fission and fusion rates led to a 41% increase in fragmentation (Iqbal & Hood, 2014). During starvation, mitochondria unable to elongate are latently dysfunctional and consume cytosolic ATP to sustain their membrane potential. The survival of non-elongated mitochondria suggests a favoring for elongation; however, survival of fragmented mitochondria increases intracellular mitochondrial architectural heterogeneity (Gomes *et al*, 2011). These three cases demonstrate increased architectural heterogeneity under nutrient stress. Apart from the mitochondrial genome, metabolic stress or pathology increase morphological heterogeneity at the level of fusion and fission rates.

In the pancreatic beta-cell, mitochondria go through frequent fusion and fission events that are changed by altered nutrient exposure (Stiles & Shirihai, 2012). Thus, fission and fusion are strong modifiers of mitochondrial heterogeneity. Under pathological conditions such as T2D, the balance of fusion and fission leans in favor of fission and reduction in

fusion(Molina *et al*, 2009b; Zorzano *et al*, 2009). Beta-cells are susceptible to chronic exposure to high glucose levels, a condition termed glucotoxicity. Glucotoxicity has been shown to inhibit mitochondrial fusion and induce mitochondrial fragmentation. Further increasing the duration of exposure to high glucose concentrations exacerbates the degree of architectural heterogeneity so much that the degree of changes becomes pathological fragmentation. As glucose concentration increases, there is a reduction in the mitochondrial fission protein, Fis1. In this pathological state, morphology is altered and fragmentation occurs whereby Fis1 impairs ATP production and insulin secretion(Wada & Nakatsuka, 2016; Twig *et al*, 2008c; Heart *et al*, 2006). Under glucolipotoxic conditions, high glucose and high fatty acid levels, beta-cell mitochondria become more fragmented, resulting in reduced glucose-stimulated insulin secretion (Molina *et al*, 2009b). Although there was an overall average reduction in the fusion rate of treated cells, fusion rates varied both intercellularly and intracellularly. Fusion rate was measured by the diffusion rate of GFP in mitochondria expressing photo-activatable mitochondrially targeted GFP (PAGFPmt). Focusing specifically on intracellular measurements, mitochondria with more branched networks had greater fusion rates than less branched mitochondria. At the time, mitochondria reported to perform fusion at higher rates were termed super fusers (Molina *et al*, 2009b). More recent literature suggests super fusers and mitochondria of reduced fusion may be two separate populations of mitochondria within the same cell (further discussed in Section 3). Another established feature of T2D is reduced circulating insulin levels due to decreased beta-cell mass caused by beta-cell apoptosis (Donath & Halban, 2004; Nasteska & Hodson, 2018). In a cultured beta-cell model, high glucose concentrations induce the functional outturn of

apoptosis; however, inhibition of mitochondrial fission prevents beta-cell apoptosis (Men *et al*, 2009). Reiterating fission and fusion are strong modifiers of mitochondrial heterogeneity and the consequences thereof.

Mitochondrial fragmentation is not only limited to the pancreatic beta-cell; increased fission has also been observed in kidney biopsies of diabetic human patients (Zhan *et al*, 2013). Recent work modeling renal ischemia-reperfusion, nephrotoxicity, and hyperglycemia-induced kidney injury have all demonstrated increased mitochondrial fragmentation (Zhan *et al*, 2013; Bhargava & Schnellmann, 2017; Kang *et al*, 2015). The above studies suggest increased morphological heterogeneity as an associated phenomenon. Specifically, intracellular variability in the degree of mitochondrial fragmentation has been observed to be associated with renal pathology. Different pharmacological approaches have been used to overcome the loss of mitochondrial performance in kidney diseases; of these, a predominant target is the Ser/Thr protein kinase 5'AMP-activated kinase (AMPK). Activation of AMPK downregulates ATP-consuming pathways and shifts the metabolic state towards catabolism, and long-term activation yields mitochondrial biogenesis (Kodiha *et al*, 2018). In the clinical setting, AMPK activity is enhanced by the antidiabetic drug metformin. To study the pathway more in the context of kidney disease, Kodiha *et al*. induced pathology through AMPK inhibition. The pathological model elicited fragmentation; however, intracellular morphological changes were not homogenous—rather, the degree of fragmentation differed by subcellular region. For the most part, the degree of architectural change was compound-specific and observed to correlate with mitochondrial compartmentalization (Kodiha *et al*, 2018).

Increased intracellular fragmentation was associated with the pathological model of AMPK inhibition. If inhibiting intracellular fragmentation is no longer feasible, is it still feasible to ameliorate pathology by reducing intercellular fragmentation? In both 2D and 3D EM micrographs of control tubular cells, a large intercellular population of long and filamentous mitochondria was observed. In sharp contrast, mitochondria of tubular cells injured by ischemia/reperfusion were completely fragmented. Looking broadly at the intercellular population, ischemia/reperfusion fragmented 42% of the cellular population (Brooks *et al*, 2009). Upon pharmacological blockade of mitochondrial fission in ischemically injured cells, attenuation of tubular cell apoptosis, tissue damage, and renal injury was observed (Brooks *et al*, 2009). Perhaps intracellular heterogeneity occurs in the early stages of pathology, and once a threshold has been surpassed intercellular heterogeneity is reached. Mitochondrial fragmentation has been observed to occur early in pathology and contributes to the subsequent development of mitochondrial membrane permeabilization, release of apoptogenic factors, and cellular apoptosis (Nowak *et al*, 2011). Inhibition of intercellular mitochondrial fragmentation has been observed to protect against tubular cell apoptosis and renal injury. Benefits in reversing morphological changes suggest the pathological shortcomings of increasing mitochondrial heterogeneity both intracellularly and intercellularly. Thus, mediators of fusion and fission would identify possible targets for preventing and treating kidney diseases, such as acute renal failure (Brooks *et al*, 2009).

Kidney function depends on oxidative metabolism to support its high energy demand to maintain electrolyte homeostasis, acid-base homeostasis, and reabsorption of nutrients. Energy depletion is a key contributor to the development and progression of

kidney diseases including acute kidney injury (AKI) (Bhargava & Schnellmann, 2017), chronic kidney disease (CKD) (Kang *et al*, 2015), and diabetic and glomerular nephropathy. Mitochondrial fatty acid oxidation (FAO) serves as the preferred fuel source supporting ATP production in the kidney, and its dysfunction results in ATP depletion and lipotoxicity (Nowak *et al*, 2011; Kang *et al*, 2015; Bhargava & Schnellmann, 2017). FAO dysfunction elicits tubular injury, inflammation, and subsequent progression of fibrosis (Kang *et al*, 2015; Jang *et al*, 2020; Hall & Schuh, 2016). Miguel *et al*. assessed intracellular morphological alterations in cortical proximal tubule cells by transmission electron microscopy. At basal conditions, most mitochondria were elongated and localized to the basolateral part of the kidney cells. In contrast, in the 100 μ M palmitate-treated primary mouse kidney epithelial cells, fewer mitochondria were localized to the basolateral region and exhibited a fragmented, small, and round appearance. Upon overexpression of the fatty acid shuttling enzyme, CPT1A, morphological alterations induced by fatty acids were abrogated in renal epithelial cells. The gain of function in FAO by CPT1A overexpression protected proximal tubules from fibrosis. In Miguel *et al*.’s study, defective FAO was observed in fibrotic kidneys from control mice of various fibrosis models, including the unilateral ureteral obstruction (UUO), folic acid nephropathy injury (FAN) model, and adenine-induced renal failure (AND). Overexpression of CPT1A in the mentioned fibrotic models counteracted impaired FAO and maintained comparable rates of FAO to that of healthy kidneys. The UUO, FAN, and AND models were all utilized to assess the benefits of recovering FAO at different stages whereby fibrosis occurred. The UUO model’s inflammation and fibrosis evident at 7 days due to obstruction to renal blood flow and glomerular filtration rate. The FAN model’s interstitial fibrosis in the chronic

phase induced by high folic acid dosage. The AND model further complements renal failure models as a reflection of tubulointerstitial disease stemming from tubular toxicity of adenine metabolites. Miguel et al. postulate to preserve mitochondrial morphology, appropriate levels of CPT1A and metabolic function are necessary to maintain ATP demand (Miguel *et al*, 2020). Heterogeneity in this example is intriguing as the phenomenon of fragmentation is associated with the pathological impairment of reduced FAO through unknown mechanisms.

Under pathology, the balance between mitochondrial fusion and fission is disrupted, whereby fusion is reduced and the rate of fission is increased. The observed increases in intracellular fission occur to varying degrees, yet the outcome remains the same: altered mitochondrial function. Excess nutrient-induced mitochondrial fragmentation in islets significantly reduced insulin secretion. Additionally, an increase in the population of fragmented proximal tubule mitochondria consistently yielded reduced FAO. Overall, increased morphological heterogeneity is associated with metabolic defects seen in diabetic islets and kidney diseases (**Figure 2**).

3. Overview of mitochondrial fatty acid oxidation.

Lipid metabolism is critical in the liver for controlling glucose production through the regulation of mitochondrial fatty acid oxidation (FAO). In the liver, FAO also serves an additional role in producing ketone bodies as an important fuel for extrahepatic organs. The liver thus serves as a metabolic hub by providing glucose and ketone bodies during starvation and, conversely, storing glucose and fat after feeding.

Depending on the tissue and its metabolic demand, fatty acids are either converted to

triglycerides or membrane phospholipids or oxidized in the mitochondria for energy production. Before oxidation of fatty acids within the mitochondrial matrix, fatty acids must permeate the mitochondrial membrane. Long-chain acyl-CoA synthetase, located on the mitochondrial outer membrane, first activate fatty acids to acyl-CoAs. Then carnitine acyltransferases catalyze the transesterification between acyl-CoA esters and L-carnitine to yield carnitine esters permeable to the mitochondrial outer membrane. The specific carnitine acyltransferase involved is dependent on the length of the fatty acyl moiety to be transported. Carnitine palmitoyltransferases (CPTs) I and II facilitate the transport of long-chain acyl groups into the mitochondrial matrix and enabling FAO. In the presence of increased glucose concentrations import of fatty acids to hepatic mitochondria via CPT-1 is inhibited by a glucose-metabolism product, malonyl-CoA. Malonyl-CoA levels are elevated in hepatocytes after feeding, serving as a shut-off switch for FAO by inhibiting beta-oxidation and promoting anabolic processes.

3.1. Regulation of CPT1.

CPT1's physiologically important role in regulating mitochondrial FAO identifies CPT1 as a potential pharmacological target for the treatment of metabolic lipid disorders. Three isoforms of CPT1 have been identified currently, a liver isoform (CPT1A), a heart/skeletal muscle isoform (CPT1B), and a brain isoform (CPT1C). A characteristic differentiating the three isoforms is their sensitivity to inhibition by malonyl-CoA. The liver isoform, CPT1A, has a tenfold higher K_i for malonyl-CoA making it the prevailing enzyme that accomplishes the rate-limiting step in FAO (Casals *et al*, 2016; McGarry & Brown, 1997). Additionally, the sensitivity of CPT-1A to malonyl-CoA inhibition changes during the transition of fed to

fasting states, generating an amplification system to control FAO.

Rat liver CPT1 has been identified to contain two malonyl-CoA binding sites. The first site has a greater binding affinity to malonyl-CoA and is not susceptible to acyl-CoA competition. The second acyl-CoA binding site, in which palmitoyl-CoA is bound, is located near CPT1's catalytic site (López-Viñas *et al*, 2007). Pharmacological activators of CPT1 acting on these sites have been shown to stimulate CPT1 activity, increase FAO, energy production, liver fat and weight loss. The present study will examine FAO in the context of regulating CPT1 through these two acyl-CoA binding sites.

3.2. Contribution of CPT1 to pathology.

In obese and insulin resistant Zucker diabetic (ZDF) rats, a rodent with a non-functioning leptin receptor, skeletal muscle confer a reduction in Mfn2 expression, resulting in smaller mitochondrial size (Putti *et al*, 2015). It has also been shown in the pancreatic beta-cell, that changes in malonyl-CoA fuel-sensing signaling is important in the pathogenesis of glucolipotoxicity. In order to prevent apoptosis induced by glucolipotoxicity, FAO is favored through activation of AMPK (Ruderman & Prentki, 2004). In the diabetic patient, the affinity of CPT-1A for malonyl-CoA decreases and the activity of CPT-1A is increased (Cook & Gamble, 1987). Additionally, ZDF rats, have shown increased hepatic FAO rates, even in the presence of high nutrient levels, indicating a potential change in the regulation of CPT-1 (UNGER & Orci, 2001). In alignment with previous studies, sensitivity of CPT-1A has been observed to decrease when its tertiary structure is altered due to changes in membrane structure (López-Viñas *et al*, 2007). However, these mechanistic adaptations differ between cell types and currently no

mechanism in increased hepatic FAO despite intact insulin signaling has been established. A potential mechanism will be discussed in chapter 2.

4. The role of mitochondrial oxidative function in liver in health and NAFLD.

Despite constituting ~2-4% of total body weight, the liver is responsible for 15% of organismal oxygen consumption in humans (Rolfe & Brown, 1997). This large ratio of respiration/liver weight demonstrates that hepatocytes are highly enriched with mitochondria consuming oxygen to produce ATP. Accordingly, 60% of the organismal mitochondrial ATP demand imposed by glucose production and ureagenesis is covered by hepatocytes, with the remaining 40% covered by the kidney (Rolfe & Brown, 1997). Thus, liver is the main organ providing glucose and ketone bodies to other tissues when nutrients are scarce. During fasting, fatty acids released from adipose tissue are oxidized by hepatocyte mitochondria, generating ketones and supplying the ATP that fuels gluconeogenesis and ureagenesis. It is estimated that fasting increases mitochondrial fat oxidation 10-fold (McGarry & Foster, 1980). Urea is produced inside mitochondria from the ammonia and bicarbonate generated by hepatic amino-acid catabolism, which is also upregulated during fasting as an additional source of ATP and carbons for gluconeogenesis.

In the fed state, hepatocytes conserve and store nutrients to fulfill their specialized function of providing nutrients to other tissues when food is scarce. To this end, insulin action in hepatocytes increases glucose storage as glycogen and transforms dietary glucose into lipids. The carbon intermediates required for lipid synthesis and the ATP needed to energize anabolism are provided by mitochondria. Specifically, glucose-

derived pyruvate oxidation in mitochondria elevates the synthesis of citrate, which is then consumed to generate the carbon precursor of *de novo* synthesized fatty acids, namely malonyl-CoA. Then, these new fatty acids are esterified into triglycerides and packed into lipid droplets and lipoproteins. Remarkably, malonyl-CoA promotes lipoprotein and lipid droplet expansion as well by blocking the entry of fatty acids into the mitochondria to prevent their oxidation (McGarry & Foster, 1980). Importantly, large intrahepatic lipid droplets by histology are not observed in healthy livers and hepatocytes can re-uptake secreted lipoproteins. Thus, lipids storage units inside healthy hepatocytes are highly dynamic, with this dynamism being an ATP demanding process. In all, mitochondrial oxidative function is highly active in the fed and fasted state, as mitochondria participate both in the production and consumption of glucose and lipids.

Hepatic steatosis or fatty liver is defined as the visualization of large lipid droplets in hepatocytes by histology. Simple steatosis is the first stage of NAFLD, which can progress to non-alcoholic steatohepatitis (NASH), characterized by liver inflammation, increased hepatocyte ballooning, cell death and some degree of fibrosis. The pro-inflammatory state of NASH can eventually lead to cirrhosis and hepatocarcinoma.

Fatty liver can occur when glucose and fatty acid availability exceeds both the capacity of adipose tissue to store energy and the demand for ATP of hepatocytes. Accordingly, steatosis is not exclusively generated by the positive energy balance associated with diet-induced obesity or over-eating. Lipodystrophy, a pathology primarily caused by an inability of adipose tissue to store fatty acids, induces hepatic steatosis and hyperinsulinemia as well. Interestingly, 25.3% of individuals with NAFLD are lean, suggesting that NAFLD prevalence is increasing independently of obesity and genetic

lipodystrophy (Young *et al*, 2020).

Hyperinsulinemia is deemed a major driver of simple steatosis, as hyperinsulinemia can develop in obese, lean and lipodystrophic individuals (Young *et al*, 2020; Bril *et al*, 2014). However, prolonged fasting in normo-insulinemic healthy mice can induce fatty liver as well, indicating that hepatic steatosis can occur independently of hyperinsulinemia. In the case of normo-insulinemic fasting, hepatic steatosis is explained by white adipose tissue releasing more fatty acids and glycerol than needed for liver mitochondria to cover their demand for ATP. This fatty acid excess is stored into intrahepatic lipid droplets to prevent free-fatty acid mediated toxicity, while concurrently allowing hepatocytes to have a reservoir of fatty acids.

The requirement of mitochondrial function to oxidize fat, generate ketones and increase hepatic glucose production, as well as to increase lipid synthesis and storage, raises a simple question: Should we decrease or increase mitochondrial oxidative function in liver to reverse hepatic steatosis and decrease hepatic glucose production? The answer is further complicated by the fact that mitochondrial respiration regulates intracellular signaling by releasing reactive oxygen species (ROS), particularly hydrogen peroxide (H_2O_2). At low concentrations, H_2O_2 produced by mitochondria can transduce a signal modulating the activity of multiple enzymes. These include kinases and phosphatases, such as Protein Tyrosine Phosphatase 1B, that regulate transcriptional programs determining gluconeogenesis, lipogenesis and insulin sensitivity (Jais *et al*, 2014; Loh *et al*, 2009). In this context, how will a change in mitochondrial oxidative function impact H_2O_2 -regulated mechanisms controlling glucose and lipid metabolism in hepatocytes?

In sections 5 and 6, we will review recent studies to answer these questions, as well as identify some proposed approaches that target mitochondria to combat NAFLD and hyperglycemia.

5. Overview whereby decreased mitochondrial oxidative function contributes to NAFLD

A decrease in mitochondrial ATP-synthesizing respiration was observed in mouse models with simple steatosis or with NASH, concluding that fat accumulates in liver because their mitochondria cannot oxidize enough fatty acids (**Figure 3**). Accordingly, genetic and diet-induced obesity lowers mitochondrial respiration measured in isolated mouse hepatocytes (Arruda *et al*, 2014; Boland *et al*, 2020). Mechanistically, high fat diet feeding causes an excessive increase in calcium uptake by liver mitochondria that disrupts respiration and elevates ROS production (Arruda *et al*, 2014). Defective respiration and thus decreased fat consumption was attributed as a major factor driving steatosis, while mitochondrial ROS-mediated c-Jun-N terminal kinase (JNK) activation was responsible for the disruption of insulin signaling that promotes hyperglycemia (Arruda *et al*, 2014). In all, this study showed that cellular control of mitochondrial respiration by calcium released from the ER, is a major cause of mitochondrial dysfunction in simple steatosis induced by obesity.

The upregulation of hepatic ceramide (Cer) synthesis, caused by high fat diet feeding, was shown to decrease mitochondrial respiration and drive both simple steatosis and NASH in mice. Indeed, the sphingolipid Cer16:0 itself, synthesized by the enzyme CERS6, had a direct action decreasing mitochondrial fat oxidation in hepatocytes from

mice with simple steatosis. In addition, Cer16:0 decreased hepatic insulin signaling, leading to hyperglycemia (Turpin *et al*, 2014). Higher hepatic ceramide content was associated with decreased mitochondrial oxidative capacity in human NASH as well (Apostolopoulou *et al*, 2018). The inhibitory effect on mitochondrial function induced by ceramides was attributed to mitochondrial fragmentation. More specifically, by the direct interaction of ceramides with the mitochondrial and peroxisomal fission/fragmentation factor (Mff) (Hammerschmidt *et al*, 2019).

5.1. The role of mitochondrial fragmentation in the decrease in mitochondrial oxidative function observed in simple steatosis and NASH

Mitochondrial fragmentation refers to the process by which long mitochondria segregate into smaller units, which can be induced by an inhibition of fusion or an activation of fission. While mitochondrial fragmentation can amplify apoptosis (Liesa *et al*, 2009), it is unclear why mitochondrial fragmentation mediated by Mff decreases mitochondrial fat oxidation and promotes steatosis (Hammerschmidt *et al*, 2019; Galloway *et al*, 2014).

Mitochondrial fragmentation mediated by Drp1 and Mff is a physiological process that occurs in healthy cells. Mitochondrial fragmentation mediated by Drp1 was shown to increase fatty acid oxidation in adipocytes and can be recruited in other tissues as an adaptive mechanism counteracting nutrient excess (Liesa & Shirihai, 2013b; Wikstrom *et al*, 2014). Accordingly, fragmentation of mitochondria in hepatocytes by deleting the mitochondrial fusion protein Mfn1 increased mitochondrial oxidative function in mice with simple steatosis (Kulkarni *et al*, 2016).

Furthermore, fragmentation does not only allow mitochondrial oxidative function to adapt to changes in ATP demand and nutrient availability. Indeed, mitochondrial fragmentation allows autophagy to remove damaged mitochondria, a process named mitophagy (Liesa & Shirihai, 2013b; Twig *et al*, 2008b). Autophagy and thus mitophagy require intact lysosomal function, which is achieved by preserving their acidity (low pH). Remarkably, fatty acids and the concurrent increase in ceramides elevate lysosomal pH in pancreatic beta-cells and liver, which disrupts the digestive function of lysosomes and halts autophagic flux (González-Rodríguez *et al*, 2014; Trudeau *et al*, 2016; Yamane *et al*, 2017). Consequently, lysosomal dysfunction causes the accumulation of damaged mitochondria by impairing mitophagy, with lysosomal dysfunction even directly causing mitochondrial damage by releasing lysosomal components (Assali *et al*, 2019; Hughes & Gottschling, 2012). It is possible that lysosomal dysfunction and disruption in mitophagy, rather than mitochondrial fragmentation *per se*, are the main mechanisms behind ceramides decreasing mitochondrial function.

Of note, mitochondrial fragmentation induced by hepatocyte-specific deletion of the mitochondrial fusion protein Mitofusin 2 (Mfn2) exacerbates NAFLD progression, inflammation and hyperglycemia in high fat diet fed mice (Hernández-Alvarez *et al*, 2019; Sebastián *et al*, 2012a). These data could be interpreted as evidence supporting the view that mitochondrial fragmentation drives steatosis and NASH by decreasing fat oxidation. However, Mfn2 plays additional roles beyond counteracting fragmentation, explaining the opposite effects caused by Mfn2 versus Mfn1 deletion. Mfn2, but not Mfn1, regulates ER-mitochondria contacts (De Brito & Scorrano, 2008) and transfers phospholipid intermediates between mitochondria and ER, facilitating phospholipid synthesis

(Hernández-Alvarez *et al*, 2019). Thus, this role of Mfn2 promoting phospholipid synthesis could explain how Mfn2 aided to the formation of new autophagosomal membranes, which are generated from ER phospholipids (Hailey *et al*, 2010).

Major metabolic consequences of deleting Mfn2 in hepatocytes are decreased mitochondrial respiration, reduced fat oxidation, elevated ROS production and JNK activation (Hernández-Alvarez *et al*, 2019; Sebastián *et al*, 2012a). The exacerbation of NASH and the decrease in hepatic fat oxidation in mice induced by Mfn2 deletion were explained by ER stress, not by mitochondrial fragmentation (Kulkarni *et al*, 2016; Hernández-Alvarez *et al*, 2019; Sebastián *et al*, 2012a). Mfn2 deletion reduced the transfer of phospholipid intermediates between mitochondria and ER, while causing PERK hyperactivation. Prevention of ER stress in Mfn2 KO livers decreased NASH, insulin resistance and reversed the decrease in fat oxidation induced by Mfn2 deletion (Hernández-Alvarez *et al*, 2019; Sebastián *et al*, 2012a; Muñoz *et al*, 2013). Importantly, preventing ER stress in Mfn2 KO livers did not reverse hepatic steatosis, despite increasing fat oxidation (Hernández-Alvarez *et al*, 2019). Thus, it seems that the decrease in fat oxidation in Mfn2 KO livers would only contribute to inflammation. Hence, the mechanism by which Mfn2 deletion promotes hepatic steatosis is unclear. A potential mechanism will be discussed in chapter 3.

5.2. JNK can induce mitochondrial fragmentation, decrease fat oxidation and elevate mitochondrial ROS in simple steatosis and NASH

Some reports support that decreased mitochondrial fat oxidation and elevated ROS production in simple steatosis and NASH are initiated by the activation of c-Jun-N terminal

kinase (JNK), which can phosphorylate mitochondrial proteins. Exposing primary hepatocytes to high levels of fatty acids activates JNK to phosphorylate the mitochondrial protein SAB (spectrin-actin binding). The phosphorylation of SAB results in elevated mitochondrial ROS production and decreased respiration (Win *et al*, 2016). Moreover, JNK phosphorylates Mfn2 to activate its degradation (Leboucher *et al*, 2012) and blocks PPAR α -mediated upregulation of mitochondrial fat oxidation in livers from obese mice (Vernia *et al*, 2014). Accordingly, hepatocyte-specific deletion of JNK1/2 protects obese mice from hepatic steatosis, enlarges mitochondria (phenocopying Mfn2 gain-of-function) and elevates mitochondrial fatty acid oxidation via transcriptional upregulation of mitochondrial proteins (Vernia *et al*, 2014).

An important therapeutic approach aiming to treat NAFLD by promoting mitochondrial fat oxidation is the use of PPAR α and PPAR δ - dual agonists (NCT02704403, currently in Phase 3). The preclinical data supporting this approach lies in the data showing that PPAR α -mediated increases in fat oxidation occur without promoting glucose production in humans. In mice, PPAR α agonism properly mimics fasting, as mitochondrial fatty acid oxidation (FAO) is upregulated to match the ATP demand imposed by gluconeogenesis. This human-mouse difference suggests that PPAR α activation in humans might drive an uncharacterized ATP demanding process different from gluconeogenesis. Mitochondria will only increase FAO if ATP demand is increased, as ATP synthase controls respiration rates in coupled mitochondria.

Another option would be that PPAR α increases the expression of a mitochondrial uncoupler in humans. Consequently, more fatty acids would be oxidized to produce the same amount of ATP. In agreement with this hypothesis, pharmacological approaches

uncoupling mitochondria selectively in hepatocytes from rodents and non-human primates protect from hepatic steatosis (Goedeke *et al*, 2019; Perry *et al*, 2013). This uncoupler improved insulin signaling in liver and muscle as well, the latter by reducing hepatic lipid export to muscles (Goedeke *et al*, 2019; Perry *et al*, 2013). Hence, the ATP sink in humans allowing PPAR α activation to promote fat oxidation remains to be identified.

The transition from simple steatosis to NASH is associated with a decrease in mitochondrial oxidative capacity. This decrease supports that the upregulation of mitochondrial fat oxidation might be a feasible therapeutic approach to treat NASH as well. However, the decrease in mitochondrial function in NASH has been attributed to mitochondrial damage caused by ceramides (Apostolopoulou *et al*, 2018). Thus, repairing the damage, rather than stimulating the damaged mitochondria that are already there, might seem a safer approach to treat NASH.

5.3. Defects in mitophagy contribute to reduced oxidative capacity in NAFLD

Mitochondrial depolarization is the major event targeting mitochondria to autophagy (mitophagy), which is mainly caused by defective and decreased respiration. As mitochondria from livers with NASH showed decreased respiratory function, one could conclude that mitophagy is not effectively recruited in NASH. In other words, the mechanisms that repair and/or remove damaged mitochondria need to fail or be dormant to allow the presence of a large number of damaged mitochondria.

Accordingly, a recent study showed that hepatocyte-specific deletion of Parkin, an E3 ubiquitin ligase selectively targeting damaged mitochondria to mitophagy, exacerbates

fatty liver disease and insulin resistance in high-fat diet-fed mice (Edmunds *et al*, 2020). The exacerbation of NAFLD induced by Parkin deletion supports the view that mitophagy is still active in simple steatosis. Thus, the additional decrease in mitochondrial respiration observed in NASH could be triggered by the acquisition of an additional defect in mitophagy. In agreement with this conclusion, the decrease in Mfn2 activity induced by a greater activation of JNK in NASH could contribute to impaired mitophagy, as Mfn2 aids the formation of autophagosomes needed for mitophagy (Hernández-Alvarez *et al*, 2019; Hailey *et al*, 2010). These studies suggest that removing damaged mitochondria by activating mitophagy could be a promising approach to counteract simple steatosis and NASH.

In agreement with this conclusion, the *in vitro* activation of the glucagon receptor (GCGR) in primary hepatocytes isolated from mice with NASH was sufficient increased mitophagy and mitochondrial oxidative function (Boland *et al*, 2020). The activation of the glucagon receptor was achieved with a dual agonist of Glucagon-like peptide-1 receptor (GLP1R) and GCGR, named Cotadutide. Accordingly, *in vivo* treatments of mice fed an Amylin diet (AMLN, model of diet-induced NASH) with Cotadutide markedly improved liver histopathology (Boland *et al*, 2020). The ability of Cotadutide to increase mitophagy in a hepatocyte-autonomous manner supports that mitophagy is silenced in NASH, rather than irreversibly suppressed. The rescue of mitophagy and mitochondrial function induced by Cotadutide was dependent on PKA activity (Boland *et al*, 2020). Interestingly, PKA induces mitochondrial fragmentation by increasing Drp1 recruitment to mitochondria, where it binds to Mff (Cereghetti *et al*, 2008), while Drp1-mediated fragmentation is required for mitophagy as well (Liesa & Shirihai, 2013b; Twig *et al*,

2008a). Thus, Cotadutide possibly causes PKA-dependent fragmentation to facilitate mitophagy as a defense mechanism against simple steatosis and NASH. In all, the PKA-dependent benefits of Cotadutide action further support that fragmentation is a physiological process and not a synonym of mitochondrial dysfunction. Cotadutide is currently in clinical trials for NASH (NCT04019561).

6. Overview whereby mitochondrial oxidative function is not impaired in NAFLD

Not all studies have shown that mitochondrial oxidative function is decreased or impaired in simple steatosis and NASH. Indeed, no defects were observed in the respiratory function of liver mitochondria isolated from Ob/Ob mice with hepatic steatosis (Brady *et al*, 1985). Furthermore, the capacity of isolated liver mitochondria to oxidize fatty acids was even increased in Ob/Ob mice (Brady *et al*, 1985). However, and in marked contrast to the increase in FAO observed in isolated mitochondria, a decrease in mitochondrial FAO was observed in perfused livers and isolated hepatocytes from obese rats with fatty liver (McCune *et al*, 1981).

An integrated interpretation of these seemingly contradictory findings is that fatty liver does not result from a primary damage to mitochondria, but is rather caused by an alteration on how hepatocytes regulate and control mitochondrial FAO (Clouet *et al*, 1986). This decrease in FAO observed in perfused livers with steatosis was concluded to be a result from the inhibition of carnitine palmitoyl-transferase 1 (CPT1) (Brady *et al*, 1985; Clouet *et al*, 1986). The rate-limiting step of mitochondrial FAO is indeed executed by CPT1, which catalyzes the entry of long-chain fatty acid into mitochondria. An endogenous mechanism to block CPT1 activity is elevated glycolysis, which promotes

the synthesis of the CPT1 inhibitor malonyl-CoA. As a result, it could be hypothesized that obesity associated with hyperglycemia caused steatosis by blocking CPT1 and FAO in the liver, via excessive production of malonyl-CoA. This malonyl-CoA would be diluted and washed after isolating mitochondria, explaining the increase in FAO when measured in isolated mitochondria. Consequently, reducing malonyl-CoA synthesis or decreasing CPT1 sensitivity to malonyl-CoA-mediated inhibition was deemed as a strategy to prevent steatosis. In agreement with this view, the treatment of obese mice with PPAR α agonists decreased the ability of malonyl-CoA to inhibit CPT1 in isolated liver mitochondria (Henninger *et al*, 1987). The mechanism(s) by which PPAR α agonists decrease the sensitivity of CPT1 to malonyl-CoA-mediated inhibition is unclear. However, studying these mechanisms of CPT1-sensitivity to malonyl-CoA could be harnessed to reverse hepatic steatosis.

Developments in non-invasive metabolite labeling and tracing in liver allowed the quantification of FAO and mitochondrial fluxes in intact livers from mice and humans (Koliaki *et al*, 2015; Sunny *et al*, 2011). These non-invasive studies support that the suppression of FAO observed in isolated hepatocytes and perfused livers with steatosis does not occur *in vivo* (**Figure 4**). Accordingly, humans with simple steatosis and insulin resistance show elevated mitochondrial FAO and respiratory function when measured *in vivo* using non-invasive methods, and even *ex-vivo* after isolating mitochondria from liver biopsies (Koliaki *et al*, 2015; Sunny *et al*, 2011; Iozzo *et al*, 2010). Preservation of higher respiratory capacity after isolating mitochondria demonstrates that the composition of mitochondria is changed by NAFLD. From these data, one can conclude that higher FAO and mitochondrial function observed in NAFLD is not just a consequence of a change in

the cellular control of FAO and mitochondrial respiration (Koliaki *et al*, 2015). Further, this change in mitochondrial composition might reflect an adaptation to the chronic increase in gluconeogenesis and intrahepatic lipid handling induced by NAFLD, which increase the demand for mitochondrial ATP and TCA cycle intermediates (**Figure 4**). Such mitochondrial remodeling might prevent free fatty acid-mediated toxicity in hepatocytes as well.

Increased mitochondrial FAO in the liver from patients with simple steatosis and insulin resistance agrees with the hypothesis presented by McGarry titled: *What if Minkowski had been ageusic?* McGarry argued that increased FAO in liver could be a major driver of hyperglycemia in diabetes, as FAO generates ATP that will energize hepatic glucose production. Thus, if Minkowski could not have tasted glucose in the urine, but smelled the ketones in the breath resulting from FAO, diabetes treatments would have aimed to block FAO and restore lipid metabolism. Supporting McGarry's hypothesis, short term treatment of type 2 diabetic humans and obese rodents with etomoxir, a drug blocking CPT1 and thus FAO, showed positive effects on insulin sensitivity, decreased glycemia and even circulating lipids (Lundsgaard *et al*, 2020; Ratheiser *et al*, 1991). However, longer-term treatments with etomoxir exacerbated steatosis and hyperglycemia in obese rodents (Lundsgaard *et al*, 2020), demonstrating that the benefits of blocking FAO on glycemic control are only transient. It is a possibility that chronic etomoxir treatments could mimic the systemic fatty acid spillover characteristic of lipodystrophy and obesity. This spillover would outcompete the beneficial effect of etomoxir decreasing hepatic glucose production. Supporting this view, the increase in acylcarnitine intermediates due to incomplete fatty acid oxidation is associated with NAFLD (Enooku

et al, 2019; Peng *et al*, 2018), and these intermediates were shown to contribute to insulin resistance in muscle (Koves *et al*, 2008).

Remarkably, the increase in respiratory capacity and FAO are not the only changes observed in mitochondria from mice and humans with NAFLD. There is also a change in the proportion of fuels that support mitochondrial respiration (**Figure 4**). In humans and mice with fatty liver, mitochondrial pyruvate oxidation and TCA cycle flux are elevated in the fasted state, while ketogenesis does not increase (Sunny *et al*, 2011). As FAO is a major source of ketones, the lack of ketosis seemed contradictory to elevated FAO observed in obese humans with insulin resistance (Iozzo *et al*, 2010). This apparent contradiction was reconciled by data showing that FAO-derived acetyl-CoA, which is normally used for ketogenesis, is diverted to the TCA cycle in simple steatosis (Fletcher *et al*, 2019). Indeed, in healthy liver mitochondria, FAO results in a decrease of TCA cycle flux and citrate synthase activity, to facilitate ketogenesis by diverting acetyl-CoA away from citrate synthase (Garland *et al*, 1968). Thus, a key pathogenic mechanism in NAFLD could be the acquired ability of mitochondria to sustain high TCA fluxes concurrently to high rates of FAO. It is a possibility that a primary defect in the machinery synthesizing ketones is driving the elevation in TCA flux in NAFLD, by making more acetyl-CoA available to the TCA cycle (d'Avignon *et al*, 2018).

In agreement with high TCA fluxes participating in NAFLD pathogenesis, decreasing TCA cycle fluxes by deleting the mitochondrial pyruvate importer MPC1 diminishes both hepatic glucose production and inflammation in high-fat diet-fed mice (Gray *et al*, 2015; Rauckhorst *et al*, 2017). Hepatitis driven by high MPC1 activity was attributed to an increase in mitochondrial ROS production, resulting from the elevation in mitochondrial

respiration caused by perennial anabolism, concurrent with a decrease in antioxidant capacity (Rauckhorst *et al*, 2017; Satapati *et al*, 2015). However, hepatic steatosis was unchanged in liver-specific MPC1 or MPC2 KO mice fed a high-fat diet (Gray *et al*, 2015; Rauckhorst *et al*, 2017; McCommis *et al*, 2015, 2017). In this regard, MPC deletion would be expected to protect from steatosis only by decreasing *de novo* fatty acids synthesis fueled by the TCA cycle intermediate citrate generated from pyruvate, not by decreasing dietary fatty acid esterification (Duarte *et al*, 2014). Thus, preserved steatosis in high-fat diet fed (HFD) MPC KO mice is in agreement with HFD mostly inducing steatosis by increasing dietary fatty acid esterification into intrahepatic TG (Duarte *et al*, 2014).

In contrast to HFD-induced hepatic steatosis in mice, up to 38% of hepatic TG accumulated in humans with fatty liver stem from *de novo* synthesized fatty acids (Smith *et al*, 2020). This relatively high percentage opens the possibility that MPC inhibition could efficiently protect humans from steatosis by decreasing *de novo* fatty acid synthesis. The reason is that mitochondrial acetyl-CoA generated from pyruvate oxidation fuels citrate and malonyl-CoA synthesis. Accordingly, pharmacological inhibition of the enzymes responsible for malonyl-CoA synthesis, Acetyl-CoA Carboxylases (ACC1 and ACC2), reversed hepatic TG accumulation in humans (Kim *et al*, 2017). Remarkably, despite that ACC inhibition resulted in elevated mitochondrial FAO and ketogenesis as expected by unleashing CPT1 activity, blocking ACC activity markedly increased plasma lipid levels (Kim *et al*, 2017).

The increase in plasma lipids was explained by an upregulation in hepatic triglycerides synthesis (TG) selectively directed towards VLDL assembly and excretion. Elevated VLDL assembly was attributed to the transcriptional upregulation of the rate-limiting

enzyme in hepatic TG synthesis, GPAT1, as a result of increased SREBP-1c activity (Kim *et al*, 2017). However, a transcriptional upregulation of GPAT1 alone cannot explain how some fatty acids escape mitochondrial FAO and are selectively directed towards VLDL assembly. Elevated circulating levels of TG and VLDL by ACC inhibition strongly support the existence of a pool of fatty acids that escape from fat oxidizing mitochondria and are exclusively destined to VLDL synthesis. We are presenting a hypothesis on how some fatty acids escape mitochondria oxidation in chapters 2 and 4, proposing a new mechanism.

The transition from simple steatosis to NASH is associated with a reduction in total oxidative capacity measured in isolated mitochondria and liver homogenates (Koliaki *et al*, 2015; Pérez-Carreras *et al*, 2003). While Perez-Carreras *et al*. showed that the individual activities of each mitochondrial OXPHOS complex were lower in NASH patients than in lean controls, particularly ATP synthase, Koliaki *et al*. reported that NASH patients showed higher mitochondrial respiratory capacity than lean controls. The decrease in mitochondrial oxidative capacity in NASH can have two interpretations: i) it is an acquired defect in the transition to NASH that further exacerbates steatosis and ROS production (**Figure 5**) or ii) it is an adaptive mechanism to inflammation and uncontrolled steatosis, aiming to limit anabolism and ROS production from mitochondrial OXPHOS. The reduction in OXPHOS as an adaptive mechanism can explain why mitochondrial mass is preserved in patients with NASH or, in other words, why mitophagy does not eliminate these mitochondria deemed as dysfunctional based on lower OXPHOS.

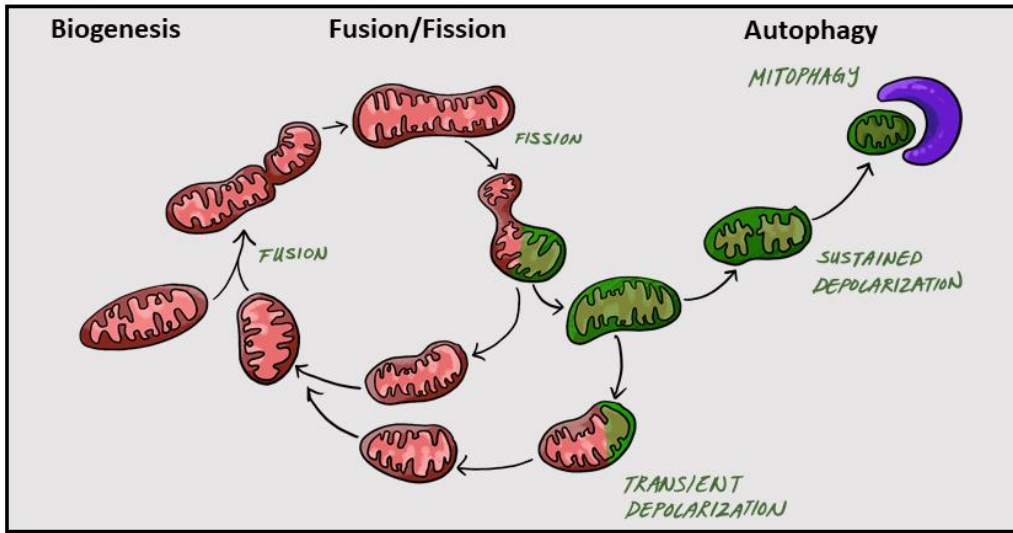
If the reduction in OXPHOS was an adaptive mechanism, one could interpret the specific reduction in complex V and increased proton leak as mitochondrial remodeling

caused by NASH, rather than damage. Proton leak together with decreased complex V would allow mitochondria to escape the limitation in fat oxidation imposed by the ATP demand while impeding an additional increase in ROS by limiting electron transport chain activity. This premise is supported by NASH patients still showing higher oxidative capacity than lean controls, but lower than in simple steatosis (Koliaki *et al*, 2015).

Overall, this study shows fission-mediated mitochondrial fragmentation is neither solely pathological nor solely compensatory. Metabolic phenotypes associated with mitochondrial fragmentation differ at different stages of disease progression. In chapter 2, we discuss how mitochondrial fragmentation may be pathological as FAO enhanced by mitochondrial fragmentation aligns with observations that fatty acids derived from adipose tissue stimulate dysregulated gluconeogenesis in obese animals, presumably due to uncontrolled beta-oxidation (Taddeo *et al*, 2017). In chapter 3, we discuss how mitochondrial fragmentation may be compensatory in alignment with observations that Mfn2KO livers decreased NASH, insulin resistance and reversed the decrease in fat oxidation (Hernández-Alvarez *et al*, 2019; Sebastián *et al*, 2012a; Muñoz *et al*, 2013).

FIGURES

A Dynamics Reduces Heterogeneity



B Dysregulation Increases Heterogeneity

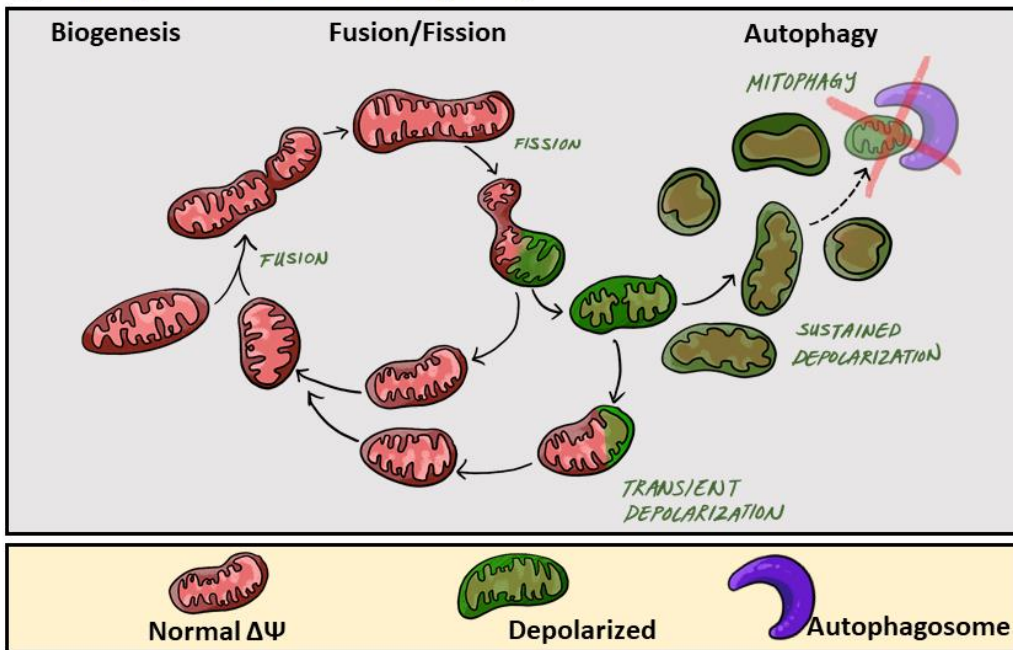


Figure 1- 1. The role of mitochondrial dynamics in mitochondrial heterogeneity.

During the mitochondrial life cycle, mitochondrial heterogeneity primarily occurs at three main phases (from left to right): biogenesis, fusion/fission, and autophagy of mitochondria (mitophagy). (A) While increases in mitochondrial heterogeneity are beneficial to cellular

health, sustained activity of the mitochondrial life cycle reduces mitochondrial heterogeneity. Specifically, fusion events result in the contents of two different mitochondria mixing, ultimately resulting in their contents becoming the same, equilibrating the mitochondrial population within the cell, and thereby decreasing intracellular heterogeneity. After fission, one daughter mitochondrion will depolarize (green) while the other will maintain normal membrane potential (red). Depolarized mitochondria will undergo one of two fates: either a transient depolarization will occur and they will slowly regain their membrane potential to fuse again (green mitochondria back to red), or they will remain depolarized and undergo mitophagy (the mitochondria will remain green). Mitophagy events remove depolarized mitochondria from the mitochondrial population, thereby reducing intracellular membrane potential heterogeneity. (B) Dysregulation and blockades within the mitochondrial life cycle lead to increases in heterogeneity. Impaired clearance of mitochondria with sustained depolarization, via mitophagy, increases the pre-autophagic pool. Increasing the pre-autophagic pool size increases intracellular heterogeneity, and the mitochondrial population now transitions from a population with a common membrane potential (red) to one with multiple membrane potentials (red and green).

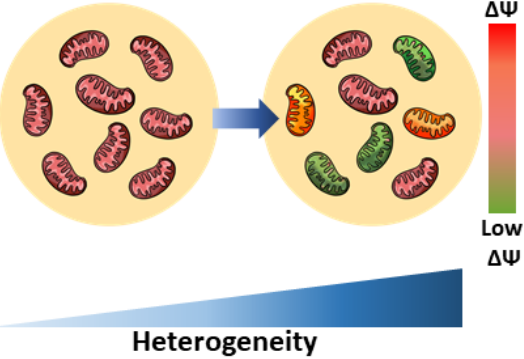
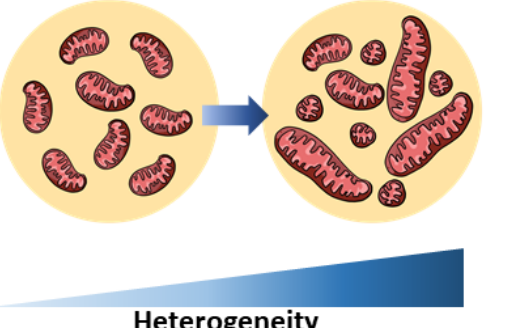
	Mitochondrial Feature	Pancreatic Beta-Cell Pathogenesis	Renal Proximal Tubule Pathogenesis
A	Membrane Potential 	<p>Unstimulated [Physiological] Normal basal insulin secretion</p> <p>Chronic GLT [Pathological] Impaired GSIS</p>	<p>Reduced FAO</p> <p>Loss of AMPK activity</p>
B	Morphology 	<p>Post-stimulated [Physiological] Normal Stimulated insulin secretion</p> <p>Chronic GLT [Pathological] Impaired GSIS</p>	<p>Membrane permeabilization</p> <p>Cellular apoptosis</p> <p>Inflammation</p> <p>Release of apoptogenic factors</p> <p>FAO dysfunction</p>

Figure 1- 2. Pathogenesis of the pancreatic beta-cell and renal proximal tubule cell induced by increased mitochondrial heterogeneity.

Mitochondrial heterogeneity under the pathological state, such as glucolipototoxicity (GLT), yields various functional readouts. **(A)** Increased mitochondrial membrane potential ($\Delta\Psi$) heterogeneity has been associated with various metabolic defects in both the pancreatic beta-cell and renal proximal tubule cell. Intracellular heterogeneity is observed by an increase in differences in $\Delta\Psi$. Reduced $\Delta\Psi$ is presented as green and increased $\Delta\Psi$ is presented as red. Mitochondria of normal $\Delta\Psi$ are presented as pink. **(B)** Architectural heterogeneity yields mitochondria varying from short to long mitochondrial lengths as a

result of varying fusion and fission rates. Increased heterogeneity in mitochondrial morphology, specifically increased short mitochondria due to reduced fusion, is associated with reductions in impaired glucose-stimulated insulin secretion (GSIS) in pancreatic beta-cells and reductions in renal fatty acid oxidation (FAO).

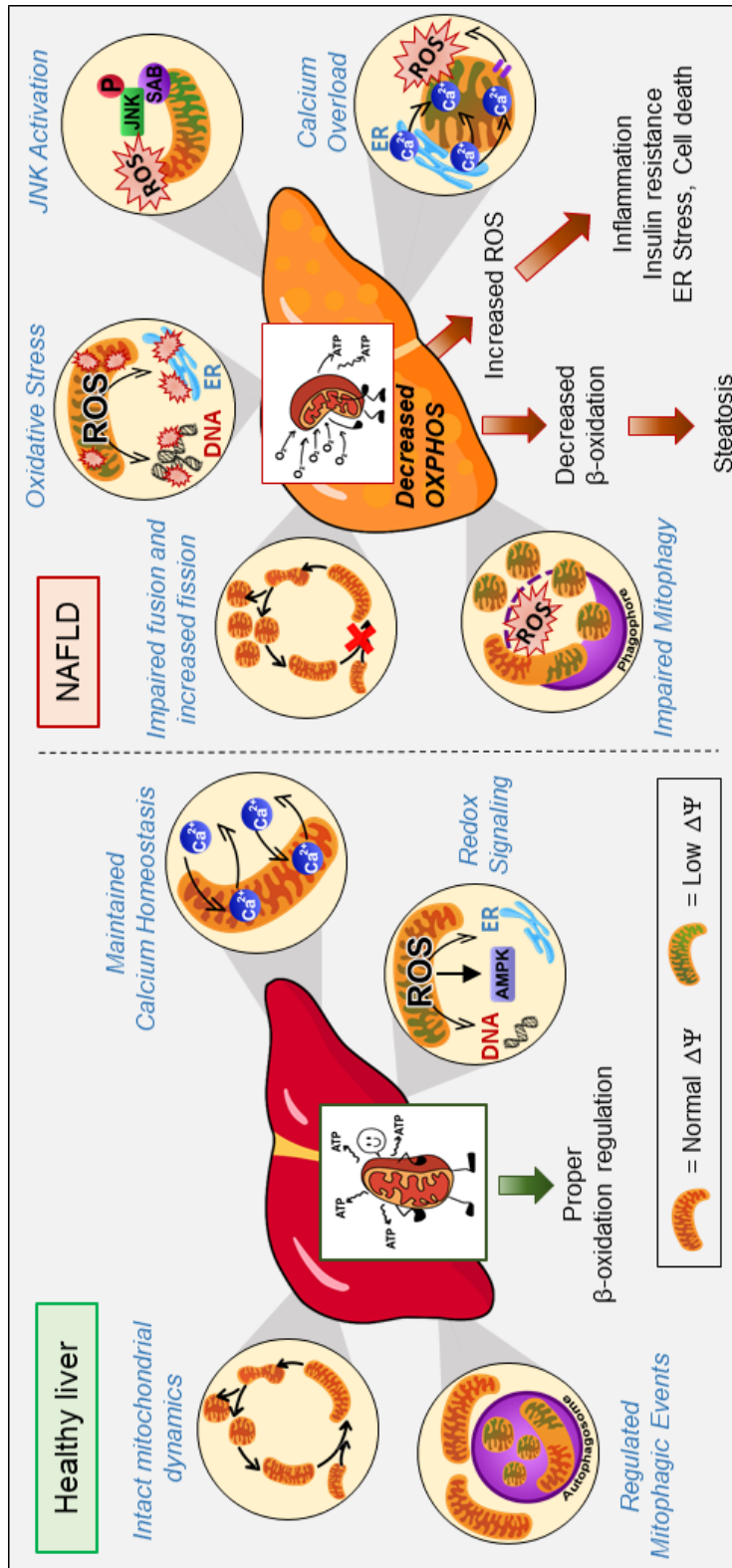


Figure 1- 3. Compromised mitochondria promote NAFLD.

Mitochondria in hepatocytes oxidize fatty acids to produce ketone bodies, as well as ATP to cover glucose production during fasting. Mitochondria rely on diverse mechanisms to preserve their function including dynamics, redox signaling, mitophagy and calcium homeostasis. In contrast to a healthy liver, mitochondria in NAFLD were reported to be fragmented, overloaded with calcium, with decreased oxidative capacity and increased ROS production, which cause JNK activation. JNK activation itself can induce these same defects in mitochondrial function as well, being a feed-forward cycle of mitochondrial defects. These mitochondrial defects in NAFLD were also explained by defective mitophagy. The decrease in fatty acid oxidation caused by this compromise in mitochondrial function was deemed to cause fat accumulation in hepatocytes, while impairing insulin signaling. JNK, c-Jun NH2-terminal Kinase.

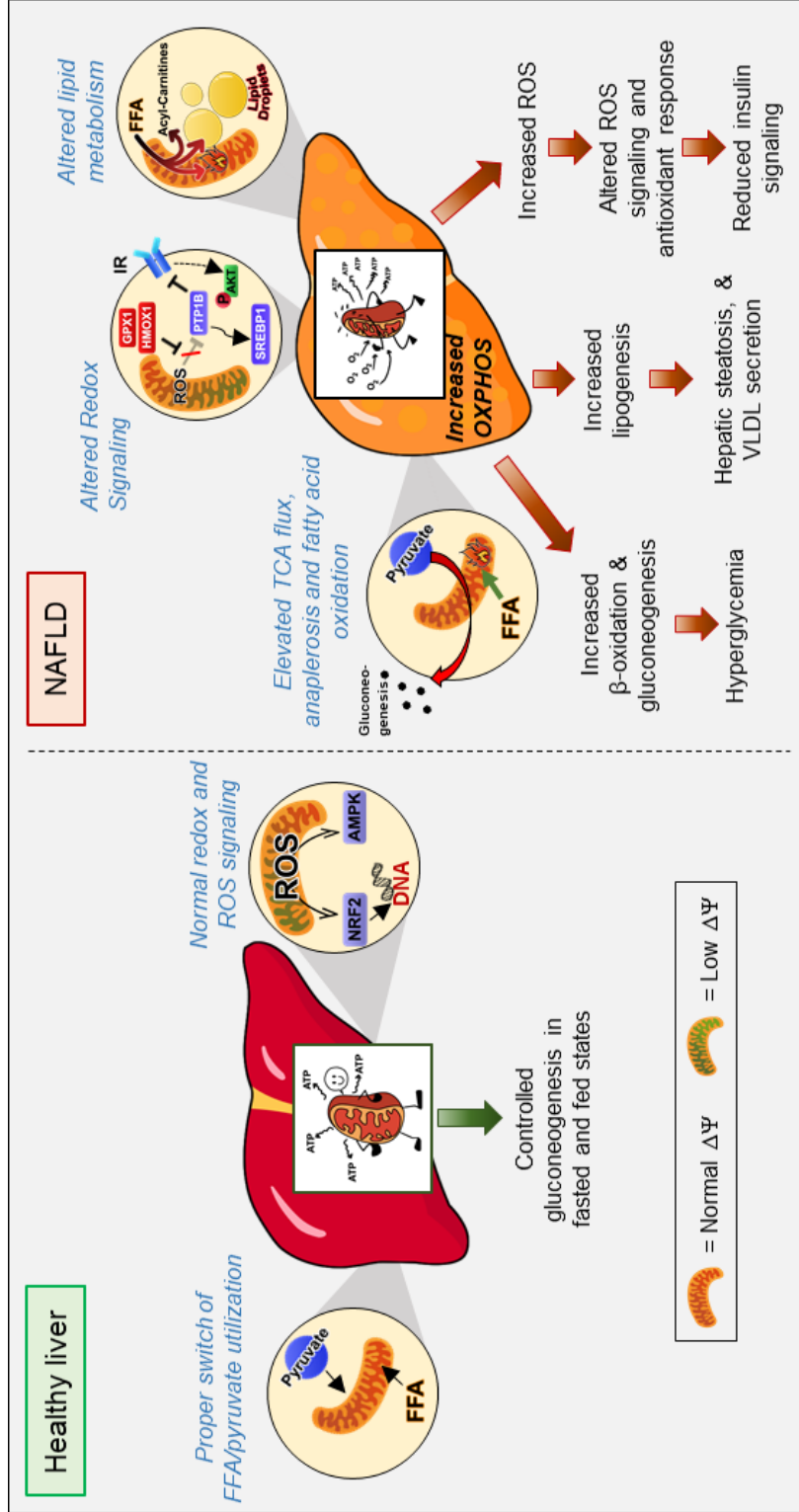


Figure 1- 4. Enhanced mitochondrial activity promote NAFLD.

As the liver supplies glucose, ketone bodies and lipids to other organs, proper control of hepatic gluconeogenesis and lipid metabolism in the fasted and fed state is essential. NAFLD is associated with increases in hepatic glucose production and lipid synthesis/storage in part due to higher glucose and lipid supply. The elevation in gluconeogenesis and lipid storage increase mitochondrial ATP demand, explaining the increase in mitochondrial oxidative capacity reported in simple steatosis and even in NASH. Interestingly, fatty liver is not only associated with increased mitochondrial fat oxidation, which normally fuels glucose production and ketogenesis, but it also increases TCA cycle flux. Further, it was proposed that increased oxidative function of mitochondria increases ROS production, which can underpin inflammation, impaired insulin signaling and cell death. Evidence suggests that increased TCA cycle flux and impaired ketogenesis cause hepatic steatosis and hyperglycemia, supporting that restoration of mitochondrial fuel preference can be a therapeutic target for NAFLD. IR, insulin resistance; GPX1, glutathione peroxidase 1; HMOX1, heme oxygenase 1; PTP1B, protein-tyrosine phosphatase 1B, SREBP1, Sterol regulatory element-binding transcription factor 1.

Healthy Liver	Hepatic Steatosis	NASH	Cirrhosis
Mitochondrial Respiration	++	+/-	-
Mitophagy	+	+/-	-
Antioxidant Defense	++	+/-	-
Mitochondria biogenesis	+	++	-
Inflammation	+	++	+++
ROS	+	++	++
Apoptosis	-	+	++

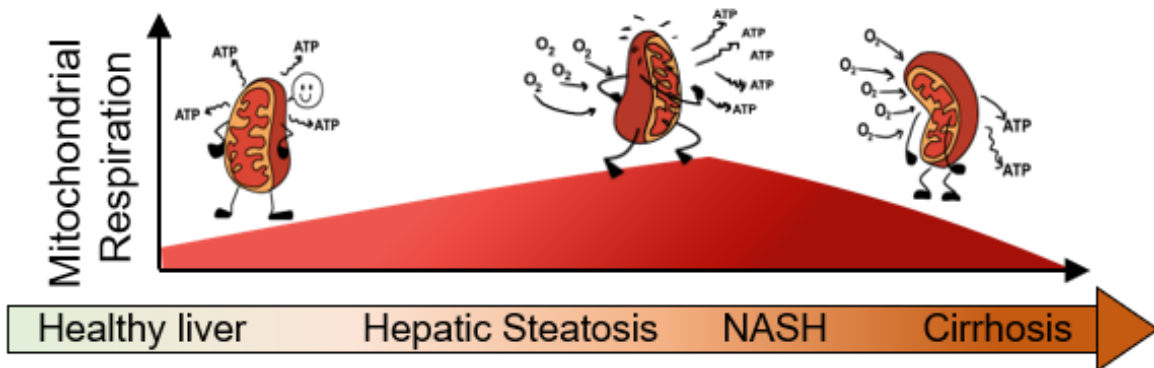


Figure 1- 5. Mitochondrial states throughout the progression of NAFLD.

In the early stages of NAFLD, namely simple steatosis, adaptative mechanisms occur to compensate for the increase in fuel availability and anabolism: mitochondrial respiration increases due to higher substrate availability and increased ATP demand, which will increase ROS production, activate mitochondrial biogenesis and antioxidant responses. As hepatocytes store more lipids and reach full storage capacity, free-fatty acid mediated toxicity impairs mitophagy and damages mitochondria. In the transition to NASH, mitochondrial function is decreased and ROS is further increased, which were deemed to be responsible for higher inflammation and cell death characteristic of NASH. However, some mouse models with antioxidant enzymes selectively deleted in hepatocytes are

protected from NASH, questioning whether the increase in ROS observed in simple steatosis and NASH contributes to the disease. In certain cases, NASH will progress to cirrhosis, meaning that hepatocytes will be replaced with cell types with fewer mitochondria, contributing to the decline in liver oxidative function.

REFERENCES

- Akkaoui M, Cohen I, Esnous C, Lenoir V, Sournac M, Girard J & Prip-Buus C (2009) Modulation of the hepatic malonyl-CoA-carnitine palmitoyltransferase 1A partnership creates a metabolic switch allowing oxidation of de novo fatty acids. *Biochem J* 420
- Apostolopoulou M, Gordillo R, Koliaki C, Gancheva S, Jelenik T, De Filippo E, Herder C, Markgraf D, Jankowiak F, Esposito I, *et al* (2018) Specific Hepatic Sphingolipids Relate to Insulin Resistance, Oxidative Stress, and Inflammation in Nonalcoholic Steatohepatitis. *Diabetes Care* 41: 1235–1243
- Arruda AP, Pers BM, Parlakgöl G, Güney E, Inouye K & Hotamisligil GS (2014) Chronic enrichment of hepatic endoplasmic reticulum-mitochondria contact leads to mitochondrial dysfunction in obesity. *Nat Med* 20: 1427–1435
- Aryaman J, Johnston IG & Jones NS (2019) Mitochondrial heterogeneity. *Front Genet* 10: 718 doi:10.3389/fgene.2018.00718 [PREPRINT]
- Assali EA, Shlomo D, Zeng J, Taddeo EP, Trudeau KM, Erion KA, Colby AH, Grinstaff MW, Liesa M, Las G, *et al* (2019) Nanoparticle-mediated lysosomal reacidification restores mitochondrial turnover and function in β cells under lipotoxicity. *FASEB J* 33: 4154–4165
- Bach D, Pich S, Soriano FX, Vega N, Baumgartner B, Oriola J, Daugaard JR, Lloberas J, Camps M, Zierath JR, *et al* (2003) Mitofusin-2 Determines Mitochondrial Network Architecture and Mitochondrial Metabolism. *J Biol Chem* 278: 17190–17197
- Baron AD, Brechtel G & Edelman S V. (1989) Effects of free fatty acids and ketone bodies on in vivo non-insulin-mediated glucose utilization and production in

humans. *Metabolism* 38: 1056–1061

Benador IY, Veliova M, Mahdavian K, Petcherski A, Wikstrom JD, Assali EA, Acín-Pérez R, Shum M, Oliveira MF, Cinti S, *et al* (2018) Mitochondria Bound to Lipid Droplets Have Unique Bioenergetics, Composition, and Dynamics that Support Lipid Droplet Expansion. *Cell Metab* 27: 869-885.e6

Bhargava P & Schnellmann RG (2017) Mitochondrial energetics in the kidney Nature Publishing Group

van der Bliek AM, Shen Q & Kawajiri S (2013) Mechanisms of mitochondrial fission and fusion. *Cold Spring Harb Perspect Biol* 5

Boland ML, Laker RC, Mather K, Nawrocki A, Oldham S, Boland BB, Lewis H, Conway J, Naylor J, Guionaud S, *et al* (2020) Resolution of NASH and hepatic fibrosis by the GLP-1R/GcgR dual-agonist Cotadutide via modulating mitochondrial function and lipogenesis. *Nat Metab* 2: 413–431

Brady LJ, Brady PS, Romsos DR & Hoppel CL (1985) Elevated hepatic mitochondrial and peroxisomal oxidative capacities in fed and starved adult obese (ob/ob) mice. *Biochem J* 231: 439–444

Bremer J, Woldegiorgis G, Schalinske K & Shrago E (1985) Carnitine palmitoyltransferase. Activation by palmitoyl-CoA and inactivation by malonyl-CoA. *Biochim Biophys Acta* 833: 9–16

Bril F, Lomonaco R, Orsak B, Ortiz-Lopez C, Webb A, Tio F, Hecht J & Cusi K (2014) Relationship between disease severity, hyperinsulinemia, and impaired insulin clearance in patients with nonalcoholic steatohepatitis. *Hepatology* 59: 2178–2187

De Brito OM & Scorrano L (2008) Mitofusin 2 tethers endoplasmic reticulum to

mitochondria. *Nature* 456: 605–610

- Brooks C, Wei Q, Cho SG & Dong Z (2009) Regulation of mitochondrial dynamics in acute kidney injury in cell culture and rodent models. *J Clin Invest* 119: 1275–1285
- Caro P, Kishan AU, Norberg E, Stanley IA, Chapuy B, Ficarro SB, Polak K, Tondera D, Gounarides J, Yin H, *et al* (2012) Metabolic Signatures Uncover Distinct Targets in Molecular Subsets of Diffuse Large B Cell Lymphoma. *Cancer Cell* 22: 547–560
- Casals N, Zammit V, Herrero L, Fadó R, Rodríguez-Rodríguez R & Serra D (2016) Carnitine palmitoyltransferase 1C: From cognition to cancer. *Prog Lipid Res* 61: 134–148
- Cereghetti GM, Stangherlin A, Martins De Brito O, Chang CR, Blackstone C, Bernardi P & Scorrano L (2008) Dephosphorylation by calcineurin regulates translocation of Drp1 to mitochondria. *Proc Natl Acad Sci U S A* 105: 15803–15808
- Chen H, Chomyn A & Chan DC (2005) Disruption of fusion results in mitochondrial heterogeneity and dysfunction. *J Biol Chem* 280: 26185–26192
- Clouet P, Henninger C & Bezard J (1986) Study of some factors controlling fatty acid oxidation in liver mitochondria of obese Zucker rats. *Biochem J* 239: 103–108
- Collins TJ, Berridge MJ, Lipp P & Bootman MD (2002) Mitochondria are morphologically and functionally heterogeneous within cells. *EMBO J* 21: 1616–1627
- Cook GA & Gamble MS (1987) Regulation of Carnitine Palmitoyltransferase by Insulin Results in Decreased Activity and Decreased Apparent K_i -Values for Malonyl-CoA*. *J Biol Chem* 262: 2050–2055
- d'Avignon DA, Puchalska P, Ercal B, Chang YJ, Martin SE, Graham MJ, Patti GJ, Han X & Crawford PA (2018) Hepatic ketogenic insufficiency reprograms hepatic

glycogen metabolism and the lipidome. *JCI insight* 3

Dai J, Liang K, Zhao S, Jia W, Liu Y, Wu H, Lv J, Cao C, Chen T, Zhuang S, *et al* (2018) Chemoproteomics reveals baicalin activates hepatic CPT1 to ameliorate diet-induced obesity and hepatic steatosis. *Proc Natl Acad Sci U S A* 115: E5896–E5905

Divakaruni AS, Hsieh WY, Minarrieta L, Duong TN, Kim KKO, Desousa BR, Andreyev AY, Bowman CE, Caradonna K, Dranka BP, *et al* (2018) Etomoxir Inhibits Macrophage Polarization by Disrupting CoA Homeostasis. *Cell Metab* 28: 490-503.e7

Donath MY & Halban PA (2004) Decreased beta-cell mass in diabetes: Significance, mechanisms and therapeutic implications. *Diabetologia* 47: 581–589
doi:10.1007/s00125-004-1336-4 [PREPRINT]

Duarte JAG, Carvalho F, Pearson M, Horton JD, Browning JD, Jones JG & Burgess SC (2014) A high-fat diet suppresses de novo lipogenesis and desaturation but not elongation and triglyceride synthesis in mice. *J Lipid Res* 55: 2541–2553

Duchen MR, Surin A & Jacobson J (2003) Imaging mitochondrial function in intact cells. *Methods Enzymol* 361: 353–389

Edmunds LR, Xie B, Mills AM, Huckestein BR, Undamatla R, Murali A, Pangburn MM, Martin J, Sipula I, Kaufman BA, *et al* (2020) Liver-specific Prkn knockout mice are more susceptible to diet-induced hepatic steatosis and insulin resistance. *Mol Metab* 41

Enooku K, Nakagawa H, Fujiwara N, Kondo M, Minami T, Hoshida Y, Shibahara J, Tateishi R & Koike K (2019) Altered serum acylcarnitine profile is associated with

the status of nonalcoholic fatty liver disease (NAFLD) and NAFLD-related hepatocellular carcinoma. *Sci Rep* 9

Fex M, Nitert MD, Wierup N, Sundler F, Ling C & Mulder H (2007) Enhanced mitochondrial metabolism may account for the adaptation to insulin resistance in islets from C57BL/6J mice fed a high-fat diet. *Diabetologia* 50: 74–83

Flavin R, Peluso S, Nguyen PL & Loda M (2010) Fatty acid synthase as a potential therapeutic target in cancer. *Futur Oncol* 6: 551–562

Fletcher JA, Deja S, Satapati S, Fu X, Burgess SC & Browning JD (2019) Impaired ketogenesis and increased acetyl-CoA oxidation promote hyperglycemia in human fatty liver. *JCI insight* 5

Frank S, Gaume B, Bergmann-Leitner ES, Leitner WW, Robert EG, Catez F, Smith CL & Youle RJ (2001) The role of dynamin-related protein 1, a mediator of mitochondrial fission, in apoptosis. *Dev Cell* 1: 515–25

Frezza C, Cipolat S, Martins de Brito O, Micaroni M, Beznoussenko G V., Rudka T, Bartoli D, Polishuck RS, Danial NN, De Strooper B, *et al* (2006) OPA1 Controls Apoptotic Cristae Remodeling Independently from Mitochondrial Fusion. *Cell* 126: 177–189

Galloway CA, Lee H, Brookes PS & Yoon Y (2014) Decreasing mitochondrial fission alleviates hepatic steatosis in a murine model of nonalcoholic fatty liver disease. *Am J Physiol - Gastrointest Liver Physiol* 307: G632–G641

Gandre-Babbe S & Blik AM van der (2008) The Novel Tail-anchored Membrane Protein Mff Controls Mitochondrial and Peroxisomal Fission in Mammalian Cells. <https://doi.org/10.1091/mbc.e07-12-1287> 19: 2402–2412

- Gao Y, Li F, Zhang A, Wang L, Tong W & Liu B (2014) Evaluation of mitochondrial divisions in mouse with type-2 diabetes and effect of glucose-oxidase on mouse islet cells RIN-m5F. *Cell Biol Int* 38: 368–373
- Garland PB, Shepherd D, Nicholls DG & Ontko J (1968) Energy-dependent control of the tricarboxylic acid cycle by fatty acid oxidation in rat liver mitochondria. *Adv Enzyme Regul* 6: 3–30
- Georgiadou E, Muralidharan C, Martinez M, Chabosseu P, Tomas A, Wern FYS, Stylianides T, Rothery SM, Gregorio A Di, Leclerc I, *et al* (2020) Pancreatic beta cell selective deletion of mitofusins 1 and 2 (Mfn1 and Mfn2) disrupts mitochondrial architecture and abrogates glucose-stimulated insulin secretion in vivo. *bioRxiv*: 2020.04.22.055384 doi:10.1101/2020.04.22.055384 [PREPRINT]
- Goedeke L, Peng L, Montalvo-Romeral V, Butrico GM, Dufour S, Zhang XM, Perry RJ, Cline GW, Kievit P, Chng K, *et al* (2019) Controlled-release mitochondrial protonophore (CRMP) reverses dyslipidemia and hepatic steatosis in dysmetabolic nonhuman primates. *Sci Transl Med* 11
- Gomes LC, Benedetto G Di & Scorrano L (2011) During autophagy mitochondria elongate, are spared from degradation and sustain cell viability. *Nat Cell Biol* 13: 589–598
- González-Rodríguez A, Mayoral R, Agra N, Valdecantos MP, Pardo V, Miquilena-Colina ME, Vargas-Castrillón J, Lo Iacono O, Corazzari M, Fimia GM, *et al* (2014) Impaired autophagic flux is associated with increased endoplasmic reticulum stress during the development of NAFLD. *Cell Death Dis* 5
- Gooptu M, Whitaker-Menezes D, Sprandio J, Domingo-Vidal M, Lin Z, Uppal G, Gong J,

- Fratamico R, Leiby B, Dulau-Florea A, *et al* (2017) Mitochondrial and glycolytic metabolic compartmentalization in diffuse large B-cell lymphoma. *Semin Oncol* 44: 204–217
- Gottlieb RA & Stotland A MitoTimer: a novel protein for monitoring mitochondrial turnover in the heart
- Gray LR, Sultana MR, Rauckhorst AJ, Oonthonpan L, Tompkins SC, Sharma A, Fu X, Miao R, Pawa AD, Brown KS, *et al* (2015) Hepatic Mitochondrial Pyruvate Carrier 1 Is Required for Efficient Regulation of Gluconeogenesis and Whole-Body Glucose Homeostasis. *Cell Metab* 22: 669–81
- Hailey DW, Rambold AS, Satpute-Krishnan P, Mitra K, Sougrat R, Kim PK & Lippincott-Schwartz J (2010) Mitochondria supply membranes for autophagosome biogenesis during starvation. *Cell* 141: 656–667
- Hall AM & Schuh CD (2016) Mitochondria as therapeutic targets in acute kidney injury. *Curr Opin Nephrol Hypertens* 25: 355–362
- Hammerschmidt P, Ostkotte D, Nolte H, Gerl MJ, Jais A, Brunner HL, Sprenger HG, Awazawa M, Nicholls HT, Turpin-Nolan SM, *et al* (2019) CerS6-Derived Sphingolipids Interact with Mff and Promote Mitochondrial Fragmentation in Obesity. *Cell* 177: 1536-1552.e23
- Heart E, Corkey RF, Wikstrom JD, Shirihai OS & Corkey BE (2006) Glucose-dependent increase in mitochondrial membrane potential, but not cytoplasmic calcium, correlates with insulin secretion in single islet cells. *Am J Physiol Metab* 290: E143–E148
- Henninger C, Clouet P, Danh HC, Pascal M & Bezard J (1987) Effects of fenofibrate

treatment on fatty acid oxidation in liver mitochondria of obese Zucker rats.

Biochem Pharmacol 36: 3231–3236

Herms A, Bosch M, Ariotti N, Reddy BJN, Fajardo A, Fernández-Vidal A, Alvarez-Guaita A, Fernández-Rojo MA, Rentero C, Tebar F, *et al* (2013) Cell-to-cell heterogeneity in lipid droplets suggests a mechanism to reduce lipotoxicity. *Curr Biol* 23: 1489–1496

Hernández-Alvarez MI, Sebastián D, Vives S, Ivanova S, Bartoccioni P, Kakimoto P, Plana N, Veiga SR, Hernández V, Vasconcelos N, *et al* (2019) Deficient Endoplasmic Reticulum-Mitochondrial Phosphatidylserine Transfer Causes Liver Disease. *Cell* 177: 881-895.e17

Hoppel C, Kerner J, Turkaly P & Tandler B (2001) Rat Liver Mitochondrial Contact Sites and Carnitine Palmitoyltransferase-I. *Arch Biochem Biophys* 392: 321–325

Hughes AL & Gottschling DE (2012) An early age increase in vacuolar pH limits mitochondrial function and lifespan in yeast. *Nature* 492: 261–265

Huynh FK, Green MF, Koves TR & Hirschey MD (2014) Measurement of fatty acid oxidation rates in animal tissues and cell lines. *Methods Enzymol* 542: 391–405

Iozzo P, Bucci M, Roivainen A, Någren K, Järvisalo MJ, Kiss J, Guiducci L, Fielding B, Naum AG, Borra R, *et al* (2010) Fatty acid metabolism in the liver, measured by positron emission tomography, is increased in obese individuals. *Gastroenterology* 139

Iqbal S & Hood DA (2014) Oxidative stress-induced mitochondrial fragmentation and movement in skeletal muscle myoblasts. *Am J Physiol - Cell Physiol* 306

Ishihara N, Fujita Y, Oka T, Mihara K, Kushnareva Y, Graber S, Kovacs I, Lee W,

- Waggoner J, Cui J, *et al* (2006) Regulation of mitochondrial morphology through proteolytic cleavage of OPA1. *EMBO J* 25: 2966–2977
- Jais A, Einwallner E, Sharif O, Gossens K, Lu TTH, Soyak SM, Medgyesi D, Neureiter D, Paier-Pourani J, Dalgaard K, *et al* (2014) Heme oxygenase-1 drives metaflammation and insulin resistance in mouse and man. *Cell* 158: 25–40
- Jang HS, Noh MR, Kim J & Padanilam BJ (2020) Defective Mitochondrial Fatty Acid Oxidation and Lipotoxicity in Kidney Diseases. *Front Med* 7: 65
doi:10.3389/fmed.2020.00065 [PREPRINT]
- Kang HM, Ahn SH, Choi P, Ko YA, Han SH, Chinga F, Park ASD, Tao J, Sharma K, Pullman J, *et al* (2015) Defective fatty acid oxidation in renal tubular epithelial cells has a key role in kidney fibrosis development. *Nat Med* 21: 37–46
- Kim CW, Addy C, Kusunoki J, Anderson NN, Deja S, Fu X, Burgess SC, Li C, Chakravarthy M, Previs S, *et al* (2017) Acetyl CoA Carboxylase Inhibition Reduces Hepatic Steatosis but Elevates Plasma Triglycerides in Mice and Humans: A Bedside to Bench Investigation. *Cell Metab* 26: 394-406.e6
- Kodiha M, Flamant E, Wang YM & Stochaj U (2018) Defining the short-term effects of pharmacological 50-AMP activated kinase modulators on mitochondrial polarization, morphology and heterogeneity. *PeerJ* 2018
- Koliaki C, Szendroedi J, Kaul K, Jelenik T, Nowotny P, Jankowiak F, Herder C, Carstensen M, Krausch M, Knoefel WT, *et al* (2015) Adaptation of hepatic mitochondrial function in humans with non-alcoholic fatty liver is lost in steatohepatitis. *Cell Metab* 21: 739–746
- Koves TR, Ussher JR, Noland RC, Slentz D, Mosedale M, Ilkayeva O, Bain J, Stevens

- R, Dyck JRB, Newgard CB, *et al* (2008) Mitochondrial overload and incomplete fatty acid oxidation contribute to skeletal muscle insulin resistance. *Cell Metab* 7: 45–56
- Kulkarni SS, Joffraud M, Boutant M, Ratajczak J, Gao AW, Maclachlan C, Hernandez-Alvarez MI, Raymond F, Metairon S, Descombes P, *et al* (2016) Mfn1 Deficiency in the Liver Protects Against Diet-Induced Insulin Resistance and Enhances the Hypoglycemic Effect of Metformin. *Diabetes* 65: 3552–3560
- Kuznetsov A V., Troppmair J, Sucher R, Hermann M, Saks V & Margreiter R (2006) Mitochondrial subpopulations and heterogeneity revealed by confocal imaging: Possible physiological role? *Biochim Biophys Acta - Bioenerg* 1757: 686–691
- Lam TKT, Carpentier A, Lewis GF, Van de Werve G, Fantus IG & Giacca A (2003a) Mechanisms of the free fatty acid-induced increase in hepatic glucose production. *Am J Physiol - Endocrinol Metab* 284
- Lam TKT, Van de Werve G & Giacca A (2003b) Free fatty acids increase basal hepatic glucose production and induce hepatic insulin resistance at different sites. *Am J Physiol Metab* 284: E281–E290
- Leboucher GP, Tsai YC, Yang M, Shaw KC, Zhou M, Veenstra TD, Glickman MH & Weissman AM (2012) Stress-induced phosphorylation and proteasomal degradation of mitofusin 2 facilitates mitochondrial fragmentation and apoptosis. *Mol Cell* 47: 547–557
- Liesa M, Palacín M & Zorzano A (2009) Mitochondrial dynamics in mammalian health and disease. *Physiol Rev* 89: 799–845 doi:10.1152/physrev.00030.2008
- [PREPRINT]

- Liesa M & Shirihaï OS (2013a) Mitochondrial Dynamics in the Regulation of Nutrient Utilization and Energy Expenditure. *Cell Metab* 17: 491–506
- Liesa M & Shirihaï OSS (2013b) Mitochondrial dynamics in the regulation of nutrient utilization and energy expenditure. *Cell Metab* 17: 491–506
- Lionetti L, Mollica MP, Donizzetti I, Gifuni G, Sica R, Pignalosa A, Cavaliere G, Gaita M, De Filippo C, Zorzano A, *et al* (2014) High-Lard and High-Fish-Oil Diets Differ in Their Effects on Function and Dynamic Behaviour of Rat Hepatic Mitochondria. *PLoS One* 9: e92753
- Loh K, Deng H, Fukushima A, Cai X, Boivin B, Galic S, Bruce C, Shields BJ, Skiba B, Ooms LM, *et al* (2009) Reactive oxygen species enhance insulin sensitivity. *Cell Metab* 10: 260–272
- López-Viñas E, Bentebibel A, Gurunathan C, Morillas M, de Arriaga D, Serra D, Asins G, Hegardt FG & Gómez-Puertas P (2007) Definition by functional and structural analysis of two malonyl-CoA sites in carnitine palmitoyltransferase 1A. *J Biol Chem* 282: 18212–24
- Lundsgaard AM, Fritzen AM, Nicolaisen TS, Carl CS, Sjøberg KA, Raun SH, Klein AB, Sanchez-Quant E, Langer J, Ørskov C, *et al* (2020) Glucometabolic consequences of acute and prolonged inhibition of fatty acid oxidation. *J Lipid Res* 61: 10–19
- Mahdavian K, Benador IY, Su S, Gharakhanian RA, Stiles L, Trudeau KM, Cardamone M, Enríquez-Zarralanga V, Ritou E, Aprahamian T, *et al* (2017) Mfn2 deletion in brown adipose tissue protects from insulin resistance and impairs thermogenesis. *EMBO Rep* 18: 1123–1138
- Masini M, Martino L, Marselli L, Bugliani M, Boggi U, Filipponi F, Marchetti P & De Tata

- V (2017) Ultrastructural alterations of pancreatic beta cells in human diabetes mellitus. *Diabetes Metab Res Rev* 33
- McCommis KS, Chen Z, Fu X, McDonald WG, Colca JR, Kletzien RF, Burgess SC & Finck BN (2015) Loss of Mitochondrial Pyruvate Carrier 2 in the Liver Leads to Defects in Gluconeogenesis and Compensation via Pyruvate-Alanine Cycling. *Cell Metab* 22: 682–694
- McCommis KS, Hodges WT, Brunt EM, Nalbantoglu I, McDonald WG, Holley C, Fujiwara H, Schaffer JE, Colca JR & Finck BN (2017) Targeting the mitochondrial pyruvate carrier attenuates fibrosis in a mouse model of nonalcoholic steatohepatitis. *Hepatology* 65: 1543–1556
- McCune SA, Durant PJ, Jenkins PA & Harris RA (1981) Comparative studies on fatty acid synthesis, glycogen metabolism, and gluconeogenesis by hepatocytes isolated from lean and obese Zucker rats. *Metabolism* 30: 1170–1178
- McGarry JD & Brown NF (1997) The mitochondrial carnitine palmitoyltransferase system. From concept to molecular analysis. *Eur J Biochem* 244: 1–14
- McGarry JD & Foster DW (1980) Effects of exogenous fatty acid concentration on glucagon-induced changes in hepatic fatty acid metabolism. *Diabetes* 29: 236–240
- Men X, Wang H, Li M, Cai H, Xu S, Zhang W, Xu Y, Ye L, Yang W, Wollheim CB, *et al* (2009) Dynamin-related protein 1 mediates high glucose induced pancreatic beta cell apoptosis. *Int J Biochem Cell Biol* 41: 879–890
- Miguel V, Tituaña J, Herrero JI, Herrero L, Serra D, Cuevas P, Barbas C, Puyol DR, Márquez-Exposito L, Ruiz-Ortega M, *et al* (2020) Renal tubule Cpt1a overexpression mitigates kidney fibrosis by restoring mitochondrial homeostasis.

bioRxiv: 2020.02.18.952440

Molina AJ a, Molina AJ a, Wikstrom JD, Wikstrom JD, Stiles L, Stiles L, Las G, Las G, Mohamed H, Mohamed H, *et al* (2009a) Mitochondrial Networking Protects Beta Cells from Nutrient Induced Apoptosis. *Diabetes* 58: 2303–2315

Molina AJA, Wikstrom JD, Stiles L, Las G, Mohamed H, Elorza A, Walzer G, Twig G, Katz S, Corkey BE, *et al* (2009b) Mitochondrial networking protects β -cells from nutrient-induced apoptosis. *Diabetes* 58: 2303–2315

Moore MP, Cunningham RP, Meers GM, Johnson SA, Wheeler AA, Ganga RR, Spencer NM, Pitt JB, Diaz-Arias A, Swi AIA, *et al* (2022) Compromised hepatic mitochondrial fatty acid oxidation and reduced markers of mitochondrial turnover in human NAFLD. *Hepatology*

Muñoz JP, Ivanova S, Sánchez-Wandelmer J, Martínez-Cristóbal P, Noguera E, Sancho A, Díaz-Ramos A, Hernández-Alvarez MI, Sebastián D, Mauvezin C, *et al* (2013) Mfn2 modulates the UPR and mitochondrial function via repression of PERK. *EMBO J* 32: 2348–2361

Mynatt RL, Greenhaw JJ & Cook GA (1994) Cholate extracts of mitochondrial outer membranes increase inhibition by malonyl-CoA of carnitine palmitoyltransferase-I by a mechanism involving phospholipids. *Biochem J* 299 (Pt 3): 761–7

Nasteska D & Hodson DJ (2018) The role of beta cell heterogeneity in islet function and insulin release. *J Mol Endocrinol* 61: R43–R60 doi:10.1530/JME-18-0011

[PREPRINT]

Nolan CJ, Leahy JL, Delghingaro-Augusto V, Moibi J, Soni K, Peyot M-LL, Fortier M, Guay C, Lamontagne J, Barbeau A, *et al* (2006a) Beta cell compensation for insulin

resistance in Zucker fatty rats: increased lipolysis and fatty acid signalling.

Diabetologia 49: 2120–2130

Nolan CJ, Madiraju MSR, Delghingaro-Augusto V, Peyot M-L & Prentki M (2006b) Fatty acid signaling in the beta-cell and insulin secretion. *Diabetes* 55 Suppl 2: S16-23

Norberg E, Lako A, Chen PH, Stanley IA, Zhou F, Ficarro SB, Chapuy B, Chen L, Rodig S, Shin D, *et al* (2017) Differential contribution of the mitochondrial translation pathway to the survival of diffuse large B-cell lymphoma subsets. *Cell Death Differ* 24: 251

Nowak G, Bakajsova D & Samarel AM (2011) Protein kinase C- ϵ on induces mitochondrial dysfunction and fragmentation in renal proximal tubules. *Am J Physiol - Ren Physiol* 301: F197–F208

Palmer JW, Tandler B & Hoppel CL (1985) Biochemical differences between subsarcolemmal and interfibrillar mitochondria from rat cardiac muscle: Effects of procedural manipulations. *Arch Biochem Biophys* 236: 691–702

Peng KY, Watt MJ, Rensen S, Willem Greve J, Huynh K, Jayawardana KS, Meikle PJ & Meex RCR (2018) Mitochondrial dysfunction-related lipid changes occur in nonalcoholic fatty liver disease progression. *J Lipid Res* 59: 1977–1986

Pérez-Carreras M, Del Hoyo P, Martín MA, Rubio JC, Martín A, Castellano G, Colina F, Arenas J & Solis-Herruzo JA (2003) Defective hepatic mitochondrial respiratory chain in patients with nonalcoholic steatohepatitis. *Hepatology* 38: 999–1007

Perry RJ, Kim T, Zhang XM, Lee HY, Pesta D, Popov VB, Zhang D, Rahimi Y, Jurczak MJ, Cline GW, *et al* (2013) Reversal of hypertriglyceridemia, fatty liver disease, and insulin resistance by a liver-targeted mitochondrial uncoupler. *Cell Metab* 18: 740–

- Poulaki A & Giannouli S (2021) Metabolic Swifts Govern Normal and Malignant B Cell Lymphopoiesis. *Int J Mol Sci* 22
- Putti R, Sica R, Migliaccio V & Lionetti L (2015) Diet impact on mitochondrial bioenergetics and dynamics. *Front Physiol* 6: 109
- Qu Q, Zeng F, Liu X, Wang QJ & Deng F (2016) Fatty acid oxidation and carnitine palmitoyltransferase I: emerging therapeutic targets in cancer. *Cell Death Dis* 7: e2226–e2226
- Quirós PM, Ramsay AJ, Sala D, Fernández-Vizarra E, Rodríguez F, Peinado JR, Fernández-García MS, Vega JA, Enríquez JA, Zorzano A, *et al* (2012) Loss of mitochondrial protease OMA1 alters processing of the GTPase OPA1 and causes obesity and defective thermogenesis in mice. *EMBO J* 31: 2117–33
- Ratheiser K, Schneeweiß B, Waldhäusl W, Fasching P, Korn A, Nowotny P, Rohac M & Wolf HPO (1991) Inhibition by etomoxir of carnitine palmitoyltransferase I reduces hepatic glucose production and plasma lipids in non-insulin-dependent diabetes mellitus. *Metabolism* 40: 1185–1190
- Rauckhorst AJ, Gray LR, Sheldon RD, Fu X, Pewa AD, Feddersen CR, Dupuy AJ, Gibson-Corley KN, Cox JE, Burgess SC, *et al* (2017) The mitochondrial pyruvate carrier mediates high fat diet-induced increases in hepatic TCA cycle capacity. *Mol Metab* 6: 1468–1479
- Rocha AG, Franco A, Krezel AM, Rumsey JM, Alberti JM, Knight WC, Biris N, Zacharioudakis E, Janetka JW, Baloh RH, *et al* (2018) MFN2 agonists reverse mitochondrial defects in preclinical models of Charcot-Marie-Tooth disease type

2A. 360: 336–341

- Rolfe DFS & Brown GC (1997) Cellular energy utilization and molecular origin of standard metabolic rate in mammals. *Physiol Rev* 77: 731–758
- Ruderman N & Prentki M (2004) AMP kinase and malonyl-CoA: targets for therapy of the metabolic syndrome. *Nat Rev Drug Discov* 3: 340–351
- Rui L (2014) Energy metabolism in the liver. *Compr Physiol* 4: 177–97
- Satapati S, Kucejova B, Duarte JAG, Fletcher JA, Reynolds L, Sunny NE, He T, Arya Nair L, Livingston K, Fu X, *et al* (2015) Mitochondrial metabolism mediates oxidative stress and inflammation in fatty liver. *J Clin Invest* 125: 4447–4462
- Schreurs M, Kuipers F & van der Leij FR (2010) Regulatory enzymes of mitochondrial β -oxidation as targets for treatment of the metabolic syndrome. *Obes Rev* 11: 380–388
- Sebastián D, Hernández-Alvarez MI, Segalés J, Sorianello E, Muñoz JP, Sala D, Waget A, Liesa M, Paz JC, Gopalacharyulu P, *et al* (2012a) Mitofusin 2 (Mfn2) links mitochondrial and endoplasmic reticulum function with insulin signaling and is essential for normal glucose homeostasis. *Proc Natl Acad Sci U S A* 109: 5523–5528
- Sebastián D, Hernández-Alvarez MI, Segalés J, Sorianello E, Muñoz JP, Sala D, Waget A, Liesa M, Paz JC, Gopalacharyulu P, *et al* (2012b) Mitofusin 2 (Mfn2) links mitochondrial and endoplasmic reticulum function with insulin signaling and is essential for normal glucose homeostasis. *Proc Natl Acad Sci U S A* 109: 5523–8
- Smith GI, Shankaran M, Yoshino M, Schweitzer GG, Chondronikola M, Beals JW, Okunade AL, Patterson BW, Nyangau E, Field T, *et al* (2020) Insulin resistance

- drives hepatic de novo lipogenesis in nonalcoholic fatty liver disease. *J Clin Invest* 130: 1453–1460
- Song JE, Alves TC, Stutz B, Šestan-Peša M, Kilian N, Jin S, Diano S, Kibbey RG & Horvath TL (2021) Mitochondrial fission governed by drp1 regulates exogenous fatty acid usage and storage in hela cells. *Metabolites* 11
- Srinivasan S, Guha M, Kashina A & Avadhani NG (2017) Mitochondrial dysfunction and mitochondrial dynamics-The cancer connection. *Biochim Biophys Acta - Bioenerg* 1858: 602–614 doi:10.1016/j.bbabi.2017.01.004 [PREPRINT]
- Stiles L & Shirihai OS (2012) Mitochondrial dynamics and morphology in beta-cells. *Best Pract Res Clin Endocrinol Metab* 26: 725–738 doi:10.1016/j.beem.2012.05.004 [PREPRINT]
- Sunny NE, Parks EJ, Browning JD & Burgess SC (2011) Excessive hepatic mitochondrial TCA cycle and gluconeogenesis in humans with nonalcoholic fatty liver disease. *Cell Metab* 14: 804–810
- Supale S, Li N, Brun T & Maechler P (2012) Mitochondrial dysfunction in pancreatic β cells. *Trends Endocrinol Metab* 23: 477–487 doi:10.1016/j.tem.2012.06.002 [PREPRINT]
- Taddeo EP, Hargett SR, Lahiri S, Nelson ME, Liao JA, Li C, Slack-Davis JK, Tomsig JL, Lynch KR, Yan Z, *et al* (2017) Lysophosphatidic acid counteracts glucagon-induced hepatocyte glucose production via STAT3. *Sci Rep* 7: 127
- Titchenell PM, Quinn WJ, Lu M, Chu Q, Lu W, Li C, Chen H, Monks BR, Chen J, Rabinowitz JD, *et al* (2016) Direct Hepatocyte Insulin Signaling Is Required for Lipogenesis but Is Dispensable for the Suppression of Glucose Production. *Cell*

Metab 23: 1154–1166

Trudeau KM, Colby AH, Zeng J, Las G, Feng JH, Grinstaff MW & Shirihai OS (2016)

Lysosome acidification by photoactivated nanoparticles restores autophagy under lipotoxicity. *J Cell Biol* 214: 25–34

Turpin SM, Nicholls HT, Willmes DM, Mourier A, Brodesser S, Wunderlich CM, Mauer J,

Xu E, Hammerschmidt P, Brönneke HS, *et al* (2014) Obesity-induced CerS6-dependent C16:0 ceramide production promotes weight gain and glucose intolerance. *Cell Metab* 20: 678–686

Twig G, Elorza A, Molina AJA, Mohamed H, Wikstrom JD, Walzer G, Stiles L, Haigh SE,

Katz S, Las G, *et al* (2008a) Fission and selective fusion govern mitochondrial segregation and elimination by autophagy. *EMBO J* 27: 433–446

Twig G, Elorza A, Molina AJA, Mohamed H, Wikstrom JD, Walzer G, Stiles L, Haigh SE,

Katz S, Las G, *et al* (2008b) Fission and selective fusion govern mitochondrial segregation and elimination by autophagy. *EMBO J* 27: 433–446

Twig G, Hyde B & Shirihai OS (2008c) Mitochondrial fusion, fission and autophagy as a

quality control axis: The bioenergetic view. *Biochim Biophys Acta - Bioenerg* 1777: 1092–1097

UNGER RH & Orci L (2001) Diseases of liporegulation: new perspective on obesity and

related disorders. *FASEB J* 15: 312–321

Vernia S, Cavanagh-Kyros J, Garcia-Haro L, Sabio G, Barrett T, Jung DY, Kim JK, Xu

J, Shulha HP, Garber M, *et al* (2014) The PPAR α -FGF21 hormone axis contributes to metabolic regulation by the hepatic JNK signaling pathway. *Cell Metab* 20: 512–525

- Wada J & Nakatsuka A (2016) Mitochondrial dynamics and mitochondrial dysfunction in diabetes. *Acta Med Okayama* 70: 151–158 doi:10.18926/AMO/54413 [PREPRINT]
- Wajchenberg BL (2010) Clinical Approaches to Preserve β -Cell Function in Diabetes. In pp 515–535. Springer, Dordrecht
- Wang L, Ishihara T, Ibayashi Y, Tatsushima K, Setoyama D, Hanada Y, Takeichi Y, Sakamoto S, Yokota S, Mihara K, *et al* (2015) Disruption of mitochondrial fission in the liver protects mice from diet-induced obesity and metabolic deterioration. *Diabetologia* 58: 2371–2380
- Whitley BN, Lam C, Cui H, Haude K, Bai R, Escobar L, Hamilton A, Brady L, Tarnopolsky MA, Dengle L, *et al* (2018) Aberrant Drp1-mediated mitochondrial division presents in humans with variable outcomes Human Molecular Genetics, Vol. 00, No. 0 Human Molecular Genetics, Vol. 00, No. 0. *Hum Mol Genet* 27: 3710–3719
- Wikstrom JD, Katzman SM, Mohamed H, Twig G, Graf S a., Heart E, Molina AJ a, Corkey BE, De Vargas LM, Danial NN, *et al* (2007) Beta-Cell mitochondria exhibit membrane potential heterogeneity that can be altered by stimulatory or toxic fuel levels. *Diabetes* 56: 2569–2578
- Wikstrom JD, Mahdavian K, Liesa M, Sereda SB, Si Y, Las G, Twig G, Petrovic N, Zingaretti C, Graham A, *et al* (2014) Hormone-induced mitochondrial fission is utilized by brown adipocytes as an amplification pathway for energy expenditure. *EMBO J* 33: n/a-n/a
- Wikstrom JD, Twig G & Shirihai OS (2009) What can mitochondrial heterogeneity tell us about mitochondrial dynamics and autophagy? *Int J Biochem Cell Biol* 41: 1914–

1927 doi:10.1016/j.biocel.2009.06.006 [PREPRINT]

- Win S, Than TA, Min RWM, Aghajan M & Kaplowitz N (2016) c-Jun N-terminal kinase mediates mouse liver injury through a novel Sab (SH3BP5)-dependent pathway leading to inactivation of intramitochondrial Src. *Hepatology* 63: 1987–2003
- Wolf DM, Segawa M, Kondadi AK, Anand R, Bailey ST, Reichert AS, Bliet AM, Shackelford DB, Liesa M & Shirihai OS (2019) Individual cristae within the same mitochondrion display different membrane potentials and are functionally independent. *EMBO J* 38
- Xiong J & Zhao WL (2018) Targetable Metabolic Vulnerability in Diffuse Large B-Cell Lymphoma. *EBioMedicine* 28: 5–6
- Yamane M, Moriya S & Kokuba H (2017) Visualization of ceramide channels in lysosomes following endogenous palmitoyl-ceramide accumulation as an initial step in the induction of necrosis. *Biochem Biophys reports* 11: 174–181
- Young S, Tariq R, Provenza J, Satapathy SK, Faisal K, Choudhry A, Friedman SL & Singal AK (2020) Prevalence and Profile of Nonalcoholic Fatty Liver Disease in Lean Adults: Systematic Review and Meta-Analysis. *Hepatol Commun* 4: 953–972
- Zhan M, Brooks C, Liu F, Sun L & Dong Z (2013) Mitochondrial dynamics: Regulatory mechanisms and emerging role in renal pathophysiology. *Kidney Int* 83: 568–581
doi:10.1038/ki.2012.441 [PREPRINT]
- Zhang W, Bu SY, Mashek MT, O-Sullivan I, Sibai Z, Khan SA, Ilkayeva O, Newgard CB, Mashek DG & Unterman TG (2016) Integrated Regulation of Hepatic Lipid and Glucose Metabolism by Adipose Triacylglycerol Lipase and FoxO Proteins. *Cell Rep* 15: 349–359

Zhou X, Zhu X, Zeng H & Zeng CH (2021) Fatty acid metabolism in adaptive immunity.

FEBS J

Zorova LD, Popkov VA, Plotnikov EY, Silachev DN, Pevzner IB, Jankauskas SS,

Babenko VA, Zorov SD, Balakireva A V., Juhaszova M, *et al* (2018) Mitochondrial membrane potential. *Anal Biochem* 552: 50–59

Zorzano A, Liesa M & Palacín M (2009) Role of mitochondrial dynamics proteins in the

pathophysiology of obesity and type 2 diabetes. *Int J Biochem Cell Biol* 41: 1846–1854 doi:10.1016/j.biocel.2009.02.004 [PREPRINT]

Zorzano A, Liesa M, Sebastián D, Segalés J & Palacín M (2010) Mitochondrial fusion

proteins: Dual regulators of morphology and metabolism

CHAPTER 2

Mitochondrial architecture controls fatty acid utilization by regulating CPT1 sensitivity to malonyl-CoA

The work describe in this chapter has been submitted to the EMBO Journal and is currently under revision:

Jennifer Ngo*, Dong Wook Choi*, Anthony Molina, Linsey Stiles, Nathaniel Miller, Siyouneh Bagdasharian, Anthony Jones, Brett Roach, Kristen Kim, Karel Erion, Sam B Sereda, Jakob D Wikstrom, Evan Taddeo, Ajit Divakaruni, David Chan, Barbara E Corkey, Marc Liesa, Orian Shirihai**, Nika Danial**. (2022) Mitochondrial architecture controls fatty acid utilization by regulating CPT1 sensitivity to malonyl-CoA. *EMBO Journal*.

*, ** contributed equally

Copyright 2022

The EMBO Journal

I was co-first author of this work and conducted the imaging and in vitro experiments. Dong Wook Choi conducted experiments in the DLBCL model, and Anthony Molina and Linsey Stiles conducted experiments in the Mfn2KO animal model. Professor Orian Shirihai and I wrote the manuscript.

ABSTRACT

Mitochondrial architecture has long been associated with metabolic flexibilities, although the precise causalities and the underlying mechanisms are still enigmatic. Herein, using multiple cellular models where the physiological relevance of fatty acid is well-established, we showed that mitochondrial fragmentation is highly associated with fatty acid oxidation (FAO) rates. Furthermore, forced mitochondrial elongation using Mfn2 over-expression or Drp1 depletion significantly decreased FAO rates, while Mfn2 KO leads to enhanced FAO rates, suggesting that mitochondrial fragmentation is functionally coupled with fatty acid utilization. Such manipulations also changed FAO-regulated cellular physiologies including gluconeogenesis in hepatocytes, insulin secretion in islet beta-cells, and cell survival of various DLBCL cancer subtypes. Notably, the increased FAO upon mitochondrial fragmentation is attributed to decreased CPT1 sensitivity to malonyl-CoA, the endogenous CPT1 inhibitor, consistent with the observation that such biochemical connections are fatty acid chain length-specific; mitochondrial fragmentation specifically facilitates long chain-fatty acid oxidation (LCFAO), but not short chain fatty acid oxidation. Taken together, our study provides a biochemical and mechanistic explanation of how mitochondrial architecture links cellular metabolic needs to differential fuel utilization, such as LCFAO, which may be implicated in a myriad of human physiologies and pathologies.

INTRODUCTION

Mitochondrial dynamics maintain quality control of energy metabolism. Cells in nutrient-rich environment tend to keep their mitochondria in a fragmented state while cells under starvation reveal the opposite phenotype, mitochondrial elongation. Arrest of mitochondrial fusion (and not increased fission) is largely responsible for mitochondrial fragmentation in conditions which mimic obesity, suggesting that mitochondrial fusion proteins, mitofusin 1& 2 (Mfn1 & Mfn2) and optic atrophy 1 (Opa1), may be involved in the regulation of morphology in response to an excess nutrient supply. Functionally, previous studies have shown liver-specific ablation of Mfn2 in mice led to numerous metabolic abnormalities, characterized by glucose intolerance and enhanced hepatic gluconeogenesis (Sebastián *et al*, 2012b). Conversely, other groups have shown disruption of hepatic mitochondrial fission, through depletion of dynamin-related protein 1 (DRP1), results in elongated mitochondria, improved glucose tolerance, and decreased gluconeogenesis (Mynatt *et al*, 1994; Wang *et al*, 2015). Similarly, fragmented mitochondria of beta-cell specific Mfn1/2 dKO displayed impaired glucose sensing, insulin secretion, and glucose homeostasis (Georgiadou *et al*, 2020). In the same context, OMA1 knockout mice revealed disruption of the mitochondrial fusion-fission equilibrium (OMA1-Opa1 interaction) led to increased obesity due to the inability to fragment and thus favored fatty acids (Quirós *et al*, 2012). Although investigations implicate mitochondrial fragmentation and elongation as bioenergetic adaptations to various metabolic demands and nutrient availability, no known mechanism has been resolved (Frank *et al*, 2001; Liesa & Shirihai, 2013b).

Impairment of mitochondrial function and the mitochondrial network has been

associated with obesity related diseases. In the obese and insulin-resistant Zucker diabetic (ZDF) rats, which express a non-functioning leptin receptor (Ob-Rb), skeletal muscle displayed a reduction in the fusion protein, Mfn2, thereby yielding fragmented mitochondria (Putti *et al*, 2015). The reduced Mfn2 expression was also seen, clinically, in skeletal muscle of obese type 2 diabetic patients (Bach *et al*, 2003). Additionally, ZDF rats have shown increased hepatic fatty acid oxidation (FAO) rates, indicating a potential change in CPT-1A regulation due to changes in mitochondrial architecture (Ruderman & Prentki, 2004). Similarly, lean rats fed a high fat diet rich in saturated fatty acids manifested hepatic fat accumulation and an increase in mitochondrial fatty acid utilization. Interestingly, this high saturated fatty acid diet also decreased Mfn2 and increased fission processes (Lionetti *et al*, 2014). Moreover, pancreatic beta-cells of ZDF rats and beta-cells chronically treated with elevated FFA at high glucose levels revealed mitochondrial dysfunction and fragmentation (Liesa & Shirihai, 2013b; Ruderman & Prentki, 2004). Although elevated glucose levels increased malonyl-CoA levels, it was shown that FAO was favored as a fuel source and was sufficient in preventing glucolipotoxicity-induced apoptosis. Additionally, brown adipose tissue preferentially oxidizes fatty acids upon complete mitochondrial fragmentation and depolarization, supporting the observed correlation of mitochondrial fragmentation and fuel preference for FAO (Liesa & Shirihai, 2013b). In previous studies, enhanced respiratory capacity and preference for lipids as the main energy source were observed in liver specific Mfn1 ablated mitochondria with increased expression of ETC complexes and a highly fragmented mitochondrial network (Kulkarni *et al*, 2016). Thus, whether increased FAO capacity and increased HGP are due to changes in mitochondrial morphology have not yet been determined. Although it

has been demonstrated in multiple cell types that an excess nutrient environment promotes mitochondrial fragmentation and a switch to FAO, there currently remains no known mechanism of increased FAO. Several factors can account for increased fatty acid utilization, including higher expression of enzymes involved in mitochondrial beta-oxidation and the ETC machinery, and increased mitochondrial mass.

FAO is a multi-step process largely occurring in the mitochondria where the liver produces energy by shortening very-long chain fatty acids to produce Acetyl-CoA and ketone bodies. This process is highly regulated, however, long-chain acyl-CoAs (chains comprised of 12 or more carbons) are not permeable across the mitochondrial inner membrane therefore, carnitine palmitoyl transferase 1 (CPT-1) is required for shuttling long-chain acyl-CoAs into the mitochondria from the cytoplasm. CPT-1 thereby plays a central role in regulating FAO as the rate-limiting step (Cook & Gamble, 1987). In the presence of increased glucose concentrations, import of fatty acids to mitochondria via CPT-1 is inhibited by malonyl-CoA, a glucose-metabolism product. malonyl-CoA thereby serves as a shut-off switch for FAO by inhibiting beta-oxidation and promoting anabolic processes. It is important to note that there are three isoforms of CPT1: CPT-1A (liver), CPT-1B (muscle), and CPT-1C (brain), all of which have tissue-specific distribution (Flavin *et al*, 2010; Schreurs *et al*, 2010). Due to this tissue-specific distribution, the sensitivity of each isoform to their endogenous inhibitor, malonyl-CoA, differs greatly. The liver isoform, CPT-1A, has a tenfold higher K_i for malonyl-CoA making it the prevailing enzyme that accomplishes the rate-limiting step in FAO (Casals *et al*, 2016; McGarry & Brown, 1997). Additionally, the sensitivity of CPT-1A to malonyl-CoA inhibition changes during the transition of fed to fasting states, generating an amplification system to control

FAO. In the diabetic patient, the affinity of CPT-1A for malonyl-CoA decreases and the activity of CPT-1A is increased (Cook & Gamble, 1987). In alignment with previous studies, sensitivity of CPT-1A has been observed to decrease when its tertiary structure is altered due to changes in membrane structure (López-Viñas *et al*, 2007). Here, we demonstrate mitochondrial architecture affects CPT1 sensitivity to malonyl-CoA in hepatocytes, B-cell lymphomas, and in islets, which, in turn, controls FAO. Mitochondrial morphology not only play a role in preferential fuel utilization, but the unique differences between tissues indicate morphology is important to bioenergetics and pathophysiology (Wajchenberg, 2010; Titchenell *et al*, 2016; Zhang *et al*, 2016).

EXPERIMENTAL PROCEDURES

Animals

C57BL/6J male mice (8 weeks old) were obtained from The Jackson Laboratory. At 9 weeks old, mice were put on a custom diet from Research Diets (D09100310) containing 40% fat, 20% fructose, and 2% cholesterol or a control diet (PicoLab Rodent Diet 20 5053) for 14-19 weeks (23-28 weeks of age). All animal care was in accordance with National Institutes of Health guidelines and University of California, Los Angeles (UCLA), institutional animal care and use committee approval (UCLA protocol #16–018). Mice were housed at the UCLA Animal Resources Facility in a 12-h/12-h light-dark cycle and maintained at 20–22.2°C. Animals were provided water and food ad libitum until the day of islet isolation.

All animal procedures for primary hepatocytes cultures were approved by the Institutional Animal Care and Use Committee of Dana-Farber Cancer Institute. Mice were

put on a standard chow diet and were housed at a barrier facility in a 12-h/12-h light-dark cycle and maintained at 20–22.2°C. Animals were provided water and food ad libitum until the day of hepatocytes isolation.

Plasmids, Lentivirus, and Cell Culturing

Clonal HepG2 cells were cultured in low glucose (5mM) Dulbecco's Modified Eagle Medium (Ref#31600-026) supplemented with 10% FBS, 50 U/ml penicillin, and 5mM HEPES buffer. For excess nutrient conditions, cells were incubated for 19hrs in 25mM Dulbecco's Modified Eagle Medium (Ref#12100-038) supplemented with 2% FBS, 50 U/ml penicillin, 5mM HEPES buffer, and 250µM 4:1 palmitate: BSA.

Clonal INS1 cells were cultured in RPMI-1640 media supplemented with 10% FBS, 10 mM HEPES buffer, 1 mM pyruvate, 50 µM 2-β-mercaptoethanol, 50 U/ml penicillin and 50 µg/ml streptomycin. 1×10^5 cells were seeded per cell culture microplate (Seahorse Bioscience) well the day prior to experiment as described previously (Wikstrom et al. 2012). For excess nutrient conditions, cells were incubated for 19hrs in 20mM RPMI-1640 media supplemented with 10% FBS, 10 mM HEPES buffer, 1 mM pyruvate, 50 µM 2-β-mercaptoethanol, 50 U/ml penicillin and 50 µg/ml streptomycin and 300µM 4:1 palmitate: BSA.

All DLBCL-OxPhos (Toledo and Pfeiffer) and BCR cell lines (DHL4, DHL6 were cultured in RPMI supplemented with 10% fetal bovine serum, 2 mM glutamine, 2 mM HEPES, and 1% penicillin/streptomycin with following exception. HBL1 cells were grown in the aforementioned medium supplemented with 1% sodium pyruvate. Ly3, Ly10 cells

were cultured in IMDM containing 20% fetal bovine serum or human serum AB (Gemini, West Sacramento, CA), respectively.

Viruses and siRNAs used for genetic modifications include Mfn2KD (Ad-miR2 encoding for 5 miRNAs against Mfn2; PMID: 22427360), dnDrp1 (welgen; gift from the Van Der Blik lab; PMID:18200046), Drp1 siRNA (ambion; AM51331; ID#19561; lot#ASO2814C), and Mfn2OE (Virovek; lot#17-606).

Respirometry

Respirometry in Intact Islet & INS1 Cells

Respirometry of whole murine islets and isolated INS1 cell mitochondria were performed using the Seahorse Bioscience XF 24 and XF96 platform (Agilent Technologies, Santa Clara, CA) as previously described (Ferrick et al., 2008). Wild type islets, β Mfn2 KO, chow, and HFD islets were isolated and allowed to recover after isolation in culture overnight before respirometry was performed.

For XF24 assays, an 80-micron screen kept islets in place directly over the oxygen sensors. After 3 days, mitochondria were isolated and respirometry was performed using the Seahorse XF 24. Data was normalized by islet number and size. Drug concentrations were as follows: 5 μ M oligomycin, 1 μ M FCCP, 5 μ M rotenone, and 5 μ M antimycin A (Sigma). In order to ensure the number of mitochondria was consistent between groups; 40 μ g of protein was loaded into every well.

For XF96 assays, islets (1–6 per well) were seeded in 1 μ L/well Matrigel in a poly-d-lysine-coated XF96 plate and size matched between conditions. Islets were incubated at 37°C for 3.5 min to solidify the Matrigel before the addition of 100–150 μ L/well Seahorse assay media (XF Base Media Minimal DMEM, pH 7.4, supplemented with 3

mmol/L glucose and 0.1% FBS). Islets were incubated at 37°C for 1 hr before starting the assay (without CO₂) (Wu et al.,2007). For port injections, indicated nutrients/compounds were injected in port A (final concentrations in figure legends) followed by oligomycin (final concentration 4.5 µmol/L) in port B, FCCP diluted in a mixture of 80% sodium pyruvate and 20% of 1:1 l-leucine/l-glutamine (final concentration 1 µmol/L FCCP in 11.4 mmol/L sodium pyruvate and 2.9 mmol/L each of leucine/glutamine) in port C, and antimycin A (final concentration 2.5 µmol/L) in port D.

For respirometry experiments in INS1 cells, cells were transfected with a micro RNA mfn2 KD delivered by adenovirus at a MOI of 500. After 3 days, respirometry was performed using the Seahorse XF 96. Prior to the assay, INS1 cells were incubated for 1hr in 100–150 µL/well Seahorse assay media (XF Base Media Minimal DMEM, pH 7.4, supplemented with 2 mmol/L glucose, 1mM sodium pyruvate, and 2mM l-glutamine) at 37°C (without CO₂) (Wu et al.,2007). For port injections, indicated nutrients/compounds were injected in port A (final concentrations in figure legends) followed by oligomycin (final concentration 3 µmol/L) in port B, FCCP diluted in sodium pyruvate (final concentration 1 µmol/L FCCP in 11.4 mmol/L sodium pyruvate) in port C, and antimycin A (final concentration 2 µmol/L) in port D.

Respirometry in isolated mitochondria from DLBCLs

OCR measurement was carried out using the XF24 extracellular flux analyzer instrument and the AKOS algorithm v1.5.069 software (Seahorse Bioscience Inc., Chicopee, MA). Briefly, the heavy membrane fraction containing mitochondria isolated as mentioned in this section was loaded on XF24 V7 plates at 15 ug/well in 100 uL of mitochondria assay solution (MAS; 70 mM sucrose, 220 mM mannitol, 10 mM KH₂PO₄,

5 mM MgCl₂, 2 mM HEPES pH 7.2, 1 mM EGTA, 0.2% defatted BSA). 300 µl MAS was added on top of the samples, and the plates were incubated at 37°C for 10 min. Different mitochondrial respiratory states was measured in as previously described (Chance and Williams, 1955). Briefly, OCR was measured in 4 to 6 min periods with 30 s intervals between measurements for 37 min. State II respiration (non-phosphorylating state) was measured following addition of respiratory substrates including of glutamate/malate or succinate at 5 mM each in 100 µl MAS. For state III and IV, measurement, 2 mM ADP and 4 µM oligomycin were sequentially added in plates using the instrument's individual injection ports. Following oligomycin administration, 4 µM of the uncoupler FCCP and antimycin A (AA) were consecutively added into the plate for the experimental quality control assessment in all experiments.

Respirometry in Permeabilized Cells

HepG2 and INS1 cells were permeabilized using 8-12nM XF PMP reagent (Agilent Technologies, Santa Clara, CA). Respirometry assay was performed in MAS buffer (220 mM mannitol, 70 mM sucrose, 10 mM KH₂PO₄, 5 mM MgCl₂, 2 mM HEPES, and 1 mM EGTA) supplemented with 0.5mM malic acid and 0.2% BSA. The following substrates were used: 5 mM pyruvate, 5 mM malate, 5 mM succinate, 2 µM rotenone, 40µM palmitoyl-CoA, 0.5 mM carnitine, 40µM palmitoyl-carnitine, 4 mM ADP, 0.5 µM malonyl-CoA, and 3 µM etomoxir (Sigma-Aldrich, St. Louis, MO). The following compounds were injected: 6 µM oligomycin (Calbiochem, San Diego, CA), 3 µM Carbonyl cyanide 4-(trifluoromethoxy) phenylhydrazone (FCCP; Sigma-Aldrich, St. Louis, MO), 4 µM antimycin A (Sigma-Aldrich, St. Louis, MO). Oxygen consumption rates were measured using the Seahorse XF96 extracellular flux analyzer (Agilent Technologies, Santa Clara,

CA). All respiratory modulators were used at ideal concentrations titrated during preliminary experiments (not shown) and oxygen consumption rates were recorded for up to 15 min due to the toxicity of these compounds. After the assay, cells were fixed using 4% paraformaldehyde (Thermo Fisher Scientific, Roskilde, Denmark) and normalized by cell count. Cells were stained with 1 µg/mL Hoechst 33342 (Thermo Fisher Scientific, Roskilde, Denmark) then imaged using an Operetta high-throughput imaging device (PerkinElmer, Waltham, MA) with 350/461nm (EX/EM) under 2x or 10x objectives. All the OCR values were subtracted from the lowest antimycin OCR.

Confocal Microscopy and Immunostaining

Confocal microscopy was performed on live cells in glass bottom dishes (MatTek, Ashland, MA) using an inverted Leica TCS SP2 confocal microscope or a Zeiss LSM 710 DUO with a plan apochromat 100x (NA = 1.4) oil immersion objectives. Super-resolution live-cell imaging was performed on a Zeiss LSM880 using a 63x Plan-Apochromat oil-immersion lens and AiryScan super-resolution detector with humidified 5% CO₂ chamber on a temperature-controlled stage (37°C). Mitochondria were stained with 15nM Tetramethylrhodamine Ethyl Ester Perchlorate (TMRE) (Invitrogen, Eugene, OR.) or with 200 nM MitoTracker green (MTG) (Thermo Fisher Scientific, Roskilde, Denmark) for 45 minutes prior to imaging. Insulin promoter mediated paGFP expression in the mitochondrial matrix was induced by lentiviral transduction. The generation of these constructs was previously described in detail (Molina and Shirihai, 2009). MTG was excited with 488 nm laser and TMRE was excited with 561 nm laser.

For immunostaining, cells were plated on poly-D-lysine coated coverslips 72 hrs prior imaging. Cells were fixed at 4% vol/vol paraformaldehyde (PFA) for 15 min at room

temperature. After washing two times in PBS, cells were incubated in 50mM NH₄Cl for 10min at room temperature to block unspecific antibody binding by the PFA. The 50mM NH₄Cl was aspirated and cells were incubated in 20mM glycine in PBS for 10min. Afterwards, cells were then incubated in permeabilization buffer (2 µl/ml Triton X-100 and 0.5 mg/ml sodium deoxycholate in PBS, pH 7.4) for 15 min at room temperature. Subsequently, cells were blocked with 10% FBS for 1 hr at room temperature. Next, cells were incubated with 1:200 primary antibody of GPR75/Mortalin (Abcam, ab110325) at 4 °C overnight. The next day, cells were washed in PBS and incubated with 1:200 primary antibody of TOM20 (Santa Cruz, Tom20 FL-145) at 4 °C for overnight. On the last day, cells were incubated with 1:500 Anti-Rabbit Alexa Fluor 488 (Thermo, A11008) or Anti-Mouse Alexa Fluor 568 antibodies (Thermo, A11004) for 1 hr at room temperature, and samples were kept in PBS. A Zeiss LSM 880 confocal microscope in Airyscan mode was used for super-resolution imaging, with a 488 nm Argon laser and Zeiss 63x/1.4NA oil immersion objective.

Analysis of Mitochondrial Morphology

At least 3 separate experiments and 30 cells per condition per experiment were collected for all three cell types, the cells were individualized as areas of interest using FIJI ImageJ software (<https://fiji.sc/>). Identifying mitochondria within areas of interest were individualized through the CellProfiler cell image analysis software (<https://cellprofiler.org/>). To minimize background, images were subjected to a median filter. Segmentation of mitochondria was performed by utilizing a global, three-class, otsu-thresholding method and minimizing the weighted-variance to shape. Identified objects were then subjected to automated mitochondrial form factor (the degree of branching (FF;

perimeter $2/4\pi$ *area)), eccentricity, and aspect ratios (the proportional relationship between width and height) were measured. Data are presented as symbols that represent average form factor, eccentricity, and aspect ratio per cell. Mitochondrial fission is expected to decrease form factor towards a value of 1, decrease eccentricity towards a value of 0, and decrease the aspect ratio. Representative images shown were adjusted in brightness and contrast for better visualization.

Isotope tracing analysis

For stable isotope tracing analysis, primary hepatocytes or DLBCLs with genetic manipulation (dnDrp1 or Mfn2 expression) or pharmacological activation of CPT1 (C75 (C5490, Sigma-Aldrich): 80 uM, 3hr or Baicalin (572667, Sigma-Aldrich): 100 uM, 3hr) were cultured in aforementioned media supplemented with the ^{13}C isotope tracer of interest. Isotope tracers were employed at the following concentrations: 200 uM BSA-conjugated U- ^{13}C -palmitate, 50 uM 1- ^{13}C hexanoic acids (all from Cambridge Isotope Laboratories, Tewksbury, MA). Cells were incubated for 2 h prior to the harvest.

Metabolite extraction and derivatization

Metabolite extraction was carried out as previously described (PMID: 24550282; 24348278; 32694660). Briefly, primary hepatocytes cells were gently washed twice on the plates with 1 mL of ice-cold isotonic saline solution (0.9% NaCl), whereas DLBCLs were pelleted in 1.5 mL eppendorf tube, followed by two times of washes with the ice-cold isotonic saline solution. After the washes, metabolites were extracted in 350 μL of ice-cold 80% methanol solution supplemented with 2 $\mu\text{g}/\text{mL}$ norvaline (as an internal control). The cells were sonicated at high intensity with a 10 sec on/off cycle for 10 min at 4 $^{\circ}\text{C}$ using a BioRuptor (UCD-200 TM, Diagenode). Samples were then pelleted for 10

min at 16,400 rpm at 4 °C. The supernatants were transferred into new vials for drying overnight in a vacuum centrifuge (Labconco, Kansas City, MO) at 4 °C. Dried extracts were desolved in 10 mg/mL methoxylamine in pyridine (Sigma Aldrich). After the incubation for 30 min at 37 °C, the samples were derivatized with 70 µL of N-methyl-N-tert-butyldimethylsilyltrifluoroacetamide (MTBSTFA, Sigma) for 1 h at 70 °C.

Metabolite analysis by GC-MS

GC-MS for metabolite analysis were carried out as previously described (PMID: 24550282; 24348278; 24304688; 32694660). Briefly, samples were run on an Agilent 5977B mass selective detector coupled to a 7890B gas chromatograph (Agilent Technologies, Santa Clara, CA) with a 7693 autosampler and a DB-5MS+DG capillary column (30 m plus 10 m Duraguard® by Agilent Technologies). Data collection was conducted in electron ionization set at 70 eV. 1 µL of the derivatized sample was injected in splitless mode at 280 °C (inlet temperature), using helium as a carrier gas with a flow rate of 1.5512 mL/min. The quadrupole was set at 150 °C with GC/MS interface at 285 °C. The oven program for all the metabolite analyses initiated at 60 °C held for 1 min, then increased at a rate of 10 °C/min until 320 °C. Data were minded in full scan mode (1–600 m/z). All metabolites measured in this study were previously validated standards with mass spectra and retention times (PMID: 24348278).

GC-MS data analysis

Integration of peak area was performed using MassHunter Quantitative Analysis (Agilent Technologies). Measurement of carbon flux was conducted using previously developed algorithms including natural isotope enrichment correction and mass isotope distributions (MIDs) (PMID: 24304688, 24304688, 32694660, 24304688, 17035687).

Hepatic Glucose Production

Primary hepatocytes in six-well plates were cultured in M199 media supplemented with 1% BSA overnight. The medium was then replaced with 1 ml of glucose-free DMEM without phenol red, supplemented with 20 mM sodium lactate and 2 mM sodium pyruvate. After a 6 hr incubation, 200 μ l of the medium was collected and pelleted at 3,000 rpm for 2 mins to remove floating cells or cell debris, then 30 μ l of the supernatants was taken to measure the glucose concentration with a colorimetric glucose assay kit (GAGO20-1KT, Sigma-Aldrich). The readings were normalized to the total protein concentration measured by BCA kit (23227, Thermo Fisher Scientific, Roskilde, Denmark).

Western Blot

Primary antibodies used include anti-Mfn2 (ab56889, AbCam, Cambridge, MA), anti-Beta-Actin (NB600-501, Novus Biologicals, Littleton, CO), anti-porin (ab61273, AbCam, Cambridge, MA), anti-CPT1A [C1C2] (GTX114337, GeneTex, Irvine, CA), and anti-vinculin (V9131, Sigma-Aldrich).

Cell lysates were diluted in Laemmli sample buffer (100 mM Tris-HCl, 2% SDS, 10% glycerol, 0.1% bromophenol blue) containing 5% β -mercaptoethanol. After heating at 95°C, proteins were separated by SDS-PAGE and transferred onto PVDF membranes. Membranes were blocked with 5% non-fat milk or 5% BSA and detection of individual proteins was carried out by blotting with specific primary antibody against CPT1A [C1C2] (GeneTex, 1:1000), Mfn2 (Abcam, 1:1,000), VDAC (Abcam, 1:1,000), beta-actin (1:1,000, Santa Cruz), and vinculin (Sigma-Aldrich, 1:10,000). Proteins of interest were detected by chemiluminescence using a secondary peroxidase-linked anti-rabbit (1:10,000) or anti-mouse (1:10,000) and a detection system.

Pa-GFP activation and imaging of mitochondria

Photoconversion of PA-GFPmt to its active (fluorescent) form was achieved by using 2-photon laser (750nm) to give a 375 nm photon-equivalence at the focal plane. This allowed for selective activation of regions that have submicron thickness and are less than 0.5 μm^2 . Using the multi-track scanning mode of the Zeiss LSM-710 microscope and the Zeiss LSM-880, red-emitting TMRE was excited with a 1 mW 543 nm helium / neon laser set at 0.3% and emission was recorded through a BP 650–710nm filter. Activated PA-GFPmt protein was excited using a 25 mW 488 nm argon laser set at 0.2%. Emission was recorded through a BP 500–550 nm filter. Prior work from our lab has determined optimal concentrations of probes and laser power to avoid photobleaching in our models (Twig et al. 2008), which was utilized in this study to avoid similar artifacts.

Measuring entrapment of ^{14}C -CO₂ from 14C-Palmitate

To test the production of CO₂ from palmitate, whole islets from 7-month-old female animals (25 islets per condition; n= 4; 400 islets total) were washed twice in PBS and preincubated for 30 min in 3mM glucose Krebs buffer (no BSA). Islets were then placed on a 5 min ice bath. Preincubation media was aspirated and islets were incubated in various buffer conditions (3mM glucose, 15mM glucose, or 10uM etomoxir in Krebs Buffer) 24 hrs at room temperature in the presence of 10uM of palmitate spiked with 0.2 μCi of 14C-U-palmitate. To trap the produced CO₂, Whatman paper was placed in the top of the tube and embedded in 2 drops of base (B-phenylethylamine) from a 1mL syringe w/ 23 gauge 1 ¼ inch needle. Acidification vials were prepared with 2 drops of 6M H₂SO₄. The ^{14}C CO₂ trapped by this reaction was quantified by scintillation. (PMID: 24862277, 9632669, 1654856)

Generation and genotyping of β Mfn2KO mice

The generation of Mfn2loxP mice has been previously described by Hsiuchen Chen (Chen et al., 2007). Briefly, ES clones (129 strain) carrying targeted mutations were injected into C57BL/6 blastocysts. Founder chimeric mice were bred to Black Swiss mice, and agouti offspring were bred to FLPeR mice to remove the neomycin resistance cassette. Resulting mice were maintained as homozygous stocks (Farley et al., 2000). B6. Cg-Tg(Ins2-cre)25Mgn/J mice (RIP-Cre) were obtained from JAX mice (Bar Harbor, ME.) and bred with homozygous Mfn2loxP to generate F1, double heterozygous mice. F1 mice were then bred with the original Mfn2loxP mice in order to generate the β Mfn2KO mice. Littermates include Mfn2loxP +/+ RIP-Cre -/- and Mfn2 +/- RIP-Cre -/- which were used as WT controls. In addition, Mfn2loxP +/- RIP-Cre +/- were tested and found to possess a mild phenotype.

Genotyping was performed by PCR of tail snip lysates (Viagen, DirectPCR, Los Angeles, CA.) obtained during the weaning of pups. Floxed Mfn2 transgene was detected using GoTaq Green Master Mix (Promega, Madison, WI.) and the following primers: gaa gta ggc agt ctc cat cg and ccc aag aag agc atg tgt gc. The unexcised conditional band is 810bp and the WT is 710 bp. Cre transgene was detected in the same samples by following the genotyping protocol provided by JAX Mice using the following primers: gcg gtc tgg cag taa aaa cta tc and gtg aaa cag cat tgc tgt cac tt.

Islet Isolation

Islets were isolated from 23–30-week-old mice through collagenase P injection into the bile duct, as previously described (Wikstrom et al. 2012; Lacy and Kostianovsky 1967), with minor modifications. Briefly, excised pancreata were digested in a 37°C water

bath for 8–10 min, and the digested tissue was washed with RPMI medium containing 1% fatty acid-free BSA. Isolated islets were then cultured overnight at 37°C in 5% CO₂ in mouse islet medium (11 mmol/L glucose RPMI medium + 10% FBS + 100 units/mL penicillin, and 100 µg/mL streptomycin) before experiments.

Insulin Secretion

Islets were cultured in RPMI 1640 media supplemented with 10% FBS and 50 U/ml penicillin and 50 µg/ml streptomycin overnight prior to insulin secretion assay. Insulin secretion was run in quintuplicate and collected in a parallel fashion. Islets were washed and preincubated for 30 min in modified Krebs-Ringer bicarbonate buffer (KRB) containing (in mM) 119 NaCl, 4.6 KCl, 5 NaHCO₃, 2 CaCl₂, 1 MgSO₄, 0.15 Na₂HPO₄, 0.4 KH₂PO₄, 20 HEPES, 2 glucose, 0.05% BSA, pH 7.4. This was followed by a 30 min incubation in media containing either 3 mM or 15 mM glucose. Media was collected and stored at –20°C for insulin measurement. Insulin was measured by radioimmunoassay (LINCO Research Inc., St. Charles, MO.). Normalization was performed by cell count then by lysing the cells and measuring total insulin content. In order to measure insulin secretion, islets from three different animals were measured per genotype. For each animal in the same samples whereby insulin secretion was assessed, islet insulin content was then measured in triplicate. For each measurement, six islets were lysed and diluted for insulin and protein measurements. Insulin was measured using the HTRF Insulin Assay (Cisbio Bioassays, Bedford, MA). Total protein was measured using the Bio-Rad Protein Assay, which is based on the Bradford method. Insulin content is presented as nanograms of insulin per milligram of total protein. Insulin concentration of the samples was calculated from an insulin standard curve (0–20 ng/mL or 0–100 ng/mL).

Palmitate-induced secretion was performed acutely, islets were incubated in media containing 0.4mM palmitate in addition to either 3mM or 15mM glucose for 30mins. Fatty acid sensitive secretion was performed with addition of 3 μ M etomoxir.

DLBCL survival

The cell viability of DLBCLs infected with adenovirus expressing dnDrp1 or Mfn1 was measured using the Annexin V: FITC Apoptosis Detection Kit (BD Bioscience) followed by flow cytometry.

Mitochondria isolation for CPT1 assay

DLBCLs or primary hepatocytes were resuspended in mitochondria isolation buffer (MIB; 200 mM mannitol, 70 mM sucrose; 1 mM EGTA; 10 mM HEPES, pH 7.4) supplemented with protease inhibitors, followed by homogenization with 20 strokes of a teflon-glass homogenizer. The nuclei and cell debris were pelleted at 1000 \times g for 5 min and the supernatant containing crude mitochondria was washed with MIB buffer twice. The resultant pellet including mitochondria-enriched heavy membrane (HM) fraction was resuspended in MIB for subsequent CPT1 enzyme activity assays.

CPT1 activity

CPT1 activity was measured according to a colorimetric assay established previously with slight modification (PMID:16542821, 21733226). Briefly, 15 μ g of isolated heavy membrane fractions containing mitochondria was loaded into the 96 well plates and filled up to 200 μ l with reaction buffer (2 mM DTNB, 116 mM Tris-HCl (pH 8.0), 2.5 mM EDTA, and 0.2 % Triton-X 100). The plates were incubated at RT for 20 mins to eliminate all pre-existing reactive thiol group in the heavy membrane fraction, then 100

mM palmitoyl CoA (Sigma-Aldrich) and 1 mM carnitine (Sigma-Aldrich), CPT1 substrate and cofactor respectively, were subsequently added to initiate the CPT1 assay reaction. After another 20 mins of incubation, release of CoA-SH from palmitoyl-CoA, as a readout of CPT1 activity, was spectrophotometrically determined at 412 nm using a Versa Max microplate reader (Molecular Devices, USA) in kinetics mode with 10 sec intervals for a total assay time of 1 hour.

Representative Images

Representative images were generated using FIJI (<https://fiji.sc/>). Images were cropped for detail, separated into respective channels, and the window and level parameters were adjusted identically per channel in all images to emphasize the fluorescent structures in the images without manipulation of raw pixel values.

Images were then inserted in PowerPoint software. For super-resolution microscopy experiments assessing mitochondrial architecture, the aim is to show morphological changes. In the GPR75/Mortalin and PAGFPmt experiments photo-correction was used to enhance the brightness of all images by increasing it by 40% and increasing the contrast by 40% for illustrative purposes.

Western blot images were also transferred to PowerPoint. When Brightness/Contrast were applied, it was done equally to control and experimental groups including all blot area.

Statistical Analysis

Data are expressed as means \pm SD, or as means \pm SEM when indicated in figure legends, of at least three independent experiments or animals per group. Each independent experiment with at least three technical replicates per condition. P values were calculated

using Graphpad Prism software by unpaired two-tailed t test, one-way ANOVA with Sidak or Dunnett multiple comparisons test, two-way ANOVA with Tukey multiple comparisons test, or linear regression. Statistical significance was set at $P < 0.05$.

Supplemental Materials and Methods:

Preparation of 4:1 Palmitate-BSA conjugates

Palmitic acid at 400 mM was solubilized in DMSO. BSA free fatty acids (FFA BSA) (Sigma Aldrich) was dissolved in PBS and warmed up to 45°C with continuous stirring. Solubilized palmitate was added to BSA at 45°C with continuous stirring (for a final concentration of 4 mM in 6.7% BSA). The conjugated palmitate-BSA was aliquoted and stored at -80°C.

qPCR

Total RNA was isolated from islets using the Qiagen RNesay Plus Mini Kit. cDNA was obtained from RNA by a reverse transcriptase reaction using Applied Biosystems High Capacity cDNA Reverse Transcription Kit. Changes in gene expression were detected with SYBR Green. All samples were normalized to 18S content, which served as an endogenous control.

Tissue Collection and Shotgun Lipidomics Analysis

Samples were cultured on 6- well plates and trypsinized then resuspended in 250ml-500ml phosphate buffered saline (PBS), pelleted, and stored at -80C prior to extraction. A modified Bligh and Dyer extraction [Hsieh W-Y] is carried out on samples. Prior to biphasic extraction, an internal standard mixture consisting of 70 lipid standards across 17 subclasses is added to each sample (AB Sciex 5040156, Avanti 330827, Avanti

330830, Avanti 330828, Avanti 791642). Following two successive extractions, pooled organic layers are dried down in a Thermo SpeedVac SPD300DDA using ramp setting 4 at 35°C for 45 min with a total run time of 90 min. Lipid samples are resuspended in 1:1 methanol/dichloromethane with 10mM Ammonium Acetate and transferred to vials (Thermo 10800107) for analysis.

Samples are analyzed on the Sciex Lipidyzer Platform with an expanded targeted acquisition list consisting of 1450 lipid species across 17 subclasses. Differential Mobility Device on Lipidyzer was tuned with EquiSPLASH LIPIDOMIX (Avanti 330731). Instrument settings, tuning settings, and MRM list available upon request. Data analysis performed on an in-house data analysis platform comparable to the Lipidyzer Workflow Manager [BK U]. Quantitative values were normalized to cell counts.

Histology

Whole pancreata were excised, placed in a tissue cassette, and submerged in 4% paraformaldehyde for at least 24 hours. Tissues were embedded in paraffin, sectioned (5µm), and stained with Hematoxylin and Eosin for visualization. Images were taken using an inverted Olympus IX71 microscope equipped with a 40X dry objective and color camera (Photometrics CoolSnap HQ).

RESULTS

Mitochondrial fatty acid utilization is associated with mitochondrial morphology

To assess the correlation between mitochondrial architecture and the capacity to utilize fatty acids, we studied the relationship between mitochondrial architecture and on fatty acid oxidation (FAO) in cells exposed to different levels of fatty acids as well as in cells where genes affecting mitochondrial architecture were manipulated (Figure 1A). The

capacity to oxidize fatty acids was measured as the maximal oxygen consumption fueled by 40 μ M palmitoyl-CoA + 5mM carnitine and induced by ADP. To control the concentrations of Palmitoyl-CoA, carnitine and ADP, and to remove other substrates, cells were permeabilized using Perfringolysin O. Permeabilization enables entry of substrates, while maintaining structural integrity of the mitochondria and its interaction with other organelles. Cells were permeabilized before respirometry analysis was initiated. To verify that cells were indeed permeabilized we measured oxygen consumption rates (OCR) in the absence of ADP prior to any injections (Figure 1B). Lack of detectible OCR in the absence of ADP, with elevated OCR upon addition of ADP is an indication that cells are permeabilized. To quantify the isolated contribution of fatty acids to the measured OCR, the capacity to oxidize fatty acids was determined by measuring the etomoxir-sensitive component of OCR. Etomoxir was used at 3 μ M, a concentration that was shown to block CPT1 without depleting the CoA pool (Figure 1B)(Divakaruni *et al*, 2018). To quantify mitochondrial fragmentation and elongation, each experimental group was also analyzed for Aspect Ratio (AR) of all mitochondria within each cell. Aspect Ratio is defined as the measurement of the long axis over the short axis. AR is utilized as a readout for mitochondrial elongation, where an AR of 2 would indicate a mitochondrion that is two times longer than it is wide. As such, a higher AR value indicates a more elongated mitochondrion, while a smaller AR value indicates a more fragmented mitochondrion. Treatment of HepG2 cells with Glucose (25mM) in combination with palmitate (250 μ M) increased the occurrence of shorter mitochondria (Figure 1Bi). Confocal images of mitochondria stained with TMRE had an averaged cellular AR of 2.183 ± 0.144 a.u (SEM). Respirometry analysis of cells exposed to identical treatment

yielded an average of 3.056 ± 0.409 (pmoles/min)/1000 cells \pm SEM of FA-oxidation as determined by Etomoxir-sensitive, palmitoyl-CoA+ carnitine-induced OCR. Opposite to mitochondrial fragmentation is elongation. To assess the effects of mitochondrial elongation on FAO we overexpressed the dominant negative form of Drp1 (dnDrp1; Drp1 K38A) which has been shown to very effectively inhibit mitochondrial fission and induce elongation (Whitley *et al*, 2018). Cells were transduced with an adenovirus expressing dnDRP1 and analyzed 48 hours after transduction (Figure 1Bii). Expression of DnDrp1 induced hyper-elongation of mitochondria as determined by AR analysis (2.906 ± 0.0452 a.u). Respirometry analysis of cells exposed to identical treatment with dnDRP1 yielded an average of 1.516 ± 0.2309 (pmoles/min)/1000 cells \pm SEM of FA-oxidation as determined by Etomoxir-sensitive, palmitoyl-CoA+ carnitine-induced OCR. When combining the data obtained from cells with fragmented and those with elongated mitochondria we found that the correlation between mitochondrial architecture and the capacity to utilize fatty acids spans across a large spectrum of architectural changes including perturbations that fragment as well as those that elongate the mitochondria (Figure 1B, C).

Respirometry determined the capacity to utilize fatty acids. To determine if mitochondrial architecture changes fuel preference in the presence of a diverse set of nutrients (glucose and amino acids) we employed metabolite tracing. Fuel preference for FAO was determined as the incorporation of palmitate-derived carbons into the TCA cycle intermediates using gas-chromatography/mass spectrometry (GC/MS) (Figure 1D). [U- $^{13}\text{C}_{16}$] palmitate, glucose, and glutamine were concurrently provided to HepG2 cells and primary hepatocytes for 48 hr. Enrichment of ^{13}C in TCA cycle metabolites was quantified

in polar metabolite extracts from total lysates. To confirm fragmented mitochondria have an increased preference for fatty acids as suggested by respirometry, mitochondrial fusion was inhibited through knockdown of Mfn2 in HepG2 cells using an Ad-miR2 (encoding for 5 miRNAs against Mfn2; Mfn2-KD) (Sebastián *et al*, 2012b). Fragmentation by Mfn2KD resulted in a two-fold increase in $^{13}\text{C}_{16}$ -palmitate incorporation (Viral Control: 4.638 ± 3.659 (SD) or 2.112 (SEM) percent enrichment from $^{13}\text{C}_{16}$ -palmitate; Mfn2KD: 10.2378 ± 1.354 (SD) or 0.782 (SEM) percent enrichment from $^{13}\text{C}_{16}$ -palmitate) (Figure 1E). Forced mitochondrial elongation via knockout of Drp1 in primary mouse hepatocytes (Figure 1F) reduced the incorporation of ^{13}C from labeled palmitate into citrate thus indicating mitochondrial elongation decreased FAO. To address the possibility that Drp1 plays a role in fatty acid metabolism independent of its GTPase activity, we also utilized Drp1 K38A (in which GTPase activity is inactivated) and observed reduced incorporation of ^{13}C from labeled palmitate (Figure 1G). Collectively, our data indicate mitochondrial architecture dictates the capacity to oxidize fatty acids in the hepatic mitochondria.

Changes to fatty acid utilization induced by mitochondrial architecture are reflected in hepatic glucose production

FAO has been shown to contribute to hepatic glucose production by providing ATP which is required for gluconeogenesis (GNG) (Satapati *et al*, 2015; Rui, 2014; Lam *et al*, 2003a, 2003b; McCune *et al*, 1981; Baron *et al*, 1989). Since mitochondrial architecture affects FAO, we tested if changes to mitochondrial architecture affect GNG by measuring hepatic glucose production (HGP). Primary hepatocytes isolated from mice were cultured in 6-well plates overnight, the media was then replaced with glucose-free DMEM, and HGP was measured by examining the glucose present after 6 hrs (Figure 1 H, I, J).

Hepatocytes isolated from mice injected with the dnDrp1 siRNA (Expanded View Figure 1A) had a 40% reduction (0.6533 ± 0.0321 units) in hepatic glucose secretion as compared to the siRNA control (0.97 ± 0.0466 units) (Figure 1H). Whereas Drp1 knockout hepatocytes (Expanded View Figure 1B) showed a 30% reduction in glucose production (Figure 1I). To eliminate the possibility that reduced glucose production is limited to fission events we also assessed HGP in elongated mitochondria induced by hyper fusion, by overexpression of Mitofusin 2 (Mfn2OE). Mfn2OE using adenovirus in mouse primary hepatocytes resulted in mitochondrial elongation as determined by western blot. Mfn2OE primary hepatocytes displayed a ~70% reduction (0.3536 ± 0.1022 units) in hepatocyte glucose secretion compared to control (0.9309 ± 0.04139 units) (Figure 1J).

Hepatic mitochondria displayed more elongated mitochondria yielded reduced FAO whereas mitochondria more structurally fragmented had higher rates of FAO. To assess if this phenomenon exists in another system we utilized a model observed to dynamically alter their mitochondrial architecture in the face of different nutrient conditions.

Obesity models yield reduction in Mfn2 levels and mitochondrial fragmentation in beta-cells

Diabetes and obesity have been shown to induce mitochondrial fragmentation in the pancreatic beta-cells (Masini *et al*, 2017; Supale *et al*, 2012; Gao *et al*, 2014). This observation has also been modeled in vitro by long term exposure to an excess nutrient environment (Molina *et al*, 2009a). Molina *et al*. developed an in vitro model using a clonal beta-cell line, INS1, where a high-nutrient environment (20mM glucose/400 μ M palmitate; glucolipotoxicity) inhibit mitochondrial fusion and induce fragmentation (Molina *et al*, 2009a; Stiles & Shirihai, 2012). Moreover, beta-cells from obese animals have been

shown to increase FAO and secret insulin in response to fatty acids (Nolan *et al*, 2006a). As such, the beta-cell is another system where mitochondrial fragmentation may change the cellular response to lipids. To determine if mitochondrial fragmentation in beta-cells increased FAO, INS1 cells were incubated for 19hrs with 20mM glucose/400 μ M palmitate (glucolipotoxicity; GLT) and, mitochondrial fragmentation was confirmed by image analysis (Figure 2A, B). We examined alterations to morphology that were induced by 24 hrs exposure to excess nutrient culture conditions using confocal imaging of mitochondria in intact cells stained with MitoTracker Green and TMRE (Figure 2A). Mitochondria of the control group (11mM glucose) largely consisted of intermediate shaped mitochondria of similar membrane potential. Mitochondria from INS1 cells incubated in excess nutrient largely displayed puncta-like mitochondria of various membrane potentials. To further validate visual observations that excess nutrient conditions yielded more fragmented mitochondria we quantified mitochondrial fragmentation by AR (Figure 2B). Exposure to 20mM glucose/400 μ M palmitate significantly reduced mitochondrial length (AR= 2.41 ± 0.00471 a.u.; 3 replicates, n=148 cells, p-value ≤ 0.0001) as compared to mitochondria in the control group cultured in 11mM glucose control (AR= 2.669 ± 0.00389 a.u.; 3 replicates, n=219 cells).

Upon verifying mitochondria were more fragmented under GLT, the capacity to oxidize fatty acids was determined by permeabilized respirometry (Figure 2C). FAO capacity was, then assessed by measuring oxygen consumption in permeabilized cells exposed to palmitoyl CoA plus carnitine, in the presence and absence of etomoxir. Cells with fragmented mitochondria yielded a higher capacity to oxidize palmitoyl-CoA + carnitine (12.562 ± 0.5166 (pmoles O₂/min)/1000 cells; n =4, p-value ≤ 0.05) versus control (9.75

± 0.9663 (pmoles O₂/min)/1000 cells; n =5). To determine if under excess nutrient conditions, the increase in FAO is a direct consequence of mitochondrial fragmentation we next determined the molecular mechanism of nutrient-induced fragmentation in the beta-cells. We rationalized that the isolated contribution of fragmentation to changes in beta-cell FAO could only be determined if we could identify the molecular mechanism behind the fragmentation observed in models of diet-induced diabetes. By identifying the molecular mechanism, we can study the effect of fragmentation independently of exposure to excess nutrient.

A previous study by Molina et. al. indicated that an excess nutrient environment directly affects mitochondrial fusion, suggesting that mitochondrial fusion proteins levels or function may be affected. We examined the levels of the mitochondrial fusion protein, Mfn2, in high fat diet fed mice. C57BL/6J mice were placed on a high fat diet (HFD, 58% kcal from fat, New Brunswick, NJ.) for 12 weeks. Islets were isolated from three mice per group at weeks 1, 2, 3, 5, and 7. Western blot analysis of Mfn2 revealed that during weeks 1-5 there are no significant changes in Mfn2 protein levels; however, by week 7, a statistically significant decrease in Mfn2 expression of 27% was observed (Expanded View Figure 2A). By week 12, Mfn2 expression levels were reduced by 67 % compared with control mice (Figure 2D). Interestingly, Mfn2 mRNA levels from islets of the same cohort of animals is not decreased indicating that the change in Mfn2 protein is not due to decreased transcription and could be attributable to an increase in degradation (Expanded View Figure 2B). These results suggest that either weight, poor glycemic control, or both contribute to the reduction of whole islet Mfn2 levels. To determine the isolated contribution of weight gain, insulin resistance, and hyperglycemia to Mfn2 levels,

we examined islets isolated from Zucker rats (Figure 2E). Three animals from each experimental group (Zucker Lean, Zucker Fatty, Zucker Diabetic Lean, and Zucker Diabetic Fatty) were assayed at eight weeks of age. Comparison of the Zucker fatty and the Zucker diabetic to their corresponding lean control showed that Mfn2 was reduced in the Zucker diabetic (by 41%, p-value ≤ 0.05), but not in the Zucker fatty (Figure 2E).

Mfn2-deficient beta-cells display fragmented mitochondrial morphology

To determine the isolated contribution of reduced Mfn2 levels to the observed increase in FAO, we knocked out Mfn2 in the pancreatic beta-cell and examined islet FAO in the absence of excess nutrients. We created a mouse lacking Mfn2 in insulin secreting cells by using the Cre/LoxP system. Rat Insulin Promoter (RIP)-mediated Cre expression produced excision of Mfn2 (β -Mfn2KO) in beta-cells of the islets of Langerhans. β -Mfn2KO animals are viable and litter sizes are similar to breedings between lox homozygous mice. Tissue specific excision of Mfn2 from isolated pancreatic islets was confirmed by western blot and PCR (Expanded View Figure 2C, 2D, 2E). Comparison of Mfn2 expression in other tissues (liver, muscle, heart, fat, thymus, and brain) obtained from β -Mfn2KO indicates that these tissues are not significantly affected (Expanded View Figure 2C, 2D, 2E).

Following isolation, islets were dispersed and cells were plated for confocal microscopy. Mitochondria were stained using TMRE. Beta-cells were identified by expression of an insulin promotor driven fluorescent protein (pa-GFP) that was transduced using an adenoviral vector. Mitochondrial fragmentation was only evident in beta-cells obtained from β Mfn2KO samples (3 mice). We determined Mfn2 deletion was sufficient to induce a fragmented mitochondrial network compared to WT littermates via

confocal microscopy (Figure 2F).

Enhanced fatty acid utilization increases secretion at non-stimulating glucose levels

Having confirmed that Mfn2 deletion induces mitochondrial fragmentation, we set out to determine the effect of Mfn2 deletion on fatty acid utilization in the islet. Rates of FAO were measured in isolated islets as the levels of $^{14}\text{C-CO}_2$ produced from oxidized ^{14}C -labeled palmitate (Huynh *et al*, 2014). An increase in basal beta-oxidation was observed in Mfn2KO islets (12.603 ± 0.8046 $^{14}\text{C-CO}_2$ pmoles; 100 islets/condition; n=4 female, p-value ≤ 0.01) compared to control (8.862 ± 0.5562 $^{14}\text{C-CO}_2$ pmoles; 100 islets/condition; n=4 female) (Figure 2G). The observed altered fatty acid metabolism indicate Mfn2-null beta-cells have greater preference to oxidize fatty acids. To address the possibility that increased FAO was due to an increase in Alpha cells in Mfn2KO islets, islets were stained for glucagon and insulin, assessed for islet composition. The ratio of beta-cells to alpha cells in both control and Mfn2KO islets were unchanged, indicating changes to FAO are not due to changes in islet composition (Expanded View Figure 2F).

To test the effects of Mfn2 deletion on islet function, namely insulin secretion, was measured in islets isolated from LoxP homozygous wild type and β -Mfn2KO mice. Mfn2 deletion induced a 2.5x fold increase ($5.99 \times 10^{-4} \pm 1.82 \times 10^{-4}$ ng/mL/content) (Figure 2I) in basal insulin secretion in unstimulated islets (under 3mM glucose), compared to WT islets ($2.24 \times 10^{-4} \pm 6.77 \times 10^{-5}$ ng/mL/content). Mfn2 deletion did not affect glucose stimulated insulin secretion, as revealed by a 30-minute 15mM glucose stimulation test (WT: $1.74 \times 10^{-4} \pm 5.11 \times 10^{-4}$ ng/mL/content, β -Mfn2KO islets: $1.74 \times 10^{-4} \pm 3.19 \times 10^{-4}$ ng/mL/content) (Figure 2H). On average, there was no difference in the average islet size between the two groups. However, to eliminate the possibility that insulin secretion levels

are affected by islet size, the diameter of isolated islets was measured and the average islet diameter was size matched. Furthermore, we eliminated the possibility that insulin secretion was affected by insulin content (Expanded View Figure 2G). There was no significant change in insulin content between size matched control (3196 ng insulin/mg protein) and β -Mfn2KO (2763 ng insulin/mg protein) islets (p-value of 0.193) (Expanded View Figure 2G). Increased mitochondrial membrane potential has also been shown to induce insulin secretion, to eliminate the possibility that membrane potential enhanced insulin response we assessed membrane potential by measuring the fluorescence intensity of the membrane potential dependent dye, TMRE, over MitoTracker Green. β -Mfn2KO islets yielded reduced in membrane potential indicating observed insulin defects are not due to enhanced mitochondrial membrane potential (Expanded View Figure 2H).

Previous studies demonstrated that, unique to islets from obese animals, is their ability to respond to acute palmitate with elevated insulin secretion even at non-stimulatory glucose concentrations (Fex *et al*, 2007; Nolan *et al*, 2006b, 2006a). If increased fatty acid utilization by Mfn2-null islets translates to fatty acid-induced secretion, this could provide an explanation for increased insulin secretion in the absence of glucose stimulation. Next, we determined the effect of Mfn2 deletion on the secretory response to acute palmitate stimulation at non-stimulatory glucose concentrations (3mM glucose).

While in WT islets acute palmitate treatment did not increase insulin secretion (WT: $2.24 \times 10^{-4} \pm 6.77 \times 10^{-5}$ ng/mL/content, WT+palmitate: 0.20323 ± 0.004462) Mfn2KO islets responded to acute palmitate stimulation with a 2fold increase in insulin secretion (Mfn2KO: $5.99 \times 10^{-4} \pm 1.82 \times 10^{-4}$ ng/mL/content; Mfn2KO +palmitate: 0.042958 ± 0.008441) (Figure 2I). Overall, our data indicates Mfn2-deficient beta-cells have

increased sensitivity to fatty acids.

Mfn2 mimetic peptide reverses the effect of glucolipotoxicity on mitochondrial architecture and insulin secretion.

The results thus far indicated that reduction in Mfn2, on its own can induce mitochondrial fragmentation as well as increased fatty acid utilization and insulin secretion at non-stimulatory glucose. To determine if restoration of Mfn2 function can restore mitochondrial architecture and secretion glucolipotoxicity we utilized an Mfn2 mimetic peptide. The mitofusin mimetic peptide, Mfn-TAT P374-384, was shown to stabilize a fusion-permissive open conformation of endogenous Mfn2 where Mfn2 activity is still present (Rocha *et al*, 2018). Islets from high fat diet fed mice were dispersed and cells were treated overnight with 1 μ M Mfn-TAT P374-384. The Mfn2 mimetic increased mitochondrial length in dispersed islets cells from high fat diet fed mice (CHOW vehicle: AR= 1.507 \pm 0.0022 a.u. n=39 islets; HFD + vehicle: AR=1.4997 \pm 0.0014 a.u. n= 42 islets; CHOW + Mfn-TAT P374-384: AR= 1.4907 \pm 0.0038 a.u. n=55 islets; HFD + Mfn-TAT P374-384: AR= 1.634 \pm 0.0035 a.u. n=31 islets). By stabilizing the fusion-permissive conformation of Mfn2, changes to mitochondrial morphology induced by high fat diet were diminished (Figure 2J, K). To control for non-specific Mitofusin effects, we tested the effect of Mfn-TAT P374-384 in Mfn1&2 null MEF cells where we found a small non-significant effect on mitochondrial architecture (Expanded View Figure 3) (Mfn1/2 dKO + vehicle: AR= 1.80949 \pm 0.159069 (SD) 0.079535 (SEM); Mfn1/2 dKO + Mfn-TAT P374-384: AR = 1.6966 \pm 0.069092 (SD) 0.034546 (SEM); P value: 0.5571).

We next tested the capacity of the Mfn2 mimetic to restore secretion at non-stimulatory glucose concentrations. Islets isolated from diet-induced obese mice and β -Mfn2KO islets

had significantly higher insulin secretion at 3mM glucose (01.411 ± 0.179 ng/ml insulin per islet; n=7 mice) compared to lean (0.795 ± 0.067 ng/ml insulin per islet; n=10 mice) and WT control mice (Figure 2L). Treatment of islets isolated from HFD with the Mfn2 mimetic reduced secretion at 3mM glucose (0.593 ± 0.163 ng/ml insulin per islet; n=8 mice) as compared to control islets (0.717 ± 0.127 ng/ml insulin per islet; n=8 mice) (Figure 2L). Our observation that fragmentation and hyper basal insulin secretion, provoked by diabetic and high nutrient conditions, can be normalized by a Mfn2 mimetic links beta-cell dysfunction to enhanced fatty acid sensitivity induced by mitochondrial fragmentation. To eliminate the possibility reduced secretions were a result of non-responsive islets, islets from the same mice were also assessed for their response to stimulation by glucose (Expanded View Figure 3H). Islets from all groups yielded greater insulin secretion as a response to glucose stimulation compared to non-stimulatory conditions indicating islets are responsive.

Increases to plasma levels of long-chain fatty acids in combination with increased sensitivity to fatty acids have been observed to stimulate metabolic pathways including hepatic glucose production and insulin secretion. We demonstrate mitochondrial morphology regulates these processes in the liver and pancreatic beta-cell by modulating the degree at which FAO occurs. Having assessed the metabolic reprogramming associated with mitochondrial morphology, we then asked what are the physiological outcomes in a model where FAO influences cell survival.

Metabolically distinct subsets of diffuse large B-Cell lymphoma cells primed for beta-oxidation display more fragmented mitochondria

Diffuse large B-cell lymphomas (DLBCLs) are a genetically heterogeneous group of

tumors that metabolically handle different substrates based on their genetic expression profile (Caro *et al*, 2012). DLBCLs displaying up-regulation of genes encoding the B-cell receptor (BCR-DLBCL) have been identified to yield higher glycolytic flux. Whereas DLBCLs enriched in genes involved in mitochondrial oxidative phosphorylation (OxPhos-DLBCL) have been characterized for increased mitochondrial FAO and palmitate to be their predominant respiratory fuel (Figure 3D) (Caro *et al*, 2012) . Understanding metabolic differences occur between DLBCL subsets we then asked if mitochondrial morphology differed between subsets reliant on expressing BCR or OxPhos genes for survival. Previously, we showed more fragmented mitochondria had greater preference to oxidize fatty acids, thus we hypothesized OxPhos-DLBCLs would have a greater propensity for fragmented mitochondria. Analysis of 3D reconstructed images of mitochondrion stained with MitoTracker Green (Figure 3A) confirmed OxPhos-DLBCL cells had reduced mitochondrion area compared to BCR-DLBCLs (Figure 3B). To confirm reduced mitochondrion area was an indication of fragmentation and not increased swelling, we show that the OxPhos-DLBCL subsets, Pfeiffer and Toledo, had a higher population of fragmented mitochondria than BCR-DLBCLs (Figure 3C). The reverse was true of BCR-DLBCLs comprising of greater amounts of elongated mitochondria (Figure 3D). Organelles were classified according to form factor values into those with short ($FF \leq 2$), intermediate ($2 \leq FF \leq 4$), and long ($FF > 4$) morphology. Our DLBCL data thereby supports our findings in hepatic and beta-cell mitochondria, mitochondria with a higher capacity to utilize fatty acids are more fragmented.

Forced elongation of primarily fragmented diffuse large B-Cell lymphoma cell mitochondria reduces FAO capacity and hinders cell survival

OxPhos-DLBCLs were observed to have greater mitochondrial fat oxidation (Figure 3E) and a larger population of fragmented mitochondria. Next, we sought to determine whether mitochondrial elongation would reduce the preference for mitochondrial fat oxidation. To test this hypothesis, we analyzed the incorporation of [U-¹³C₁₆] palmitate in Mfn2 OE Pfeiffer and Toledo OxPhos-DLBCL (Figure 3F) and dnDrp1 Pfeiffer and Toledo OxPhos-DLBCL (Figure 3G) as compared to control. Both models of mitochondrial elongation led to significant reduction in incorporation of [U-¹³C₁₆] palmitate. Hyper fusion by Mfn2 OE OxPhos-DLBCLs led to a 30% reduction in FAO (0.6884 ± 0.06326 % enrichment from ¹³C-palmitate) as compared to control (0.9779 ± 0.02528 % enrichment from ¹³C-palmitate). Inhibition of fission by dnDrp1 OxPhos-DLBCLs yielded a 25% reduction in FAO (0.7569 ± 0.02531 % enrichment from ¹³C-palmitate) as compared to control. Thus our data indicate the capacity to utilize fatty acids as an oxidative fuel in the mitochondria is dependent on mitochondrial morphology.

Metabolic reprogramming is an adaptation for cell survival in disease progression and altering lipid metabolism has the ability to modulate downstream survival in DLBCL (Caro *et al*, 2012; Xiong & Zhao, 2018). In OxPhos-DLBCLs, utilization of palmitate as a primary fuel source is vital to cell survival and disruption or ablation of such capacity contribute to cell death. We reasoned that if modulating mitochondrial architecture in OxPhos-DLBCLs had a profound effect on lipid metabolism, then such metabolic changes would affect cell survival. To assess if cell survival was affected by the reduction in FAO we measured cell viability as compared to control by an Apoptosis Detection Kit. In Mfn2OE OxPhos-DLBCLs, the observed reduction in fatty acid utilization was reflected in a 20% reduction (81.315 ± 3.096 units) in cell survival compare to control OxPhos-DLBCLs (Figure 3H).

Additionally, dnDrp1 OxPhos-DLBCLs had a 30% reduction in cell survival (66.954 ± 1.479 units) (Figure 3I). This observation further strengthens the findings that mitochondrial architecture plays a role in the preference to utilize fatty acids to fuel mitochondrial ATP production, and reductions to FAO are well correlated to physiology associated with reductions to mitochondrial FAO.

Mitochondrial architecture specifically alters CPT1-dependent fatty acid oxidation

Fatty acid utilization can be enhanced in several ways, through favoring exogenous fatty acids over stored fatty acids or through enhancing fatty acid import into the mitochondria. FAO is contributed by fatty acids of different chain lengths. Short-chain and medium-chain fatty acids can freely diffuse into the mitochondria whereas long-chain fatty acids cannot. To enter the mitochondria, long-chain fatty acids are esterified with carnitine in the cytoplasm and then are able to be transported into the mitochondria by carnitine palmitoyl transferase 1 (CPT1). To determine if the regulation of fatty acid entry into the mitochondria is influenced by mitochondrial architecture, we assessed the incorporation of a long-chain CoA ([U- $^{13}\text{C}_{16}$]-palmitate) versus a medium chain-CoA ([U- $^{13}\text{C}_6$] hexanoic acid) (Figure 4A). In both conditions whereby OxPhos-DLBCLs exhibit elongated mitochondria (Mfn2OE OxPhos-DLBCLs and dnDrp1 OxPhos-DLBCLs), we observed reduced incorporation of long chain fatty acids (Figure 4B & 4C). In the same Mfn2OE OxPhos-DLBCLs and dnDrp1 OxPhos-DLBCLs, no changes to incorporation of hexanoic acid was observed compared to control (Figure 4B & 4C). Similarly, elongated mitochondria from dnDrp1 and Drp1KO primary mouse hepatocytes displayed no changes to the incorporation of hexanoic acid into the TCA cycle compared to control (Figure 4F & 4G). The observed data suggests mitochondrial architecture alters FAO in

a CPT1-dependent manner.

Under physiological conditions long-chain fatty acid oxidation (LCFAO) is tightly regulated by CPT1 (McGarry & Brown, 1997). CPT1, however, has varying sensitivity to its endogenous inhibitor, malonyl-CoA, depending on physiological states. CPT1 sensitivity is increased in obesity or diabetic rats administered insulin and decreased in starvation and T2DM (Akkaoui et al, 2009). Furthermore, membrane structure and fluidity influence the efficiency of CPT1, thus we focused on fatty acid shuttling by CPT1 and its regulation by malonyl-CoA (Hoppel et al, 2001). We hypothesized that mitochondrial elongation enhances the sensitivity of CPT1 to malonyl-CoA thereby reducing FAO. We further hypothesize mitochondrial fragmentation would yield opposite sensitivities to favor and enhance FAO. We tested such hypotheses by accessing CPT1 activity upon inhibition with malonyl-CoA in mitochondrial fractions purified from OxPhos-DLBCL. At 100 μ M of malonyl-CoA, dnDrp1 OxPhos-DLBCL cells displayed significantly lower CPT1 activity ($11.143\% \pm 4.975$ activity remaining) as compared to control OxPhos-DLBCL ($38.742\% \pm 4.641$ remaining activity) (Figure 5A), suggesting that elongated mitochondria have higher CPT1 sensitivity to malonyl-CoA. At a greater resolution, utilizing various malonyl-CoA concentrations, we observed an exponential hypersensitivity to malonyl-CoA in dnDrp1 primary mouse hepatocytes (Figure 5B). Additionally, in INS1 cells yielding fragmented mitochondria induced by nutrient overload (20mM glucose + 400 μ M palmitate) we observed reduced sensitivity to malonyl-CoA inhibition (Expanded View Figure 4). These findings suggest CPT1 of elongated mitochondria are more sensitive to malonyl-CoA inhibition resulting in reduced LCFAO whereas, the CPT1 of fragmented mitochondria are less sensitive to malonyl-CoA inhibition and thus enhance LCFAO.

To exclude the possibility that observed changes in LCFAO are due to CPT1 activity, FAO was measured in dnDrp1 OxPhos-DLBCL cells treated with C75 and baicalin, two pharmacological CPT1 activators with different action modes (Figure 5C). Mechanistically, C75 competes with malonyl-CoA for CPT1's CoA binding site thereby reversing malonyl-CoA inhibition (Bremer *et al*, 1985). Whereas baicalin activates CPT1 by binding to CPT1's catalytic site; however, baicalin cannot rescue CPT1 activity if malonyl-CoA is present and binds to CPT1's CoA moiety (Dai *et al*, 2018). C75 treatment of dnDrp1 (Figure 5D) and Mfn2OE (Figure 5E) primary mouse hepatocytes significantly rescued and enhanced [U-¹³C] palmitate incorporation into citrate (DnDrp1: 0.9428 ± 0.0189 units, Mfn2: 1.0068 ± 0.0655 units). Whereas treatment with baicalin did not reverse the observed reductions in LCFAO in dnDrp1 (0.6503 ± 0.0138 units) and Mfn2OE (0.635 ± 0.0842 units). These observations suggest changes to the degree at which LCFAO occur are not due to CPT1 activity rather it is by the interaction of CPT1 with malonyl-CoA. Overall our data reveals mitochondrial architecture alters FAO by changing CPT1 sensitivity to malonyl-CoA (Figure 5F).

DISCUSSION & FUTURE DIRECTIONS

Mitochondrial dynamics has long been associated with bioenergetic adaptation to metabolic demand (Liesa & Shirihai, 2013b). We show in several cellular models that mitochondrial fragmentation favors beta oxidation and elongated mitochondria yielded reduced capacity to oxidize fatty acids. Only differences in incorporation of fatty acid-derived carbons into the TCA cycle was observed between long chain versus short chain-fatty acids, leading us to assess CPT1 activity and sensitivity. Compared to fragmented mitochondria, we show CPT1 of elongated mitochondria had increased sensitivity to

malonyl-CoA, marked by greater inhibition of long chain-fatty acid incorporation in the presence of malonyl-CoA and increased FAO capacity when C75 prevents malonyl-CoA binding. Whereas fragmented mitochondria have reduced CPT1 sensitivity to malonyl-CoA. Therefore, our work supports the idea that mitochondrial dynamics also serves as an adaptive mechanism to metabolic demand in addition to being essential to mitochondrial quality control.

Role of mitochondrial morphology in FAO

In agreement with previous studies, mitochondrial fragmentation in Mfn1LKO mice enhanced fatty acid utilization (Kulkarni *et al*, 2016) and inhibition of fission in Drp1KO HeLa cells decreased FAO (Song *et al*, 2021), the present study showed that mitochondrial morphology dictates the capacity to oxidize long-chain fatty acids. Although Kulkarni *et al* proposed fatty acid utilization was enhanced from metabolic cage studies, the observed reduction in acylcarnitine species agrees with increased fatty acid utilization (Kulkarni *et al*, 2016). One would predict an increase in FAO would result in either no changes to lipid droplet accumulation or a decrease at basal conditions; however, both studies revealed an enhanced lipid droplet size despite FAO occurring in opposite directions. Therefore, this observation allowed us to predict changes to lipid droplet accumulation can occur independent of beta oxidation as a result of mitochondrial morphology. Additionally, HeLa cells are not metabolically similar to primary hepatocytes and thereby the physiological relevance may be absent, suggesting the fragmentation and presence of LD can be explained by esterification before steatosis occurs and excess FAs are oxidized to prevent lipotoxicity. To address this challenge, FAO was determined in 2 manners, by the capacity to oxidize one substrate in a permeabilized system and by

assessing the amount of carbon-derived fatty acids incorporated into the TCA. Through both methods we identified fragmented mitochondria yielded greater capacity and greater preference for fatty acids. On the other hand, elongated mitochondria displayed reduced capacity and preference. These findings are consistent with mitochondrial morphologies associated with brown adipocyte peridroplet mitochondria and cytoplasmic mitochondria (Benador *et al*, 2018). Peridroplet mitochondria, observed to be more elongated, can promote TG synthesis and expand lipid droplets. Moreover, cytoplasmic mitochondria diverge both functionally and morphologically, they specialize in oxidizing fatty acids and appear more fragmented. Our observations in the capacity to undergo FAO as a result of the degree in fragmentation is further supported by previous findings in increased FAO as a result of mitochondrial fragmentation in the brown adipocyte (Mahdavian *et al*, 2017). Overall, our data suggests the degree of mitochondrial length dictates the preference for fatty acids in multiple cell types.

To address the mechanism of mitochondrial fragmentation in response to an excess nutrient environment, we examined Mfn2, which previous studies have shown is reduced in models of obesity and excess nutrients in muscle and adipose tissue (Bach *et al.*, 2003; Le Blanc *et al.*, 2012; Pich *et al.*, 2005; Sorianello *et al.*, 2012). Treatment of INS1 cells in excess nutrient resulted in mitochondrial fragmentation, reduction in Mfn2 expression, and increased ADP-induced oxygen consumption in response to palmitoyl-CoA + carnitine in the media. In a rat model of obesity, Zucker fatty rat, we report a decrease in Mfn2 expression in the beta-cell, an observation absent in Zucker lean rats. This indicates that obesity alone is insufficient to decrease islet Mfn2 and that reduction in Mfn2 may be linked to uncompensated hyperglycemia. Furthermore, deletion of Mfn2

in the beta-cell resulted in fragmented mitochondria in the absence of an excess nutrient environment. Genetic ablation of Mfn2 in mice resulted in increased basal insulin secretion without changing insulin content. Deletion of Mfn2 also enhanced the capacity of FFAs to promote insulin secretion under low glucose. This mimics previous findings from the Prenkti group showing islets from obese rats are more sensitive to fatty acid-induced insulin secretion at basal glucose (C J Nolan et al., 2006). Taken together, the forced fragmentation of mitochondria elicited a shift at basal glucose concentrations to FFA for oxidation and insulin secretion. Consistent with this observation, loss of Mfn2 resulted in increased FFA oxidation in INS1 cells with Mfn2KD. This phenotype suggests an important role for FFA metabolism in beta-cells and insulin secretion. Insulin secretion in response to fatty acids may be of particular importance in states of insulin resistance or diabetes because these patients often have increased circulating triglyceride (Seigneur et al., 1994). Deleting Mfn2 in brown adipose tissue (BAT) mitochondria increases their capacity for ATP-generating fat oxidation (Mahdavian et al., 2017). In this regard, we showed that deletion of Mfn2 in beta-cells increased respiratory capacity linked to ATP synthesis under low glucose. The preferred nutrient of beta-cells to oxidize in low levels of low glucose is fatty acids. Thus, our data demonstrate that inhibiting Mfn2 provides an enhanced capacity to uptake and utilize fatty acids for ATP synthesis in beta-cells under low glucose settings.

Impaired CPT1 regulation may explain unregulated HGP amid insulin signaling

Type 2 diabetic models with intact hepatic insulin signaling have displayed increased glucose production as a result of excess circulating FFAs, largely attributed to adipocyte lipolysis, but the mechanism as to how hepatic glucose production becomes

non-suppressible remains unclear (Titchenell *et al*, 2016). We show the biological relevance of our findings; our study indicates hepatic mitochondrial morphology contributes to hepatic glucose production levels by regulating FAO. Under conditions of increased FFA, mitochondria fragment and enhance FAO. Moreover in the presence of high malonyl-CoA levels, malonyl-CoA insensitive CPT1 in rat hepatocytes counteracted inhibition of oleate induced FAO amid insulin signaling (Akkaoui *et al*, 2009). Revealing malonyl-CoA insensitive CPT1 was highly effective in counteracting regulatory effects of insulin. These findings as well as our own strengthen CPT1 sensitivity as an essential driving force for hepatic LCFAO and can explain the increase in hepatic glucose production despite the presence of insulin signaling.

CPT1 as a mechanism to increasing beta-cell sensitivity to FFAs

Our data suggests that Mfn2 downregulation may be involved in the switch in response from short term to long term exposure in palmitate by controlling the dose response of insulin secretion in beta-cells. This hypothesis is further supported by our observations of reduced islet Mfn2 expression in HFD fed mice and ZDF rats. Previous studies have shown an increase in glycerolipid/free fatty acid (GL/FFA) cycling in response to HFD in rats (C J Nolan *et al.*, 2006; Christopher J. Nolan & Prentki, 2008; Christopher J Nolan *et al.*, 2006). It is thought that this cycle alters insulin secretion through signaling intermediates, such as monoacylglycerols (MAGs), which activate exocytotic machinery via Munc13 (Marc Prentki, Matschinsky, & Madiraju, 2013). Given that Mfn2 deletion results in similar effects, it is conceivable that GL/FFA cycling could increase sensitivity to exogenous fatty acids in our system, particularly given their increased utilization by beta-cells. Other studies have shown an important role for the cell

membrane fatty acid receptor GPR40 in the augmentation of insulin secretion by FFA (El-Azzouny et al., 2014). These two potential mechanisms are not mutually exclusive; increased cycling could also contribute to increased release of FFA from the cell, which GPR40 responds to by enhancing insulin secretion.

In this study, we propose the switch in fuel preference centers on CPT1 and its rate-limiting control of mitochondrial FA oxidation. CPT1 is expressed in beta-cells (Assimacopoulos-Jeannet et al., 1997) and controls the entry of fatty acids conjugated to carnitine into mitochondria (McGarry, Mannaerts, & Foster, 1977; Newgard & McGarry, 1995). CPT1 sensitivity to malonyl-CoA have been observed to be modulated by membrane fluidity, and mitochondrial membrane fluidity is increased in the livers of high-fat diet fed Wistar rats (Aoun et al., 2012), a condition shown to decrease CPT1 sensitivity to inhibition by Mal-CoA (Faye et al., 2005). Conceivably, the reduced sensitivity to inhibition on CPT1 would increase FAO in the face of excess nutrients, consistent with compensatory behavior to detoxify the excess lipids. However, this compensation could become pathological if it induced increased insulin secretion at a non-stimulatory glucose concentration, contributing to hyperinsulinemia prior to insulin resistance. Because mitochondrial fragmentation is observed in high-fat diet fed animals, mitochondrial membrane fluidity presents an attractive target to study the control of fuel preference.

Potential implications of CPT1 sensitivity in OxPHOS-DLBCL metabolic adaptability

Microenvironment plays a role in establishing the gene expression profile (GEP) of DLBCL (Poulaki & Giannouli, 2021). The subsequent metabolic features accompanied by specific DLBCL subsets dictate tumor metabolism and provide heterogeneity in fuel utilization which ensures pro-survival and proliferation (Zhou et al, 2021). By fine tuning

their metabolic adaptability studies have shown increased resistance to mitochondrial apoptosis (Gooptu *et al*, 2017). In combination with the microenvironment influencing GEP and increased FAO capacity having proven beneficial (Moore *et al*, 2022), it is possible that under nutrient rich environments OxPHOS-DLBCL are preferred over BCR-DLBCLs. The preference of OxPHOS- DLBCL for fatty acids as a fuel substrate under nutrient excess will also impede lipotoxicity. CPT1-dependent LCFAO has been observed to be protective in cancer cells and inhibition of CPT1 or reliance on SC-FAO and MC-FAO suppresses cancer growth. Not only does increased FAO enable ATP production under metabolic stress but also protects cells from apoptosis by clearing cytoplasmic LCFA and impede lipotoxicity (Norberg *et al*, 2017). In the event FA uptake is impeded, having a more fragmented morphology serves as a compensatory mechanism to enhance FA uptake. It is then possible to promote cellular proliferation and reduce lipotoxicity by selecting for a GEP and mitochondrial morphology best adapted to lipid rich environments. Mitochondrial fragmentation will enhance FAO through reduction of CPT1 sensitivity. Whether enhanced FAO is due to OxPHOS-DLBCL GEP or mitochondrial fragmentation remains unknown. Since OxPHOS-DLBCL rely on FAO as their main source of ATP, any changes to FAO capacity translates to energy depletion (Qu *et al*, 2016) and thereby a potential explanation to the observed reduction in cell viability when forced mitochondrial elongation reduced FAO. The alterations in malonyl-CoA sensitivity as a result of mitochondrial morphology can thereby overcome energy depletion by allowing the import of FA despite presence of malonyl-CoA. However, a limitation to this study is the assumption that only one CPT1 isoform is present. It is feasible the observed changes in malonyl-CoA sensitivity is contributed by the differential presence of CPT1A

vs CPT1B, isoforms with different malonyl-CoA sensitivities.

Conclusion

This work provides evidence that mitochondrial dynamics can affect mitochondrial fuel utilization and preference and metabolic processes associated with LCFAO through alteration of CPT1 sensitivity to its endogenous inhibitor, malonyl-CoA. As such this study suggests two possibilities to treating metabolic diseases: 1) restoration of mitochondrial architecture or 2) altering CPT1's CoA binding site to restore malonyl-CoA sensitivity.

FIGURES

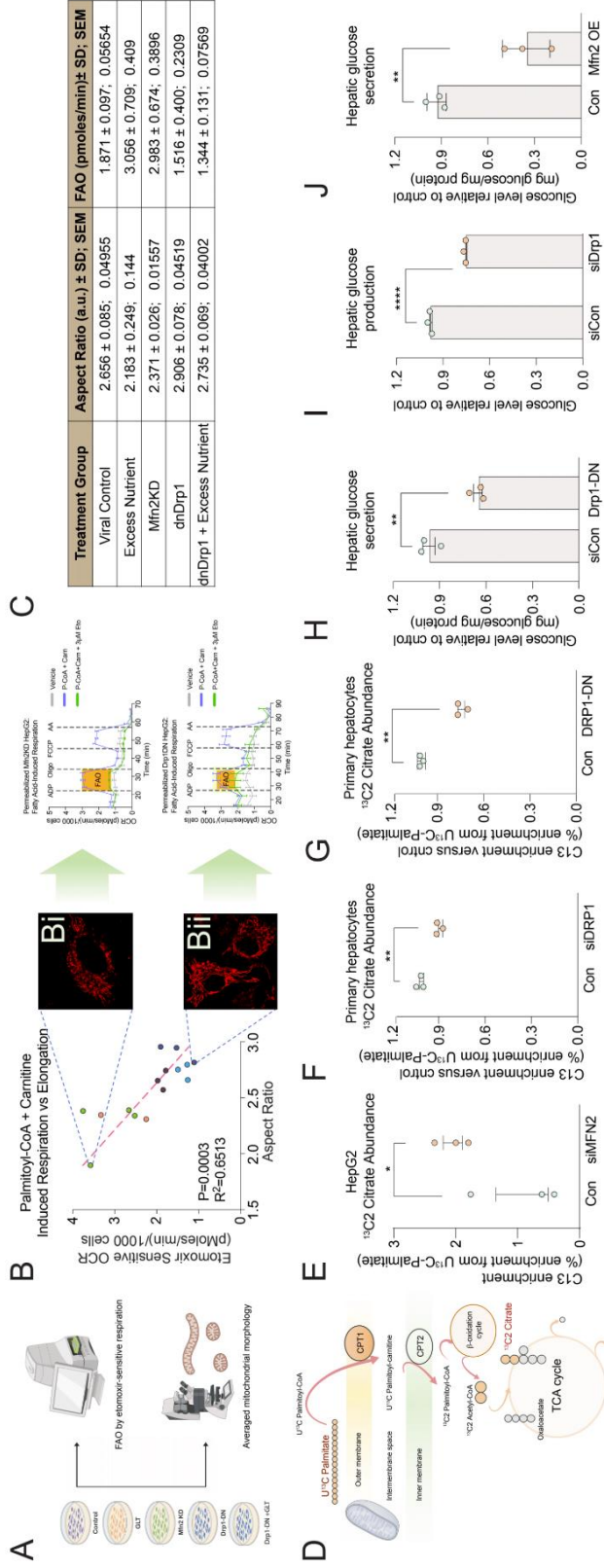


Figure 1

Figure 2- 1. Hepatic mitochondrial fatty acid utilization and glucose production is associated with mitochondrial morphology.

Schematic representation of experimental approach to assessing mitochondrial morphology using confocal microscopy in parallel to assessing the capacity to utilize fatty acids through respirometry. **B, C.** Correlation of mitochondrial length (AR; long axis/ short axis) to etomoxir sensitive oxygen consumption rates. (B) Highest etomoxir sensitive OCR correlated to lowest AR as seen in confocal images. Confocal images of HepG2 mitochondria stained with 15nM TMRE. Live-cell super-resolution confocal imaging of HepG2 cells stained with TMRE (red). Scale bar = 10 μ m. Oxygen consumption data represents n= 6 replicates from 3-5 individual experiments. Data represents n= 20-50 cells from 3 individual experiments. (C) Quantification of changes in aspect ratio (a.u.) and mitochondrial capacity to utilize fatty acids (pmoles/min)/1000 cells. **D.** Schematic representation of experimental approach to measuring fatty acid utilization using stable isotope tracing analysis. **E.** Effect of mitochondrial fragmentation on HepG2 fuel preference toward fatty acid. [U-¹³C] palmitate tracing in HepG2 cells with adenoviral expression Mfn2KD. Data show C13 enrichment of [U-¹³C] palmitate into citrate. Data were normalized to cell count for each individual replicate. n = 3 biological replicates. *P < 0.05 compared to vehicle by Student's t-test. **F, G.** Effect of mitochondrial elongation on hepatic fuel preference toward fatty acid. [U-¹³C] palmitate tracing in hepatocytes with adenoviral expression Drp1KO and dnDrp1. Data show C13 enrichment of [U-¹³C] palmitate into citrate. Data were normalized to viral control for each individual replicate. n = 3 biological replicates. **P < 0.01 compared to vehicle by Student's t-test. **H, I, J.** Hepatic glucose production in primary hepatocytes with adenoviral expression of Mfn2

OE (Figure 1H), Drp1-DN (Figure 1I), or Drp1 siRNA transfection (Figure 1J) $n = 3$ biological replicates. ** $P < 0.01$, *** $P < 0.001$ compared to vehicle by Student's t-test.

Data information: All data are presented as mean \pm SD or as mean \pm SEM.

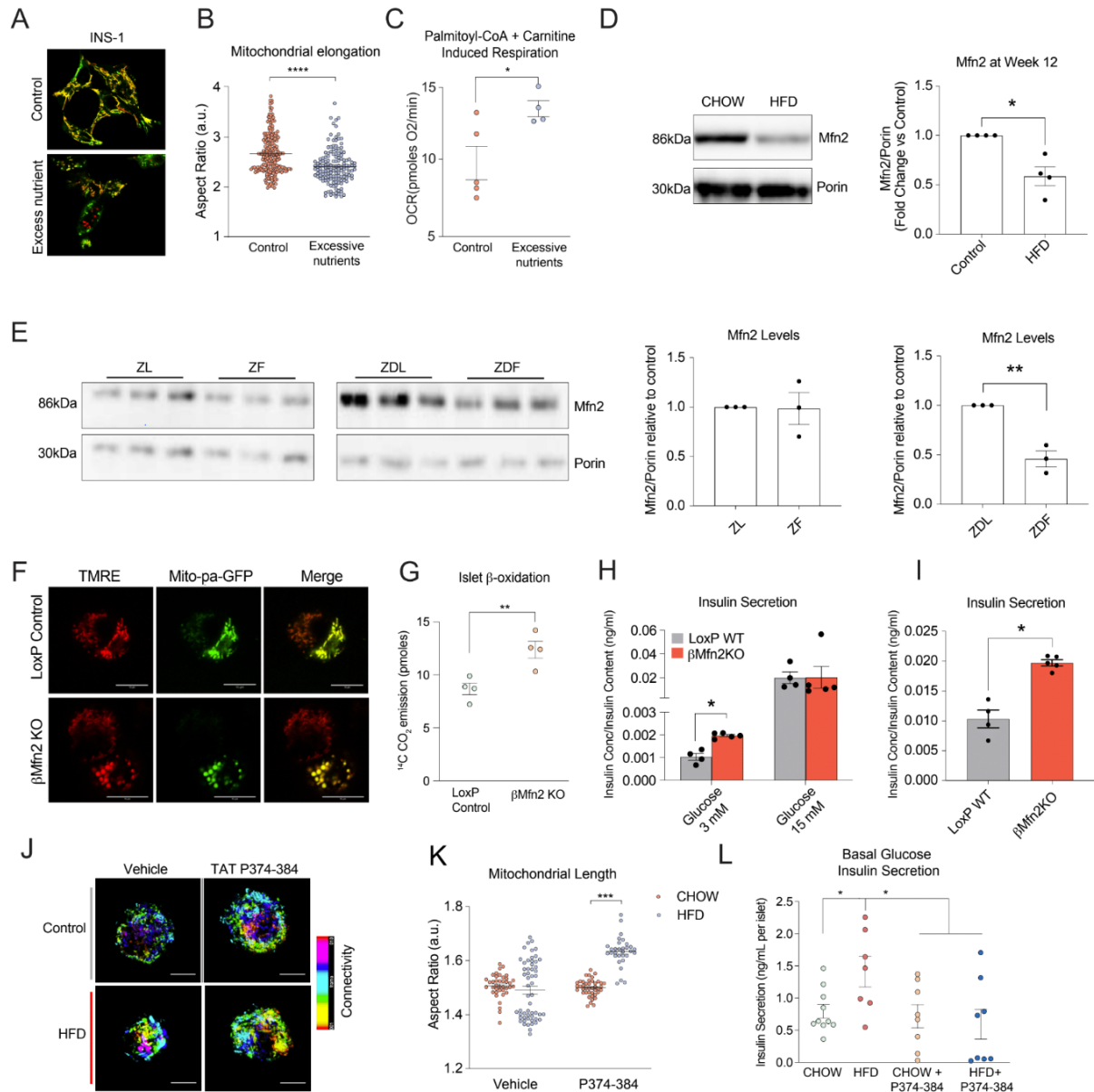


Figure 2

Figure 2- 2. Mitochondrial fragmentation induced by Mfn2 in beta-cells increases fatty acid sensitivity

Representative images of live-cell super-resolution confocal imaging of INS1 cells stained with TMRE (red) and MitoTracker Green. Scale bar = 10 μ m. INS1 cells were exposed

to control or excess nutrients (GLT; 20mM glucose and 0.4mM palmitate) media for 19 hrs. **B.** INS1 cells subjected to GLT were significantly more fragmented as indicated by reductions to aspect ratio. n = 20-30 cells from 3 individual experiments. ****P < 0.0001 compared to vehicle by Student's t-test. **C.** INS1 cells yielding greater presence of fragmented mitochondria had increased fatty acid utilization. n = 6 technical replicates from 4 individual experiments. *P < 0.05 compared to vehicle by Student's t-test. **D.** Western blot analysis of protein lysates obtained from islets isolated from male C57BL/6J mice fed a CHOW or HFD for 12 weeks. HFD mice reveal a decrease in Mfn2. Actin and Porin expression were equal in both sets of mouse islets tested (n=3 for each group). Representative western blot and densitometric analyses demonstrating decreased Mfn2 expression in mouse islets after 12 weeks of HFD. **E.** Islets isolated from 8-week-old Zucker Lean (ZL), Zucker Fatty (ZF), Zucker Diabetic Lean (ZDL), and Zucker Diabetic Fatty (ZDF) and tested for Mfn2 protein expression (n=3 per group). Densitometric analyses of Mfn2/porin indicates that there is a 41% decrease in Mfn2 expression in ZDF rats compared to ZDL control (p<0.05) and no difference between ZF and ZL mice. Data information: In (A,B, D–F, G-I), data are presented as mean \pm SEM. *P \leq 0.05 and ****P \leq 0.0001 (Student's t-test). **F.** Representative confocal images of islet mitochondria labeled with TMRE and mito-paGFP (insulin promoter). beta-cells were identified by 2-photon mediated photoconversion of paGFP. Representative confocal images of beta-cells and non beta-cells (no GFP expression) from dispersed islets. Mitochondrial fragmentation is only evident in the beta-cells obtained from β Mfn2KO samples. (n= 3 mice per group). Scale bars: 10 μ m. **2G.** Mfn2KO islets exhibit greater production of ¹⁴CO₂ from labeled palmitate. Data presented as 100 islets/condition; n=4 female mice.

****P < 0.01** compared to vehicle by Student's t-test. **2H.** β Mfn2KO islets exhibit increased basal insulin secretion with no changes to GSIS. n=7 and 8 animals for WT and β Mfn2KO respectively, performed in technical triplicates, $p \leq 0.05$ by student's t-test. **2I.** Mfn2 excision in the beta-cell increases fatty acid sensitivity. Insulin secretion in response to 0.4mM palmitate. β Mfn2KO animals display the increased basal insulin secretion. When 0.4mM palmitate is added with 3mM glucose, β Mfn2KO demonstrate a statistically significant increase in insulin secretion, which is not observed in control islets. Data is shown as mean \pm standard deviation; n = 4 per group. **2J.** Confocal images of islets isolated from CHOW and HFD fed mice fixed in PFA and stained for GRP75. Scale bars: 10 μ m. **2K.** Quantitative analysis of mitochondrial morphology markers, aspect ratio (D), form factor (E), and eccentricity (F) of CHOW and HFD islets isolated from mice (n = 30 islets/mice for each genotype; n=4 mice/group). *****P < 0.001** compared to vehicle by Student's t-test. **2L.** HFD islets exhibit increased basal secretion compared to CHOW. Treatment with a Mfn2 open permissive peptide reduces basal secretion. n = 30 islets/mice for each genotype; n=4 mice/group. ***P < 0.05** compared to vehicle by Student's t-test.

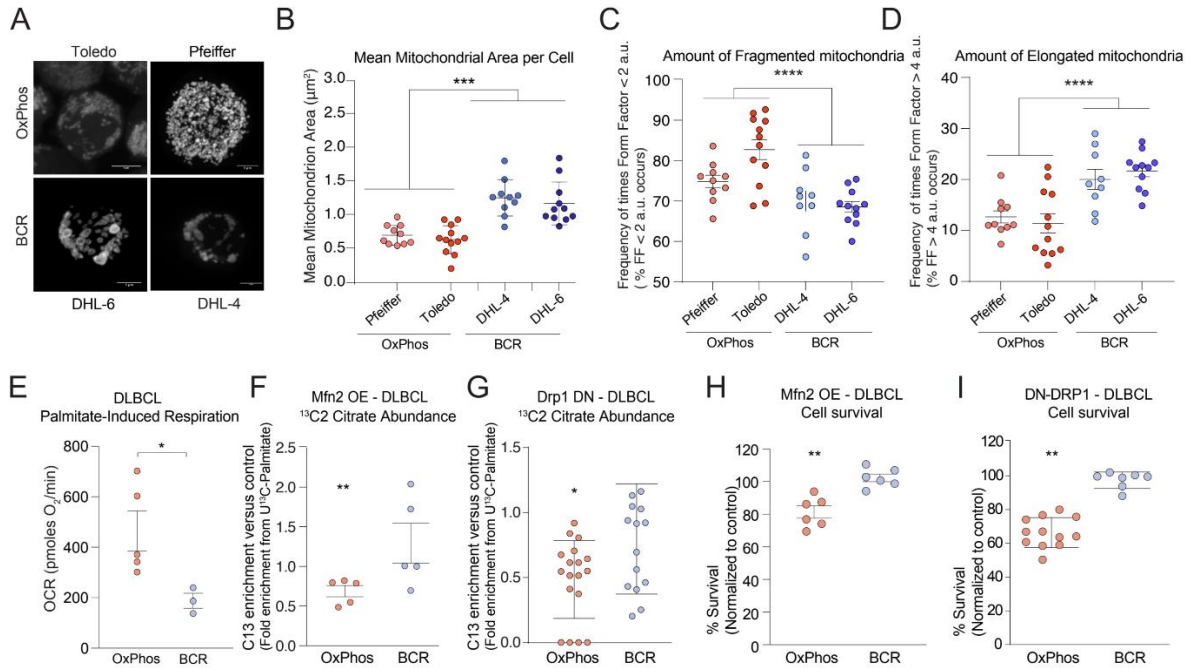


Figure 3

Figure 2- 3. Mitochondrial elongation reduces OxPHOS-DLBCL FAO and impairs cell survival

A. Representative images of live-cell super-resolution confocal imaging of OxPHOS-DLBCL subsets Toledo and Pfeiffer and BCR-DLBCL subsets DHL-6 and DHL-4. Cells stained with MitoTracker Green. Scale bar = 10 µm. **B.** BCR-DLBCL cells yielding greater mean mitochondrion area. n =10 cells. ***P < 0.001 compared to vehicle by Student's t-test. **C.** OxPHOS-DLBCL cells yielding greater presence of fragmented mitochondria. n =10 cells. ****P < 0.0001 compared to vehicle by Welch's t-test. **D.** BCR-DLBCL cells yielding greater presence of elongated mitochondria. n =10 cells. ****P < 0.0001 compared to vehicle by Welch's t-test. **E.** Basal OCR on palmitate in DLBCL subsets. Each dot of the graph represents OCR values assessed in different DLBCL cell lines. 7–13 independent OCR values for each cell line were measured in 4 DLBCL-OxPhos or 3

DLBCL-BCR cell lines. $n = 3$ biological replicates. $*P < 0.05$ compared to vehicle by Student's t-test. **F, G.** C13 enrichment in citrate in DLBCL subsets with lentiviral expression of Mfn2 (Figure 3F) Drp1-DN (Figure 3G). Each dot of graphs represents a technical replicate of a measurement in 2 different DLBCL-OxPhos and DLBCL-BCR cell lines (Figure 3F), or 4 different DLBCL-OxPhos and DLBCL-BCR cell lines (Figure 3G). $n=3$ biological replicates. $**P < 0.01$ compared to vehicle by Student's t-test. $*P < 0.05$, $**P < 0.01$ compared to vehicle by Student's t-test. **H, I.** Cell viability assessed in DLBCL subsets following lentiviral expression of Mfn2 (Figure 3H) and Drp1-DN (Figure 3I). Each dot of graphs represents a technical replicate of a measurement in 2 different DLBCL-OxPhos and DLBCL-BCR cell lines (Figure 3H), or 4 different DLBCL-OxPhos or DLBCL-BCR cell lines (Figure 3I). $n=3$ biological replicates. $**P < 0.01$ compared to vehicle by Student's t-test.

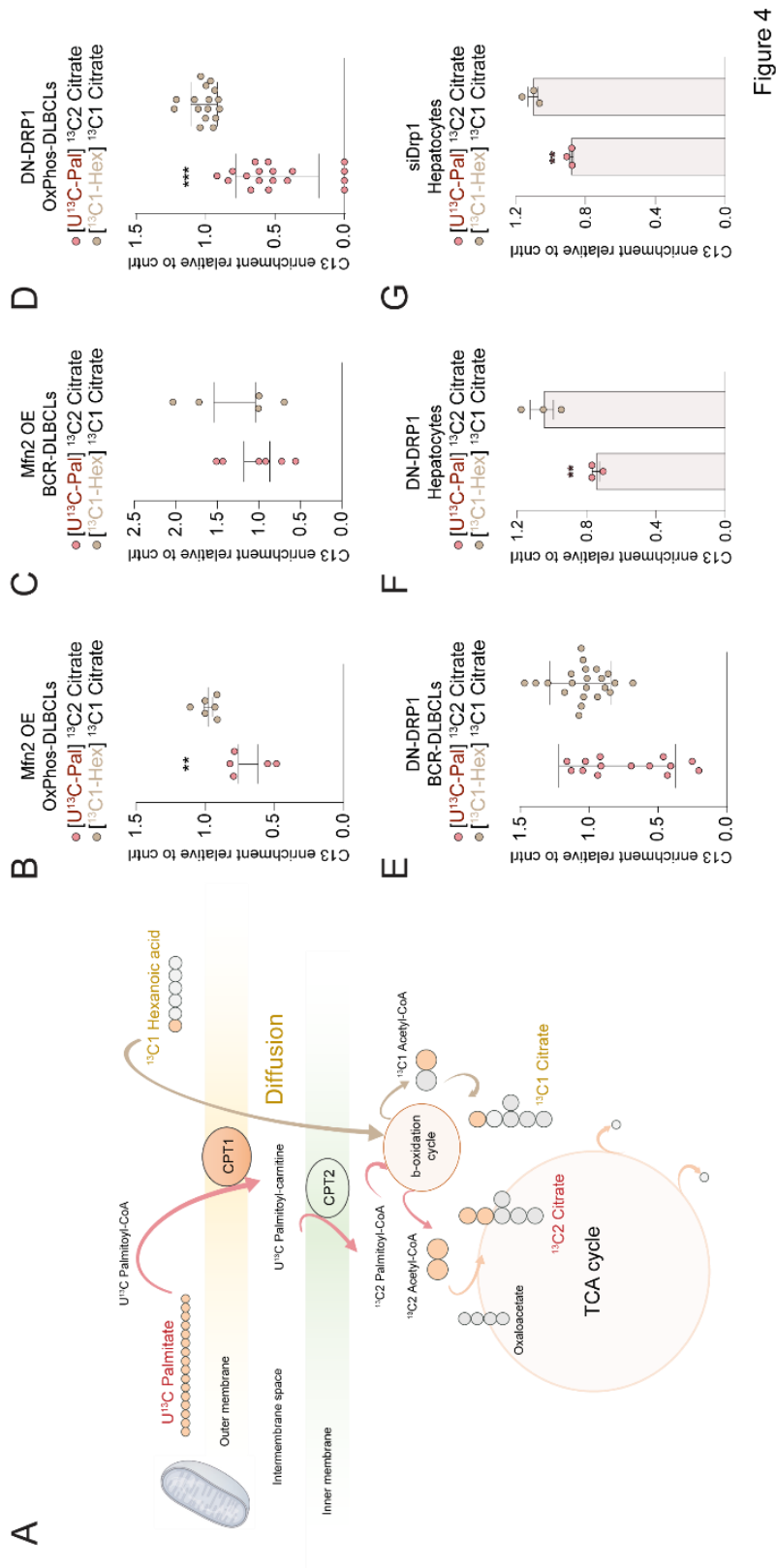


Figure 2- 4. Mitochondrial architecture specifically alters CPT1-dependent FAO

A. Schematics representation of experimental approach to measuring short chain vs long chain fatty acid utilization using stable isotope tracing analysis. **B, C.** Citrate C13 enrichment following [U-¹³C] palmitate or [1-¹³C] hexanoic acid treatment in OxPhos-DLBCL (Figure 4B) or BCR-DLBCL (Figure 4C) with lentiviral expression of Mfn2. Each dot of graphs represents a technical replicate from a measurement in 2 different DLBCLS-OxPhos (Figure 4D) or DLBCLS-BCR (Figure 4E) cell lines. n=3 biological replicates. **P < 0.01 compared to vehicle by Student's t-test. **D, E.** Citrate C13 enrichment following [U-¹³C] palmitate or [¹³C1] hexanoic acid treatment in OxPhos-DLBCL (Figure 4D) or BCR-DLBCL (Figure 4E) with lentiviral expression of Drp1-DN. Each dot represents a technical replicate from a measurement in 4 different DLBCLS-OxPhos (Figure 4D) or DLBCLS-BCR (Figure 4E) cell lines. n=3 biological replicates. ***P < 0.001 compared to vehicle by Student's t-test. **F, G.** Citrate 13C enrichment following [U-¹³C] palmitate or [¹³C1] hexanoic acid treatment in primary hepatocytes with lentiviral expression of Drp1-DN (Figure 4F) or transfection of siRNA against Drp1 (Figure 4G). n=3 biological replicates. **P < 0.01 compared to vehicle by Student's t-test.

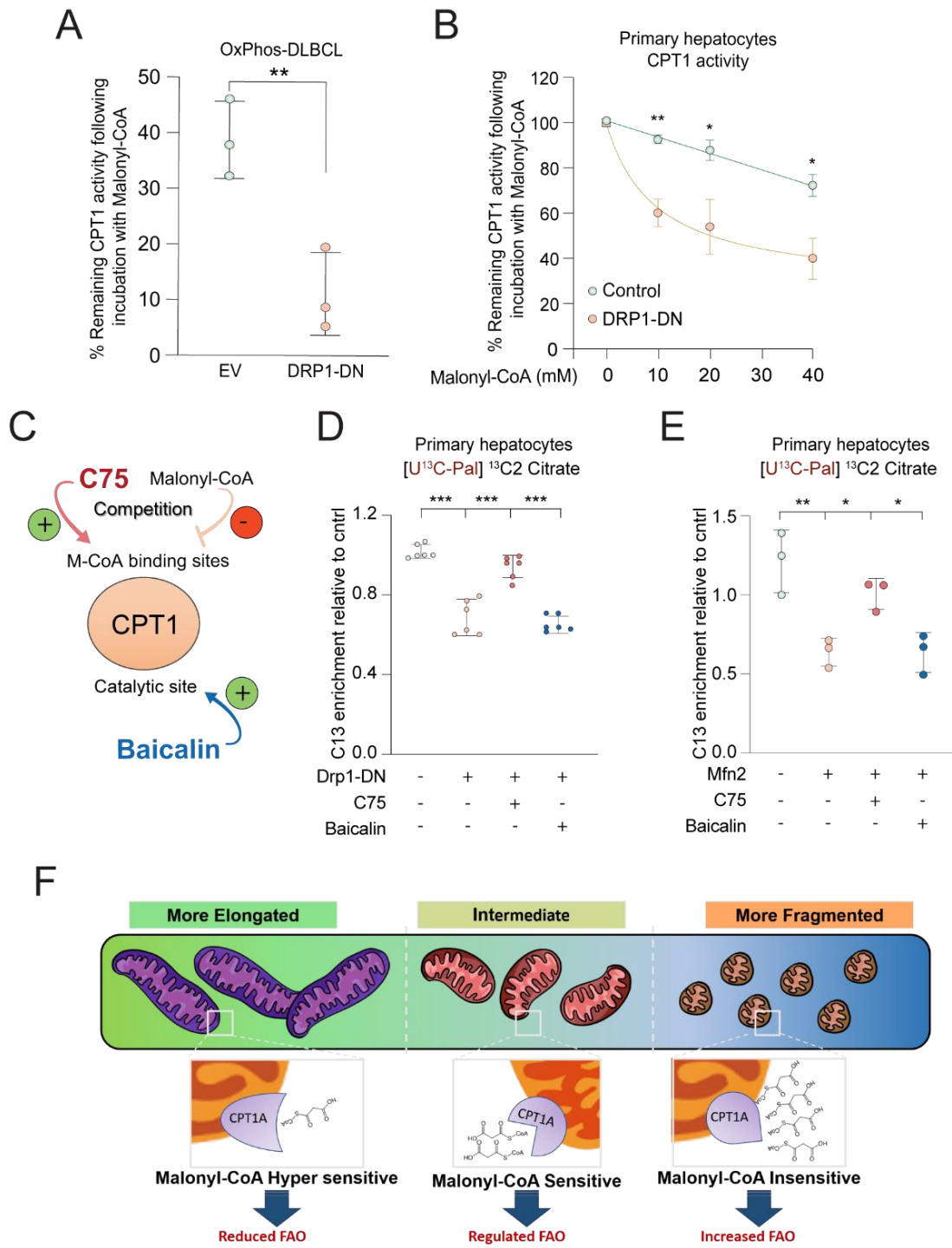


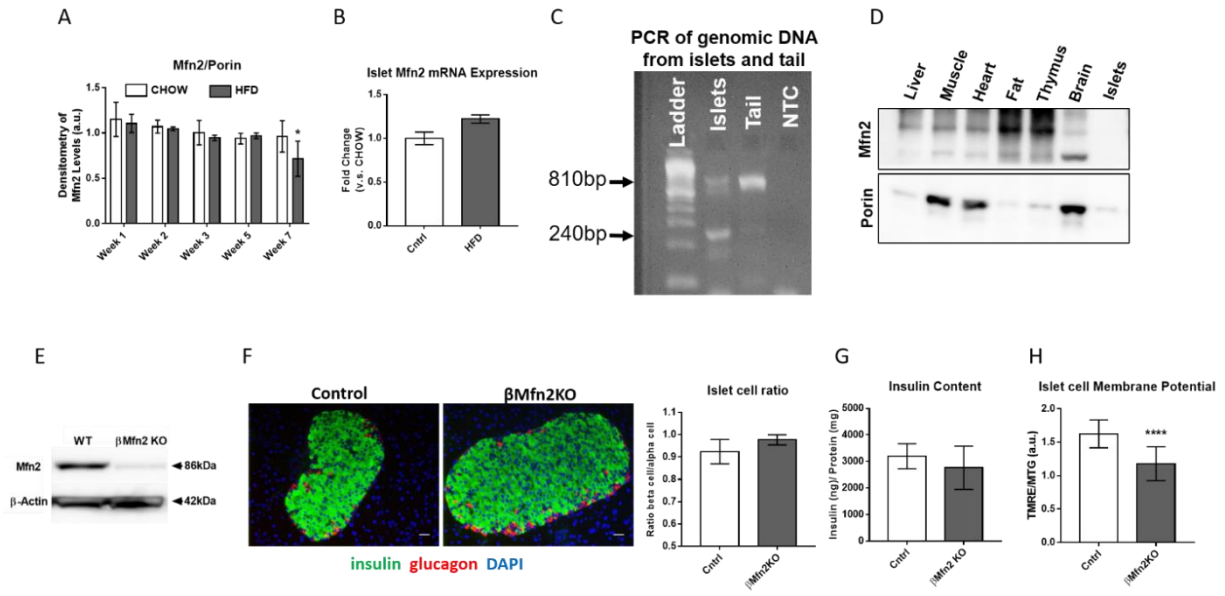
Figure 5

Figure 2- 5. Mitochondrial architecture specifically alters the interaction between CPT1 and Malonyl-CoA

CPT1 activity measured in the presence of 100 μ M of malonyl-CoA in heavy membrane fraction including mitochondria purified from OxPhos-DLBCL (Toledo) following lentiviral expression of DRP1-DN. $n=3$ biological replicates. $**P < 0.01$ compared to vehicle by Student's t-test. **B.** CPT1 activity assessed in the presence of malonyl-CoA at different concentration (10, 20, 30, or 40 μ M) in heavy membrane fraction including mitochondria purified from primary hepatocytes following adenoviral expression of DRP1-DN. $n=3$ biological replicates. $*P < 0.05$, $**P < 0.01$ compared to vehicle by Student's t-test. **C.** Schematics depicting mechanisms underlying C75 and baicalin activation of CPT1. C75 activates CPT1 by binding to a CPT1 region shared with malonyl-CoA, allowing for its competitive inhibition of malonyl-CoA suppression of CPT1, while baicalin binding to CPT1 catalytic site provokes CPT1 activation. **D, E.** Citrate ^{13}C enrichment in uniformly labelled palmitate ($U^{13}C$ palmitate)-treated primary hepatocytes upon C75 (20 μ M) or baicalin (100 μ M) treatment following Drp1-DN (Figure 6D) or Mfn2 expression (Figure 6E). $n=3$ biological replicates. $*P < 0.05$, $**P < 0.01$, $***P < 0.01$ compared between each sample by one-way ANOVA. **F.** Schematic representation of proposed mechanism by which mitochondrial morphology regulates fatty acid oxidation through CPT1 sensitivity to malonyl-CoA.

Expanded View Figure 2- 1. Drp1 reduction verification in hepatocytes

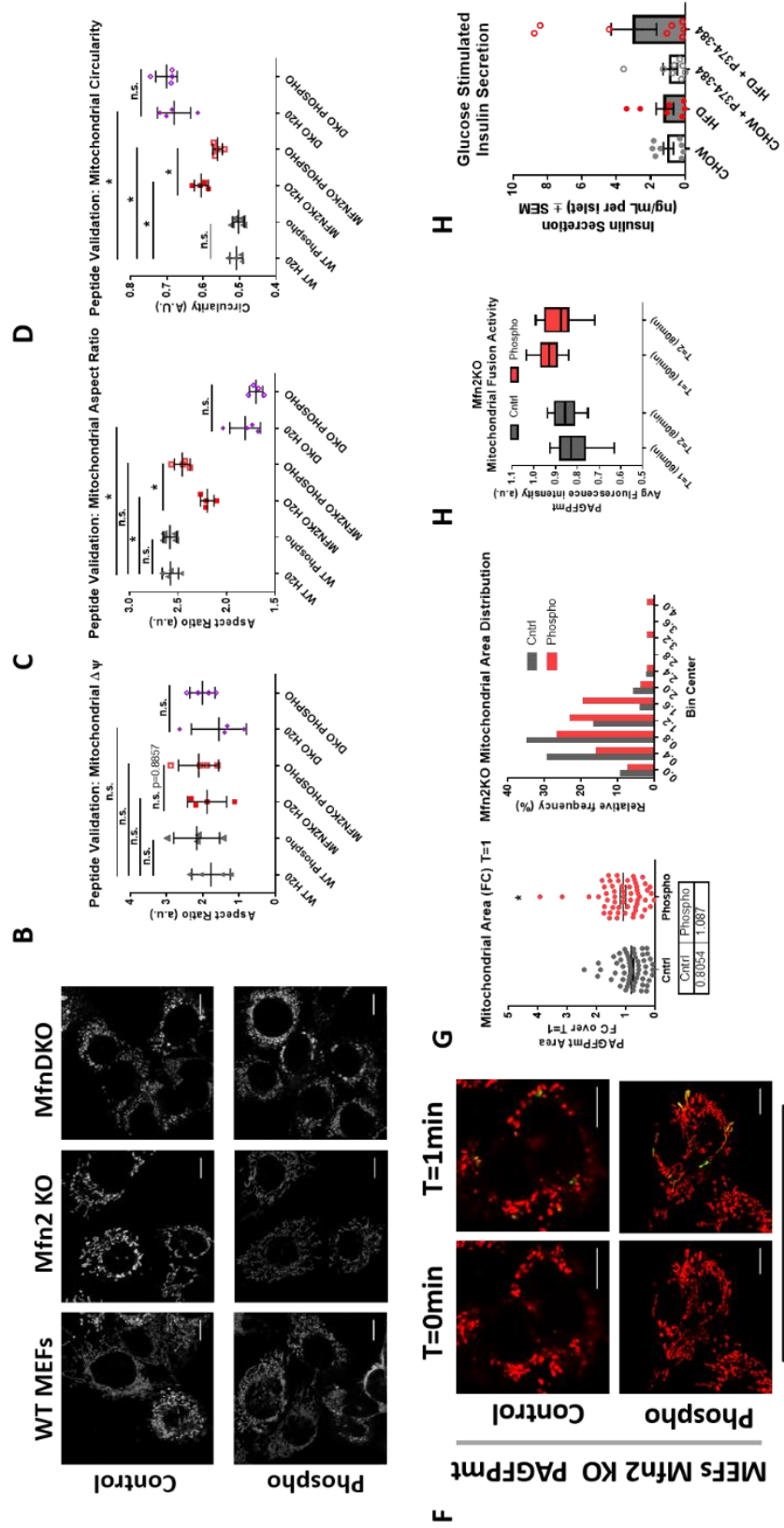
EV1A. Representative blots of Drp1 and beta-actin from primary hepatocytes of dnDrp1 and control. **EV1B.** Representative blots of Drp1 and beta-actin from primary hepatocytes of Drp1 KO and control.



Expanded View Figure 2- 2. Beta-cell specific Mfn2KO islet verification

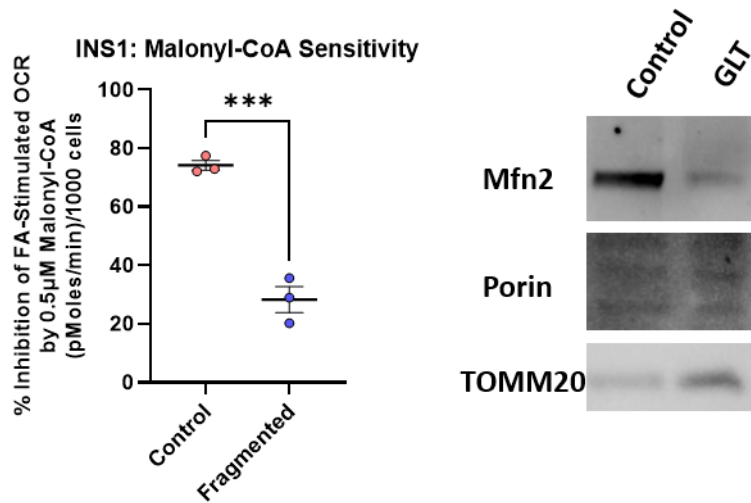
EV2A. Mfn2 protein levels are decreased in pancreatic islets under HFD. Male C57BL/6J mice were provided with a high fat or a control diet for 12 weeks. Western blot analysis of protein lysates obtained from islets isolated from HFD mice reveal a decrease in Mfn2 starting at week 7. Mouse islets tested (N=3). *P < 0.5 compared to vehicle by Student's t-test. **EV2B.** No differences in Mfn2 mRNA were observed in β Mfn2KO islets compared with control islets. **EV2C.** Mfn2 LoxP PCR of genomic DNA obtained from a tail sample and islets from a β Mfn2KO animal. Lane 1 is the PCR product obtained using islet DNA as the template, the product is present at a 240bp excised band demonstrating knockout of Mfn2. Any residual unexcised 810bp band is contributed by other cell types in the islet that would have Mfn2 excised under RIP. Lane 2 is the PCR product obtained using tail lysates and is present as the unexcised 810bp band. Lane 3 is the no template control. **EV2D.** Tissue specificity of the beta-cell specific Mfn2 knockout was measured in tissue samples obtained from a β Mfn2KO mouse. Mfn2 expression was measured by western

blot and was found to be present at varying degrees in all tissues tested except for isolated pancreatic islets. **EV2E.** Representative blots of Mfn2 and beta-actin from islets of β Mfn2KO and control littermates. Any present Mfn2 is attributed to non-beta-cell islet cells in β Mfn2KO islets. **EV2F.** Immunohistochemical staining of pancreatic sections reveal that the ratio of beta-cells stained with anti-insulin (green) compared to α -cells stained with anti-glucagon antibody (red) in β Mfn2KO sections is not changed in comparison to control; nuclei are stained with DAPI (blue). IHC also demonstrates the increase in islet size in the KO sections. **EV2G.** No differences in insulin content were observed in β Mfn2KO islets compared with control islets (n=3 mice per group; technical triplicates of 10 islets each from each animal). **EV2H.** β Mfn2KO islets yielded significant reductions to membrane potential as compared with control islets. Cells were stained with TMRE (red) and MitoTracker Green. (n=3 mice per group; technical triplicates of 10 islets each from each animal). ****P < 0.0001 compared to vehicle by Student's t-test.



Expanded View Figure 2- 3. Mfn2-TAT peptide validation

EV3A. Representative images of live-cell super-resolution confocal imaging of WT, Mfn2KO, and Mfn2DKO MEFs stained with TMRE (red) and MitoTracker Green. Scale bar = 10 μ m. **EV3B.** Mfn2-TAT peptide did significantly change mitochondrial membrane potential. Cells were stained with TMRE (red) and MitoTracker Green. **EV3C, D.** Mfn2-TAT peptide only changed mitochondrial morphology in Mfn2KO MEF cells. n = 30-50 cells from 4 individual experiments. *P < 0.5 compared to vehicle by Student's t-test. **EV3F, G, H.** Representative confocal images and quantification of Mfn2KO MEF cells mitochondria labeled with TMRE and mito-paGFP (insulin promoter). Enhanced fusion was identified by 2-photon mediated photoconversion of paGFP. Mitochondrial fusion is only evident in Mfn2KO MEF cells treated with the Mfn2-TAT peptide. Scale bars: 10 μ m. **EV3I.** Treatment with a Mfn2 open permissive peptide does not impair insulin secretion as islets exhibit a response to glucose. n = 30 islets/mice for each genotype; n=4 mice/group. **EV3J.** HFD mice display increased basal secretion. Insulin secretion at 3mmol/L glucose (NGSIS) (A) or 16.7mmol/L glucose (GSIS). In isolated mouse islets from CHOW fed and High fat fed-mice (HFD). (n = 7-10 independent experiments).



Expanded View Figure 2- 4. CPT1 sensitivity in INS1 cells

EV4A. CPT1 sensitivity measured in the presence of 0.5 uM of malonyl-CoA in permeabilized INS1 cells following GLT (20mM glucose + 400 uM palmitate) treatment. n=3 biological replicates. ***P < 0.001 compared to control by Student's t-test. **EV4B.** Representative blots of Mfn2, porin, and TOMM20 from INS1 cells of GLT (20mM glucose + 400 uM palmitate) and control INS1 cells.

REFERENCES

- Akkaoui M, Cohen I, Esnous C, Lenoir V, Sournac M, Girard J & Prip-Buus C (2009) Modulation of the hepatic malonyl-CoA-carnitine palmitoyltransferase 1A partnership creates a metabolic switch allowing oxidation of de novo fatty acids. *Biochem J* 420
- Baron AD, Brechtel G & Edelman S V. (1989) Effects of free fatty acids and ketone bodies on in vivo non-insulin-mediated glucose utilization and production in humans. *Metabolism* 38: 1056–1061
- Benador IY, Veliova M, Mahdaviani K, Petcherski A, Wikstrom JD, Assali EA, Acín-Pérez R, Shum M, Oliveira MF, Cinti S, *et al* (2018) Mitochondria Bound to Lipid Droplets Have Unique Bioenergetics, Composition, and Dynamics that Support Lipid Droplet Expansion. *Cell Metab* 27: 869-885.e6
- Bremer J, Woldegiorgis G, Schalinske K & Shrago E (1985) Carnitine palmitoyltransferase. Activation by palmitoyl-CoA and inactivation by malonyl-CoA. *Biochim Biophys Acta* 833: 9–16
- Caro P, Kishan AU, Norberg E, Stanley IA, Chapuy B, Ficarro SB, Polak K, Tondera D, Gounarides J, Yin H, *et al* (2012) Metabolic Signatures Uncover Distinct Targets in Molecular Subsets of Diffuse Large B Cell Lymphoma. *Cancer Cell* 22: 547–560
- Dai J, Liang K, Zhao S, Jia W, Liu Y, Wu H, Lv J, Cao C, Chen T, Zhuang S, *et al* (2018) Chemoproteomics reveals baicalin activates hepatic CPT1 to ameliorate diet-induced obesity and hepatic steatosis. *Proc Natl Acad Sci U S A* 115: E5896–E5905
- Divakaruni AS, Hsieh WY, Minarrieta L, Duong TN, Kim KKO, Desousa BR, Andreyev AY, Bowman CE, Caradonna K, Dranka BP, *et al* (2018) Etomoxir Inhibits Macrophage Polarization by Disrupting CoA Homeostasis. *Cell Metab* 28: 490-

503.e7

- Fex M, Nitert MD, Wierup N, Sundler F, Ling C & Mulder H (2007) Enhanced mitochondrial metabolism may account for the adaptation to insulin resistance in islets from C57BL/6J mice fed a high-fat diet. *Diabetologia* 50: 74–83
- Gao Y, Li F, Zhang A, Wang L, Tong W & Liu B (2014) Evaluation of mitochondrial divisions in mouse with type-2 diabetes and effect of glucose-oxidase on mouse islet cells RIN-m5F. *Cell Biol Int* 38: 368–373
- Gooptu M, Whitaker-Menezes D, Sprandio J, Domingo-Vidal M, Lin Z, Uppal G, Gong J, Fratamico R, Leiby B, Dulau-Florea A, *et al* (2017) Mitochondrial and glycolytic metabolic compartmentalization in diffuse large B-cell lymphoma. *Semin Oncol* 44: 204–217
- Hoppel C, Kerner J, Turkaly P & Tandler B (2001) Rat Liver Mitochondrial Contact Sites and Carnitine Palmitoyltransferase-I. *Arch Biochem Biophys* 392: 321–325
- Huynh FK, Green MF, Koves TR & Hirschey MD (2014) Measurement of fatty acid oxidation rates in animal tissues and cell lines. *Methods Enzymol* 542: 391–405
- Kulkarni SS, Joffraud M, Boutant M, Ratajczak J, Gao AW, Maclachlan C, Hernandez-Alvarez MI, Raymond F, Metairon S, Descombes P, *et al* (2016) Mfn1 Deficiency in the Liver Protects Against Diet-Induced Insulin Resistance and Enhances the Hypoglycemic Effect of Metformin. *Diabetes* 65: 3552–3560
- Lam TKT, Carpentier A, Lewis GF, Van de Werve G, Fantus IG & Giacca A (2003a) Mechanisms of the free fatty acid-induced increase in hepatic glucose production. *Am J Physiol - Endocrinol Metab* 284
- Lam TKT, Van de Werve G & Giacca A (2003b) Free fatty acids increase basal hepatic

- glucose production and induce hepatic insulin resistance at different sites. *Am J Physiol Metab* 284: E281–E290
- Liesa M & Shirihai OSS (2013) Mitochondrial dynamics in the regulation of nutrient utilization and energy expenditure. *Cell Metab* 17: 491–506
- Mahdaviani K, Benador IY, Su S, Gharakhanian RA, Stiles L, Trudeau KM, Cardamone M, Enríquez-Zarralanga V, Ritou E, Aprahamian T, *et al* (2017) Mfn2 deletion in brown adipose tissue protects from insulin resistance and impairs thermogenesis. *EMBO Rep* 18: 1123–1138
- Masini M, Martino L, Marselli L, Bugliani M, Boggi U, Filipponi F, Marchetti P & De Tata V (2017) Ultrastructural alterations of pancreatic beta cells in human diabetes mellitus. *Diabetes Metab Res Rev* 33
- McCune SA, Durant PJ, Jenkins PA & Harris RA (1981) Comparative studies on fatty acid synthesis, glycogen metabolism, and gluconeogenesis by hepatocytes isolated from lean and obese Zucker rats. *Metabolism* 30: 1170–1178
- McGarry JD & Brown NF (1997) The mitochondrial carnitine palmitoyltransferase system. From concept to molecular analysis. *Eur J Biochem* 244: 1–14
- Molina AJ a, Molina AJ a, Wikstrom JD, Wikstrom JD, Stiles L, Stiles L, Las G, Las G, Mohamed H, Mohamed H, *et al* (2009) Mitochondrial Networking Protects Beta Cells from Nutrient Induced Apoptosis. *Diabetes* 58: 2303–2315
- Moore MP, Cunningham RP, Meers GM, Johnson SA, Wheeler AA, Ganga RR, Spencer NM, Pitt JB, Diaz-Arias A, Swi AIA, *et al* (2022) Compromised hepatic mitochondrial fatty acid oxidation and reduced markers of mitochondrial turnover in human NAFLD. *Hepatology*

- Nolan CJ, Leahy JL, Delghingaro-Augusto V, Moibi J, Soni K, Peyot M-LL, Fortier M, Guay C, Lamontagne J, Barbeau A, *et al* (2006a) Beta cell compensation for insulin resistance in Zucker fatty rats: increased lipolysis and fatty acid signalling. *Diabetologia* 49: 2120–2130
- Nolan CJ, Madiraju MSR, Delghingaro-Augusto V, Peyot M-L & Prentki M (2006b) Fatty acid signaling in the beta-cell and insulin secretion. *Diabetes* 55 Suppl 2: S16-23
- Norberg E, Lako A, Chen PH, Stanley IA, Zhou F, Ficarro SB, Chapuy B, Chen L, Rodig S, Shin D, *et al* (2017) Differential contribution of the mitochondrial translation pathway to the survival of diffuse large B-cell lymphoma subsets. *Cell Death Differ* 24: 251
- Poulaki A & Giannouli S (2021) Metabolic Swifths Govern Normal and Malignant B Cell Lymphopoiesis. *Int J Mol Sci* 22
- Qu Q, Zeng F, Liu X, Wang QJ & Deng F (2016) Fatty acid oxidation and carnitine palmitoyltransferase I: emerging therapeutic targets in cancer. *Cell Death Dis* 7: e2226–e2226
- Rocha AG, Franco A, Krezel AM, Rumsey JM, Alberti JM, Knight WC, Biris N, Zacharioudakis E, Janetka JW, Baloh RH, *et al* (2018) MFN2 agonists reverse mitochondrial defects in preclinical models of Charcot-Marie-Tooth disease type 2A. *360*: 336–341
- Rui L (2014) Energy metabolism in the liver. *Compr Physiol* 4: 177–97
- Satapati S, Kucejova B, Duarte JAG, Fletcher JA, Reynolds L, Sunny NE, He T, Arya Nair L, Livingston K, Fu X, *et al* (2015) Mitochondrial metabolism mediates oxidative stress and inflammation in fatty liver. *J Clin Invest* 125: 4447–4462

- Sebastián D, Hernández-Alvarez MI, Segalés J, Sorianello E, Muñoz JP, Sala D, Waget A, Liesa M, Paz JC, Gopalacharyulu P, *et al* (2012) Mitofusin 2 (Mfn2) links mitochondrial and endoplasmic reticulum function with insulin signaling and is essential for normal glucose homeostasis. *Proc Natl Acad Sci U S A* 109: 5523–8
- Song JE, Alves TC, Stutz B, Šestan-Peša M, Kilian N, Jin S, Diano S, Kibbey RG & Horvath TL (2021) Mitochondrial fission governed by drp1 regulates exogenous fatty acid usage and storage in hela cells. *Metabolites* 11
- Stiles L & Shirihai OS (2012) Mitochondrial dynamics and morphology in beta-cells. *Best Pract Res Clin Endocrinol Metab* 26: 725–738 doi:10.1016/j.beem.2012.05.004 [PREPRINT]
- Supale S, Li N, Brun T & Maechler P (2012) Mitochondrial dysfunction in pancreatic β cells. *Trends Endocrinol Metab* 23: 477–487 doi:10.1016/j.tem.2012.06.002 [PREPRINT]
- Titchenell PM, Quinn WJ, Lu M, Chu Q, Lu W, Li C, Chen H, Monks BR, Chen J, Rabinowitz JD, *et al* (2016) Direct Hepatocyte Insulin Signaling Is Required for Lipogenesis but Is Dispensable for the Suppression of Glucose Production. *Cell Metab* 23: 1154–1166
- Whitley BN, Lam C, Cui H, Haude K, Bai R, Escobar L, Hamilton A, Brady L, Tarnopolsky MA, Denge L, *et al* (2018) Aberrant Drp1-mediated mitochondrial division presents in humans with variable outcomes *Human Molecular Genetics*, Vol. 00, No. 0 *Human Molecular Genetics*, Vol. 00, No. 0. *Hum Mol Genet* 27: 3710–3719
- Xiong J & Zhao WL (2018) Targetable Metabolic Vulnerability in Diffuse Large B-Cell Lymphoma. *EBioMedicine* 28: 5–6

Zhou X, Zhu X, Zeng H & Zeng CH (2021) Fatty acid metabolism in adaptive immunity.

FEBS J

CHAPTER 3

Decreasing DRP1 expression in liver activates the mitochondrial integrated stress response and exacerbates NASH

The work describe in this chapter has been submitted to Hepatology and is currently
under revision:

Janos Steffen*, Jennifer Ngo*, Sheng-Ping Wang*, Kevin Williams, Fritz Kramer, George
Ho, Carlos Rodriguez, Krishna Yekkala, Chidozie Amuzie, Russell Bialecki, Lisa
Norquay, Andrea Nawrocki, Mark Erion, Alessandro Pocai, Orian Shirihai, Marc Liesa.
(2022) Decreasing DRP1 expression in liver activates the mitochondrial integrated
stress response and exacerbates NASH. *Hepatology*

*contributed equally

Copyright 2022

Hepatology

I was co-first author of this work and conducted the biochemical experiments. Janos
Steffen and Sheng-Ping assisted with quantitative PCR analysis and animal models,
respectively. Professor Marc Liesa and I wrote the manuscript.

ABSTRACT

Aims: Non-alcoholic fatty liver disease (NAFLD) increases Drp1-mediated mitochondrial fragmentation in hepatocytes. Deletion and inhibition of hepatic Drp1 in early life prevents high fat diet-induced liver steatosis in mice. However, whether Drp1 knockdown (Drp1 KD) can reverse established steatohepatitis (NASH) in mice is unknown. Hepatocyte-restricted delivery of siRNA conjugated to N-acetyl-galactosamine (GalNAc) is a safe and non-toxic approach to manipulate gene expression in liver, which is currently approved by the FDA and EMA to treat genetic forms of liver disease. Thus, we aimed to decrease Drp1 function in liver from adult mice with established NASH using GalNAc-siRNA mediated delivery.

Methods: To determine Drp1 KD safety, C57BL/6J mice fed a chow-diet for 26 weeks were injected weekly with vehicle (PBS) or GalNAc-Drp1-siRNA for 4 weeks. Mice with established NASH (26 week-GAN diet) were injected weekly with GalNAc-Drp1-siRNA for 12 weeks. Liver steatosis and damage were assessed by histology, by quantifying AST and ALT and by gene expression measurements of inflammation and fibrosis markers. Liver NEFA and triglycerides were quantified by GC/MS. Mitochondrial mass and function were determined in liver homogenates. Western blots of Oma1, Opa1, phosphorylated EIF2alpha, as well as transcriptional analyses of Atf4 and Atf4-regulated genes determined ISR engagement.

Results: In control mice, Drp1 KD in liver decreased body weight, elevated circulating AST and ALT and increased the expression of pro-inflammatory and fibrosis markers in liver. Decreased body weight was largely explained by reduced food intake caused by Gdf15 actions, as Gdf15 receptor (Gfral) KO prevented the decrease in food intake and

mitigated weight loss induced by Drp1 KD. ISR can explain increased hepatic Gdf15 expression, as Drp1 KD caused ER stress and Oma1 activation, elevated EIF2alpha phosphorylation and Atf4 expression. While NASH was not sufficient to activate OMA1, Drp1 KD in mice with NASH activated OMA1 and exacerbated ER stress, ISR, inflammation, fibrosis and induced hepatocyte necrosis.

Conclusion: Drp1-mediated mitochondrial fragmentation is an adaptative mechanism in NASH that prevents ISR overactivation and ER stress to limit fibrosis, inflammation, and necrosis. The elevation in Gdf15 actions induced by Drp1 KD might represent an adaptive response reducing the nutrient load to hepatocytes when their mitochondria are dysfunctional. Our study argues against blocking Drp1-mediated fragmentation in hepatocytes to combat NASH.

INTRODUCTION

No pharmacological agents are available to treat non-alcoholic steatohepatitis (NASH), a disease that is expected to become the first cause for liver transplantation in Western societies (Burra *et al*, 2020). The presence of lipid accumulation inside hepatocytes, together with hepatocyte ballooning and lobular inflammation, is used to diagnose NASH (Burra *et al*, 2020). Given that intrahepatic lipid accumulation can precede hepatitis and fibrosis, it is thought that the initial changes in hepatic lipid metabolism play a major role in initiating inflammation. Accordingly, preclinical studies and clinical trials testing pharmacological approaches to combat NASH aim to reverse lipid accumulation by directly targeting lipid metabolism in hepatocytes. Some of these approaches include the use of molecules that increase mitochondrial fatty acid oxidation in hepatocytes (Goedeke *et al*, 2019; Boland *et al*, 2020), inhibit enzymes catalyzing lipid synthesis, as well as molecules that limit dietary fat and carbohydrate availability to hepatocytes and concurrently stimulate catabolism (Boland *et al*, 2020).

Mitochondria are central determinants of lipid metabolism in fatty liver disease (Shum *et al*, 2020). In patients with insulin resistance and fatty liver, fat oxidation in mitochondria is still upregulated to support the increased demand for both ATP and carbon intermediates that sustain elevated glucose production (Izzo *et al*, 2010). The upregulation in mitochondrial function in NAFLD not only includes elevated fat oxidation, but also elevated TCA fluxes (Sunny *et al*, 2011) that provide carbon intermediates that fuel fatty acids synthesis (McGarry *et al*, 1977). Different studies support that a non-compensated increase in mitochondrial ROS production resulting from the permanent increase in mitochondrial function can be the trigger to initiate hepatitis (Koliaki *et al*,

2015) . Therefore, targeting mitochondria is an appealing approach to resolve hepatic lipid accumulation, counteract oxidative damage, and potentially treat NASH.

Mitochondrial function and ROS production are strongly determined by the ability of an individual mitochondrion to engage in fusion and fission and move inside the cell, processes collectively known as mitochondrial dynamics (Liesa *et al*, 2009) . The shape of mitochondria itself and their intracellular location not only determines their function synthesizing ATP and producing ROS, but also the removal of damaged units by mitophagy (Liesa & Shirihai, 2013) . As multiple stresses that primarily increase ROS production, impair mitochondrial ATP synthesis and/or activate cell death cause mitochondrial fragmentation, there was an early interest to block Drp11-mediated fragmentation to treat diseases associated with mitochondrial dysfunction. In the context of NAFLD, previous studies in mice determined the effect of hepatocyte-restricted Drp11 inhibition preventing NAFLD induced by high fat diet feeding (Galloway *et al*, 2014; Wang *et al*, 2015) . Constitutive hepatic Drp11 deletion largely prevented body fat gain, glucose intolerance and hepatic steatosis by increasing systemic energy expenditure. The increase in energy expenditure was shown to be caused by an increase in Fgf21 secretion to the circulation, because of elevated hepatic ER stress and liver damage. However, decreasing Drp11 activity by expressing a dominant negative form of DRP1L (K38A) reversed steatosis without causing liver damage (Galloway *et al*, 2014) . The proposed mechanism for protection from steatosis was improved lipid excretion via lipoproteins to increase body fat mass, as well as an increasing in mitochondrial uncoupling that elevated fat expenditure (Galloway *et al*, 2014) . This latter study supported that a Drp1L knock-down approach could held promise to reverse not just simple steatosis, but NASH as well.

Delivery of siRNA conjugated to N-acetylgalactosamine (GalNAc) is a safe, non-toxic approach to knockdown genes specifically in hepatocytes. Indeed, the FDA and EMA approved a GalNAc-siRNA therapy for acute hepatic porphyria, a liver disease with an onset mostly in females ranging from 14-45 years old (Wang *et al*, 2018; Mullard, 2018) . Therefore, GalNAc mediated delivery of Drp1l siRNA in mice with established NASH is the best approach to determine whether Drp1l KD holds any promise to reverse NASH. The reason is the previous studies deleted or decreased DRP1L activity post-natally or prior to high fat diet feeding (8-weeks old), meaning that Drp1l activity was decreased at an age that holds little translational relevance. In this study, we define the safety of Drp1l hepatic knock down in healthy but older mice (26 weeks-old) and in mice with established NASH (after 26 weeks of GAN diet feeding). We define a novel effect of DRP1L KD in adult liver, which supports that DRP1L inhibition might not be a safe approach to different liver diseases.

EXPERIMENTAL PROCEDURES

Animal handling

All procedures described below were approved by the Janssen Institutional Animal Care and Use Committee and carried out in accordance with the Guide for the Care and Use of Laboratory Animals.

Effect of Drp1 KD in lean mice

13 weeks old male C57BL/6 mice fed regular chow diet were maintained in a 12/12 h light-dark cycle with free access to food and water in a temperature-controlled environment (22°C). These mice were treated with a weekly subcutaneous injection of either PBS or Drp1 GalNAc-siRNA (10 mg/kg, 5 ml/kg) for a total of four doses. Weekly

body weight was monitored. 7 days post the 4th dose, mice were euthanized via CO₂. The whole liver was weighed, and liver fat mass was measured by EchoMRI.

In vivo NASH efficacy study in GAN diet induced NASH mouse model

Male C57BL/6 mice were switched to GAN diet (Research Diets, D09100310, 40% fat, 22% fructose and 2% cholesterol) at 6 weeks old at Taconic Farms. GAN mice and 8 age-matched lean mice fed regular chow (5053; LabDiet, 5% dietary fat; 3.42 kcal/g) were obtained from Taconic Farms (Germantown, NY) at 28 weeks old. Mice were 30 weeks old (24 weeks post GAN diet feeding) at beginning of siRNA treatment. 2 days before treatment, EDTA plasma was collected via tail bleeds for baseline ALT/AST measurement. GAN mice were assigned into PBS and Drp1 GalNAc siRNA groups based on body weight, and ALT/AST (n=12/group). Eight PBS-treated age-matched chow fed mice served as blank controls. Mice were treated with a weekly subcutaneous injection of either PBS or Drp1 GalNAc-siRNA (10mg/kg, 5ml/kg). 9 weeks post treatment, mice were dosed with D₂O (intraperitoneal, 20 mg/kg) followed by adding 8% D₂O in drinking water for the remaining of the study. Weekly food intake and body weight were monitored. 12 weeks post treatment, mice were euthanized via CO₂ after food removal for 3 h. EDTA plasma was collected via cardiac puncture and reserved for further analysis. The whole liver was weighed, and liver fat mass was measured by EchoMRI.

ALT/AST

Plasma analytes were assayed on the VET-AXCEL clinical analyzer (Alfa Wassermann), as per manufacturer's instructions. The ALT (Alfa Wassermann Cat# SA1052), AST (Alfa Wassermann Cat# SA1053), TCHOL (Alfa Wassermann Cat# SA1010), TRIG (Alfa Wassermann Cat# SA1023) reagents and tests were calibrated with the GEMCAL calibrator (Alfa Wassermann, Cat# S1-33) and quality controls tested with Chemical Controls level 1 and 2 (Alfa Wassermann

Cat# C1-4 and C1-5 respectively). All calibrations and reagents QCs were performed on a weekly basis before each test run.

Gdf15, Fgf21, Timp-1 ELISA

Plasma Timp-1 (R&D Systems, MTM100), Gdf15 (R&D Systems, MGD150) and Fgf21 (EMD Millipore Corporation, EZRMFGF21-26K) were measured according to the supplied product's protocol.

Liver morphometric analyses

The right medial and left lateral lobes were sectioned and immersion-fixed in phosphate-buffered 10% formaldehyde for 48 h and then switched to 70% EtOH. The lobes were embedded in blocks of paraffin. All blocks were sectioned into 5 µm paraffin sections and slides were stained with hematoxylin and eosin (H&E) or Picrosirius red (PSR). The pathologist was initially blinded to the treatment groups.

The PSR-stained slides were examined microscopically, and deposition of PSR-stained collagen was diagnosed as fibrosis. Fibrosis was scored according to the following six fibrosis stages:

0 = Staining noted in central vein and portal region (background).

1 = Occasional positive staining strands extend into parenchyma from the capsule, central vein or portal region.

2 = Positive staining strands extend into parenchyma from central vein or portal region and bridge with each other (up to 3 bridging/section).

3 = Positive staining strands extend into parenchyma from central vein or portal region and bridge with each other (more than 3 bridging/section).

4 = Positive staining strands extend into parenchyma from central vein or portal region,

bridging with each other and form a circumscribing pattern (up to 3 circumscribing areas/section).

5 = Positive staining strands extend into parenchyma from central vein or portal region, bridging with each other and form a circumscribing pattern (more than 3 circumscribing areas/section)

The H&E-stained sections were examined microscopically, and histopathological findings were recorded and graded as described below.

- Necrosis 0 (not clearly increased above background), 1 (slight increase in single cell necrosis or rare large foci of necrosis), 2 (notable increase in single cell necrosis), 3 (abundant single cell necrosis).
- Biliary/oval cell hyperplasia, 0 (not present), 1 (minimal), 2 (mild), 3 (moderate), 4 (marked), or 5 (severe)
- Pigmented Macrophages 0 (not present), 1 (minimal), 2 (mild), 3 (moderate), 4 (marked), or 5 (severe)
- Macrovesicular and Microvesicular Steatosis: scored on a 0-5 scale based on a 20% gradient for the extent of the sample affected.
- Inflammation (according to Liang et, al, 2014) # of inflammatory foci -defined as a cluster of 5 or more cells/5 100x fields) 0 (<0.5), 1 (0.5-1.0) 2 (1.0-2.0), 3 (≥2)
- Degeneration/Hypertrophy (adapted from Kleiner et. al and Liang et. al)-0 (none present) 1 (slight degeneration/enlargement of hepatocytes) 2 (many cells with prominent degeneration/hypertrophy)

A NAS score for each sample was generated by calculating the sum of macro and microvesicular steatosis, degeneration/hypertrophy, and inflammation.

Quantitative assessment of Immunohistochemistry (IHC)

Paraffin embedded slides were de-paraffinated in xylene and rehydrated in series of graded ethanol. Type I collagen (Southern Biotech, 1310-01), alpha-smooth muscle actin (α -Sma) (Abcam, Ab124964) and Cd11b (AbCam, 133357) IHC are performed using standard procedures. Briefly, after antigen retrieval and blocking of endogenous peroxidase activity, slides are incubated with primary antibody. The primary antibody is detected using a polymeric HRP-linker antibody conjugate. Next, the primary antibody is visualized with DAB as chromogen. Finally, sections are counterstained in hematoxylin and cover-slipped. IHC-positive staining is quantified by image analysis using the VIS software (Visiopharm, Denmark). The quantitative estimates of IHC-positive staining are calculated as an area fraction.

Liver hydroxyproline synthesis measurement

Hydroxyproline synthesis analysis was performed by Metabolic Solutions, Inc. A piece of liver was snap-frozen in liquid nitrogen and stored at -80°C for collagen synthesis. An aliquot (10 mg) of liver was weighed and re-suspended in a 1N HCl solution containing $2\ \mu\text{g}$ m+6 labeled hydroxyproline ($^{13}\text{C}_5^{15}\text{N}$ -OHP). Samples were hydrolyzed at 100°C for 24 hours. A dowex cleanup column is used to remove HCl. Samples are eluted with ammonium hydroxide and dried with nitrogen gas. Hydroxyproline was derivatized using the method described by March (March, 1975) with modifications by Matthews, Persola and Campbell (Matthews *et al*, 1990). The propyl ester is added by addition of $100\ \mu\text{L}$ 1-propanol/acetyl chloride (5:1 v/v). Samples are incubated at 90°C for 20 min. The

propylation reagents are evaporated by nitrogen gas and heat (60-70°C). The heptafluorobutyric ester is formed by the addition of 100 µl 0.1M diethylamine in hexane and 10 µl heptafluorobutyric acid (Sigma Aldrich) with incubation at 60°C for 20 min. All reagents are evaporated with nitrogen gas and heat (60-70°C). The sample is reconstituted with 100 µL ethyl acetate. The isotopic enrichment is determined by gas chromatography–mass spectrometric analysis using methane negative chemical ionization (Agilent 5975 EI/CI MSD with an Agilent 7890 GC). A Phenomenex ZB-1MS capillary column is used to separate the derivative of phenylalanine. Selected ion chromatograms are obtained by monitoring ions m/z 545, 546 and 551 for unlabeled HyPro, M+1 HyPro and $^{13}\text{C}_5^{15}\text{N}$ -OHP, respectively. Incorporation of 2H into OHP was calculated as the molar fraction of molecules with one excess mass unit above the natural abundance fraction (EM1). Fractional turn over (f) was calculated as the ratio of the EM1 value in protein-bound OHP to the maximal value possible at the body water enrichment present, which has been empirically determined to be $1.1 * \text{Body Water Enrichment}$ (i.e., $f = \text{EM1} / (1.1 * \text{BW})$). The principle behind this calculation has previously been described by Gardner, J.L., et al. (Gardner *et al*, 2007).

Additionally, OHP content in each sample was determined by comparing the abundance in the $m+6$ 551 m/z channel representing the $^{13}\text{C}_5^{15}\text{N}$ -OHP internal standard in each sample with that the $m+0$ 545 m/z ion. A set of standards with known OHP/ $^{13}\text{C}_5^{15}\text{N}$ -OHP concentration ratios was analyzed alongside the samples.

Plasma body water samples were analyzed for deuterium enrichment by cavity ring-down spectroscopy using a Liquid Water Isotope Analyzer with automated injection system, version 2 upgrade (Los Gatos Research). Plasma proteins were removed by

adding approximately 5 mg zinc sulfate monohydrate to 25-50 μ l plasma in a microcentrifuge tube. Samples were vortexed and spun at 8,000 rpm to precipitate proteins. The plasma protein-free supernatant was injected 8 times and the average of the last three measurements used for data analysis. A standard curve was run before and after samples for calculation of deuterium enrichment as delta per mil (parts per thousand) relative to Vienna Standard Mean Ocean Water (VSMOW). Intra-run precision is less than 2 delta per mil (parts per thousand) and inter-run precision is less than 3.5 delta per mil. Delta per mil is converted to atom percent deuterium by a calculation described previously.

CALCULATIONS:

Body water: Mice were labeled with D₂O by bolus and drinking water to achieve a constant exposure of D₂O during the label period of approximately 2.5%. Plasma samples were analyzed for deuterium enrichment.

Excess M1 (%EM1): This quantity represents the degree of isotopic incorporation of deuterium into OHP mediated by collagen synthesis *in vivo*.

Fractional synthesis of OHP ("f"): This quantity represents the percentage of collagen that was newly-synthesized during the period of label incorporation.

OHP concentration: The absolute amount of OHP found in the 10 mg piece of liver analyzed by Metabolic Solutions was determined in mass terms by introducing a known amount of ¹³C₅¹⁵N-OHP prior to further processing. The ratio of m0 (representing OHP) to m+6 (representing the ¹³C₅¹⁵N-OHP standard) in samples was converted to the OHP content of the sample analyzed, which was divided by grams used to obtain a hydroxyproline concentration value for the tissue. Note that by multiplying fractional

synthesis (f) with total OHP concentration, one can determine the total mass of OHP in newly-synthesized collagen.

Respirometry on Previously Frozen Liver Samples

Frozen tissues were thawed in ice-cold PBS, minced with scissors, and homogenized in a Potter-Elvehjem (Teflon-glass) homogenizer. Tissue samples were placed in 2 ml of ice-cold MAS buffer (70mM sucrose, 220mM mannitol, 5mM KH₂PO₄, 5mM MgCl₂, 1mM EGTA, 2mM HEPES pH 7.4) and homogenized via 6-9 strokes. Homogenates were then centrifuged at 1,000 g for 10 min at 4°C; then, the supernatant was collected. Protein concentration was determined with the Pierce™ BCA Protein Assay Kit (Thermo Fisher).

Liver homogenates (8µg per well) were loaded into a Seahorse XF96 microplate in 20 µl of MAS. The loaded plate was centrifuged at 2,000 g for 5 min at 4°C (with no brakes). Subsequently, an additional 130 µl of MAS buffer containing cytochrome c (10 µg/ml, final concentration) was added to each well. Substrate injections were as follows: 1mM NADH or 5mM succinate + 2µM rotenone were injected at port A; 2µM rotenone + 4µM antimycin A at port B; 0.5mM TMPD + 1mM ascorbic acid at port C; and 50mM azide at port D. Substrate injections allow for assessment of mitochondrial respiratory capacity through Complex I, Complex II, and Complex IV (Acin-Perez *et al*, 2020; Osto *et al*, 2020).

Seahorse Data Analysis

Wave software (Agilent) was used to export oxygen consumption rates (OCR). Rates were normalized by protein and mitochondrial content (via MTDR) to GraphPad Prism v7.02. Complex I-, II-, and IV-dependent respiration was calculated by the following formulas:

- I. Maximal Complex I respiratory complex = OCRNADH – OCRantimycin
- II. Maximal Complex II respiratory complex = OCRSuccinate+Rotenone – OCRantimycin
- III. Maximal Complex IV respiratory complex = OCRTMPD+Ascorbate – OCRazide

Mitochondrial Quantification using MitoTracker Deep Red (MTDR)

For MTDR mitochondrial content quantification, 20 µl of liver homogenate (8 µg) was seeded per well on a clear-bottom black 96-well plate (Corning) in 100µl of MAS containing MitoTracker Deep Red (Thermo Fisher) (0.5µM MTDR final concentration) and incubated at 37°C for 10 min. Plates were centrifuged at 2,000 g for 5 min at 4°C (no brake), and supernatant was carefully removed. Finally, 100 µl of MAS was added per well. MTDR was excited at 625nm and its emission recorded at 670 nm. Mitochondrial content was calculated as MTDR signal (minus background fluorescence) per milligram of protein. Plates were imaged using the Spark 20M Microplate Reader (TECAN). Alternatively, a plate reader or high-throughput microscope maybe used (Acin-Perez *et al*, 2020; Osto *et al*, 2020).

Tissue Collection and Shotgun Lipidomics Analysis

Frozen tissues (50-100 mg) were transferred to extraction tubes with PBS. A modified Bligh and Dyer extraction (Hsieh *et al*, 2021) is carried out on samples. Prior to biphasic extraction, an internal standard mixture consisting of 70 lipid standards across 17 subclasses is added to each sample (AB Sciex 5040156, Avanti 330827, Avanti 330830, Avanti 330828, Avanti 791642). Following two successive extractions, pooled organic layers are dried down in a Thermo SpeedVac SPD300DDA using ramp setting 4 at 35°C for 45 min with a total run time of 90 min. Lipid samples are resuspended in 1:1

methanol/dichloromethane with 10mM Ammonium Acetate and transferred to robovials (Thermo Fisher 10800107) for analysis.

Samples are analyzed on the Sciex Lipidyzer Platform with an expanded targeted acquisition list consisting of 1450 lipid species across 17 subclasses. Differential Mobility Device on Lipidyzer was tuned with EquiSPLASH LIPIDOMIX (Avanti 330731). Instrument settings, tuning settings, and MRM list available upon request. Data analysis performed on an in-house data analysis platform comparable to the Lipidyzer Workflow Manager (BK, 2018). Quantitative values were normalized to cell counts.

RNA isolation and q-PCR

Livers were collected in RNAlater. Total RNA was isolated from liver tissue using the TRIZol reagent (Thermo Fisher) and further purified with the RNeasy 96 QIAcube HT Kit and QIAcube HT (Qiagen). The obtained total RNA was then reverse transcribed into cDNA using the SuperScript™ IV VILO™ Master Mix (Thermo Fisher) and PCRs were run on a QuantStudio™ 12K Flex Real-Time PCR System using TaqMan Gene Expression Assays and TaqMan Fast Advanced Master Mix (Thermo Fisher). All mRNA expression level were normalized to *Ppia*. The $2^{-\Delta\Delta Ct}$ method was used to calculate relative gene expression levels.

Gene name	Thermo Fisher Catalog number
<i>Ppia</i>	Mm02342430-g1
<i>Col1a1</i>	Mm00801666-g1

<i>Acta2</i>	Mm00725412-s1
<i>Timp1</i>	Mm01341361-m1
<i>Tgfb1</i>	Mm00178820-m1
<i>Il6</i>	Mm00446190-m1
<i>Tnf</i>	Mm00443258-m1
<i>Adgre1</i>	Mm00802529-m1
<i>Ccl2</i>	Mm00441242-m1
<i>Dnm1l</i>	Mm01342903_m1
<i>Cpt1a</i>	Mm01231183_m1
<i>Acaca</i>	Mm01304257_m1
<i>Acacb</i>	Mm01204671_m1
<i>Fasn</i>	Mm00662319_m1
<i>Dgat1</i>	Mm00515643_m1
<i>Dgat2</i>	Mm00499536_m1
<i>Asns</i>	Mm00803785_m1
<i>Sesn2</i>	Mm00460679_m1
<i>Chac1</i>	Mm00509926_m1

<i>Mthfd2</i>	Mm00485276_m1
<i>Atf3</i>	Mm00476032_m1
<i>Ddit3</i>	Mm01135937_g1
<i>Trib3</i>	Mm00454879_m1
<i>Col3a1</i>	Mm00802331_m1
<i>Cd68</i>	Mm03047343_m1

Immunoblot

Frozen liver tissue was cut on dry ice into approximately 50-60mg pieces and transferred to chilled Lysing Matrix M, 2 ml tubes (MP Biomedicals). Tissue Extraction Reagent II (Thermo Fisher) supplemented with PhosSTOP™ and cOmplete™, EDTA-free Protease Inhibitor Cocktail (Roche Life Science) was added to a final buffer to tissue ratio of 15 µL buffer/mg tissue. Liver tissue was homogenized using the preset mouse liver program on the FastPrep-24™ 5G system (MP Biomedicals) and then centrifuged for 15 min at 21000 xg, 4°C. The supernatant was transferred to a new 1.5 ml tube and the protein concentration was determined with the Pierce™ BCA Protein Assay Kit (Thermo Fisher). 25µg of total protein were denatured at 70°C for 10 min and separated on Novex™ WedgeWell™ 4 to 20%, Tris-Glycine gels (Thermo Fisher) and then transferred on nitrocellulose iBlot™ 2 Transfer Stacks using the iBlot 2 Dry Blotting System (Thermo Fisher). Membranes were blocked in Intercept® (TBS) Blocking Buffer (Licor) for 60 min and then exposed to the primary antibody overnight at 4°C. After

applying the secondary antibodies, the membranes were scanned on an Odyssey® CLx Imaging System (Licor). Densitometric analyses were performed with the Image Studio software (Licor).

Antibodies

Antigen	Dilution	Vendor	Catalogue number
Opa1	1:3000	BD Bioscience	612607
Mfn1	1:1000	Proteintech	13798-1-AP
Mfn2	1:1000	Proteintech	12186-1-AP
Oma1	1:1000	Cell Signaling	95473
β -Actin	1:20000	Proteintech	66009-1-Ig
Gapdh	1:5000	Santa Cruz	sc-365062
Chop	1:1000	Cell Signaling	2895S
p-eIF2 α	1:1000	Cell Signaling	3398S
eIF2 α	1:1000	Thermo Fisher	AHO0802
Dlp1/Drp1	1:1000	BD Bioscience	611113
Atf6	1:1000	Proteintech	24169-1-AP
Xbp1s	1:1000	Biologend	658802

Statistical Analysis

Comparisons between groups were made by one-way analysis of variance (ANOVA). Differences were considered statistically significant at $p < 0.05$. In the figures, asterisks denote statistical significance (* $p < 0.05$; ** $p < 0.01$; *** $p < 0.001$; **** $p < 0.0001$). Data were analyzed with GraphPad Prism v7.02.

RESULTS

Drp1 knockdown in hepatocytes induces liver damage and Gdf15 secretion, resulting in decreased body weight and food intake.

Hepatocyte specific Drp1 inhibition using a Drp1-dominant negative form (K38A) protected diet-induced obese mice from both liver damage and steatosis (Galloway, wang). Consequently, we hypothesized that knocking down Drp1 specifically in hepatocytes using FDA approved N-acetyl-galactosamine (GalNAc)-siRNA conjugates could be an ideal approach to counteract NASH. First, we chose 26-week-old lean mice, which is equivalent in age to a 30-year-old human, to test GalNAc-Drp1-siRNA knockdown efficacy and potential safety issues. One of the most effective ways to knockdown a gene in humans without safety problems using GalNAc siRNAs is a regimen of 4 weekly injections of low conjugates concentrations (Fitzgerald *et al*, 2017) . Hence, we performed 4 injections of GalNAc siRNA to knockdown Drp1 in mice, which induced an 80% decrease in *Drp1* mRNA and almost ablation of the protein (Figure 1A, 2D). After the second injection of GalNAc siRNA, mice started to stop gaining body weight, which resulted in net loss of body weight after four injections (Figure 1B,C). Circulating ALT and AST levels were increased 24- and 8-fold respectively after four injections (Figure 1D), without changes in liver weight (Figure 1E). Liver histology revealed clear signs of

hepatocyte damage, including necrotic hepatocytes and oval cell hyperplasia (Figure 1F). Furthermore, the expression of fibrogenic (*Col1a1*, *Col3a1*, *Acta1* and *Tgfb1*) and pro-inflammatory genes (*Timp1*, *Ccl2*, *Cd68*, *Adgre1*) were increased by Drp1 knockdown in these same chow diet fed mice (Figure 1G, H).

One of the major pathways initiated by hepatocytes that induces weight loss is the secretion of hepatokines. In the case of Drp1 KO mice, hepatocytes were shown to secrete Fgf21, which induced weight loss by increasing systemic energy expenditure (Wang *et al*, 2015). We found that four injections of GalNAc-Drp1-siRNA also increased circulating Fgf21 level and further led to a release of Gdf15 into the plasma (Figure 1I). Elevated Gdf15 level have been associated with weight loss by decreasing food intake (Patel *et al*, 2019). In this regard, the GalNAc-Drp1-siRNA injections caused a reduction in food intake (Figure 1J), supporting that Gdf15 could be playing a major role in body weight loss induced by Drp1 KD. As the dependency of the effects of hepatic Drp1 inhibition on Gdf15 were unknown, we determined the effects of Drp1 knockdown in Gdf15 receptor (GDNF family receptor alpha-like) knockout mice (Gfral KO). We found that Gfral KO mice preserved weight gain even after 4 injections of GalNAc-Drp1-siRNA, showing just a 3.3% reduction in total body weight, when compared to 11.4% reduction in body weight in WT mice (Figure 1K). Indeed, Drp1 knockdown was unable to decrease food intake in Gfral KO mice (Figure 1J), supporting that the major cause for the decrease in body weight induced by Drp1 was a reduction in food intake. Drp1 KD in Gfral KO animals compared to chow-fed Drp1 KD animals yielded no differences in serum liver injury markers (ALT and AST) and nutritional stress biomarkers (Fgf21 and Gdf15) (Supplemental Figure 1). This indicates that Gdf15 contributes to the observed body

weight loss in the Drp1 KD mice, but the increases in ALT, AST, Fgf21, and Gdf15 all occur independent of Gdf15, suggesting liver specific Drp1 KD induces hepatic stress in chow-fed mice.

Increased NEFA in Liver-specific DRP1 knockdown attributed to defects in the ETC

Steatohepatitis occurs when accumulation of fat in the liver causes inflammation and cell death. To understand the observed liver injury in response to Drp1 knockdown, mice livers were assessed for hepatic lipid composition. Liver non-esterified fatty acids (NEFA) and triglycerides (TG) were quantified by GC/MS. Drp1 KD in lean healthy mice yielded significant increases of NEFA species (3.88 ± 0.278) compared to control (2.99 ± 0.16) and a reduced capacity to esterify fatty acids into TGs (Figure 2A). Composition of NEFA species lead to differential lipotoxic effects (Hetherington *et al*, 2016), specifically palmitate and oleate-induced lipotoxicity is crucial for the pathogenesis of nonalcoholic fatty liver disease (Malhi & Gores, 2008). Drp1 mice had an increase in palmitate levels and more so in oleate levels (0.7009 ± 0.0515) versus control (0.4623 ± 0.0245). The increase in NEFA and development of lipotoxicity can explain the observed increases to inflammatory markers when Drp1 is knocked down.

As mitochondria play an important role in fatty acid utilization, we assessed the role of mitochondrial function and the contribution of the ETC by measuring respiration in frozen liver samples. Furthermore, it has recently been shown that a shift in substrate utilization from glucose to fatty acids results in the degradation of Complex I to mediate increases in ROS (Adela Guara *et al*, 2016). Complex I activity was assessed by oxygen consumption analysis stimulated by NADH under pyruvate and malate, complex II was assessed by succinate and rotenone, and complex IV was assessed by averaging the

maximal oxygen consumption stimulated by TMPD/ascorbate under both pyruvate and malate and succinate and malate. Despite significant reductions to complex I and complex II activity in Drp1 knockdown animals, no changes were observed of complex IV activity (Figure 2B). Reductions in complex I oxidative capacity could be explained by increased NEFA as observed previously in fibroblasts (Adela Guara *et al*, 2016) and fasting mouse livers (Lapiente-Brun *et al*, 2013). In the presence of elevated free fatty acids, lipotoxicity can be prevented by increasing mitochondrial fatty acid oxidation (FAO). Reductions of mRNA levels of proteins regulating fatty acid oxidation (*Cpt1a* and *Acacb*), fatty acid synthesis (*Fasn*), and triglyceride synthesis (*Dgat2*) all suggest the inability for mitochondria to undergo fission prevents proper FAO (Figure 2C). Increased *Aca-alpha* mRNA levels suggests increased formation of Malonyl-CoA and thereby inhibiting the progression of FAO. Reductions to *Dgat2*, the enzyme responsible for catalyzing the esterification of fatty acyl-CoAs and diacylglycerols to triacylglycerols, support the subtle decrease in TG of Drp1 KD mice. The inability to synthesize triglycerides has been shown to improve hepatic steatosis but exacerbate liver damage (Yamaguchi *et al*, 2007).

Drp1 KD in lean mice increases Oma1 activity and activates the mitochondrial integrated stress response

Elevated levels of NEFA, in part due to reductions in complex I activity, can trigger inflammation, elevate ROS formation, and impinge on mitochondria. Mitochondria undergo a series of fission and fusion events to maintain quality control and mitochondrial stress activates the inner membrane protease Oma1 leading to the cleavage of long isoforms of fusion protein Opa1 (L-Opa1) (Baker *et al*, 2014). Immunoblotting revealed a robust Drp1 knockdown and reductions to mitochondrial fusion proteins, Mfn1, Mfn2, as

well as cleavage of L-Opa1 in Drp1 KD mice compared to control (Figure 2D). Reductions in Mfn1/2 levels suggest that the cell attempts to decrease mitochondrial fusion to remove damaged mitochondria caused by increased NEFA. Observations of increased short Opa1 isoforms (S-Opa1) suggests Oma1 activation and cleavage of L-Opa1 resulting in loss of mitochondrial bioenergetics and the activation of the mitochondrial integrated stress response (ISR). To assess for Oma1 activation and whether or not the ISR is stimulated to initiate an apoptotic cascade via the Oma1-Dele11-Hri-Atf4 pathway (Blais *et al*, 2004), we performed immunoblots of liver extracts and probed for eIF2 alpha, phosphorylation of eIF2 alpha, Chop, and Oma1 (Figure 2E). Ablation of Drp1 reveals reduced Oma1 protein level, consistent to Oma1 activation and processing of Opa1. Reduced Oma1 protein level are due to Oma1 activation and autocatalytic cleavage rather than decreased gene expression, because we could not detect any changes in Oma1 mRNA level in mice injected with Drp1 GalNAc siRNAs compared to control animals (supplementary figure 2). Furthermore, we observe elevated levels of eIF2 alpha phosphorylation, eIF2 alpha, and upregulation of Chop (Figure 2E).

Using quantitative RT-PCR (qRT-PCR) we validated activation of the Atf4 mediated mitochondrial integrated stress response by measuring multiple transcripts downstream of p-eIF2 (*Atf3* and *Ddit3*) and other well-known Atf4-regulated genes (*Asns*, *Sesn2*, *Chac1*, *Mthfd2* and *Trib3*) (Palam *et al*, 2015; Lopez *et al*, 2007; Forsström *et al*, 2019) (Figure 2F). These result show that Oma1 activation is upstream of Opa1 processing and Atf4 activation. Oma1 is activated by increasing ROS levels upon NEFA accumulation and FFA-mediated degradation of complex I. Activation of Atf3 as a second stage event of ISR suggests Atf4 activation is adaptive and not cause for changes to

mitochondrial function. Perhaps Atf4 senses mitochondrial dysfunction and mitigates it by downregulating mitochondrial biogenesis and increasing antioxidants.

Knockdown of Drp1 in GAN-fed mice induces hepatic injury

Liver injury and activation of the ISR argue against using Drp1 knockdown as a therapeutic approach in the liver. Although the only beneficial outcome was weight loss, the observed weight loss was induced by Gdf15 as a response to liver injury. However, is it possible that ablation of Drp1 has more beneficial outcomes in a NASH model? To assess whether or not Drp1 knockdown is beneficial in a NASH liver model, 30-week-old mice were fed a Gubra-Amylin NASH (GAN) diet for 36 weeks and injected with the Drp1 siRNA after 24 weeks of diet (Figure 3A). The GAN diet has demonstrated clinical translatability with histopathological, transcriptional and metabolic aspects of the human disease (Hansen *et al*, 2020). Highlighting the suitability of the GAN mouse model for identifying therapeutic targets for NASH as opposed to using diet-induced obese or high fat diet-fed models. Drp1 mRNA levels were reduced in the GAN diet fed control mice but not to the same extent as those receiving the siRNA. The 50% greater reduction of Drp1 mRNA in the GAN diet fed mice with Drp1 knockdown vs the control GAN diet fed mice is sufficient to identify outcomes due to Drp1 KD (Figure 3A). Compared to GAN-fed control mice, GAN-fed Drp1 KD mice showed significantly reduced body weight, reduced liver fat mass (hepatic lipid accumulation), total cholesterol, plasma triglyceride, plasma glucose levels at termination (Figure 3B-F) and insulin level (supplementary figure 3A). Despite reductions to plasma lipid and glucose levels (Figure 3E, F), liver injury markers, ALT and AST, remain high relative to chow-fed control mice (Figure 3G-H), suggesting liver injury is still present in Drp1 ablated NASH models. Furthermore,

decreased plasma glucose levels may occur when damaged liver cannot utilize glucose. Previous literature has shown hepatic knockout of Drp1 protected mice from diet induced obesity (Wang *et al*, 2015). Since no appreciable differences were observed in food intake between HFD- fed control mice and HFD-fed Drp1LKO mice, Wang *et. al.* proposed weight loss was due to upregulation of Fgf21. Increased levels of Fgf21 would increase energy expenditure in the form of adipocyte thermogenesis and increased lipid utilization (Wang *et al*, 2015). In our GAN diet NASH model, Fgf21 levels were not significantly increased (Figure 3I). Thus, observed weight-loss cannot be attributed to Fgf21 levels in our model. In the lean mice, Drp1 KD yielded significant increases to Gdf15 and Gfral KO reversed weight loss effects (Figure 3C, K). Here, the NASH diet overrides weight-loss induced by Gdf15 (Figure 3J). The lack of differences in Gdf15 between the GAN model versus the chow model can be explained by energy intake. Ultimately, the GAN model has a higher caloric intake compared to chow fed mice, perhaps why Gdf15 levels are not reduced in Drp1 KD GAN fed mice but are reduced in Drp1 KD chow-fed mice.

Drp1 knockdown in GAN-fed mice hyper activates the IRS and NEFA accumulation

Presence of liver injury in the GAN model led us to investigate if mitochondrial dysfunction and the IRS persists under Drp1 KD. Mitochondrial fusion and fission are compensatory mechanisms to cellular milieu. In lean mice, ablation of Drp1 lead to the reduction of complex I activity (Figure 2B). In GAN diet fed animals, the lack of metabolic flexibility under nutrient overload led to exacerbation of the IRS. Mitochondrial dysfunction has changed under the GAN diet and now both Complex I and Complex II activity is significantly reduced (Figure 4A). Markedly, fatty acid synthesis (*Fasn*) did not change between lean control and GAN diet fed mice but FAO genes (*Cpt1a* and *Acac alpha*) were

increased in GAN compared to control. Suggesting the compensatory mechanism of increasing beta oxidation in the presence of increased hepatic lipid accumulation. Further supported by reduction in triglyceride synthesis genes (*Dgat1* & *Dgat2*) (Figure 4B), whereby lipogenesis is reduced as lipolysis occurs. In the GAN-fed mice, Drp1 KD animals are not able to compensate for the increased nutrient supply. Both *Dgat2* and *Cpt1a* are reduced in the Drp1 KD GAN model (Figure 4B). Indicating the inability to oxidize lipids or properly store lipids in Drp1 KD livers thereby elevating NEFA levels and promoting lipotoxicity (Figure 4C). Our results show inhibiting mitochondrial fission promotes Oma1 activation and hyper activates the ISR (Figure 4D, E, supplementary Figure 3C). Immunoblots reveal Oma1 activation, cleavage of L-Opa1, phosphorylation of eIF2 alpha, and activation of the ATF stress response pathway (Figure 4D). qRT-PCR measurements further confirm activation of Atf4 and ISR as genes associated with the ISR are upregulated (Figure 4E). In NASH models, metabolic flexibility is required to mediate hepatic lipid accumulation and downstream fibrosis. The loss of metabolic flexibility further exacerbates NASH phenotypes. The GAN diet itself does not induce Oma1 activation and Opa1 processing (Figure 4D), which provides indirect proof that Oma1 activation selectively induced by Drp1 KD might be responsible for crossing the threshold to over-activate Atf4 and cause cell death.

DRP1 ablation under the NASH diet exacerbates hepatic fibrosis and inflammation

In agreement with Drp1 KD inducing a greater IRS response, inflammation (*Tgf-beta*, *Tnf-alpha*, and *IL-6*) and fibrosis markers (*Col1a1*, *alpha-SMA*, and *plasma Timp-1*) were all significantly upregulated compared to control GAN mice (Figure 5A, B). Increased inflammation and fibrosis were observed in histology sections (Figure 5C, D)

and quantifications yielded increased fibrosis and inflammation (*Col1a1*, *alpha-SMA*, and *CD11b*) (Figure 5E).

Increased fibrosis was further confirmed by the presence of hydroxyproline produced by hepatic stellate cells. Hydroxyproline as a biomarker for liver fibrogenesis progression has shown significant correlations to HSC activation during liver fibrosis (Gabr *et al*, 2017). Consistent to observed fibrosis in histology section, Drp1I KD GAN mice yielded significant increases to both total hydroxyproline and newly made hydroxyproline (Figure 5F, G). Our findings identify multiple stimuli activating EIF2alpha phosphorylation are triggered by Drp1 KD (ER stress via Perk and Oma1 activation). These multiple stimuli (ER stress, Oma1 activation and even potentially mitochondrial ROS) are converging to activate Atf4. This convergence fits with the necrosis only seen in Drp1 KD under GAN diet (Figure 5H), as Atf4 inducers are elevated by the GAN diet itself (Figure 4D, E). Adding the extra stimulation by Drp1 KD on top of GAN feeding can explain an increase in cell death. Taken together, these data imply that Drp1 knockdown in the liver exacerbates hepatic inflammation and fibrosis and worsens NASH.

DISCUSSION & FUTURE DIRECTIONS

Drp1LKO mice and dnDrp1 mice have shown decreased fat mass and protection from high-fat diet induced obesity (Galloway *et al*, 2014; Wang *et al*, 2015). Thus, we hypothesized that knocking down Drp1 specifically in hepatocytes using FDA approved GalNAc-siRNA conjugates could be an ideal approach to counteract NASH. We found Drp1IKD in C57B/6J lean mice resulted in decreased body weight, elevated circulating AST and ALT, and increased expression of pro-inflammatory and fibrosis markers in the liver. Observed total body weight loss was attributed to reduced food intake mediated by

GDF15 as GFRAL null mice (GDF15 receptor) prevented decreased food intake and weight loss induced by Drp1IKD. Increased levels of GDF15, whose expression is regulated by the ISR, indicate Drp1IKD induced ER stress and OMA1 activation and further explains elevated EIF2alpha phosphorylation and ATF4 expression. In our NASH model, we observed elevated levels of AST, ALT, and fibrosis but no activation of OMA1. While Drp1IKD in mice with NASH was sufficient to activate OMA1 and exacerbate ER stress, ISR, inflammation, fibrosis and induce hepatocyte necrosis.

GDF15 has been differentiated from satiety hormones and is identified as a circulating biomarker of mitochondrial disease and at times the degree of expression is correlated to disease severity (Sharma *et al*, 2021; Montero *et al*, 2016; Chung *et al*, 2017; Fujita *et al*, 2015). In our study, GDF15 is increased in Drp1IKD and fits well as a biomarker of cellular stress as Drp1IKD mice yield elevated levels of inflammation and fibrosis. Additionally, GDF15 have shown to reduce food intake in various species and to alter food choice (O’Rahilly, 2017). Patel *et. al.* observed mice overexpressing GDF15 lost weight secondary to reduced food intake. And GFRAL null mice were slightly heavier (Patel *et al*, 2019; Hsu *et al*, 2017). This aligns with our observed weight loss under Drp1IKD mice and loss of reduced weight in GFRAL null Drp1IKD mice and suggests the GDF15-GFRAL axis as a critical player to stress pathway-induced weight loss. As well as increased GDF15, we observed increased FGF21 in Drp1IKD mice. Previous literature attributed weight loss and increased FGF21 in Drp1LiKO mice to increased energy expenditure and expression of thermogenic genes to utilize lipids (Wang *et al*, 2015). However, in the study, food intake was not changed between control and Drp1LiKO mice and, in our model, Drp1IKD mice in the lean had significant reductions. It is therefore not

feasible to attribute weight loss in our study to increased energy expenditure when significant reductions were observed in food intake and reversed when food intake was corrected by GFRAL KO. An important feature to note is differences in both studies, genetic background, age, diet, and method of Drp1 ablation of the mouse model utilized in the Wang et al study.

Increased liver GDF15 mRNA in lean animals can be explained by increased levels of FFA and reduced incorporation to triacylglycerols. Increased lipid droplet formation in livers have shown to enhance hepatosteatosis but does not adversely affect hepatic health or glucose metabolism (Trevino *et al*, 2015). The inability of Drp1KD livers to properly form triacylglycerols will contribute to metabolic and mitochondrial stress. Upon changes to the metabolic state, the ETC has been observed to reconfigure expression of complexes and supercomplex formation in response to substrate shift from glucose to FA (Lapiente-Brun *et al*, 2013; Adela Guara *et al*, 2016). These findings align with our observations of increased FFA and a decline in CI and CII oxidative capacity in Drp1KD lean animals. Our data suggests impaired Drp1 activity increases ROS by enhancing electron flux in the presence of greater FFA. To mediate ROS, Drp1KD cells will reconfigure the ETC and degrade CI (Adela Guara *et al*, 2016). In the future, it will be relevant to assess CI +CIII supercomplex formation under reduced Drp1 activity. Although we observed reductions to CI and CII activity and no changes to CIV activity, flox/cre Drp1KO mice fed a HFD diet by Wang et al observed no changes to CII and CIV activity, suggesting the importance of when the intervention occurs.

The autocatalytic degradation of OMAI serves as a stress-sensor and results in the complete protein turnover to restore mitochondrial network or damage (Baker *et al*,

2014). This aligns with our observation of enhanced mitochondrial stress under Drp1IKD mice where FGF21 and GDF15 is enhanced, and increased Oma1 activity activates the ISR. Previous studies have shown ablation of Drp1 activates the ISR and cytokine expression of Fgf21 in the brain, but how the ISR is activated is not fully addressed (Wang *et al*, 2015; Restelli *et al*, 2018). Restelli *et. al.* proposed the ISR is activated when Drp1 deletion alters ER-mitochondria contact, modifying membrane curvature, and thereby activating the ER stress sensor PERK (Restelli *et al*, 2018). Heme deprivation and changes to amino acid sensitivity as a result of Drp1 ablation were proposed to be potential activators of eIF2 alpha (Restelli *et al*, 2018). But the exact mitochondrial mechanism to how Drp1 ablation leads to Perk activation remains unclear. Our data identifies reduced Drp1 function activates OMA1 via NEFA accumulation and subsequently activation of the ISR. These results show that Oma1 activation is upstream of Opa1 processing and Atf4 activation. Oma1 is activated by increasing ROS levels upon NEFA accumulation and FFA-mediated degradation of CI. These findings show DRP1L knockdown elicits an integrated stress response consistent with the UPR pathway by increasing NEFA and impairing Complex I. Activation of Atf3 as a second stage event of ISR suggests Atf4 activation is adaptive and not cause for changes to mitochondrial function. Perhaps Atf4 senses mitochondrial dysfunction and mitigates it by downregulating mitochondrial biogenesis, gene transcripts, and increasing antioxidants. It is also possible reduced CI activity and impaired NADH oxidation contributes to ISR activation, elevated levels of cytosolic NADH/NAD⁺ have been shown to deplete asparagine levels and triggering the ISR (Mick *et al*, 2020). Supplementation of aspartate attenuated the ISR activation as measured by Ddit3 transcripts. It is interesting to

speculate if this mechanism is operative in our system as well, in future studies we can investigate the NADH/NAD⁺ and aspartate levels.

To assess the effects of reducing Drp1 activity as a potential therapeutic in a NASH liver model, 30-week-old mice were fed a GAN diet for 36 weeks and injected with the Drp1 siRNA after 24 weeks of diet. Inhibition of Drp1 activity has been observed to protect from obesity, reductions in steatosis, and no changes to body weight in B6sJL HFD models (Galloway *et al*, 2014). It was consistent to see increases to ALT and AST levels between lean control and calorically modified models, as well as reduced ALT and no changes to AST in animals of reduced Drp1 between our study and the Galloway study. However, in this study the NASH model reveals increased steatosis and no reductions in AST, FGF21, or GDF15 levels in Drp1KD GAN-fed mice. GDF15 is produced by almost any cell type in response to ISR activation and in states of long-term caloric excess, as is the case with a GAN diet for 36 weeks, circulating GDF15 levels rise (Patel *et al*, 2019). Thus, GDF15 is increased in the NASH model and no reductions to GDF15 in the Drp1KD GAN fed animal suggests metabolic stress is still present. No reductions in weight despite increased GDF15 levels in Drp1KD GAN fed animals can be explained by the higher caloric consumption.

A previous study demonstrated autophagy deficiency in muscle led to protection against obesity and insulin resistance by inducing FGF21 and increasing FAO and energy expenditure. The group also noted, autophagy deficiency resulted in mitochondrial morphology similar to mitochondria found in Drp1LiKO mice on HFD (Kim *et al*, 2012). If we apply these observations to our study, perhaps reduced Drp1 activity prevents damaged mitochondria from undergoing mitophagy and as a compensatory mechanism,

FGF21 is enhanced as an attempt to handle the nutrient overload on top of impaired Drp1 activity. Additionally, reductions to ETC activity is different in the GAN model than the lean. Independent of the lean study and unlike previous studies yielding protection from diet-induced obesity by inhibiting fission, Drp1 knockdown does not promote pro-adaptive responses in the GAN model. In GAN diet fed animals, the lack of metabolic flexibility under nutrient overload lead to a different reconfiguration of the ETC as compared to lean animals and further exacerbation of the IRS. Mitochondrial dysfunction has changed under the GAN diet with CII activity having significantly been reduced (Figure 4A). Perhaps the reversal of Complex I reduction can be explained by CII downregulation (Adela Guara et al, 2016). Guara et al has observed reductions to CIV stalled CoQ dependents, leading to the prevention of beta oxidation and the eventual degradation of CI. This observation aligns with our study in that GAN/Drp1KD animals exhibit reduced CI and CIV oxidative capacity as well as reductions to beta oxidation gene transcripts. The mitochondrial phenotype we observe is explained better by the model of selective ETC reconfiguration, rather than just by a defect in mitophagy leading to an accumulation of damaged mitochondria that oxidize fewer fatty acids. A defect in mitophagy would decrease the activity of all complexes and also elevate mitochondrial mass. The selective degradation of CI suggests that it is a regulated process, rather than a mitochondrial carnage. The Atf4 response could indeed be mitigating some of the defects in mitophagy due to Drp1 deletion. Furthermore, Oma1 activation was not observed in the GAN model alone and activation was only observed in GAN/Drp1KD animals suggesting reduced Drp1 activity enhances cellular stress and activation of the IRS. The significant increases to hepatic necrosis only under the GAN/Drp1KD can thereby be explained by Drp1

reduction exacerbating fibrosis and inflammation. However, it still remains unclear what are the chain of events, is ETC remodeling occurring before Oma1 activation or is Oma1 activation occurring before ETC remodeling and the subsequent Atf4 and FGF21 signaling, this will require further investigation.

In this study, inhibiting Drp1 activity neither mediated NASH nor reduced steatosis. However, we do acknowledge our results may differ from previous literature due to differences in approach and model. We utilized the FDA approved GalNAc regime which includes PBS as a control rather than an siRNA control, similar to human trials, perhaps more work can be done to address the use of other placebos and mitochondrial fission protein siRNAs which are outside the scope of this study (Fitzgerald *et al*, 2017; Mullard, 2018). Overall, further work is required to assess the true benefits of inhibiting Drp1-dependent fission in combating obesity. This will involve the assessment of inhibiting fission both in a Drp1-dependent manner and inhibiting fission in a Drp1-independent manner. Our study has also shown ETC reconfiguration may differ between lean and NASH models, it would contribute to the field to investigate whether or not supercomplex formation is involved and if so if it is different. Nevertheless, our data suggests downregulation of Drp1L could be a poor target to relieve nutrient overload in the liver and more studies should be done before consideration as a therapeutic approach to reversing established NASH.

FIGURES

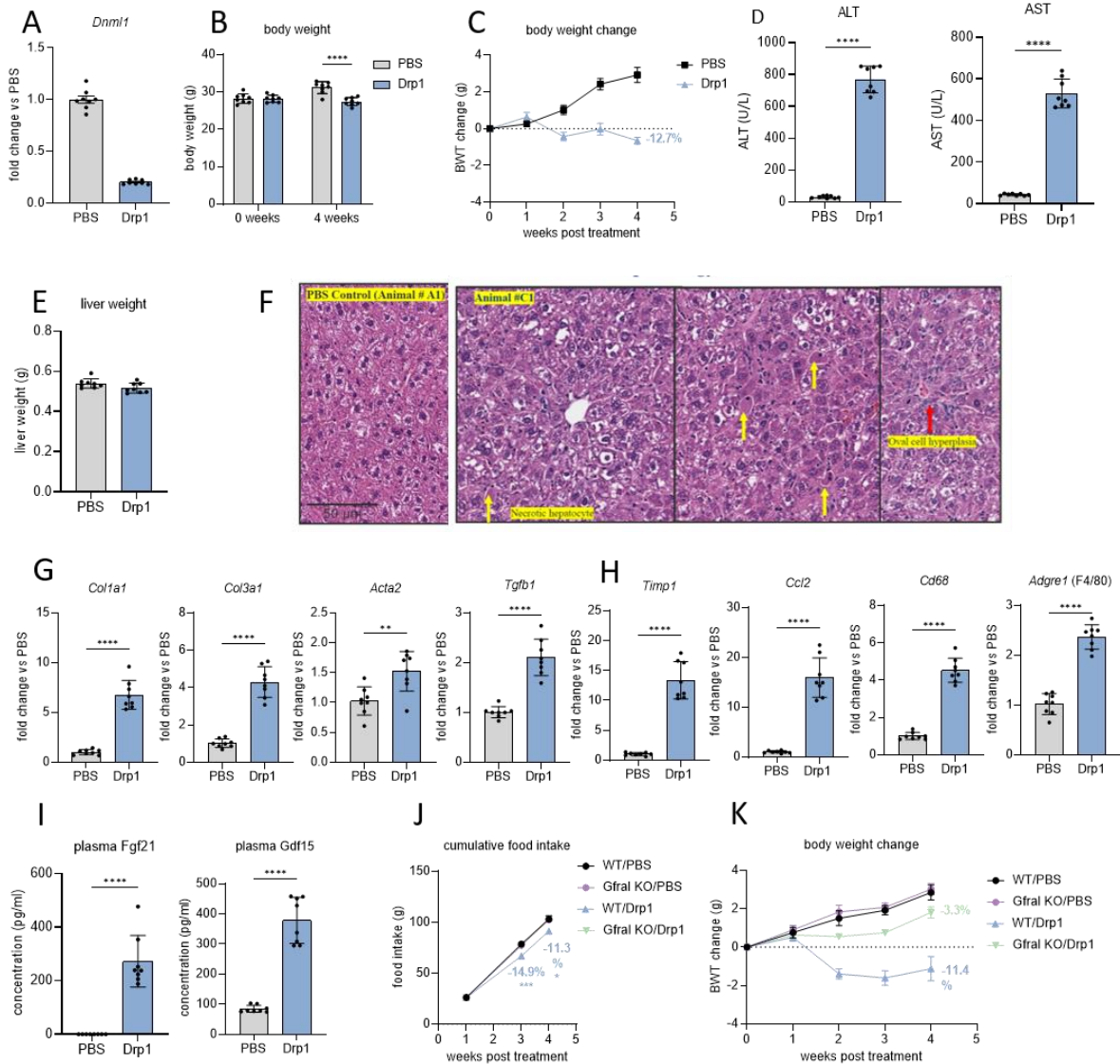


Figure 3- 1. Hepatocyte specific knockdown of Drp1 causes liver damage, inflammation, fibrosis and bodyweight loss due to Gdf15 mediated reduced food intake

A) Lean male C57BL/6 mice were injected with PBS (control) or GalNAc Drp1 siRNA (Drp1) weekly for 4 weeks. Liver *Dnm1l* mRNA level was analyzed by qPCR. B) Total mice body weights at the beginning (0 weeks) and after 4 weeks of PBS or GalNAc Drp1 siRNA treatment. C) Body weight changes at each week of PBS or GalNAc Drp1 siRNA

injection. D) ALT and AST level after 4 weeks of weekly injections with PBS or GalNAc Drp1 siRNA. D) Final liver weight after 4 weeks. F) Hematoxylin and Eosin (H&E) staining of livers from control (PBS) or GalNAc Drp1 siRNA treated mice at week 4. G) Liver gene expression analysis of fibrogenic and H) inflammatory genes by qPCR. I) Plasma Fgfg21 and Gdf15 protein level measured after 4 weeks. H) Food intake at each week of PBS or GalNAc Drp1 siRNA (Drp1) injected lean male wild type or Gfral knockout (KO) C57BL/6 mice. I) As in G, body weight changes were measured. All data presented are the mean±SD. *p<0.05, ***p<0.001, ****p<0.0001 one-way ANOVA

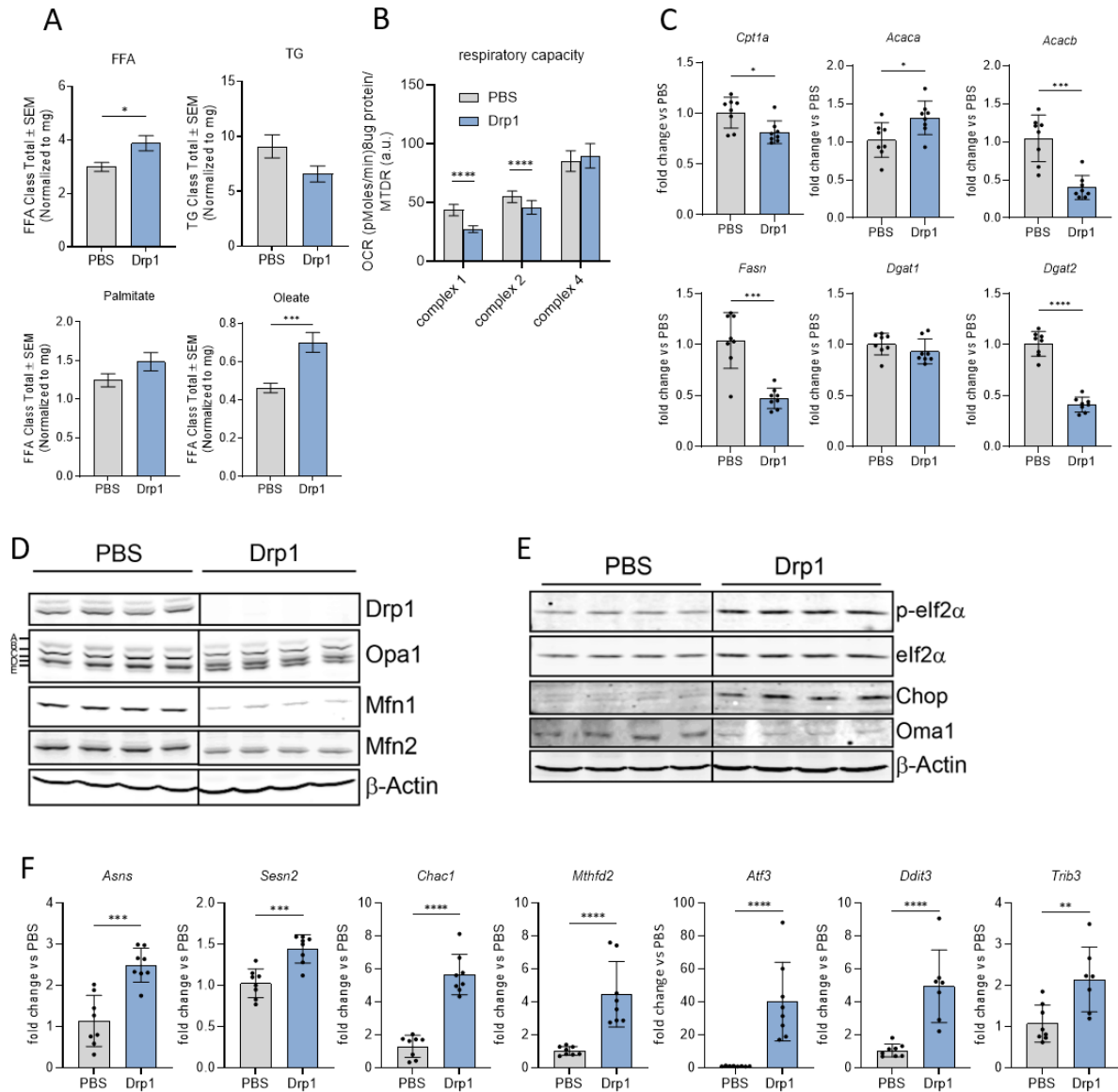


Figure 3- 2. Drp1 ablation reduces mitochondrial respiration and activates the ATF4 mediated ISR

A) C57BL/6 mice were treated weekly with PBS (control) or GalNAc Drp1 siRNA (Drp1). At week 4, livers were isolated and free fatty acids (FFA), triglycerides (TG), palmitate and oleate were measured by mass spectrometry. B) The activity of mitochondrial ETC complexes I, II and IV

were measured in livers of mice treated for 4 weeks with PBS or GalNAc Drp1 siRNA (Drp1). C) Liver gene expression analysis of indicated genes at week 4. D) Immunoblot of liver extracts with specific antibodies for Drp1, Opa1, Mfn1, Mfn2 and β -Actin. Different Opa1 splice variants are indicated. E) The liver protein levels of integrated stress response (ISR) proteins were analyzed by immunoblot with specific antibodies. F) Liver gene expression analysis of ISR and ER-stress related genes by qPCR. All data presented are the mean \pm SD. * $p < 0.05$, ** $p < 0.01$, *** $p < 0.001$, **** $p < 0.0001$ one-way ANOVA

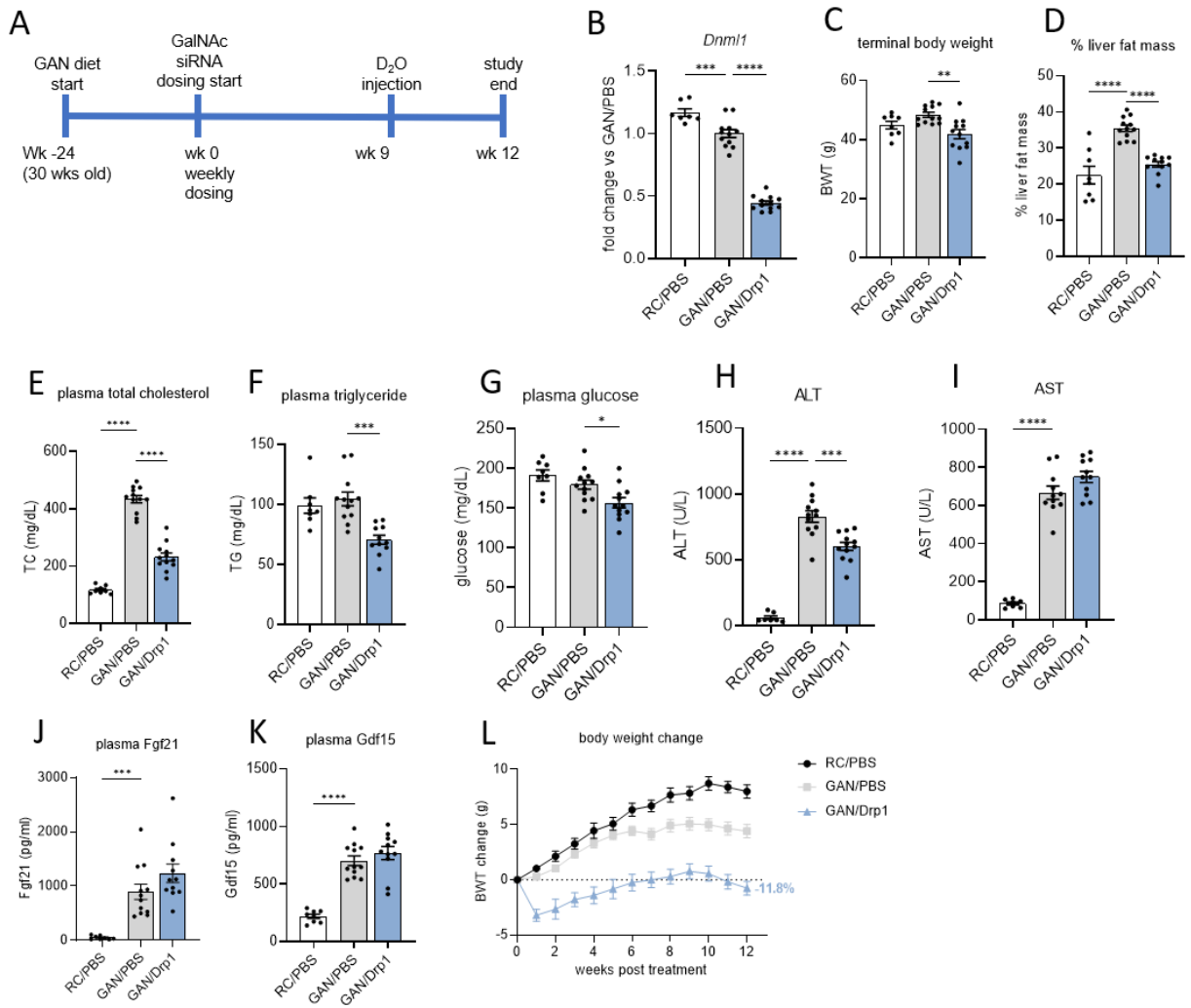


Figure 3- 3. Improved plasma metabolic profile in mice on GAN diet by Drp1 knockdown

A) Study design for testing hepatocyte specific Drp1 knockdown efficacy in the preclinical NASH GAN mouse model. Mice were fed regular chow (RC) or GAN diet for 24 weeks before they were treated weekly with PBS (control) or GalNac Drp1 siRNA (Drp1) for 12 weeks. At week 9, D₂O was injected to measure the production of hydroxyproline, indicator for ongoing fibrosis. B) Liver *Dnm1* mRNA levels were analyzed by qPCR at the end of the study. C) Terminal body weights of each mouse at the study end. D) Percent

of liver fat mass in mice on regular chow or GAN diet and treatment with PBS or GalNAc Drp1 siRNA. E) Final plasma cholesterol (TC) F) triglycerides (TG) G) and glucose level. H) ALT and I) AST level after weekly injections with PBS or GalNAc Drp1 siRNA for 12 weeks in mice on regular chow or GAN diet. J) Final plasma Fgf21 and K) Gdf15 protein level. K) Body weight changes at each week of PBS or GalNAc Drp1 siRNA injected mice on regular chow or GAN diet. All data presented are the mean \pm SD. * $p < 0.05$, ** $p < 0.01$, *** $p < 0.001$, **** $p < 0.0001$ one-way ANOVA

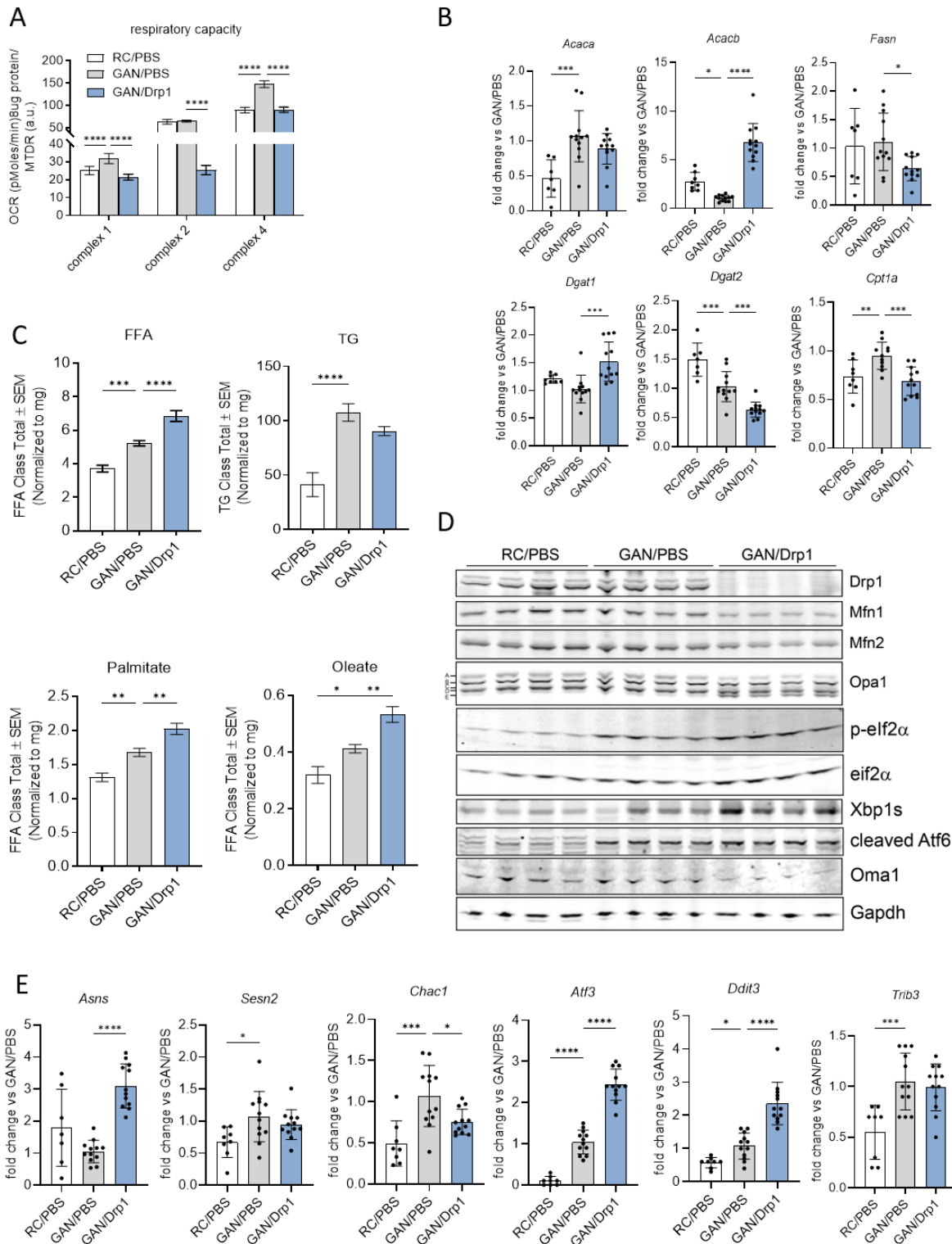


Figure 3- 4. Reduced respiratory capacity and accumulation of FFA upon Drp1 knockdown activates the ISR in mice on GAN diet

A) C57BL/6 mice on regular chow or GAN diet for 24 weeks were treated weekly with PBS (control) or GalNAc Drp1 siRNA (Drp1) for 12 weeks. Livers were isolated and the activity of mitochondrial ETC complexes 1, 2 and 4 were measured. B) Liver gene expression analysis of genes involved in lipid metabolism. C) Lipidomics analysis of free fatty acids (FFA), triglycerides (TG), palmitate and oleate in livers of mice on regular chow or GAN diet treated for 12 weeks with PBS or GalNAc Drp1 siRNA (Drp1). D) Immunoblot of liver extracts with specific antibodies for Drp1, Opa1, Mfn1, Mfn2, p-eIF2 α , eIF2, Xbp1s, Atf6, Oma1 and Gapdh. Different Opa1 splice variants are indicated. E) Liver gene expression analysis of integrated stress response (ISR) and ER-stress related genes by qPCR. All data presented are the mean \pm SD. *p<0.05, ** p<0.01, ***p<0.001, ****p<0.0001 one-way ANOVA

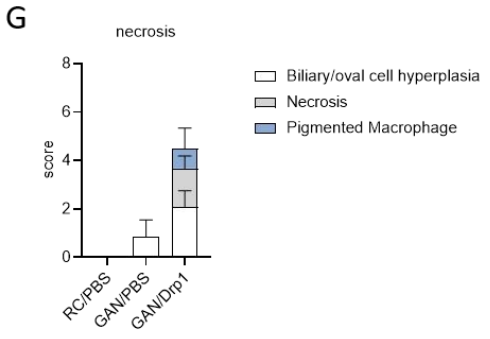
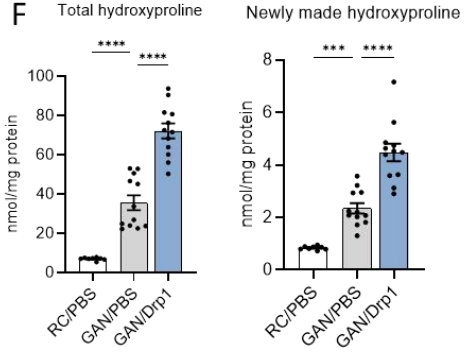
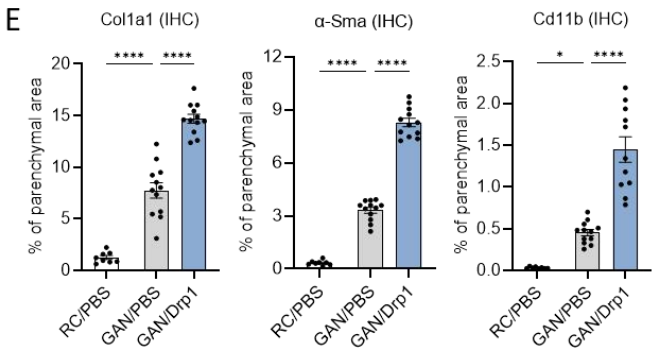
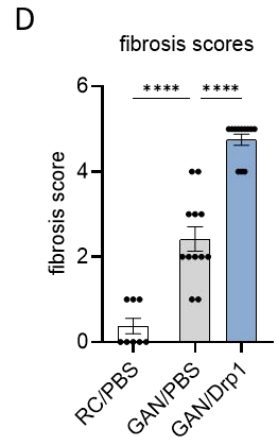
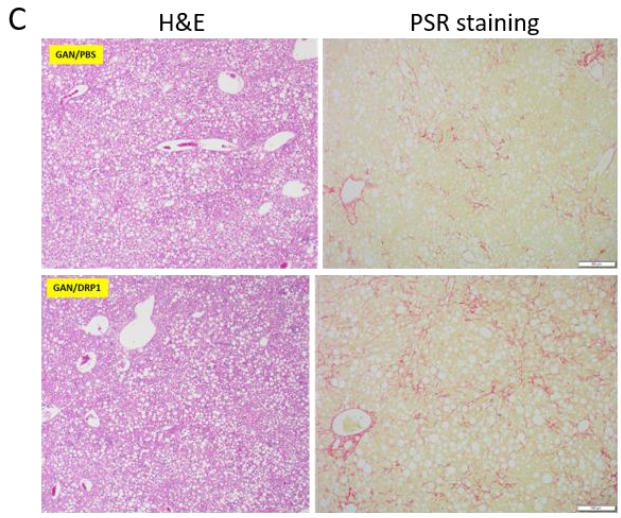
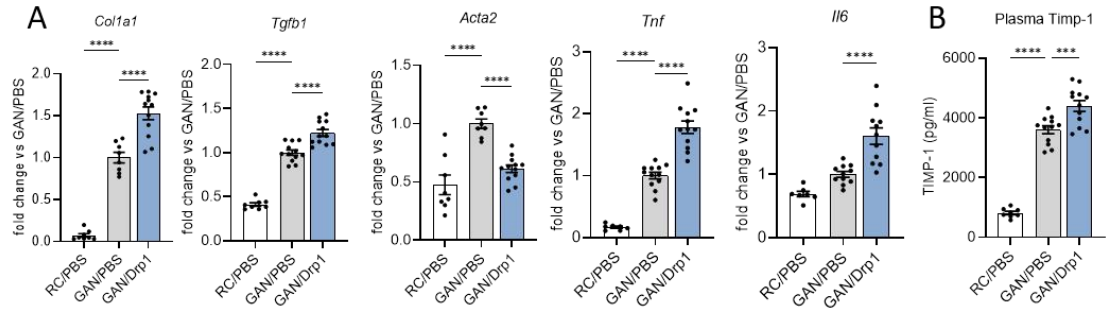
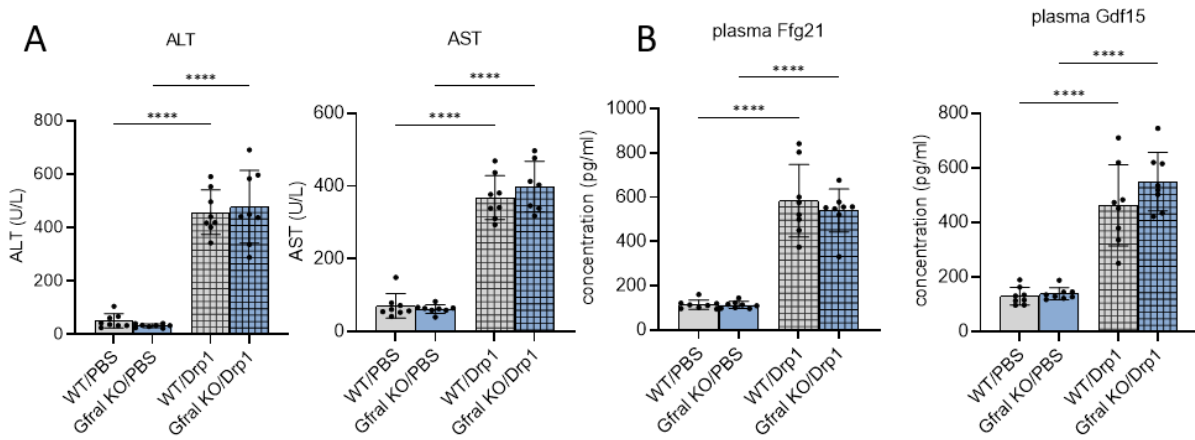


Figure 3- 5. Hepatocyte specific Drp1 knockdown worsens fibrosis and inflammation in GAN mice

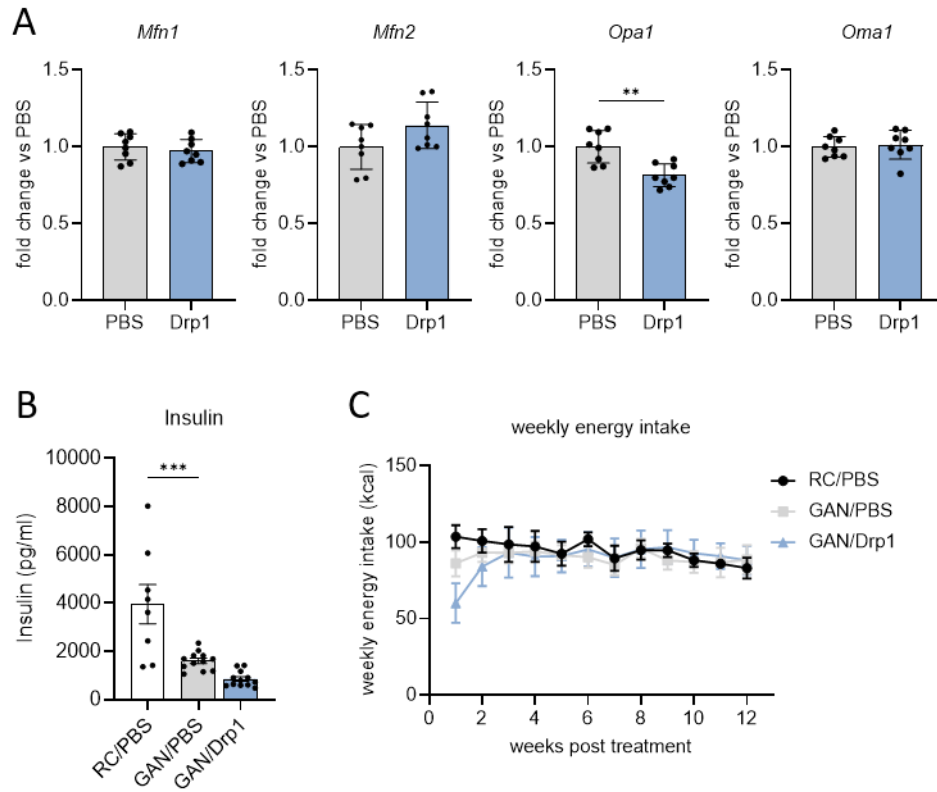
A) Gene expression of *Col1a1*, *Tgfb*, *Acta2*, *Tnf*, and *Il6* was analyzed in livers from C57BL/6 mice on regular chow or GAN diet for 24 weeks and then treated weekly with PBS (control) or GalNAc Drp1 siRNA (Drp1) for additional 12 weeks. B) Plasma Timp-1 protein level. C) Hematoxylin and Eosin (H&E) and Picrosirius Red (PSR) staining of livers from control (PBS) or GalNAc Drp1 siRNA treated mice on GAN diet. D) Histological quantification of Picrosirius Red staining in livers from indicated mice. E) Quantification of liver immunohistochemistry (IHC) staining for *Col1a1*, α -Sma and Cd11b F) Mass spectrometry analysis of total liver hydroxyproline and newly made hydroxyproline. G) Histopathological changes within the livers from mice on regular chow or GAN diet and treatment with PBS or GalNAc Drp1 siRNA. All data presented are the mean \pm SD. * $p < 0.05$, *** $p < 0.001$, **** $p < 0.0001$ one-way ANOVA

SUPPLEMENTAL FIGURES



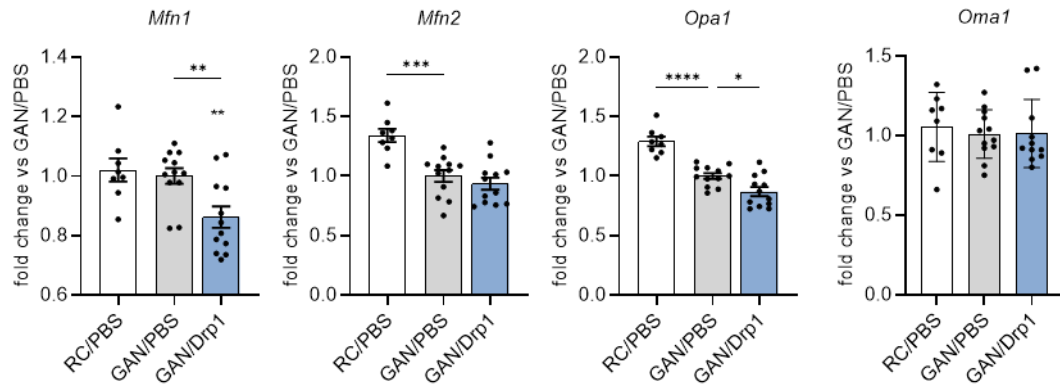
Expanded View Figure 3- 1

A) ALT and AST level in wildtype or Gfral KO mice after 4 weeks of weekly injections with PBS or GalNAc Drp1 siRNA (Drp1). B) Final plasma Fgf21 and Gdf15 protein level. All data presented are the mean \pm SD. ****p<0.0001 one-way ANOVA



Expanded View Figure 3- 2

A) Liver *Mfn1*, *Mfn2*, *Opa1* and *Oma1* mRNA level were analyzed by qPCR. B) Insulin level in male C57BL/6 mice injected with PBS (control) or GalNAc Drp1 siRNA on regular chow or GAN diet. C) Weekly food intake presented as caloric intake in mice of PBS (control) or GalNAc Drp1 siRNA on regular chow or GAN diet. All data presented are the mean±SD. *p<0.05, ** p<0.01, ***p<0.001, ****p<0.0001 one-way ANOVA



Expanded View Figure 3- 3.

Lean male C57BL/6 mice were injected with PBS (control) or GalNAc Drp1 siRNA (Drp1) weekly for 4 weeks. Liver *Mfn1*, *Mfn2*, *Opa1* and *Oma1* mRNA level were analyzed by qPCR. All data presented are the mean \pm SD. ** p<0.01 one-way ANOVA

REFERENCES

- Acin-Perez R, Benador IY, Petcherski A, Veliova M, Benavides GA, Lagarrigue S, Caudal A, Vergnes L, Murphy AN, Karamanlidis G, *et al* (2020) A novel approach to measure mitochondrial respiration in frozen biological samples. *EMBO J* 39
- Adela Guara A, Perales-Clemente E, Calvo E, Cido Navas P, Vazquez J, Enriquez JA, Guara A, Acın-Perez R, Loureiro-Lopez M, Pujol C, *et al* (2016) The CoQH₂/CoQ Ratio Serves as a Sensor of Respiratory Chain Efficiency.
- Baker MJ, Lampe PA, Stojanovski D, Korwitz A, Anand R, Tatsuta T & Langer T (2014) Stress-induced OMA1 activation and autocatalytic turnover regulate OPA1-dependent mitochondrial dynamics. *EMBO J* 33: 578–593
- BK U (2018) Direct Infusion-Tandem Mass Spectrometry (DI-MS/MS) Analysis of Complex Lipids in Human Plasma and Serum Using the Lipidizer™ Platform. *Methods Mol Biol* 1730: 227–236
- Blais JD, Filipenko V, Bi M, Harding HP, Ron D, Koumenis C, Wouters BG & Bell JC (2004) Activating transcription factor 4 is translationally regulated by hypoxic stress. *Mol Cell Biol* 24: 7469–7482
- Boland ML, Laker RC, Mather K, Nawrocki A, Oldham S, Boland BB, Lewis H, Conway J, Naylor J, Guionaud S, *et al* (2020) Resolution of NASH and hepatic fibrosis by the GLP-1R/GcgR dual-agonist Cotadutide via modulating mitochondrial function and lipogenesis. *Nat Metab* 2: 413–431
- Burra P, Becchetti C & Germani G (2020) NAFLD and liver transplantation: Disease burden, current management and future challenges. *JHEP Reports* 2
- Chung HK, Ryu D, Kim KS, Chang JY, Kim YK, Yi HS, Kang SG, Choi MJ, Lee SE,

- Jung SB, *et al* (2017) Growth differentiation factor 15 is a myomitokine governing systemic energy homeostasis. *J Cell Biol* 216: 149–165
- Fitzgerald K, White S, Borodovsky A, Bettencourt BR, Strahs A, Clausen V, Wijngaard P, Horton JD, Taubel J, Brooks A, *et al* (2017) A Highly Durable RNAi Therapeutic Inhibitor of PCSK9. *N Engl J Med* 376: 41–51
- Forsström S, Jackson CB, Carroll CJ, Kuronen M, Pirinen E, Pradhan S, Marmyleva A, Auranen M, Kleine IM, Khan NA, *et al* (2019) Fibroblast Growth Factor 21 Drives Dynamics of Local and Systemic Stress Responses in Mitochondrial Myopathy with mtDNA Deletions. *Cell Metab* 30: 1040-1054.e7
- Fujita Y, Ito M, Kojima T, Yatsuga S, Koga Y & Tanaka M (2015) GDF15 is a novel biomarker to evaluate efficacy of pyruvate therapy for mitochondrial diseases. *Mitochondrion* 20: 34–42
- Gabr SA, Alghadir AH, Sherif YE & Ghfar AA (2017) Hydroxyproline as a Biomarker in Liver Disease. 471–491
- Galloway CA, Lee H, Brookes PS & Yoon Y (2014) Decreasing mitochondrial fission alleviates hepatic steatosis in a murine model of nonalcoholic fatty liver disease. *Am J Physiol - Gastrointest Liver Physiol* 307: G632–G641
- Gardner JL, Turner SM, Bautista A, Lindwall G, Awada M & Hellerstein MK (2007) Measurement of liver collagen synthesis by heavy water labeling: effects of profibrotic toxicants and antifibrotic interventions. *Am J Physiol Gastrointest Liver Physiol* 292
- Goedeke L, Peng L, Montalvo-Romeral V, Butrico GM, Dufour S, Zhang XM, Perry RJ, Cline GW, Kievit P, Chng K, *et al* (2019) Controlled-release mitochondrial

protonophore (CRMP) reverses dyslipidemia and hepatic steatosis in dysmetabolic nonhuman primates. *Sci Transl Med* 11

Hansen HH, Ægidius HM, Oró D, Evers SS, Heebøll S, Eriksen PL, Thomsen KL, Bengtsson A, Veidal SS, Feigh M, *et al* (2020) Human translatability of the GAN diet-induced obese mouse model of non-alcoholic steatohepatitis. *BMC Gastroenterol* 20: 1–12

Hetherington AM, Sawyez CG, Zilberman E, Stoianov AM, Robson DL & Borradaile NM (2016) Differential Lipotoxic Effects of Palmitate and Oleate in Activated Human Hepatic Stellate Cells and Epithelial Hepatoma Cells. *Cell Physiol Biochem* 39: 1648–1662

Hsieh W-Y, Williams KJ, Su B & Bensinger SJ (2021) Profiling of mouse macrophage lipidome using direct infusion shotgun mass spectrometry. *STAR Protoc* 2: 100235

Hsu JY, Crawley S, Chen M, Ayupova DA, Lindhout DA, Higbee J, Kutach A, Joo W, Gao Z, Fu D, *et al* (2017) Non-homeostatic body weight regulation through a brainstem-restricted receptor for GDF15. *Nature* 550: 255–259

Iozzo P, Bucci M, Roivainen A, Någren K, Järvisalo MJ, Kiss J, Guiducci L, Fielding B, Naum AG, Borra R, *et al* (2010) Fatty acid metabolism in the liver, measured by positron emission tomography, is increased in obese individuals. *Gastroenterology* 139

Kim KH, Jeong YT, Oh H, Kim SH, Cho JM, Kim YN, Kim SS, Kim DH, Hur KY, Kim HK, *et al* (2012) Autophagy deficiency leads to protection from obesity and insulin resistance by inducing Fgf21 as a mitokine. *Nat Med* 2012 191 19: 83–92

Koliaki C, Szendroedi J, Kaul K, Jelenik T, Nowotny P, Jankowiak F, Herder C,

- Carstensen M, Krausch M, Knoefel WT, *et al* (2015) Adaptation of hepatic mitochondrial function in humans with non-alcoholic fatty liver is lost in steatohepatitis. *Cell Metab* 21: 739–746
- Lapuente-Brun E, Moreno-Loshuertos R, Acín-Pérez R, Latorre-Pellicer A, Colaś C, Balsa E, Perales-Clemente E, Quirós PM, Calvo E, Rodríguez-Hernández MA, *et al* (2013) Supercomplex assembly determines electron flux in the mitochondrial electron transport chain. *Science* 340: 1567–1570
- Liesa M, Palacín M & Zorzano A (2009) Mitochondrial dynamics in mammalian health and disease. *Physiol Rev* 89: 799–845 doi:10.1152/physrev.00030.2008
[PREPRINT]
- Liesa M & Shirihi OSS (2013) Mitochondrial dynamics in the regulation of nutrient utilization and energy expenditure. *Cell Metab* 17: 491–506
- Lopez AB, Wang C, Huang CC, Yaman I, Li Y, Chakravarty K, Johnson PF, Chiang CM, Snider MD, Wek RC, *et al* (2007) A feedback transcriptional mechanism controls the level of the arginine/lysine transporter cat-1 during amino acid starvation. *Biochem J* 402: 163–173
- Malhi H & Gores GJ (2008) Molecular mechanisms of lipotoxicity in nonalcoholic fatty liver disease. *Semin Liver Dis* 28: 360–369
- March J (1975) A modified technique for the quantitative analysis of amino acids by gas chromatography using heptafluorobutyric n-propyl derivatives. *Anal Biochem* 69: 420–422
- Matthews DE, Pesola G & Campbell RG (1990) Effect of epinephrine on amino acid and energy metabolism in humans. *Am J Physiol* 258

- McGarry JD, Mannaerts GP & Foster DW (1977) A possible role for malonyl-CoA in the regulation of hepatic fatty acid oxidation and ketogenesis. *J Clin Invest* 60: 265–270
- Mick E, Titov D V., Skinner OS, Sharma R, Jourdain AA & Mootha VK (2020) Distinct mitochondrial defects trigger the integrated stress response depending on the metabolic state of the cell. *Elife* 9
- Montero R, Yubero D, Villarroja J, Henares D, Jou C, Rodríguez MA, Ramos F, Nascimento A, Ortez CI, Campistol J, *et al* (2016) GDF-15 Is Elevated in Children with Mitochondrial Diseases and Is Induced by Mitochondrial Dysfunction. *PLoS One* 11
- Mullard A (2018) FDA approves landmark RNAi drug. *Nat Rev Drug Discov* 17: 613
- O’Rahilly S (2017) GDF15-From Biomarker to Allostatic Hormone. *Cell Metab* 26: 807–808
- Osto C, Benador IY, Ngo J, Liesa M, Stiles L, Acin-Perez R & Shirihai OS (2020) Measuring Mitochondrial Respiration in Previously Frozen Biological Samples. *Curr Protoc Cell Biol* 89
- Palam LR, Gore J, Craven KE, Wilson JL & Korc M (2015) Integrated stress response is critical for gemcitabine resistance in pancreatic ductal adenocarcinoma. *Cell Death Dis* 2015 610 6: e1913–e1913
- Patel S, Alvarez-Guaita A, Melvin A, Rimmington D, Dattilo A, Miedzybrodzka EL, Cimino I, Maurin AC, Roberts GP, Meek CL, *et al* (2019) GDF15 Provides an Endocrine Signal of Nutritional Stress in Mice and Humans. *Cell Metab* 29: 707-718.e8
- Restelli LM, Oettinghaus B, Halliday M, Agca C, Licci M, Sironi L, Savoia C, Hench J,

- Tolnay M, Neutzner A, *et al* (2018) Neuronal Mitochondrial Dysfunction Activates the Integrated Stress Response to Induce Fibroblast Growth Factor 21. *Cell Rep* 24: 1407
- Sharma R, Reinstadler B, Engelstad K, Skinner OS, Stackowitz E, Haller RG, Clish CB, Pierce K, Walker MA, Fryer R, *et al* (2021) Circulating markers of NADH-reductive stress correlate with mitochondrial disease severity. *J Clin Invest* 131
- Shum M, Ngo J, Shirihai OS & Liesa M (2020) Mitochondrial oxidative function in NAFLD: friend or foe? *Mol Metab*: 101134
- Sunny NE, Parks EJ, Browning JD & Burgess SC (2011) Excessive hepatic mitochondrial TCA cycle and gluconeogenesis in humans with nonalcoholic fatty liver disease. *Cell Metab* 14: 804–810
- Trevino MB, Mazur-Hart D, Machida Y, King T, Nadler J, Galkina E V., Poddar A, Dutta S & Imai Y (2015) Liver Perilipin 5 Expression Worsens Hepatosteatosis But Not Insulin Resistance in High Fat-Fed Mice. *Mol Endocrinol* 29: 1414–1425
- Wang B, Rudnick S, Cengia B & Bonkovsky HL (2018) Acute Hepatic Porphyrrias: Review and Recent Progress. *Hepatol Commun* 3: 193–206
- Wang L, Ishihara T, Ibayashi Y, Tatsushima K, Setoyama D, Hanada Y, Takeichi Y, Sakamoto S, Yokota S, Mihara K, *et al* (2015) Disruption of mitochondrial fission in the liver protects mice from diet-induced obesity and metabolic deterioration. *Diabetologia* 58: 2371–2380
- Yamaguchi K, Yang L, McCall S, Huang J, Xing XY, Pandey SK, Bhanot S, Monia BP, Li YX & Diehl AM (2007) Inhibiting triglyceride synthesis improves hepatic steatosis but exacerbates liver damage and fibrosis in obese mice with nonalcoholic

steatohepatitis. *Hepatology* 45: 1366–1374

CHAPTER 4

Discussion & Future Directions

1. A second job for the mitochondrial life cycle

Within this thesis, I have demonstrated that mitochondrial dynamics regulates FAO, particularly at the level of CPT1 regulation (Chapter 2). Other works have suggested mitochondrial morphology not only play a role in preferential fuel utilization, but the unique differences between tissues indicate morphology is important to bioenergetics and pathophysiology (Wajchenberg, 2010; Titchenell *et al*, 2016; Zhang *et al*, 2016; Liesa & Shirihai, 2013). Furthermore, previous studies have mitochondrial morphology impacts CPT1 activity and tertiary structure (López-Viñas *et al*, 2007; Song *et al*, 2021). We investigated the role of mitochondrial dynamics in FAO under various conditions known to elongate and fragment mitochondrial morphology. We first established our model in HepG2 cells then expanded our work into primary hepatocytes, INS1 cells, primary beta-cells, and DLBCL cells and further confirmed the degree of FAO was determined by mitochondrial length.

Diabetes and obesity have been shown to induce mitochondrial fragmentation in the pancreatic beta-cells (Masini *et al*, 2017; Supale *et al*, 2012; Gao *et al*, 2014). This observation has also been modeled in vitro by long term exposure to an excess nutrient environment (Molina *et al*, 2009). Within the mitochondrial life cycle, mitochondria undergo a series of fission and fusion events as a response to bioenergetic adaptation and quality control. Mitochondrial fragmentation has been identified both as a precursor to mitophagy and as an association with disease onset. We then asked, is mitochondrial fragmentation under obese conditions a maladaptive response or a compensatory mechanism? To do so, we assessed liver health by impairing mitochondrial fission in an animal model of NASH (Chapter 3).

Investigating the process of mitochondrial fission and ultimately impairing the mitochondrial life cycle revealed the role of mitochondrial dynamics can be extended past quality control, modulating fuel preference to meet metabolic demands. Perhaps modulating the sensitivity of CPT1 or membrane-bound proteins is thus a compensatory mechanism.

2. Investigation of inhibiting fission as a therapeutic revealed novel role for mitochondrial morphology in FFA metabolism

In chapter 3, we show that inhibiting mitochondrial fission enhanced NEFA accumulation, altered the ETC, induced ER stress, and activated the mitochondrial ISR. Other labs have shown inhibition of hepatic? mitochondrial fission protects from diet-induced obesity as noted by reductions in TG content and to some degree mtROS (Table 1). In an effort to dissect the role of mitochondrial morphology as a compensatory mechanism under nutrient excess, we impaired mitochondrial fission by knocking down Drp1 through GalNAC siRNA delivery in lean animals and in a NASH model (induced by GAN-diet feeding). Impaired fission in NASH animals resulted in OMA1 activation, ER stress, hyper activation of the IRS, and hepatocyte necrosis only seen in the GAN/Drp1KD. At the same time FAO associated genes were reduced and accumulation of NEFA was observed. Taken together, inhibition of mitochondrial fragmentation under nutrient excess impaired metabolic flexibility and enhanced NASH phenotypes. Consistent with this observation, mitochondria forced to be elongated via Drp1 KO and dnDrp1 yielded reduced FAO capacity (Chapter 2). Other labs have also shown the inability to undergo FAO under nutrient excess results in insulin insensitivity and NAFLD onset (Trevino *et al*, 2015; Moore *et al*, 2022). This phenotype suggests an important role

for mitochondrial fragmentation in excess nutrient environments and in liver health.

3. Potential for mitochondrial heterogeneity to influence malonyl-CoA sensitivity and FAO

Studying malonyl-CoA sensitivity poses unique challenges due to the sensitivity of the assay necessary to capture differential inhibitory responses at small concentrations of malonyl-CoA. In chapter 2, we assessed malonyl-CoA sensitivity through respirometry under cellular permeabilization, isolation of membrane fractions to binding of malonyl-CoA, and multiple pharmacological activators of CPT1 acting on different binding sites. Although the data consistently revealed elongated mitochondria yielded hypersensitivity to malonyl-CoA and reduced sensitivity upon fragmentation, a limitation to our study is the inability to account for mitochondrial heterogeneity. Expression of CPT1 isoforms contribute to regulation of FAO not only in different tissues but also under fed and fasted states (Flavin *et al*, 2010; Schreurs *et al*, 2010). Our lab has previously demonstrated the existence of peridroplet mitochondria (PDM) and cytoplasmic mitochondria (CM) in the brown adipocyte. Both subsets of mitochondria have their own unique lipid metabolism, thereby suggesting differences in CPT1 expression. These findings then suggest, if peridroplet mitochondria and cytoplasmic mitochondria exist in the liver then the observed changes to CPT1 sensitivity may be an underestimation.

Furthermore, our findings of mitochondrial dynamics regulating FAO capacity combined with observations of mitochondrial subpopulations lead to the question: Is CPT1 sensitivity altered in different mitochondrial subpopulations? In particular to those characterized to be more fragmented? And to what degree do the different CPT1 isoforms contribute to changes in FAO? Future experiments should assess CPT1 interaction with

malonyl-CoA in different mitochondrial subpopulations and if differential expression of isoforms recapitulate our findings that fragmented mitochondria have reduced CPT1 sensitivity. Further studies should be conducted to observe if changing CPT1 sensitivity alters the mitochondrial subpopulation to shift towards another mitochondrial subpopulation by using a CPT1-insensitive mutant. Be more specific about what "CPT1-insensitive mutant" means. It is insensitive to malonyl-CoA? It is not active to shuttle fatty acid? Will a CPT1-insensitive cytoplasmic mitochondria now transition into peridroplet-like mitochondria? Genetic manipulation of CPT1 would be a useful tool to investigate the interplay of morphology, metabolic regulation, and mitochondrial heterogeneity.

On the other hand, our findings can explain the differences in the observed mitochondrial subpopulations. As the role of PDM has been well characterized to be a potential therapeutic to sequester fat and prevent lipotoxicity (Veliova *et al*, 2020), the potential for CMs to have reduced malonyl-CoA sensitivity can be a proposed therapeutic in preventing NEFA accumulation by enhancing FAO.

4. Mitochondrial subpopulations influence cellular function

Mitochondrial heterogeneity in both pathological and physiological states has been observed to yield functional heterogeneity, if not an association with a phenomenon of interest. Intracellular mitochondrial heterogeneity in the physiological state has largely been attributed to the presence of various subpopulations (**Figure 1**). When mitochondrial subpopulations begin to lose their unique traits, cellular function is altered, and early stages of pathology are observed (as discussed in Chapter 1). The detrimental decline in mitochondrial subpopulation heterogeneity can explain the loss of compensatory mechanisms (as reviewed by Shum *et al*. (Shum *et al*, 2020)). Observation of disease

onset due to loss of organellar heterogeneity has also been observed in lipid droplets (Herms *et al*, 2013). This section will highlight known mitochondrial subpopulations and their influence on cellular function.

To date, the exact role of mitochondria bound to lipid droplets remains unanswered in hepatocytes. We will discuss how mitochondrial dynamics can clarify the conundrum of the role of mitochondrial oxidative function in hepatic steatosis. Particularly, why measurements of mitochondrial function in intact livers and in isolated mitochondria both reveal increased oxidative function induced by steatosis, while measurements in primary hepatocytes and perfused livers showed the opposite.

These characteristics of PDM in BAT have a strong resemblance with the functional changes in mitochondrial function observed when hepatic lipogenesis is elevated. As a result, we expect that increasing the interaction of hepatocyte mitochondria to lipid droplets would promote steatosis. The published studies characterizing the role of PLIN5 in liver support this expectation. Indeed, hepatic PLIN5 gain-of-function increased the number of lipid droplets and induced steatosis in hepatocytes, as we showed in brown adipocytes (Wang *et al*, 2015a; Trevino *et al*, 2015). Remarkably though, hepatic steatosis induced by PLIN5 did not cause hyperglycemia or hepatic inflammation and even protected from high-fat diet-induced insulin resistance (Trevino *et al*, 2015). On the other hand, the deletion of PLIN5 in hepatocytes resulted in PPAR α activation, which elevated mitochondrial FAO and prevented hepatic steatosis at the expense of causing hepatic damage and inflammation (Wang *et al*, 2015a). Thus, PLIN5 loss-of-function in liver resembles cold-induced activation of thermogenic FAO in BAT, which decreases the number of mitochondria attached to lipid droplets by an unclear mechanism.

In summary, hepatic PLIN5 traps the dietary excess of fatty acids into lipid droplets, protecting from insulin resistance and from liver damage induced by high-fat diet feeding. Furthermore, PLIN5 loss-of-function in hepatocytes demonstrates that PPAR α activation and elevated mitochondrial FAO will not be beneficial if the capacity of hepatocytes to sequester fatty acid excess into lipid droplets is impaired. Consequently, one could envision that a therapeutic strategy for NAFLD would require a concurrent increase in the capacity of PDM to sequester fatty acids and cytosolic mitochondria oxidizing fat (**Figure 2**).

5. Three distinct mitochondrial sub-populations could regulate hepatic steatosis in opposite ways in NAFLD

Like the physically segregated PDM and CM in BAT, we propose that hepatocytes also harbor a first sub-population of segregated mitochondria similar to BAT PDM, which will be specialized to support dietary fatty acid esterification into TG. Hepatic PDM could be defined by mitochondria anchored to the lipid droplet via PLIN5, a lipid droplet protein that binds mitochondria in multiple tissues, or via other uncharacterized proteins.

In addition to dietary fatty acid esterification into TG, hepatocytes can synthesize new fatty acids and assemble lipoproteins in the ER. These lipoproteins carry TG, cholesterol and phospholipids, allowing their export from the hepatocyte to the plasma. We propose that a second sub-population of segregated mitochondria, the ER-anchored mitochondria, will have their CPT1 activity inhibited and will be supporting lipoprotein assembly and *de novo* fatty acid synthesis. We further propose that these ER-mitochondria will have a limited capacity to execute FAO, similar to PDM. Finally, we propose a third distinct sub-population of mitochondria, the cytosolic mitochondria (CM),

which will be specialized in oxidizing fatty acids (**Figure 2**).

The existence of ER-anchored mitochondria can explain how a pool of fatty acids escape FAO and can be selectively directed towards lipoprotein assembly (VLDL), as these mitochondria would have CPT1 and thus FAO inhibited. Such a subpopulation of specialized mitochondria could explain why ACC inhibition reduces intrahepatic TG content in mice, while increasing VLDL secretion (Kim *et al*, 2017). The segregation of mitochondria caused by their interaction with the ER would allow these ER-mitochondria to have a different protein composition and/or post-translational modifications, inhibiting their capacity to oxidize fatty acids. An interesting property could be that these mitochondria selectively carried CPT1B, the isoform of CPT1 that is highly sensitive to malonyl-CoA inhibition. As hyperinsulinemia promotes lipogenesis, hyperinsulinemia might explain why ER-mitochondria contacts are increased in mice with insulin resistance and simple steatosis (Arruda *et al*, 2014).

PLIN5 gain-of-function in liver causes cytosolic lipid droplet expansion without increasing VLDL export and plasma lipids (Trevino *et al*, 2015). This published study supports that PLIN5, and potentially PDM, are not increasing de novo lipogenesis or the assembly of lipoproteins in the ER. We thus propose that, instead of PLIN5, one of the important mediators to segregate mitochondria to generate ER-anchored lipogenic mitochondria is DGAT2 (Stone *et al*, 2009). DGAT2 catalyzes the last step of TG synthesis and is located in the mitochondria-associated membranes (MAM) of the ER. Furthermore, DGAT2 itself can promote the association of mitochondria to the ER and DGAT2 deletion decreases steatosis and hypertriglyceridemia (Gluchowski *et al*, 2019). Mfn2 is also known to participate in ER-mitochondria contacts (De Brito & Scorrano,

2008) and Mfn2 deletion in hepatocytes causes hepatic steatosis(Hernández-Alvarez *et al*, 2019; Sebastián *et al*, 2012; Muñoz *et al*, 2013). Thus, it is a possibility that steatosis induced by Mfn2 KO is caused by dysfunctional and/or unstable ER-mitochondria contacts, limiting the ability of mitochondria to support VLDL assembly. Limited or impaired transfer of phospholipid precursors and ATP between mitochondria and ER could affect both lipoprotein assembly, as well as fatty acid esterification into TG in the ER. Therefore, an impairment in VLDL assembly caused by Mfn2 deletion could cause the re-routing of fatty acids and TG into cytosolic lipid droplets. This specific role of Mfn2 on VLDL assembly could explain why the reversal of ER stress, inflammation, decreased FAO and insulin resistance in liver-specific Mfn2 KO mice does not decrease hepatic steatosis (Liesa *et al*, 2009; González-Rodríguez *et al*, 2014; Trudeau *et al*, 2016).

The hypothetical scenario that ER-mitochondria and PDM in liver are functionally separated from cytosolic mitochondria can explain the divergence of the effects reported on mitochondrial oxidative function in NAFLD. Segregating mitochondria into 3 different populations inside one hepatocyte means that the oxidative function of each population can be completely independent. The functional independence of each segregated population can explain why TCA cycle flux and FAO rates measured in vivo are concurrently increased in NAFLD, despite FAO and TCA being competing fluxes that can cancel each other in isolated mitochondria (Garland *et al*, 1968).

6. Challenges and considerations to be made when studying intracellular heterogeneity

While there is significant evidence that different mitochondrial subpopulations may be present in certain tissue types, dissecting this heterogeneity can prove to be challenging.

Mitochondrial heterogeneity has been attributed to different biochemical properties including respiratory or enzymatic activity, membrane potential, morphology, calcium levels, etc., and while these traits may fluctuate in the same direction across different cell types, their functional heterogeneity may not be the same. Often the greatest question is whether or not the observed phenotypes are due to background noise as a result of technical difficulties in separating individual mitochondrial populations (Duchen *et al*, 2003; Noske *et al*, 2008; Woods, 2017; Kuznetsov *et al*, 2006). Characterization of mitochondrial heterogeneity thus becomes exceptionally difficult when a portion of measured heterogeneity may stem from the noise generated during isolation, data acquisition, and data analysis. For example, in the case of measuring mitochondrial heterogeneity using single-plane confocal microscopy, a large variance can be generated since not all mitochondria are localized in the same focal plane. When mitochondria are not in the same focal plane, the results exclude mitochondria that are elongating towards a different axis or are covered by another organelle. This potential noise can only be properly assessed with 3D reconstruction at 22 °C, where mitochondrial movement is slowed down when compared to traditional measurement temperatures of 37 °C (Collins *et al*, 2002).

Alternatively, noise may be generated in the processing leading up to imaging, specifically during the mitochondrial isolation process, as in the separation of brown adipocyte PDM and cytoplasmic mitochondria. Although the isolation method may have impacted the characterization of PDM and cytoplasmic mitochondria, Benador *et al*. verified the unique population traits by overexpression of the mitochondria–lipid droplet tethering protein to highlight biochemical differences observed in the mitochondrial

subpopulations(Benador *et al*, 2018; Ngo *et al*, 2021).

The establishment of methods to separate the proposed mitochondrial populations (CM, PDM, and ER-bound mitochondria) will be essential to demonstrate their existence and specialization in hepatocytes. One approach could be to use PLIN5 to pull down PDM and DGAT2 to pull down ER-anchored mitochondria, with mitochondria that did not bind to PLIN5 and DGAT2 being cytosolic mitochondria that oxidize fatty acids. Then, we could compare their capacity to synthesize citrate and oxidize fatty acids, as well as their sensitivity to malonyl-CoA-mediated inhibition of FAO. We expect that cytosolic mitochondria will be the population with the highest FAO capacity and lowest sensitivity to malonyl-CoA-mediated FAO inhibition. On the other hand, lipogenic mitochondria (PDM and ER-mito) will have higher citrate synthase activity, higher sensitivity to malonyl-CoA-mediated FAO inhibition and lower FAO capacity. Another approach would be to identify specific mitochondrial proteins acting as biomarkers for each population. Once identified, these biomarkers could be used to visualize them using microscopy or to quantify their relative abundance. However, it is difficult to anticipate the existence of an exclusive protein that defines each population. We would rather expect a differential enrichment of certain proteins.

The analysis of mitochondrial diversity has important implications for the diagnosis and treatment of various mitochondrial disorders. The processing and imaging techniques being used for these studies have a major role in the impact and discovery of these studies. Advancement in mitochondrial isolation, analysis, and imaging techniques will thus open promising avenues for utilizing mitochondrial heterogeneity in clinical research.

7. Current and hypothetical therapies targeting liver mitochondria to treat

NAFLD and hyperglycemia

Mitochondrial function is maintained through a complex interplay between cellular ATP demand, nutrient availability, the ability of mitochondria to communicate energetic and redox stress, as well as the response of mitochondria to energetic imbalances. NAFLD is primarily a consequence of an energetic, redox and hormonal imbalance in hepatocytes, leading to excessive exposure of mitochondria to nutrients relative to their ATP demand. Moreover, mitochondria in NAFLD are facilitating anabolism and lipid synthesis when it is not needed. Therefore, one way to cure NAFLD could be to reduce the anabolic activity of mitochondria or alternatively decreasing nutrient load by activating mitochondrial function to eliminate these nutrients. Here, we will list current approaches that are targeting mitochondria to treat NAFLD and propose novel approaches based on our hypothesis of mitochondrial segregation in hepatocytes.

Modulating mitophagy could decrease lipogenesis in the liver, by targeting lipogenic mitochondria for degradation. Indeed, preclinical studies suggested that mitochondrial quality control and mitophagy are reduced in NAFLD, with the restoration of mitophagy preventing or reversing some features of simple steatosis and NASH (Yamada *et al*, 2018; Wang *et al*, 2015c; Zhou *et al*, 2019). One could hypothesize that lipogenic mitochondria accumulate in simple steatosis and NASH because hyperinsulinemia and hyperlipidemia suppress their elimination by mitophagy. Treatment with a natural molecule that restores mitophagy, namely Urolithin A (Ryu *et al*, 2016), improves glucose homeostasis and protects mice from hepatic steatosis (Toney *et al*, 2019). Accordingly, current drugs improving steatosis and NASH in humans, such as metformin and liraglutide, increase mitophagy in rodent models of simple steatosis and NASH (Song *et*

al, 2016; Yu *et al*, 2019). Cotadutide, which targets GLP1R and GCGR and improves NASH, enhances mitophagy too (Boland *et al*, 2020). Of note, Cotadutide mimics glucagon action, implying that mitophagy of lipogenic mitochondria might be a new mechanism by which glucagon decreases lipogenesis. Understanding whether hepatic GCGR activation can selectively target lipogenic mitochondria for mitophagy would resolve the conundrum on how eliminating mitochondria, which oxidize fatty acids, can counteract steatosis. AMPK activators could potentially eliminate lipogenic mitochondria and even replace them with fat oxidizing mitochondria (EQ *et al*, 2016).

Alternatively, mitophagy can be improved by restoring lysosomal function, as hepatic lysosomal acidity is lower in NAFLD (González-Rodríguez *et al*, 2014; Fukuo *et al*, 2014; Inami *et al*, 2011). Lysosomes are essential for autophagy/mitophagy and can determine hepatic TG content (Singh *et al*, 2009). Therapies aiming at restoring lysosomal function could represent a new strategy to attenuate NAFLD (Zeng *et al*, 2019).

Another way to prevent steatosis, without inducing hyperglycemia, is by increasing FAO in mitochondria without increasing ATP synthesis (uncoupled), which would prevent an increase in glucose production. Although mitochondrial uncouplers are cardiotoxic and their action in muscle cause malignant hyperthermia (Grundlingh *et al*, 2011; Dying to be thin: a dinitrophenol related fatality - PubMed), a novel approach that delivered the active form of a mitochondrial uncoupler exclusively to hepatocytes showed a remarkable improvement in safety. This hepatic-specific uncoupler decreased hepatic steatosis and insulin resistance in obese rats, improved liver function and prevented fibrosis in a rat model of NASH (Perry *et al*, 2013, 2015) and in dysmetabolic nonhuman primates (Goedeke *et al*, 2019). Other mild uncouplers delivered systemically, such as BAM15,

improved systemic glucose homeostasis and insulin resistance, showing efficacy in mouse models of NAFLD (Alexopoulos *et al*, 2020).

As elevated oxidative damage is associated with all stages of NAFLD, different studies aimed to improve mitochondrial function by using antioxidants. These trials tested mostly hydrophilic antioxidants and have provided inconclusive data. Remarkably, vitamin E is one of the few lipophilic antioxidants tested for NASH, which was also inconclusive. A meta-analysis showed that vitamin E ingestion was associated with decreased liver steatosis, but not with improved fibrosis (Said & Akhter, 2017). Moreover, vitamin E at high doses correlated with higher cancer and stroke incidence (Klein *et al*, 2011; Schürks *et al*, 2010).

Dietary antioxidants that specifically decreased ROS in mitochondria showed benefits in mouse models of NAFLD, but their efficacy in treating NAFLD in humans has not been proven. One antioxidant tested in humans is silymarin, which is a mixture of flavonoligans with the major active component being silybinin (Taleb *et al*, 2018). Silymarin decreased oxidative damage in different subcellular compartments by decreasing mitochondrial respiratory chain activity (Detaille *et al*, 2008). Clinical trials revealed that treatment with Silymarin decreased circulating AST and ALT levels and improved liver histology in participants with simple steatosis or NASH (Wah Kheong *et al*, 2017; Zhong *et al*, 2017). Systemic treatments with compounds scavenging ROS inside mitochondria, such as mitoQ or mito-tempol, protected rodents from the metabolic syndrome, but evidence in humans is still missing. Moreover, studies restricting the actions of these mitochondrial antioxidants to hepatocytes are still missing (Mercer *et al*, 2012; Ni *et al*, 2016). Therefore, it is unknown if the benefits stemming from these

antioxidant treatments are explained by their actions on the liver or in other tissues.

While the protection from NAFLD induced by hepatocyte-specific deletion of GPX1 and HMOX1 in mice is a proof-of-concept that excessive antioxidant function can promote NAFLD, no therapeutic strategies and trials aimed to decrease antioxidant activity in human livers. As a result, targeting maladaptive and redundant antioxidant systems is a largely unexplored therapeutic avenue in NAFLD. It would be interesting to determine whether some of the current NAFLD treatments can decrease the expression of certain antioxidant systems. Strong candidates as maladaptive antioxidants would be among the ones induced by inflammation and decreased by GLP1R-GCGR agonism.

Furthermore, regulating mitochondrial dynamics and architecture could be a new therapeutic strategy to combat NAFLD. Enhancing the attachment of mitochondria to lipid droplets could protect from fatty acid-mediated toxicity during feeding. On the other hand, promoting the detachment of mitochondria during fasting could enhance fat oxidation and elimination. Such a strategy would restore the ability of liver to handle lipids and would prevent inflammation associated with lipotoxicity. Studies modulating mitochondrial architecture have also proven promising outcomes dependent on the stage of disease progression (**Table 1**).

In all, we conclude that novel therapeutic approaches to treat NAFLD can be provided by: i) approaches limiting mitochondrial-driven synthesis of lipids and glucose, ii) removing maladapted mitochondria by mitophagy or iii) decreasing the action of maladaptive and redundant antioxidant systems.

8. Remaining questions in the field

Remaining questions for future investigation in mitochondrial morphology and liver

disease

ETC structural organization is modulated by dedicated chaperones and assembly factors, mitochondrial membrane morphology, and membrane lipid composition. How much of this dictates CPT1 sensitivity and mitochondrial FAO? If the changes to FAO is not solely influenced by CPT1 sensitivity then how much of the changes to FAO is influenced by ETC restructuring? Considering the different CPT1 isoforms present, is it possible for only one isoform to have changes to malonyl-CoA sensitivity, whereas the other isoform remains unchanged? The mitochondrial translation pathway supports the central metabolic feature of OxPhos-DLBCLs in increasing mitochondrial energy transduction as a survival mechanism. How much of a bioenergetic impact is mitochondrial translational pathway playing?

We observe mitochondrial dynamics to be a compensatory mechanism, to what degree is inhibiting fission beneficial as observed in Table 1? Is there an appropriate pause point in treatment? Various studies have indicated inhibition of fission results in enhanced mitochondrial IRS but yielded beneficial fat mass and TG reduction, what are the effects of inhibiting fission long term? In tissues such as proximal tubules, impaired mitochondrial function and presence of enlarged swollen mitochondria are highly present in early stages of a disease model but mitochondrial oxidative capacity recovers after 16 weeks. Will long term inhibition of fission reduce activation of the IRS?

9. Conclusion

The goal of this research was to elucidate the role of mitochondrial morphology and function in mitochondrial fatty acid oxidation and whether or not this served as a compensatory mechanism under disease states. We have provided evidence

demonstrating that mitochondrial morphology governs fatty acid oxidation rates and may underlie pathological changes in hepatocyte, islet, and DLBCL metabolism. Multiple tissues utilize fatty acids, express some isoform of CPT1, and respond to nutrient overload. Thus, this work explored one of many regulatory mechanisms responsible for unregulated fatty acid oxidation. Further research is needed to understand the exact disease progression at which mitochondrial dynamics serves as a compensatory mechanism or maladaptive response.

Figures

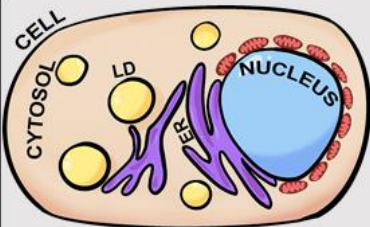
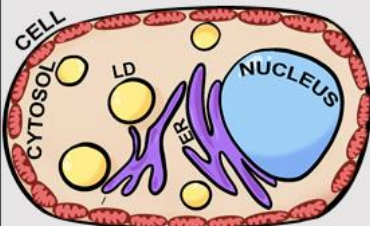
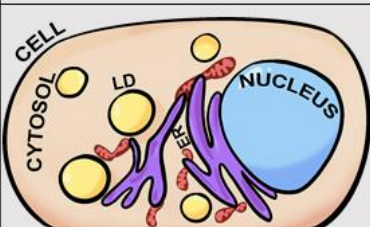
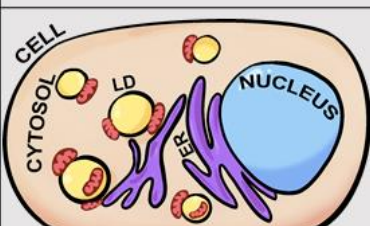
	Localization	Morphology	Membrane Potential	$\frac{ATP}{ADP}$	$mtCa^{2+}$
A	 <p>CELL CYTOSOL LD NUCLEUS ER Perinuclear Mitochondria</p>	Shorter	Higher $\Delta\Psi$	Lower	Lower
B	 <p>CELL CYTOSOL LD NUCLEUS ER Peripheral Mitochondria</p>	Elongated	Lower $\Delta\Psi$	Higher	Higher
C	 <p>CELL CYTOSOL LD NUCLEUS ER ER-Bound Mitochondria</p>	Intermediate	Higher $\Delta\Psi$	No Change	Higher
D	 <p>CELL CYTOSOL LD NUCLEUS ER Peridroplet Mitochondria</p>	Elongated	Undetermined	Higher	Undetermined

Figure 4- 1. Mitochondrial subpopulations reveal unique mitochondrial traits.

Diagram of a typical cell containing nuclei (blue), lipid droplets (LD) (yellow), endoplasmic reticulum (ER) (purple), cytoplasm (peach), and mitochondria (red ovals). Proposed model of distinct mitochondrial subpopulations observed across several cell types.

Mitochondria of specific subcellular localizations have unique traits demonstrating that not all mitochondria are homogeneous under physiological states. Based on previous studies (Collins *et al*, 2002; Kuznetsov *et al*, 2004; Mahdaviyani *et al*, 2017; Benador *et al*, 2018; Al-Mehdi *et al*, 2012; B, 2000; Lonergan *et al*, 2007; Rizzuto *et al*, 1998; CAC *et al*, 2019; Park *et al*, 2001; Marchi *et al*, 2014) we observed the presence of 4 mitochondrial subpopulations: perinuclear, peripheral, ER-bound, and peridroplet mitochondria. The 4 mitochondrial subpopulations have been observed to exhibit differences in morphology, membrane potential, ATP/ADP ratios, and mitochondrial calcium ($_{mt}Ca^{2+}$) levels. Mitochondrial length is dictated from longest length (elongated), intermediate length, and shortest length (shorter). Higher substrate concentrations are dictated as higher, and reduced substrate concentrations are dictated as lower in the table according to mitochondrial subpopulation. **(A)** Perinuclear mitochondria, localized to the nucleus, display higher membrane potential and reduced mitochondrial length. **(B)** Peripheral mitochondria, bordering the plasma membrane, display increases in mitochondrial length. **(C)** ER-bound mitochondria, tethered to the endoplasmic reticulum, yield higher mitochondrial calcium levels. **(D)** Peridroplet mitochondria, attached to lipid droplets, display elongated mitochondria compared to those in the cytosol.

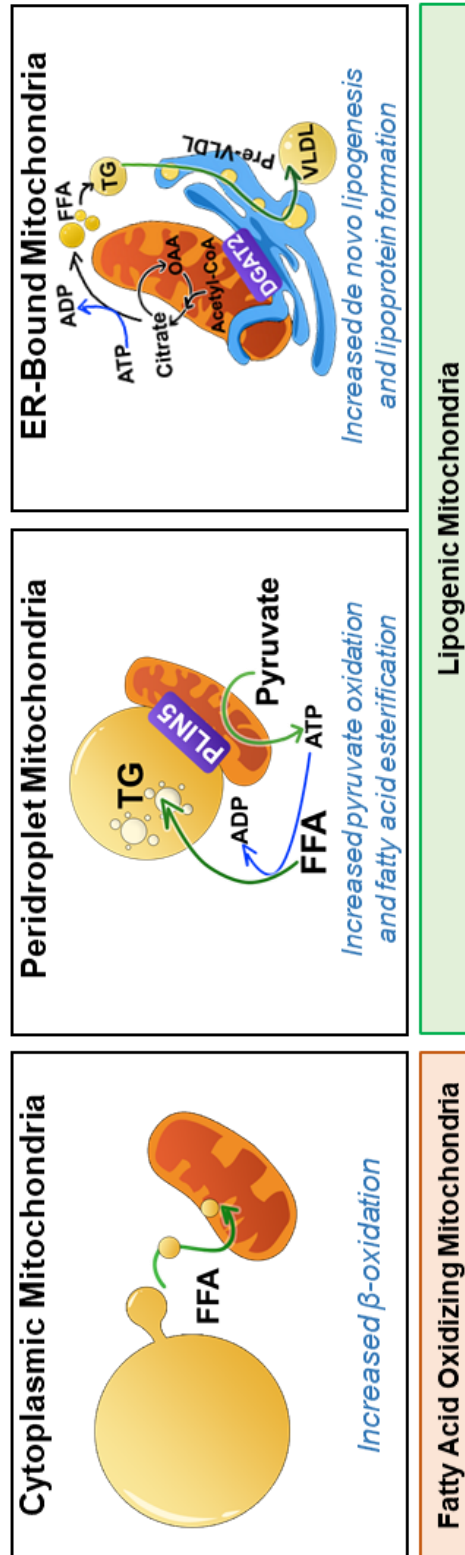


Figure 4- 2. Proposed model of three distinct mitochondrial populations in hepatocytes.

Mitochondria attached to different organelles were shown to have distinct functions, demonstrating that not all mitochondria in the same cell are homogeneous. This concept supports that: 1) Different mitochondria can be specialized in a specific task: some mitochondria in hepatocytes can be specialized in synthesizing lipids, while other mitochondria can oxidize lipids. 2) Localizing mitochondria close to their targeted organelles or compartments have the advantage to exchange metabolites or molecules more efficiently. The functional segregation of mitochondria can be determined by their anchorage to specific organelle, which prevents motility and thus fusion between the different subpopulations. Based partly on our previous work (Benador *et al*, 2018), we propose the existence of 3 mitochondrial populations in hepatocytes: 1) Cytosolic mitochondria, which are responsible for fatty acid oxidation, ketone bodies production and ureagenesis to support glucose production; 2) mitochondria attached to lipid droplets, namely peridroplet mitochondria (PDM), which promote the esterification of fatty acids into triglycerides and; 3) the ER-anchored mitochondria, which are responsible for fatty acid synthesis, lipoprotein assembly and excretion. VLDL, very-low-density lipoprotein.

Model	Animal Background	Diet	Mitochondrial Architecture	Bioenergetics	Lipid Metabolism	Histology	Stress Markers	Conclusion & Observation	Reference
DLP1 K38A (dTg [rTA/K38A]) via doxycycline-inducible	B6SJL/129 8-12 week-old	CHOW + 200mg/kg doxycycline	Long & entangled, ball-shaped mitochondria connected by tubular	Increased basal OCR; Increased p+ leak; no changes to CI, CII, & CIV (via Ad-DLP-K38A)	N/A	N/A	Reduced oxidative stress under STZ-induced hyperglycemia	Beneficial; Expression in diabetic conditions normalizes ROS levels and attenuates oxidative damage	Galloway et. al., 2012
	B6SJL/129 30-week-old	HFD + 200mg/kg doxycycline	N/A (HFD control yielded fragmentation)	Basal OCR no change; Increased p+ leak (via Ad-DLP-K38A)	Reduced oil red; reduced TG	Reduced steatosis; Reduced lipid infiltration (3x fold)	Reduced fatty infiltrates & oxidative/nitrate stress (nitrotyrosine signal)	Beneficial; Increased BW; Reduced ALT; Enhanced p+ leak reduced oxidative stress	Galloway et. al., 2014;
Drp1LKO via flox/cre	C57BL/6J 18-24 week-old	CHOW	N/A	No changes to OCR	No changes to total lipid, NEFA, & TG; Lipogenic genes reduced	Reduced inflammatory cellular infiltration	Increased ER stress; Fgf21 unchanged	No change to BW; Increased AST & ALT; Increased ER stress	Wang et. al., 2015
		HFD	Dispersed & swollen; Fewer but increased area (HFD control yielded fragmentation)	No changes to OCR	No changes to total lipid, NEFA, TG, & serum NEFA; Reduced serum TG; Adipocyte lipolytic genes increased	Increased inflammation & inflammatory cellular infiltration	Increased ER stress, Atf3, Trib3, CHOP, p-eIF2 α ; Increased Fgf21	Beneficial; Reduced BW & fat mass; No changes to food intake; improved glucose tolerance; ER stress induces Fgf21 to increase EE and reduce fat mass	
MFFLKO via flox/cre	C57BL/6J 30-week-old	NCD	Enlarged & tubular	No changes to OCR	No significant differences	Mild infiltration of inflammatory cells & ballooning	No changes to inflammatory/ER stress genes. Only Atf3 increased	Increased ALT; no NASH phenotypes	Takeichi et. al., 2021
		HFD	Megamitochondria, diffusely distributed aberrant mitochondria, larger cristae, small MAMs	Reduced OCR	Reduced FAO & TG secretion; Increased lipid accumulation & TG content	Increased macrovesicular steatosis & ballooning; Increased NAFLD score	Increased inflammatory & ER stress genes, Atf3, Trib3, & CHOP; Fgf21 unchanged	Detrimental; No change to BW or food intake; Ablation provokes ER stress, reduces TG secretion and made HFD more susceptible to NASH onset	

Model	Animal Background	Diet	Mitochondrial Architecture	Bioenergetics	Lipid Metabolism	Histology	Stress Markers	Conclusion & Observation	Reference
Fis1 OE via adenovirus (Ad-Fis1)	C57BL/6 10-20 week old	CHOW	Fragmentation	N/A	N/A	N/A	Increased ISR genes (in vitro)	N/A	Yae-Huei et al., 2022
		HFD	Enlarged	CI no change; CII & CIV increased	FFA no change; TG decreased; Reduced serum lipids	TG content decreased	Reduced mROS; Activation of IRS; Increased Atf5 & Ddit3	Beneficial; Promotes mitophagy, reduces oxidative stress, and improves glucose homeostasis; Improved insulin tolerance; IRS activation & inhibition of IFN-I signaling helps glucose metabolism	
Fis1 KD (Ad-shFis1)	C57BL/6 10-20 week old	4 week HFD	N/A	N/A	N/A	N/A	Increased mROS & impaired mitophagy	Reduced glucose tolerance	Yae-Huei et al., 2022

Table 1. Proposed models of modulating fission as a therapeutic approach to NASH & NAFLD.

References

- Al-Mehdi AB, Pastukh VM, Swiger BM, Reed DJ, Patel MR, Bardwell GC, Pastukh V V., Alexeyev MF & Gillespie MN (2012) Perinuclear mitochondrial clustering creates an oxidant-rich nuclear domain required for hypoxia-induced transcription. *Sci Signal* 5: ra47–ra47
- Alexopoulos SJ, Chen SY, Brandon AE, Salamoun JM, Byrne FL, Garcia CJ, Beretta M, Olzomer EM, Shah DP, Philp AM, *et al* (2020) Mitochondrial uncoupler BAM15 reverses diet-induced obesity and insulin resistance in mice. *Nat Commun* 11
- Arruda AP, Pers BM, Parlakgöl G, Güney E, Inouye K & Hotamisligil GS (2014) Chronic enrichment of hepatic endoplasmic reticulum-mitochondria contact leads to mitochondrial dysfunction in obesity. *Nat Med* 20: 1427–1435
- Aryaman J, Johnston IG & Jones NS (2019) Mitochondrial heterogeneity. *Front Genet* 10: 718 doi:10.3389/fgene.2018.00718 [PREPRINT]
- B O (2000) Pathophysiological and protective roles of mitochondrial ion channels. *J Physiol* 529 Pt 1: 23–36
- Benador IY, Veliova M, Mahdaviani K, Petcherski A, Wikstrom JD, Assali EA, Acín-Pérez R, Shum M, Oliveira MF, Cinti S, *et al* (2018) Mitochondria Bound to Lipid Droplets Have Unique Bioenergetics, Composition, and Dynamics that Support Lipid Droplet Expansion. *Cell Metab* 27: 869-885.e6
- Boland ML, Laker RC, Mather K, Nawrocki A, Oldham S, Boland BB, Lewis H, Conway J, Naylor J, Guionaud S, *et al* (2020) Resolution of NASH and hepatic fibrosis by the GLP-1R/GcgR dual-agonist Cotadutide via modulating mitochondrial function and lipogenesis. *Nat Metab* 2: 413–431

Boutant M, Kulkarni SS, Joffraud M, Ratajczak J, Valera-Alberni M, Combe R, Zorzano A & Cantó C (2017) Mfn2 is critical for brown adipose tissue thermogenic function.

EMBO J 36: 1543–1558

De Brito OM & Scorrano L (2008) Mitofusin 2 tethers endoplasmic reticulum to mitochondria. *Nature* 456: 605–610

CAC F, PC R, CS E & RW K (2019) MIGA2 Links Mitochondria, the ER, and Lipid Droplets and Promotes De Novo Lipogenesis in Adipocytes. *Mol Cell* 76: 811-825.e14

Collins TJ, Berridge MJ, Lipp P & Bootman MD (2002) Mitochondria are morphologically and functionally heterogeneous within cells. *EMBO J* 21: 1616–1627

Detaille D, Sanchez C, Sanz N, Lopez-Novoa JM, Leverve X & El-Mir MY (2008) Interrelation between the inhibition of glycolytic flux by silibinin and the lowering of mitochondrial ROS production in perfused rat hepatocytes. *Life Sci* 82: 1070–1076

Duchen MR, Surin A & Jacobson J (2003) Imaging mitochondrial function in intact cells. *Methods Enzymol* 361: 353–389

Dying to be thin: a dinitrophenol related fatality - PubMed

Dzeja PP, Bortolon R, Perez-Terzic C, Holmuhamedov EL & Terzic A (2002) Energetic communication between mitochondria and nucleus directed by catalyzed phosphotransfer. *Proc Natl Acad Sci U S A* 99: 10156–10161

EQ T, S H, J C, TL L, OC L, K H, NP Y, H C, F P, DC C, *et al* (2016) Metabolism. AMP-activated protein kinase mediates mitochondrial fission in response to energy stress. *Science* 351: 275–281

Fukuo Y, Yamashina S, Sonoue H, Arakawa A, Nakadera E, Aoyama T, Uchiyama A,

- Kon K, Ikejima K & Watanabe S (2014) Abnormality of autophagic function and cathepsin expression in the liver from patients with non-alcoholic fatty liver disease. *Hepato Res* 44: 1026–1036
- Galloway CA, Lee H, Brookes PS & Yoon Y (2014) Decreasing mitochondrial fission alleviates hepatic steatosis in a murine model of nonalcoholic fatty liver disease. *Am J Physiol - Gastrointest Liver Physiol* 307: G632–G641
- Galloway CA, Lee H, Nejjari S, Jhun BS, Yu T, Hsu W & Yoon Y (2012) Transgenic control of mitochondrial fission induces mitochondrial uncoupling and relieves diabetic oxidative stress. *Diabetes* 61: 2093–2104
- Garland PB, Shepherd D, Nicholls DG & Ontko J (1968) Energy-dependent control of the tricarboxylic acid cycle by fatty acid oxidation in rat liver mitochondria. *Adv Enzyme Regul* 6: 3–30
- Gluchowski NL, Gabriel KR, Chitraju C, Bronson RT, Mejhert N, Boland S, Wang K, Lai ZW, Farese R V. & Walther TC (2019) Hepatocyte Deletion of Triglyceride-Synthesis Enzyme Acyl CoA: Diacylglycerol Acyltransferase 2 Reduces Steatosis Without Increasing Inflammation or Fibrosis in Mice. *Hepatology* 70: 1972–1985
- Goedeke L, Peng L, Montalvo-Romeral V, Butrico GM, Dufour S, Zhang XM, Perry RJ, Cline GW, Kievit P, Chng K, *et al* (2019) Controlled-release mitochondrial protonophore (CRMP) reverses dyslipidemia and hepatic steatosis in dysmetabolic nonhuman primates. *Sci Transl Med* 11
- González-Rodríguez A, Mayoral R, Agra N, Valdecantos MP, Pardo V, Miquilena-Colina ME, Vargas-Castrillón J, Lo Iacono O, Corazzari M, Fimia GM, *et al* (2014) Impaired autophagic flux is associated with increased endoplasmic reticulum stress

during the development of NAFLD. *Cell Death Dis* 5

Grundlingh J, Dargan PI, El-Zanfaly M & Wood DM (2011) 2,4-dinitrophenol (DNP): a weight loss agent with significant acute toxicity and risk of death. *J Med Toxicol* 7: 205–212

Herms A, Bosch M, Ariotti N, Reddy BJN, Fajardo A, Fernández-Vidal A, Alvarez-Guaita A, Fernández-Rojo MA, Rentero C, Tebar F, *et al* (2013) Cell-to-cell heterogeneity in lipid droplets suggests a mechanism to reduce lipotoxicity. *Curr Biol* 23: 1489–1496

Hernández-Alvarez MI, Sebastián D, Vives S, Ivanova S, Bartoccioni P, Kakimoto P, Plana N, Veiga SR, Hernández V, Vasconcelos N, *et al* (2019) Deficient Endoplasmic Reticulum-Mitochondrial Phosphatidylserine Transfer Causes Liver Disease. *Cell* 177: 881-895.e17

Inami Y, Yamashina S, Izumi K, Ueno T, Tanida I, Ikejima K & Watanabe S (2011) Hepatic steatosis inhibits autophagic proteolysis via impairment of autophagosomal acidification and cathepsin expression. *Biochem Biophys Res Commun* 412: 618–625

Kim CW, Addy C, Kusunoki J, Anderson NN, Deja S, Fu X, Burgess SC, Li C, Chakravarthy M, Previs S, *et al* (2017) Acetyl CoA Carboxylase Inhibition Reduces Hepatic Steatosis but Elevates Plasma Triglycerides in Mice and Humans: A Bedside to Bench Investigation. *Cell Metab* 26: 394-406.e6

Klein EA, Thompson IM, Tangen CM, Crowley JJ, Lucia S, Goodman PJ, Minasian LM, Ford LG, Parnes HL, Gaziano JM, *et al* (2011) Vitamin E and the risk of prostate cancer: the Selenium and Vitamin E Cancer Prevention Trial (SELECT). *JAMA* 306:

1549–1556

Kodiha M, Flamant E, Wang YM & Stochaj U (2018) Defining the short-term effects of pharmacological 50-AMP activated kinase modulators on mitochondrial polarization, morphology and heterogeneity. *PeerJ* 2018

Kuznetsov A V. & Margreiter R (2009) Heterogeneity of mitochondria and mitochondrial function within cells as another level of mitochondrial complexity. *Int J Mol Sci* 10: 1911–1929 doi:10.3390/ijms10041911 [PREPRINT]

Kuznetsov A V., Schneeberger S, Renz O, Meusbürger H, Saks V, Usson Y & Margreiter R (2004) Functional heterogeneity of mitochondria after cardiac cold ischemia and reperfusion revealed by confocal imaging. *Transplantation* 77: 754–756

Kuznetsov A V., Troppmair J, Sucher R, Hermann M, Saks V & Margreiter R (2006) Mitochondrial subpopulations and heterogeneity revealed by confocal imaging: Possible physiological role? *Biochim Biophys Acta - Bioenerg* 1757: 686–691

Liesa M, Palacín M & Zorzano A (2009) Mitochondrial dynamics in mammalian health and disease. *Physiol Rev* 89: 799–845 doi:10.1152/physrev.00030.2008 [PREPRINT]

Liou Y-H, Personnaz J, Jacobi D, Knudsen NH, Chalom MM, Starost KA, Nnah IC & Lee C-H (2022) Hepatic Fis1 regulates mitochondrial integrated stress response and improves metabolic homeostasis. *JCI insight*

Lonergan T, Bavister B & Brenner C (2007) Mitochondria in stem cells. *Mitochondrion* 7: 289–296 doi:10.1016/j.mito.2007.05.002 [PREPRINT]

Mahdaviani K, Benador IY, Su S, Gharakhanian RA, Stiles L, Trudeau KM, Cardamone

- M, Enríquez-Zarralanga V, Ritou E, Aprahamian T, *et al* (2017) Mfn2 deletion in brown adipose tissue protects from insulin resistance and impairs thermogenesis. *EMBO Rep* 18: 1123–1138
- Marchi S, Patergnani S & Pinton P (2014) The endoplasmic reticulum-mitochondria connection: One touch, multiple functions. *Biochim Biophys Acta - Bioenerg* 1837: 461–469 doi:10.1016/j.bbabi.2013.10.015 [PREPRINT]
- Mercer JR, Yu E, Figg N, Cheng KK, Prime TA, Griffin JL, Masoodi M, Vidal-Puig A, Murphy MP & Bennett MR (2012) The mitochondria-targeted antioxidant MitoQ decreases features of the metabolic syndrome in ATM^{+/-}/ApoE^{-/-} mice. *Free Radic Biol Med* 52: 841–849
- Mootha VK, Bunkenborg J, Olsen J V., Hjerrild M, Wisniewski JR, Stahl E, Bolouri MS, Ray HN, Sihag S, Kamal M, *et al* (2003) Integrated Analysis of Protein Composition, Tissue Diversity, and Gene Regulation in Mouse Mitochondria. *Cell* 115: 629–640
- Muñoz JP, Ivanova S, Sánchez-Wandelmer J, Martínez-Cristóbal P, Noguera E, Sancho A, Díaz-Ramos A, Hernández-Alvarez MI, Sebastián D, Mauvezin C, *et al* (2013) Mfn2 modulates the UPR and mitochondrial function via repression of PERK. *EMBO J* 32: 2348–2361
- Ngo J, Benador IY, Brownstein AJ, Vergnes L, Veliova M, Shum M, Acín-Pérez R, Reue K, Shirihai OS & Liesa M (2021) Isolation and functional analysis of peridroplet mitochondria from murine brown adipose tissue. *STAR Protoc* 2: 100243
- Ni R, Cao T, Xiong S, Ma J, Fan GC, Lacefield JC, Lu Y, Tissier S Le & Peng T (2016) Therapeutic inhibition of mitochondrial reactive oxygen species with mito-TEMPO

- reduces diabetic cardiomyopathy. *Free Radic Biol Med* 90: 12–23
- Noske AB, Costin AJ, Morgan GP & Marsh BJ (2008) Expedited approaches to whole cell electron tomography and organelle mark-up in situ in high-pressure frozen pancreatic islets. *J Struct Biol* 161: 298–313
- Park MK, Ashby MC, Erdemli G, Petersen OH & Tepikin A V. (2001) Perinuclear, perigranular and sub-plasmalemmal mitochondria have distinct functions in the regulation of cellular calcium transport. *EMBO J* 20: 1863–1874
- Perry RJ, Kim T, Zhang XM, Lee HY, Pesta D, Popov VB, Zhang D, Rahimi Y, Jurczak MJ, Cline GW, *et al* (2013) Reversal of hypertriglyceridemia, fatty liver disease, and insulin resistance by a liver-targeted mitochondrial uncoupler. *Cell Metab* 18: 740–748
- Perry RJ, Zhang D, Zhang XM, Boyer JL & Shulman GI (2015) Controlled-release mitochondrial protonophore reverses diabetes and steatohepatitis in rats. *Science* 347: 1253–1256
- Rizzuto R, Pinton P, Carrington W, Fay FS, Fogarty KE, Lifshitz LM, Tuft RA & Pozzan T (1998) Close contacts with the endoplasmic reticulum as determinants of mitochondrial Ca²⁺ responses. *Science (80-)* 280: 1763–1766
- Ryu D, Mouchiroud L, Andreux PA, Katsyuba E, Moullan N, Nicolet-Dit-Félix AA, Williams EG, Jha P, Lo Sasso G, Huzard D, *et al* (2016) Urolithin A induces mitophagy and prolongs lifespan in *C. elegans* and increases muscle function in rodents. *Nat Med* 22: 879–888
- Said A & Akhter A (2017) Meta-Analysis of Randomized Controlled Trials of Pharmacologic Agents in Non-alcoholic Steatohepatitis. *Ann Hepatol* 16: 538–547

- Schürks M, Glynn RJ, Rist PM, Tzourio C & Kurth T (2010) Effects of vitamin E on stroke subtypes: meta-analysis of randomised controlled trials. *BMJ* 341: 1033
- Sebastián D, Hernández-Alvarez MI, Segalés J, Sorianello E, Muñoz JP, Sala D, Waget A, Liesa M, Paz JC, Gopalacharyulu P, *et al* (2012) Mitofusin 2 (Mfn2) links mitochondrial and endoplasmic reticulum function with insulin signaling and is essential for normal glucose homeostasis. *Proc Natl Acad Sci U S A* 109: 5523–5528
- Shum M, Ngo J, Shirihai OS & Liesa M (2020) Mitochondrial oxidative function in NAFLD: friend or foe? *Mol Metab*: 101134
- Singh R, Kaushik S, Wang Y, Xiang Y, Novak I, Komatsu M, Tanaka K, Cuervo AM & Czaja MJ (2009) Autophagy regulates lipid metabolism. *Nature* 458: 1131–1135
- Song YM, Lee WK, Lee YH, Kang ES, Cha BS & Lee BW (2016) Metformin Restores Parkin-Mediated Mitophagy, Suppressed by Cytosolic p53. *Int J Mol Sci* 17
- Stone SJ, Levin MC, Zhou P, Han J, Walther TC & Farese R V. (2009) The endoplasmic reticulum enzyme DGAT2 is found in mitochondria-associated membranes and has a mitochondrial targeting signal that promotes its association with mitochondria. *J Biol Chem* 284: 5352–5361
- Takeichi Y, Miyazawa T, Sakamoto S, Hanada Y, Wang L, Gotoh K, Uchida K, Katsuhara S, Sakamoto R, Ishihara T, *et al* (2021) Non-alcoholic fatty liver disease in mice with hepatocyte-specific deletion of mitochondrial fission factor. *Diabetologia*
- Taleb A, Ahmad KA, Ihsan AU, Qu J, Lin N, Hezam K, Koju N, Hui L & Qilong D (2018) Antioxidant effects and mechanism of silymarin in oxidative stress induced

- cardiovascular diseases. *Biomed Pharmacother* 102: 689–698
- Toney AM, Fan R, Xian Y, Chaidez V, Ramer-Tait AE & Chung S (2019) Urolithin A, a Gut Metabolite, Improves Insulin Sensitivity Through Augmentation of Mitochondrial Function and Biogenesis. *Obesity (Silver Spring)* 27: 612–620
- Trevino MB, Mazur-Hart D, Machida Y, King T, Nadler J, Galkina E V., Poddar A, Dutta S & Imai Y (2015) Liver Perilipin 5 Expression Worsens Hepatosteatosis But Not Insulin Resistance in High Fat-Fed Mice. *Mol Endocrinol* 29: 1414–1425
- Trudeau KM, Colby AH, Zeng J, Las G, Feng JH, Grinstaff MW & Shirihai OS (2016) Lysosome acidification by photoactivated nanoparticles restores autophagy under lipotoxicity. *J Cell Biol* 214: 25–34
- Wah Kheong C, Nik Mustapha NR & Mahadeva S (2017) A Randomized Trial of Silymarin for the Treatment of Nonalcoholic Steatohepatitis. *Clin Gastroenterol Hepatol* 15: 1940-1949.e8
- Wang C, Zhao Y, Gao X, Li L, Yuan Y, Liu F, Zhang L, Wu J, Hu P, Zhang X, *et al* (2015a) Perilipin 5 improves hepatic lipotoxicity by inhibiting lipolysis. *Hepatology* 61: 870–882
- Wang L, Ishihara T, Ibayashi Y, Tatsushima K, Setoyama D, Hanada Y, Takeichi Y, Sakamoto S, Yokota S, Mihara K, *et al* (2015b) Disruption of mitochondrial fission in the liver protects mice from diet-induced obesity and metabolic deterioration. *Diabetologia* 58: 2371–2380
- Wang L, Liu X, Nie J, Zhang J, Kimball SR, Zhang H, Zhang WJ, Jefferson LS, Cheng Z, Ji Q, *et al* (2015c) ALCAT1 controls mitochondrial etiology of fatty liver diseases, linking defective mitophagy to steatosis. *Hepatology* 61: 486–496

- Wikstrom JD, Katzman SM, Mohamed H, Twig G, Graf S a., Heart E, Molina AJ a, Corkey BE, De Vargas LM, Danial NN, *et al* (2007) Beta-Cell mitochondria exhibit membrane potential heterogeneity that can be altered by stimulatory or toxic fuel levels. *Diabetes* 56: 2569–2578
- Woods DC (2017) Mitochondrial Heterogeneity: Evaluating Mitochondrial Subpopulation Dynamics in Stem Cells. *Stem Cells Int* 2017 doi:10.1155/2017/7068567 [PREPRINT]
- Yamada T, Murata D, Adachi Y, Itoh K, Kameoka S, Igarashi A, Kato T, Araki Y, Haganir RL, Dawson TM, *et al* (2018) Mitochondrial Stasis Reveals p62-Mediated Ubiquitination in Parkin-Independent Mitophagy and Mitigates Nonalcoholic Fatty Liver Disease. *Cell Metab* 28: 588-604.e5
- Yu X, Hao M, Liu Y, Ma X, Lin W, Xu Q, Zhou H, Shao N & Kuang HY (2019) Liraglutide ameliorates non-alcoholic steatohepatitis by inhibiting NLRP3 inflammasome and pyroptosis activation via mitophagy. *Eur J Pharmacol* 864
- Zeng J, Shirihai OS & Grinstaff MW (2019) Degradable Nanoparticles Restore Lysosomal pH and Autophagic Flux in Lipotoxic Pancreatic Beta Cells. *Adv Healthc Mater* 8
- Zhong S, Fan Y, Yan Q, Fan X, Wu B, Han Y, Zhang Y, Chen Y, Zhang H & Niu J (2017) The therapeutic effect of silymarin in the treatment of nonalcoholic fatty disease: A meta-analysis (PRISMA) of randomized control trials. *Medicine (Baltimore)* 96
- Zhou T, Chang L, Luo Y, Zhou Y & Zhang J (2019) Mst1 inhibition attenuates non-alcoholic fatty liver disease via reversing Parkin-related mitophagy. *Redox Biol* 21

Zorov DB, Juhaszova M & Sollott SJ (2006) Mitochondrial ROS-induced ROS release:

An update and review. *Biochim Biophys Acta - Bioenerg* 1757: 509–517

doi:10.1016/j.bbabbio.2006.04.029 [PREPRINT]

Appendix I

Isolation and Functional Analysis of Mitochondria Bound to Lipid Droplets from Murine Brown Adipose Tissue.

The work described in this chapter has been reproduced from:

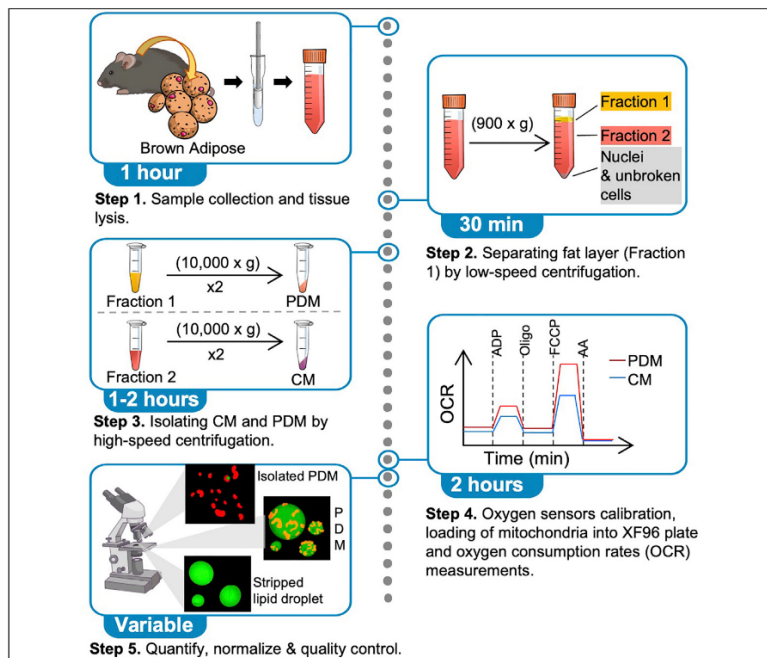
Ngo J., Benador I.Y., Brownstein A., Vergnes L., Veliova M., Shum M., Acín-Pérez R., Reue K.,
Shirihai O.S., Liesa M. Isolation and Functional Analysis of Mitochondria Bound to Lipid
Droplets from Murine Brown Adipose Tissue. STAR Protocols. 2020. doi:
10.1016/j.xpro.2020.100243.

Copyright 2020

Jennifer Ngo, Ilan Benador, Alex Brownstein, Laurent Vergnes, Michaela Veliova, Michael
Shum, Rebeca Acín-Pérez, Karen Reue, Orian Shirihai, Marc Liesa.

Protocol

Isolation and functional analysis of peridroplet mitochondria from murine brown adipose tissue



Mitochondria play a central role in lipid metabolism and can bind to lipid droplets. However, the role and functional specialization of the population of peridroplet mitochondria (PDMs) remain unclear, as methods to isolate functional PDMs were not developed until recently. Here, we describe an approach to isolate intact PDMs from murine brown adipose tissue based on their adherence to lipid droplets. PDMs isolated using our approach can be used to study their specialized function by respirometry.

Jennifer Ngo, Ilan Y. Benador, Alexandra J. Brownstein, ..., Karen Reue, Orian S. Shirihai, Marc Liesa

jngo@chem.ucia.edu (J.N.)
ilan.benador-shen@steward.org (I.Y.B.)
oshirihai@mednet.ucla.edu (O.S.S.)
mliesa@mednet.ucla.edu (M.L.)

Highlights

Isolation of peridroplet mitochondria (PDMs) from brown adipose tissue is described

The function of murine PDMs is analyzed using 96-well format respirometry

QC steps of PDM isolation by imaging and protein biochemistry are defined

Ngo et al., STAR Protocols 2, 100243
March 19, 2021 © 2020 The Author(s).
<https://doi.org/10.1016/j.xpro.2020.100243>





Protocol

Isolation and functional analysis of peridroplet mitochondria from murine brown adipose tissue

Jennifer Ngo,^{1,2,3,6,8,*} Ilan Y. Benador,^{1,6,*} Alexandra J. Brownstein,^{1,3} Laurent Vergnes,^{3,4} Michaela Veliova,^{1,3} Michael Shum,^{1,3} Rebeca Acín-Pérez,^{1,3} Karen Reue,^{3,4,5} Orian S. Shirihai,^{1,3,7,*} and Marc Liesa^{1,3,5,7,9,*}

¹Department of Medicine, Division of Endocrinology and Department of Molecular and Medical Pharmacology, David Geffen School of Medicine at UCLA, Los Angeles, CA 90095, USA

²Department of Chemistry and Biochemistry at UCLA, Los Angeles, CA 90095, USA

³Metabolism Theme, David Geffen School of Medicine at UCLA, Los Angeles, CA 90095, USA

⁴Department of Human Genetics, David Geffen School of Medicine at UCLA, Los Angeles, CA 90024, USA

⁵Molecular Biology Institute at UCLA, Los Angeles, CA 90095, USA

⁶These authors contributed equally

⁷These authors contributed equally

⁸Technical contact

⁹Lead contact

*Correspondence: jngo@chem.ucla.edu (J.N.), ilan.benador-shen@steward.org (I.Y.B.), oshirihai@mednet.ucla.edu (O.S.S.), mliesa@mednet.ucla.edu (M.L.)
<https://doi.org/10.1016/j.xpro.2020.100243>

Summary

Mitochondria play a central role in lipid metabolism and can bind to lipid droplets. However, the role and functional specialization of the population of peridroplet mitochondria (PDMs) remain unclear, as methods to isolate functional PDMs were not developed until recently. Here, we describe an approach to isolate intact PDMs from murine brown adipose tissue based on their adherence to lipid droplets. PDMs isolated using our approach can be used to study their specialized function by respirometry.

For complete information on the use and execution of this protocol, please refer to Benador et al. (2018).

Before you begin

⌚ Timing: 4 h

1. Prepare batches of the Mitochondrial Isolation Buffer (MIB), Mitochondrial Assay Solution (MAS) and respirometry substrates solutions. The use of batch preparations reduces variability across independent isolations. Storage at -20°C of these buffers in single-use aliquots for 6 months is recommended, as freeze-thawing cycles can damage respirometry substrates. For MAS + GDP without substrates, single-use aliquots of 20 mL will provide sufficient buffer for the 96 wells in a plate/assay. For buffers containing 10 \times respirometry substrates with and without ADP, single-use aliquots of 1.5 and 2 mL respectively will provide sufficient buffer for one 96-well plate/assay. Refer to [Materials and equipment](#) tables for more details about the buffers that are stored at -20°C and buffers that are prepared on the day of the assay.

⚠ **CRITICAL:** Adding respirometry substrates, such as pyruvate and malate, will acidify the MAS. Thus, the pH needs to be adjusted to pH 7.2 after adding substrates: $\text{pH} \leq 6$ inhibits mitochondrial respiration.



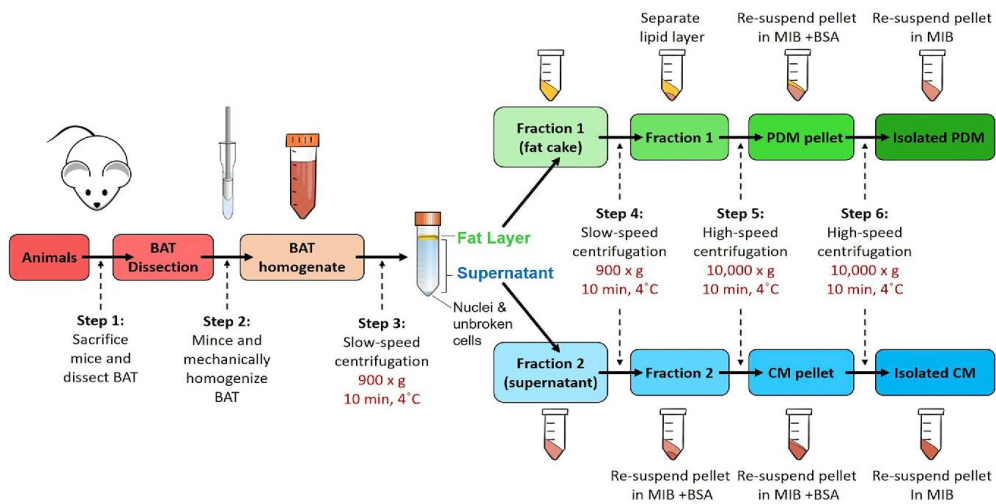


Figure 1. Schematic representation of peridroplet mitochondria (PDMs) isolation procedure

Brown adipose tissue (BAT) is dissected from mice and homogenized with glass-Teflon Dounce homogenizer. Low-speed centrifugation generates a floating fat layer containing PDMs (fraction 1) and a supernatant containing cytoplasmic mitochondria (CMs, fraction 2). High-speed centrifugation strips and pellets PDMs from lipid droplets (LDs) and pellets CM mitochondria from the supernatant. Note that some traditional BAT mitochondrial isolation protocols discard the fat layer and/or begin with a high-speed centrifugation step.

- MIB stocks should be prepared with and without BSA. BSA is needed to trap free fatty acids released during adipose tissue homogenization, which can uncouple and damage mitochondria. However, BSA will interfere with the protein quantification assay needed to determine the yield of isolated mitochondria. Thus, the buffer without BSA is only used for the final resuspension of the mitochondrial pellet (Figure 1).

⚠ **CRITICAL:** All solutions, materials, and equipment should be pre-cooled to 4°C (or ice-cold) before isolation and remain ice-cold throughout the protocol. These low and non-freezing temperatures preserve the integrity of mitochondria during the isolation procedure.

- The cartridge containing the oxygen sensors from Agilent Seahorse must be hydrated for at least 4 h before the assay. It is recommended that the template and protocol for the respirometry assay in the XF96 Analyzer software be created before isolation. The respirometry protocol is as follows:

Steps	Time	Cycles
Calibration		
Mix	2 min 0 s	2
Delay	2 min 0 s	
Mix	0 min 24 s	1
Measure	4 min 0 s	
Mix	0 min 48 s	
Injection, port A (ADP)		
Mix	0 min 40 s	1
Measure	4 min 0 s	

(Continued on next page)



Continued		
Steps	Time	Cycles
Mix	0 min 20 s	1
Measure	4 min 0 s	
Mix	0 min 48 s	
Injection, port B (oligomycin)		
Mix	0 min 30 s	2
Delay	2 min 0 s	
Measure	4 min 0 s	1
Mix	0 min 48 s	
Injection, port C (FCCP)		
Mix	0 min 24 s	2
Measure	4 min 0 s	
Mix	0 min 48 s	1
Injection, port D (antimycin A)		
Mix	0 min 24 s	4
Measure	4 min 0 s	

Key resources table

REAGENT or RESOURCE	SOURCE	IDENTIFIER
Biological samples		
Interscapular brown adipose tissue from 12 week-old C57BL/6J mice	Jackson Laboratory	Cat#000664
Chemicals, peptides, and recombinant proteins		
Fatty acid-free bovine serum albumin	EMD Millipore	Cat#126575
BODIPY 493/503 (4,4-difluoro-1,3,5,7,8-pentamethyl-4-bora-3a,4a-diaza-s-indacene)	Thermo Fisher Scientific	Cat#D3922
MitoTracker deep red FM	Thermo Fisher Scientific	Cat#M22426
MitoTracker green FM	Thermo Fisher Scientific	Cat#M7514
GDP (guanosine 50-diphosphate sodium type I)	Sigma-Aldrich	Cat#G7127
Pyruvic acid	Fisher	Cat#PB356
L-(-)-Malic acid	Sigma-Aldrich	Cat#M6413
Ultrapure dimethyl sulfoxide (DMSO)	Amresco	Cat#N182
KCl	Sigma-Aldrich	Cat#31248
KH ₂ PO ₄	Sigma-Aldrich	Cat#P5655
MgCl ₂	Sigma-Aldrich	Cat#M0250
Ultrapure water	Invitrogen	Cat#10977-015
Succinic acid	Sigma-Aldrich	Cat#S9512
Rotenone	Sigma-Aldrich	Cat#R8875
Palmitoyl-L-carnitine chloride	Sigma-Aldrich	Cat#P1645
ADP (adenosine 5'-diphosphate monopotassium)	Sigma-Aldrich	Cat#A5285
Oligomycin A	Calbiochem	Cat#495455
FCCP	ENZO	Cat#BML-CM120-0010
Antimycin A	ENZO	Cat#ALX380075M010
PBS	Sigma	Cat#P3813
Sucrose	Fisher	Cat#L-12686
HEPES	Fisher	Cat#M-12211
EGTA	Sigma	Cat#E3889
Critical commercial assays		
Pierce BCA	Thermo Fisher Scientific	Cat#23225
Software and algorithms		
ImageJ	N/A	https://imagej.net/

(Continued on next page)

<i>Continued</i>		
REAGENT or RESOURCE	SOURCE	IDENTIFIER
Seahorse Wave Software	Agilent	www.agilent.com/en/product/cell-analysis/real-time-cell-metabolic-analysis/xf-software/seahorse-wave-desktop-software-740897nline
Excel, Prism, or spreadsheet software	Microsoft, GraphPad	https://www.graphpad.com/scientific-software/prism/
Other		
Glass/smooth Teflon Dounce homogenizer 10 mL	Thomas	Cat#3431D76
50 mL conical tubes	Nunc/Falcon	N/A
2 mL microfuge tubes	Eppendorf	N/A
1.5 mL microfuge tubes	Eppendorf	N/A
Surgical scissors	Fine Science Tools	Cat#91401-12
Graefe forceps	Fine Science Tools	Cat#11150-10
Fine surgical scissors	Fine Science Tools	Cat#91460-11
Noyes scissors	Fine Science Tools	Cat#15011-12
6-well plate or petri dishes	N/A	N/A
Ice buckets	N/A	N/A
Syringe and 23G needle (for exsanguination)	BD Precision Glide	Cat#305143
Sorvall ST 16R	Thermo Scientific	75004241
TX-200 swinging bucket rotor and multi-well plate adaptor	Thermo Scientific	75003658
Microcentrifuge	Eppendorf	5417C
1 mm glass slide	Fisher Scientific	Cat#22-034-985
#1.5 thickness coverslips	Zeiss	Cat#10474379
Confocal fluorescence microscope	Zeiss	LSM880
XF96 Extracellular Flux Analyzer	Agilent	XF96 Analyzer

Materials and equipment

Mitochondrial isolation buffer (MIB)			
Reagent	Stock concentration	Final concentration	Volume/weight
Sucrose	n/a	250 mM	0.855 g
HEPES	n/a	5 mM	11.91 mg
EGTA	n/a	2 mM	7.60 mg
ddH ₂ O	n/a	n/a	10 mL
Total	n/a	n/a	10 mL

Stir at 20°C–25°C until dissolved; bring to pH 7.2 using KOH or HCl, as Na⁺ can affect mitochondrial function. Store at –20°C for 6 months, single-use aliquots of 1 mL (<1 mL used per group of 6 mice).

Mitochondrial isolation buffer (MIB) + BSA			
Reagent	Stock concentration	Final concentration	Volume/weight
Sucrose	n/a	250 mM	17.11 g
HEPES	n/a	5 mM	238.31 mg
EGTA	n/a	2 mM	152.14 mg
BSA	n/a	2% (w/v)	2 mg/200 mL
ddH ₂ O	n/a	n/a	200 mL
Total	n/a	n/a	200 mL

▲ **CRITICAL:** Use fatty acid-free BSA and pH with KOH, as Na⁺ can affect mitochondrial function. Store at –20°C for 6 months in single-use aliquots of 20 mL, with a total of 7–17 mL being used per group of 6 mice, depending on tissue weight.



Mitochondria assay solution (MAS)			
Reagent	Stock concentration	Final concentration	Volume/weight
KCl	n/a	155 mM	2.143 g
KH ₂ PO ₄	n/a	10 mM	340.225 mg
MgCl ₂	n/a	2 mM	101.65 mg
HEPES	n/a	5 mM	297.875 mg
EGTA	n/a	1 mM	95.09 mg
BSA	n/a	0.1% (w/v)	0.25 g
ddH ₂ O	n/a	n/a	250 mL
Total	n/a	n/a	250 mL

⚠ **CRITICAL:** Use fatty acid-free BSA and pH using KOH, as Na⁺ can affect mitochondrial function. Store at –20°C for 6 months.

Respirometry substrate stock solutions			
Reagent	Stock concentration	Solvent	
Pyruvate	0.5 M, pH 7.2	MAS + GDP	
Malate	0.5 M, pH 7.2	MAS + GDP	
Succinate	0.5 M, pH 7.2	MAS + GDP	
Rotenone	40 mM	DMSO	
Palmitoyl-carnitine	10 mM	95% v/v ethanol	

⚠ **CRITICAL:** Adjust pH to 7.2. Rotenone is a poisonous reagent that must be handled with gloves and disposed of in accordance with safety data provided by supplier. Store solutions for 6 months with the exception of palmitoyl-carnitine (3 months) and rotenone (1 year).

Mitochondrial stress compounds		
Reagent	Stock concentration	Solvent
Oligomycin	20 mM	DMSO
FCCP	20 mM	DMSO
Antimycin A	40 mM	DMSO

⚠ **CRITICAL:** Oligomycin, FCCP, and antimycin A are poisonous reagents that need to be handled with gloves and disposed of in accordance with safety data provided by supplier. Store at –20°C for <1 year, aliquots for 10 assays.

MAS + GDP (UCP1 inhibitor)			
Reagent	Stock concentration	Final concentration	Volume/weight
GDP	n/a	1 mM	88.6 mg
MAS	n/a	n/a	200 mL
Total	n/a	n/a	200 mL

Store at –20°C for 6 months in single-use aliquots of 20 mL, which will provide buffer for 96 wells (1 plate/assay).

Complex I driven respiration (MAS + GDP + pyruvate + malate)			
Reagent	Stock concentration	Final concentration	Volume/weight
Pyruvate	0.5 M	50 mM	2 mL
Malate	0.5 M	50 mM	2 mL
MAS + GDP buffer	n/a	n/a	16 mL
Total	n/a	n/a	20 mL

This is a 10× solution that is loaded directly into the wells of a XF96 plate, together with mitochondria in MAS + GDP. Store at –20°C for 6 months in single-use aliquots of 2 mL, which will provide buffer for 96 wells (1 plate/assay).

Complex I driven State 3 respiration (MAS + GDP + pyruvate + malate + ADP)			
Reagent	Stock concentration	Final concentration	Volume/weight
ADP	n/a	35 mM	263.16 mg
MAS + GDP + PM buffer	n/a	n/a	15 mL
Total	n/a	n/a	15 mL

This is a 10× solution that is loaded into port A of the XF96 cartridge to induce maximal ATP synthesis (State 3 respiration). Store at –20°C for 6 months in single-use aliquots of 1.5 mL, which will provide buffer for 96 wells (1 plate/assay, 15 μL × 96 wells = 1.44 mL).

Complex II driven respiration (MAS + GDP + succinate + rotenone)			
Reagent	Stock concentration	Final concentration	Volume/weight
Succinate	0.5 M	50 mM	2 mL
Rotenone	40 mM	20 μM	10 μL
MAS + GDP buffer	n/a	n/a	18 mL
Total	n/a	n/a	20 mL

⚠ **CRITICAL:** Rotenone is a poisonous reagent that must be handled with gloves and disposed of in accordance with safety data provided by supplier. This is a 10× solution loaded into the wells of a XF96 plate, together with mitochondria in MAS + GDP. Store at –20°C for 6 months in single-use aliquots of 2 mL, which will provide buffer for 96 wells (1 plate/assay).

Complex II driven respiration (MAS + GDP + succinate + rotenone + ADP)			
Reagent	Stock concentration	Final concentration	Volume/weight
ADP	n/a	35 mM	263.16 mg
MAS + GDP + SR buffer	n/a	n/a	15 mL
Total	n/a	n/a	15 mL

This is a 10× solution that is loaded into port A of the XF96 cartridge to induce maximal ATP synthesis (State 3). Store at –20°C for 6 months in single-use aliquots of 1.5 mL, which will provide buffer for 96 wells (1 plate/assay, 15 μL × 96 wells = 1.44 mL).

Fatty acid-fueled respiration (MAS + GDP + palmitoyl-carnitine)			
Reagent	Stock concentration	Final concentration	Volume/weight
Palmitoyl-carnitine	10 mM	40 μM	80 μL
Malate	0.5 M	1 mM	40 μL
MAS + GDP buffer	n/a	n/a	20 mL
Total	n/a	n/a	20 mL

This is a 10× solution that is loaded into the Seahorse well, together with mitochondria in MAS + GDP. Store at –20°C for 3 months in single-use aliquots of 2 mL, which will provide buffer for 96 wells (1 plate/assay).

Fatty acid-fueled State 3 respiration (MAS + GDP + palmitoyl-carnitine + ADP)			
Reagent	Stock concentration	Final concentration	Volume/weight
ADP	n/a	35 mM	263.16 mg
MAS + GDP + PC buffer	n/a	n/a	15 mL
Total	n/a	n/a	15 mL

This is a 10× solution loaded into port A of the XF96 cartridge to induce maximal ATP synthesis (State 3). Store at −20°C for 6 months in single-use aliquots of 1.5 mL, which will provide buffer for 96 wells (1 plate/assay, 15 μL × 96 wells = 1.44 mL).

State 4o respiration (MAS + GDP + substrate + oligomycin)			
Reagent	Stock concentration	Final concentration	Volume/weight
Oligomycin	20 mM	40 μM	4 μL
MAS + GDP + substrate	n/a	n/a	2 mL
Total	n/a	n/a	2 mL

Add oligomycin (poisonous) to MAS + GDP on the day of the assay. This is a 10× solution that is loaded into port B of the XF96 cartridge to block ATP synthesis (16.6 μL × 96 wells = 1.59 mL).

Maximal respiration (MAS + GDP + substrate + FCCP)			
Reagent	Stock concentration	Final concentration	Volume/weight
FCCP	20 mM	40 μM	4 μL
MAS + GDP + substrate	n/a	n/a	2 mL
Total	n/a	n/a	2 mL

Add FCCP (poisonous) to MAS + GDP on the day of the assay. This is a 10× solution that is loaded into port C of the XF96 cartridge to induce maximal respiration (18.5 μL × 96 wells = 1.78 mL).

MAS + GDP + substrate + antimycin A			
Reagent	Stock concentration	Final concentration	Volume/weight
Antimycin A	40 mM	40 μM	2 μL
MAS + GDP + substrate	n/a	n/a	2 mL
Total	n/a	n/a	2 mL

Add antimycin A (poisonous) to MAS + GDP on the day of the assay. This is a 10× solution that is loaded into port D of the XF96 cartridge to block mitochondrial respiration (20.5 μL × 96 wells = 1.97 mL).

Mitochondria and lipid droplet imaging dye stock solutions		
Reagent	Stock concentration	Solvent
BODIPY 493/503	1 mM	DMSO
MitoTracker green FM	1 mM	DMSO
MitoTracker deep red FM	1 mM	DMSO

Store at −20°C in aliquots of 10 μL for 6 months.

Imaging solution A		
Reagent	Stock concentration	Volume/weight
BODIPY 493/503	1 mM	1 μL
MitoTracker red	1 mM	1 μL
MAS + GDP + PM buffer	n/a	1 mL
Total	n/a	1 mL

Imaging solution B		
Reagent	Stock concentration	Volume/weight
MitoTracker Green	1 mM	1 μ L
MitoTracker red	1 mM	1 μ L
MAS + GDP + PM buffer	n/a	1 mL
Total	n/a	1 mL

⚠ **CRITICAL:** Imaging solution A and B should be prepared freshly on the day of the assay.

Step-by-step method details

This mitochondrial isolation protocol uses the Agilent Seahorse XF96 Analyzer to analyze respiratory function. Note that oxygen consumption can be analyzed in these isolated mitochondrial fractions using other equipment as well. The primary adjustment that might be required when using other equipment is to increase the amount of mitochondrial mass loaded per measurement.

Sample collection

⌚ Timing: 30 min

The first section of this protocol describes the dissection and preparation of murine brown adipose tissue, prior to its mechanical lysis to liberate mitochondria and lipid droplets. We are currently adapting this protocol to other mouse and human tissues, which will be described in a separate publication.

Note: The number of mice needed for effective isolation of PDMs varies according to tissue lipid content. A sufficient amount of lipids is required to effectively form a buoyant fat layer on the surface of the homogenate (see [Figure 2](#)). Fewer animals can be used if mice have higher lipid content due to age, diet, or genetic manipulation. This protocol has been optimized for BAT isolation from 6 mice, with dissected BAT weights per mouse varying between 80–300 mg. Thus, a minimum of 480 mg of tissue is needed.

⚠ **CRITICAL:** The buoyancy of lipid droplets is the process that separates peridroplet mitochondria (PDMs) from the other mitochondria.

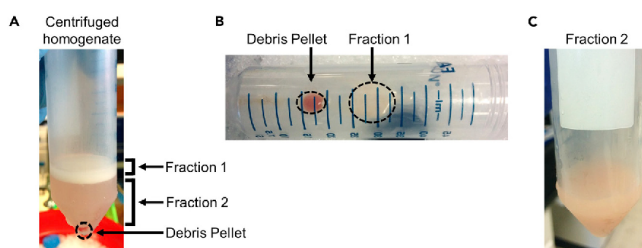


Figure 2. Separation of the fat layer containing PDMs by low-speed centrifugation

(A) Image of 50 mL Falcon tube containing BAT homogenate after first low-speed centrifugation (step 3). Note the separation of fraction 1, containing the fat layer and peridroplet mitochondria (PDMs), from fraction 2, containing cytosolic mitochondria (CMs).

(B and C) (B) Fraction 1 in the decanted original Falcon tube after pouring (C) the supernatant containing CMs, namely fraction 2, into a clean tube.



1. Euthanize mice one-by-one using isoflurane and secondary cervical dislocation as approved by your institutional animal care and use committee in compliance with US Public Health Service Regulation. Cervical dislocation should be performed carefully to avoid tearing interscapular brown adipose tissue at the base of the neck.

⚠ **CRITICAL:** Isoflurane must be handled in a fume hood, as it is a volatile anesthetic.

2. Exsanguinate mice by cardiac puncture using a syringe with a 23G needle to minimize blood within the isolated BAT.
3. Dissect interscapular BAT from 6 male 12-week-old C57BL/6J mice and immediately place in 6-well plate or petri dish containing ice-cold PBS.
4. Use surgical scissors and forceps to separate BAT from connective tissue, muscle, and white adipose tissue, preferably using a dissection microscope.
5. Weigh pooled BAT tissue from 6 mice (480 mg minimum) and mince it into ~2mm pieces with scissors or razors.
6. Re-suspend tissue pieces in 10:1 (volume: weight) in ice-cold MIB + BSA.

Tissue and cell mechanical lysis

⌚ **Timing:** 10 min

⚠ **CRITICAL:** All tubes and materials must be ice-cold and remain ice-cold throughout the protocol.

7. Disrupt tissue with 9–10 strokes in ice-cold glass/Teflon Dounce homogenizer until the MIB and tissue appear as a homogenous solution, with the Dounce head moving smoothly through the solution.

⚠ **CRITICAL:** Do not use detergents or soaps to clean the homogenizer, as they can disrupt mitochondrial membranes. Use warm water and clean brushes. For samples with higher content of connective tissue, a glass-glass loose Dounce homogenizer is recommended. As glass can break during homogenization, one should be mindful of sharps hazards.

Separating fat cake by low-speed centrifugation

⌚ **Timing:** 20 min

Peridroplet mitochondria (PDMs) are separated from cytosolic mitochondria (CMs) during the low-speed centrifugation step, which also separates nuclei, insoluble cell debris and unbroken tissue (Figure 2A).

8. Transfer homogenate into ice-cold 50mL Falcon tube (Corning) and centrifuge $900 \times g$ (low speed) for 10 min at 4°C, using a centrifuge with swinging bucket rotor.

⚠ **CRITICAL:** When using a swinging bucket rotor, measure the distance between the center of the rotor and the center of the liquid homogenate mass within the tube, when in horizontal position, in order to transform $900 \times g$ into the actual rpm needed.

$$rcf (g) = 1.12 \times \text{radius (mm)} \times \left(\frac{\text{rpm}}{1,000} \right)^2$$

9. Carefully pour the supernatant, which is fraction 2 that contains CMs, into a new ice-cold falcon tube (Figure 2C). A cell strainer (70–100 μm) can be used to prevent debris or loose fat to mix with the CM fraction. Pouring will leave the fat layer on the side of the tube, which is fraction 1 that contains PDMs, and the pellet in the original tube (Figure 2B).
10. By keeping the tube horizontally, scrape fraction 1 into a second and clean ice-cold 50 mL tube and re-suspend in 4 mL of MIB + BSA buffer (Figure 2B).

Alternatives: Use a P1000 micropipette with 1/3 of its tip cut, collect fraction 1, and transfer it to a clean tube. Cutting 1/3 of the tip increases its bore size, which prevents tip clogging when aspirating the fat layer. Collecting fat layer by pipetting is not the preferred option, as fat can remain attached to the tip and thus lost. Consequently, this alternative should only be used if the fat layer does not remain intact and adherent to the side of the tube, after pouring fraction 2 to a clean tube. See [Troubleshooting, problem 1](#).

⚠ CRITICAL: It is critical that sufficient tissue is homogenized to generate a compact and floating fat layer on the surface of the homogenate. See [Troubleshooting, problem 1](#) if a floating layer is absent.

⚠ CRITICAL: Save 1 μL of fraction 1 for peridroplet mitochondria imaging, as a quality control assessment.

11. Discard the original 50 mL tube that contains the pelleted unbroken cells, nuclei, and debris.
12. Repeat the low-speed centrifugation on fraction 1 re-suspended in 4 mL of MIB + BSA and on fraction 2 in the new tube, to further eliminate debris.

⚠ CRITICAL: Fractions 1 and 2 must be completely cleared of debris prior to high-speed centrifugation steps. If necessary, perform a third low-speed centrifugation. If a residual lipid layer is generated after a second slow spin of fraction 2, discard it and do not pool it with clean fraction 1.

Isolating CMs and PDMs by high-speed centrifugation

⌚ Timing: 1 h 30 min

By using high-speed centrifugation, PDMs will be separated from fraction 1 and cytosolic mitochondria (CMs) from fraction 2.

13. Transfer clean fraction 1 and fraction 2 to 2mL Eppendorf tubes and centrifuge at $10,000 \times g$ for 10 min at 4°C using a microfuge (Figure 3A).
14. Discard the lipid layer and supernatants generated after centrifuging Fractions 1 and 2.
 - a. Use a P1000 pipette to physically scrape the lipid layer and gently evacuate residual lipids before removing supernatant. This step is to prevent the lipids from mixing with the PDM pellet.
 - ⚠ CRITICAL:** Save at least 1 μL of the discarded lipid layer for quality control measurements.
 - b. The pellet obtained from fraction 1 will contain PDMs and the pellet from fraction 2 will contain CMs (Figure 3B).
 - c. Re-suspend pellets in 200 μL MIB + BSA and transfer them to clean 1.5 mL tubes.

⚠ CRITICAL: There should be minimal lipid content floating after high-speed centrifugation of fraction 2. The presence of large amounts of lipid in fraction 2 can indicate a

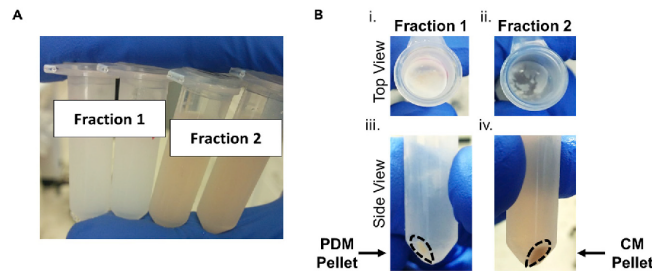


Figure 3. Mitochondrial isolation by high-speed centrifugation

(A) Re-suspended fraction 1 in MIB + BSA and fraction 2 before high-speed centrifugation.
(B) Top and side views of the mitochondrial pellets generated from high-speed centrifugation of fraction 1 and fraction 2. Note that fraction 2 after high-speed centrifugation should have minimal fat layer compared to fraction 1.

contamination of CMs with PDMs. Refer to “Separating Fat Cake by Low-Speed Centrifugation” steps to optimize slow centrifugation steps and minimize lipid content in fraction 2.

15. Repeat high-speed centrifugation step to wash residual lipids and non-mitochondrial contents with MIB + BSA.
16. Following the second high-speed centrifugation, remove supernatant and preserve washed pellets with mitochondria.

⚠ **CRITICAL:** There should be no visible lipid layer at this step. Perform additional centrifugation steps until no lipid layer is observed.

17. Gently re-suspend mitochondrial pellets by pipetting up and down (do not use vortex) in ice-cold MIB without BSA and determine protein concentration by BCA assay (Thermo). When re-suspending pellet in MIB, aim for a concentration of $\sim 10 \mu\text{g}/\mu\text{L}$ (1:2–1:3 volume pellet: buffer). These ratios result in re-suspending fraction 1 in 20–40 μL and fraction 2 in 40–60 μL of buffer.

⚠ **CRITICAL:** Use MIB without BSA for protein determination, as BSA will cause an overestimation of protein content in the mitochondrial fractions. See [Troubleshooting, problems 1 and 2](#).

⏸ **Pause point:** Isolated CMs and PDMs can be pelleted and stored long-term at -80°C . Frozen and thawed mitochondria can be used to measure maximal respiratory capacity, with the exception of mitochondrial coupled respiration ([Acin-Perez et al., 2020](#); [Osto et al., 2020](#)). It is recommended to determine the protein concentration before use.

Functional assessment of PDMs and CMs by respirometry

⌚ **Timing:** 1 h

Here we describe how to measure oxidative function of PDMs and CMs under different fuels, using the Seahorse XF96 analyzer from Agilent Technologies. This equipment allows the use of minimal amounts of biological sample, namely 2–4 μg of protein per measurement. Respiration can be measured in these same fractions using other equipment measuring oxygen consumption, but the amount of mitochondria loaded will likely need to be increased. Consult “Before You Begin” section to prepare the equipment and XF96 cartridge before starting the assay.

18. Load the cartridge with 15 μL MAS + ADP in port A, 16.6 μL MAS + oligomycin in port B, 18.5 μL MAS + FCCP in port C, and 20.5 μL MAS + antimycin A in Port D (see Tables with Solution composition in Materials and Methods section).

Alternatives: As basal respiration with substrates in the absence of ADP is functionally equivalent to respiration under oligomycin, one can plate mitochondria already with ADP, then add 15 μL MAS + oligomycin in port A, 16.6 μL MAS + FCCP in port B, 18.5 μL MAS + antimycin A in port C and 20.5 μL MAS + TMPD/Ascorbate in Port D to determine maximal complex IV activity. This alternative is critical for models with less healthy or less resilient mitochondria. Starting at state 3 reduces the time of the assay itself and of mitochondria being hyperpolarized. The reason is that hyperpolarized, highly respiring mitochondria are not as stable at 37°C. See [Troubleshooting, problem 3](#).

19. Load the protocol prepared the day before the assay, press start, and place the utility plate containing the hydrated sensor cartridge, with its ports loaded, into the XF96 analyzer to begin oxygen and pH sensor calibration. Calibration takes 30 min, during which one can load mitochondria into the XF96 cell culture microplate.
20. For each mitochondrial fuel, generate a master mix with sufficient volume for at least triplicate measures (3 wells), with up to three different fuels assessed per sample. Each well will contain 2–4 μg mitochondria in 20 μL MAS + the substrate to be assessed (pyruvate + malate, succinate + rotenone or palmitoyl-carnitine + malate). Thus, each master mix will contain at least a total of 60 μL with 6–12 μg of mitochondria per substrate to cover triplicates.
21. Load 20 μL of each master mix into individual wells of the microplate using a P20 pipette. Mitochondria show higher respiratory rates under succinate + rotenone. Thus, 2 μg of mitochondria should be loaded under succinate + rotenone and 4 μg for the other substrates.
 - a. Centrifuge the plate at 2,000 $\times g$ for 5 min at 4°C using a swinging bucket rotor with plate carriers and running with the rotor brakes off, to sediment mitochondria at the bottom surface of the well.

⚠ CRITICAL: Load mitochondria in the center of the well. If mitochondria attach to the wall of the well, oxygen consumption will not be properly measured. Turn OFF centrifuge brake and allow the rotor to reduce speed gradually, so that the plate is not shook by a sudden decrease in speed and mitochondria can stay at the center of the well.

22. Add 115 μL MAS + GDP + substrate using multichannel pipette at a 45° angle to the top of each chamber well. Total volume in the well is going to be 135 μL . The total volume needs to be accurate, as 10 \times solutions for ADP (15 + 135 = 150 μL), oligomycin (16.6 + 150 = 166.6 μL), FCCP (18.5 + 166.6 = 185.1 μL), and antimycin A (20.5 + 185.1 = 205.6 μL) will be injected from the ports on top.

⚠ CRITICAL: The additional 115 μL of MAS should be added gradually, to prevent detaching mitochondria from the bottom of the well. Mitochondria can be visualized by bright field or fluorescent microscopy, using a 40 \times –63 \times objective. A homogenous layer of bacteria-like structures (mitochondria) should be observed on the surface of the well (see [Figure 5B](#)).

23. Warm the Seahorse plate with mitochondria in a 37°C incubator for 5 min before loading the plate into the XF96 Analyzer.
24. Replace the utility plate with the Seahorse plate loaded with mitochondria and start the assay. Assay duration is around 1 h.

Data analysis

⌚ Timing: 1 h

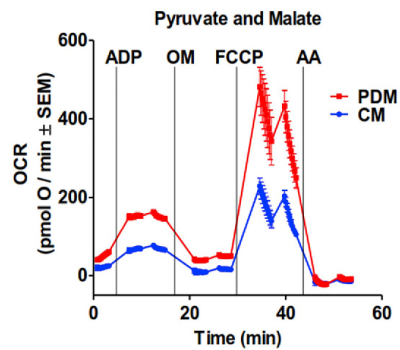


Figure 4. Respiriometry assay of isolated PDMs versus CMs from brown adipose tissue
Representative trace of oxygen consumption rates (OCR) of isolated PDMs and CMs fueled by pyruvate + malate. ADP, oligomycin, FCCP, and antimycin A were sequentially injected to assess mitochondrial respiratory states. The injection of ADP in port A increases, oligomycin decreases, and FCCP increases respiration only when mitochondria are intact after isolation. Antimycin A blocks respiration, leaving some oxygen consumption attributed to other mitochondrial processes (i.e., ROS generation). 4–6 technical replicates per group. Data are expressed as mean \pm SEM. Adapted from Benador et al. (2018).

25. Export Point-to-point oxygen consumption rates (OCRs) of individual wells from Seahorse instrument (Figure 4).
26. Check that the oxygen tension traces are linear in each measurement, as a quality control parameter. Non-linear traces do not allow a reliable calculation of OCR.
27. Using Microsoft Excel, perform the following calculations described with the OCR values measured in each individual well. For each calculation, the OCR under Antimycin A is subtracted from other values to obtain the OCR that corresponds to mitochondrial respiratory function. This is because Antimycin-resistant oxygen consumption cannot arise from mitochondrial respiration, since Antimycin A blocks electron transfer from complex III to complex IV, with complex IV being responsible for respiration (reducing oxygen to water).
 - a. State 2: Subtract minimal OCR value following antimycin A injection from maximal OCR value at the start of the assay. State 2 represents respiration of mitochondria with fuels, without ATP synthesis, as ADP should be absent.
 - b. State 3: Subtract minimal OCR value following antimycin A injection from maximal OCR value following ADP injection. See [Troubleshooting, problem 3](#) if poor response to ADP is observed.
 - c. State 4o: Subtract minimal OCR value following antimycin A injection from minimal OCR value following oligomycin injection (mitochondria with fuels, with ATP synthase blocked, functionally equivalent to state 2).
 - d. Maximal: Subtract minimal OCR value following antimycin A injection from maximal OCR value following FCCP injection. See [Troubleshooting, problem 4](#) if OCR is unstable.

Quality control

⌚ Timing: variable

To assess the quality of isolated mitochondria, Option A describes a quantitative parameter to assess integrity of mitochondrial function after isolation. Option B describes a microscopic assessment of the lipid droplets with mitochondria still attached by fluorescence microscopy and the presence of lipid droplets in the PDM fraction. Option C describes measuring the relative mitochondrial protein content in each fraction by biochemical techniques, to determine correspondence of protein loaded to the respirometry assay with mitochondria loaded. Option D describes assessing mitochondrial function by membrane potential analysis.

28. Option A: The respiratory control ratio (RCR) is the ratio between state 3/state 2 or state 3/state 4o respiration and can be used as a quantitative measure of mitochondrial inner membrane

damage. Physical damage to the mitochondrial inner membrane is indicated by RCR values < 4, when respiring under pyruvate + malate, or < 2, when respiring with succinate + rotenone or palmitoyl-carnitine + malate. A similar or greater fold increase in OCR should be seen after injecting FCCP.

29. Option B: Measurement of mitochondria and lipid droplet (LD) content by fluorescence microscopy.
 - a. Combine 1 μ L of non-stripped fat layer (Figure 3A), 1 μ L stripped fat layer and 1 μ L isolated PDMs (Figure 3B) with 1 μ L Imaging solution A.
 - b. Place 1 μ L of each sample- Imaging solution A mix on a #1.5H coverglass and cover with an additional coverglass.
 - c. Place the coverglass on a confocal microscope stage and image BODIPY using 488 nm laser for excitation and collect fluorescence emission at 500–550 nm. Using a separate track, image MitoTracker with 633 nm excitation and collect emission at 650–700 nm. Use 20 \times lens for low-magnification imaging of LD content (Figure 5) (Benador et al., 2018).
 - d. The non-stripped fat layer should have mitochondria closely attached to lipid droplets (Figure 5A) and the isolated PDM fraction should not have lipid droplets (Figure 5B). The stripped fat layer should have little to no mitochondria (Figure 5C).
30. Option C: Quantification of total mitochondrial content in each fraction by western Blot.
 - a. Combine 1–10 μ g isolated mitochondria and boil at 95 $^{\circ}$ C for 5 min.
 - b. Run and transfer an SDS gel as specified by gel apparatus manufacturer.
 - c. Probe for the relative content of mitochondrial markers, such as TOMM20 or VDAC and quantify per microgram of protein loaded.

⚠ CRITICAL: The semi-quantitative data obtained from Option B can provide evidence that functional differences detected between samples of different types do not arise from differential enrichment of PDMs in the isolated fraction. Option C is an essential step when comparing PDMs from different tissues or mice with different ages or genetic manipulations.

Alternatives: Evaluate mitochondrial content by mass spectroscopy proteomic analysis using MitoCarta 2.0 to estimate mitochondrial protein content.

31. Option D: Assessment of mitochondrial function by membrane potential imaging.
 - a. Combine 1 μ L of isolated mitochondria with 1 μ L Imaging solution B.
 - b. Place 1 μ L of mitochondria-solution B mix on a #1.5H coverglass and cover with an additional coverglass.
 - c. Place the coverglass on microscope stage and image MitoTracker green using 488 nm laser excitation and 500–550 nm emission. Using a separate track, image MitoTracker red with 633 nm excitation and 650–700 nm emission (Figures 5D and 5E).

Note: MitoTracker red staining is more sensitive to differences in membrane potential, while MitoTracker green is less sensitive. Therefore, mitochondria with intact membrane potential will stain with both green and red (Figures 5D and 5E), while depolarized mitochondria will only stain green (Benador et al., 2018).

Expected outcomes

Normal respiration patterns shared by PDMs and CMs

Basal or State 2 oxygen consumption rate (OCR) is generally between 30–60 pmol O₂/min (Figure 4) (Benador et al., 2018). After the injection of ADP, OCR increases at least 4-fold in mitochondria under pyruvate and malate and at least 2-fold with other substrates. Subsequent injection by oligomycin yields a drop in OCR to basal or State 2 values (see [Troubleshooting, Problem 3](#) if this is not the case). The third injection with the mitochondrial uncoupler FCCP must induce a similar increase in

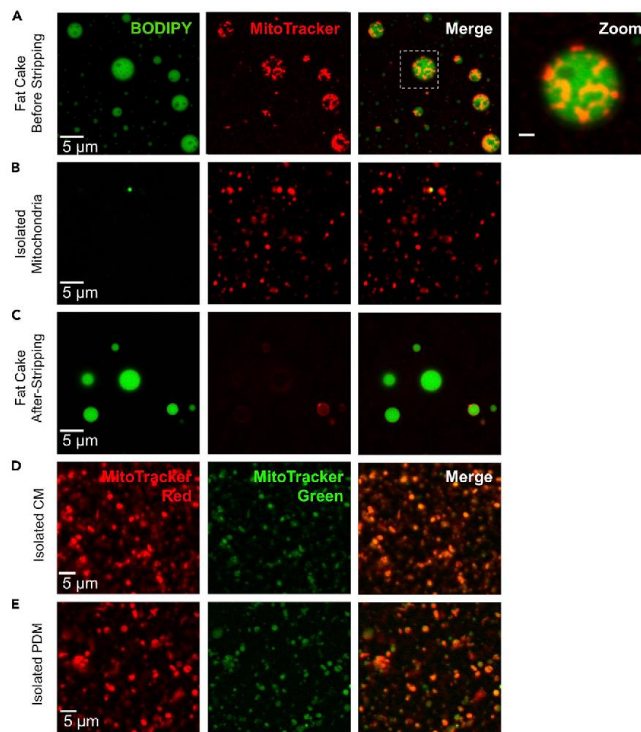


Figure 5. Confocal fluorescence microscopy of isolated PDMs

(A) Images of re-suspended fraction 1 before high-speed centrifugation stained with the lipid droplet dye BODIPY (green) and the mitochondrial dye MitoTracker red. Note the localization of mitochondria to lipid droplet surface. (B) Image of re-suspended PDM pellet stained with mitochondrial marker MitoTracker red. Isolated PDMs have little to no lipid droplets. (C) Images of re-suspended fraction 1 after high-speed centrifugation, stained with the lipid droplet dye BODIPY (green) and the mitochondrial dye MitoTracker red. Note the lack of mitochondria. (D) Images of isolated mitochondria from fraction 2 (CMs) stained with MitoTracker green and MitoTracker red. (E) Images of isolated mitochondria from fraction 1 (PDMs) stained with MitoTracker green and MitoTracker red. Scale bars, 5µm. Adapted from Benador et al. (2018).

OCR or higher than the increase induced by ADP. The last injection, antimycin A, blocks electron transfer from complex III to complex IV causing an immediate drop in OCR. Rates after antimycin A injection are typically under 10 pmol O₂/min and reflects other processes that consume oxygen, but are not respiration (i.e., ROS generation). See [Troubleshooting, Problem 4](#) if rates are unstable.

Functional differences between CMs and PDMs

When comparing BAT CMs and PDMs, PDMs assayed using pyruvate and malate as substrate typically display a 2-fold higher OCR rates than CMs under state 3 (maximal ATP-synthesizing respiration induced by ADP injection), as well as in maximal respiration (under FCCP, [Figure 4](#)). OCR values are generally between 100–300 pmol O₂/min for CMs and 200–600 pmol O₂/min for PDMs. The higher values of OCR observed in PDMs compared to CMs are observed when mitochondria respire under succinate and rotenone as well (Benador et al., 2018). See [Troubleshooting, Problems 2 and 4](#).

Confocal images of isolated fat layer and peridroplet mitochondria

Fluorescent staining and imaging of mitochondria and LD in the fat layer will reveal numerous mitochondria attached to LDs (Figure 5A). High-speed centrifugation strips mitochondria from LDs, resulting in a pellet containing PDMs without large lipid droplets and only showing 5% of total BODIPY fluorescence (Figure 5B). Indeed, this 5% is confined to very small LD, smaller than some mitochondria. Accordingly, the stripped fat layer shows that 95% of mitochondria have been removed, with only 5% of MitoTracker red signal retained in the stripped fat layer (Figure 5C) (Benador et al., 2018).

Limitations

Separating fraction 1 from fraction 2 can be problematic. Yield of PDMs may diminish due to an ineffective formation and buoyancy of the fat layer that constitutes fraction 1. Ineffective formation can be caused by insufficient tissue, lower total lipid content, or tissue harboring lipid droplets of very small size.

Separation of PDMs by differential centrifugation may preferentially select for PDMs attached to large lipid droplets (LDs), which are more buoyant. Small LDs with insufficient buoyancy could potentially be lost or potentially contaminate fraction 2.

The PDM fraction might be constituted by a heterogeneous population, with PDMs behaving differently when attached to large lipid droplets, when compared to small lipid droplets. Our current approach of PDM isolation pools PDMs attached to small and to large lipid droplets together.

This protocol strips PDMs from lipid droplets by high-speed centrifugation, which means that it is a possibility that centrifugation may potentially not detach mitochondria that have a very strong interaction with lipid droplets.

Mass spectrometry analyses reveal that the crudely isolated CMs and PDMs are equally contaminated with other organelles and cellular compartments, mostly the endoplasmic reticulum (ER). Qualitative analyses reveal that 50% of the proteins detected in PDM and CM fractions are mitochondrial.

This protocol has been optimized for BAT from male C57BL/6J mice but could be extrapolated to other organisms. Optimization for other tissues is needed and we are currently developing protocols for other tissues, including liver and white adipose tissue.

Troubleshooting

Problem 1

Low yield of CMs and/or PDMs.

Potential solution

Sample yields, particularly of PDMs, will differ based on the age, diet, and genetic background of the animal, as these factors determine total lipid content and lipid droplet size.

Due to the presence of multiple washes and centrifugation steps, there is high risk of losing material (mitochondria and fat). This can be minimized by increasing the amount of tissue used.

The mechanical separation of fraction 1 from fraction 2 using a plastic micropipette tip can cause fat to adhere to the tip, resulting in loss of material, including PDMs. We recommend cutting 1/3 of the P1000 tip to increase bore size and pipetting slowly to minimize sample loss in step 10.

Problem 2

CM and PDM preparations do not yield differences in biochemical and functional assays.



Potential solution

Due to the crude separation of fraction 1 from fraction 2, there is the potential for PDM and CM cross contamination, particularly PDM contamination of the CM fraction. The presence of a remaining lipid layer remaining in fraction 2 after high-speed centrifugation increases the likelihood of PDM-CM cross contamination. It is recommended to collect fraction 1 with more supernatant, rather than trying to get fraction 1 without any fraction 2 (supernatant) after the low-speed centrifugation.

If contamination is suspected (i.e., a fat layer is present after high-speed centrifugation of fraction 2), it will be confirmed by respirometry. PDMs have higher ATP-linked respiration and capacity to oxidize pyruvate.

PDM and CM protein concentrations may not have been accurately assessed. Since step 14 requires a MIB+BSA wash, residual BSA could remain after MIB resuspension in step 17 and will interfere with accurate protein quantification. If the amount of starting material is large, we recommend a second centrifugation of the mitochondria pellet with MIB lacking BSA. However, it should be noted that mitochondria are more prone to damage when samples are highly diluted, so we do not recommend a secondary resuspension if starting material/mitochondrial pellet is small. If normalization by total protein content is not reliable due to BSA contamination, alternative normalization could be performed: by staining the XF96 plate with MitoTracker deep red (MTDR) and measuring red fluorescence in the well or by immunoblotting. With the first approach, samples can be normalized by MTDR staining either prior or after respirometry (Acin-Perez et al., 2020). Normalization by immunoblot can be performed using TOMM20 and Porin levels.

Problem 3

PDMs and CMs are uncoupled or show poor responses to ADP and FCCP.

Potential solution

We recommend increasing the concentration of BSA utilized in MIB buffer and ensuring that GDP is included in the buffer. BSA is needed to trap free fatty acids released during adipose tissue homogenization, which can damage the mitochondrial inner membrane and/or activate UCP1. The addition of BSA should reduce levels of free fatty acids, and the inclusion of GDP will inhibit UCP1 and uncoupled respiration. Uncoupled PDMs could also result from physical damage incurred during homogenization. To minimize potential physical damage, ensure that the Dounce homogenizer was not washed with detergents and reduce the number of strokes to 6 during homogenization.

Another explanation is that mitochondria are not resilient to the assay. In this case, start the respirometry assay in state 3, with the mitochondria having saturating ADP concentrations when plated, to shorten the time of mitochondria being hyperpolarized (see Alternative after step 18).

Problem 4

Oxygen consumption rates are unstable, giving a transient peak with very high values that subsequently decrease.

Potential solution

Ensure that mitochondria are seeded at an appropriate amount per well. Optimal seeding conditions should be determined experimentally, with lower amounts required when mitochondria use succinate and rotenone. Basal oxygen consumption rates (substrates without ADP) should not exceed 250–275 pmol O₂/min.

If high respiration rates persist after decreasing the amount of mitochondria loaded, we recommend reducing measurement times in the respirometry assay protocol commands.

Resource availability**Lead contact**

Further information and requests for resources and reagents should be directed to and will be fulfilled by the Lead Contact, Dr. Marc Liesa (mliesa@mednet.ucla.edu).

Materials availability

This study did not generate any unique materials or reagents.

Data and code availability

We did not generate any unique datasets or code.

Acknowledgments

M.L. is funded by UCLA-DDRC NIH P30DK41301, 1R01AA026914-01A, and the Seed Award of DG SOM to K.R., M.L., and L.V. O.S.S. is funded by R01 DK099618-05. We thank Linsey Stiles at the Mitochondria and Metabolism Core at UCLA.

Author contributions

Conceptualization, I.B., J.N., O.S.S., and M.L.; investigation, I.B., J.N., A.B., M.V., M.S., R.A.P., and L.V.; writing – original draft, J.N. and I.B.; writing – review & editing, J.N., I.B., L.V., R.A.P., K.R., O.S.S., and M.L.; funding acquisition, K.R., O.S.S., and M.L.; supervision, R.A.P., K.R., O.S.S., and M.L.

Declaration of interests

The authors declare no competing interests.

References

Acin-Perez, R., Benador, I.Y., Petcherski, A., Veliova, M., Benavides, G.A., Lagarrigue, S., Caudal, A., Vergnes, L., Murphy, A.N., Karamanlidis, G., et al. (2020). A novel approach to measure mitochondrial respiration in frozen biological samples. *EMBO J.* 39, e104073.

Benador, I.Y., Veliova, M., Mahdavian, K., Petcherski, A., Wikstrom, J.D., Assali, E.A., Acin-Perez, R., Shum, M., Oliveira, M.F., Cinti, S., et al. (2018). Mitochondria bound to lipid droplets have unique bioenergetics, composition, and dynamics that support lipid droplet expansion. *Cell Metab.* 27, 869–885.e6.

Osto, C., Benador, I.Y., Ngo, J., Liesa, M., Stiles, L., Acin-Perez, R., et al. (2020). Measuring mitochondrial respiration in previously frozen biological samples. *Current Protocols in Cell Biology* 89, <https://doi.org/10.1002/cpcb.116>.

Appendix II

Measuring mitochondrial respiration in previously frozen biological samples.

The work described in this chapter has been reproduced from:

Osto C., Benador I.Y., Ngo J., Liesa M., Stiles L., Acin-Perez R., Shirihai O. Measuring mitochondrial respiration in previously frozen biological samples. *Currents Protocols in Cell Biology*. 2020. 89, e116. doi: 10.1002/cpcb.116.

Copyright 2020

Corey Osto, Ilan Benador, Jennifer Ngo, Marc Liesa, Linsey Stiles, Rebeca Acín-Pérez, Orian Shirihai.

Measuring Mitochondrial Respiration in Previously Frozen Biological Samples

Corey Osto,^{1,2} Ilan Y. Benador,^{2,3,4} Jennifer Ngo,^{3,5} Marc Liesa,^{1,2,3}
Linsey Stiles,^{1,2,3,7} Rebeca Acin-Perez,^{2,3,7} and Orian S. Shirihai^{1,2,3,4,6,7}

¹Department of Molecular and Medical Pharmacology, University of California, Los Angeles, California

²Metabolism Theme, David Geffen School of Medicine, University of California, Los Angeles, California

³Department of Medicine, Endocrinology, David Geffen School of Medicine, University of California, Los Angeles, California

⁴Nutrition and Metabolism, Graduate Medical Sciences, Boston University School of Medicine, Boston, Massachusetts

⁵Department of Chemistry and Biochemistry, University of California, Los Angeles, California

⁶Molecular Biology Institute, University of California, Los Angeles, California

⁷Corresponding authors: OShirihai@mednet.ucla.edu; acinperez@mednet.ucla.edu; LStiles@mednet.ucla.edu

Measuring oxygen consumption allows for the role of mitochondrial function in biological phenomena and mitochondrial diseases to be determined. Although respirometry has become a common approach in disease research, current methods are limited by the necessity to process and measure tissue samples within 1 hr of acquisition. Detailed by Acin-Perez and colleagues, a new respirometry approach designed for previously frozen tissue samples eliminates these hurdles for mitochondrial study. This technique allows for the measurement of maximal respiratory capacity in samples frozen for long-term storage before testing. This protocol article describes the optimal tissue isolation methods and the combination of substrates to define electron transport chain function at high resolution in previously frozen tissue samples. © 2020 The Authors.

Basic Protocol 1: Sample collection, storage, and homogenization for previously frozen tissue respirometry

Basic Protocol 2: Running a Seahorse respirometry assay using previously frozen tissue samples

Basic Protocol 3: Normalization to mitochondrial content for previously frozen tissue respirometry

Keywords: frozen • mitochondria • OCR • respirometry

How to cite this article:

Osto, C., Benador, I. Y., Ngo, J., Liesa, M., Stiles, L., Acin-Perez, R., & Shirihai, O. (2020). Measuring mitochondrial respiration in previously frozen biological samples. *Current Protocols in Cell Biology*, 89, e116. doi: 10.1002/cpcb.116

INTRODUCTION

Impaired mitochondrial respiration plays a key role in metabolic, aging-related, and cardiovascular disease (Liesa, Palacín, & Zorzano, 2009; Wallace, 2011). Mitochondrial respiration results from the transfer of electrons between complexes I, II, III,



Current Protocols in Cell Biology e116, Volume 89
Published in Wiley Online Library (wileyonlinelibrary.com).
doi: 10.1002/cpcb.116

© 2020 The Authors. This is an open access article under the terms of the Creative Commons Attribution License, which permits use, distribution and reproduction in any medium, provided the original work is properly cited.

Osto et al.

1 of 17

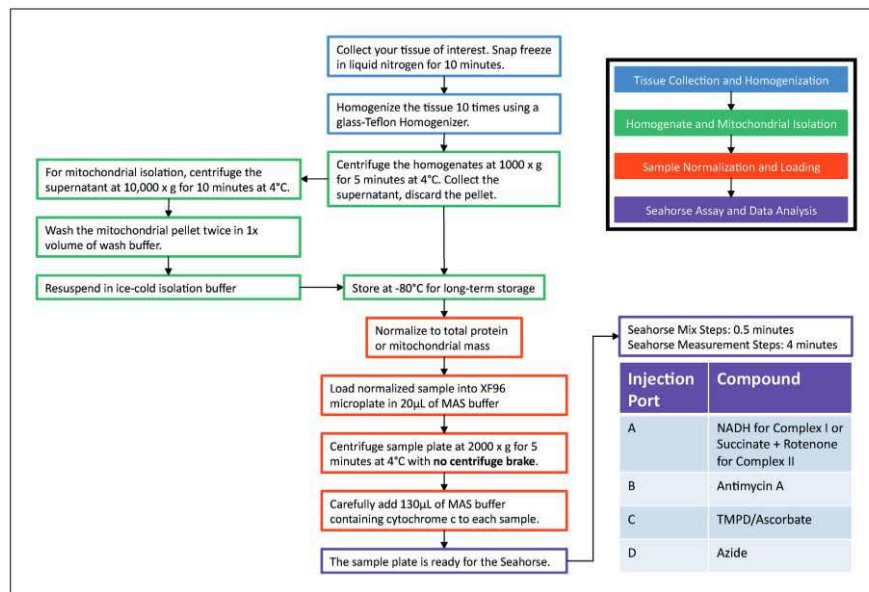


Figure 1 Flowchart of the frozen tissue respirometry protocol detailing the most important steps. The sections of the protocol are outlined in the top right box, which will be referred to in subsequent figures.

and IV, with complex IV reducing oxygen to water; thus, oxygen consumption integrates electron transport activity from complexes I/II through IV. However, mitochondrial respirometry analysis currently requires processing and measurement of the living tissue sample within an hour of being taken from the patient. This requirement is set by the need to preserve the integrity of the inner mitochondrial membrane, needed both for integrated electron transfer between the complexes as well as to preserve the coupling of electron transfer to ATP synthesis. Consequently, the need to use fresh tissue to assess integrated electron transport activity makes respirometry analysis largely unfeasible for standard clinical practice and clinical studies. This limitation has significantly stalled scientific progress and virtually excluded the possibility of translating some discoveries in mitochondrial physiology into improved patient care. Here we describe a methodology to assess mitochondrial respirometry capacity in previously frozen biological specimens. This procedure (see flowchart in Fig. 1) overcomes the fundamental limitation of conventional respirometry approaches that require freshly isolated tissue, and also allows for the use of less biological material. Furthermore, our approach also allows for the use of a combination of substrates that permits selective measurements of respiratory capacity driven by complex I, II, or IV alone, resembling previous methods for determining isolated electron transport chain complex activity.

Detailed in Acin-Perez et al. (2020), the maximal respiratory capacity measured from frozen tissues using this assay is comparable to that measured in fresh tissue (Figure 2A). Freeze-thawing impairs mitochondrial respiration by disrupting and permeabilizing the mitochondrial inner membrane, which releases electron carriers that support the electron transport chain (Figure 2C). However, the interaction of electron transport complexes (supercomplexes) remains intact under freeze-thawing conditions, allowing for integrated electron transport as seen in fresh tissues. This article, therefore, provides instructions to rescue the defects induced by freeze-thawing, as well as to control the entry of electrons into the electron transport system by providing different electron carriers.

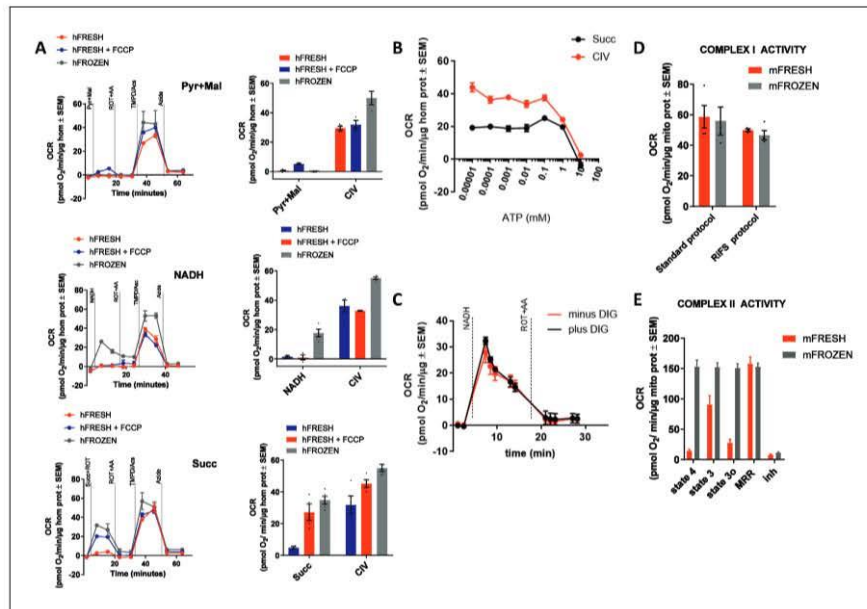


Figure 2 Respiriometry measurements of complex I, II, and IV comparing fresh versus frozen tissue protocols. (A) The Seahorse traces and associated OCR (oxygen consumption rate) quantifications of mouse liver homogenates. hFresh represents liver homogenate which was isolated and tested without being frozen. TMPD is added to a subset of the hFresh samples to uncouple the mitochondria to survey complex activity separately from ATP-linked respiration. hFrozen represents liver homogenates which underwent the frozen respirometry protocol. While complex IV was surveyed using TMPD/ascorbate for all three assays, the top graph was first stimulated with pyruvate + malate, the middle with NADH, and the bottom with succinate + rotenone. (B) Succinate + rotenone and TMPD + ascorbate-dependent oxygen consumption rate measured in the presence of a titration of ATP concentrations. (C) Oxygen consumption rate in response to NADH injection for frozen liver homogenate treated with or without digitonin to control whether the mitochondria are fully broken and substrates can directly fuel the electron transport chain. (D) Complex I and complex II activity (measured as oxygen consumption rate). (E) Oxygen consumption rates of fresh and frozen mitochondria respiring under succinate+rotenone. Fresh mitochondria respond to ADP, oligo, FCCP, and AA, whereas frozen mitochondria, being uncoupled from the beginning, only respond to AA.

As our procedure allows for the specific measurement of oxygen consumed by complex IV, mitochondrial isolation is no longer necessary, allowing for the use of homogenates to measure mitochondrial function, significantly simplifying tissue preparation (described in Basic Protocol 1).

The methodology described in this article is broken up into three subsections: Basic Protocol 1 for sample collection, storage, and homogenization for respirometry on previously frozen tissue; Basic Protocol 2 for running a Seahorse respirometry assay using previously frozen tissue samples; and Basic Protocol 3 for normalization to mitochondrial content for respirometry on previously frozen tissue (optional). Figure 1 provides a graphical representation of this method from start to finish. Basic Protocol 1 describes the process of dissecting a sample, freezing a sample for storage, and homogenizing a sample for a more simplified sample preparation. Basic Protocol 2 details the loading of the XF96 Seahorse sample plate, describes the compounds to be loaded into the Seahorse cartridge injection ports, and lays out the Seahorse protocol steps to measure respirometry in previously frozen tissues. Basic Protocol 3 describes how to use MitoTracker Deep Red staining to normalize samples to mitochondrial content rather than whole protein

content. Completion of this series of protocols will allow users to progress from removing a tissue of interest from a specimen, freeze the tissue for later study, and set up a Seahorse assay to obtain complex I, II, and IV functional readings from the previously frozen tissue sample.

SAMPLE COLLECTION, STORAGE, AND HOMOGENIZATION FOR PREVIOUSLY FROZEN TISSUE RESPIROMETRY

The following protocol details how tissue samples should be collected and stored prior to being analyzed using the previously frozen tissue respirometry assay. In this protocol, the tissue of interest will be isolated from the organism and frozen for long-term storage. Samples will then be manually homogenized and isolated via centrifugation, or, optionally mitochondria may be isolated from the homogenate. Finally, a BCA protein assay will be performed to normalize the samples either for immediate loading or for normalization to mitochondrial mass (described in Basic Protocol 3). If the protocol is followed accurately, the samples should progress from whole tissue to a homogenate or mitochondrial isolate that is ready for normalized loading on a Seahorse sample plate in Basic Protocol 2.

This sample preparation protocol is optimized for mouse liver isolation. See Troubleshooting (Table 3) for alterations to be made for the collection, preparation, and measurement of other tissue types using the frozen tissue respirometry method.

Materials

Mice
Phosphate-buffered saline (PBS; Sigma, P3813)
Liquid nitrogen (optional)
1× MAS buffer (see recipe)
Collagenase Type II (Worthington Biochemical, 4174; optional)
BCA Protein Assay Kit (ThermoFisher, 23225, or equivalent)

Scissors and other dissection tools
Glass-glass or glass-Teflon Dounce homogenizer
Refrigerated centrifuge

Additional reagents and equipment for euthanasia of mice ((see Current Protocols article: Donovan & Brown, 2006)

Tissue collection

1. Euthanize mice using isoflurane anesthesia followed by cervical dislocation (see Current Protocols article: Donovan & Brown, 2006) as approved by Institutional Guidelines for Animal Care in compliance with U.S. Public Health Service Regulations.
2. Dissect the tissue of interest, wash with PBS, and optionally mince with scissors.
When possible, dissections should be done on ice to keep the tissue as cold as possible.
3. Snap freeze in liquid nitrogen. For long-term storage, store the frozen tissue at -80°C .

Liver samples have been shown to have little loss in respirometry results if stored at room temperature or 4°C for up to 3 hr prior to being snap frozen (Fig. 3A).

Though snap freezing is the most ideal method of tissue preparation, the tissue may be immediately stored at -80°C or at -20°C for up to 4 hr prior to being stored at -80°C without affecting the respirometry results (Fig. 3B).

Tissue homogenization

4. Thaw samples in ice-cold PBS and mince with pre-chilled scissors or razor blades.

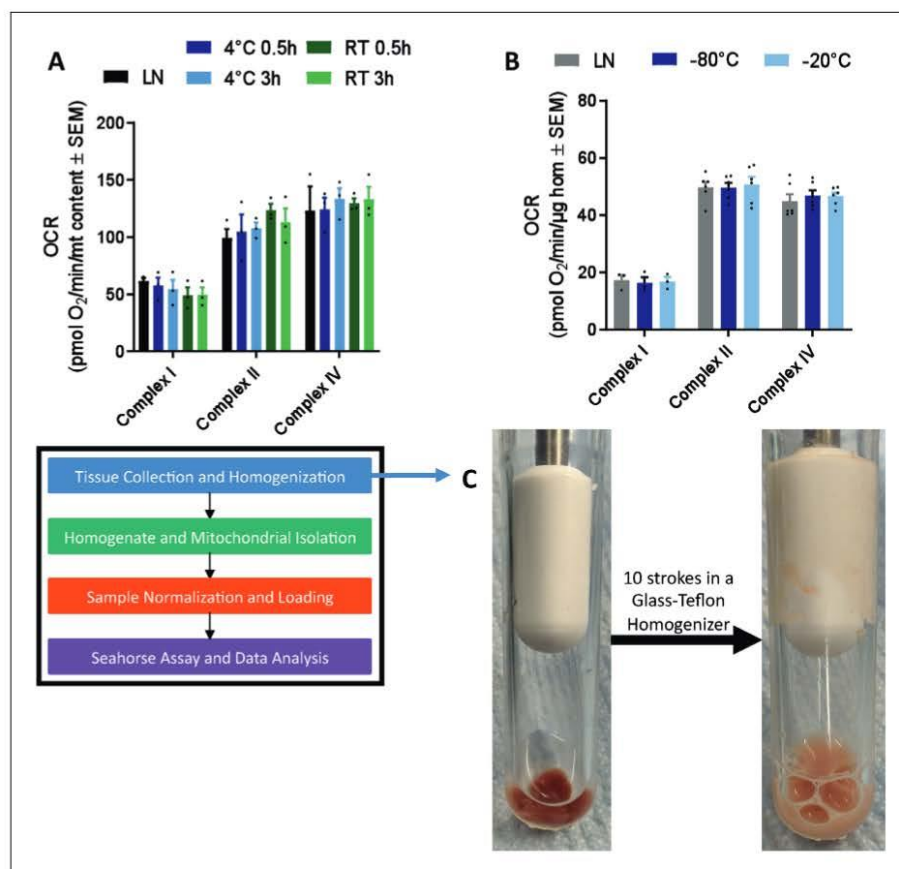


Figure 3 Tissue collection and homogenization. (A) Complex I, complex II, and complex IV oxygen consumption rates of mouse liver homogenates. Liquid nitrogen (LN) samples were immediately snap-frozen after isolation: 4°C 0.5 hr and 4°C 3 hr were kept at 4°C for 0.5 and 3 hr, respectively after isolation prior to being snap-frozen. RT 0.5 hr and RT 3 hr were kept at room temperature for 0.5 and 3 hr, respectively after isolation prior to being snap-frozen. (B) Complex I, complex II, and complex IV oxygen consumption rates of mouse liver homogenates. LN homogenates were isolated then snap-frozen in liquid nitrogen prior to storage at -80°C . -80°C samples were isolated then stored at -80°C until homogenization. -20°C samples were isolated then stored at -20°C for 4 hr before being stored at -80°C until homogenization. (C) Mouse liver before and after 10 strokes of homogenization using a glass-Teflon homogenizer.

- Homogenize using 250 μl to 500 μl per 10 mg of tissue of ice-cold MAS buffer using the appropriate homogenizer (Fig. 3C illustrates this process). For liver, brown adipose tissue, brain, kidney, lung, and skeletal muscle, use ten to twenty strokes in a glass-Teflon Dounce homogenizer. For heart and white adipose tissue, use twenty strokes in a glass-glass Dounce homogenizer.

CRITICAL: For muscle tissue, incubate homogenized tissue in collagenase Type II (0.25 mg/ml final concentration) in MAS at 37°C for 30 min prior to centrifugation.

Our studies have shown that using smaller-volume homogenizers (e.g., using a 7-ml homogenizer rather than a 15-ml homogenizer when working with <5 ml of sample material) results in less sample retention in the homogenizer and produces better homogenization.

Osto et al.

5 of 17

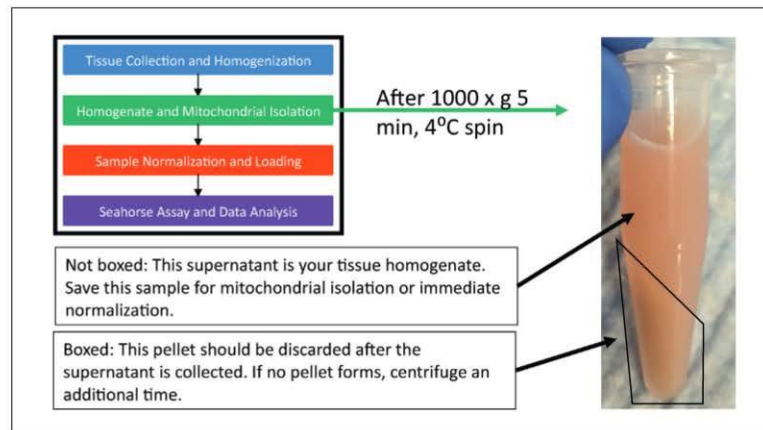


Figure 4 Homogenate isolation from frozen tissues. After homogenization, the homogenate must be isolated from the cellular debris. This is performed using a $1000 \times g$ centrifugation for 5 min at 4°C . Highlighted in this figure is the pellet resulting from this centrifugation (boxed) and the supernatant (not boxed). The supernatant is your tissue homogenate, which should be collected and may be used for normalization prior to respirometry, for mitochondrial isolation, or for non-respirometry assays like Blue Native Gel Electrophoresis. The pellet should be discarded.

6. Centrifuge homogenates 5 min at $1000 \times g$, 4°C .

CRITICAL: If using swinging-bucket centrifuge, measure the precise distance between rotor center and the center of mass of the liquid homogenate in the tube in the horizontal swinging position in order to correctly calculate the g to rpm conversion:

$$\text{rcf (g)} = 1.12 * \text{radius (mm)} * \left(\frac{\text{rpm}}{1,000} \right)^2$$

7. Collect the resulting supernatant as the homogenate sample. Discard the pellet (Fig. 4). The supernatant (tissue homogenate) may be stored at -80°C for long-term storage.

This sample may also be used for other assays like enzymatic assays, western blots, or Blue Native gel electrophoresis.

8. If you are running the sample as a tissue homogenate, perform a BCA protein assay to normalize your samples according to protein content prior to loading on the Seahorse XF96 sample plate (Fig. 5B, Method 1). If you are normalizing according to mitochondrial content, perform a BCA protein assay and continue with the steps detailed in the optional Basic Protocol 3 (Fig. 5B, Method 2). If you are isolating mitochondria from the tissue homogenate, proceed with the following steps for mitochondrial isolation protocol.

Mitochondrial isolation from homogenate (optional)

9. If mitochondrial isolation is desired, centrifuge the rest of the homogenate preparation (the supernatant from the above centrifugation) 10 min at $10,000 \times g$, 4°C .
10. Optionally, wash mitochondrial pellets twice in $1 \times$ volume of MAS buffer, each time centrifuging as in step 9.
11. Re-suspend final mitochondrial pellet in ice-cold MAS buffer.
12. Perform a BCA protein assay using the mitochondrial homogenates. This may be used to normalize the sample according to protein content for loading, or optionally

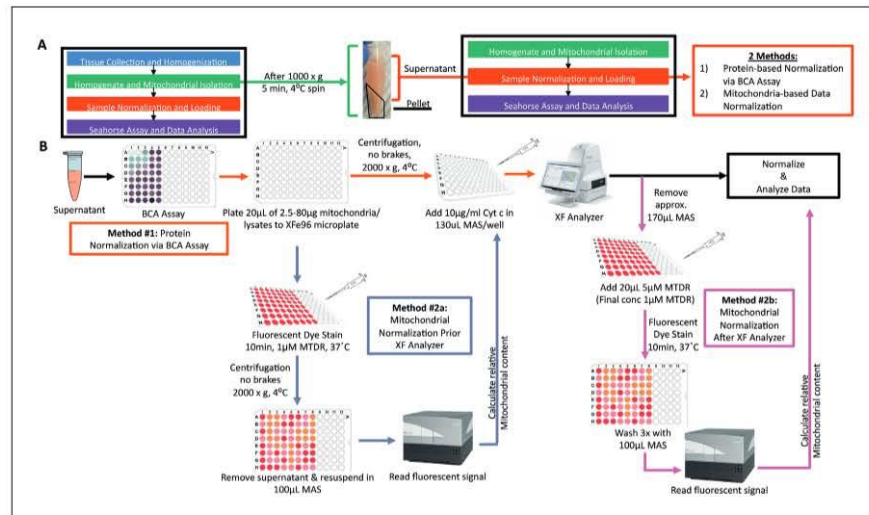


Figure 5 Normalization and loading of tissue homogenates or mitochondrial isolates. Normalization may be performed in one of two ways: protein normalization using a BCA assay or mitochondrial mass normalization using MTDR dye. Method 1 describes the protein-based normalization using the BCA assay. Method 2a describes mitochondrial normalization performed prior to running the XF96 Seahorse plate. Method 2b describes mitochondrial normalization performed after running the XF96 Seahorse plate.

to prepare for mitochondrial mass normalization using MitoTracker Deep Red dye as described in Basic Protocol 2.

Sample data

Figures 3C and 4 depict the results one should obtain after sample collection. Figure 3C shows a mouse liver sample that has been homogenized using a glass-Teflon homogenizer. Figure 4 shows the same sample after centrifugation, highlighting the pellet formed (which should be discarded) and the supernatant (which should be saved). If this sample separation does not occur after centrifugation, you should repeat the centrifugation step a second time.

RUNNING A SEAHORSE RESPIROMETRY ASSAY USING PREVIOUSLY FROZEN TISSUE SAMPLES

This protocol will detail the process of loading normalized samples onto an XF96 Seahorse plate, loading the Seahorse cartridge with compound injections, and running samples on the Seahorse platform. Samples will be loaded onto a XF96 sample plate, then centrifuged and diluted before loading the plate onto the Seahorse. Additionally, this protocol describes the loading of the Seahorse cartridge with compound injections. If this protocol is followed accurately, an operator will be capable of loading samples onto an XF96 sample plate, loading compound injections into a Seahorse cartridge, and running the plates on a Seahorse XF96 system. While this protocol is optimized for use with the Seahorse platform, with optimization, it could be adjusted to work with other respirometry platforms like the Oroboros.

Materials

- Tissue homogenates or mitochondrial isolates (Basic Protocol 1)
- 1 × MAS buffer (see recipe)

BASIC
PROTOCOL 2

Osto et al.

7 of 17

Cytochrome *c* (Sigma, C2506)
Alamethicin (Sigma, A4665; optional)
NADH (Sigma, N8129)
Succinate (Sigma, S9512)
Rotenone (Sigma, R8875)
Antimycin A (ENZO, ALX380075M010)
TMPD (Sigma, 87890)
Ascorbic acid (Fisher, A61-100)
Sodium azide (Sigma, S8032)
Potassium hydroxide (KOH)
Hydrochloric acid (HCl)

Seahorse XF96 flux pack (Agilent 102416-100)
Swinging-bucket centrifuge with plate carrier adapter
Multichannel pipettes
Seahorse XF96 instrument

1. Load homogenates or mitochondrial isolates, based on your BCA normalization results, into a Seahorse XF96 microplate (from the Seahorse XF96 flux pack) in 20 μ l of MAS buffer. Optimal loading concentration will vary depending on the sample material, but for most samples a concentration between 2.5 and 20 μ g of sample per well will be sufficient. See Table 3 in the Troubleshooting section of this document for approximate loading concentrations for different tissue types.

Coating the XF96 plate with substrates promoting cell adhesion like laminin, Cell-Tak, and poly-D-lysine has been shown to not improve performance.

2. Centrifuge the loaded plate 5 min at 2000 \times g, 4°C, using a plate carrier.

CRITICAL: Turn OFF the centrifuge brake and let buckets slow down by themselves. Sudden deceleration due to braking will result in uneven distribution of materials on the bottom of the plate.

3. Carefully add 130 μ l (or enough to achieve a final volume of 150 μ l) per well of 1 \times MAS buffer containing cytochrome *c* (10 μ g/ml, final concentration) for homogenates, or the same volume of MAS buffer alone for isolated mitochondria.

CRITICAL: For brain and lung homogenates, add alamethicin (10 μ g/ml, final) to the MAS buffer containing cytochrome *c* to allow complete membrane permeabilization to substrates.

4. Load the cartridge to deliver 25 μ l of the following injections (Fig. 6A):
 - a. Port A: NADH (1 mM) for complex I assessment, or 5 mM succinate + 2 μ M rotenone for complex II assessment.
 - b. Port B: Antimycin A (4 μ M)
 - c. Port C: TMPD + ascorbic acid (0.5 mM TMPD + 1 mM ascorbic acid)
 - d. Port D: Sodium azide (50 mM) at port D.

All compound injections should be diluted in 1 \times MAS buffer. When making the TMPD + ascorbate solution, add 0.5 mM TMPD into 1 mM ascorbate and adjust the solution to pH 7.2 using potassium hydroxide (KOH) and hydrochloric acid (HCl). NADH and TMPD/ascorbate solutions must be made freshly on the day of the assay, but all other compound injections can be made ahead of time and stored at -20°C until time of use.

5. Mix and measure times for the Seahorse run protocol are 0.5 and 4 min, respectively. If a protocol includes an oligomycin injection, a 2-min wait time should be included between the injection of oligomycin and the 4-min measurement period (Fig. 6B).

Figure 6B describes a typical Seahorse program.

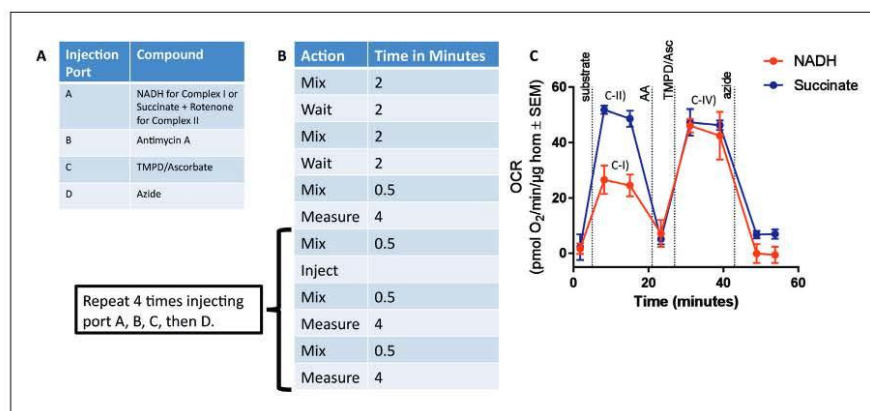


Figure 6 A standard frozen tissue respirometry method, compound injections, and Seahorse trace. (A) An example frozen respirometry Seahorse protocol. (B) Sample compounds for injection ports for the measurement of complex I or complex II oxygen consumption in frozen tissues. (C) An optimal Seahorse trace measuring ETC complexes I, II, and IV. Red trace represents NADH and complex IV dependent and blue trace represents succinate and complex IV dependent respiration. (C-I) NADH-induced respiration, representative of complex I activity. (C-II) Succinate + rotenone-induced respiration, representative of complex II activity. (C-IV) TMPD + ascorbate-induced respiration, representative of complex IV activity.

Sample data

Figure 6C depicts a representative Seahorse trace for a standard assay which measures complex I, II, and IV in mouse liver homogenates. Figure 6C-I and C-II highlight the complex I NADH peak and complex II succinate + rotenone peak, respectively. Figure C-IV highlights the complex IV TMPD + ascorbate peaks from the complex I and complex II samples. This Seahorse trace not only has distinct peaks for all substrate injections, but also has strong and distinct responses to the inhibitors (antimycin A and azide) used in the assay, making it an optimal-looking trace.

NORMALIZATION TO MITOCHONDRIAL CONTENT FOR PREVIOUSLY FROZEN TISSUE RESPIROMETRY (OPTIONAL)

The following protocol describes normalization of the results from respirometry samples according to mitochondrial content. Homogenates or mitochondrial isolates (made in Basic Protocol 1) will undergo MitoTracker Deep Red (MTDR) staining and measurement. Using this data, samples can be normalized based on their mitochondrial content rather than using a whole protein measurement.

Materials

- Tissue homogenates or mitochondrial isolates (Basic Protocol 1) or Seahorse sample plate from Basic Protocol 2
- 1 × MAS buffer (see recipe)
- MitoTracker Deep Red FM (MTDR; Thermo, M22426)
- Clear, flat-bottom, black 96-well plate (Corning, 3904 or equivalent)
- Seahorse XF96 flux pack (Agilent 102416-100) including sample plate
- Multichannel pipette
- Refrigerated centrifuge with plate adapter
- Fluorescence plate reader or high-throughput microscope

Normalizing to mitochondrial content

For protein content-based normalization using homogenates or mitochondrial isolates, use the BCA protein data previously generated (in Basic Protocol 1) to load

BASIC
PROTOCOL 3

Osto et al.

9 of 17

equivalent protein amounts in the XF96 Seahorse plate as described in Basic Protocol 2 (Fig. 5B, Method 1). Normalization for mitochondrial content using MitoTracker Deep Red (MTDR) may be performed before or after running the Seahorse sample plate.

While MTDR normalization can be performed at any step after BCA values have been generated, loading onto the Seahorse sample plate is exclusively done based on BCA values. Normalization to mitochondrial content should only be done after oxygen consumption rate (OCR) values are obtained.

Normalizing to mitochondrial content before running a Seahorse experiment (Fig. 5B, Method 2a)

- 1a. Perform protein normalization via BCA assay as described above (Basic Protocol 1).
- 2a. On a clear, flat-bottom, black, 96-well plate, seed 2.5–80 μg of mitochondria or lysate sample (according to protein normalization values) in 100 μl of MAS buffer containing MTDR at 1 μM final concentration.

If your sample material is limited, MTDR normalization may be done in the XF96 sample plate afterwards, or using a sister plate loaded alongside the XF96 sample plate.
- 3a. Incubate the sample plus dye at 37°C for 10 min.
- 4a. Remove the dye by centrifuging the sample 5 min at 2000 $\times g$, 4°C, with no brake for deceleration. Carefully remove the supernatant and resuspend in 100 μl of MAS buffer.
- 5a. Measure fluorescence in a plate reader or high-throughput microscope using a clear-bottom black 96-well plate (Corning 3904 or equivalent). MTDR is excited at 625 nm and emits at 670 nm.
- 6a. Calculate relative mitochondrial content after controlling for background fluorescence using a blank well.

Normalizing to mitochondrial content after running a Seahorse experiment (Fig. 5B, Method 2b)

- 1b. Remove the Seahorse sample plate from the Seahorse machine.
- 2b. Carefully, without agitation of the sample material at the bottom of the Seahorse sample plate, remove the MAS buffer from the plate until approximately 80 μl of liquid remains in each well.
- 3b. Add 20 μl of 5 μM MTDR in MAS buffer to each sample such that each sample now has 100 μl of liquid with a final MTDR concentration of 1 μM .
- 4b. Incubate the sample plus dye at 37°C for 10 min. Ensure that the incubation period is no more than 10 min; too long of an incubation period can result in high background MTDR fluorescence.
- 5b. Add 100 μl of MAS buffer without MTDR to each sample. Remove 100 μl of solution from each well. Perform this washing procedure up to three times.
- 6b. Measure fluorescence in a plate reader or high-throughput microscope.

MTDR is excited at 625 nm and emits at 670 nm.
- 7b. Calculate relative mitochondrial content after controlling for background fluorescence using a blank well. For absolute quantification, use an isolated mitochondria standard.

Table 1 Sample MTDR Plate Reader Assay Data^a

Sample number	Raw absorbance units (AU)	Raw AU – background	µg protein loaded via BCA	(Raw AU – background)/(µg protein)
Background	1940			
1	21540	19600	10	1960
2	19411	17471	10	1747.1
3	23593	21653	10	2165.3
4	36932	34992	10	3499.2
5	41933	39993	10	3999.3
6	18971	17031	10	1703.1
7	34057	32117	10	3211.7
8	39941	38001	10	3800.1
9	49203	47263	10	4726.3

^aThis figure shows an example data set of MTDR readings from mouse liver homogenate samples. The user will be generating data to fill the “raw absorbance units” and “µg protein loaded via BCA” columns of the table. The “raw absorbance units” column will be filled with the absorbance readings from the plate reader or high-throughput microscope taking MTDR measurements. The “µg protein loaded” via BCA will be filled with the amount of protein loaded (calculated via BCA) into the well for the MTDR reading. Using these two values, the final column titled “(Raw AU - background)/(µg protein)” can be calculated by dividing the raw absorbance minus background and the µg protein loaded via BCA. Normalizing your samples based upon the values in this column will result in equivalent sample loading based upon mitochondrial content.

Sample data

Table 1 showcases data from a MTDR plate reader assay to normalize mouse liver by mitochondrial content before loading a Seahorse sample plate. The columns titled “raw absorbance units” and “µg of protein loaded via BCA” will be filled in by the user based on the plate reader results and the amount of protein added to the plate for the MTDR reading (determined via BCA). Dividing the raw absorbance minus the background absorbance and the µg of protein loaded results in the data in the farthest right column entitled “(Raw AU - background)/(µg protein),” which is now a reading of mitochondrial content per µg of protein in the sample. Normalization may then be performed such that the OCR values obtained are normalized to measurements of OCR per mitochondrial content.

REAGENTS AND SOLUTIONS

MAS buffer, 1×

- 70 mM sucrose (Fisher, L-12686)
- 220 mM mannitol (Sigma, M9546)
- 5 mM KH₂PO₄ (Sigma, P5655)
- 5 mM MgCl₂ (Sigma, M0250)
- 1 mM EGTA (Sigma, E4378)
- 2 mM HEPES (Corning, 25-060-CI)

Adjust to pH 7.4 using potassium hydroxide (KOH) or hydrochloric acid (HCl). Store up to 1 year or longer at –20°C.

COMMENTARY

Background Information

Mitochondrial respiration results in the transfer of electrons between electron transport chain complexes I, II, III, and IV, with

complex IV reducing oxygen to water. With oxygen playing a primary and crucial role in the process, respirometry platforms like the Seahorse or Oroboros use the measurement

Osto et al.

11 of 17

of oxygen consumption rate as a surrogate marker for mitochondrial activity. Current mitochondrial respirometry techniques for *in vivo* samples require that the processing and measurement of the living tissue sample happen within an hour of isolation from the specimen. This requirement is set by the need to preserve the integrity of the inner mitochondrial membrane, needed both for integrated electron transfer between the complexes as well as to preserve the coupling of electron transfer to ATP synthesis. Although freeze-thawing disrupts and permeabilizes the mitochondrial inner membrane, our novel respirometry method overcomes this challenge to allow for previously frozen tissue samples to be measured. Mitochondrial supercomplexes remain intact despite freeze-thawing; therefore, we have developed a set of substrates that are capable of measuring complex I, II, and IV through measurement of these supercomplexes. While this assay cannot measure coupled mitochondrial respiration, as can be done in fresh tissue respirometry, freezing tissues allows for long-term tissue storage and simplified sample processing through use of tissue homogenates, thereby enabling respirometry experiments that are less time-intensive, require less tissue processing, and are less expensive, facilitating large-scale respirometry research studies when compared to current respirometry methods.

Critical Parameters

Multiple parameters within this methodology are critical to obtaining good results from your respirometry run. In Basic Protocol 1, the most critical parameter to success is the homogenization step. If there is too little homogenization, mitochondria will not be released from the cell, resulting in low yield; too much homogenization might impact the mitochondrial supercomplexes. We have provided guidelines for the types of homogenizers and the number of strokes required for different tissues, but this could be a variable to optimize if you are getting suboptimal mitochondrial yield from your tissue samples.

Basic Protocol 2 is likely the part of the procedure that is most sensitive to certain experimental parameters. The most important parameter in this basic protocol is that centrifugation steps be done with the centrifuge brake turned OFF. Braking during deceleration of the centrifuge can result in an uneven distribution of the sample across the bottom of the Seahorse sample plate, adversely effecting OCR results and reproducibility. A centrifuge

with the capability of having the brake turned off is necessary for best performance in this assay. An additional variable to consider for this part of the assay is how much sample is being loaded onto the sample plate. Too little sample and OCR values will be very low, but having too much sample can result in oxygen depletion and inconsistent responses to the compound injections (diagnosing these issues is discussed in the Troubleshooting, below). We recommend titrating your sample material to find the optimal loading concentrations that provide the best Seahorse results.

Basic Protocol 3 has few parameters that are critical to results, but it must be noted that while normalization to mitochondrial content is optional, it provides an additional analysis technique that may explain differences in respiration due to samples having differing numbers of mitochondria. An example of where this may be impactful is if two samples have the same OCR reading, but one sample has fewer mitochondria that have higher respiratory capabilities and the other has many mitochondria that have low respiratory capabilities. In this scenario, normalizing the data to mitochondrial content could elucidate these differences.

Troubleshooting

This troubleshooting section is designed to account for issues specific to frozen tissue respirometry, although traditional Seahorse troubleshooting techniques will likely also apply to this technique. Figure 6C displays a representative Seahorse trace for a standard assay measuring complexes I, II, and IV in liver homogenates. Table 2 describes factors that may cause poor respirometry results. Additionally, this table catalogs how to diagnose these errors and the potential solutions to improve respirometry sample performance. This protocol was initially optimized for frozen liver respirometry, but many other tissue types have been successfully tested using this procedure, with some modifications. Table 3 compiles some of the potential optimizations in tissue collection and respirometry when using alternative tissue types with this protocol. Further examples of respirometry results using alternative tissue types including Seahorse traces can be found in Acin-Perez et al. (2020); also see Table 3.

Statistical Analysis

When the Seahorse run is complete, export the oxygen consumption rates (OCRs) from the Agilent Wave software and (if applicable)

Table 2 Troubleshooting

Observation	Etiology	Solution	Additional confirmation of etiology
Low respiration	Insufficient mitochondrial mass	Remeasure respiration using a larger amount of sample material. Alternatively, using mitochondrial isolates rather than whole tissue homogenate can improve the results when using lower-mitochondrial-mass samples.	Confirm your mitochondrial content using the assays described in Basic Protocol 3
	Homogenate too dilute/low mitochondrial mass to total protein ratio	Concentrating the sample material by centrifuging at very high speeds and resuspending in a lower volume can limit the amount of non-mitochondrial “debris” that may clog the pores of the Seahorse plate. Additionally, titrating the amount of sample loaded into the Seahorse plate may also improve performance.	This can be common in tissues like WAT, which may have a lot of non-mitochondrial “debris” that can block the pores of the Seahorse plate. This phenotype commonly causes high variability between samples, oxygen depletion, and possible lack of response to compound injections.
	Tissue degradation	Ensure that all samples, buffers, and equipment are kept ice-cold during all steps of the procedure to prevent tissue degradation from occurring	Confirm that the mitochondrial supercomplexes of your sample are intact using Blue Native Gel-Electrophoresis (BNE)
	Incomplete uncoupling or permeabilization	Add 10 µg/ml final concentration of alamethicin (or your chosen permeabilization agent) to the assay buffer	Permeability and distribution of some compounds may be limited in samples that contain a large proportion of lipids or membranes.
	Over-permeabilization	Titrate the digitonin until supercomplexes are intact and respiration is elicited with membrane-impermeable substrate NADH	Confirm that the mitochondrial supercomplexes of your sample (after detergent addition) are intact using Blue Native Gel-Electrophoresis (BNE)
	Insufficient cytochrome <i>c</i>	Titrate cytochrome <i>c</i> for your samples	Measure cytochrome <i>c</i> in your preparation and supernatant.
	Excess mitochondrial mass (oxygen depletion)	Down-titrate the amount of sample loaded into the wells to prevent oxygen depletion	Check the oxygen traces generated during the run in the Seahorse software. Sharply declining and/or negative oxygen values (examples shown in Fig. 7A) are associated with oxygen depletion.

(Continued)

Table 2 Troubleshooting, *continued*

Observation	Etiology	Solution	Additional confirmation of etiology
	Mitochondria are not evenly distributed on the bottom of the sample plate	If a centrifuge brake is applied when spinning down the sample plate, it is possible that the mitochondria will not be evenly distributed along the bottom of the wells of the Seahorse plate	Viewing the sample plate under a microscope prior to running the Seahorse will determine if the mitochondria are not evenly distributed along the bottom of the plate
No NADH response	Incomplete permeabilization	Add 10 µg/ml final concentration of alamethicin (or your chosen permeabilization agent) to the assay buffer	
No succinate + rotenone response	Old stocks of succinate/rotenone	Remake the stocks of succinate + rotenone	After prolonged storage, succinate + rotenone may begin to precipitate out of solution
No antimycin A response	Non-mitochondrial respiration	Running a mitochondrial isolation rather than homogenates can be used to reduce or even eliminate non-mitochondrial respiration impacting the results	Incomplete inhibition of OCR by antimycin A can be common in some human samples. This typically represents non-mitochondrial respiration: can impact OCR under antimycin A.
No TMPD/ascorbate response	pH imbalance	Adjust the solution to reach pH 7.4 using HCl and KOH	Test the pH of the TMPD + ascorbate solution to ensure it is pH 7.4
After compound injection, measurement 1 is dramatically different from measurement 2	Oxygen depletion	Down-titrate the amount of sample loaded into the wells to prevent oxygen depletion. Adding a wait or mixing step in between measurement 1 and measurement 2 can allow oxygen levels to equilibrate between measurements to eliminate variability between the two measurements.	Check the oxygen traces generated during the run in the Seahorse software. Sharply declining and/or negative oxygen values (examples shown in Fig. 7A-B) are associated with oxygen depletion.
	NADH depletion	Higher injection concentrations of NADH, multiple NADH injections, or decreasing mitochondrial loading can alleviate potential NADH depletion	For complex I measurement, it is possible that with high mitochondrial loading in certain cell types, NADH depletion may occur after measurement 1
TMPD + ascorbate-induced OCR is lower than complex I/II OCR values	Excess mitochondrial mass	Decrease the amount of sample loaded into the sample plate	Diminished TMPD values can occur as a result of oxygen depletion related to having too much mitochondrial mass loaded

Table 3 Tissue Type Adjustments

Tissue type	Tissue collection/isolation	Respirometry considerations	Approximate loading amounts
Heart	A glass-glass Dounce homogenizer should be used to more thoroughly disrupt the tissue for the best results		1-2 µg
White adipose tissue	A glass-glass Dounce homogenizer should be used to more thoroughly disrupt the tissue for the best results. Spin samples at 20,000 to 25,000 × g to further concentrate the sample and potentially remove the fat from the mitochondria.	Using more concentrated samples can increase rates above baseline and improve response to compounds in the Seahorse plate (Fig. 7C)	10-15 µg
Muscle	Increasing the number of homogenization strokes can improve the results with fibrous tissues like muscle. Alternatively, using collagenase type II at 0.25 mg/ml final concentration during homogenization can aid in the tissue homogenization process.		6-8 µg
Human samples- white adipose tissue, liver, tumor samples, etc.	Human tissues often have more connective tissue and therefore require more strokes with the homogenizer or enzymatic digestion for the best results	Human tissues often respire at lower rates than mouse tissues or cell lines. To compensate for this, more sample should be loaded into the Seahorse plate.	Human liver: 15-20 µg, human adipose tissue: 10-15 µg, human tumor: 8-12 µg
Cell pellets	Alamethicin addition may help further permeabilize the cells. Necessity for further permeabilization is largely cell-type dependent and should be titrated prior to use in respirometry.		Depends on cell type
Brain	Cells from the brain can often be very membrane rich. To compensate for this, alamethicin may be added to further permeabilize the cells for improved respirometry performance.		6-10 µg

normalize by mitochondrial mass (MTDR readings) in Microsoft Excel. Calculate complex I-, II-, and IV-dependent respiration by the following formulas:

a. Maximal respiratory capacity through complex I:

$$OCR_{NADH} - OCR_{antimycin}$$

b. Maximal respiratory capacity through complex II:

$$OCR_{succinate+rotenone} - OCR_{antimycin}$$

c. Maximal respiratory capacity through complex IV:

$$OCR_{TMPD+Ascorbate} - OCR_{azide}$$

Calculating the complex I to complex IV or complex II to complex IV ratio may serve as an alternative measurement of complex respiratory capacity.

Osto et al.

15 of 17

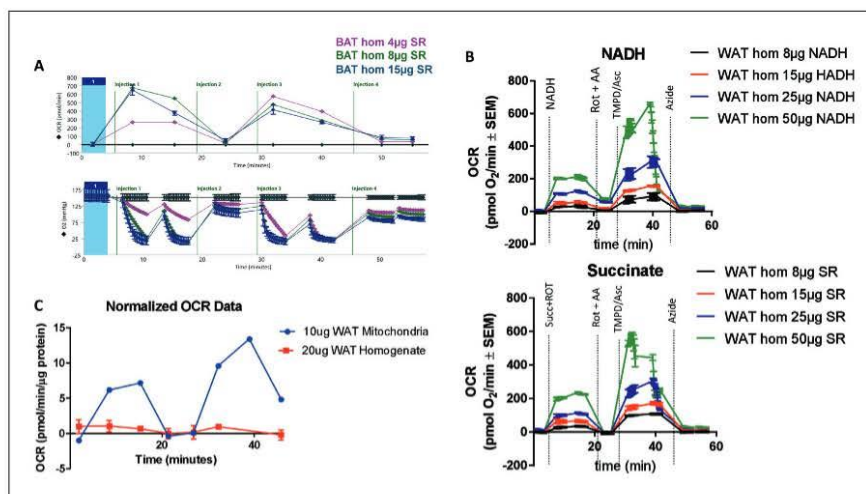


Figure 7 Troubleshooting frozen tissue respirometry Seahorse traces. (A) A brown adipose tissue (BAT) sample exhibiting signs of oxygen depletion. The top graph of A shows OCR, and the bottom graph shows oxygen levels. At 4 µg of loaded sample, oxygen levels deplete linearly for both measurements after injection 1. As more sample is loaded, oxygen depletion becomes less linear, and between the two measurements oxygen levels do not fully recover, both of which are signs of oxygen depletion affecting respiration results. (B) A white adipose tissue (WAT) sample exhibiting inconsistencies between measurement 1 and measurement 2 after compound addition. With 50 µg of WAT loaded, measurement 2 after TMPD/ascorbate addition begins high, but drops dramatically as the measurement cycle continues, ultimately affecting the overall respirometry trace. When the sample input is decreased, measurements normalize and the drop in measured OCR is not observed. (C) A white adipose tissue (WAT) sample measured at 20 µg as a homogenate and measured at 10 µg after concentrating the sample by pelleting the sample and resuspending in a lower volume.

Understanding Results

Figure 6C exhibits a representative Seahorse trace. The trace in red corresponds to a complex I peak (Figure 6C-I) followed by a complex IV peak (Figure 6C-IV) induced by NADH and TMPD/ascorbate, respectively. The trace in blue corresponds to a complex II peak (Figure 6C-II) followed by an additional complex IV peak (Figure 6C-IV) induced by succinate/rotenone and TMPD/ascorbate, respectively. This sample responds to all substrate and inhibitor injections and has relatively low standard deviations for each measurement across the three replicates tested. When analyzing the data, the primary data points of importance will be Figure 6C.D, the complex I respiration induced by NADH addition, Figure 6C.C-II, the complex II respiration induced by succinate addition, and Figure 6C.C-IV, the complex IV respiration induced by TMPD + ascorbate addition. The measurements after antimycin A injection and azide injection are used primarily as background controls where the antimycin A measurement represents any respiratory activity not produced by the non-mitochondrial respiration

of the electron-transport chain complexes, and the azide measurement represents any non-mitochondrial respiratory activity still in the sample. Figure 7 showcases Seahorse traces which are not ideal. The Troubleshooting section, above, describes potential reasons for why certain traces may look like those in Figure 7.

Time Considerations

Basic Protocol 1 will take approximately 2 hr for 15 samples, not including dissection of the tissue of interest from the specimen (the time to do this will depend on the specimen and tissue being used). This time is largely based on manual homogenization of the samples; an automated system of tissue homogenization could dramatically decrease the sample processing time, although these methods would need to be optimized for the purpose of this assay. Basic Protocol 2 will take approximately 2 hr to set up for 15 samples, then the Seahorse run will take approximately 90 min, with no user input required. This process could be easily scaled up for more samples with multiple Seahorse instruments, where larger

volumes of each compound injection could be made for multiple Seahorse cartridges. Basic Protocol 3 will take approximately 30-60 min for 15 samples. In total, 15 samples will take approximately 6 hr, although this time can be split between 1 day of sample processing and storage and 1 day of running the Seahorse assay.

Acknowledgments

A special thanks to all authors and contributors involved in Acin-Perez et al. (2020) for the foundational work surrounding this assay. The authors would like to thank Alexandra Brownstein and Shai Rambod as well as Drs. Ajit Divakaruni, Michael Shum, Daniel Dagan, Evan Taddeo, Alex Van der Blik, Jose Antonio Enriquez, and Amy Wang for scientific discussions and valuable advice. This work was supported by UAB-UCSD O'Brien Center P30 DK079337 (VMDU), UAB Nathan Shock Center P30 G050886 (VMDU), HL110349 (RT), U54 DK120342 (KR and LV), R56AG060880 (JW), R01AG055518 (JW), K02AG059847 (JW), R21AR072950 (JW), UCLA Older Americans Independence Center P30AG028748 (JW), R01DK099618-05 (OSS), R01CA232056-01 (OSS), R21AG060456-01 (OSS), R21AG063373-01 (OSS), ADA Grant No. 1-19-IBS-049 (OSS), R01AA026914-01A1 (ML), and Swiss National Science Foundation Grant No. 320030_170062 (FA). This work was supported by the NIH grant number 1R41ES031043-01A1.

Author Contributions

Corey Osto: Conceptualization; data curation; formal analysis; methodology; project administration; visualization; writing-original draft; writing-review & editing. **Ilan Y. Benedor:** Conceptualization; data curation; formal analysis; investigation; methodology; project administration; writing-original draft; writing-review & editing. **Jennifer Ngo:** Data curation; visualization;

writing-original draft; writing-review & editing. **Linsey Stiles:** Conceptualization; data curation; formal analysis; investigation; methodology; project administration; supervision; validation; writing-original draft; writing-review & editing. **Rebeca Acin-Perez:** Conceptualization; data curation; formal analysis; investigation; methodology; project administration; supervision; validation; writing-original draft; writing-review & editing. **Marc Liesa:** Conceptualization; funding acquisition; methodology; project administration; resources; writing-review & editing. **Orian Shirihai:** Conceptualization; funding acquisition; methodology; project administration; resources; supervision; writing-review & editing.

Literature Cited

- Acin-Perez, R., Benador, I. Y., Petcherski, A., Veliova, M., Benavides, G. A., Lagarrigue, S., ... Shirihai, O. S. (2020). A novel approach to measure mitochondrial respiration in frozen biological samples. *The EMBO Journal*, *39*(13), e104073. doi: 10.15252/embj.2019104073.
- Donovan, J., & Brown, P. (2006). Euthanasia. *Current Protocols in Immunology*, *73*, 1.8.1-1.8.5. doi: 10.1002/0471142735.im0108s73.
- Liesa, M., Palacín, M., & Zorzano, A. (2009). Mitochondrial dynamics in mammalian health and disease. *Physiological Reviews*, *89*(3), 799-845. doi: 10.1152/physrev.00030.2008.
- Wallace, D. C. (2011). Bioenergetic origins of complexity and disease. *Cold Spring Harbor Symposium on Quantitative Biology*, *76*, 1-16. doi: 10.1101/sqb.2011.76.010462.

Internet Resources

<https://www.agilent.com/en/products/cell-analysis/how-to-run-an-assay>

The Agilent Seahorse website provides valuable information on the reagents and equipment required for a standard Seahorse assay. Our protocol encompasses many of the special considerations to be made for a Seahorse run using previously frozen tissue, but Agilent provides a protocol for a standard Seahorse assay on their website.

Appendix III

Parkin Regulates Adiposity by Coordinating Mitophagy with Mitochondrial Biogenesis in White Adipocytes.

The work describe in this chapter has been submitted to Nature Metabolism and is currently under revision:

Timothy M. Moore, Lijing Cheng, Dane M. Wolf, Jennifer Ngo, Mayuko Segawa, Xiaopeng Zhu, Alexander R. Strumwasser, Yang Cao, Bethan L. Clifford, Alice Ma, Philip Scumpia, Orian Shirihai, Thomas Q de Aguiar Vallim, Markku Laakso, Aldonis J. Lusic, Andrea L. Hevener, Zhenqi Zhou (2021) Parkin regulates adiposity by coordinating mitophagy with mitochondrial biogenesis in white adipocytes. *Nature metabolism*

*contributed equally

Copyright 2021

Nature Metabolism

Parkin Regulates Adiposity by Coordinating Mitophagy with Mitochondrial Biogenesis in White Adipocytes

Timothy M. Moore^{1, #}, Lijing Cheng^{2, #}, Dane M. Wolf³, Jennifer Ngo³, Mayuko Segawa³, Xiaopeng Zhu⁴, Alexander R. Strumwasser³, Yang Cao¹, Bethan L. Clifford¹, Alice Ma³, Philip Scumpia², Orian Shirihai³, Thomas Q de Aguiar Vallim^{1, 5}, Markku Laakso⁶, Aldons J. Lusis^{1, 7}, Andrea L. Hevener³, Zhenqi Zhou^{3, 8*}

¹Division of Cardiology, Department of Medicine, University of California, Los Angeles, California USA 90095 USA

²Division of Dermatology, Department of Medicine, University of California, Los Angeles, California USA 90095 USA

³Division of Endocrinology, Diabetes, and Hypertension, Department of Medicine, University of California, Los Angeles, California USA 90095 USA

⁴Division of Pediatric Endocrinology, Department of Pediatrics UCLA Children's Discovery and Innovation Institute, Department of Medicine, University of California, Los Angeles, California USA 90095 USA

⁵Department of Biological Chemistry, David Geffen School of Medicine, University of California, Los Angeles, California USA 90095 USA

⁶Institute of Clinical Medicine, Internal Medicine, University of Eastern Finland and Kuopio University Hospital, Kuopio, Finland

⁷Department of Human Genetics, David Geffen School of Medicine, University of California, Los Angeles, California 90095 USA

⁸Molecular Biology Institute, University of California, Los Angeles, California 90095 USA

These authors contributed equally

* Correspondence

Dr. Zhenqi Zhou
UCLA
Division of Endocrinology, Diabetes, and Hypertension
Department of Medicine
650 Charles E. Young Dr. S. CHS 33-260
Los Angeles, CA 90095
zhenqizhou@mednet.ucla.edu

SUMMARY

Parkin, an E3 ubiquitin ligase, plays an essential role in mitochondrial quality control. However, the mechanisms by which Parkin connects mitochondrial homeostasis to cellular metabolism in adipose tissue remain unclear. Here, we demonstrate that *Park2* gene (encodes Parkin) deletion specifically from adipose tissue protects mice against high-fat diet and aging-induced obesity. Despite a mild reduction in mitophagy, mitochondrial DNA (mtDNA) content and mitochondrial function are significantly increased in *Park2* deficient white adipocytes. Moreover, *Park2* gene deletion robustly elevates mitochondrial biogenesis by increasing Pgc1 α protein stability through mitochondrial superoxide-activated Nqo1. Both *in vitro* and *in vivo* studies show that Nqo1 overexpression elevates Pgc1 α protein level and mtDNA content and enhances mitochondrial activity in mouse and human adipocytes. Taken together, our findings indicate that Parkin regulates mitochondrial homeostasis by balancing mitophagy and Pgc1 α -mediated mitochondrial biogenesis in white adipocytes, suggesting a potential therapeutic target in adipocytes to combat obesity and obesity-associated disorders.

INTRODUCTION

Mitochondrial dysfunction contributes to the pathogenesis of metabolic disorders such as obesity⁽¹⁾. Mitochondria are highly dynamic organelles that play essential roles in energy metabolism, heat production, generation of oxygen radicals, calcium signaling, and apoptosis⁽²⁻⁶⁾. To maintain metabolic health, mitochondrial selective autophagy (mitophagy), mitochondrial biogenesis, and various mitochondrial protein degradation processes coordinately control the quality of mitochondria^(6,7).

Mitophagy involves the recognition of damaged mitochondria by the autophagosome through microtubule-associated protein 1 light chain 3 (LC3) adapters in ubiquitin-dependent and independent mechanisms^(8,9). PTEN-induced putative kinase 1 (Pink1, encoded by *Park6*) and E3 ubiquitin-protein ligase Parkin are known to function in ubiquitin-dependent mitophagy, while other proteins such as TBC1 domain family member 15 (Tbc1d15) and Nip3-like protein X (Nix) contribute to ubiquitin-independent mitophagy⁽⁹⁻¹²⁾.

Emerging evidence has shown that low mitochondrial content and activity contribute to adipocyte hypertrophy and metabolic disorders⁽¹³⁻¹⁸⁾. Therefore Parkin-mediated mitophagy in adipocytes has attracted increasing attention. Numerous studies indicate that Parkin not only protects mitochondrial function against metabolic stress induced by obesity⁽¹⁹⁾, but also plays an essential role in adipose tissue browning and beige adipocyte thermogenesis⁽²⁰⁻²²⁾. However, how adipose tissue Parkin maintains mitochondrial health and regulates glucose homeostasis in adipose tissue remain inadequately understood^(20,21,23).

Here we sought to determine whether adipose Parkin regulates cellular metabolism and adiposity. To address this, we generated *Park2* knockdown 3T3-L1 preadipocytes (*Parkin^{KD}*) and a mouse model by deleting the *Park2* gene specifically in adipose tissue (*Parkin^{Adi}*). We determined that adipose-specific *Park2* deletion prevents both high-fat diet (HFD) and aging-induced obesity. Mechanistic studies revealed that Parkin deletion slightly impaired mitophagy in adipocytes and elevated mitochondrial superoxide level, which increased the protein level of Nqo1. Moreover, Nqo1 enhances the protein stability of Pgc1 α and accelerates mitochondrial biogenesis. Collectively, our findings suggest a new role for Parkin in regulating mitochondrial homeostasis in white adipocytes and a potential therapeutic target for combating obesity.

MATERIALS AND METHODS

METSIM studies

Genetic association and gene expression analyses were conducted on data collected from the metabolic syndrome in men (METSIM) study as previously described. METSIM adipose array data are available from Gene Expression Omnibus (GSE70353)⁽²⁴⁾. Gene-trait relationships presented here were obtained from 770 male participants (age of 45 to 70 years). All data generated from tissue samples were obtained from previously published studies as reported. No new human samples were acquired for the generation of this manuscript.

Animals

The University of California, Los Angeles Institutional Animal Care and Use Committee approved this study. All animal care, maintenance, surgeries, and euthanasia were conducted in accordance with this Institutional Animal Care and Use Committee and the National Institutes of Health. Parkin floxed mice (a gift from Ted Dawson) were crossed with adiponectin Cre mice (The Jackson Laboratory, #010803) to generate animals with Parkin deletion in adipose tissue specifically (Parkin^{Adi}). Whole body parkin null mice were obtained from the Jackson Laboratory (#006582). Mice were studied under normal chow (NC) and 45 % high fat diet (HFD, Research Diets, D12451)-fed conditions. Mouse sex is indicated in the figure legends for each experiment. Blood was drawn from 6-hour-fasted male mice and analyzed for circulating factors: glucose (HemoCue), insulin, and leptin (Meso Scale Discovery, CA). After a 2-week recovery, intraperitoneal glucose tolerance tests (IPGTT, 1 g/kg dextrose), and intraperitoneal insulin tolerance tests (IPITT, 0.7 U/kg) were performed on male mice following 6 hours fast as previously described⁽²⁵⁾.

Metabolic analysis

Body fat and lean mass were determined by NMR (Bruker). Oxygen consumption, carbon dioxide production, and respiratory exchange ratio were determined using Promethion metabolic screening system (Sable Systems).

Cell culture and transfections

The stromal vascular fraction (SVF) cells from inguinal white adipose tissue (iWAT), eWAT, or BAT of C57BL6/J wild-type mice (The Jackson Laboratory, #000664) were cultured in DMEM/F12 medium with 10 % FBS as described⁽²⁶⁾. Then the cells were cultured 2 days in DM1 medium (DMEM medium, 10 % FBS, 5 µg/ml insulin, 1 µM Dexamethasone, 0.5 mM IBMX, and 1 µM rosiglitazone), 2 days in DM2 medium (DMEM/F12 medium with 10 % FBS plus 5 µg/ml insulin), and 6 additional days in DMS medium. The primary adipocytes from BAT were differentiated in (DMEM/F12 medium with 10 % FBS, 5 µg/ml insulin, 0.5 µM Dexamethasone, 0.125 mM Indomethacin, 1 nM T3, 0.5 mM IBMX, and 1 µM GW1929). 3T3-L1 preadipocytes were cultured cells in DM1 after 100% confluent for two days and in DM2 (DMEM medium, 10 % FBS, and 5 µg/ml insulin) for two days before replacement with DMS (DMEM medium and 10 % FBS) for 2-3 days. Primary human subcutaneous pre-adipocytes were purchased from ATCC (PCS-210-010) and differentiated to adipocytes according to the protocol provided (ATCC, PCS-500-050). Briefly, pre-adipocytes were incubated for 48 hours before initiating differentiation via adipocyte differentiation initiation medium for 96 hours. After this period, cells were cultured in adipocyte differentiation maintenance medium for an extra 3 days then incubated with or without 2×10^7 PFU/ml adenovirus carrying human NQO1 (Vector Biolabs, ADV-217023) for another 5 days. To achieve Park2 knockdown (KD), lentiviral particles carrying shRNA targeted to Park2 or scramble shRNA (Sigma-Aldrich) (multiplicity of infection = 3) were used to transduce 3T3-L1 preadipocytes. To inhibit Nqo1 activity, differentiated adipocytes were treated with the Nqo1 inhibitor (100 µM Dicoumarol, Santa Cruz Biotechnology, CAS66-76-2,) or (400 nM ES936, Santa Cruz Biotechnology, CAS192829-78-3) for 24 hrs. To overexpress Nqo1 in adipocytes (Nqo1^{OE}), 3T3-L1 pre-adipocytes were transfected with pcDNA3-Nqo1-flag (Addgene, #61729) and selected with 500 µg/ml G418 for 4 weeks. Cells were harvested and Nqo1 overexpression was confirmed by immunoblot.

AAV injection

Mice were anesthetized with isoflurane and fixed into a supine position. The midventral line region was shaved and cleaned with ethanol. A 1.5-2 cm midline incision was made in the skin followed by separation of the underlying musculature to expose the epididymal white adipose tissue (eWAT). 2.5×10^{11} GC/ μ l of AAV8-hAdp-m-Nqo1 (AAV8-Nqo1) (Vector Biolabs, AAV-266028) dissolved in 50 μ l of saline was injected directly into the left eWAT. The same amount of control virus (Vector Biolabs, AAV-7077) and saline volume was injected into the other side of eWAT. The body wall was sutured and the wound was closed with wound clips. Animals recovered on a heating pad. To prevent infection, sulfamethoxazole (0.48 mg/ml) and trimethoprim (0.096 mg/ml) via an oral suspension was supplied. Animals were observed daily for any signs of inflammation. 7 days after surgery, the wound clips were removed. Tissues were harvested 4 weeks after virus injection.

Fluorescence microscopy

All imaging was performed using a Zeiss LSM880 confocal microscope. Super-resolution imaging was performed with a 63x apochromat oil-immersion lens and an AiryScan super-resolution detector. All images analysis was performed using Fiji (ImageJ, NIH)⁽²⁷⁾. To quantify mitophagy, adipocytes were transduced with adenoviral mCherry-GFP-Fis1 (a generous gift from Oran Shirihai) for 3 days. The fluorescent signals were captured and analyzed. In studies assessing membrane potential, cells were labeled with MitoTracker Green (MTG; Invitrogen) and Tetramethylrhodamine, Ethyl Ester, Perchlorate (TMRE; Invitrogen). Mitochondrial superoxide was stained by MitoSOX in the live 3T3-L1 adipocytes. Fluorescence was quantified by confocal microscopy and analyzed in Fiji.

ROS Detection

Hydrogen peroxide and superoxide were detected using ROS/superoxide detection assay kit (Abcam, ab139476). Briefly, 3T3-L1 adipocytes were cultured in 96 well plate and incubated in ROS/Superoxide detection solution with or without ROS inducer for 1 hour in the dark. The fluorescent signals were detected by fluorescent microplate reader and standard fluorescein (excitation/emission = 488/520 nm) and rhodamine (excitation/emission = 550/610 nm). The signals were normalized to protein content in each well.

Mitochondrial DNA

Total DNA was extracted from cells using DNeasy Blood and Tissue kit (Qiagen). For mouse adipocytes, primers for mitochondrial encoded cytochrome c oxidase III (mtCO3) for mtDNA and 18S for nuclear DNA were used to assess mtDNA content. The ratio of mtCO3 to 18S was used to determine mtDNA content. For human adipocytes, primers for mitochondrially encoded tRNA leucine 1 for mtDNA and beta-2-microglobulin (B2M) for nuclear DNA were used to determine mtDNA content. The ratio of mtCO3 to 18S was used to determine mtDNA content.

Mitochondrial respiration

Mitochondrial respiration in 3T3-L1 preadipocytes and differentiated adipocytes was measured using an XF96 Extracellular Flux Analyzer (Seahorse Biosciences). Briefly, cells were plated and grown to confluence on a 96-well plate. Measurements of oxygen consumption were made continuously while cells were sequentially treated with oligomycin (ATP synthase inhibitor), FCCP (an uncoupling agent), and rotenone/myxothiazol (inhibitors of complex I /III of the electron transport chain).

Immunoblot analysis

Mouse tissue samples were pulverized in liquid nitrogen and homogenized in RIPA lysis buffer containing freshly added complete EDTA-Free protease (Roche) and Phosphatase Inhibitor Cocktail 2 (Sigma-Aldrich). All lysates were centrifuged and resolved by SDS-PAGE. Samples were transferred to PVDF membranes and subsequently probed with the following antibodies for protein detection: Parkin (Cell Signaling #2132), Pink1 (Cayman Chemicals, #10006283), p62 (Progen Biotechnik GmbH), actin (Santa Cruz Biotechnology, sc-47778), Lc3b (Novus, NB100), GAPDH (Invitrogen, AM4300), F4/80 (Santa Cruz Biotechnology, sc-377009), Pgc1 α (EMD

Millipore, AB3242; Abcam, ab191838; and Abcam, ab106814), Hsp90 (Cell Signaling #4877), OXPHOS (Abcam, ab110413), Nqo1 (Novus, NB200-209; Abcam, ab80588), p53 (Santa Cruz Biotechnology, sc-126), Mono- and polyubiquitinated conjugates recombinant monoclonal antibody (ENZO lifeSCIENCES, ENZ-ABS840), Paris (Abcam, ab130867), total OXPHOS rodent antibody cocktail (Abcam, ab110413), Hmgb1 (Abcam, ab18256), α -Tubulin (Santa Cruz Biotechnology, sc-5286), AlexaFluor 488 goat anti rabbit IgG (Invitrogen, A11088), or AlexaFluor 568 goat anti mouse IgG (Invitrogen, A11004). Densitometric analysis was performed using BioRad Quantity One image software (Bio-Rad).

Co-immunoprecipitation

3T3-L1 adipocytes (approximately 1.7×10^7 cells / each) were lysed in the lysis buffer (10 mM Hepes-KOH, pH 7.9, 0.5% NP-40, 140 mM NaCl, 10 mM KCl, 1.5 mM MgCl₂ and protease inhibitors) by dounce on ice. The lysate was centrifuged at 16,000 g for 15 min at 4°C, and the resulting supernatant was used for immunoprecipitation. After preincubation of each supernatant with 20 μ l of Protein A/G magnetic beads (Thermo Scientific, Cat #: 88802) at 4°C for 1 hour the pre-cleared supernatant was incubated with 4 μ g anti-Pgc1 α antibody and 30 μ l Protein A/G magnetic beads at 4°C overnight with rotation. After washing 4 times with lysis buffer, the bound proteins were eluted from the beads by boiling in SDS sample buffer. The eluted proteins were analyzed by Western blotting as described above.

Protein synthesis assay

Protein synthesis was determined by using Protein Synthesis Assay Kit (Cayman chemical, Cat # 601100). Briefly, differentiated adipocytes were treated with O-Propargyl-Puromycin (OPP) working solution and followed with cell-based assay fixative buffer. Washed adipocytes were incubated with 5 FAM-Azide staining solution for 30 minutes at room temperature. Nuclei were stained with Hoechst 33342 for 10 minutes. FITC (excitation/emission = 485/535 nm) signal was detected by a fluorescent plate reader. Nuclei were counted by the Operetta high content imaging system (PerkinElmer).

Immunohistochemistry

Formalin fixed adipose tissues were sectioned and stained for H&E. Following deparaffinization, rehydration, heat-induced epitope retrieval, and permeabilization, slides were blocked with 5 % BSA and incubated with the antibody F4/80 antibody overnight inside a humidified chamber at 4°C. After incubating with the goat anti-mouse IgG-Alexa Fluor 568 for 1 hour at room temperature. Images were captured under fluorescent microscope (Zesis).

Quantitative RT-PCR

Mouse tissue samples were homogenized using Trizol reagent and RNA was isolated using RNeasy Mini QIAcube Kit with DNase digestion (Qiagen). For RNA isolation from cells, lyses occurred using RLT buffer (Qiagen) with 2-Mercaptoethanol. RNA was isolated from lysed cells using the RNeasy Plus kit per the manufacturer's instructions. cDNA synthesis was performed using 1 μ g of RNA with iSuperscript reverse transcriptase (Bio-Rad). PCR reactions were prepared using PowerUp SYBR Green Master Mix (Applied Biosystems). All PCRs are performed in a Quantstudio 5 Real-Time PCR system (Applied Biosystems). Quantification of a given gene, expressed as relative mRNA level compared with control, was calculated after normalization to a standard housekeeping gene (18S or ACTIN). Primer pairs were designed using Primer 3 Input software (Version 0.4.0) or previously published sequences. Primer sets were selected spanning at least one exon-exon junction when possible and were checked for specificity using BLAST (Basic Local Alignment Search Tool, NCBI). The specificity of the PCR amplification was confirmed by melting curve analysis ensuring that a single product with its characteristic melting temperature was obtained. See Table S1 for a list of the primers used.

RNA Sequencing and Analysis

A homogenous portion of frozen adipose samples were homogenized using a tissue homogenizer in Trizol. RNA was isolated using the Qiagen RNeasy Mini QIAcube Kit following the manufacturer's instructions. Isolated RNA was checked for concentration using a NanoDrop and

purity using the Agilent TapeStation. Only samples with RIN > 7.0 were used. Libraries were prepared using the KAPA mRNA HyperPrep Kit following the manufacturer's instructions. The resulting libraries were combined into two pools and sequenced on an Illumina HiSeq 3000 within the UCLA TCGB core facility following in house established protocols. Raw reads were checked for quality using FastQC, aligned to the Mus musculus GRCm38, and then counted using Mus musculus GRCm38 version 97. Alignment and counting occurred using Rsubread v 2.4.2⁽²⁸⁾. Raw counts were then analyzed for differential gene expression using the DESeq2 v1.30.0⁽²⁹⁾.

Statistics

Values presented are expressed as means \pm SEM unless otherwise indicated. Statistical analyses were performed using Student's t-test when comparing two groups of samples or one-way analysis of variance (ANOVA) with Tukey's post hoc comparison for identification of significance within and between groups using GraphPad Prism 9 (GraphPad Software). Significance was set a priori at $P < 0.05$. For RNA Sequencing analysis, significance was set as FDR < 0.05.

RESULTS

Parkin is elevated during adipogenesis.

Mitophagy, the degradation of mitochondria by autophagic machinery, controls beige adipocyte maintenance⁽²¹⁾. However, the role of mitophagy in white adipocytes and how it relates to adiposity are not well elucidated. We identified over 70 single nucleotide polymorphisms (SNPs) near or within the human *PARK2* gene (encodes Parkin protein) positively associate with BMI in a series of genome-wide association studies (GWAS) from PhenoScanner (a database of human genotype-phenotype associations)^(30,31). Therefore, we examined whether mitophagy-related genes *Park2* and *Park6* (encodes Pink1 protein) are altered during murine adipocyte differentiation. We found both *Park2* and *Park6* genes were markedly elevated during the differentiation of 3T3-L1 and 10T1/2 cells as well as in primary adipocytes of iWAT and brown adipose tissue (BAT) (Figures 1A-B, S1A-B). Consistently, Parkin protein levels were increased in mature adipose tissues (iWAT and eWAT) and differentiated adipocytes in multiple fat depots (Figures 1C-E). To determine whether Parkin level is elevated during diet-induced adipogenesis, we fed both male and female wild-type (WT) mice with HFD for 6 weeks. Parkin protein level was only elevated in eWAT of male, but not female WT mice (Figures. 1F-G, S1C-D). Increased *Park2* gene expression during the differentiation of 3T3-L1 cells indicates potentially enhanced Parkin-mediated mitophagy. However, this finding was not accordant with elevated mtDNA content that we and others have found (Figure S1E)^(32,33). These potentially conflicting findings suggest that Parkin may be involved in the dynamic regulation of mitochondrial homeostasis during adipogenesis.

Parkin deletion in adipose tissue prevents HFD and aging-induced obesity.

To investigate the role of Parkin in adipogenesis, we studied both female and male whole-body Parkin knockout mice (Parkin^{KO}). Only male Parkin^{KO} mice showed reduced body weight and fat mass (Figures S2A-D), indicating a sexual dimorphism with the respect to the role of Parkin in regulating fat mass. Therefore, we will exert the following experiments on male mice. To further explore the role of Parkin in male adipose tissue, we generated adipose tissue-specific *Park2* knockout mice (Parkin^{Adi}). Parkin protein levels were reduced in the adipose tissue of Parkin^{Adi} mice but not in liver and skeletal muscle even after HFD feeding (Figures S2E-G). We found body weight and fat mass were significantly lower than the control *fff* mice after HFD feeding, suggesting that Parkin depletion in adipose tissue is protective against diet-induced obesity (Figures 2A-B, and S2H-I). Both glucose tolerance and insulin tolerance were improved in Parkin^{Adi} mice (Figures 2C-D). Moreover, histological analysis of the adipose tissue indicates a reduction in adipocyte area in eWAT, iWAT, and BAT (Figure 2E, S2J).

To understand the impact of Parkin deletion on transcriptome in white adipose tissue, we performed RNA-seq and enrichment analysis on eWAT from HFD-fed control *fff* and Parkin^{Adi} mice. The downregulated genes were enriched in immune-related pathways and biological processes, including macrophage migration and leukocyte regulation (Figure. 2F). Indeed, we confirmed reduced macrophage infiltration in the eWAT of Parkin^{Adi} mice by immunofluorescent staining of F4/80 (Figure. 2G). Gene expression of several pro-inflammatory factors including *Tnfa*, *Mcp1*, and *F4/80* in eWAT as well as pro-inflammatory cytokine Il-6 in the plasma were dramatically reduced in Parkin^{Adi} vs. control *fff* mice (Figures S2K-L).

Parkin mediated mitophagy is pivotal for metabolic health^(34,35). Although Parkin^{Adi} mice show reduced fat weight gain during HFD-feeding compared to control *fff* mice, the long-term effects of Parkin deletion under normal dietary conditions is unknown. To examine the impact of adipose tissue Parkin throughout life, we investigated whether this genetic manipulation would impact aging-associated weight gain. Parkin^{Adi} mice showed a reduction in body weight throughout adulthood without perturbation of lifespan (Figure S2M). Although adipocyte size was not altered between genotypes, Parkin^{Adi} mice showed improved glucose and insulin tolerance (Figures S2N-

Q). Taken together, adipose tissue-specific Parkin deletion prevents both HFD-feeding and aging-induced adiposity and disrupted glucose homeostasis.

Loss of Parkin in BAT fail to prevent HFD-feeding induced obesity.

Cold stress stimulates mitophagy in brown adipose tissue (BAT) ^(22,36,37). Consistently, we found cold stress strikingly increased *Ucp1* gene expression but decreased *Park6* and *Park2* gene expression in BAT (Figure S3A). Because we found *Parkin*^{Adi} mice had higher body temperature at 2 months of age (Fig. S3B), we would like to illustrate the role of Parkin in BAT using brown adipose tissue-specific Parkin knockout mouse model (*Parkin*^{BAT}). Parkin protein levels were reduced in BAT and iWAT but not in other tissues (Fig. S3B). Although mtDNA content was significantly increased in BAT of *Parkin*^{BAT} mice, fat mass and glucose homeostasis were not different between genotypes (Figures S3D-F), suggesting that Parkin expression in BAT does not contribute to the lean phenotype and improved glucose homeostasis observed in *Parkin*^{Adi} and *Parkin*^{KO} mice.

Parkin deletion increases energy expenditure and mitochondrial activity.

To elucidate the mechanisms by which Parkin controls metabolism, we performed indirect calorimetry and found increased oxygen consumption and energy expenditure but reduced RER during the dark phase in body weight-matched *Parkin*^{Adi} vs. control *fff* mice (Figures S4A-B). This occurred independent of food intake, water consumption, and total physical activity (Figures S4A-D and S4C-I).

Reduced RER in *Parkin*^{Adi} mice suggests an increased utilization of lipid for energy production. This observation led us to further analyze the lipid metabolism in the adipose tissues. We found that lipid transfer gene *Mtp*, lipid synthesis genes (*Srebp1c* and *Acc1*), and fatty acid oxidation genes (*Ppara*, *Cpt1a*, *Cpt1b*) were significantly increased in eWAT of *Parkin*^{Adi} vs. control *fff* mice (Figure 3E). In addition, the protein levels of phosphorylated hormone-sensitive lipase (HSL) at Ser563 were robustly elevated in the eWAT of *Parkin*^{Adi} mice (Figure 3F). Collectively, Parkin deletion alters the gene expression that impact lipid synthesis and oxidation in eWAT and could suggest alterations in mitochondrial oxidative metabolism.

We and others have shown that mitochondrial mass and function are impaired in the context of obesity and type-2 diabetes in humans and rodents ^(1,15,25) (Figures 3G-H and S4J). Furthermore, we found that both mtDNA encoded genes and mtDNA copy number were elevated regardless of diet or fat pad depot in *Parkin*^{Adi} compared with control *fff* mice (Figures 3I-J; Figure S4K-L). To explore the impact of Parkin deletion on mitochondrial function, we knocked down the *Park2* in 3T3-L1 cells (*Parkin*^{KD}) and found mtDNA copy number was increased 2.3 folds in *Parkin*^{KD} vs. control (Scr) adipocytes (Figure S4O and 3K). Increased mtDNA copy number was also observed in the eWAT of whole-body Parkin knockout mice (*Parkin*^{KO}) (Figures S4M-N and S4P).

Consistent with our mouse studies, *Parkin*^{KD} adipocytes also displayed a reduction in lipid levels (Figure S4Q). Moreover, increased mitochondrial oxygen consumption rate in both *Parkin*^{KD} preadipocyte and adipocytes measured by Seahorse XF analyzer indicates mitochondrial function was enhanced as a consequence of Parkin reduction (Figure 3L). We also observed a dramatic increase in mitochondrial membrane potential and aspect ratio (Figures 3M and S4R), reflecting a healthy mitochondrial population in *Parkin*^{KD} adipocytes. Taken together, our in vitro and in vivo findings confirm our observation in mice that reduction in Parkin expression promotes mitochondrial function in adipocytes.

Parkin mediates both mitophagy and mitochondrial biogenesis in adipocytes.

Mitochondrial content is regulated by a balance between mitophagy and mitochondrial biogenesis⁽⁸⁾. Because mitophagy relies on the autophagic machinery and our data suggests lacking Parkin impacts mitochondrial abundance and function, we next examined the protein

levels of autophagy makers p62 and LC3BI/II. Only p62 protein was reduced but no change of the protein levels of LC3BI and LC3BII in the eWAT of HFD-fed Parkin^{A^{di}} vs. control *f/f* mice (Figure 4A-B). Red fluorescent protein (RFP) signal is typically maintained despite the acidic lysosomal environment (pH 4 to 5) whereas green fluorescent protein (GFP) loses fluorescence in this pH range^(38,39). Using the adenoviral GFP-mCherry-Fis1, we assessed the turnover of mitochondria by lysosome and observed a decreased number of mitolysosome puncta indicating a reduction of mitophagy in Parkin^{KD} vs. control (Scr) adipocytes (Figure 4C-D). Next, we accessed the protein levels of mitochondrial biogenesis markers. Surprisingly, the protein level of Pgc1 α was strikingly elevated in both eWAT of HFD-fed Parkin^{A^{di}} mice and Parkin^{KD} adipocytes compared with controls (Figure 4E-F). Outer mitochondrial membrane protein Vdac1 and Sdhb were also significantly elevated in Parkin^{A^{di}} mice (Figure 4E). Because the gene expression of Pgc1 α was not changed in eWAT of both NC and HFD-fed Parkin^{A^{di}} mice (Figure 3I), we hypothesized that Parkin deletion may promote post-translational modification of Pgc1 α to enhance the protein stability. Next, we blocked protein synthesis with cycloheximide (CHX) and determined that the protein level of Pgc1 α was elevated in Parkin^{KD} adipocytes (Figure 4G). These findings suggest that Parkin may control mitochondrial homeostasis by coordinating mitophagy with mitochondrial biogenesis in adipocytes.

Elevated Nqo1 stabilizes Pgc1 α protein in Parkin knockdown adipocytes.

To identify the mechanisms underlying Pgc1 α protein stability in the context of Parkin knockdown, we investigated the impact of Nqo1 expression on Pgc1 α in adipocytes, as Nqo1 was previously shown to modulate Pgc1 α protein⁽⁴⁰⁾. Both the protein and mRNA levels of Nqo1 were elevated in eWAT of HFD-fed Parkin^{A^{di}} mice and Parkin^{KD} adipocytes (Figures 5A-D). Similar to Pgc1 α , Nqo1 protein stability was also significantly elevated in Parkin^{KD} adipocytes following treatment with the protein synthesis inhibitor cycloheximide (CHX) (Figure 5E).

Nqo1 is known to interact with Pgc1 α in an NADH-dependent manner⁽⁴⁰⁾. To confirm the protein association of Pgc1 α and Nqo1 in adipose tissues, we performed co-immunoprecipitation using eWAT protein lysates of WT mice. We determined that Pgc1 α associates with Nqo1 in white adipose tissues (Figure 6F). To further confirm Nqo1 preserves the protein level of Pgc1 α , we next tested whether pharmacological inhibition of Nqo1 activity or genetical knocking down Nqo1 in adipocytes could decrease the protein level of Pgc1 α . We treated adipocytes with the Nqo1 inhibitors Dicoumarol or ES936 and observed that Pgc1 α protein was decreased in Parkin^{KD} adipocytes compared with untreated (Figures 5G and S5A). Nqo1 and Parkin double knock down reduced the protein level of Pgc1 α in Parkin^{KD} preadipocytes, although this difference did not reach statistical significance (Figure S5B). Furthermore, we found Nqo1 inhibitor Dicoumarol increased the protein ubiquitination of Pgc1 α in 3T3-L1 adipocytes (Figure 5H). Together, our findings suggest Pgc1 α associates with Nqo1 in white adipose tissue and increased Nqo1 protein stabilizes Pgc1 α protein in adipocytes with reduced Parkin expression.

Mitochondrial superoxide increases Nqo1 and Pgc1 α in Parkin deleted adipocytes.

Because Nqo1 is induced by oxidative stress⁽⁴¹⁻⁴³⁾, we examined oxidative stress in Parkin^{KD} adipocytes and determined that superoxide levels were significantly increased (Figures 5I and S5C). Since mitochondria are a primary source of superoxide, we treated Parkin^{KD} adipocytes with Menadione, a redox-cycling quinone that produces toxic levels of mitochondrial superoxide, Menadione increased protein levels of both Nqo1 and Pgc1 α in adipocytes (Figure 5J). Moreover, H₂O₂ administration could also elevate the protein levels of both Nqo1 and Pgc1 α in 3T3-L1 adipocytes at 50-100 μ M (Figure 5K). However, N-acetyl cysteine (NAC), which generates hydroperosulfides with direct antioxidation activity, did not change the protein levels of Nqo1 and Pgc1 α in adipocytes (Figure S5D). MitoQ, a mitochondrial-matrix-targeted antioxidant, suppressed the protein levels of both Nqo1 and Pgc1 α (Figures 5L and S5E). In response to low-dose of oxidative stress, Nrf2 induces the expression of cytoprotective genes such as Nqo1⁽⁴⁴⁾.

Indeed, Nrf2 gene expression is elevated in eWAT of Parkin^{Adi} mice (Figure S5F), suggesting elevated superoxide activates Nrf2-induced Nqo1, which enhances Pgc1 α protein stability in Parkin deleted adipocytes.

Nqo1 overexpression elevates Pgc1 α protein level in adipocytes.

We and others have found that Nqo1 gene expression is positively associated with adiposity in humans and mice (Figures S6A and S7A-B)⁽⁴⁵⁾. However, a recent study show that whole-body Nqo1 transgenic mice prevented HFD-induced obesity and insulin resistance⁽⁴³⁾, suggesting Nqo1 gene expression may not be concordant with its protein level. Indeed, we found that Nqo1 gene expression, but not the protein level, was significantly increased in eWAT of Ob/+ mice (Figures 6A-B). To investigate the impact of Nqo1 expression on mitochondrial function and lipid metabolism, we overexpressed Nqo1 in 3T3-L1 adipocytes (Nqo1^{OE}). We observed a reduction of lipid levels that corresponded with an increased expression of mtDNA-encoded genes, Pgc1 α mRNA and protein levels, mitochondrial proteins, mtDNA content, and mitochondrial oxygen consumption rate in Nqo1^{OE} adipocytes (Figures 6C-G and S6B). Nqo1 overexpression did not change mitochondrial membrane potential, but strikingly altered mitochondrial morphology by diminishing mitochondrial aspect ratio (the ratio between centerline length and average width) (Figures S6C-D). To determine the impact of Nqo1 overexpression upon adipogenesis, we profiled adipogenesis gene expression and found a dramatic suppression of *C/EBpa*, *Fabp4*, *Adiponectin*, and *Leptin* in Nqo1^{OE} vs. control (Scr) adipocytes (Figure S6E). Additionally, both Nqo1 protein stability and mitophagy were elevated, while protein synthesis was decreased in Nqo1^{OE} adipocytes (Figures S6F-H).

To explore the role of Nqo1 *in vivo*, we contralaterally injected AAV8-Control or AAV8-Nqo1 into eWAT of HFD-fed WT mice so that each mouse served as its own control (Figure 6H). AAV8-Nqo1 significantly decreased adipocyte area, elevated Sdhb and Ndufb8 protein levels, mtDNA content, and mtDNA encoded genes (Figures 6I-M, S6I-J).

Overexpression of NQO1 in human adipocytes increases PGC1 α protein and improves mitochondrial respiration.

Human adipose NQO1 gene expression positively associates with PARK2 gene expression in the Metabolic Syndrome in Men (METSIM) study (Figure 7A). Therefore, we overexpressed human NQO1 in differentiated human subcutaneous adipocytes with adenoviral NQO1-IRES-GFP (Ad-NQO1). Ad-NQO1 not only robustly elevated NQO1 protein, but also increased the protein level of PGC1 α (Figures 7B, S7C). Consistent with the findings from Nqo1^{OE} adipocyte and AAV8-Nqo1 injected mice, NQO1 overexpression in human adipocytes also significantly elevated mtDNA content and basal mitochondrial activity and mildly decreased lipid levels (Figures 7C-7D, S7D-S7E). Furthermore, elevated NQO1 also suppressed the adipogenesis gene *C/EBpa* (Figure 7E). Altogether, our findings suggest that NQO1 controls mitochondrial function and *C/EBpa* expression that contribute to the inhibition of adipogenesis in human adipocytes.

DISCUSSION

In this study, we provide evidence that the E3 ubiquitin protein ligase Parkin controls mitochondrial homeostasis in human and rodent white adipocytes. Beyond its regulatory role in mitophagy, Parkin prevents the turnover of the mitochondrial biogenesis master regulator Pgc1 α through Nqo1 in white adipocytes. Stabilized Pgc1 α protein drives increased mitochondrial abundance and function which combats HFD- and aging-induced obesity.

Mitochondrial homeostasis, regulated by a balance of mitophagy and mitochondrial biogenesis, involves in the pathogenesis of obesity and other metabolic disorders⁽⁸⁾. Consistent with other published work, we obtained the paradoxical result that both mitochondrial number and mitophagy protein Parkin were increased during adipogenesis *in vitro* and *in vivo*⁽⁴⁶⁾. Herein, we investigated this apparent inconsistent observation by studying Parkin-regulated mitochondrial homeostasis and whole-body metabolism using adipose tissue-specific *Park2* deletion mouse model. We show that Parkin deletion ameliorates HFD-feeding and aging-induced adiposity and improves glucose homeostasis. Supporting the lean phenotype that we observed in the Parkin^{A_{di}} mouse model, we consistently found smaller adipocytes, suppressed inflammation, increased energy expenditure, and elevated mitochondrial activity from multiple cohorts.

Parkin-mediated mitophagy has been shown to play an important role in the beige-to-white adipocyte transition^(20,21,47). Our findings agree with published work showing that cold stress downregulates *Park2* gene level in BAT⁽²²⁾. Multilocularity of brown adipocytes and higher body temperature of Parkin^{A_{di}} mice led us to hypothesize that Parkin deletion in BAT may contribute to the lean phenotype and improved glucose homeostasis. We tested this notion by deleting *Park2* gene specifically in BAT. Unfortunately, Parkin^{BAT} mice did not recapitulate the phenotypes we observed in Parkin^{A_{di}} mice, where Parkin was deleted from both white and brown adipocytes. Thus, our findings suggest that Parkin expression in BAT may be dispensable in the regulation of adiposity.

Pgc1 α regulates mitochondrial biogenesis by activating a variety of transcription factors⁽⁴⁸⁻⁵⁰⁾, which could benefit adipose tissue and systemic metabolism^(51,52). Our *in vitro* and *in vivo* studies suggest that Parkin deletion robustly elevates Pgc1 α protein stability. The increase in Pgc1 α led to a direct increase in markers of mitochondrial biogenesis including elevated mtDNA copy number and the level of mitochondrial gene expression⁽⁵³⁾. Consistent with previous pre-clinical and clinical findings, we found increased mtDNA content and mtDNA encoded gene expression in Parkin-deleted adipocytes, suggesting that loss of Parkin specifically in adipose tissue prevented diet-induced obesity⁽⁵⁴⁾. Together, our findings highlight that Parkin, in addition to controlling mitophagy, plays a central role in regulating mitochondrial biogenesis in the prevention of adipocyte hypertrophy.

Numerous studies have shown that pharmacological stimulation of Nqo1 or whole-body Nqo1 overexpression ameliorates obesity^(43,55-59). We confirmed and extended these findings by showing that Nqo1 overexpression selectively in white adipocytes enhances mitochondrial activity and lipid metabolism. Our findings provide an opportunity for further studies to examine the metabolic regulation of Nqo1 *in vivo*.

A previous study suggested that Nqo1 interacts with Pgc1 α in an NADH-dependent manner by inhibiting degradation of Pgc1 α , but not canonical ubiquitin-mediated pathways⁽⁴⁰⁾. In our study, we found Dicoumarol administration increased Pgc1 α ubiquitination in adipocytes, suggesting Nqo1 may inhibit Pgc1 α degradation through the ubiquitin-dependent pathway. However, we did not rule out that the Dicoumarol treatment may be working through alternative mechanisms to inhibit Pgc1 α degradation. Further thorough examination of the mechanisms of Nqo1-mediated Pgc1 α degradation are needed.

We showed that Parkin deletion from adipocytes enhanced mitochondrial function by elevating both mitochondrial respiration and mitochondrial membrane potential. A consequence of increased mitochondrial metabolism in Parkin-deleted adipocytes was an elevation of mitochondrial reactive oxygen species (mtROS). The cellular effects of ROS are largely

dependent on the species itself, its concentration, and likely time of exposure. ROS are important physiological molecules to regulate intracellular signaling pathways⁽⁶⁰⁾. Studies have shown that NADPH oxidase (NOX) derived ROS are important modulators of adipogenesis and adipose tissue function^(61,62). Our findings suggest that low concentration of mitochondrial superoxide in Parkin-deleted adipocytes may activate cytoprotective signals to maintain adipocyte health.

In conclusion, our research shows that Parkin not only regulates mitophagy but also mitochondrial biogenesis in white adipocytes through inhibiting Nqo1 increased protein stabilization of Pgc1 α . These findings suggest that Parkin regulates mitochondrial hemostasis and energy metabolism in WAT, suggesting that Parkin is a viable therapeutic target to combat obesity and obesity-associated disorders.

ACKNOWLEDGMENTS

We would like to thank Dr. Ted M. Dawson at the Johns Hopkins University for providing us Parkin flox mice. We thank undergraduate students Julia Zhou at University of California San Diego for analyzing the adipocyte size.

AUTHOR CONTRIBUTIONS

Z.Z., T.M.M., L.C., and A.L.H conceived and designed the experiments. Z.Z., T.M.M., A.R.S., and X.Z. performed *in vivo* studies in Parkin^{Adi} and Parkin^{BAT} mouse models. Z.Z., T.M.M., X.Z., A.R.S., Y.C., and P.S. conducted the sample collection and subsequent experimental analysis. B.L.C., and T.Q.d.A.V. performed indirect calorimetry studies. M.L. provided data from the METSIM studies. Z.Z. and T.M.M. performed all adipocyte culture studies and mtDNA copy number. L.C. performed all AAV injection studies. D.M.W., J.N., M.S. conducted the studies related to mitochondrial respirometry and confocal microscopy. Z.Z., T.M.M., L.C., X.Z., A.R.S., Y.C., B.L.C., P.S. T.Q.d.A.V., M.L., O.S., A.L.H, and A.J.L. analyzed the data. T.M.M., L.C., A.L.H, A.J.L., and Z.Z. wrote the manuscript.

FUNDING

Z.Z. was supported by NIH grant (DK125354). A.L.H. was supported by NIH grants (DK109724, P30DK063491). A.J.L. was supported by NIH grants U54 DK120342 and DK117850. T.M.M. was supported by the UCLA Intercampus Medical Genetics Training Program (T32GM008243), NRSA predoctoral fellowship (F31DK108657), Carl V. Gisolfi Memorial Research grant from the American College of Sports Medicine, and a predoctoral graduate student award from the Dornsife College at the University of Southern California.

DECLARATION OF INTERESTS

The authors declare no competing interests.

REFERENCE

1. Bournat, J. C., and Brown, C. W. (2010) Mitochondrial dysfunction in obesity. *Curr Opin Endocrinol Diabetes Obes* **17**, 446-452
2. McBride, H. M., Neuspiel, M., and Wasiak, S. (2006) Mitochondria: more than just a powerhouse. *Curr Biol* **16**, R551-560
3. Nunnari, J., and Suomalainen, A. (2012) Mitochondria: in sickness and in health. *Cell* **148**, 1145-1159
4. Bray, N. (2019) Many makes of mitochondria. *Nat Rev Neurosci* **20**, 645
5. Detmer, S. A., and Chan, D. C. (2007) Functions and dysfunctions of mitochondrial dynamics. *Nat Rev Mol Cell Biol* **8**, 870-879
6. Palikaras, K., Lionaki, E., and Tavernarakis, N. (2015) Balancing mitochondrial biogenesis and mitophagy to maintain energy metabolism homeostasis. *Cell Death Differ* **22**, 1399-1401
7. Ni, H. M., Williams, J. A., and Ding, W. X. (2015) Mitochondrial dynamics and mitochondrial quality control. *Redox Biol* **4**, 6-13
8. Altshuler-Keylin, S., and Kajimura, S. (2017) Mitochondrial homeostasis in adipose tissue remodeling. *Sci Signal* **10**
9. Yoo, S. M., and Jung, Y. K. (2018) A Molecular Approach to Mitophagy and Mitochondrial Dynamics. *Mol Cells* **41**, 18-26
10. Yamano, K., Fogel, A. I., Wang, C., van der Bliek, A. M., and Youle, R. J. (2014) Mitochondrial Rab GAPs govern autophagosome biogenesis during mitophagy. *Elife* **3**, e01612
11. Hanna, R. A., Quinsay, M. N., Orogo, A. M., Giang, K., Rikka, S., and Gustafsson, A. B. (2012) Microtubule-associated protein 1 light chain 3 (LC3) interacts with Bnip3 protein to selectively remove endoplasmic reticulum and mitochondria via autophagy. *J Biol Chem* **287**, 19094-19104
12. Novak, I., Kirkin, V., McEwan, D. G., Zhang, J., Wild, P., Rozenknop, A., Rogov, V., Lohr, F., Popovic, D., Occhipinti, A., Reichert, A. S., Terzic, J., Dotsch, V., Ney, P. A., and Dikic, I. (2010) Nix is a selective autophagy receptor for mitochondrial clearance. *EMBO Rep* **11**, 45-51
13. Diaz-Vegas, A., Sanchez-Aguilera, P., Krycer, J. R., Morales, P. E., Monsalves-Alvarez, M., Cifuentes, M., Rothermel, B. A., and Lavandero, S. (2020) Is Mitochondrial Dysfunction a Common Root of Noncommunicable Chronic Diseases? *Endocr Rev* **41**
14. Wilson-Fritch, L., Nicoloso, S., Chouinard, M., Lazar, M. A., Chui, P. C., Leszyk, J., Straubhaar, J., Czech, M. P., and Corvera, S. (2004) Mitochondrial remodeling in adipose tissue associated with obesity and treatment with rosiglitazone. *J Clin Invest* **114**, 1281-1289
15. Heinonen, S., Buzkova, J., Muniandy, M., Kaksonen, R., Ollikainen, M., Ismail, K., Hakkarainen, A., Lundbom, J., Lundbom, N., Vuolteenaho, K., Moilanen, E., Kaprio, J., Rissanen, A., Suomalainen, A., and Pietilainen, K. H. (2015) Impaired Mitochondrial Biogenesis in Adipose Tissue in Acquired Obesity. *Diabetes* **64**, 3135-3145

16. Bogacka, I., Xie, H., Bray, G. A., and Smith, S. R. (2005) Pioglitazone induces mitochondrial biogenesis in human subcutaneous adipose tissue in vivo. *Diabetes* **54**, 1392-1399
17. Rong, J. X., Qiu, Y., Hansen, M. K., Zhu, L., Zhang, V., Xie, M., Okamoto, Y., Mattie, M. D., Higashiyama, H., Asano, S., Strum, J. C., and Ryan, T. E. (2007) Adipose mitochondrial biogenesis is suppressed in db/db and high-fat diet-fed mice and improved by rosiglitazone. *Diabetes* **56**, 1751-1760
18. Ruegsegger, G. N., Creo, A. L., Cortes, T. M., Dasari, S., and Nair, K. S. (2018) Altered mitochondrial function in insulin-deficient and insulin-resistant states. *J Clin Invest* **128**, 3671-3681
19. Cui, C., Chen, S., Qiao, J., Qing, L., Wang, L., He, T., Wang, C., Liu, F., Gong, L., Chen, L., and Hou, X. (2018) PINK1-Parkin alleviates metabolic stress induced by obesity in adipose tissue and in 3T3-L1 preadipocytes. *Biochem Biophys Res Commun* **498**, 445-452
20. Taylor, D., and Gottlieb, R. A. (2017) Parkin-mediated mitophagy is downregulated in browning of white adipose tissue. *Obesity (Silver Spring)* **25**, 704-712
21. Lu, X., Altshuler-Keylin, S., Wang, Q., Chen, Y., Henrique Sponton, C., Ikeda, K., Maretich, P., Yoneshiro, T., and Kajimura, S. (2018) Mitophagy controls beige adipocyte maintenance through a Parkin-dependent and UCP1-independent mechanism. *Sci Signal* **11**
22. Cairo, M., Campderros, L., Gavaldà-Navarro, A., Cereijo, R., Delgado-Angles, A., Quesada-Lopez, T., Giral, M., Villarroya, J., and Villarroya, F. (2019) Parkin controls brown adipose tissue plasticity in response to adaptive thermogenesis. *EMBO Rep* **20**
23. Corsa, C. A. S., Pearson, G. L., Renberg, A., Askar, M. M., Vozheiko, T., MacDougald, O. A., and Soleimanpour, S. A. (2019) The E3 ubiquitin ligase parkin is dispensable for metabolic homeostasis in murine pancreatic beta cells and adipocytes. *J Biol Chem* **294**, 7296-7307
24. Vangipurapu, J., Stancakova, A., Pihlajamaki, J., Kuulasmaa, T. M., Kuulasmaa, T., Paananen, J., Kuusisto, J., Ferrannini, E., and Laakso, M. (2011) Association of indices of liver and adipocyte insulin resistance with 19 confirmed susceptibility loci for type 2 diabetes in 6,733 non-diabetic Finnish men. *Diabetologia* **54**, 563-571
25. Zhou, Z., Moore, T. M., Drew, B. G., Ribas, V., Wanagat, J., Civelek, M., Segawa, M., Wolf, D. M., Norheim, F., Seldin, M. M., Strumwasser, A. R., Whitney, K. A., Lester, E., Reddish, B. R., Vergnes, L., Reue, K., Rajbhandari, P., Tontonoz, P., Lee, J., Mahata, S. K., Hewitt, S. C., Shirihai, O., Gastonbury, C., Small, K. S., Laakso, M., Jensen, J., Lee, S., Drevon, C. A., Korach, K. S., Lusis, A. J., and Hevener, A. L. (2020) Estrogen receptor alpha controls metabolism in white and brown adipocytes by regulating Polg1 and mitochondrial remodeling. *Sci Transl Med* **12**
26. Rajbhandari, P., Thomas, B. J., Feng, A. C., Hong, C., Wang, J., Vergnes, L., Sallam, T., Wang, B., Sandhu, J., Seldin, M. M., Lusis, A. J., Fong, L. G., Katz, M., Lee, R., Young, S. G., Reue, K., Smale, S. T., and Tontonoz, P. (2018) IL-10

- Signaling Remodels Adipose Chromatin Architecture to Limit Thermogenesis and Energy Expenditure. *Cell* **172**, 218-233 e217
27. Schindelin, J., Arganda-Carreras, I., Frise, E., Kaynig, V., Longair, M., Pietzsch, T., Preibisch, S., Rueden, C., Saalfeld, S., Schmid, B., Tinevez, J. Y., White, D. J., Hartenstein, V., Eliceiri, K., Tomancak, P., and Cardona, A. (2012) Fiji: an open-source platform for biological-image analysis. *Nat Methods* **9**, 676-682
 28. Liao, Y., Smyth, G. K., and Shi, W. (2019) The R package Rsubread is easier, faster, cheaper and better for alignment and quantification of RNA sequencing reads. *Nucleic Acids Res* **47**, e47
 29. Love, M. I., Huber, W., and Anders, S. (2014) Moderated estimation of fold change and dispersion for RNA-seq data with DESeq2. *Genome Biol* **15**, 550
 30. Staley, J. R., Blackshaw, J., Kamat, M. A., Ellis, S., Surendran, P., Sun, B. B., Paul, D. S., Freitag, D., Burgess, S., Danesh, J., Young, R., and Butterworth, A. S. (2016) PhenoScanner: a database of human genotype-phenotype associations. *Bioinformatics* **32**, 3207-3209
 31. Kamat, M. A., Blackshaw, J. A., Young, R., Surendran, P., Burgess, S., Danesh, J., Butterworth, A. S., and Staley, J. R. (2019) PhenoScanner V2: an expanded tool for searching human genotype-phenotype associations. *Bioinformatics* **35**, 4851-4853
 32. Xiao, D., Powolny, A. A., and Singh, S. V. (2008) Benzyl isothiocyanate targets mitochondrial respiratory chain to trigger reactive oxygen species-dependent apoptosis in human breast cancer cells. *J Biol Chem* **283**, 30151-30163
 33. Aquilano, K., Lettieri Barbato, D., and Rosa, C. M. (2015) The multifaceted role of nitric oxide synthases in mitochondrial biogenesis and cell differentiation. *Commun Integr Biol* **8**, e1017158
 34. Onishi, M., Yamano, K., Sato, M., Matsuda, N., and Okamoto, K. (2021) Molecular mechanisms and physiological functions of mitophagy. *EMBO J* **40**, e104705
 35. Kitada, M., and Koya, D. (2021) Autophagy in metabolic disease and ageing. *Nat Rev Endocrinol* **17**, 647-661
 36. Lu, Y., Fujioka, H., Joshi, D., Li, Q., Sangwung, P., Hsieh, P., Zhu, J., Torio, J., Sweet, D., Wang, L., Chiu, S. Y., Croniger, C., Liao, X., and Jain, M. K. (2018) Mitophagy is required for brown adipose tissue mitochondrial homeostasis during cold challenge. *Sci Rep* **8**, 8251
 37. Yau, W. W., Wong, K. A., Zhou, J., Thimmukonda, N. K., Wu, Y., Bay, B. H., Singh, B. K., and Yen, P. M. (2021) Chronic cold exposure induces autophagy to promote fatty acid oxidation, mitochondrial turnover, and thermogenesis in brown adipose tissue. *iScience* **24**, 102434
 38. Livingston, M. J., Wang, J., Zhou, J., Wu, G., Ganley, I. G., Hill, J. A., Yin, X. M., and Dong, Z. (2019) Clearance of damaged mitochondria via mitophagy is important to the protective effect of ischemic preconditioning in kidneys. *Autophagy* **15**, 2142-2162
 39. McWilliams, T. G., Prescott, A. R., Allen, G. F., Tamjar, J., Munson, M. J., Thomson, C., Muqit, M. M., and Ganley, I. G. (2016) mito-QC illuminates mitophagy and mitochondrial architecture in vivo. *J Cell Biol* **214**, 333-345

40. Adamovich, Y., Shlomai, A., Tsvetkov, P., Umansky, K. B., Reuven, N., Estall, J. L., Spiegelman, B. M., and Shaul, Y. (2013) The protein level of PGC-1alpha, a key metabolic regulator, is controlled by NADH-NQO1. *Mol Cell Biol* **33**, 2603-2613
41. Kasai, S., Shimizu, S., Tataru, Y., Mimura, J., and Itoh, K. (2020) Regulation of Nrf2 by Mitochondrial Reactive Oxygen Species in Physiology and Pathology. *Biomolecules* **10**
42. Ross, D., and Siegel, D. (2017) Functions of NQO1 in Cellular Protection and CoQ10 Metabolism and its Potential Role as a Redox Sensitive Molecular Switch. *Front Physiol* **8**, 595
43. Di Francesco, A., Choi, Y., Bernier, M., Zhang, Y., Diaz-Ruiz, A., Aon, M. A., Kalafut, K., Ehrlich, M. R., Murt, K., Ali, A., Pearson, K. J., Levan, S., Preston, J. D., Martin-Montalvo, A., Martindale, J. L., Abdelmohsen, K., Michel, C. R., Willmes, D. M., Henke, C., Navas, P., Villalba, J. M., Siegel, D., Gorospe, M., Fritz, K., Biswal, S., Ross, D., and de Cabo, R. (2020) NQO1 protects obese mice through improvements in glucose and lipid metabolism. *NPJ Aging Mech Dis* **6**, 13
44. Zucker, S. N., Fink, E. E., Bagati, A., Mannava, S., Bianchi-Smiraglia, A., Bogner, P. N., Wawrzyniak, J. A., Foley, C., Leonova, K. I., Grimm, M. J., Moparthy, K., Ionov, Y., Wang, J., Liu, S., Sexton, S., Kandel, E. S., Bakin, A. V., Zhang, Y., Kaminski, N., Segal, B. H., and Nikiforov, M. A. (2014) Nrf2 amplifies oxidative stress via induction of Klf9. *Mol Cell* **53**, 916-928
45. Palming, J., Sjöholm, K., Jernas, M., Lystig, T. C., Gummesson, A., Romeo, S., Lonn, L., Lonn, M., Carlsson, B., and Carlsson, L. M. (2007) The expression of NAD(P)H:quinone oxidoreductase 1 is high in human adipose tissue, reduced by weight loss, and correlates with adiposity, insulin sensitivity, and markers of liver dysfunction. *J Clin Endocrinol Metab* **92**, 2346-2352
46. Shi, X., Burkart, A., Nicoloso, S. M., Czech, M. P., Straubhaar, J., and Corvera, S. (2008) Paradoxical effect of mitochondrial respiratory chain impairment on insulin signaling and glucose transport in adipose cells. *J Biol Chem* **283**, 30658-30667
47. Wrighton, K. H. (2016) Metabolism: Mitophagy turns beige adipocytes white. *Nat Rev Mol Cell Biol* **17**, 607
48. Puigserver, P., Wu, Z., Park, C. W., Graves, R., Wright, M., and Spiegelman, B. M. (1998) A cold-inducible coactivator of nuclear receptors linked to adaptive thermogenesis. *Cell* **92**, 829-839
49. Wu, Z., Puigserver, P., Andersson, U., Zhang, C., Adelmant, G., Mootha, V., Troy, A., Cinti, S., Lowell, B., Scarpulla, R. C., and Spiegelman, B. M. (1999) Mechanisms controlling mitochondrial biogenesis and respiration through the thermogenic coactivator PGC-1. *Cell* **98**, 115-124
50. Virbasius, J. V., and Scarpulla, R. C. (1994) Activation of the human mitochondrial transcription factor A gene by nuclear respiratory factors: a potential regulatory link between nuclear and mitochondrial gene expression in organelle biogenesis. *Proc Natl Acad Sci U S A* **91**, 1309-1313

51. Komen, J. C., and Thorburn, D. R. (2014) Turn up the power - pharmacological activation of mitochondrial biogenesis in mouse models. *Br J Pharmacol* **171**, 1818-1836
52. Svensson, K., and Handschin, C. (2014) Modulation of PGC-1alpha activity as a treatment for metabolic and muscle-related diseases. *Drug Discov Today* **19**, 1024-1029
53. Popov, L. D. (2020) Mitochondrial biogenesis: An update. *J Cell Mol Med* **24**, 4892-4899
54. Chella Krishnan, K., Vergnes, L., Acin-Perez, R., Stiles, L., Shum, M., Ma, L., Mouisel, E., Pan, C., Moore, T. M., Peterfy, M., Romanoski, C. E., Reue, K., Bjorkegren, J. L. M., Laakso, M., Liesa, M., and Lusis, A. J. (2021) Sex-specific genetic regulation of adipose mitochondria and metabolic syndrome by Ndufv2. *Nat Metab*
55. Hwang, J. H., Kim, D. W., Jo, E. J., Kim, Y. K., Jo, Y. S., Park, J. H., Yoo, S. K., Park, M. K., Kwak, T. H., Kho, Y. L., Han, J., Choi, H. S., Lee, S. H., Kim, J. M., Lee, I., Kyung, T., Jang, C., Chung, J., Kweon, G. R., and Shong, M. (2009) Pharmacological stimulation of NADH oxidation ameliorates obesity and related phenotypes in mice. *Diabetes* **58**, 965-974
56. Houtkooper, R. H., Canto, C., Wanders, R. J., and Auwerx, J. (2010) The secret life of NAD⁺: an old metabolite controlling new metabolic signaling pathways. *Endocr Rev* **31**, 194-223
57. Kim, Y. H., Hwang, J. H., Noh, J. R., Gang, G. T., Kim, D. H., Son, H. Y., Kwak, T. H., Shong, M., Lee, I. K., and Lee, C. H. (2011) Activation of NAD(P)H:quinone oxidoreductase ameliorates spontaneous hypertension in an animal model via modulation of eNOS activity. *Cardiovasc Res* **91**, 519-527
58. Lee, J. S., Park, A. H., Lee, S. H., Lee, S. H., Kim, J. H., Yang, S. J., Yeom, Y. I., Kwak, T. H., Lee, D., Lee, S. J., Lee, C. H., Kim, J. M., and Kim, D. (2012) Beta-lapachone, a modulator of NAD metabolism, prevents health declines in aged mice. *PLoS One* **7**, e47122
59. Choi, W. H., Ahn, J., Jung, C. H., Jang, Y. J., and Ha, T. Y. (2016) beta-Lapachone Prevents Diet-Induced Obesity by Increasing Energy Expenditure and Stimulating the Browning of White Adipose Tissue via Downregulation of miR-382 Expression. *Diabetes* **65**, 2490-2501
60. Finkel, T. (2011) Signal transduction by reactive oxygen species. *J Cell Biol* **194**, 7-15
61. Den Hartigh, L. J., Omer, M., Goodspeed, L., Wang, S., Wietecha, T., O'Brien, K. D., and Han, C. Y. (2017) Adipocyte-Specific Deficiency of NADPH Oxidase 4 Delays the Onset of Insulin Resistance and Attenuates Adipose Tissue Inflammation in Obesity. *Arterioscler Thromb Vasc Biol* **37**, 466-475
62. Issa, N., Lachance, G., Bellmann, K., Laplante, M., Stadler, K., and Marette, A. (2018) Cytokines promote lipolysis in 3T3-L1 adipocytes through induction of NADPH oxidase 3 expression and superoxide production. *J Lipid Res* **59**, 2321-2328

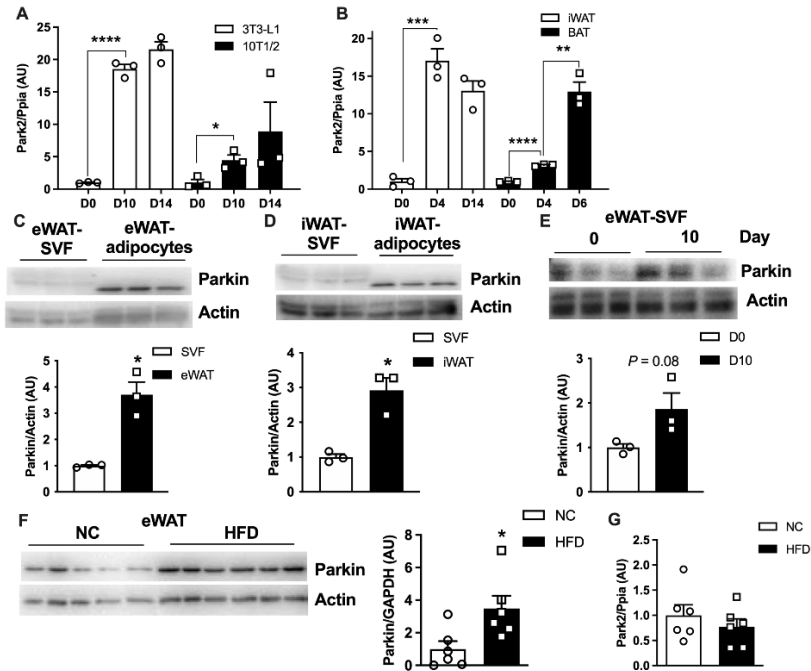


Figure 1. Parkin is elevated in white adipocytes during adipogenesis and by HFD feeding of mice.

(A and B) mRNA level of *Park2* during differentiation of 3T3-L1 and 10T1/2 adipocytes and primary adipocytes from iWAT and BAT (n=3 biological replicate). Western blot analysis (top of panel) and corresponding densitometric quantification (bottom of panel; normalized to Actin) of Parkin in (C) eWAT, (D) iWAT vs. SVF fractions, (E) SVF fractions from eWAT vs. 10 day-differentiated primary adipocytes (n=3 biological replicate). (F) Western blot analysis of Parkin and (G) mRNA level of *Park2* in eWAT from normal chow-fed vs. HFD-fed male WT C57BL6/J mice. The bar graph on the right is the densitometric quantification of Parkin protein level normalized to Actin (n=5-6 mice per group). Data are presented as mean \pm SEM. * $P < 0.05$, ** $P < 0.01$, *** $P < 0.001$, **** $P < 0.0001$.

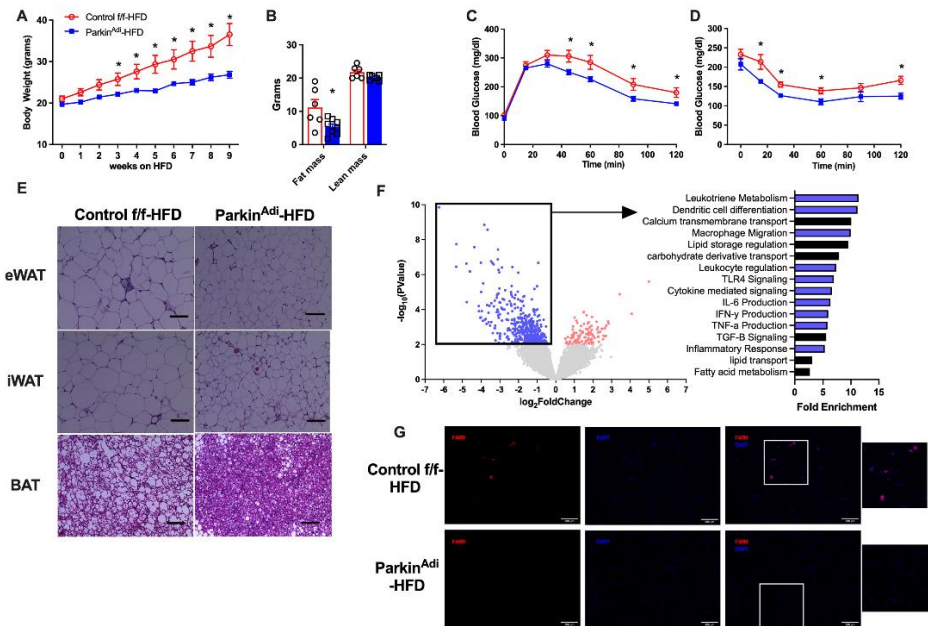


Figure 2. Adipose-specific deletion of Parkin ameliorates high-fat diet and aging-induced obesity and glucose tolerance.

(A) Body weight of HFD-fed Control *f/f* and *Parkin^{Adi}* mice (n=6-8 mice per group). (B) Body consumption of Control *f/f* and *Parkin^{Adi}* mice following a 9-week HFD (n=6-8 mice per group). (C and D) Glucose tolerance and insulin tolerance tests performed on HFD-fed Control *f/f* and *Parkin^{Adi}* mice (n=7 mice per genotype). (E) H&E-stained sections of eWAT, iWAT, and BAT from 9 weeks HFD-fed mice; scale bars = 50 μ m. (F) Volcano plots and enrichment analysis of RNA sequencing results from eWAT of HFD-fed *Parkin^{Adi}* vs. Control *f/f* mice (n=4 mice per genotype). (G) Immunofluorescent staining of F4/80 and DAPI in the eWAT of HFD-fed Control *f/f* and *Parkin^{Adi}* mice. Data are presented as mean \pm SEM. * $P < 0.05$.

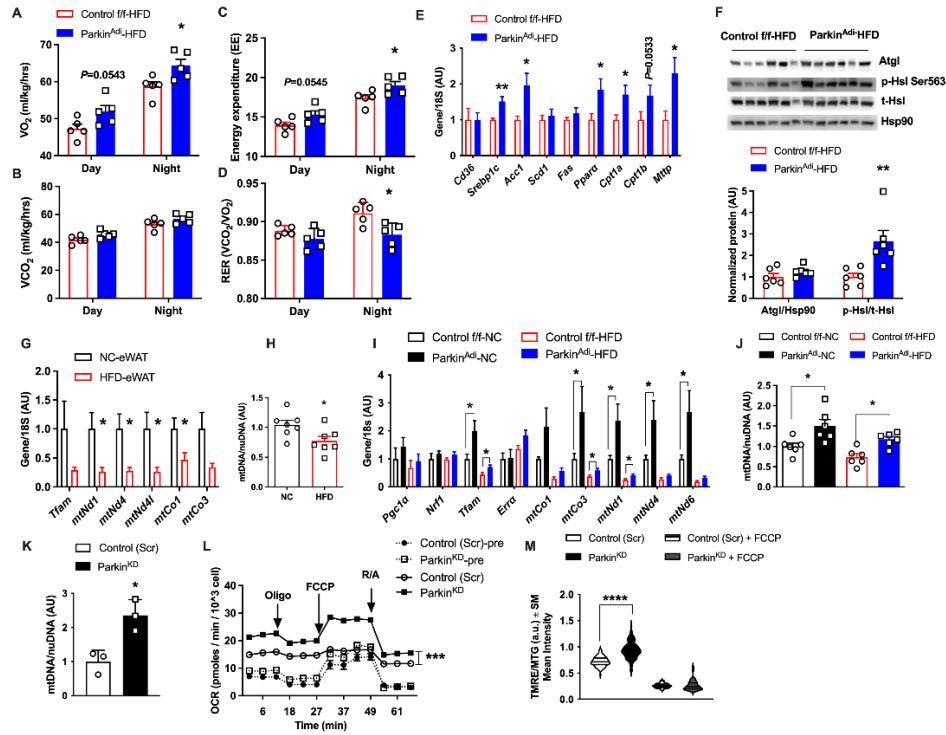


Figure 3. Parkin deletion elevates energy expenditure and mitochondrial activity in adipocytes.

(A) Oxygen consumption, (B) CO₂ production, (C) energy expenditure (EE), and (D) respiratory exchange ratio (RER) of HFD-fed male Control *ff* and *Parkin*^{Adi} mice fed a HFD for 4 weeks (n=5 mice per genotype). (E) mRNA levels of lipid metabolism genes in the eWAT of HFD-fed Control *ff* and *Parkin*^{Adi} mice (n=6-8 mice per genotype). (F) Western blots and densitometric analysis of Atgl, phospho-Hsl Ser563, and total Hsl protein in eWAT of HFD-fed Control *ff* and *Parkin*^{Adi} mice (n=6 mice per genotype). (G) mRNA levels of mitochondrial and related genes in the eWAT of WT mice fed with NC and HFD (n=5 mice per diet). (H) Relative mtDNA copy number in the eWAT of mice fed with NC and HFD (n=7 per diet). (I) mRNA levels of mitochondrial and related genes in the eWAT of Control *ff* and *Parkin*^{Adi} mice fed with NC and HFD (n=5-7 mice per genotype per diet). (J and K) Relative mtDNA copy number in the eWAT of Control *ff* and *Parkin*^{Adi} mice fed with NC and HFD (n=6 mice per genotype per diet) and in the differentiated 3T3-L1 Control (Scr) and *Parkin*^{KD} adipocytes (n=3 biological replicate). (L) Mitochondrial oxygen consumption rate of preadipocytes (dash line) and differentiated adipocytes (solid line) of 3T3-L1 cells (n=4 biological replicate). (M) Normalized mitochondrial membrane potential (TMRE)/mitochondrial tracker green (MTG) of the differentiated 3T3-L1 Control (Scr) and *Parkin*^{KD} adipocytes treated with vehicle (DMSO) and FCCP (n=39-102 cells per group). Data are presented as mean ± SEM. * $P < 0.05$, ** $P < 0.01$, *** $P < 0.001$, **** $P < 0.0001$.

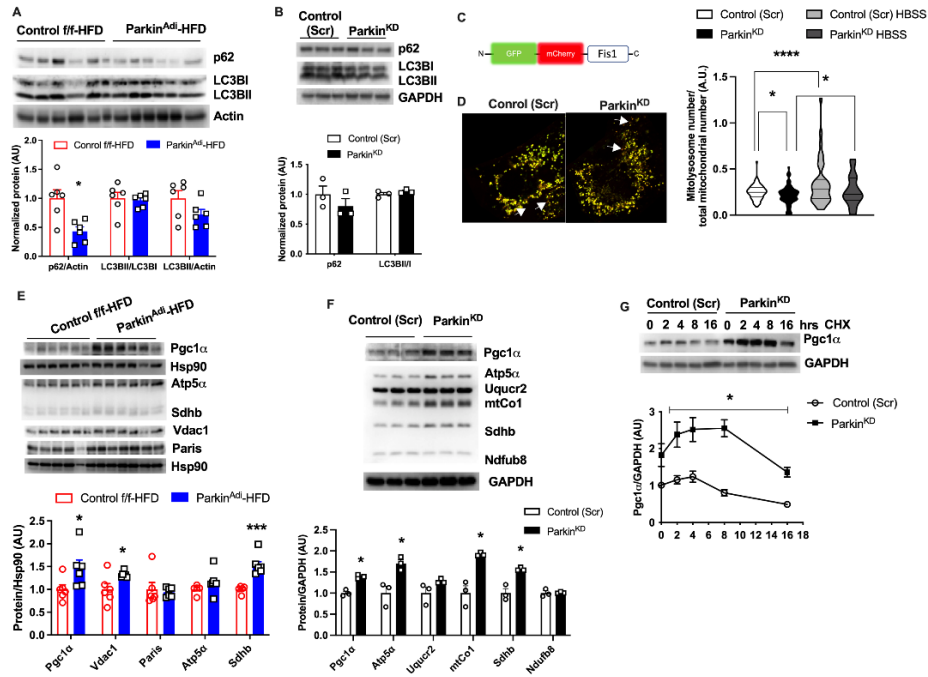


Figure 4. Parkin deletion slightly impairs mitophagy but extended Pgc1 α protein stability in adipocytes.

(A and B) Western blot analysis of autophagy markers p62 and LC3 in the eWAT of HFD-fed Control *f/f* and *Parkin^{Adi}* mice fed with HFD ($n=6$ mice per genotype) and in differentiated adipocytes of Control (Scr) and *Parkin^{KD}* ($n=3$ biological replicate). The bar graphs at the bottom are the densitometric quantification of protein level normalized to Actin or GAPDH. (C) Adenoviral GFP and mCherry Fis1 probe used for mitophagy quantification. (D) Fluorescent microscopy analysis of mitophagy signals in Control (Scr) and *Parkin^{KD}* adipocytes ($n=25-91$ cells per group). The graph on the right is the quantification of mitolysosome number in differentiated 3T3-L1 Control (Scr) and *Parkin^{KD}* adipocytes cultured in the normal medium or in HBSS for 4 hours ($n=25-72$ cells per group). (E) Western blot and densitometry analysis of Pgc1 α , Vdac1, and Paris (normalized to Hsp90) in eWAT of HFD-fed Control *f/f* and *Parkin^{Adi}* mice fed with HFD ($n=6$ mice per genotype). (F) Western blot and densitometry analysis of Pgc1 α and OXPHOS proteins in the differentiated Control (Scr) and *Parkin^{KD}* adipocytes ($n=3$ biological replicate). (G) Western blot and densitometry analysis of Pgc1 α (normalized to GAPDH) in the differentiated 3T3-L1 Control (Scr) and *Parkin^{KD}* adipocytes treated with 100 $\mu\text{g/ml}$ CHX at the indicated time. ($n=3$ biological replicate). Data are presented as mean \pm SEM. * $P < 0.05$, *** $P < 0.001$.

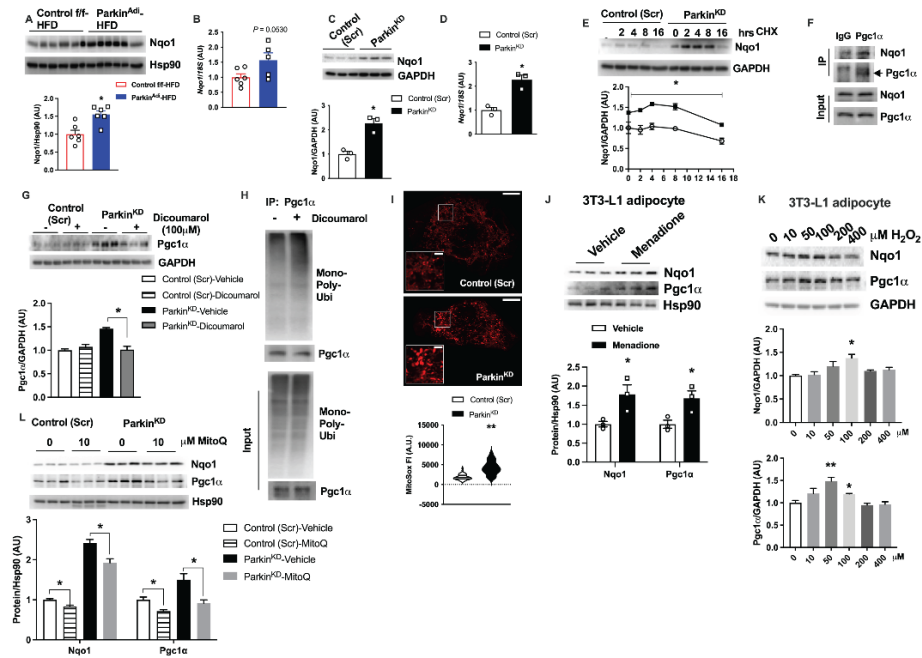


Figure 5. Adipose-specific Parkin deletion enhances Pgc1 α protein stability by elevating Nqo1.

(A and C) Western blot and densitometry analysis of Nqo1 in eWAT of HFD-fed Control *f/f* and Parkin^{Adi} mice fed with HFD (n=5-6 mice per genotype; normalized to Hsp90) and in differentiated adipocytes of Control (Scr) and Parkin^{KD} (n=3 biological replicate; normalized to GAPDH). (B and D) mRNA level of *Nqo1* in eWAT of HFD-fed Control *f/f* and Parkin^{Adi} mice fed with HFD (n=6 mice per genotype) and in differentiated adipocytes of Control (Scr) and Parkin^{KD} (n=3 biological replicate). (E) Western blot and densitometry analysis of Nqo1 (normalized to GAPDH) in the differentiated 3T3-L1 Control (Scr) and Parkin^{KD} adipocytes treated with 100 μ g/ml CHX at the indicated time. (n=3 biological replicate). (F) Co-immunoprecipitation analysis of Pgc1 α and Nqo1 in the lysates of eWAT. (G) Western blot and densitometry analysis of Pgc1 α (normalized to GAPDH) in the differentiated 3T3-L1 Control (Scr) and Parkin^{KD} adipocytes treated with vehicle and Dicumarol (Nqo1 inhibitor) (n=3 biological replicate). (H) Co-immunoprecipitation of Pgc1 α in differentiated 3T3-L1 Control (Scr) and Parkin^{KD} adipocytes treated with vehicle or Dicumarol. (I) Images of MitoSox staining and quantification of MitoSox fluorescent intensity in Control (Scr) and Parkin^{KD} adipocytes (n=35-47 cells per group). (J) Western blot and densitometry analysis of Pgc1 α and Nqo1 (normalized to Hsp90) in 3T3-L1 adipocytes treated with vehicle and 5 μ M Menadione for 24 hours (n=3 biological replicate). (K) Western blot and densitometry analysis of Pgc1 α and Nqo1 (normalized to GAPDH) in 3T3-L1 adipocytes treated with H₂O₂ at indicated concentration for 24 hours (n=3 biological replicate). (L) Western blot and densitometry analysis of Pgc1 α and Nqo1 (normalized to Hsp90) in Control (Scr) and Parkin^{KD} adipocytes treated with vehicle or MitoQ (10 μ M) for 24 hours (n=3 biological replicate). Data are presented as mean \pm SEM. * $P < 0.05$, ** $P < 0.01$.

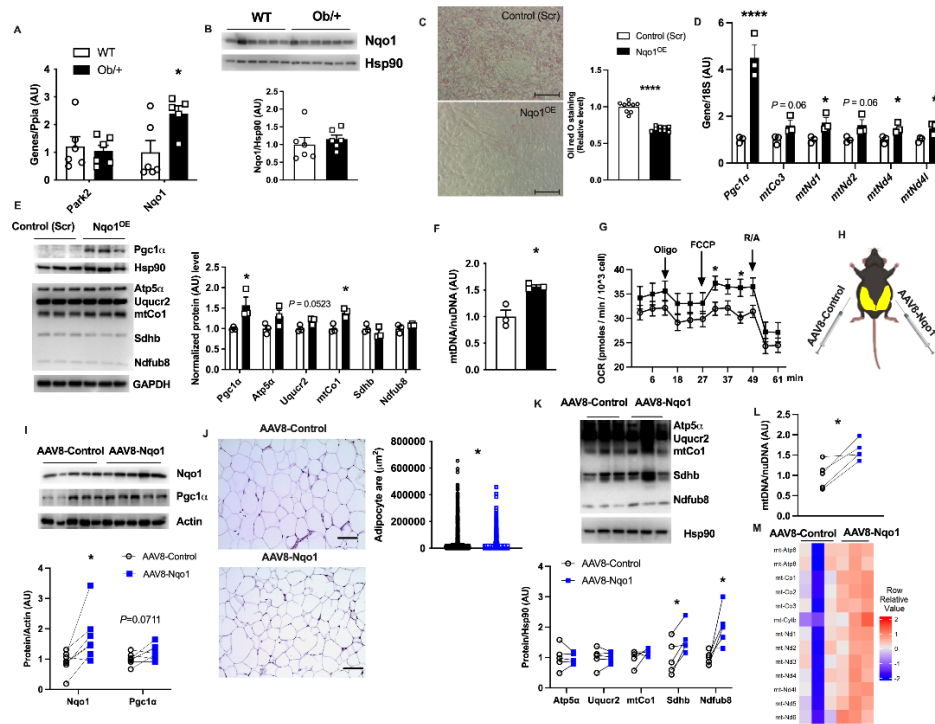


Figure 6. Overexpression of Nqo1 enhances mitochondrial biogenesis *in vitro* and *in vivo*.

(A) mRNA level of *Park2* and *Nqo1* (B) western blot analysis of Nqo1 in the eWAT of WT and Ob/+ mice (n=5-6 mice per genotype). (C) Oil Red O staining and the quantification of Oil Red O in differentiated 3T3-L1 Control (Scr) and Nqo1^{OE} adipocytes (n=9 biological replicate). (D) mRNA level of mitochondrial and related genes in the differentiated 3T3-L1 Control (Scr) and Nqo1^{OE} adipocytes (n=3 biological replicate). (E) Western blot and densitometry analysis of Pgc1 α and OXPHOS proteins (normalized to Hsp90 or GAPDH) in the differentiated 3T3-L1 Control (Scr) and Nqo1^{OE} adipocytes (n=3 biological replicate). (F) mtDNA content of the differentiated 3T3-L1 Control (Scr) and Nqo1^{OE} adipocytes (n=3 biological replicate). (G) Mitochondrial oxygen consumption rate of the differentiated 3T3-L1 Control (Scr) and Nqo1^{OE} adipocytes (n=5 biological replicate). (H) Experimental design for AAV8 injection in HFD-fed male WT mice. (I) Western blot and densitometry analysis of Nqo1 and Pgc1 α proteins (normalized to Actin) in eWAT of AAV-Control or AAV-Nqo1 injected mice (n=7 mice per group). (J) H&E-stained sections of the eWAT from AAV-Control or AAV-Nqo1 injected mice; scale bars = 50 μ m; The dot graph on the right is the quantified adipocyte area from H&E-stained sections of the eWAT from HFD-fed Control *f/f* and Parkin^{Adi} mice (n=1603-1932 adipocytes per group). (K) Western blot and densitometry analysis of OXPHOS protein levels (normalized to Hsp90) in eWAT of AAV-Control or AAV-Nqo1 injected mice (n=5 mice per group). (L) mtDNA content of the eWAT from AAV-Control or AAV-Nqo1 injected mice (n=5 mice per group). (M) Heatmap of mtDNA encoded genes from RNA sequencing results in AAV8-Control or AAV8-Nqo1

injected eWAT (n=3 mice per group). Data are presented as mean \pm SEM. * $P < 0.05$, ** $P < 0.01$, *** $P < 0.001$.

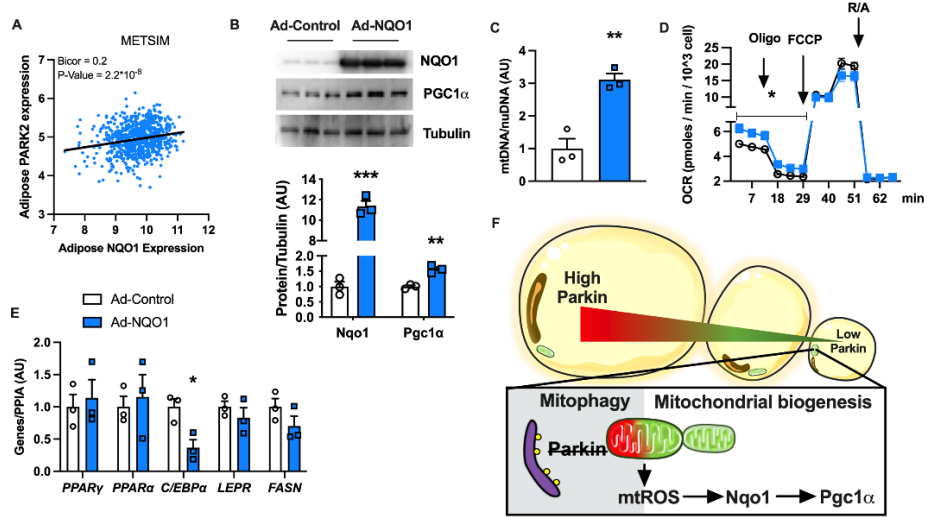
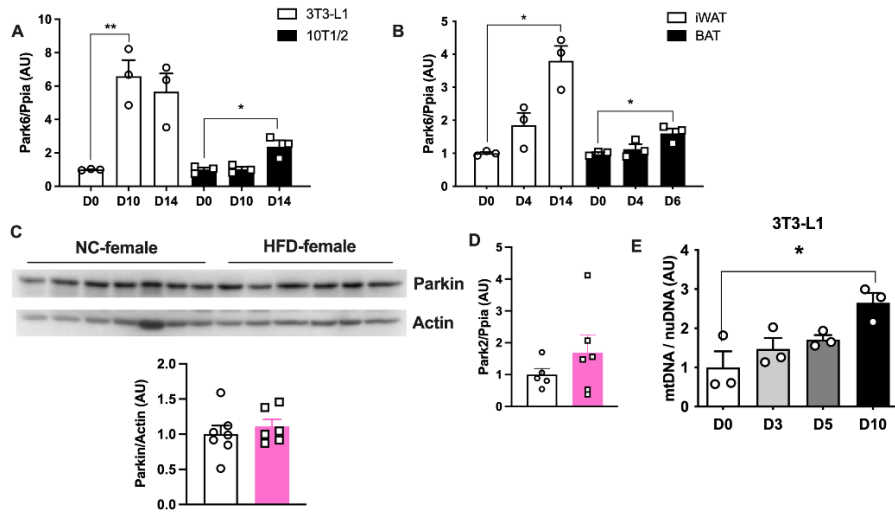


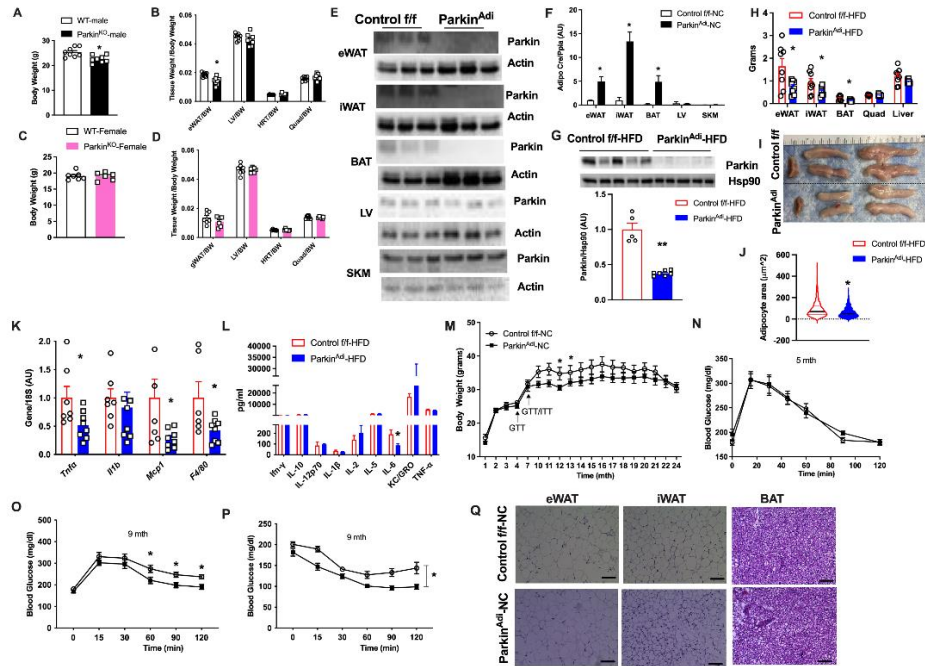
Figure 7. Overexpression of NQO1 in human SubQ adipocytes elevates mtDNA content and improves mitochondrial function.

(A) The correlation of NQO1 and PARK2 gene expression in human subcutaneous adipose tissues from men participated in the METSIM study (n=770). (B) Western blot and densitometry analysis of Nqo1 and Pgc1 α protein levels in ad-Control and ad-NQO1 treated primary human subcutaneous adipocytes (n=3 biological replicate). (C, D, and E) mtDNA content, mitochondrial oxygen consumption rate, and adipogenesis gene expression of ad-Control and ad-NQO1 treated primary human subcutaneous adipocytes (n=3 biological replicate). (F) Schematic view of Parkin regulates adiposity by coordinating mitophagy with mitochondrial biogenesis in white adipocytes. Data are presented as mean \pm SEM. * $P < 0.05$, ** $P < 0.01$.



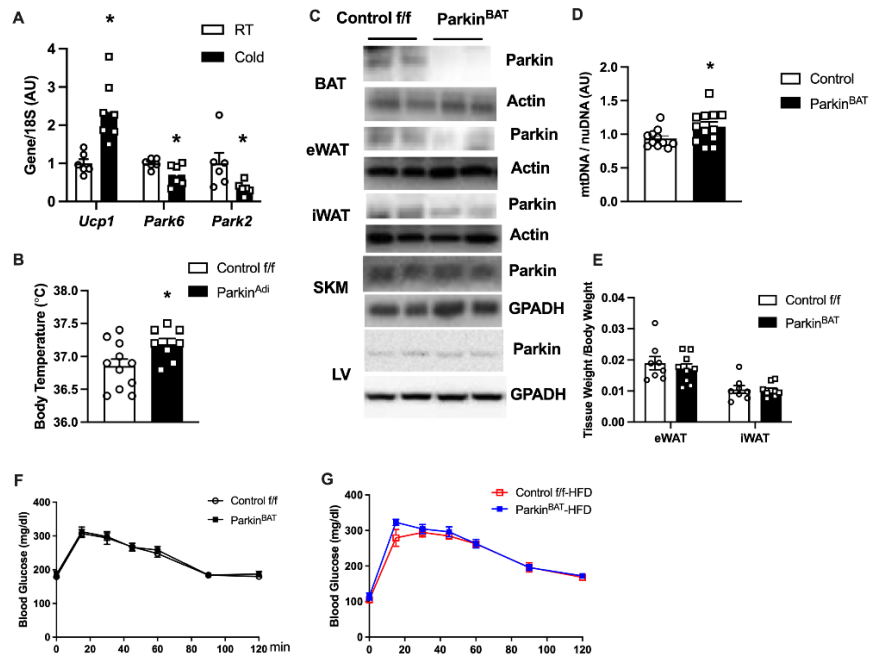
Suppl. Figure 1: Pink1 and parkin expression during the differentiation of primary adipocytes and 3T3-L1 preadipocytes.

(A) mRNA level of *Park6* during the differentiation of 3T3-L1 and 10T1/2 adipocytes (n=3 biological replicate); (B) primary adipocytes from iWAT and BAT (n=3 biological replicate). (C) Western blot analysis and (D) mRNA level of Parkin in the gonadal white adipose tissues of NC vs. HFD-fed female mice (n=6-7 mice per diet). (E) mtDNA content of 3T3-L1 preadipocytes at day 0, day 3, day 5, and day 10 of the differentiation (n=3 biological replicate). Data are presented as mean \pm SEM. * $P < 0.05$, ** $P < 0.01$, *** $P < 0.001$.

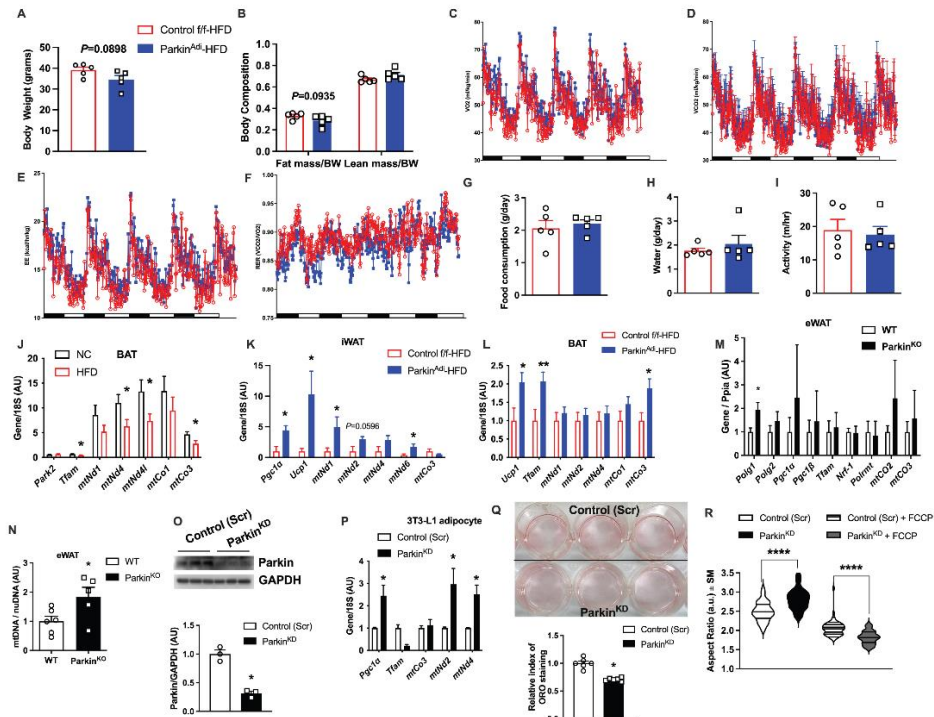


Suppl. Figure 2: Body composition and histology of Parkin knockout mice.

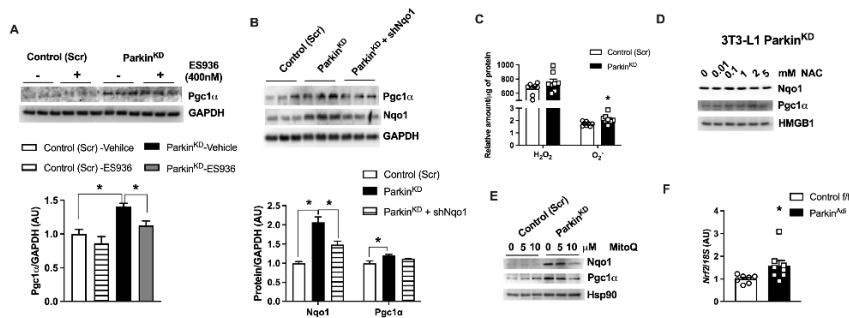
(A and B) Body weight and body composition of NC-fed male WT and whole-body Parkin knockout ($Parkin^{KO}$) mice ($n=6$ mice per genotype). (C and D) Body weight and body composition of NC-fed female WT and whole-body Parkin knockout mice ($n=6-7$ mice per genotype). (E) Western blots analysis of Parkin in the eWAT, iWAT, BAT, liver (LV), and skeletal muscle (SKM) of Control *f/f* vs. $Parkin^{Adi}$ mice fed with NC ($n=3$ mice per genotype). (F) Adiponectin Cre expression in the eWAT, iWAT, BAT, LV, and SKM of male Control *f/f* and $Parkin^{Adi}$ mice ($n=3$ mice per genotype). (G) Western blots analysis of Parkin in eWAT of Control *f/f* vs. $Parkin^{Adi}$ mice fed with HFD ($n=5-7$ mice per genotype). (H) Tissue weight of HFD-fed Control *f/f* and $Parkin^{Adi}$ mice ($n=7-8$ mice per genotype). (I) Images of adipose tissues. (J) Quantified adipocyte area from H&E-stained sections of eWAT from HFD-fed Control *f/f* and $Parkin^{Adi}$ mice ($n=330-533$ adipocytes per genotype). (K) mRNA levels of inflammatory genes in the eWAT of HFD-fed Control *f/f* and $Parkin^{Adi}$ mice ($n=6-8$ mice per genotype). (L) The levels of inflammatory cytokines and chemokines in the plasma of HFD-fed Control *f/f* and $Parkin^{Adi}$ mice ($n=6-7$ mice per genotype). (M) Body weight of NC-fed male Control *f/f* and $Parkin^{Adi}$ mice ($n=6-10$ mice per genotype). (N, O, and P) Glucose tolerance test and insulin tolerance test performed on 5 months old and 9 months old NC-fed Control *f/f* and $Parkin^{Adi}$ mice ($n=6-7$ mice per genotype). (Q) H&E-stained sections of eWAT, iWAT, and BAT from NC-fed mice; scale bars = 50 μ m. Data are presented as mean \pm SEM. * $P < 0.05$.



Suppl. Figure 3: Brown adipose-specific Parkin deletion does not impact glucose homeostasis. (A) mRNA levels of *Ucp1*, *Park6*, and *Park2* genes in the BAT of male mice housed in room temperature (RT) or cold room for 4 hours (4°C) (n=6 mice per group). (B) Body temperature of 2 months old NC-fed Control *f/f* and *Parkin^{Adi}* mice (n=8-11 mice per genotype). (C) Western blots analysis of Parkin in the BAT, eWAT, iWAT, SKM, and LV of Control *f/f* and *Parkin^{BAT}* mice (n=2 per genotype). (D) mtDNA content of the BAT from Control *f/f* and *Parkin^{BAT}* mice (n=11-12 mice per genotype). (E) eWAT and iWAT tissue weight of Control *f/f* and *Parkin^{BAT}* mice (n=8-9 mice per genotype). (F and G) Glucose tolerance analysis of NC-fed and HFD-fed Control *f/f* and *Parkin^{BAT}* mice (n=4-7 mice per genotype). Data are presented as mean ± SEM. * $P < 0.05$

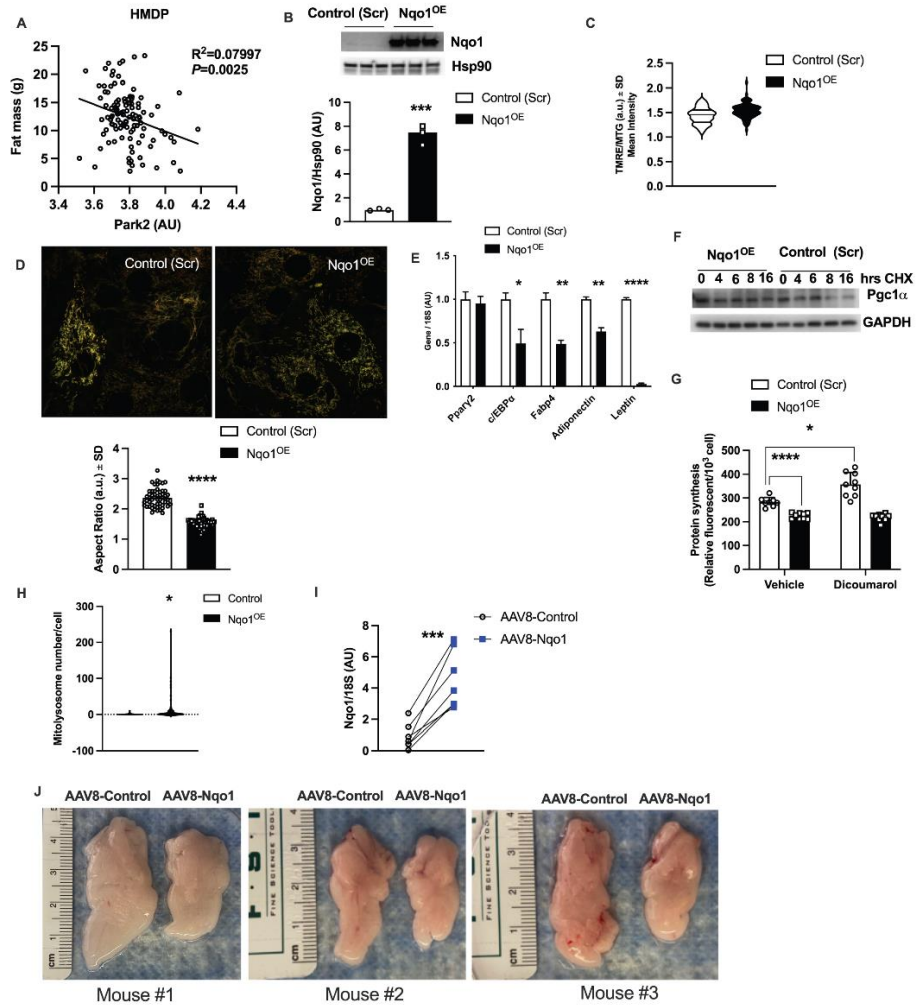


Suppl. Figure 4: Parkin deletion elevates energy expenditure and mitochondrial activity in adipocytes. (A and B) Body weight and body composition of 4 weeks of HFD-fed Control *f/f* and *Parkin^{Adi}* mice that housed in the chamber (n=5 mice per genotype). (C, D, E, and F) recording oxygen consumption, CO2 production, EE, and RER of HFD-fed Control *f/f* and *Parkin^{Adi}* mice for 4 days (n=5 mice per genotype). (G, H, and I) Food consumption per day, water consumption per day, and total activity of HFD-fed Control *f/f* and *Parkin^{Adi}* mice (n=5 mice per genotype). (J, K, L, and M) mRNA levels of mitochondrial and related genes in the BAT of mice fed with NC and HFD (n=6 mice per genotype), in the BAT of Control *f/f* and *Parkin^{Adi}* mice fed with HFD (n=7 mice per genotype), in the iWAT of HFD-fed Control *f/f* and *Parkin^{Adi}* mice (n=6 mice per genotype), in the eWAT of WT and *Parkin^{KO}* mice fed with NC (n=4-5 mice per genotype). (N) mtDNA content in the eWAT of WT and *Parkin^{KO}* mice (n=5-6 mice per genotype). (O) Western blot and densitometry analysis of Parkin (normalized to GAPDH) in 3T3-L1 Control (Scr) and *Parkin^{KD}* adipocytes. (n=3 biological replicate). (P) mRNA levels of mitochondrial genes in 3T3-L1 Control (Scr) and *Parkin^{KD}* adipocytes (n=3 biological replicate). (Q) Oil O Red staining and the quantification analysis of ORO in the differentiated Control (Scr) and *Parkin^{KD}* adipocytes (n=3 biological replicate). (R) Mitochondrial aspect ratio analysis of Control (Scr) and *Parkin^{KD}* adipocytes (n=39-102 cells per group). Data are presented as mean \pm SEM. * $P < 0.05$, ** $P < 0.01$, *** $P < 0.001$, **** $P < 0.0001$.



Suppl. Figure 5: Nqo1 preserves Pgc1α protein in adipocytes.

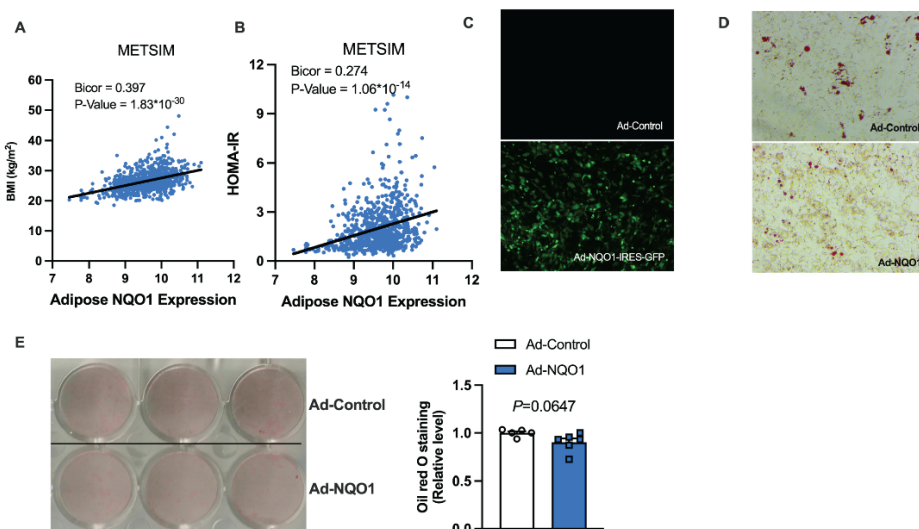
(A and B) Western blot and densitometry analysis of Pgc1α and Nqo1 (normalized to GAPDH) in the differentiated 3T3-L1 Control (Scr) and Parkin^{KD} adipocytes treated with vehicle or ES936 (Nqo1 inhibitor) and in 3T3-L1 Control (Scr), Parkin^{KD}, and Parkin^{KD} + shNqo1 3T3-L1 preadipocytes (n=3 biological replicate). (C) Relative amount of H₂O₂ and O₂ in differentiated adipocytes of Control (Scr) and Parkin^{KD} (n=8 biological replicate). (D and E) Western blot analysis of Pgc1α and Nqo1 in the indicated concentration of NAC or MitoQ treated 3T3-L1 adipocytes. (F) mRNA level of *Nrf2* in the eWAT of HFD-fed Control *f/f* and Parkin^{Adi} mice (n=7-8 mice per genotype). Data are presented as mean ± SEM. * *P* < 0.05, ** *P* < 0.01, *** *P* < 0.001, **** *P* < 0.0001.



Suppl. Figure 6: Overexpression of Nqo1 enhances mitochondrial biogenesis *in vitro* and *in vivo*.

(A) *Park2* gene expression in adipose tissue from male HMDP mice (4 mice per strain, ~100 strains) versus fat mass (g). (B) Western blot and densitometry analysis of Nqo1 protein level (normalized to Hsp90) in the differentiated 3T3-L1 Control (Scr) and Nqo1^{OE} adipocytes (n=3 biological replicate). (C) Normalized mitochondrial membrane potential (TMRE)/mitochondrial tracker green (MTG) of the differentiated 3T3-L1 Control (Scr) and Nqo1^{OE} adipocytes (n=55-77 cells per group). (D) Mitochondrial morphology of the differentiated 3T3-L1 Control (Scr) and Nqo1^{OE} adipocytes. The bar graph at the bottom is the normalized aspect ratio (n=55-77 cells per group). (E) mRNA of

adipogenesis genes: *Ppar2*, *C/Ebpa*, *Fabp4*, *Adiponectin*, *Leptin* in the differentiated 3T3-L1 Control (Scr) and Nqo1^{OE} adipocytes (n=3 biological replicate). (F) Western blot analysis of Pgc1 α in the differentiated 3T3-L1 Control (Scr) and Nqo1^{OE} adipocytes treated with 100 μ g/ml CHX at the indicated time. (G) Protein synthesis rate of the differentiated 3T3-L1 Control (Scr) and Nqo1^{OE} adipocytes treated with vehicle or Dicoumarol (n=8-9 biological replicate). (H) Normalized mitolysosome number in the differentiated 3T3-L1 Control (Scr) and Nqo1^{OE} adipocytes (n=39-54 cells per group). (I) mRNA level of Nqo1 in the eWAT of AAV8 injected mice (n=7 mice per group). (J) Image of the eWAT of AAV8-Control or AAV8-Nqo1 injected mice. Data are presented as mean \pm SEM. * $P < 0.05$, *** $P < 0.001$, **** $P < 0.0001$.



Suppl. Figure 7: Overexpression of NQO1 in human SubQ adipocytes elevates mtDNA content and improves mitochondrial function.

(A and B) The association of human subcutaneous adipose NQO1 gene expression with BMI and HOMA-IR from METSIM study (n=770). (C) Validating NQO1 overexpression in ad-Control and ad-NQO1 treated primary human subcutaneous adipocytes. (D and E) Oil Red O staining of ad-Control and ad-NQO1 treated primary human subcutaneous adipocytes. The bar graph on the right is the densitometry of oil red o staining in the adipocytes (n=5-6 biological replicate).

Table S1. Primer list

Species	Gene	Forward	Reverse
Mouse	18S	CGCCGCTAGAGGTGAAATTCT	CGAACCTCCGACTTTCGTTCT
	Acc1	CTGAAGCAGATCCGCAGCTT	GGTGAGATGTGCTGGGTCATG
	Adipo Cre	AGGTGTAGAGAAGGCACTTAG	CTAATCGCCATCTTCCAGCAGG
	Adiponectin	TGTTGGAATGACAGGAGCTGAA	CACACTGAAGCCTGAGCGATAC
	c/Ebpa	CCCCACTCAGCTTACAACAGG	CACCCACAAAGCCCAGAAAC
	Cd36	TCCAGCCAATGCCTTTGC	TGGAGATTACTTTTTCAGTGCAGAA
	Cpt1a	CCAGGCTACAGTGGGACATT	GAACTTGCCCATGTCCTTGT
	Erra	GGAGGACGGCAGAAGTACAAA	GCGACACCAGAGCGTTCAC
	F4/80	TTTGGCTATGGGCTTCCAGTC	GCAAGGAGGACAGAGTTTATCGTG
	Fabp4	TTCGATGAAATCACCGCAGA	GGTCGACTTTCATCCCCTT
	Fas	TGCTCCCAGCTGCAGGC	GCCCGGTAGCTCTGGGTGTA
	Il1b	GACGGCACACCCACCCT	AAACCGTTTTTCCATCTTCTTT
	Leptin	GAGACCCCTGTGTCGGTTC	CTGCGTGTGTGAAATGTCATTG
	Mcp1	CAGCCAGATGCAGTTAACGC	GCTGCTGGTGATCCTCTTG
	mtCo1	TCCAACCTCATCCCTTGACATC	TCCTGCTATGATAGCAAACACT
	mtCo3	GCAGGATTCTTCTGAGCGTTCT	GTCAGCAGCCTCCTAGATCATGT
	mtNd1	GTTGGTCCATACGGCATT	TGGGTGTGGTATTGGTAGGG
	mtNd2	CGCCCCATTCCACTTCTGATT	TTAAGTCCTCCTCATGCCCT
	mtNd4	GCCTGATTACTGCCACTAATA	GGTCCCTCATCGGGTAATAA
	mtNd4l	ACCTCACCATAGCCTTCTCAC	TAGTCTACAGCTGCTTCGC
	mtNd6	ACAACCTATATATTGCCGC	GATATACGACTGCTATAGCTA
	Mtp	CGTGGTCAAAGGGCTTATTC	TCGCGATACCACAGACTGAA
	Nqo1	TTCTCTGGCCGATTCAGAGT	GGCTGCTTGGAGCAAATAG
	Nrf1	GAA CTG CCA ACC ACA GTC AC	CGT CTG GAT GGT CAT TTC AC
	Nrf2	CTCGCTGAAAAAGAAGTGG	CGGTCCAGGATTCAGAGAG
	Park2	GGAAGCCATAGCTGGAGTTG	AAACCTGACAGAAACGCTGG
	Park6	GGATGTCGTCCTGAAGGGAG	GCTTCGCTGGAGGAACCTG
	Polg1	TAGCTGGCTGGTCCAAGAGT	CGACGTGGAGGTCTGCTT
	Polg2	CCGTTTTCCAGCGTAGTCTC	TTCTGTGTGGCCTGGCTATT
	Polrmt	CTCATCTCAGGTGTGCCCTC	TCTGCAGCTCAAGAAGGAGC
	Ppara	CCTGAACATCGAGTGTCAATAT	GGTCTTCTTCTGAATCTTGCAGCT GGT TCT ACT TTG ATC GCA CTT TG
	Pparg2	TCA CAA GAG CTG ACC CAA TGG	TGAAGTGGTGTAGCGACCAA
	Ppargc1a	TGAGGACCGCTAGCAAGTTT	GCTCTCGTCCTTCTTCCCTCA
	Ppargc1b	CTGAGTCAAAGTCACTGGCG	GCGTGGGCAGGATGAAG
	Scd1	TGGGTTGGCTGCTTGTG	GGAGCCATGGATTGCACATT
	Srebp1c	GCTCCAGAGAGGAGCCCAG	

	Tfam	AGC TTG TAA ATG AGG CTT GGA	AGA TGT CTC CGG ATC GTT TC
	Tnfa	CAC AAG ATG CTG GGA CAG TGA	TCC TTG ATG GTG GTG CAT GA
	Ucp1	GGAAAGGGACGACCCCTAATC	CCGGCAACAAGAGCTGACA
Human	ACTIN	GATGAGATTGGCATGGCTTT	GTCACCTTCACCGTTCCAGT
	B2M	TGCTGTCTCCATGTTTGATGTATCT	TCTCTGCTCCCCACCTCTAAGT
	c/EBPa	CTAGAGATCTGGCTGTGGGG	TCATAACTCCGGTCCCTCTG
	FASN	CTGGCTCAGACACTCTATCC	CAGGTTGTCCCTGTGATCCT
	LPER	AGGACGAAAGCCAGAGACAA	AAATGCCTGGGCCTCTATCT
	PPARa	ATGGCATCCAGAACAAGGAG	TCCCGTCTTTGTTTCATCACA
	PPARg	GCTGTGCAGGAGATCACAGA	GGGCTCCATAAAGTCACCAA
	tRNA-Leu	CACCCAAGAACAGGGTTTGT	TGGCCATGGGTATGTTGTTA

Appendix IV

ABCB10 exports mitochondrial biliverdin, driving metabolic maladaptation in obesity.

The work described in this chapter has been reproduced from:

Shum M, Shintre C, Althoff T, Gutierrez V, Segawa M, Saxberg AD, Martinez M, Adamson R, Young MR, Faust B, Gharakhanian R, Su S, Krishnan K, Mahdavian K, Veliova M, Wolf D, Ngo J, Nocito L, Stiles L, Abramson J, Lusi A, Hevener A, Zoghbi ME, Carpenter EP, Liesa M. ABCB10 exports mitochondrial biliverdin, driving metabolic maladaptation in obesity. *Science Translational Medicine*. 2021. doi: 10.1126/scitranslmed. abd1869.

Copyright 2021

Michael Shum, Chitra A Shintre, Thorsten Althoff, Vincent Gutierrez, Mayuko Segawa, Alexandra D Saxberg, Melissa Martinez, Roslin Adamson, Margaret R Young, Belinda Faust, Raffi Gharakhanian, Shi Su, Karthickeyan Chella Krishnan, Kiana Mahdavian, Michaela Veliova, Dane M Wolf, Jennifer Ngo, Laura Nocito, Linsey Stiles, Jeff Abramson, Aldons J Lusi, Andrea L Hevener, Maria E Zoghbi, Elisabeth P Carpenter, Marc Liesa.

METABOLISM

ABCB10 exports mitochondrial biliverdin, driving metabolic maladaptation in obesity

Michael Shum^{1,2,3†}, Chitra A. Shintre⁴, Thorsten Althoff⁵, Vincent Gutierrez^{1,2,3}, Mayuko Segawa^{1,2,3}, Alexandra D. Saxberg⁶, Melissa Martinez⁶, Roslin Adamson⁴, Margaret R. Young⁴, Belinda Faust^{4‡}, Raffi Gharakhanian^{1,2,3}, Shi Su⁷, Karthickeyan Chella Krishnan^{8,9}, Kiana Mahdavian^{1,7}, Michaela Veliova², Dane M. Wolf^{1,7}, Jennifer Ngo^{1,2,3,10}, Laura Nocito⁷, Linsey Stiles^{1,2}, Jeff Abramson⁵, Aldons J. Lusis^{8,11,12}, Andrea L. Hevener¹, Maria E. Zoghbi^{6§}, Elisabeth P. Carpenter^{4‡§}, Marc Liesa^{1,2,3*}

Although the role of hydrophilic antioxidants in the development of hepatic insulin resistance and nonalcoholic fatty liver disease has been well studied, the role of lipophilic antioxidants remains poorly characterized. A known lipophilic hydrogen peroxide scavenger is bilirubin, which can be oxidized to biliverdin and then reduced back to bilirubin by cytosolic biliverdin reductase. Oxidation of bilirubin to biliverdin inside mitochondria must be followed by the export of biliverdin to the cytosol, where biliverdin is reduced back to bilirubin. Thus, the putative mitochondrial exporter of biliverdin is expected to be a major determinant of bilirubin regeneration and intracellular hydrogen peroxide scavenging. Here, we identified ABCB10 as a mitochondrial biliverdin exporter. ABCB10 reconstituted into liposomes transported biliverdin, and ABCB10 deletion caused accumulation of biliverdin inside mitochondria. Obesity with insulin resistance up-regulated hepatic ABCB10 expression in mice and elevated cytosolic and mitochondrial bilirubin content in an ABCB10-dependent manner. Revealing a maladaptive role of ABCB10-driven bilirubin synthesis, hepatic ABCB10 deletion protected diet-induced obese mice from steatosis and hyperglycemia, improving insulin-mediated suppression of glucose production and decreasing lipogenic SREBP-1c expression. Protection was concurrent with enhanced mitochondrial function and increased inactivation of PTP1B, a phosphatase disrupting insulin signaling and elevating SREBP-1c expression. Restoration of cellular bilirubin content in ABCB10 KO hepatocytes reversed the improvements in mitochondrial function and PTP1B inactivation, demonstrating that bilirubin was the maladaptive effector linked to ABCB10 function. Thus, we identified a fundamental transport process that amplifies intracellular bilirubin redox actions, which can exacerbate insulin resistance and steatosis in obesity.

INTRODUCTION

Hydrogen peroxide produced by mitochondria not only can damage cells but is also a central molecule participating in signaling transduction (1). Consequently, pro- and antioxidant systems are key regulators of metabolism and can play tissue-specific roles. Liver is one

of the tissues with the highest antioxidant capacity and largest variety of antioxidant systems. Both prooxidants and antioxidants are concurrently elevated in insulin-resistant and steatotic livers and are distributed to distinct microdomains based on their chemical properties. A well-studied antioxidant of the hydrophilic environment is glutathione. The lipophilic environment, which includes membranes, has its own antioxidant systems that are less studied. Among them are ubiquinol, melatonin, α -lipoic acid, and bilirubin (2). Bilirubin is a particularly interesting antioxidant due to its lipophilicity, cell-autonomous and ubiquitous production from heme degradation, and its presence in different organelles (3, 4).

Heme is an essential cofactor present in all cell types because it is part of mitochondrial cytochromes and oxygen carrier proteins. However, free heme is toxic because it can cause oxidative damage (5). Consequently, all cells prevent heme-induced toxicity by degrading heme to biliverdin. Biliverdin is soluble and is transformed by cytosolic biliverdin reductase (BLVRA) to lipophilic bilirubin (6, 7). Bilirubin and biliverdin are both released from the cytosol to the bloodstream. Plasma bilirubin concentrations are higher (1 to 25 μ M) than biliverdin (0.12 to 0.01 μ M), which is explained by the efficient and ubiquitous conversion of biliverdin to bilirubin and the faster excretion of biliverdin. Biliverdin can be directly excreted to the bile (8), whereas solubilization of bilirubin is required for its efficient excretion. Bilirubin solubilization is achieved by conjugating bilirubin to glucuronic acids, a reaction catalyzed by UDP glucuronosyltransferase family 1 member A1 (UGT1A1) in the endoplasmic reticulum (ER) lumen of hepatocytes (9).

¹Department of Medicine, Division of Endocrinology, David Geffen School of Medicine at UCLA, 650 Charles E. Young Dr., Los Angeles, CA 90095, USA. ²Department of Molecular and Medical Pharmacology, David Geffen School of Medicine at UCLA, 650 Charles E. Young Dr., Los Angeles, CA 90095, USA. ³Molecular Biology Institute at UCLA, 611 Charles E. Young Drive East, Los Angeles, CA 90095-1570, USA. ⁴Center for Medicines Discovery, University of Oxford, Oxfordshire OX3 7DQ, UK. ⁵Department of Physiology, University of California, Los Angeles, 650 Charles E. Young Dr., Los Angeles, CA 90095, USA. ⁶Department of Molecular Cell Biology, School of Natural Sciences, University of California, Merced, 5200 North Lake Rd., Merced, CA 95343, USA. ⁷Evans Biomedical Research Center, Boston University School of Medicine, 650 Albany St., Boston, MA 02118, USA. ⁸Department of Human Genetics, David Geffen School of Medicine at UCLA, 650 Charles E. Young Dr., Los Angeles, CA 90095, USA. ⁹Department of Pharmacology and Systems Physiology, University of Cincinnati College of Medicine, 231 Albert Sabin Way, Cincinnati, OH 45267-0575, USA. ¹⁰Department of Chemistry and Biochemistry, University of California, Los Angeles, Los Angeles, CA 90095, USA. ¹¹Department of Medicine, Division of Cardiology, David Geffen School of Medicine at UCLA, 650 Charles E. Young Dr., Los Angeles, CA 90095, USA. ¹²Department of Microbiology, Immunology and Molecular Genetics, David Geffen School of Medicine at UCLA, 650 Charles E. Young Dr., Los Angeles, CA 90095, USA.

*Corresponding author: Email: mliesa@mednet.ucla.edu

†Present address: Department of Molecular Medicine, Faculty of Medicine, Université Laval, Québec City G1V 0A6, Canada.

‡Present address: Vertex Pharmaceuticals Ltd., Jubilee Drive, Milton Park, Abingdon OX14 4RZ, UK.

§These authors contributed equally to this work.

The lipophilicity of unconjugated bilirubin allows its passive diffusion through cellular membranes, including mitochondrial membranes (10). Kernicterus, a neurological disease resulting from excessive plasma bilirubin concentrations (>300 μM), damages brain mitochondria (11). The detrimental effect of high bilirubin concentrations on mitochondrial function can be reproduced in vitro because 100 μM bilirubin added to isolated mitochondria completely blocks their adenosine 5'-triphosphate (ATP) synthesis capacity (12). In contrast, 100 μM biliverdin has no effects on isolated mitochondrial function (12). Moreover, bilirubin decreases mitochondrial OXPHOS (oxidative phosphorylation) efficiency (12), scavenges lipid peroxides, and decreases H_2O_2 content at low micromolar, even nanomolar, concentrations (6, 7).

Consequently, the intracellular pool of free bilirubin must be tightly regulated to prevent the toxic actions of bilirubin on mitochondria and execute its beneficial actions when needed. The lipophilic nature of bilirubin and higher hydrophilicity of biliverdin impose a mechanistic challenge on the regulation of their intracellular pools. Bilirubin can cross membranes by passive diffusion and equilibrate across the ER, mitochondria, and cytosol (10). When bilirubin scavenges H_2O_2 , it is oxidized to form biliverdin, which cannot cross membranes easily. There is functional evidence that an uncharacterized biliverdin exporter is present in the plasma membrane of hepatocytes and is required to export biliverdin to the bile (8). However, whether mitochondria export biliverdin is unknown. Biliverdin cannot be converted back to bilirubin in the mitochondrial matrix because BLVRA is absent (13, 14). Therefore, mitochondria can regulate bilirubin synthesis by controlling the export of biliverdin. The regulation of mitochondrial biliverdin export and its consequences on the cellular pool of bilirubin, as well as on mitochondrial bilirubin content, are currently undefined.

The ATP-binding cassette (ABC) transporter ABCB10 is located in the inner mitochondrial membrane (15–18) and is highly expressed in the liver and bone marrow. ABCB10 is essential for hemoglobinization during primitive erythropoiesis, and ABCB10 deletion causes defects in hemoglobin synthesis that are rescued by treatments with antioxidants. This rescue by antioxidants demonstrates that ABCB10 is not essential for heme synthesis per se but rather protects from oxidative stress induced by high heme content (16). Hepatocytes are ranked second after differentiating erythrocytes as the cells with the highest rates of heme synthesis in their mitochondria (19). Disturbed heme homeostasis and changes in mitochondrial function in the liver are associated with insulin resistance and fatty liver disease (20), and ABCB10 is the only gene that encodes for a mitochondrial transporter related to heme homeostasis with intronic variants associated with type 2 diabetes (21, 22). However, the function of ABCB10 in the liver, its role in insulin resistance, and the cargo transported by ABCB10 are unknown.

Here, we demonstrate that ABCB10 is a mitochondrial biliverdin exporter that increases bilirubin production. We find that ABCB10 up-regulation is necessary for the increase in mitochondrial bilirubin content induced by obesity, which leads to a redox state that promotes hepatic steatosis and insulin resistance. In all, we define a mitochondrial transport process that becomes maladaptive in obesity.

RESULTS

ABCB10 exports biliverdin, which increases bilirubin synthesis

ABCB10 has been mostly studied in differentiating red blood cells (15–18, 23). Because the substrate exported by ABCB10 is unknown,

the mechanism by which ABCB10 protected from oxidative damage is uncharacterized (16). However, previous data provided key insights about the nature of ABCB10 cargo. Treating ABCB10 knockout (KO) red blood cell precursors with antioxidants rescues heme biosynthesis, showing that ABCB10 is not essential to transport heme intermediates and heme itself (16, 24). Instead, the cargo transported by ABCB10 is expected to counteract oxidative stress and to be produced during heme synthesis.

In this context, the next logical molecules to test as ABCB10 cargo were the products of heme metabolism, biliverdin, and its redox pair bilirubin (fig. S1A). ABC transporters harness energy from the hydrolysis of ATP to facilitate the conformational changes necessary to execute transport cycles. Thus, ABCB10 adenosine triphosphatase (ATPase) activity is expected to increase in the presence of its cargo (24, 25). We found that biliverdin, but not bilirubin, caused a twofold increase in ABCB10 ATPase activity in purified human ABCB10 reconstituted into nanodiscs (Fig. 1A). Maximal ATPase activation was achieved at biliverdin concentrations of 2.5 to 5 μM with a Michaelis constant of 143.6 nmol of biliverdin/mg of protein per minute and a V_{max} (maximal rate) of 323 nmol of Pi/mg of protein per minute (Fig. 1B). Moreover, other heme-related molecules previously hypothesized to be transported by ABCB10, including heme precursors aminolevulinic acid and protoporphyrin IX, as well as hemin, did not change ABCB10 ATPase activity (26, 27). Together, these results support that biliverdin is the strongest heme-related candidate as cargo transported by ABCB10.

To directly determine whether ABCB10 transports biliverdin across membranes, we reconstituted human ABCB10 into sealed liposomes. For ABC transporters that carry a substrate away from the ATP domain, cargo accumulation inside liposomes can be achieved by adding ATP in the incubation media. The reason is that ATP cannot cross the membrane of a sealed liposome and, thus, ATP is not accessible to transporters inserted in the opposite orientation. As a result, ABCB10 molecules with their ATP-binding domain facing the incubation media will be the only ABCB10 molecules transporting cargos, allowing the cargo to accumulate inside liposomes (Fig. 1C).

With ATP in the media, we observed a linear increase in radioactive biliverdin accumulation in ABCB10 liposomes, approaching a plateau 15 to 30 min after adding radioactive biliverdin (Fig. 1D). In the absence of ATP, we detected a minor and linear increase in radioactive biliverdin content in liposomes. We attributed the ATP-independent increase in biliverdin accumulation to the expected binding of biliverdin to lipids and maybe to ABCB10 itself but without being transported. This ATP-independent increase in biliverdin accumulation was subtracted to calculate the maximal amount of biliverdin transported by ABCB10. After 60 min of incubation, 135 nmol of biliverdin/mg of ABCB10 protein accumulated into the liposomes (Fig. 1D). To further confirm the specificity of ABCB10-mediated biliverdin transport, we tested the ability of other heme-related molecules, as well as unlabeled biliverdin, to compete for ABCB10-mediated labeled biliverdin uptake. As expected, unlabeled biliverdin (1 μM , threefold higher than labeled) blocked labeled biliverdin uptake, whereas the other physiological heme-related molecules did not (fig. S2). In all, these data support that the only heme-related molecule transported by ABCB10 is biliverdin.

Because bilirubin is synthesized in the cytosol from biliverdin by biliverdin reductase (BLVRA), our expectation was that ABCB10-mediated biliverdin export would increase cytosolic bilirubin

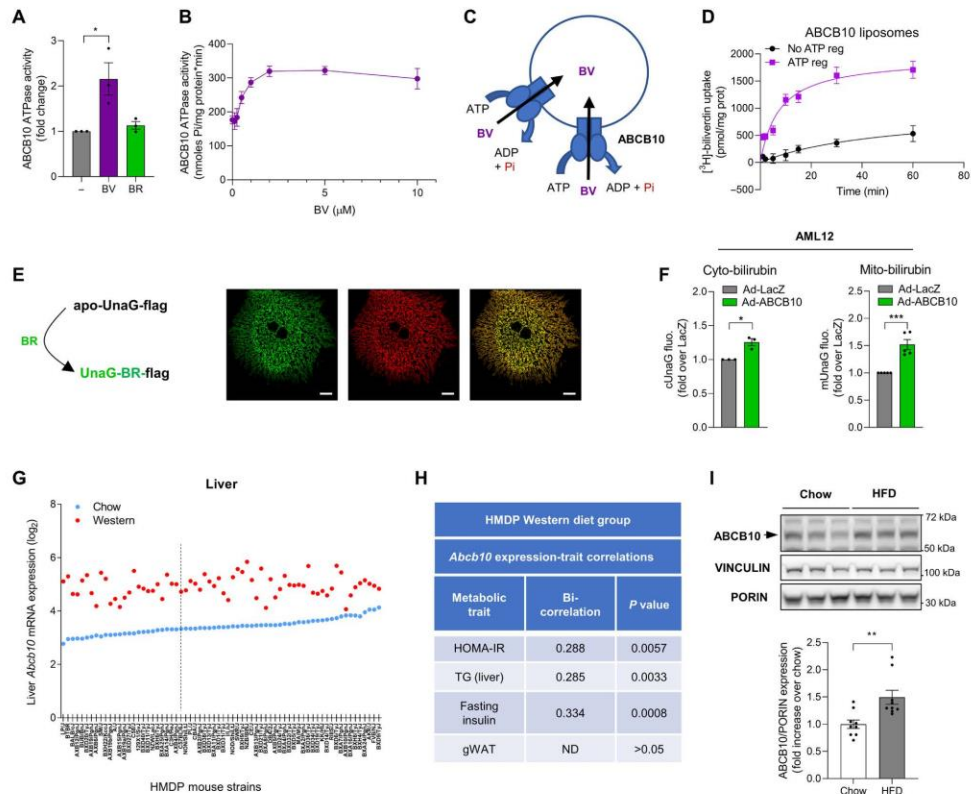


Fig. 1. ABCB10 exports mitochondrial biliverdin to increase bilirubin synthesis and is positively associated with insulin resistance and steatosis. (A) ATPase activity of ABCB10 reconstituted into nanodiscs in the presence of biliverdin (BV; 5 μ M) or bilirubin (BR; 5 μ M). $n = 3$ independent experiments. (B) Michaelis-Menten plot of ABCB10 ATPase activity with increasing biliverdin concentrations. $n = 7$ independent experiments. (C) Scheme of ABCB10 orientation in sealed liposomes. ADP, adenosine 5'-diphosphate. (D) 3 H-biliverdin accumulation into sealed ABCB10 liposomes determined with or without ATP for the indicated times. Graph was plotted using one-phase association equation, mean of $n = 5$ independent transport experiments \pm SEM, from two independent protein and liposome preparations. (E) UnaG-Flag protein fluorescence upon reversible binding to bilirubin, with high-resolution confocal images of primary mouse hepatocytes expressing the bilirubin sensor in mitochondria (mito-UnaG or mUnaG) showing colocalization with the mitochondrial dye TMRE. Scale bars, 20 μ m. (F) AML12 mouse hepatocytes cotransduced with adenovirus encoding LacZ or ABCB10 with cytosolic UnaG (cUnaG) or mUnaG to measure bilirubin. $n = 3$ to 5 independent experiments. (G) Hepatic *Abcb10* mRNA content measured in 68 strains (x axis) of the HMDP fed chow (blue) or Western diet (red), including C57BL/6J (dashed line). (H) Biweight midcorrelation values between hepatic *Abcb10* transcript content with the metabolic trait measured in the Western diet-fed HMDP mice, with nominal P values shown ($n = 102$ strains). gWAT, gonadal white adipose tissue, ND, not detected. (I) ABCB10 expression in liver lysates from WT mice fed an HFD (45% kcal as fat). $n = 9$ mice per group. Mann-Whitney U test, * $P < 0.05$, ** $P < 0.01$, and *** $P < 0.001$.

production and availability (fig. S3). If this expectation was correct, then ABCB10 gain of function would increase bilirubin content in the cytosol of hepatocytes. Then, higher cytosolic bilirubin availability would lead to an increase in mitochondrial bilirubin through passive diffusion across mitochondrial membranes (10). The availability of a fluorescent and reversible bilirubin sensor, the eel protein UnaG (Fig. 1E) (4, 28), allowed us to perform real-time measurements of cytosolic and mitochondrial bilirubin in live cells. UnaG was successfully targeted to the mitochondrial matrix of

mouse primary hepatocytes, as shown by its colocalization with Tetramethylrhodamine, ethyl ester (TMRE) (Fig. 1E). UnaG fluorescence successfully reported mitochondrial bilirubin content, as shown by the increase in UnaG fluorescence after adding bilirubin to the media (fig. S4, A and B) (3, 4). Increasing ABCB10 expression in alpha mouse liver 12 (AML12) hepatocytes elevated both cytosolic and mitochondrial bilirubin contents (Fig. 1F and fig. S5), supporting that ABCB10-mediated biliverdin export was sufficient to increase bilirubin synthesis.

Hepatic ABCB10 expression is higher in diet-induced obese mice and is associated with greater steatosis and insulin resistance

Because insulin resistance induces hepatic redox stress and intronic *ABCB10* variants are associated with type 2 diabetes in humans (21, 22), we analyzed hepatic *Abcb10* expression in the Western diet-fed Hybrid Mouse Diversity Panel (HMDP). The HMDP is a collection of 102 mouse strains with obesity, insulin resistance, and hepatic steatosis (29). *Abcb10* mRNA content in the liver is elevated by Western diet feeding in 68 of the 102 HMDP strains, with 68 being the number of strains with matched chow diet feeding. The increase in ABCB10 expression ranged 2- to 10-fold depending on the strain (Fig. 1G). Analyzing the 102 Western diet-fed HMDP strains, we found a positive correlation between hepatic *Abcb10* expression and the severity of steatosis and insulin resistance (Fig. 1H and fig. S6, A and B). Accordingly, liver *Abcb10* expression showed positive and significant correlations with liver triglyceride (TG) content ($P = 0.0033$), HOMA-IR (Homeostatic Model Assessment for Insulin Resistance) values ($P = 0.0057$), and fasting insulin concentrations ($P = 0.0008$) (Fig. 1H and fig. S6, A to C). Correlations were determined via midweight bicorrelation analyses as reported (29). No significant ($P > 0.05$) correlations of liver *Abcb10* expression with gonadal fat mass were detected (Fig. 1I and fig. S6D). Thus, hepatic ABCB10 up-regulation was not a reflection of the different susceptibility among HMDP strains to develop obesity. Last, ABCB10 protein was also increased in the liver from C57BL/6j mice fed a 45% high-fat diet (HFD) (Fig. 1J).

ABCB10 is dispensable for normal hepatocyte function in mice

The liver is ranked second in the list of tissues with the highest ABCB10 content and heme synthesis rates (30). To determine the physiological relevance of ABCB10-mediated biliverdin export in hepatocytes, we first tested the effects of deleting ABCB10 in hepatocytes from control lean mice by generating *Abcb10* liver-specific KO (LKO) mice (fig. S7). *Abcb10* excision was confirmed by amplification of the Cre-excised *Abcb10* genomic sequence and elimination of ABCB10 protein from primary hepatocytes isolated from LKO mice (Fig. 2, A and B). Phenotypically, LKO mice were healthy with normal body weight, glucose tolerance, hepatic lipid content, and mitochondrial function (Fig. 2, C to G). In marked contrast to erythroid cells (16), ABCB10 is not essential for viability, mitochondrial function, or heme homeostasis in hepatocytes. If ABCB10 exported biliverdin in hepatocytes in vivo, then biliverdin would accumulate in ABCB10 KO mitochondria. Relative quantifications of mitochondrial biliverdin content revealed a 79% increase in isolated mitochondria from LKO mice, showing that the absence of ABCB10 caused accumulation of biliverdin in mitochondria (Fig. 2H). As expected from a decrease in bilirubin synthesis induced by an abrogation of ABCB10-mediated biliverdin export, ABCB10 deletion decreased both cytosolic and mitochondrial bilirubin contents in primary hepatocytes (Fig. 2, I and J). These data indicate that mitochondrial biliverdin export by ABCB10 contributes to bilirubin production in mouse hepatocytes and that neither ABCB10 deletion nor elevated mitochondrial biliverdin is deleterious for normal liver function in mice.

Hepatic ABCB10 deletion protects diet-induced obese mice from insulin resistance

The positive correlation between hepatic ABCB10 expression and insulin resistance suggested two possible roles for ABCB10:

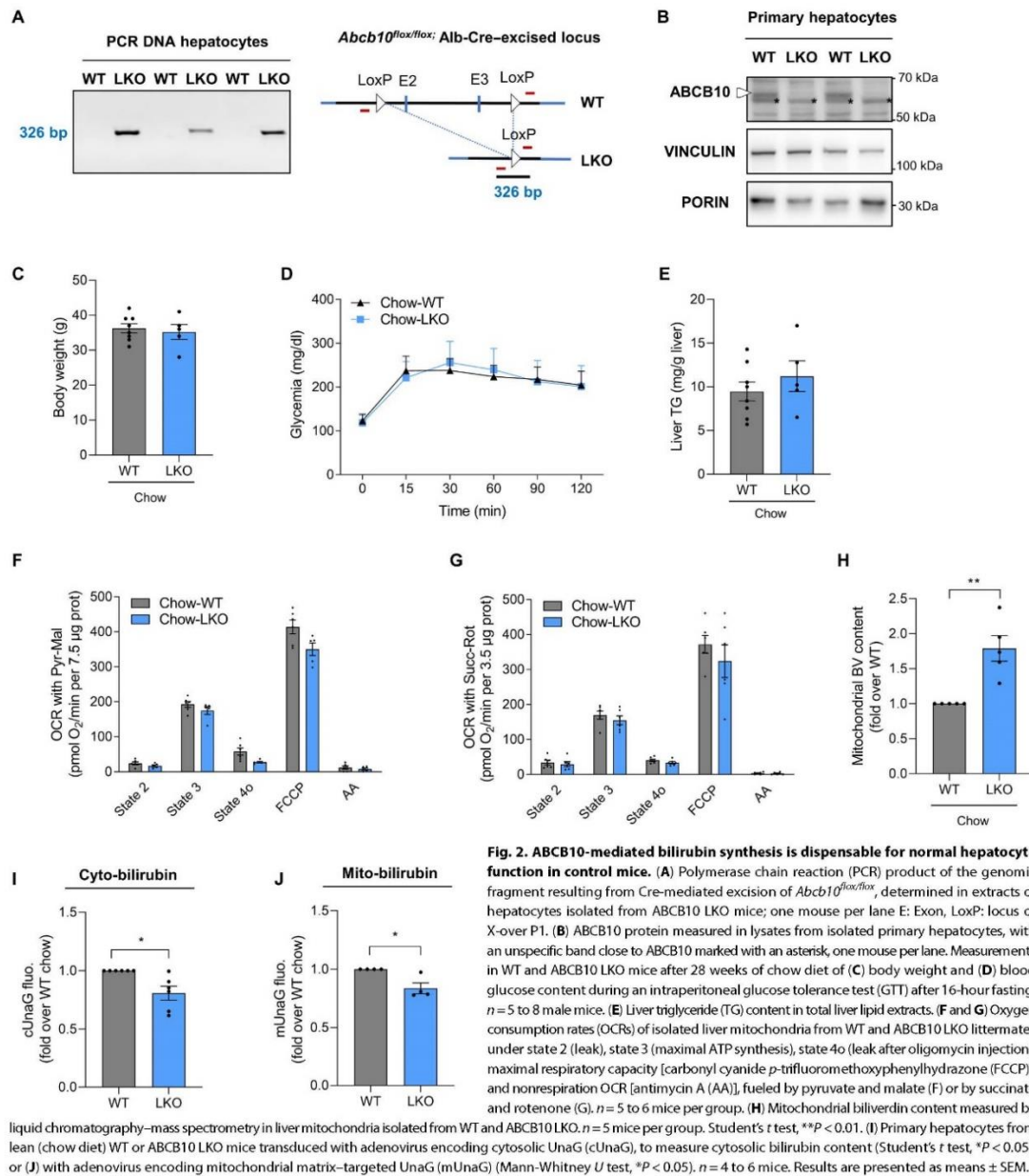
Either ABCB10 exacerbates insulin resistance, or ABCB10 ineffectively counteracts insulin resistance. Supporting the first role, ABCB10 LKO mice were protected from glucose intolerance induced by HFD, showing improved glucose clearance during a glucose tolerance test (GTT) without changes in insulinemia (Fig. 3, A and B) and a prolonged action of insulin maintaining lower glycemia during an insulin tolerance test (ITT) (Fig. 3C). ABCB10 deletion decreased fasting glucose concentrations, without changing fasting insulin (Fig. 3, D and E). A 7.2% decrease in body weight without changes in food intake was observed in HFD-fed LKO mice, which was explained by lower fat mass (Fig. 3, F to H).

The improvement in the glycemic profiles of LKO mice could be a result of a decrease in hepatic glucose production and an improvement in insulin action suppressing hepatic glucose production. Consequently, to test whether changes in hepatic glucose production in LKO mice were independent of decreased body weight, we used weight-matched HFD-fed LKO and wild-type (WT) mice (Fig. 3I) to perform hyperinsulinemic-euglycemic clamps (Fig. 3J). These clamp experiments revealed that glucose infusion rates in weight-matched HFD-fed LKO mice were 48% higher than in WT littermates (Fig. 3K). Hepatic glucose production was markedly decreased, and the ability of insulin to suppress hepatic glucose production was improved in HFD-fed LKO mice (Fig. 3, L and M). Higher suppression of hepatic glucose production by insulin, without a change in insulin-stimulated glucose disappearance rates (Fig. 3N), indicated that protection from insulin resistance in LKO mice was largely restricted to the liver. Thus, these data support that ABCB10 deletion in the liver might not protect the muscle from insulin resistance.

ABCB10 impairs insulin signaling in primary human and mouse hepatocytes

Although hepatic glucose production rates can be determined by extrahepatic tissues, impaired insulin signal transduction in the liver can augment hepatic glucose production and is a reliable biomarker of hepatocyte-autonomous insulin resistance (31–33). To determine whether ABCB10 deletion improved insulin sensitivity in a hepatocyte-autonomous manner, we isolated primary hepatocytes from weight-matched HFD-fed WT and ABCB10 LKO mice and determined insulin action ex vivo. To this end, we measured the effects of insulin treatment on the insulin receptor (INSR) and AKT phosphorylation in cultured primary hepatocytes. After 5-min treatment of 10 nM insulin, HFD-fed LKO primary hepatocytes showed a twofold improvement in the action of insulin increasing INSR Tyr^{1162/1163} and AKT Ser⁴⁷³ phosphorylation, when compared to hepatocytes from HFD-fed WT littermates (Fig. 4A). In healthy primary human hepatocytes with ABCB10 knocked down (40%) (fig. S8A), a similar improvement in insulin action on INSR Tyr^{1162/1163} phosphorylation was observed (Fig. 4B).

To test whether elevated ABCB10 function was sufficient to decrease insulin signaling in human hepatocytes, we used adenoviral transduction to increase ABCB10 expression (fig. S8B). The ability of insulin (10 nM) to induce INSR and AKT phosphorylation was decreased both in mouse AML12 and in primary human hepatocytes with increased ABCB10 expression (Fig. 4, C and D). Last, we restored ABCB10 expression ex vivo via adenoviral transduction of primary hepatocytes isolated from HFD-fed ABCB10 LKO mice. We found that the improvement in insulin action phosphorylating INSR and AKT in LKO hepatocytes was reversed by ABCB10 re-expression (fig. S9).



Our data show that high ABCB10 expression promotes a hepatocyte-autonomous disruption in insulin signaling in mouse and human hepatocytes. Accordingly, ABCB10 deletion in HFD-fed mice improved insulin signaling, decreased hepatic glucose production, and increased the action of insulin suppressing hepatic glucose production in HFD-fed mice.

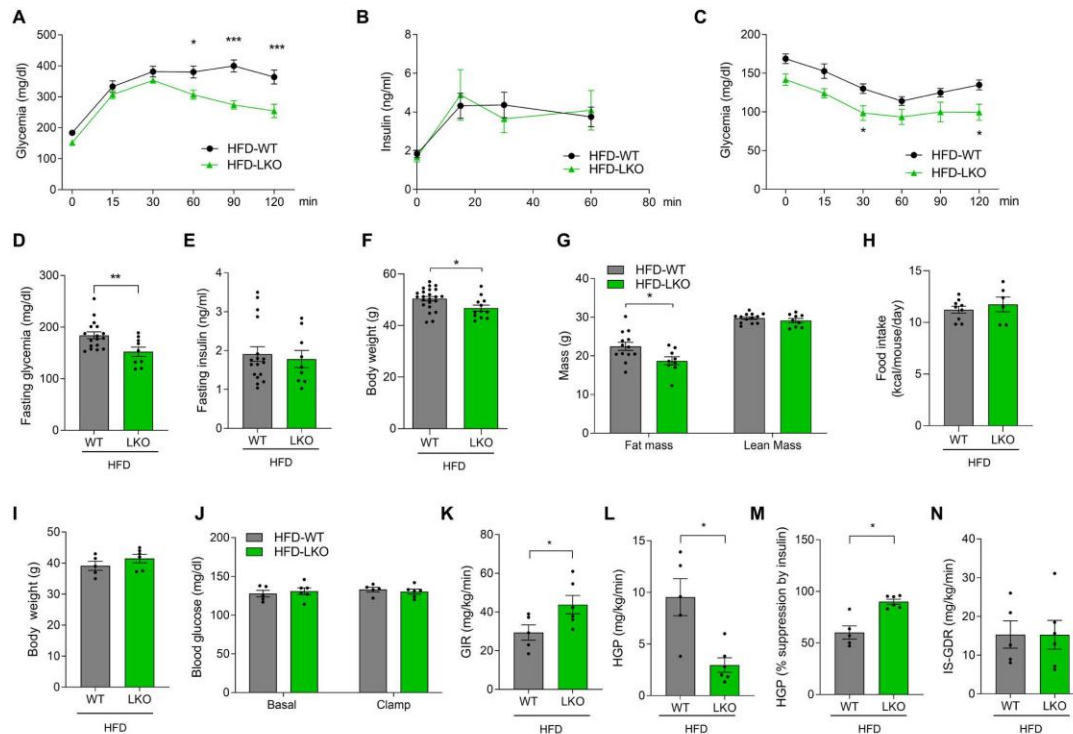


Fig. 3. Hepatic ABCB10 deletion protects from HFD-induced insulin resistance and increases insulin-mediated suppression of hepatic glucose production. (A to N) WT and ABCB10 LKO male mice were fed a HFD and (A) blood glucose, and (B) plasma insulin were measured after 16-hour fasting during GTT at 28 weeks of diet. Two-way ANOVA, $^*P < 0.05$ and $^{***}P < 0.001$. $n = 9$ to 17 mice per group. (C) Insulin tolerance test (ITT) performed after a 6-hour fasting at 26 weeks of HFD. Two-way ANOVA, $^*P < 0.05$. $n = 11$ to 19 mice per group. (D) Fasting glycemia and (E) fasting insulinemia values from (A) and (B). (F) Body weight of WT and LKO mice after 30 weeks of HFD. $n = 9$ to 23 mice per group. Student's t test, $^*P < 0.05$ and $^{**}P < 0.01$. (G) Lean and fat mass of HFD-fed WT and LKO mice determined by EchoMRI at 30 weeks of diet. $n = 9$ to 13 mice per group. Student's t test, $^*P < 0.05$. (H) Daily food intake in WT or ABCB10 LKO mice. (I to N) Hyperinsulinemic-euglycemic clamps in weight-matched HFD-fed WT and ABCB10 LKO mice at 30 weeks of diet. $n = 5$ to 6 mice per group. (I) Body weight of clamped mice with (J) blood glucose concentration at basal state and during the clamps. (K) Glucose infusion rates (GIRs). Student's t test, $^*P < 0.05$. (L) Hepatic glucose production (HGP). Student's t test, $^*P < 0.05$. (M) Insulin suppression of HGP. Student's t test, $^*P < 0.05$. (N) Insulin-stimulated glucose disappearance rate (IS-GDR). Results are presented as means \pm SEM.

Hepatic ABCB10 deletion increases mitochondrial respiration, protects against steatosis, and counteracts hyperlipidemia in diet-induced obese mice

To investigate why HFD-fed ABCB10 LKO mice showed decreased fat mass, we measured their energy balance using indirect calorimetry. No significant changes ($P > 0.05$) were detected in their food intake, fecal lipids (Fig. 5, A and B), or total physical activity (fig. S10A). In contrast, we detected a significant ($P < 0.05$) increase in oxygen consumption (VO_2) and energy expenditure (EE) in HFD-fed LKO mice at night (fed state) when using covariate statistics to model VO_2 and EE values at an equal body weight between genotypes (Fig. 5, C and D). HFD-fed LKO mice showed an elevation in carbohydrate oxidation, revealed by higher respiratory exchange ratio values (RER) at night (Fig. 5E). Thus, increased RER showed that the decrease in body fat in LKO mice was associated with increased carbohydrate expenditure, rather than elevated fat expenditure. Accordingly, we did not observe changes in circulating fibroblast growth factor 21 in ABCB10

LKO mice (fig. S10B), a factor secreted by the liver that increases systemic EE by promoting fat oxidation (34).

Higher mitochondrial oxidative function in hepatocytes was previously shown to improve insulin signaling (20, 35). To test whether ABCB10 deletion increased mitochondrial function in diet-induced obese mice, we isolated mitochondria and primary hepatocytes from livers of HFD-fed ABCB10 LKO mice and measured their respiratory capacity. Respiration coupled to ATP synthesis was increased both in isolated mitochondria and in primary hepatocytes isolated from HFD-fed ABCB10 LKO mice (Fig. 5, F and G). Maximal respiratory capacity was increased in primary hepatocytes from HFD-fed LKO mice as well (Fig. 5H). These changes in mitochondrial function occurred in the absence of changes in mitochondrial biogenesis markers, such as PGC-1 α [peroxisome proliferator-activated receptor γ coactivator-1 α] or TFAM (transcription factor A, mitochondrial) (fig. S10C), and without a coordinated up-regulation in the subunits of mitochondrial

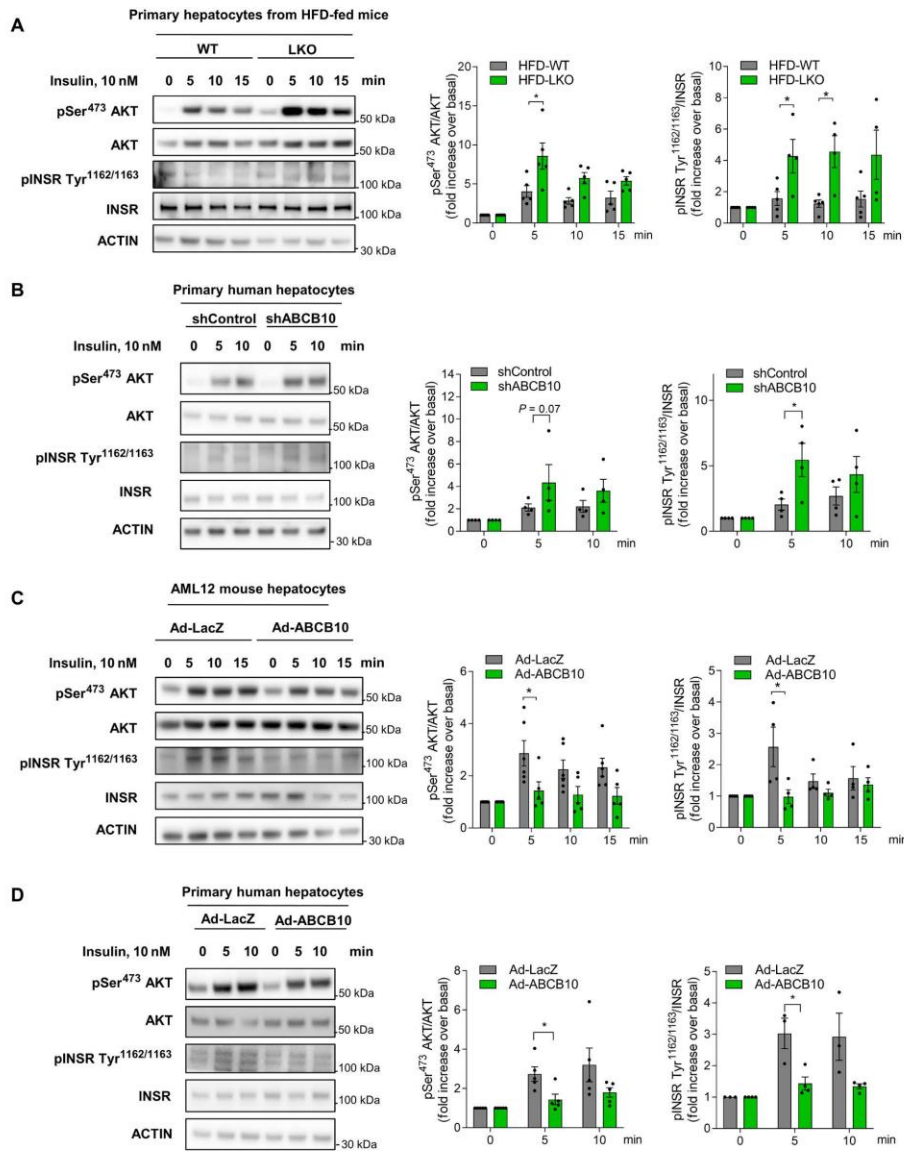


Fig. 4. ABCB10 is sufficient to impair insulin signaling in mouse and human primary hepatocytes. (A) Western blots detecting pSer⁴⁷³ AKT and pTyr^{1162/1163} INSR in total lysates of primary hepatocytes isolated from HFD-fed WT and LKO mice. Hepatocytes were serum-starved (o/n) and treated with 10 nM insulin for the indicated times. *n* = 4 to 5 independent experiments. (B) Human hepatocytes were transduced with lentivirus encoding shControl (sh001) or shABCB10. Two days after transduction, hepatocytes were serum-starved (6 hours) and treated with 10 nM insulin for the indicated times. Western blots of pSer⁴⁷³ AKT and pTyr^{1162/1163} INSR in total lysates. *n* = 4 independent experiments. (C) Mouse AML12 hepatocytes were transduced with Adenovirus (Ad) encoding LacZ or ABCB10. Two days after transduction, hepatocytes were serum-starved (6 hours) and treated with 10 nM insulin for the indicated times. Western blots of pSer⁴⁷³ AKT and pTyr^{1162/1163} INSR. *n* = 4 to 6 independent experiments. (D) Human primary hepatocytes transduced with Ad-LacZ and Ad-ABCB10. Two days after transduction, hepatocytes were serum-starved (6 hours) and treated with 10 nM insulin for the indicated times. Western blots detecting pSer⁴⁷³ AKT and pTyr^{1162/1163} INSR in total lysates. *n* = 3 to 5 independent experiments. Means ± SEM, **P* < 0.05, one-way ANOVA.

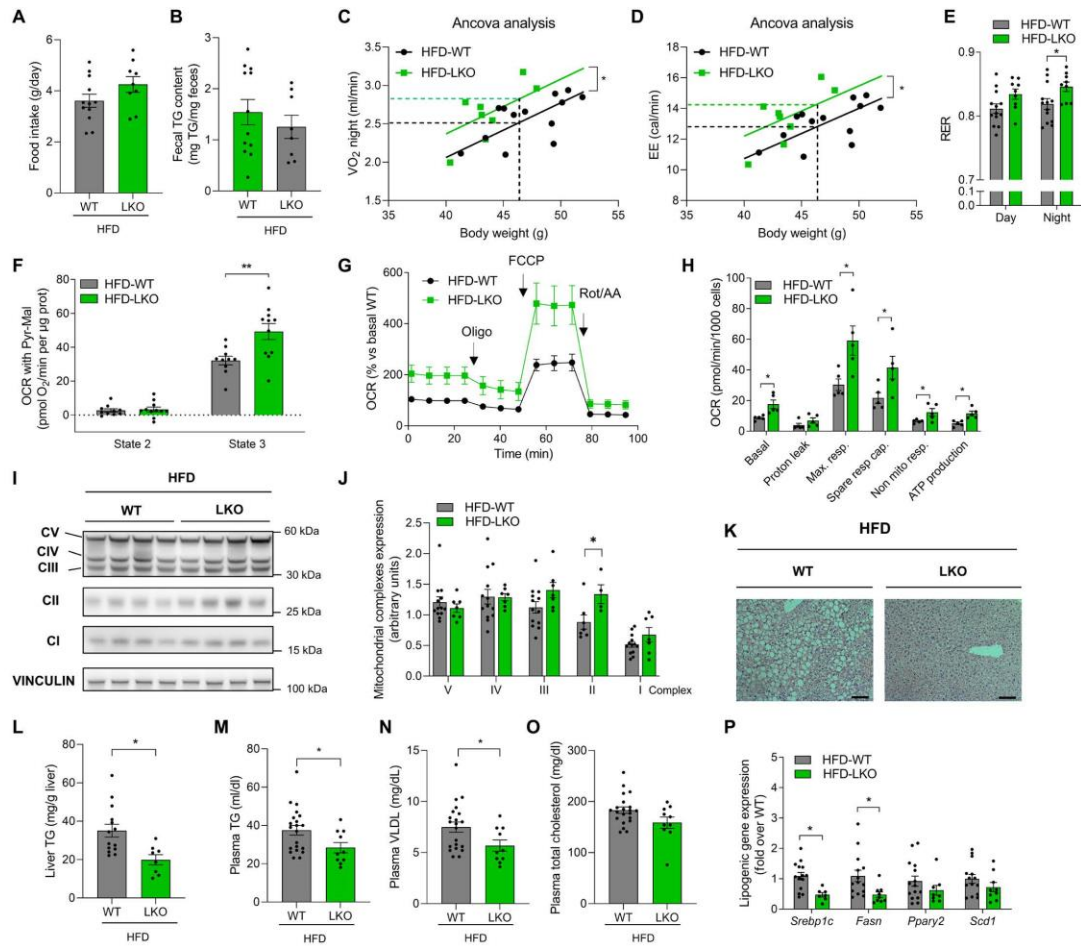


Fig. 5. Hepatic ABCB10 deletion increases mitochondrial energy expenditure and protects from hepatic steatosis and hyperlipidemia induced by high-fat diet. (A to O) Measurements in WT and ABCB10 LKO male mice fed a high-fat diet (HFD) for 30 to 32 weeks. (A) Food intake of each individual mouse over a 48-hour period and (B) TG content measured in feces collected in the metabolic cages ($n = 8$ to 12 mice). (C) Covariate analysis of VO_2 and (D) energy expenditure (EE) versus total body weight measured using indirect calorimetry. Dashed lines represent the average body weight values modeled to determine VO_2 and EE in each group. $*P < 0.05$ using ANCOVA. $n = 8$ to 13 mice per group. (E) Respiratory exchange ratio (RER). Student's t test, $*P < 0.05$. $n = 8$ to 13 mice per group. (F) Oxygen consumption rates (OCR) from isolated liver mitochondria under state 2 (leak) and state 3 (maximal ATP synthesis) fueled by pyruvate (Pyr) and malate (Mal). $n = 10$ to 12 mice per group. Student's t test, $**P < 0.01$. (G) OCR traces showing basal, ATP-synthesizing (oligomycin sensitive), and maximal respiration (induced by FCCP) and (H) their bar graph quantification measured in intact primary hepatocytes isolated from $n = 5$ mice per group. Student's t test, $*P < 0.05$. (I and J) Mitochondrial complex I to V subunits' protein content in total liver lysates, with vinculin as loading control. $n = 7$ to 13 mice per group. Student's t test, $*P < 0.05$, WT versus LKO. (K) Hematoxylin and eosin staining of liver sections. Scale bars, 100 μ m. (L) Liver TG content in total liver lipid extracts. $n = 8$ to 14 mice per group. Student's t test, $*P < 0.05$. (M) Plasma TG, (N) plasma very-low-density lipoprotein (VLDL), and (O) plasma total cholesterol concentration. $n = 10$ to 21 mice per group. Student's t test, $*P < 0.05$. (P) Expression of lipogenic genes *Srebp1c*, *Fasn*, *Atgl*, *Ppar γ 2*, and *Scd1* measured by quantitative PCR of complementary DNA retrotranscribed from HFD-fed WT and LKO mouse livers. $n = 7$ to 15 mice per group. Student's t test, $*P < 0.05$. Results presented as means \pm SEM.

complexes I, III, IV, and V (Fig. 5, I and J). Together, our data showed that ATP-synthesizing capacity (OXPHOS) was improved per unit of mitochondria with ABCB10 deleted. In this regard, we observed a 50% up-regulation exclusively in complex II content

(Fig. 5, I and J). The specific up-regulation of complex II in ABCB10 KO mitochondria suggests that bilirubin might not only be decreasing electron transfer activity as previously reported (12) but also might decrease the total content of complex II. These data support that the

Downloaded from <https://www.science.org> at University of California Los Angeles on December 31, 2021

regulation of complex II content could be an additional mechanism by which bilirubin is decreasing mitochondrial function and reactive oxygen species production.

Because hepatic steatosis is associated with insulin resistance and metabolic dysfunction, we measured lipid content and lipogenic gene expression in livers from HFD-fed LKO mice. Liver histology revealed decreased lipid droplet area in livers from HFD-fed LKO mice (Fig. 5K), which was confirmed by the 40% reduction in total TG content (Fig. 5L). Moreover, HFD-fed LKO mice showed a significant ($P < 0.05$) reduction in plasma TG and very-low-density lipoprotein concentrations and a nonsignificant ($P > 0.05$) decrease in plasma cholesterol content (Fig. 5, M to O). Last, HFD-fed LKO mice showed a 50% decrease in the mRNA content of the master regulator of lipogenesis *Srebp1c* and its downstream target, fatty acid synthase (*Fasn*) (Fig. 5P). Together, these data support that decreased hepatic TG synthesis can contribute to protection from steatosis and hyperlipidemia in LKO mice.

ABCB10 expression induced by HFD hinders cytosolic and mitochondrial H₂O₂-redox signaling by elevating cellular bilirubin content

Our data show that ABCB10 gain of function was sufficient to increase mitochondrial bilirubin content in hepatocytes. However, the effects on obesity and insulin resistance on mitochondrial bilirubin content have not been measured. Consistent with the increase in ABCB10 expression induced by HFD, HFD feeding elevated both mitochondrial and cytosolic bilirubin contents by 50% in isolated primary hepatocytes, and these HFD-induced increases were completely prevented by ABCB10 deletion (Fig. 6, A and B). In addition, we validated that the total content of the bilirubin sensor UnaG was not altered by ABCB10 deletion (fig. S11), as expected, given that UnaG was delivered via viral transduction. Furthermore, ABCB10 deletion did not change the content of proteins involved in heme catabolism [heme oxygenase 1 (HMOX1)], bilirubin synthesis (BLVRA) (fig. S12), or excretion (ABCC2) (fig. S13A). Moreover, the expression of the main enzyme involved in free bilirubin conjugation, UGT1A1, was not changed by ABCB10 deletion (fig. S13B). UGT activity, mostly determined by UGT1A1, showed a nonsignificant ($P > 0.05$) decrease in ABCB10 KO livers, which could be reflecting an unsuccessful compensation trying to preserve free bilirubin content (fig. S13C). Together, these data support that a major driver of increased intrahepatic bilirubin content induced by HFD was bilirubin synthesis from mitochondrial biliverdin exported by ABCB10.

A major action of bilirubin is to decrease H₂O₂ content and mitochondrial OXPHOS, a source of H₂O₂. H₂O₂ released by mitochondria generates signals that improve insulin signaling and prevent hepatic steatosis (20, 36). Thus, as expected from decreased bilirubin content in ABCB10 KO hepatocytes, we explored whether ABCB10 deletion caused an increase in mitochondrial H₂O₂ release and H₂O₂-mediated actions regulating the activity of redox-sensitive proteins. Using ratiometric roGFP2 (reduction-oxidation sensitive green fluorescence protein 2) probes, we measured H₂O₂ and its action on the glutathione redox state [oxidized glutathione (GSSG)/glutathione (reduced form) (GSH)] in live primary murine hepatocytes. Concurrently with higher mitochondrial and cytosolic H₂O₂ content (Fig. 6, C and D), both mitochondrial and cytosolic GSSG/GSH were increased in live hepatocytes isolated from HFD-fed LKO mice (Fig. 6, E and F). The magnitude of the elevation in H₂O₂ content

and of the GSSG/GSH ratio (ranging 25 to 40%), together with improved mitochondrial respiration, shows that the increase in H₂O₂ induced by hepatic ABCB10 deletion was not in the toxic range.

Protein tyrosine phosphatase 1B (PTP1B) is increased by HFD feeding and plays a dual maladaptive action: PTP1B directly dephosphorylates Tyr^{1162/1163} in INSR, blocking insulin signaling, and activates a different signaling cascade that increases *Srebp1c* expression (37–39). Furthermore, PTP1B oxidative inactivation is one of the mechanisms by which mitochondrial H₂O₂ release was demonstrated to protect from insulin resistance and hepatic steatosis (20). Consequently, we determined the effects of ABCB10 deletion in HFD-fed mice on PTP1B activity. By immunoprecipitating endogenous PTP1B from total lysates of primary hepatocytes, we found that HFD-fed ABCB10 LKO mice showed a ~30% decrease in PTP1B phosphatase activity (Fig. 6G).

In sum, ABCB10-driven increases in cellular bilirubin content generate a redox state favoring insulin resistance and steatosis, by disrupting mitochondrial H₂O₂ actions on insulin signaling (fig. S14). To determine the causal role of bilirubin in these redox changes, we next aimed to restore bilirubin content in ABCB10 KO hepatocytes and test its effects on redox and PTP1B activity (Fig. 7A).

Bilirubin supplementation reverses the redox benefits induced by ABCB10 deletion in diet-induced obese mice

Supplementing primary hepatocytes isolated from HFD-fed LKO mice with physiological bilirubin concentrations (10 μM) effectively restored mitochondrial and cytosolic bilirubin to WT concentrations (Fig. 7A and fig. S4C). Moreover, the slope of the fold increase in UnaG fluorescence over time after adding bilirubin was the same in WT and LKO hepatocytes (fig. S4, A and B), supporting that the capacity of extracellular bilirubin to reach both the cytosol and the mitochondrial matrix was not changed by ABCB10 deletion. One could hypothesize that the lower content of bilirubin in LKO could accelerate the entry of bilirubin into hepatocytes. However, our data showing the absence of an acceleration suggest that the occupancy of bilirubin acceptor(s) by other competing molecules could be increased by ABCB10 deletion or that intracellular bilirubin content is not a parameter strongly determining bilirubin entry rates.

We next tested the relationship between decreased bilirubin and the redox changes induced by ABCB10 deletion. Restoring bilirubin in HFD-fed LKO hepatocytes brought mitochondrial H₂O₂ content and GSSG/GSH back to HFD-fed WT values (Fig. 7, B and C). In WT hepatocytes, HFD feeding significantly ($P < 0.05$) increased only cytosolic H₂O₂ content, and, accordingly, bilirubin supplementation significantly ($P < 0.05$) decreased only cytosolic H₂O₂ in HFD-fed WT hepatocytes (Figs. 6C and 7B).

As ABCB10 deletion increased mitochondrial OXPHOS, which can elevate H₂O₂ release, we tested whether restoring bilirubin content could reverse the positive effects on mitochondrial respiration observed in ABCB10 KO hepatocytes. Bilirubin (10 μM) reversed the increase in mitochondrial OXPHOS observed in primary hepatocytes from HFD-fed ABCB10 LKO mice without changing OXPHOS in WT hepatocytes (Fig. 7, D and E). The acute nature of bilirubin actions on mitochondria was further supported by the reversal of increased respiration when bilirubin was added to liver mitochondria isolated from HFD-fed LKO mice (Fig. 7F).

We determined whether bilirubin-mediated reversal of ABCB10 KO actions on mitochondrial redox affected PTP1B activity. Bilirubin induced a nonsignificant ($P > 0.05$) increase in PTP1B activity

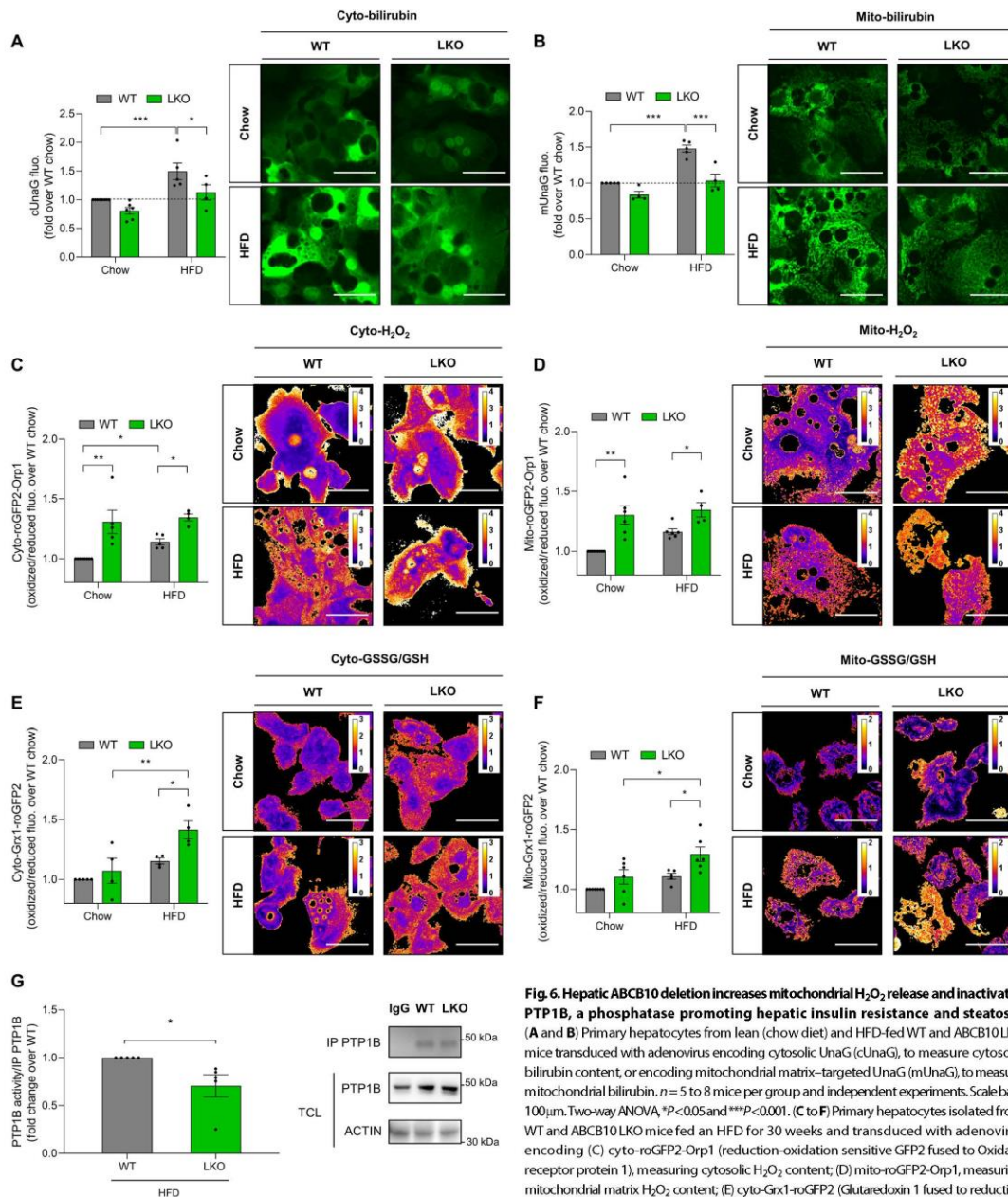
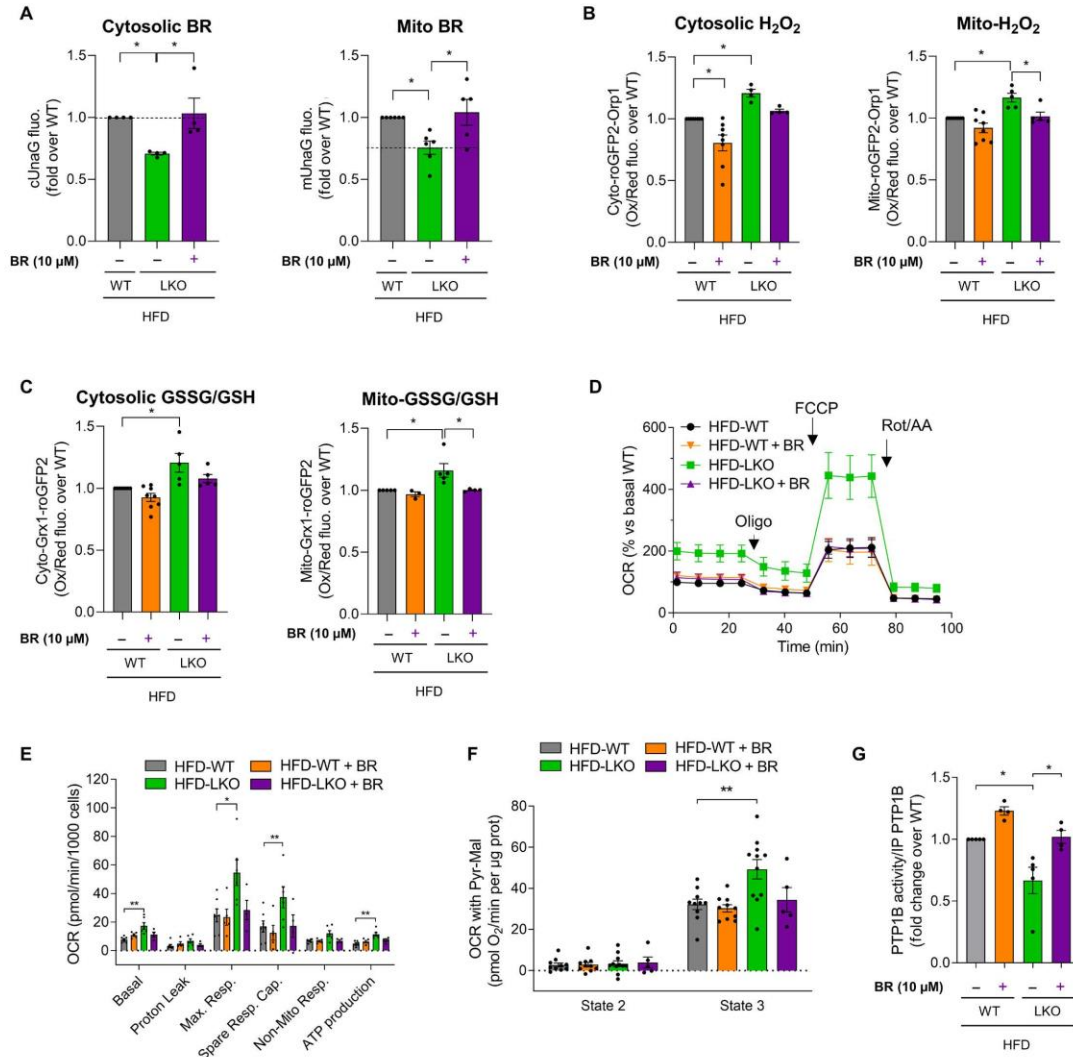


Fig. 6. Hepatic ABCB10 deletion increases mitochondrial H₂O₂ release and inactivates PTP1B, a phosphatase promoting hepatic insulin resistance and steatosis. (A and B) Primary hepatocytes from lean (chow diet) and HFD-fed WT and ABCB10 LKO mice transduced with adenovirus encoding cytosolic UnaG (cUnaG), to measure cytosolic bilirubin content, or encoding mitochondrial matrix-targeted UnaG (mUnaG), to measure mitochondrial bilirubin. *n* = 5 to 8 mice per group and independent experiments. Scale bars, 100 μm. Two-way ANOVA, **P* < 0.05 and ****P* < 0.001. (C to F) Primary hepatocytes isolated from WT and ABCB10 LKO mice fed an HFD for 30 weeks and transduced with adenovirus encoding (C) cyto-roGFP2-Orp1 (reduction-oxidation sensitive GFP2 fused to Oxidant receptor protein 1), measuring cytosolic H₂O₂ content; (D) mito-roGFP2-Orp1, measuring mitochondrial matrix H₂O₂ content; (E) cyto-Grx1-roGFP2 (Glutaredoxin 1 fused to reduction sensitive GFP2), measuring cytosolic GSSG/GSH; or (F) mito-Grx1-roGFP2, measuring mitochondrial GSSG/GSH. The ratio of green fluorescence emitted by oxidized roGFP2 divided by reduced roGFP2 is proportional to H₂O₂ content (Orp1) and GSSG/GSH (Grx1), respectively. Scale bars, 100 μm. *n* = 4 to 9 mice per group and independent isolations. Two-way ANOVA, **P* < 0.05 and ***P* < 0.01. (G) PTP1B activity measured in primary hepatocytes isolated from HFD-fed WT and ABCB10 LKO mice by immunoprecipitating (IP) PTP1B in total cell lysates (TCL) and measuring its phosphatase activity. *n* = 5 mice per group and independent isolations. Mann-Whitney *U* test, **P* < 0.05. Results presented as means ± SEM.

Downloaded from https://www.science.org at University of California Los Angeles on December 31, 2021



Downloaded from https://www.science.org at University of California Los Angeles on December 31, 2021

Fig. 7. Bilirubin supplementation reverses the redox benefits induced by hepatic ABCB10 deletion in diet-induced obese mice. (A) Live imaging of cUnaG and mUnaG average fluorescence intensity to quantify cytosolic and mitochondrial bilirubin in hepatocytes isolated from HFD-fed ABCB10 LKO mice and then treated with vehicle [dimethyl sulfoxide (DMSO)] and 10 μM bilirubin. Effects of the same bilirubin treatments on (B) cytosolic and mitochondrial matrix H₂O₂ content and (C) Grx1-roGFP2 and mito-Grx1-roGFP2 measuring cytosolic and mitochondrial GSSG/GSH. *n* = 3 to 8 mice per group. Two-way ANOVA, **P* < 0.05. (D) Respiration traces of primary hepatocytes treated with vehicle (DMSO) or 10 μM bilirubin (16 hours), isolated from HFD-fed WT and ABCB10 LKO mice. (E) Bar graph of respiration traces in (D) ± SEM. *n* = 3 to 7 mice per group. Two-way ANOVA, **P* < 0.05 and ***P* < 0.01. (F) Liver mitochondria isolated from HFD-fed WT and ABCB10 LKO mice respiring under state 2 (leak) and state 3 (maximal ATP synthesis) fueled by pyruvate (Pyr) and malate (Mal), with vehicle (DMSO) or 10 μM bilirubin (BR). *n* = 5 to 11 mice per group. Two-way ANOVA, ***P* < 0.01. (G) Phosphatase activity measured in immunoprecipitated PTP1B from primary hepatocytes treated with vehicle (DMSO) or 10 μM bilirubin (BR) (16 hours) and isolated from HFD-fed WT and ABCB10 LKO mice. *n* = 4 to 5 mice per group. Two-way ANOVA, **P* < 0.05. Results presented as means ± SEM.

in WT hepatocytes from HFD mice (Fig. 7G), consistent with bilirubin decreasing cytosolic H_2O_2 content (Fig. 7B) and thus PTP1B oxidative inactivation (40). Last, the same bilirubin treatments completely reversed the reduction of PTP1B activity observed in ABCB10 KO hepatocytes isolated from HFD-fed mice (Fig. 7G). Together, these results show that bilirubin is the major effector of ABCB10-mediated redox actions in hepatocytes from HFD-fed mice (fig. S15).

DISCUSSION

We have identified that ABCB10 exports biliverdin out of the mitochondria to amplify bilirubin synthesis. Our cell-free approach using human ABCB10 reconstituted in vesicles demonstrates that ABCB10 transports biliverdin from the matrix to the intermembrane space (IMS) domain of ABCB10. Mitochondrial biliverdin export was confirmed *in vivo* by the accumulation of biliverdin in ABCB10 KO mitochondria isolated from mouse liver. Up to this study, it was known that ABCB10 supported hemoglobin synthesis in differentiating erythrocytes, by preventing oxidative damage associated with heme synthesis (25, 30). Thus, how does biliverdin export protect from oxidative damage?

We find that mitochondrial biliverdin export executed by ABCB10 increases the availability of biliverdin destined for bilirubin synthesis, because the enzyme transforming biliverdin to bilirubin is located in the cytosol (BLVRA). Bilirubin is an effective antioxidant that scavenges H_2O_2 and, due to its lipophilic nature, effectively crosses mitochondrial membranes (10). Accordingly, elevating ABCB10 expression is sufficient to increase cytosolic and mitochondrial bilirubin contents. BLVRA can be associated with the cytosolic side of the ER (41, 42), an organelle with tight interactions with mitochondria in the liver from insulin resistant mice (43). This tight interaction means that biliverdin exported by mitochondria can be readily transformed to bilirubin in ER-mitochondria contact areas, a microdomain that could facilitate a preferential trafficking of bilirubin to mitochondria.

Initially, we expected that hepatic ABCB10 deletion would exacerbate insulin resistance and steatosis in obese mice by increasing oxidative damage and disrupting insulin signaling (44, 45). However, we obtained the opposite results. Mitochondrial OXPHOS and insulin signaling were improved in hepatocytes from diet-induced obese ABCB10 LKO mice, concurrent with mild increases in mitochondrial and cytosolic H_2O_2 content. Our study is not the first example showing that a protein that hinders H_2O_2 actions in hepatocytes promotes insulin resistance and steatosis. Hepatocyte-specific deletion of glutathione peroxidase 1 (GPX1 LKO mice), a mitochondrial and cytosolic enzyme that removes H_2O_2 , and hepatocyte-specific decreases in cytosolic biliverdin production achieved by deleting Heme Oxygenase 1 (HMOX1 LKO mice) induced the same benefits as ABCB10 deletion. In GPX1 LKO and HMOX1 LKO mice, an improvement in insulin sensitivity was explained by the posttranslational oxidative inactivation of the phosphatase PTP1B (20, 36).

PTP1B is maladaptive in obesity because it blocks insulin signaling transduction and promotes lipid synthesis in the liver (37, 46). The increase in mitochondrial H_2O_2 release as a result of GPX1 and HMOX1 deletion leads to the oxidative inactivation of the catalytic cysteine in PTP1B. Hepatocyte-specific deletion or 50% down-regulation of PTP1B activity is sufficient to protect mice from diet-induced obesity insulin resistance and steatosis (37, 46). Accordingly, we found that ABCB10 deletion decreased PTP1B phosphatase

activity (30%) in hepatocytes from HFD-fed mice, similarly to what was reported for GPX1 and HMOX1 deletion. However, the benefits induced by hepatic ABCB10 deletion on metabolic health are greater when compared to PTP1B deletion (37). These phenotypic differences support that ABCB10 deletion induces additional benefits beyond PTP1B inactivation. We propose that the increase in mitochondria function and EE observed in ABCB10 LKO mice are responsible for these additional benefits. In this regard, we demonstrated that decreased mitochondrial bilirubin content induced by ABCB10 deletion is responsible for improved mitochondrial function, a benefit that is not expected when PTP1B is deleted.

Other approaches inducing systemic increases in heme catabolism or in plasma bilirubin were shown to protect from metabolic dysfunction in obesity (47). However, mitochondrial bilirubin content was not measured in this study, meaning that it is possible that mitochondrial bilirubin was decreased by these other approaches. In this regard, bilirubin generated from mitochondrial biliverdin might preferentially act on different subcellular sites than imported bilirubin or bilirubin generated from biliverdin produced in the cytosol. This preferential action could be achieved by confining bilirubin to a microdomain (ER-mitochondria contact areas) to restrict its action on specific targets. Thus, we propose that mechanisms controlling BLVRA trafficking to different cytosolic microdomains might be a major determinant of adaptive and maladaptive bilirubin actions.

Controversy exists on whether bilirubin can be synthesized in the mitochondrial matrix, with one study detecting BLVRA in the inner mitochondrial membrane (48). This study did not determine whether the catalytic domain of BLVRA responsible for bilirubin synthesis was facing the matrix or the IMS (48). The authors showed that isolated liver mitochondria can transform exogenous biliverdin to bilirubin. The transformation of exogenously added biliverdin supports that, if BLVRA was located in the inner membrane, the domain responsible for bilirubin synthesis could be facing the IMS to access exogenous biliverdin more easily. Moreover, it is unknown how BLVRA translocates from the cytosol to the inner membrane because no mitochondrial targeting sequence is present in BLVRA. Last, other independent studies could not reproduce BLVRA detection in mitochondria, including MitoCarta (13, 14). Our data showing the existence of an active mitochondrial biliverdin export support that bilirubin is not synthesized in the matrix. Lack of matrix bilirubin synthesis or in the inner membrane face of the IMS could be justified by the need to prevent bilirubin bursts damaging the mitochondrial inner membrane. Bilirubin is a lipophilic molecule that can strongly bind to membranes and fatty acid binding proteins. Bilirubin can make the membrane leaky to protons at low concentrations and completely block electron transfer at higher concentrations (12).

The maladaptive and nonessential role of hepatic ABCB10 function further supports that bilirubin is the major effector of ABCB10 actions. Bilirubin availability in hepatocytes *in vivo* cannot be severely impaired by eliminating ABCB10-mediated biliverdin export. ABCB10 KO hepatocytes can still synthesize bilirubin from biliverdin generated in the cytosol and import bilirubin from the blood (70% of bilirubin synthesis is extrahepatic) (9). Moreover, our data show that biliverdin accumulation in liver mitochondria induced by ABCB10 deletion is not toxic in mice. This conclusion can apply to erythroid cells as well, because the essential role of ABCB10 supporting heme synthesis in erythroid cells was rescued by antioxidant treatments (16). Consequently, heme biosynthesis and respiration occur

in ABCB10 KO erythroid mitochondria accumulating biliverdin when oxidative damage is prevented. The role of bilirubin actions in erythroid cells remains largely uncharacterized because the assumption is that heme molecules synthesized in erythroid mitochondria are all exported to produce hemoglobin, and none of them are degraded. Our study could potentially change our understanding of mitochondrial heme fate during erythroid differentiation.

Because ABCB10 is dispensable for mouse liver function and maladaptive in murine obesity and its role exporting biliverdin and modulating insulin signaling is conserved in humans, we propose that hepatocyte-restricted targeting of ABCB10 holds promise as an approach to be tested to counteract hepatic insulin resistance and steatosis. The main limitation of our study is that the role of ABCB10 in mouse models of more severe forms of liver disease was not determined. Thus, it is a possibility that ABCB10 could be playing a protective role when liver damage is induced by something different from an HFD model of obesity. In addition, the mechanism by which bilirubin slows down OXPHOS directly in mitochondria remains unidentified but should involve saturable binding sites.

MATERIALS AND METHODS

Study design

The aim of this study was to examine the substrate transported by ABCB10 and the role of ABCB10 in the development of insulin resistance and steatosis. To this end, we used ABCB10 reconstituted into liposomes and nanodiscs, hepatocyte-specific ABCB10 KO mice, isolated mouse primary hepatocytes, human primary hepatocytes, and AML12 murine hepatocytes. We used fluorescent sensors to quantify bilirubin, H₂O₂, and GSSG/GSH in intact hepatocytes to determine the role of ABCB10 regulating the redox state and bilirubin compartmentalization in live cells. All experiments were approved by Institutional Animal Care and Use Committee at Boston University and by the Animal Research Committee at University of California, Los Angeles (UCLA). For mouse studies, a power analysis was used to calculate the sample sizes required. For *in vitro* studies, a minimum of three independent experiments were performed, and the numbers of independent experiments (*n*) are presented in the figure legends.

Abcb10^{wt/flox} mice generation

Targeted C57BL/6J embryonic stem (ES) cells with *Abcb10* containing loxP sites flanking exons 2 to 3 and a neomycin cassette flanked by FRT (Flippase Recognition Target) sites were generated by genOway. Targeted ES cells were injected and implanted in C57BL/6J-Tyrc-2/J (albino) females at the Boston University Mouse Transgenic Core, directed by G. L. Martin and K. Ravid. Seven male chimeras containing floxed *Abcb10* were identified by coat color and bred with C57BL/6J flippase FLP recombinase females from the Jackson laboratory [B6.Cg-Tg (ACTFLPe)9205Dym/J] to excise the neomycin cassette. The offspring were bred with WT C57BL/6J, to obtain *Abcb10*^{wt/flox} mice without FLP recombinase. *Abcb10*^{wt/flox} mice were paired with B6.Cg-Tg (Alb-cre)21Mgn/J purchased from the Jackson laboratory, to generate ABCB10 LKO mice. Groups analyzed were offspring littermates from breeding pairs between *Abcb10*^{flox/flox}; *Alb-Cre*^{-/-} and *Abcb10*^{wt/flox}; *Alb-Cre*^{+/-}. WT mice are *Abcb10*^{flox/flox}; *Alb-Cre*^{+/-} and ABCB10 LKO are *Abcb10*^{flox/flox}; *Alb-Cre*^{+/-}.

Mice, diets, and metabolic and body composition measurements

Mice were provided with water and food ad libitum and housed two to five mice per cage, 12-hour light:dark cycle, and at a room temperature of 22° to 24°C. Obesity and insulin resistance were induced by HFD feeding (D12451, Research Diets; 45 kcal % fat). Lean controls were mice fed a chow diet for the same period of time. Male mice were introduced to the diets after weaning (3 to 4 weeks of age). Body weight and food intake were monitored weekly. GTTs, ITTs, and metabolic cage measurements (CLAMS) were sequentially performed in the same cohorts of mice. Mice were left 2 weeks to recover between GTT and ITT measurements. ITTs were performed at 26 weeks, and GTTs were performed at 28 weeks of diet. At 30 weeks of diet, lean and fat mass were measured using EchoMRI, using a known mass of canola oil for calibration purposes, followed by 5 days of metabolic cage measurements. Additional cohorts of mice were used at 30 weeks to perform hyperinsulinemic-euglycemic clamps and isolate primary hepatocytes. Mice were left to recover from the metabolic cage analyses for 1 week and then euthanized, with plasma and tissues harvested for biochemical analyses. Body weight, GTT, ITT, and hyperinsulinemic clamps confirmed that protection from HFD in LKO mice was preserved between 26 and 32 weeks of HFD feeding.

Statistical analyses

Data were tested for normality using Shapiro-Wilk. Excel, Graph Pad 8, and Sigma Plot 14.0 were used for statistical analyses, which included Student's *t* tests or Mann-Whitney *U* tests when comparing two groups and one-way analysis of variance (ANOVA) with Tukey or two-way ANOVA with Tukey or Holm-Sidak post hoc when comparing multiple groups of samples. Analysis of covariance (ANCOVA) was performed with Sigma Plot 14, Systat Software Inc. using the MMPC website: www.mmpc.org/shared/regression.aspx. Chemical structures of bilirubin and biliverdin were taken from PubChem and drawn with ChemDoodle software.

SUPPLEMENTARY MATERIALS

stm.sciencemag.org/cgi/content/full/13/594/eabd1869/DC1

Materials and Methods

- Fig. S1. Scheme summarizing heme catabolism to biliverdin and bilirubin.
- Fig. S2. Evidence excluding other heme-related molecules as ABCB10 cargos.
- Fig. S3. ABCB10-mediated biliverdin export increases bilirubin synthesis.
- Fig. S4. The response of UnaG fluorescence to bilirubin supplementation in WT and ABCB10 KO hepatocytes.
- Fig. S5. ABCB10 overexpression in AML12 hepatocytes.
- Fig. S6. Correlation plots between hepatic *Abcb10* transcript content and the metabolic traits determined in the HMDP.
- Fig. S7. *Abcb10* targeting strategy to generate ABCB10 LKO mice.
- Fig. S8. ABCB10 gain- and loss-of function approaches in primary human hepatocytes.
- Fig. S9. Rescuing ABCB10 expression ex vivo reverses the improvement in insulin action seen in ABCB10 LKO hepatocytes isolated from HFD-fed mice.
- Fig. S10. HFD-fed ABCB10 LKO mice show no differences in physical activity, mitochondrial biogenesis markers in the liver, or plasma fibroblast growth factor 21 concentrations.
- Fig. S11. Total protein content of cytosolic and mitochondrial UnaG is not changed by ABCB10 deletion.
- Fig. S12. No differences in hepatic HMOX1 or BLVRA content in HFD-fed ABCB10 LKO mice.
- Fig. S13. HFD-fed ABCB10 LKO mice show no changes in the bilirubin exporter ABCC2 or the main enzyme conjugating bilirubin, UGT1A1.
- Fig. S14. Summary of PTP1B actions on insulin signaling and lipogenesis and the consequences of PTP1B inactivation by H₂O₂.
- Fig. S15. The role of ABCB10 in hepatic insulin resistance and steatosis in obesity.
- Table S1. Primer sequences.
- Data File S1. Primary data for Figs. 1 to 7 in tabular format.

[View/request a protocol for this paper from Bio-protocol.](#)

REFERENCES AND NOTES

- G. S. Shadel, T. L. Horvath, Mitochondrial ROS signaling in organismal homeostasis. *Cell* **163**, 560–569 (2015).
- I. Mironczuk-Chodakowska, A. M. Witkowska, M. E. Zujko, Endogenous non-enzymatic antioxidants in the human body. *Adv. Med. Sci.* **63**, 68–78 (2018).
- T. W. Sedlak, M. Saleh, D. S. Higginson, B. D. Paul, K. R. Juluri, S. H. Snyder, Bilirubin and glutathione have complementary antioxidant and cytoprotective roles. *Proc. Natl. Acad. Sci. U.S.A.* **106**, 5171–5176 (2009).
- J.-S. Park, E. Nam, H.-K. Lee, M. H. Lim, H.-W. Rhee, In cellulo mapping of subcellular localized Bilirubin. *ACS Chem. Biol.* **11**, 2177–2185 (2016).
- D. Chiabrando, F. Vinchi, V. Fiorito, S. Mercurio, E. Tolosano, Heme in pathophysiology: A matter of scavenging, metabolism and trafficking across cell membranes. *Front. Pharmacol.* **5**, 61 (2014).
- D. E. Baranano, M. Rao, C. D. Ferris, S. H. Snyder, Biliverdin reductase: A major physiologic cytoprotectant. *Proc. Natl. Acad. Sci. U.S.A.* **99**, 16093–16098 (2002).
- R. Stocker, Y. Yamamoto, A. F. McDonagh, A. N. Glazer, B. N. Ames, Bilirubin is an antioxidant of possible physiological importance. *Science* **235**, 1043–1046 (1987).
- N. S. Nyttöf, M. A. Serrano, M. J. Monte, E. Gonzalez-Sanchez, Z. Tumer, K. Ladefoged, O. Briz, J. J. G. Marin, A homozygous nonsense mutation (c.214C→A) in the biliverdin reductase alpha gene (BVRB) results in accumulation of biliverdin during episodes of cholestasis. *J. Med. Genet.* **48**, 219–225 (2011).
- S. Erlinger, I. M. Arias, D. Dhumeaux, Inherited disorders of bilirubin transport and conjugation: New insights into molecular mechanisms and consequences. *Gastroenterology* **146**, 1625–1638 (2014).
- S. D. Zucker, W. Goessling, A. G. Hoppin, Unconjugated bilirubin exhibits spontaneous diffusion through model lipid bilayers and native hepatocyte membranes. *J. Biol. Chem.* **274**, 10852–10862 (1999).
- H. S. Schutta, L. Johnson, H. E. Neville, Mitochondrial abnormalities in bilirubin encephalopathy. *J. Neuropathol. Exp. Neurol.* **29**, 296–305 (1970).
- M. G. Mustafa, M. L. Cowger, T. E. King, Effects of bilirubin on mitochondrial reactions. *J. Biol. Chem.* **244**, 6403–6414 (1969).
- D.-J. Slebos, S. W. Rytter, M. van der Toorn, F. Liu, F. Guo, C. J. Batty, J. M. Karlsson, S. C. Watkins, H. P. Kim, X. Wang, J. S. Lee, D. S. Postma, H. F. Kauffman, A. M. K. Choi, Mitochondrial localization and function of heme oxygenase-1 in cigarette smoke-induced cell death. *Am. J. Respir. Cell Mol. Biol.* **36**, 409–417 (2007).
- S. E. Calvo, K. R. Clauser, V. K. Mootha, MitoCarta2: An updated inventory of mammalian mitochondrial proteins. *Nucleic Acids Res.* **44**, D1251–D1257 (2016).
- W. Chen, P. N. Parakkal, L. Li, E. L. Pierce, N. B. Langer, N. Takahashi-Makise, B. B. Hyde, O. S. Shirihai, D. M. Ward, J. Kaplan, B. H. Paw, Abcb10 physically interacts with mitoferrin-1 (Slc25a37) to enhance its stability and function in the erythroid mitochondria. *Proc. Natl. Acad. Sci. U.S.A.* **106**, 16263–16268 (2009).
- B. B. Hyde, M. Liesa, A. A. Borza, W. Qiu, S. E. Haigh, L. Richey, H. K. Mikkola, T. M. Schlaeger, O. S. Shirihai, The mitochondrial transporter ABC-me (ABCB10), a downstream target of GATA-1, is essential for erythropoiesis in vivo. *Cell Death Differ.* **19**, 1117–1126 (2012).
- M. Yamamoto, H. Arimura, T. Fukushige, K. Minami, Y. Nishizawa, A. Tanimoto, T. Kanekura, M. Nakagawa, S. Akiyama, T. Furukawa, Abcb10 role in heme biosynthesis in vivo: Abcb10 knockout in mice causes anemia with protoporphyria IX and iron accumulation. *Mol. Cell Biol.* **34**, 1077–1084 (2014).
- L. Tang, S. M. Bergevoet, G. Bakker-Verweij, C. L. Hartevel, P. C. Giordano, L. Nijtmans, T. de Witte, J. H. Jansen, R. A. P. Raymakers, B. A. van der Beijden, Human mitochondrial ATP-binding cassette transporter ABCB10 is required for efficient red blood cell development. *Br. J. Haematol.* **157**, 151–154 (2012).
- H. L. Bonkowski, P. R. Sinclair, J. F. Sinclair, Hepatic heme metabolism and its control. *Yale J. Biol. Med.* **52**, 13–37 (1979).
- A. Jais, E. Einwallner, O. Sharif, K. Gossens, T. T.-H. Lu, S. M. Soyad, D. Medgyesi, D. Neureiter, J. Paier-Potranj, K. Dalgaard, J. C. Duvigneau, J. Lindroos-Christensen, T.-C. Zapf, S. Amann, S. Saluzzo, F. Jantscher, P. Stiedl, J. Todoric, R. Martins, H. Oberkofler, S. Müller, C. Hauser-Kronberger, L. Kenner, E. Casanova, H. Sutterlüty-Fall, M. Bilban, K. Miller, A. V. Kozlov, F. Krempfer, S. Knapp, C. N. Lumeng, W. Patsch, O. Wagner, J. A. Pospisilik, H. Esterbauer, Heme oxygenase-1 drives metaflammation and insulin resistance in mouse and man. *Cell* **158**, 25–40 (2014).
- A. Mahajan, D. Talun, M. Thurner, N. R. Robertson, J. M. Torres, N. W. Rayner, A. J. Payne, V. Steinhilber, R. A. Scott, N. Grarup, J. P. Cook, E. M. Schmidt, M. Wuttke, C. Sarnowski, R. Mägi, J. Nano, C. Gieger, S. Trompet, C. Lecoeur, M. H. Preuss, B. P. Prins, X. Guo, L. F. Bielak, J. E. Below, D. W. Bowden, J. C. Chambers, Y. J. Kim, M. C. Y. Ng, L. E. Petty, X. Sim, W. Zhang, A. J. Bennett, J. Bork-Jensen, C. M. Brunnett, M. Canouil, K.-U. E. Kardt, K. Fischer, S. L. R. Kardia, F. Kronenberg, K. Läll, C.-T. Liu, A. E. Locke, J. Luan, I. Ntalla, V. Nylander, S. Schönherr, C. Schurmann, L. Yengo, E. P. Bottinger, I. Brandslund, C. Christensen, G. Dedoussis, J. C. Florez, I. Ford, O. H. Franco, T. M. Frayling, V. Giedraitis, S. Hackinger, A. T. Hattersley, C. Herder, M. A. Ikram, M. Ingelsson, M. E. Jørgensen, T. Jørgensen, J. Kriebel, J. Kuusisto, S. Ligthart, C. M. Lindgren, A. Linneberg, V. Lyssenko, V. Mamiakou, T. Meitinger, K. L. Mohlke, A. D. Morris, G. Nadkarni, J. S. Pankow, A. Peters, N. Sattar, A. Stančáková, K. Strauch, K. D. Taylor, B. Thorand, G. Thorleifsson, U. Thorsteinsdóttir, J. Tuomilehto, D. R. Witte, J. Dupuis, P. A. Peyser, E. Zeggini, R. J. F. Loos, P. Froguel, E. Ingelsson, L. Lind, L. Groop, M. Laakso, F. S. Collins, J. W. Jukema, C. N. A. Palmer, H. Grallert, A. Metspää, A. Dehghan, A. Kottgen, G. R. Abecasis, J. B. Meigs, J. I. Rotter, J. Marchini, O. Pedersen, T. Hansen, C. Langenberg, N. J. Wareham, K. Stefansson, A. L. Gloyn, A. P. Morris, M. Boehnke, M. I. McCarthy, Fine-mapping type 2 diabetes loci to single-variant resolution using high-density imputation and islet-specific epigenome maps. *Nat. Genet.* **50**, 1505–1513 (2018).
- Diabetes Genetics Replication And Meta-analysis (DIAGRAM) Consortium, Large-scale association analysis provides insights into the genetic architecture and pathophysiology of type 2 diabetes. *Nat. Genet.* **44**, 981–990 (2012).
- A. Seguin, N. Takahashi-Makise, Y. Y. Yien, N. C. Huston, J. C. Whitman, G. Musso, J. A. Wallace, T. Bradley, H. A. Bergonia, M. D. Kafina, M. Matsumoto, K. Igarashi, J. D. Phillips, B. H. Paw, J. Kaplan, D. M. Ward, Reductions in the mitochondrial ABC transporter Abcb10 affect the transcriptional profile of heme biosynthesis genes. *J. Biol. Chem.* **292**, 16284–16299 (2017).
- W. Qiu, M. Liesa, E. P. Carpenter, O. S. Shirihai, ATP binding and hydrolysis properties of ABCB10 and their regulation by glutathione. *PLoS ONE* **10**, e0129772 (2015).
- C. A. Shintre, A. C. W. Pike, Q. Li, J.-I. Kim, A. J. Barr, S. Goubin, L. Shrestha, J. Yang, G. Berridge, J. Ross, P. J. Stansfeld, M. S. P. Sansom, A. M. Edwards, C. Bountra, B. D. Marsden, F. von Delft, A. N. Bullock, O. Gileadi, N. A. Burgess-Brown, E. P. Carpenter, Structures of ABCB10, a human ATP-binding cassette transporter in apo- and nucleotide-bound states. *Proc. Natl. Acad. Sci. U.S.A.* **110**, 9710–9715 (2013).
- M. Martinez, G. A. Fendley, A. D. Saxberg, M. E. Zoghbi, Stimulation of the human mitochondrial transporter ABCB10 by zinc-mesoporphrin. *PLoS ONE* **15**, e0238754 (2020).
- A. D. Saxberg, M. Martinez, G. A. Fendley, M. E. Zoghbi, Production of a human mitochondrial ABC transporter in *E. coli*. *Protein Expr. Purif.* **178**, 105778 (2021).
- A. Kumagai, R. Ando, H. Miyatake, P. Greimel, T. Kobayashi, Y. Hirabayashi, T. Shimogori, A. Miyawaki, A bilirubin-inducible fluorescent protein from eel muscle. *Cell* **153**, 1602–1611 (2013).
- B. J. Bennett, R. C. Davis, M. Givolek, L. Orozco, J. Wu, H. Qi, C. Pan, R. R. S. Packard, E. Eskin, M. Yan, T. Kirchgessner, Z. Wang, X. Li, J. C. Gregory, S. L. Hazen, P. S. Gargalovic, A. J. Lusis, Genetic architecture of atherosclerosis in mice: A systems genetics analysis of common inbred strains. *PLoS Genet.* **11**, e1005711 (2015).
- O. S. Shirihai, T. Gregory, C. Yu, S. H. Orkin, M. J. Weiss, ABC-me: A novel mitochondrial transporter induced by GATA-1 during erythroid differentiation. *EMBO J.* **19**, 2492–2502 (2000).
- R. J. Perry, V. T. Samuel, K. F. Petersen, G. I. Shulman, The role of hepatic lipids in hepatic insulin resistance and type 2 diabetes. *Nature* **510**, 84–91 (2014).
- M. D. Michael, R. N. Kulkarni, C. Postic, S. F. Previs, G. I. Shulman, M. A. Magnuson, C. R. Kahn, Loss of insulin signaling in hepatocytes leads to severe insulin resistance and progressive hepatic dysfunction. *Mol. Cell* **6**, 87–97 (2000).
- R. J. Perry, J.-P. G. Camporez, R. Kursawe, P. M. Titchener, D. Zhang, C. J. Perry, M. J. Jurczak, A. Abudukadiev, M. S. Han, X.-M. Zhang, H.-B. Ruan, X. Yang, S. Caprio, S. M. Kaech, H. S. Sul, M. J. Birnbaum, R. J. Davis, G. W. Cline, K. F. Petersen, G. I. Shulman, Hepatic acetyl CoA links adipose tissue inflammation to hepatic insulin resistance and type 2 diabetes. *Cell* **160**, 745–758 (2015).
- S. Vernia, J. Cavanagh-Kyros, L. Garcia-Haro, G. Sabio, T. Barrett, D. Y. Jung, J. K. Kim, J. Xu, H. P. Shulha, M. Garber, G. Gao, R. J. Davis, The PPAR α -FGF21 hormone axis contributes to metabolic regulation by the hepatic JNK signaling pathway. *Cell Metab.* **20**, 512–525 (2014).
- R. J. Perry, T. Kim, X.-M. Zhang, H.-Y. Lee, D. Pesta, V. B. Popov, D. Zhang, Y. Rahimi, M. J. Jurczak, G. W. Cline, D. A. Spiegel, G. I. Shulman, Reversal of hypertriglyceridemia, fatty liver disease, and insulin resistance by a liver-targeted mitochondrial uncoupler. *Cell Metab.* **18**, 740–748 (2013).
- T. L. Merry, M. Tran, G. T. Dodd, S. P. Mangiafico, F. Wiede, S. Kaur, C. L. McLean, S. Andrikopoulos, T. Tiganis, Hepatocyte glutathione peroxidase-1 deficiency improves hepatic glucose metabolism and decreases steatohepatitis in mice. *Diabetologia* **59**, 2632–2644 (2016).
- M. Delibegovic, D. Zimmer, C. Kauffman, K. Rak, E. G. Hong, Y. R. Cho, J. K. Kim, B. B. Kahn, B. G. Neel, K. K. Bance, Liver-specific deletion of protein-tyrosine phosphatase 1B (PTP1B) improves metabolic syndrome and attenuates diet-induced endoplasmic reticulum stress. *Diabetes* **58**, 590–599 (2009).
- N. Krishnan, C. A. Bonham, I. A. Rus, O. K. Shrestha, C. M. Gauss, A. Haque, A. Tocilj, L. Joshua-Tor, N. K. Tonks, Harnessing insulin- and leptin-induced oxidation of PTP1B for therapeutic development. *Nat. Commun.* **9**, 283 (2018).
- S. Shimizu, S. Ujji, H. Maegawa, K. Egawa, Y. Nishio, T. Yoshizaki, K. Shi, Y. Nagai, K. Morino, K. Nemoto, T. Nakanura, M. Bryer-Ash, A. Kashiwagi, Protein-tyrosine phosphatase 1B

- as new activator for hepatic lipogenesis via sterol regulatory element-binding protein-1 gene expression. *J. Biol. Chem.* **278**, 43095–43101 (2003).
40. K. Mahadev, A. Zilberling, L. Zhu, B. J. Goldstein, Insulin-stimulated hydrogen peroxide reversibly inhibits protein-tyrosine phosphatase 1b *in vivo* and enhances the early insulin action cascade. *J. Biol. Chem.* **276**, 21938–21942 (2001).
 41. R. K. Kutty, M. D. Maines, Purification and characterization of biliverdin reductase from rat liver. *J. Biol. Chem.* **256**, 3956–3962 (1981).
 42. T. Yoshinaga, S. Sassa, A. Kappas, The occurrence of molecular interactions among NADPH-cytochrome c reductase, heme oxygenase, and biliverdin reductase in heme degradation. *J. Biol. Chem.* **257**, 7786–7793 (1982).
 43. A. P. Arruda, B. M. Pers, G. Parlakgul, E. Guney, K. Inouye, G. S. Hotamisligil, Chronic enrichment of hepatic endoplasmic reticulum-mitochondria contact leads to mitochondrial dysfunction in obesity. *Nat. Med.* **20**, 1427–1435 (2014).
 44. C. Koliaki, J. Szendroedi, K. Kaul, T. Jelenik, P. Nowotny, F. Jankowiak, C. Herder, M. Carstensen, M. Krausch, W. T. Knoefel, M. Schlensak, M. Roden, Adaptation of hepatic mitochondrial function in humans with non-alcoholic fatty liver is lost in steatohepatitis. *Cell Metab.* **21**, 739–746 (2015).
 45. N. E. Sunny, E. J. Parks, J. D. Browning, S. C. Burgess, Excessive hepatic mitochondrial TCA cycle and gluconeogenesis in humans with nonalcoholic fatty liver disease. *Cell Metab.* **14**, 804–810 (2011).
 46. A. Agouti, N. Mody, C. Owen, A. Czapek, D. Zimmer, M. Bentires-Alj, K. K. Bence, M. Delibegovic, Liver-specific deletion of protein tyrosine phosphatase (PTP) 1B improves obesity- and pharmacologically induced endoplasmic reticulum stress. *Biochem. J.* **438**, 369–378 (2011).
 47. J. Liu, H. Dong, Y. Zhang, M. Cao, L. Song, Q. Pan, A. Bulmer, D. B. Adams, X. Dong, H. Wang, Bilirubin increases insulin sensitivity by regulating cholesterol metabolism, adipokines and PPAR γ levels. *Sci. Rep.* **5**, 9886 (2015).
 48. D. P. Converso, C. Taillé, M. C. Carreras, A. Jaitovich, J. J. Poderoso, J. Boczkowski, HO-1 is located in liver mitochondria and modulates mitochondrial heme content and metabolism. *FASEB J.* **20**, 1236–1238 (2006).
 49. J. Folch, M. Lees, G. H. Sloane Stanley, A simple method for the isolation and purification of total lipides from animal tissues. *J. Biol. Chem.* **226**, 497–509 (1957).
 50. V. Ribas, B. G. Drew, Z. Zhou, J. Phun, N. Y. Kalajian, T. Soleymani, P. Daraei, K. Widjaja, J. Wanagat, T. O. de Aguiar Vallim, A. H. Fhuitt, S. Bensinger, T. Le, C. Radu, J. P. Whitelegge, S. W. Beaven, P. Tontonoz, A. J. Lusis, B. W. Parks, L. Vergnes, K. Raue, H. Singh, J. C. Bopassa, L. Toro, E. Stefani, M. J. Watt, S. Schenk, T. Akerstrom, M. Kelly, B. K. Pedersen, S. C. Hewitt, K. S. Korach, A. L. Hevener, Skeletal muscle action of estrogen receptor α is critical for the maintenance of mitochondrial function and metabolic homeostasis in females. *Sci. Transl. Med.* **8**, 334ra354 (2016).
 51. R. Steele, Influences of glucose loading and of injected insulin on hepatic glucose output. *Ann. N. Y. Acad. Sci.* **82**, 420–430 (1959).
 52. L. Nocito, A. S. Kleckner, E. J. Yoo, A. R. Jones IV, M. Liesa, B. E. Corkey, The extracellular redox state modulates mitochondrial function, gluconeogenesis, and glycogen synthesis in murine hepatocytes. *PLoS ONE* **10**, e0122818 (2015).
 53. M. Shum, K. Bellmann, P. St-Pierre, A. Marette, Pharmacological inhibition of S6K1 increases glucose metabolism and Akt signalling *in vitro* and in diet-induced obese mice. *Diabetologia* **59**, 592–603 (2016).
 54. A. J. Meyer, T. P. Dick, Fluorescent protein-based redox probes. *Antioxid. Redox Signal.* **13**, 621–650 (2010).
 55. K. Mahdavian, I. Y. Benador, S. Shu, R. A. Gharakhanian, L. Stiles, K. M. Trudeau, M. Cardamone, V. Enriquez-Zarralanga, E. Ritou, T. A. Arahmanian, M. F. Oliveira, B. E. Corkey, V. Perissi, M. Liesa, O. S. Shirihai, Mfn2 deletion in brown adipose tissue protects from insulin resistance and impairs thermogenesis. *EMBO Rep.* **18**, 1123–1138 (2017).
 56. M. E. Zoghbi, R. S. Cooper, G. A. Altenberg, The lipid bilayer modulates the structure and function of an ATP-binding cassette exporter. *J. Biol. Chem.* **291**, 4453–4461 (2016).
 57. E. R. Geertsma, N. A. B. Nik Mahmood, G. K. Schuurman-Wolters, B. Poolman, Membrane reconstitution of ABC transporters and assays of translocator function. *Nat. Protoc.* **3**, 256–266 (2008).

Acknowledgments: We thank D. Braas and T. Graeber at the UCLA Metabolomics core for the liquid chromatography-mass spectrometry measurements of biliverdin. We thank S. Matsuura, G. Martin, and K. Bavid from the Transgenic Core at Boston University for the generation of ABCB10 floxed mice. We thank T. Balon from Boston University for help with CLAMS. We thank T. Dick for the roGFP2 constructs and J.-S. Park and H.-W. Rhee for the UnaG construct. We thank B. E. Corkey, M. Fernandes de Oliveira, S. K. Fried, D. Dagan and O. S. Shirihai for input and discussions and S. B. Sereda, E. Ritou, and N. Miller for technical assistance. **Funding:** M.L. is funded by the Department of Medicine at UCLA, pilot grants from P30 DK 41301 (UCLA/DDRRC NIH), P50 AA011999 (USC-ALPD), UL1TR001881 (CTSI), P30 DK063491 (UCSD-UCLA/DERC), P30 DK046200 (BNORC), and NIH-1R01AA026914-01A1. M.E.Z. is funded by NIH-1R15GM131289-01. M. Shum is funded by the Canadian Diabetes Association, C.A.S., R.A., M.R.Y., B.F., and E.P.C. were in the SGC, a registered charity funded by AbbVie, Bayer Pharma AG, Boehringer Ingelheim, Canada Foundation for Innovation, Genome Canada, Janssen, Merck KGaA, Merck & Co., Novartis, Ontario Ministry of Economic Development and Innovation, Pfizer, São Paulo Research Foundation-FAPESP, Takeda, Innovative Medicines Initiative Joint Undertaking ULTRA-DD grant 115766, and Wellcome Trust (106169/Z/14/Z). T.A. and J.A. were funded by NIH 1R35GM135175-01, A.J.L. is funded by NIH-P01HL028481 and DK120342, and K.C.K. is funded by K99 DK120875 and AHA18POST33990256. A.L.H. is funded by NIH P30 DK063491 (UCSD-UCLA/DERC) and R01 DK109724. **Author contributions:** M.L., M. Shum, C.A.S., and E.P.C. conceptualized the project. M. Shum, C.A.S., T.A., V.G., M. Segawa, M.L., R.A., M.R.Y., B.F., E.P.C., A.D.S., M.M., M.E.Z., J.A., A.L.H., and A.J.L. provided methods. M. Shum, M.L., C.A.S., T.A., V.G., M. Segawa, E.P.C., A.D.S., M.M., M.E.Z., R.G., K.C.K., A.L.H., and M.V. analyzed data. M. Shum, T.A., M.L., C.A.S., V.G., M. Segawa, A.D.S., M.M., M.E.Z., R.G., S.S., K.M., A.L.H., M.V., D.M.W., J.N., L.N., and L.S. performed experiments. M.L., E.P.C., M.Z., A.L.H., A.J.L., and J.A. provided resources. M. Shum and M.L. wrote the original draft. M.L., E.P.C., and M.E.Z. supervised the project and acquired funds. **Competing interests:** The following competing interests are not related to this study: E.P.C. and B.F. are currently employed by Vertex Pharmaceuticals, and M.L. is a cofounder and consultant of Enspire Bio LLC. The authors declare that they have no competing interests. **Data and materials availability:** All data associated with this study are present in the paper or the Supplementary Materials. The hybrid mouse diversity panel (HMDP) data are available at <https://systems.genetics.ucla.edu>. roGFP2 constructs were obtained under a material transfer agreement with T. Dick.

Submitted 9 June 2020
Resubmitted 25 January 2021
Accepted 20 April 2021
Published 19 May 2021
10.1126/scitranslmed.abd1869

Citation: M. Shum, C. A. Shintre, T. Althoff, V. Gutierrez, M. Segawa, A. D. Saxberg, M. Martinez, R. Adamson, M. R. Young, B. Faust, R. Gharakhanian, S. Su, K. Chella Krishnan, K. Mahdavian, M. Veliova, D. M. Wolf, J. Ngo, L. Nocito, L. Stiles, J. Abramson, A. J. Lusis, A. L. Hevener, M. E. Zoghbi, E. P. Carpenter, M. Liesa, ABCB10 exports mitochondrial biliverdin, driving metabolic maladaptation in obesity. *Sci. Transl. Med.* **13**, eabd1869 (2021).

ABCB10 exports mitochondrial biliverdin, driving metabolic maladaptation in obesity

Michael ShumChitra A. ShintreThorsten AlthoffVincent GutierrezMayuko SegawaAlexandra D. SaxbergMelissa MartinezRoslin AdamsonMargaret R. YoungBelinda FaustRaffi GharakhanianShi SuKarthickeyan Chella KrishnanKiana MahdavianMichaela VellovaDane M. WolfJennifer NgoLaura NocitoLinsey StilesJeff AbramsonAldons J. LusisAndrea L. HevenerMaria E. ZoghbiElisabeth P. CarpenterMarc Liesa

Sci. Transl. Med., 13 (594), eabd1869. • DOI: 10.1126/scitranslmed.abd1869

Heme homeostasis

Mitochondrial membrane transporter ABCB10 has been linked to heme metabolism, but its exact function is unclear. Shum *et al.* show in mouse and human primary hepatocytes that ABCB10 transports biliverdin out of the mitochondria to further supply synthesis of heme metabolite bilirubin. ABCB10 liver-specific knockout mice showed enhanced mitochondrial respiration and were protected from diet-induced obesity, insulin resistance, and hepatic steatosis, which the authors in part tied to the modulation of a regulatory phosphatase upon the resulting oxidative shift. Overexpression of ABCB10 impaired insulin signaling in hepatocytes in vitro and mice on a high-fat diet expressed increased ABCB10 in the liver, implying maladaptive potential of the transporter in obesity.

View the article online

<https://www.science.org/doi/10.1126/scitranslmed.abd1869>

Permissions

<https://www.science.org/help/reprints-and-permissions>

Use of this article is subject to the Terms of service.

Science Translational Medicine (ISSN 1946-6242) is published by the American Association for the Advancement of Science, 1200 New York Avenue NW, Washington, DC 20005. The title *Science Translational Medicine* is a registered trademark of AAAS. Copyright © 2021 The Authors, some rights reserved; exclusive licensee American Association for the Advancement of Science. No claim to original U.S. Government Works.

Supplementary Materials for

ABCB10 exports mitochondrial biliverdin, driving metabolic maladaptation in obesity

Michael Shum, Chitra A. Shintre, Thorsten Althoff, Vincent Gutierrez, Mayuko Segawa, Alexandra D. Saxberg, Melissa Martinez, Roslin Adamson, Margaret R. Young, Belinda Faust, Raffi Gharakhanian, Shi Su, Karthickeyan Chella Krishnan, Kiana Mahdavian, Michaela Veliova, Dane M. Wolf, Jennifer Ngo, Laura Nocito, Linsey Stiles, Jeff Abramson, Aldons J. Lulis, Andrea L. Hevener, Maria E. Zoghbi, Elisabeth P. Carpenter, Marc Liesa*

*Corresponding author: Email: mliesa@mednet.ucla.edu

Published 19 May 2021, *Sci. Transl. Med.* **13**, eabd1869 (2021)
DOI: 10.1126/scitranslmed.abd1869

The PDF file includes:

Materials and Methods

- Fig. S1. Scheme summarizing heme catabolism to biliverdin and bilirubin.
- Fig. S2. Evidence excluding other heme-related molecules as ABCB10 cargos.
- Fig. S3. ABCB10-mediated biliverdin export increases bilirubin synthesis.
- Fig. S4. The response of UnaG fluorescence to bilirubin supplementation in WT and ABCB10 KO hepatocytes.
- Fig. S5. ABCB10 overexpression in AML12 hepatocytes.
- Fig. S6. Correlation plots between hepatic *Abcb10* transcript content and the metabolic traits determined in the HMDP.
- Fig. S7. *Abcb10* targeting strategy to generate ABCB10 LKO mice.
- Fig. S8. ABCB10 gain- and loss-of-function approaches in primary human hepatocytes.
- Fig. S9. Rescuing ABCB10 expression *ex vivo* reverses the improvement in insulin action seen in ABCB10 LKO hepatocytes isolated from HFD-fed mice.
- Fig. S10. HFD-fed ABCB10 LKO mice show no differences in physical activity, mitochondrial biogenesis markers in the liver, or plasma fibroblast growth factor 21 concentrations.
- Fig. S11. Total protein content of cytosolic and mitochondrial UnaG is not changed by ABCB10 deletion.
- Fig. S12. No differences in hepatic HMOX1 or BLVRA content in HFD-fed ABCB10 LKO mice.
- Fig. S13. HFD-fed ABCB10 LKO mice show no changes in the bilirubin exporter ABCC2 or the main enzyme conjugating bilirubin, UGT1A1.
- Fig. S14. Summary of PTP1B actions on insulin signaling and lipogenesis and the consequences of PTP1B inactivation by H₂O₂.
- Fig. S15. The role of ABCB10 in hepatic insulin resistance and steatosis in obesity.

Table S1. Primer sequences.
Legend for data file S1

Other Supplementary Material for this manuscript includes the following:

(available at stm.sciencemag.org/cgi/content/full/13/594/eabd1869/DC1)

Data File S1 (Microsoft Excel format). Primary data for Figs. 1 to 7 in tabular format.

Supplementary material

Materials and Methods

Genotyping and PCR validating Cre-mediated excision

Mouse tails (0.5 cm) and primary hepatocytes were lysed with 200 μ l and 50 μ l of Viagen direct PCR lysis reagent with proteinase K respectively. One microliter of the lysate was used to amplify ABCB10 floxed alleles using primers r11: GCAGACTGTAGGGACAAAGGCATCAC and 12: CTGAGCCGTCAGAGGTAATCG, which concurrently amplify the floxed and WT allele. To detect Cre-mediated excision of floxed ABCB10, primers 27: AGAAGCCTCCCTATTGAGCTCATGC and 26: GGAAGTGTCTCCCAAAGTTTATGTATCG, amplified a 326 bp fragment only existing after excision. The WT allele fragment flanked by these primers being too long to be amplified (see Fig. 2A).

Glucose and insulin tolerance tests (GTT, ITT)

Mice were fasted overnight for GTT and 6h for ITT, with fasting blood glucose measured before intraperitoneal injection of glucose (1g/kg weight) or insulin (Humulin, 1 mU/g weight), in a blood drop obtained from a tail nick. Then, after injection of glucose or insulin respectively, additional blood glucose measures were performed at 15, 30, 60, 90, and 120 min using *Free style* (Abbot) glucometer and glucose strips. Additional blood was collected during GTT using glass capillaries containing EDTA (Sarstedt and Fisher brand) to obtain plasma and measure insulin at time 0, 15 and 30 min by ELISA (ALPCO).

Metabolic cage measurements

O₂ consumed, CO₂ produced and physical activity (XYZ, laser beam breaks counts) were determined using Oxymax Comprehensive Lab Animal Monitoring System (CLAMS, Columbus Instruments) at the Boston University Mouse Physiology core and at UCLA. Mice were housed for 5 days in CLAMS, with data analyzed for the last 2 days, when the 3 day-acclimation period to the metabolic cages passed. RER was calculated with CLAX software (Columbus Instruments) as V_{CO_2}/V_{O_2} . Energy expenditure in

cal/min was derived from the Lusk equation: $(3.815 + 1.232 \times \text{RER}) \times \text{VO}_2$, with VO_2 in ml/min. The system was calibrated with gas of a known O_2 and CO_2 % before every experiment.

Liver and feces triglycerides

Liver and feces triglycerides were quantified by extracting their lipid fraction using a variation of the Folch method (48). Briefly, 100 mg of crushed frozen liver powder or 60 mg feces were mixed with 6 ml of Chloroform : Methanol (2:1) in glass vials, homogenized for 30 seconds, capped and incubated overnight at 4°C on a shaker. Then, 1.5 ml MgCl_2 (0.043%) was added, the mixture vortexed and centrifuged 15 min at 2000 rpm. The lower organic phase was collected with a glass pipette and transferred to a clean glass tube. The solvent was evaporated and lipids resuspended in 500 μl of 1% Triton X-100 in chloroform, with chloroform evaporated again. The lipids with Triton X-100 were finally resuspended in water, vortexing and incubating them at 65°C for 20 min. Triglycerides were measured using a colorimetric assay as described (29).

Hyper-insulinemic euglycemic clamps

Glucose clamps were performed 3 days after implanting dual catheters in the right jugular vein of mice. Mice were fasted for 6h prior to the clamp. Basal glucose turnover was determined after 90 min of constant $[3\text{-}^3\text{H}]$ D-glucose infusion (5.0 $\mu\text{Ci/h}$, 0.12 ml/h, Perkin Elmer). After basal glucose turnover rate was assessed at steady state, insulin (8 $\text{mU}\cdot\text{kg}^{-1}\cdot\text{min}^{-1}$; Novo Nordisk) plus $[3\text{-}^3\text{H}]$ D-glucose (5.0 $\mu\text{Ci/h}$) were constantly infused (2 $\mu\text{l/min}$). Exogenous glucose was simultaneously infused at a rate to maintain blood glucose at fasting levels and thus match the decrease in glycemia induced by insulin. Blood glucose concentration was clamped at ~ 130 mg/dl using a variable glucose (50% dextrose; Abbott) infusion rate (GIR). As previously described and using the Steele equation for steady state metabolism (49, 50), a tracer dilution approach was used to determine the rate of endogenous hepatic glucose production (HGP) and the insulin-stimulated glucose disposal rate above basal (IS-GDR).

Hybrid Mouse Diversity Panel (HMDP) analyses

Liver and serum were collected from transgenic male mice carrying both human *CETP* and human *APOE3* Leiden variant, fed a “Western diet” starting at 8-weeks of age (33 % kcal fat from cocoa butter, 1% cholesterol, Research Diets D10042101) and euthanized after 8 weeks of diet. The control group were the same mouse strains without the human transgenes and fed a chow diet (Ralston Purina Company). The bicor (biweight midcorrelation) function implemented in the Weighted Gene Co-expression Network Analysis R package (WGCNA) was used to calculate hepatic *Abcb10* transcript-trait correlations in the Western diet group and obtain a nominal p value for the different correlations. Gene expression data in the liver was determined by hybridization to Affymetrix HT-MG_430 PM microarrays, with *Abcb10* mRNA quantified using probe 1416403_PM. Serum and liver triglycerides were measured in the HMDP strains as described (29).

Serum triglycerides, cholesterol, and VLDL measurements

TGs and total cholesterol were measured by colorimetric assays from Sigma according to the manufacturer’s instructions. VLDL in plasma were quantified using the Friedewald calculation as described (29).

Primary mouse hepatocyte isolation and culture

This protocol was modified from our previous publication (51). Krebs-perfused livers of ketamine/xylazine anesthetized mice were digested by perfusing a type 4 collagenase solution (Worthington Biochemical Corp) through the inferior vena cava. Hepatocyte viability was determined by trypan blue exclusion, with isolations only over 70% viability being used. WT and LKO sibling pairs were used in each independent isolation experiment. Primary hepatocytes were plated in M199 medium supplemented with 100 U/ml penicillin, 100 µg/ml streptomycin, 0.1% bovine serum albumin, 500 nM dexamethasone (Sigma-Aldrich), 100 nM triiodothyronine (Sigma-Aldrich), 10 nM insulin (Actrapid, Novo Nordisk). Hepatocytes were seeded at a density of 2.5×10^5 cells/well on 6-well plates and 8000 cells/well on 96 well plates for XF96 respirometry and for live cell fluorescence imaging. After 2-4h of

seeding hepatocytes on a collagen-coated plate, media was replaced to remove unattached, dead hepatocytes with M199 medium supplemented with 100 U/ml penicillin, 100 µg/ml streptomycin, 0.1% bovine serum albumin, 500 nM dexamethasone.

AML12 and human primary hepatocytes culture

AML12 mouse hepatocytes were grown in DMEM/F12 media (ThermoFisher Scientific) supplemented with 10% (vol./vol.) FBS, insulin (0.003 mg/ml), dexamethasone (40 ng/ml), transferrin (0.005 mg/ml) and sodium selenite (5 ng/ml). 48h later, AML12 were deprived of serum for 6h prior to insulin (10 nM) treatment for the indicated times. Human primary hepatocytes were purchased from Lonza and cultured in Williams E media supplemented with 10% (vol./vol.) FBS, dexamethasone (500 nM), penicillin/streptomycin 1% (vol./vol.), insulin (10 nM), triiodothyronine (200 nM) and HEPES (15 mM). 48h later, human primary hepatocytes were deprived of serum for 6h prior to insulin (10 nM) treatment for the indicated times. For adenoviral and lentiviral transductions, hepatocytes were exposed to the MOI indicated in each method section listed below, washed and analyzed 48h later.

PTP1B activity measurements

Primary hepatocytes were homogenized in lysis buffer 48h after their isolation (20 mM Tris pH 7.6, 150 mM NaCl, 0.5 mM EDTA, protease inhibitors, and 1% Triton X-100). Lysates were centrifuged for 10 min at 12,000xg, to discard the insoluble fraction. One milligram of protein from lysates was precleared for 10 min at 4°C by incubation with 20 µl protein A/G plus agarose beads (Santa Cruz). Precleared samples were incubated for 1 h at 4°C with anti-PTP1B (Proteintech). Next, 20 µl agarose beads were added to capture PTP1B complexed to the antibody and incubated for 2 h at 4°C. Samples were washed two times with immunoprecipitation buffer and two times with phosphatase assay buffer (25 mM HEPES pH 7.2, 50 mM NaCl, 2 mM EDTA, 3 mM DTT). PTP1B activity was measured using 50 mM of para-nitrophenylphosphate (New England BioLabs) as a phosphatase substrate, according to the manufacturer's instructions. Subsequently, immunoprecipitated PTP1B samples were boiled and

subjected to immunoblotting using rabbit anti-PTP1B (R&D System). Immunoprecipitated PTP1B content was quantified by blot densitometry and PTP1B phosphatase activity was normalized to the amount of immunoprecipitated PTP1B.

Insulin signaling analyses

This protocol was modified from our previous publication (52). Briefly, serum starved primary hepatocytes were treated, for the indicated times, with saline or 10 nM insulin (Actrapid, Novo Nordisk). Insulin action was quantified by measuring the fold increase in phosphorylation of AKT and the insulin receptor (INSR) induced by insulin over the saline group, detected by Western blot.

Primary mouse hepatocyte respirometry and bilirubin treatments

Freshly isolated hepatocytes were seeded at 8000 cells/well on 96 well-plate for Seahorse respirometry (Agilent), measured 48h after isolation. One hour prior and during the assay itself, hepatocytes were cultured in DMEM with low glucose. Mitochondrial stress test compounds were added at 2 μ M oligomycin, 1 μ M FCCP, 1 μ M rotenone and 1 μ M antimycin A. Bilirubin was added at 10 μ M 16 hours prior running the respirometry assay, with bilirubin being present during respirometry.

Hepatocyte transduction and imaging of redox and bilirubin probes

The cDNAs for UnaG and roGFP2 sensors were obtained from Drs. Rhee (4) and Dick (53). Adenovirus were used to deliver ABCB10, Grx1-roGFP2 (GSSG/GSH), roGFP2-Orp1 (H_2O_2 probe) and UnaG (bilirubin probe) to primary hepatocytes, with the fluorescent probe proteins targeted either to the mitochondrial matrix or to the cytosol as described (7,8). roGFP2 and ABCB10 adenoviruses (mouse cDNA) were generated *in house* using Gateway cloning (Invitrogen) into a pAdeno-CMV vector, while UnaG cDNA was cloned into adenovirus by Welgen. Hepatocytes were exposed to adenoviruses (MOI 1 for UnaG viruses and MOI 400 for roGFP2 viruses) for 2h the same day of isolation and imaged 48h after

transduction. Live cell imaging was performed in 96-well plates at 37°C, 5% CO₂, using the Operetta Spinning Disk Fluorescent Microscope imaging system (Perkin Elmer). A Xenon lamp with the following excitation filters was used for each probe: oxidized form of roGFP2 (roGFP2ox) with Ex 460 - 490 nm and Em 500 – 550 nm; reduced form of roGFP2 (roGFP2red) with Ex 410 - 480 nm and Em 500 – 550 nm and for UnaG, Ex 460 - 490 nm and Em 500 – 550 nm. To quantify fluorescence, Columbus Perkin Elmer software was used to select cells and threshold the images to remove background fluorescence. Average fluorescence intensity values were calculated per field, containing 20-30 cells. Results for roGFP2-Orp1 and Grx1-roGFP2 were expressed as oxidized/reduced probe fluorescence ratio.

Properties of UnaG to detect bilirubin

The domain of UnaG that binds unconjugated bilirubin to generate fluorescence is a FABP (fatty acid binding protein) (28). Thus, UnaG cannot report on bilirubin bound with stronger affinity to other FABP proteins and lipids. Purified UnaG is a highly sensitive and reversible bilirubin sensor, having a K_d with bilirubin of 98 pM and reporting on concentrations as low as 20-40 pM. UnaG detects real time changes in intracellular bilirubin content in live cells. UnaG reports relative amounts of bilirubin, as no internal standards could be reliably generated in intact live cells. UnaG fluorescence is insensitive to hypoxia and continues to fluoresce after fixation, still reporting differences in bilirubin content detected prior fixation.

UGT activity assay

Microsomes were isolated from frozen WT and ABCB10 KO livers and UGT activity was measured according to the manufacturer's protocol (Biovision).

Downregulation of ABCB10 expression by shRNA

Stable short hairpin RNA (shRNA)-mediated knockdown of ABCB10 expression in primary human hepatocytes was achieved using lentiviral transduction. Human control (sh001) and ABCB10 shRNA (TRCN0000060176) encoded in pLKO.1-Puro vector (Sigma-Aldrich) were used. Lentiviruses were

produced in HEK293T cells. Human primary hepatocytes were exposed to lentivirus overnight, then washed and analyzed 48h after transduction.

Isolated mitochondria respirometry and bilirubin treatments

A differential centrifugation protocol was used to isolate mitochondria as published (54). Mitochondria were diluted in Mitochondrial Assay buffer (MAS: 70 mM sucrose, 220 mM mannitol, 10 mM KH_2PO_4 , 5 mM MgCl_2 , 2 mM HEPES, 1 mM EGTCA and 0.2% fatty acid-free BSA, pH 7.2) on ice. 25 μL of MAS with 3.5-4 μg of mitochondrial protein fraction for succinate (5mM) + rotenone (4 μM) or with 7-10 μg for pyruvate (5mM) + malate (5mM)-driven respiration were plated in a XF96-well plate. The XF96 plate was then centrifuged at 4°C at 2000xg for 5 min to sediment mitochondria to the bottom of the well, then carefully adding the rest of MAS (110 μL) on top. For bilirubin treatments, bilirubin in DMSO (10mM) was diluted 1/1000 in MAS to 10 μM , which is a physiological plasma concentration of free bilirubin. The XF96 plate was incubated 5-8 min at 37°C before loading it to the instrument measuring respiration. State 3 was induced after injection of ADP (4mM final), State 4o after injection of oligomycin (3.5 μM final), maximal after injecting FCCP (4 μM final) and antimycin A (4 μM final) to block respiration.

Western blot analyses

This protocol was modified from our previous publication (52). Cells or tissues were homogenized in lysis buffer (50 mM Tris pH 7.5, 150 mM NaCl, 2 mM EDTA, 5 mM EGTCA, 1% Triton X-100, 1% SDS, 1% sodium deoxycholate, 2 mM sodium orthovanadate, 50 mM sodium fluoride, 5 mM sodium pyrophosphate, 1 mM PMSF, 80 mM sodium β -glycerophosphate). Lysates were centrifuged for 10 min at 12,000xg. Protein concentration was determined with BCA Protein Assay Kit (Pierce). Equal amounts of proteins were separated by SDS-PAGE (4-12% (wt/vol.)) and transferred onto PVDF membrane. Membranes were blocked in 3% (wt/vol.) milk diluted in Tris pH 7.4 + 0.1% (vol./vol.) Tween (TBS-T) and incubated overnight at 4°C with the respective antibodies diluted in 3% (wt/vol.) BSA in TBS-T. Anti-phospho-INSR Tyr1162/1163 was from Invitrogen, phospho-AKT Ser 473, total AKT and INSR

were from Cell Signaling Technologies. Porin/VDAC1, vinculin and total OXPHOS complexes were from Abcam. ABCB10, PTP1B and anti-flag were from Proteintech. Anti-actin was from Millipore. BLVRA and HMOX1 were from SantaCruz.

qPCR analyses

Total RNA was extracted from liver tissues using RNeasy (QIAGEN) and TRIzol, (Invitrogen). 2 µg total RNA were reverse transcribed into cDNA (Applied Biosystems). qPCR reactions were performed using the iQ SYBR Green Supermix (Bio-Rad Laboratories). See table 1 for Primers list. Melting curve analysis was performed to control for unspecific products. *Ugt1a1* ([Mm02603337_m1](#)) and *Abcc2* ([Mm00496899_m1](#)) gene expression were measured using TaqMan probes and gene expression assay (Thermofisher). Results were normalized to acidic ribosomal phosphoprotein P0 (*Arbp*) within each sample to obtain sample-specific ΔCt values ($\text{Ct gene of interest} - \text{Ct Rplp0}$). $2_{-\Delta\Delta\text{Ct}}$ values were calculated to obtain fold expression levels, where $\Delta\Delta\text{Ct} = (\Delta\text{Ct treatment} - \Delta\text{Ct control})$.

Confocal imaging

Zeiss LSM880 with Airyscan was used to image live primary hepatocytes at 37 °C and with humidified 5% CO₂ chamber, transduced with mito-UnaG and stained with 100nM TMRE. Super-resolution imaging was performed with 40x Apochromat oil-immersion lens and AiryScan super-resolution detector.

ATPase activity of ABCB10

The codon-optimized ABCB10 gene, without mitochondrial targeting sequence, was synthesized and inserted in the pET28a-TEV vector (Gene Script) within the NdeI and BamHI sites. The N-term His-tagged protein was expressed in Rosetta 2 (DE) (Novagen) cells, extracted from the membrane with 1 % dodecyl-maltoside (DDM) and 0.1 % cholesteryl hemi-succinate (CHS), and purified using Ni-NTA resin (Qiagen) in a Low-Pressure chromatography system (BioRad). Most concentrated fractions were pooled and treated with TEV protease during dialysis (300 mM NaCl, 10 % Glycerol, 20 mM Tris-HCl pH 7.5, 0.06 % DDM, and 0.5 mM DTT), followed by batch Ni-NTA purification. Purified His-tagged free

ABCB10 was recovered from the supernatant and stored at -80°C . For reconstitution in nanodiscs, ABCB10 in detergent was mixed with *E. coli* total or polar lipids and membrane scaffold protein MSP1D1, and detergent was removed by addition of absorbent Biobeads. The reconstituted protein sample was run through a size-exclusion chromatography column (Enrich 650, BioRad) to remove aggregates. ABCB10 concentration in ABCB10-nanodisc fractions was estimated by SDS-gel electrophoresis using purified ABCB10 in detergent as standard. The ATPase activity of reconstituted ABCB10 was measured by the linked-enzyme assay, following the decrease in NADH absorbance at 340 nm during 3 to 4 hours at 37°C (55). The buffer contained: 100 mM KCl, 5 mM NaCl, 20 mM Tris-HCl pH 7.5, 5 mM Na ATP, 10 mM MgCl_2 , 3 mM phosphoenol pyruvate, 0.5 mM TCEP, 0.8 mM NADH, plus the enzymes pyruvate kinase and lactate dehydrogenase (Sigma). Biliverdin and Bilirubin (Chem Cruz) were dissolved in DMSO. See publications (26, 27) for more details on ABCB10 production and ATPase assays.

Biliverdin transport assays

ABCB10 was cloned and purified as published (25). ABCB10 was reconstituted using the method outlined in (56) with some modifications. Reconstitution was performed in a 1:1 (wt:wt) mixture of 1-palmitoyl-2-oleoyl-sn-glycero-3-phosphocholine (POPC) and 1-palmitoyl-2-oleoyl-sn-glycero-3-phosphoethanolamine (POPE) (Avanti Lipids). Chloroform solubilized lipids were dried into a glass flask under argon to form a film under vacuum for 1h. Reconstitution/ ATPase assay buffer (50 mM HEPES, 200 mM NaCl, 10 mM MgSO_4) was used to solubilize the lipids and form multilamellar vesicles, which were solubilized with 1% Triton-X100. Protein was added to the prepared lipids in a 1:10 ratio by weight and mixed. 0.1 g of SM2-Biobeads washed with ATPase buffer were added and the mixture was rotated overnight at 4°C . Fresh Biobeads were added and the incubation continued for 2h before removal of Biobeads to recover reconstituted ABCB10. Protein concentration was measured on a Coomassie blue-stained SDS/PAGE gel comparing protein staining to a BSA standard. Transport assay was performed using ABCB10-liposomes (6 μg) resuspended in 50 mM Tris, 10% Sucrose, 100 mM NaCl, pH 7.0. To

initiate the transport, no ATP buffer or ATP regenerating buffer (20 mM ATP, Creatine Kinase 2.5 mg/ml, 20mM MgSO₄, 25 mM Creatine Phosphate) in presence of ³[H]-Biliverdin (34 pmols, 10 Ci/mmol) (American Radiolabeled Chemicals) was added to each sample at 37°C. At appropriate time points, 800 µl of cold no ATP buffer were added to each sample and filtered rapidly through 0.45-µm cellulose acetate filters. After washing the filters with another 3 ml of cold buffer, the filters were dissolved in 900 µl ethyl acetate and the radioactivity in the filter was determined by scintillation counting in 3 ml Ultima Gold XR scintillation cocktail (Perkin Elmer) in a Beckman LS6500 scintillation counter. Competition assay of ³H-biliverdin transport in ABCB10-liposomes with or without ATP (ATP + regeneration buffer) was performed by using 3 mg of ABCB10-protein incubated with 34 pmols ³H-biliverdin in a 110 ml reaction (0.3 µM), competing with unlabeled biliverdin, aminolevulinic Acid (ALA) (Sigma), protoporphyrin IX (PPIX) (Sigma) or hemin (Sigma) at 0.5 µM and 1 µM. Data was analyzed using the one-phase association equation, mean of independent transport experiments and ABCB10 proteoliposome batches ± SEM.

Biliverdin measurements in isolated mitochondria by LC/MS

A differential centrifugation protocol was used to isolate mitochondria. This method preserves the integrity of the inner membrane and thus the retention of metabolites, quantitatively shown by respiratory control ratio values (>5) (Figure 1). Polar metabolites were extracted from 500 µg of mitochondrial protein using 1 ml of ice-cold 80% MeOH. Extraction was performed by vortexing samples three times for 10 sec and then centrifuged at 10,000xg for 10 min at 4°C. Both Biliverdin IX alpha (1 nmol final) and D/L-norvaline (5 nmols final) were added for standard and extraction normalization purposes. Then, samples were dried using a *speedvac* centrifuge, and reconstituted in 50 µl of 70% acetonitrile (ACN). For mass spectrometry analysis, 5 µl of each sample was injected onto a Luna NH2 (150 mm x 2 mm, Phenomenex) column. Samples were analyzed with an UltiMate 3000RSLC (Thermo Scientific) coupled to a Q Exactive mass spectrometer (Thermo Scientific). The Q Exactive was run with polarity switching

(+3.00 kV / -3.00 kV) in full scan mode with an m/z range of 65–950. Separation was achieved using 5 mM NH_4AcO (pH 9.9) and ACN. The gradient started with 15% NH_4AcO and reached 90% over 18 min, followed by an isocratic step for 9 min and reversal to the initial 15% NH_4AcO for 7 min. Biliverdin was detected at $m/z=583$ and relative quantities were calculated using EI-Maven software.

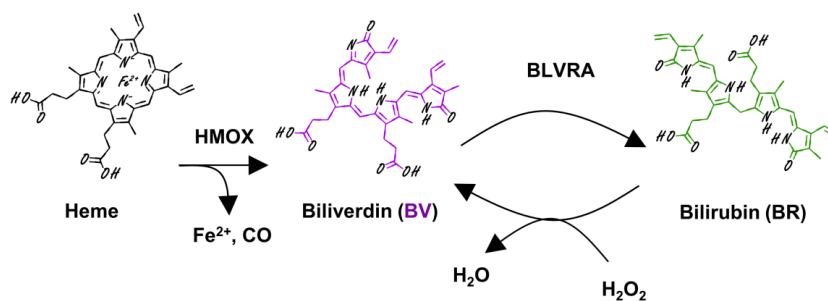


Fig. S1. Scheme summarizing heme catabolism to biliverdin and bilirubin. Heme is oxidized by heme oxygenases (HMOX) to biliverdin (BV), which is reduced to bilirubin (BR) by biliverdin reductase A (BLVRA). Hydrogen peroxide (H_2O_2) was shown to oxidize bilirubin to generate biliverdin.

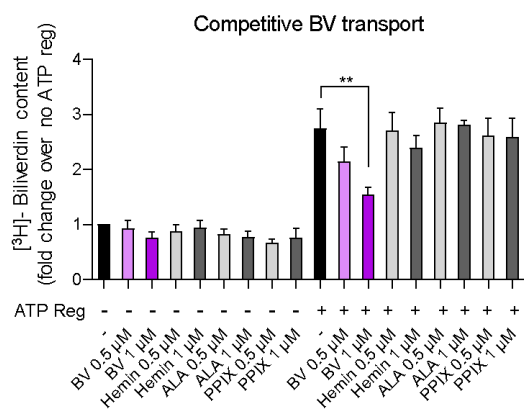


Fig. S2. Evidence excluding other heme-related molecules as ABCB10 cargos. Competition assay of ³H-biliverdin transport in ABCB10-liposomes with or without ATP regenerating buffer (ATP reg) and incubated with unlabeled biliverdin (BV), aminolevulinic acid (ALA), protoporphyrin IX (PPIX) or hemin at 0.5 μ M and 1 μ M. n=4-5 independent transport assays. **p<0.01, one-way ANOVA.

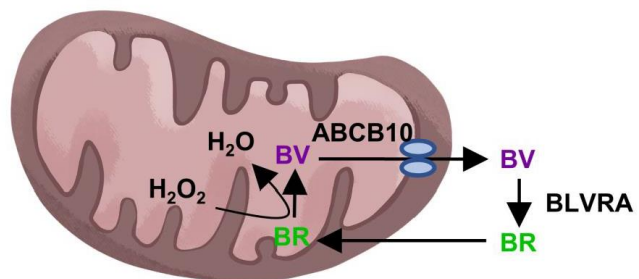


Fig. S3. ABCB10-mediated biliverdin export increases bilirubin synthesis. Scheme showing how biliverdin export increases bilirubin synthesis catalyzed by BLVRA.

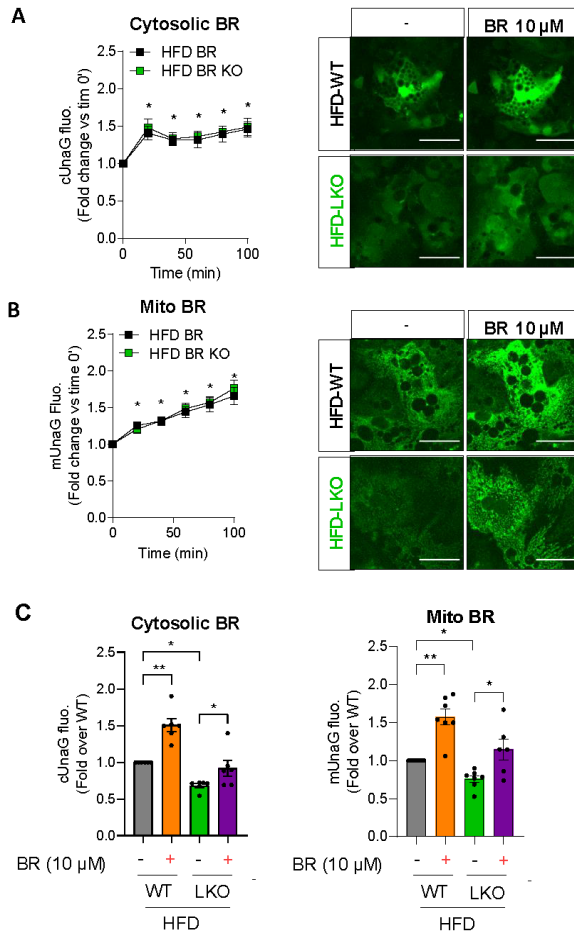


Fig. S4. The response of UnaG fluorescence to bilirubin supplementation in WT and ABCB10 KO hepatocytes. A-C) Average number of WT and ABCB10-LKO male mice fed a high fat diet (HFD) used to isolate hepatocytes \pm SEM. $n = 4$ mice/group. These hepatocytes were transduced with adenovirus encoding cytosolic UnaG (cUnaG), to measure cytosolic bilirubin, or with mitochondrial matrix targeted UnaG (mUnaG), to measure matrix bilirubin. A) Fold increase in cytosolic bilirubin and B) mitochondrial bilirubin after adding bilirubin ($10 \mu\text{M}$) to the hepatocyte culture media. This same slope supports that the capacity of extracellular bilirubin to reach the cytosol and the mitochondrial matrix is not changed by ABCB10 deletion. $*p < 0.05$ vs. time 0° min. C) Total cytosolic and mitochondrial bilirubin measured in A and B at 100 min normalized by WT concentrations, showing higher accumulation of bilirubin in WT and restoration of bilirubin in LKO. This result is consistent with lower bilirubin synthesis in the LKO. 2-way ANOVA, $*p < 0.05$, $**p < 0.01$ Scale bar, $100 \mu\text{m}$.

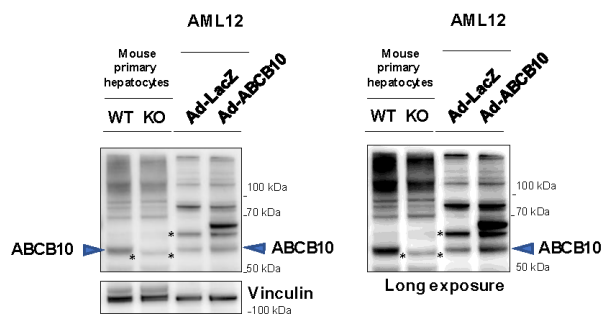


Fig. S5. ABCB10 overexpression in AML12 hepatocytes. AML12 were transduced overnight with Adenovirus (Ad) encoding for LacZ or ABCB10 and analyzed 48h after transduction. Western blots detecting ABCB10 and Vinculin in total lysates from transduced AML12 and from WT and ABCB10 KO mouse primary hepatocytes. The specific ABCB10 band is detected around 60 kDa, which is absent in the KO. One unspecific band* is running very close to ABCB10 in primary hepatocytes as shown in Fig.2 and is marked with an asterisk. An additional band is detected by ABCB10 antibody after ABCB10 overexpression, which migrates at a higher molecular weight. *Unspecific band. Representative gels of 4 different experiments.

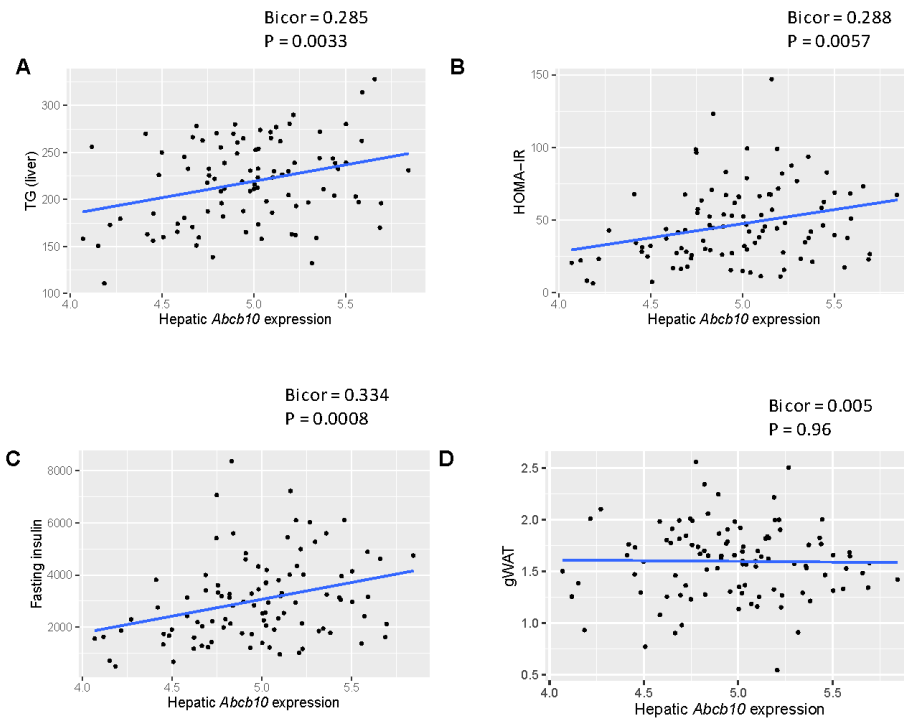


Fig. S6. Correlation plots between hepatic *Abcb10* transcript content and the metabolic traits determined in the HMDP. Biweight midcorrelation (Bicor) plots between hepatic *Abcb10* transcript levels and A) Triglycerides in the liver (TG), B) HOMA-IR (insulin resistance), C) Fasting insulin and D) Gonadal white adipose tissue mass (gWAT). Each dot represents one mouse strain of the HMDP Western diet group, a total of n=102 strains. Values of the Bicor slope and its nominal *P* value shown in each panel.

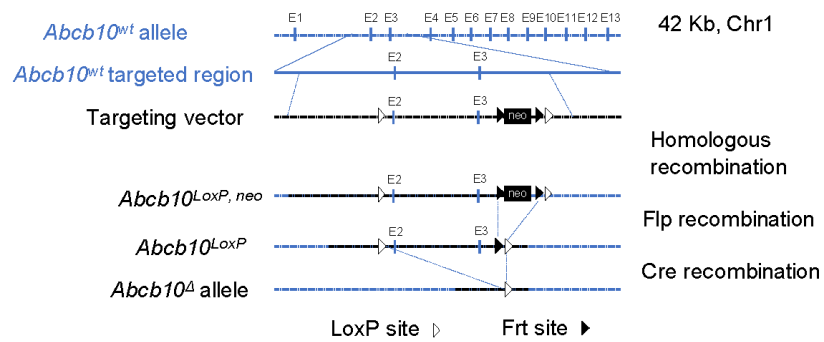


Fig. S7. *Abcb10* targeting strategy to generate ABCB10 LKO mice. ES cells from C57BL/6J were targeted with a vector containing *Abcb10* exon 2 and 3 flanked by LoxP and containing a selection cassette (Neomycin) flanked by FRT sites. Targeted ES cells were generated by genOway. The Neomycin cassette was excised by breeding mice harboring germline transmission of the floxed allele with Flp recombinase transgenic mice. *Abcb10* exons 2 and 3 were excised in hepatocytes by breeding with Albumin Cre transgenic mice.

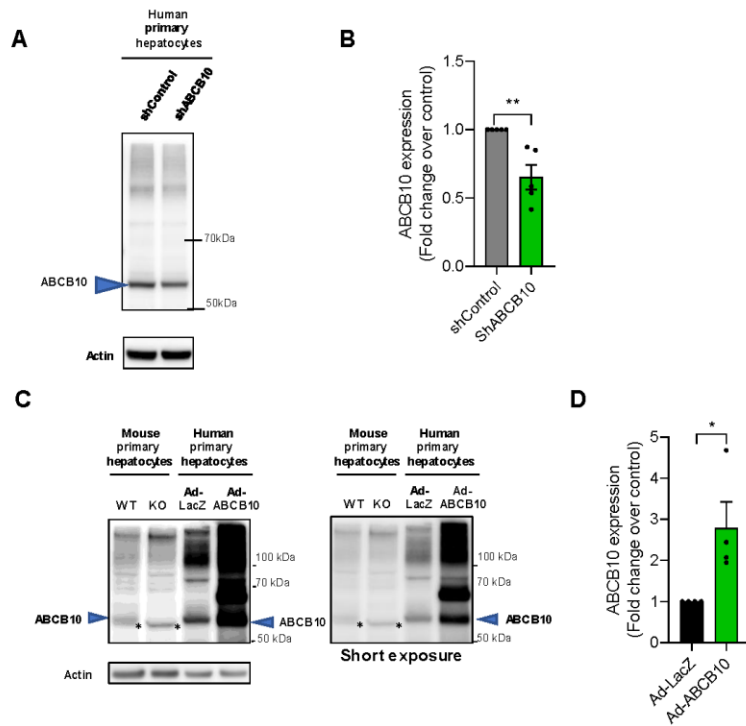


Fig. S8. ABCB10 gain- and loss-of-function approaches in primary human hepatocytes. **A)** Primary human hepatocytes transduced overnight with Ad-LacZ and Ad-ABCB10 and analyzed 48h after transduction. Western blots detecting ABCB10 and actin in total lysates from human primary hepatocytes, running lysates of mouse primary hepatocytes isolated from WT and ABCB10 LKO mice to validate ABCB10 band (60 kDa). The unspecific band close to ABCB10 is marked with an asterisk (*) and the higher molecular weight band is also observed when ABCB10 is overexpressed in human hepatocytes (see fig. S3). **B)** Primary human hepatocytes were transduced with lentivirus encoding shControl (sh001) or shABCB10. $n=5$, data are mean \pm SEM. **C-D)** Quantification of endogenous ABCB10 band (around 60 kDa) in human hepatocytes transduced with Ad-LacZ and Ad-ABCB10. Student's t test; ** $p<0.01$. $n=4$ SEM. Student's t test; * $p<0.05$.

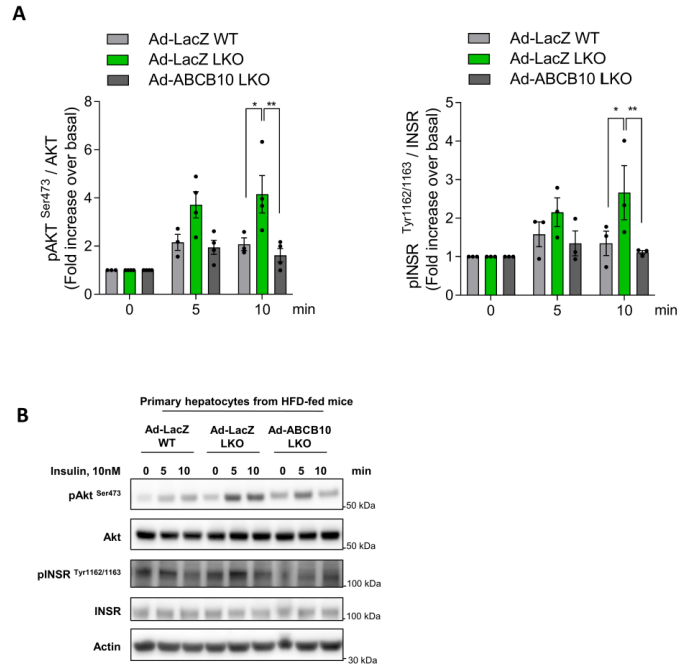


Fig. S9. Rescuing ABCB10 expression ex vivo reverses the improvement in insulin action seen in ABCB10 LKO hepatocytes isolated from HFD-fed mice. A-B) Primary mouse hepatocytes isolated from WT and ABCB10 LKO HFD-fed mice were transduced with Adenovirus (Ad) encoding LacZ or ABCB10. Two days after transduction, hepatocytes were treated with or without insulin 10 nM for the indicated minutes (min). **A**) Quantification of pSer⁴⁷³ AKT and pTyr^{1162/1163} INSR. **B**) Representative Western blots of pSer⁴⁷³ AKT and pTyr^{1162/1163} INSR, AKT, INSR. Actin was used as loading control. *p<0.05, **p<0.01 Two-way ANOVA. n=3-4 independent isolations and treatments of WT and KO hepatocyte pairs.

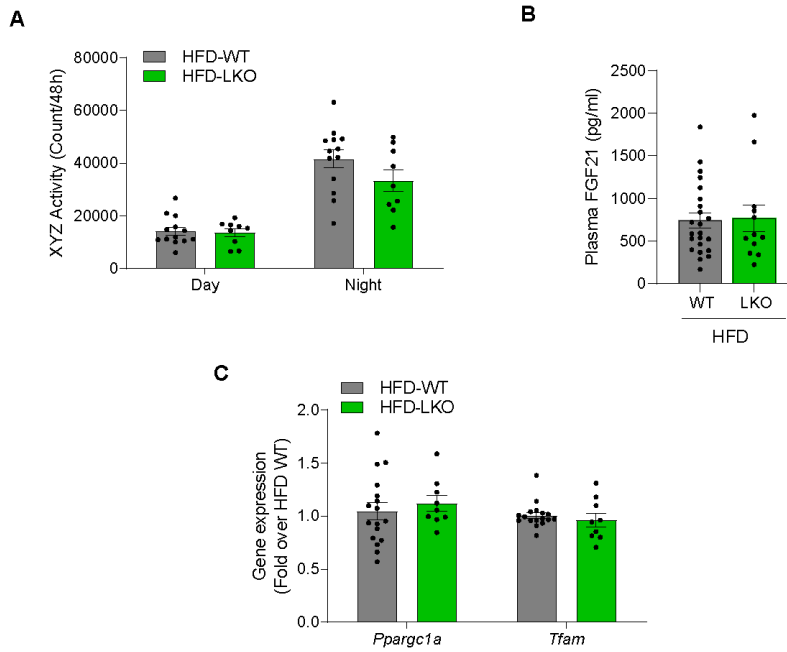


Fig. S10. HFD-fed ABCB10 LKO mice show no differences in physical activity, mitochondrial biogenesis markers in the liver, or plasma fibroblast growth factor 21 (FGF21) concentrations. A-D) Average number of WT and ABCB10-LKO male mice fed a high fat diet (HFD) \pm SEM. n = 9-23 mice/group. **A)** Physical activity as counts of laser beams breaks in XYZ over a 48h period. **B)** Plasma FGF21 and **C)** gene expression of mitochondrial biogenesis markers (*Pparg1a* aka *Pgc1 α* and *Tfam*).

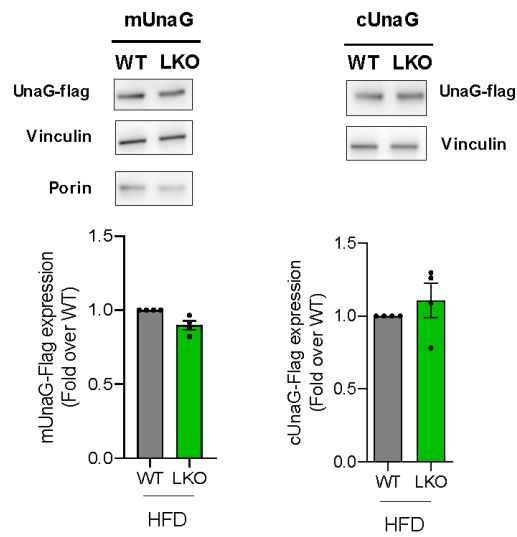


Fig. S11. Total protein content of cytosolic and mitochondrial UnaG is not changed by ABCB10 deletion. Western blot of total UnaG-flag protein expressed in HFD-fed WT and LKO primary hepatocytes, detected with anti-flag. n=4/ group.

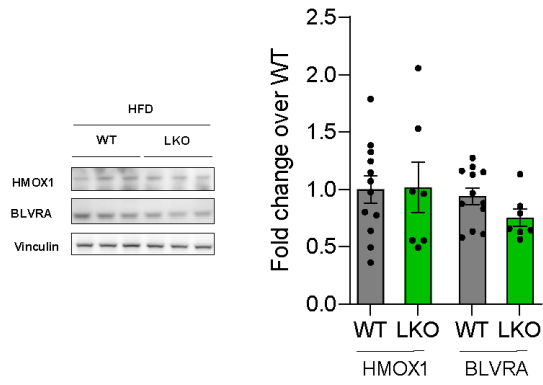


Fig. S12. No differences in hepatic HMOX1 or BLVRA content in HFD-fed ABCB10 LKO mice. Average number of WT and ABCB10-LKO male mice fed a high-fat diet (HFD) \pm SEM. n=7-12 mice/group.

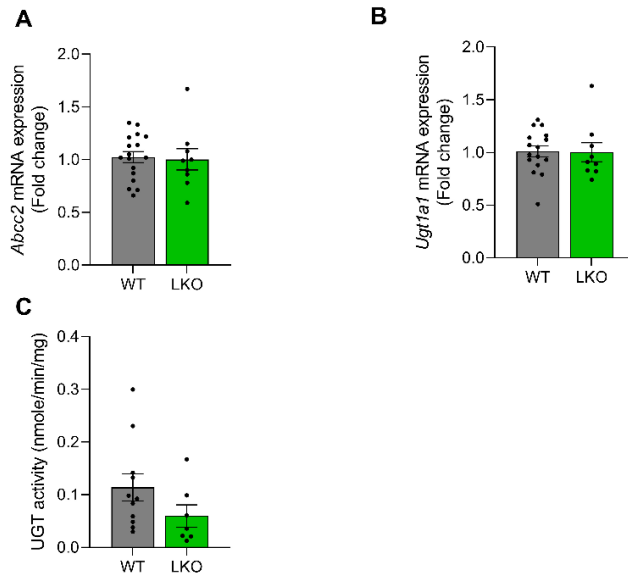


Fig. S13. HFD-fed ABCB10 LKO mice show no changes in the bilirubin exporter ABCC2 or the main enzyme conjugating bilirubin, UGT1A1. A-C) Average number of WT and ABCB10-LKO male mice fed a high-fat diet (HFD) \pm SEM. $n=9-16$ mice/group. **A)** *Abcc2* mRNA abundance and **B)** *Ugt1a1* mRNA abundance measured in total liver lysates. **C)** UGT activity measured in microsomal fractions from liver.

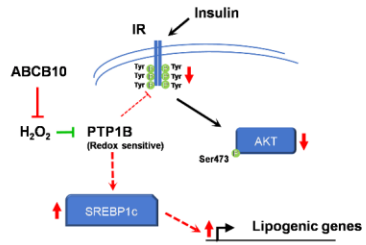


Fig. S14. Summary of PTP1B actions on insulin signaling and lipogenesis and the consequences of PTP1B inactivation by H₂O₂.

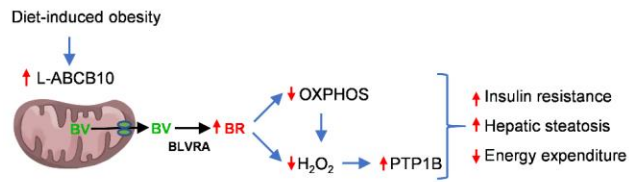


Fig. S15. The role of ABCB10 in hepatic insulin resistance and steatosis in obesity..

Table S1. Primer sequences.

Gene	Forward Primer 5' to 3'	Reverse Primer 5' to 3'
<i>Arbp</i>	AGA AAC TGC TGC TC ACA TC	CAT CAC TCA GAA TTT CAA TGG
<i>Fasn</i>	CTG GCC CCG GAG TCG CTT GAG TAT A	GGA GCC TCC GAA GCC AAA TGA
<i>Pparg1a</i>	AAG ATG AAG GTC CCC AGG CAG TAG	TGT CCG CGT TGT GTC AGG TC
<i>Pparγ</i>	ACT GCC TAT GAG CAC TTC AC	CAA TCG GAT GGT TCT TCG GA
<i>Scd1</i>	GCC CAC CAC AAG TTC TCA GA	GGG CGA TAT CCA TAG AGA TG
<i>Srebp1c</i>	GCC GGC GCC AG GAC GAG CTG GCC	CAG GAA GGC TTC CAG AGA GGA GGC
<i>Tfam</i>	CAC CCA GAT GCA AAA CTT TCA G	CTG CTC TTT ATA CTT GCT CAC AG

The following data file is available in the online version of the supplement:

Data File S1. Primary data for Figs. 1 to 7 in tabular format.

Appendix V

COQ11 deletion mitigates respiratory deficiency caused by mutations in the gene encoding the coenzyme Q chaperone protein Coq10.

The work described in this chapter has been reproduced from:

Bradley M.C., Yang K., Fernandez-del-Rio L., Ngo J., Ayer A., Tsui H.S., Stocker R., Shirihai O.S., Barros M.H., Clarke C.F. COQ11 deletion mitigates respiratory deficiency caused by mutations in the gene encoding the coenzyme Q chaperone protein Coq10. *J. Biol. Chem.* 2020. doi: 10.1074/jbc.RA119.012420.

Copyright 2020

Michelle C Bradley, Krista Yang, Lucía Fernández-Del-Río, Jennifer Ngo, Anita Ayer, Hui S Tsui, Noelle Alexa Novales, Roland Stocker, Orian S Shirihai, Mario H Barros, Catherine F Clarke.



COQ11 deletion mitigates respiratory deficiency caused by mutations in the gene encoding the coenzyme Q chaperone protein Coq10

Received for publication, December 20, 2019, and in revised form, March 17, 2020. Published, Papers in Press, March 23, 2020. DOI 10.1074/jbc.RA119.012420

Michelle C. Bradley[‡], Krista Yang[‡], Lucía Fernández-del-Río[‡], Jennifer Ngo^{‡§}, Anita Ayer^{¶||}, Hui S. Tsui[‡], Noelle Alexa Novales[‡], Roland Stocker^{¶||}, Orian S. Shirihai[§], Mario H. Barros^{**}, and Catherine F. Clarke^{††}

From the [‡]Department of Chemistry and Biochemistry, Molecular Biology Institute, UCLA, Los Angeles, California 90095-1569, the [§]Department of Molecular and Medical Pharmacology and Medicine, David Geffen School of Medicine, UCLA, Los Angeles, California 90095, the [¶]Vascular Biology Division, Victor Chang Cardiac Research Institute, Sydney, New South Wales 2010, Australia, the ^{||}St. Vincent's Clinical School, University of New South Wales Medicine, Sydney, New South Wales 2050, Australia, and the ^{**}Departamento Microbiologia, Universidade de São Paulo, São Paulo 05508-900, Brazil

Edited by Dennis R. Voelker

Coenzyme Q (Q_n) is a vital lipid component of the electron transport chain that functions in cellular energy metabolism and as a membrane antioxidant. In the yeast *Saccharomyces cerevisiae*, *coq1-coq9* deletion mutants are respiratory-incompetent, sensitive to lipid peroxidation stress, and unable to synthesize Q_6 . The yeast *coq10* deletion mutant is also respiratory-deficient and sensitive to lipid peroxidation, yet it continues to produce Q_6 at an impaired rate. Thus, Coq10 is required for the function of Q_6 in respiration and as an antioxidant and is believed to chaperone Q_6 from its site of synthesis to the respiratory complexes. In several fungi, Coq10 is encoded as a fusion polypeptide with Coq11, a recently identified protein of unknown function required for efficient Q_6 biosynthesis. Because “fused” proteins are often involved in similar biochemical pathways, here we examined the putative functional relationship between Coq10 and Coq11 in yeast. We used plate growth and Seahorse assays and LC-MS/MS analysis to show that *COQ11* deletion rescues respiratory deficiency, sensitivity to lipid peroxidation, and decreased Q_6 biosynthesis of the *coq10Δ* mutant. Additionally, immunoblotting indicated that yeast *coq11Δ* mutants accumulate increased amounts of certain Coq polypeptides and display a stabilized CoQ synthome. These effects suggest that Coq11 modulates Q_6 biosynthesis and that its absence increases mitochondrial Q_6 content in the *coq10Δcoq11Δ* double mutant. This augmented mitochondrial Q_6 content counteracts the respiratory deficiency and lipid peroxidation sensitivity phenotypes of the *coq10Δ* mutant. This

study further clarifies the intricate connection between Q_6 biosynthesis, trafficking, and function in mitochondrial metabolism.

Coenzyme Q (ubiquinone or Q)² is a benzoquinone lipid that functions as an essential electron carrier within the electron transport chain (1). Because of its redox activities, Q is a versatile electron acceptor in biological pathways such as cellular respiration, oxidation of proline and sulfide, fatty acid β -oxidation, and pyrimidine biosynthesis (1–3). The reduced hydroquinone form of Q (ubiquinol or QH₂) also serves as an important chain-breaking antioxidant shown to alleviate lipid peroxidative damage in cellular membranes (4).

For proper functional localization, Q relies on its polyisoprenoid tail to remain anchored at the mid-plane of phospholipid bilayers. The number of isoprene units (n) that comprise the polyisoprenoid tail of Q_n depends on a species-specific polyprenyl diphosphate synthase (5), with Q_{10} representing the major isoform in humans (6). Patients unable to produce adequate levels of Q_{10} display a wide variety of health issues that stem from mitochondrial dysfunction across tissues (7). Attempts to ameliorate the consequences of primary Q_{10} deficiency by early Q_{10} supplementation have been partially successful in some cases (8); however, many patients fail to demonstrate full recovery, which is related to inefficient uptake of orally-supplied Q_{10} . Because of the striking homology between human COQ genes and those of *Saccharomyces cerevisiae* (7, 9), studies of Q_6 biosynthesis in *S. cerevisiae* may provide insight

This work was supported by National Science Foundation Grant MCB-1330803 (to C. F. C.), National Institutes of Health Grant T32 GM 007185 (to H. S. T. and M. C. B.), Ruth L. Kirschstein National Service (to M. C. B. and H. S. T.), the Whitcome Individual Predoctoral Fellowship (to M. C. B.), UCLA Summer Undergraduate Research Fellowship, Department of Chemistry and Biochemistry (to K. Y.), Fundação de Amparo a Pesquisa de São Paulo-FAPESP 2013/09482-8 and 2013/07937-8 (to M. H. B.), Gates Millennium Scholars Fellowship (to J. N.), and the Eugene V. Cota Robles Fellowship (to J. N.). The authors declare that they have no conflicts of interest with the contents of this article. The content is solely the responsibility of the authors and does not necessarily represent the official views of the National Institutes of Health.

This article contains Figs. S1–S3, Tables S1 and S2, and supporting Refs. 1–8. [†] To whom correspondence should be addressed. Tel: 310-825-0771; Fax: 310-206-5213; E-mail: cathy@chem.ucla.edu.

This is an Open Access article under the [CC BY](https://creativecommons.org/licenses/by/4.0/) license.



J. Biol. Chem. (2020) 295(18) 6023–6042 6023

© 2020 Bradley et al. Published under exclusive license by The American Society for Biochemistry and Molecular Biology, Inc.

Coq10 knockout phenotypes are rescued by deletion of COQ11

into human Q₁₀ biosynthesis, leading to the discovery of potential therapeutic targets.

In *S. cerevisiae*, at least 14 nuclear-encoded mitochondrial proteins (Coq1–Coq11, Yah1, Arh1, and Hfd1) drive Q₆ biosynthesis (7, 9). Many Coq polypeptides (Coq3–Coq9, and Coq11) are localized to the matrix side of the mitochondrial inner membrane, where they organize into a high-molecular-weight multisubunit complex known as the “CoQ synthome” (7, 9). Several lines of evidence suggest that correct assembly of the CoQ synthome is necessary for efficient Q₆ biosynthesis (9–12). In fact, deletion of certain COQ genes results in decreased levels of other Coq polypeptides and contributes to a destabilized CoQ synthome in these mutants (12, 13). Recently, a protein of unknown function encoded by the ORF YLR290C was identified to associate with the CoQ synthome, via proteomic analysis of tandem affinity-purified tagged Coq proteins (14). YLR290C copurified with Coq5, Coq7, and Coq9, in addition to Q₆ and late-stage Q₆-intermediates (14). Furthermore, the *ytr290cΔ* mutant exhibited impaired *de novo* Q₆ biosynthesis, despite preserving growth on a nonfermentable carbon source (14). Given its effects on Q₆ biosynthesis and involvement with the CoQ synthome, YLR290C was renamed Coq11 (14).

In several fungi, Coq11 and Coq10 have evolved as fusion proteins (14), suggesting that Coq11 may have a functional relationship with Coq10 (15). High-throughput genetic analyses found COQ11 to correlate with both COQ2 and COQ10 (16). Whereas the *coq* mutants generally lack Q₆, the *coq10Δ* mutant is different because it produces near WT amounts of Q₆ in stationary phase and only has decreased *de novo* Q₆ biosynthesis in log phase (17, 18). Although Q₆ biosynthesis is only minimally decreased in the absence of COQ10, the *coq10Δ* mutant has decreased NADH and succinate oxidase activity and displayed sickly growth on respiratory medium (18). The *coq10Δ* mutant is sensitive to lipid peroxidation initiated by exogenously supplemented polyunsaturated fatty acids (PUFAs), indicating that the Coq10 polypeptide is also required for antioxidant protection by Q₆ (17, 19).

The NMR structure of a Coq10 ortholog in *Caulobacter crescentus* was shown to possess a steroidogenic acute regulatory protein-related lipid transfer (START) domain (20) that can directly bind Q and late-stage Q-intermediates (17). Purified Coq10 from either *S. cerevisiae* or *Schizosaccharomyces pombe* eluted with the respective species' Q isoform (18, 21). This observation has prompted speculation that Coq10 acts as a Q₆ chaperone protein required for delivery of Q₆ from its synthesis site to sites where Q₆ functions as an antioxidant and to the respiratory complexes, thereby bridging efficient *de novo* Q₆ biosynthesis with respiration (17). Recent studies have shown a spatial compartmentalization of the mitochondrial inner membrane with the identification of different sites, such as the inner boundary membrane, the cristae membrane, and the ER-mitochondrial contact sites (22–25). Thus, for optimal respiratory competence, newly-synthesized Q₆ must move from its site of synthesis (*i.e.* the ER-mitochondrial contact sites (23, 24)) to the cristae membrane where the respiratory complexes are concentrated (22). The presence of Coq10–Coq11 fusions in fungal species indicates that Coq11 may have a functional association

with the Coq10 chaperone to facilitate or regulate Q₆ transport for respiration in yeast.

In this work, the functional relationship between Coq10 and Coq11 was investigated using a series of single- and double-knockout mutants. Deletion of COQ11 alleviated the *coq10Δ* respiratory defect, increased Coq polypeptides and CoQ synthome stability, and partially rescued Q₆ production. Based on this evidence, we propose a novel function for Coq11 as a negative modulator of Q₆ biosynthesis in the mitochondria.

Results

Coq10 and Coq11 reside in similar compartments within the mitochondria

Previous phylogenetic analyses of numerous fungi revealed that Coq11-like proteins are fused to Coq10 (14). Protein fusions often indicate a functional relationship between corresponding homologs in other organisms, such as direct protein–protein interaction or operation within the same biological pathway (15). Although Coq10 and Coq11 are not physically fused in yeast (Fig. 1A), we sought to investigate whether there is a functional link between the two proteins. Because protein localization is often associated with function, we first performed mitochondrial fractionation to localize both Coq10 and Coq11. Coq10 has been localized previously (18), but fractionation was re-performed here in the context of Coq11.

S. cerevisiae mitochondria were fractionated as described under “Experimental procedures.” Purified mitochondria were incubated in hypotonic buffer to disrupt the outer membrane and release soluble components of the intermembrane space (IMS). The inner membrane was kept intact following hypotonic buffer treatment, protecting inner membrane and matrix proteins. Analysis of the fractions via immunoblot suggested that both Coq10 and Coq11 remained associated with the mitoplast fraction as opposed to colocalizing with the IMS marker cytochrome *b*₂. Mitoplasts were further fractionated after sonication to separate soluble matrix components (supernatant, S) from membrane components (pellet, P). The soluble matrix marker Hsp60 was partially released into the supernatant by sonication as demonstrated in earlier work (26). Although Coq11 remained associated with the membrane fraction, Coq10 was partially dissociated in a similar manner to Hsp60 (Fig. 1B). Previous Coq10 colocalization following sonication demonstrated that Coq10 was solely associated with the membrane fraction (18). The detection of Coq10 in the supernatant shown in Fig. 1B may be due to increased sensitivity of the polyclonal antisera used in this study.

Alternatively, mitoplasts were subjected to alkaline carbonate extraction to separate peripheral membrane components (supernatant, S) from integral membrane and matrix components (pellet, P) (27). Coq10 and Coq11 were released into the supernatant following alkaline treatment (Fig. 1B), matching the peripheral inner membrane marker Atp2 (28). There was no colocalization with the pellet fraction, marked by the integral membrane protein Cyt₁ (29). These results indicate that Coq10 and Coq11 are both peripheral inner membrane proteins, and Coq10 has additional localization to the matrix. The localization of Coq10 to the inner membrane is consistent with

Coq10 knockout phenotypes are rescued by deletion of COQ11

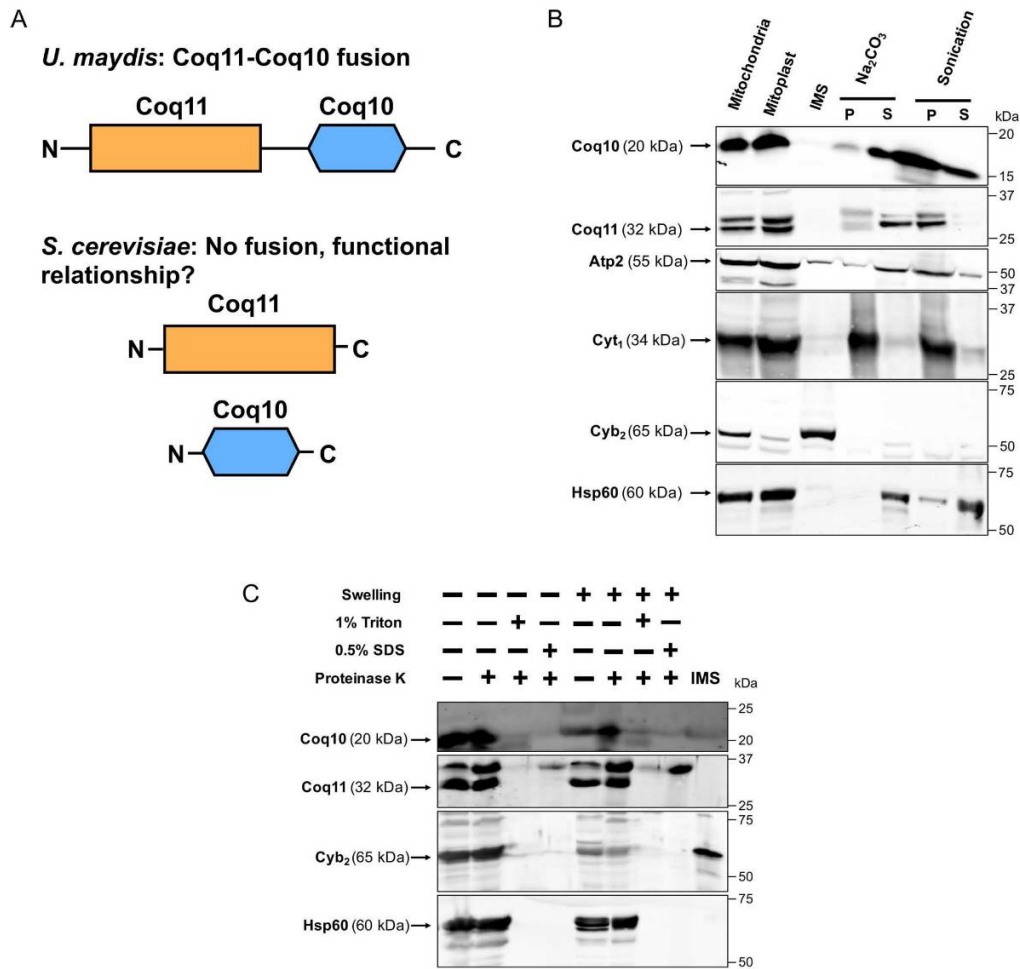


Figure 1. Coq11 and Coq10 are peripherally associated with the mitochondrial inner membrane facing the matrix, and Coq10 is additionally found in the mitochondrial matrix. *A*, Coq10 and Coq11 are fused in multiple fungi, suggesting an evolutionarily functional relationship between these proteins, although they are not found fused in *S. cerevisiae*. *B*, *S. cerevisiae* mitochondria purified from yeast strains cultured on YPGal medium were subjected to hypotonic swelling and centrifugation to separate the IMS proteins from mitoplasts. The mitoplasts were alkaline-treated (Na_2CO_3 ; pH 11.5) or sonicated and then separated by centrifugation ($100,000 \times g$ for 1 h) into supernatant (S) or pellet (P) fractions. *C*, intact mitochondria or mitoplasts were treated with $100 \mu\text{g}/\text{ml}$ proteinase K for 30 min on ice, with or without detergent. Mitochondrial polypeptide markers are as follows: *Atp2*, peripheral inner membrane protein; *Cyb₂*, intermembrane space protein; *Cyt₁*, integral inner membrane protein; and *Hsp60*, soluble matrix protein. Results are representative of two experiments.

its putative role as a START domain protein possessing a hydrophobic cavity to bind and chaperone Q_6 from its site of synthesis to complex III for respiration (17, 18). We hypothesize that dual mitochondrial matrix localization occurs when Coq10 is tightly bound to protein partners to decrease its hydrophobicity.

For better insight into the membrane association of Coq10 and Coq11, intact mitochondria or mitoplasts were treated with proteinase K in the absence or presence of two individual detergents (1% Triton X-100 or 0.5% SDS). Coq10 and Coq11 were both protected from protease treatment in purified mito-

chondria and mitoplasts, as was the matrix marker Hsp60 (Fig. 1C). When protease was used in the presence of either detergent in mitochondria or mitoplasts, all proteins became sensitive to the protease and were degraded. Expanding on the sub-fractionation results, these data indicate that Coq10 and Coq11 polypeptides are peripherally associated with the inner membrane facing the matrix side in yeast mitochondria, and Coq10 is also found in the mitochondrial matrix itself. The mitochondrial peripheral membrane association of these two proteins is also in agreement with their submitochondrial localization previously identified in a study of the yeast mitochondrial proteome (30).

Coq10 knockout phenotypes are rescued by deletion of COQ11

Table 1
Genotype and source of yeast strains

Strain	Genotype	Source
W303-1B	MAT α <i>ade2-1 his3-1,15 leu2-1,12trp1-1 ura3-1</i>	R. Rothstein ^a
BY4742	MAT α <i>his3Δ0 leu2Δ0 met15Δ0 ura3Δ0</i>	53
JM6	MAT α <i>his-4</i> ρ^0	68
JM8	MAT α <i>ade-1</i> ρ^0	68
BY4742 <i>coq1Δ</i>	MAT α <i>his3Δ0 leu2Δ0 met15Δ0 ura3Δ0 coq1::KanMX4</i>	69
BY4741 <i>coq2Δ</i>	MAT α <i>his3Δ0 leu2Δ0 met15Δ0 ura3Δ0 coq2::KanMX4</i>	69
BY4742 <i>coq3Δ</i>	MAT α <i>his3Δ0 leu2Δ0 met15Δ0 ura3Δ0 coq3::KanMX4</i>	69
BY4742 <i>coq4Δ</i>	MAT α <i>his3Δ0 leu2Δ0 met15Δ0 ura3Δ0 coq4::KanMX4</i>	69
BY4742 <i>coq5Δ</i>	MAT α <i>his3Δ0 leu2Δ0 met15Δ0 ura3Δ0 coq5::KanMX4</i>	69
BY4741 <i>coq6Δ</i>	MAT α <i>his3Δ0 leu2Δ0 met15Δ0 ura3Δ0 coq6::KanMX4</i>	Dharmacon, Inc.
BY4742 <i>coq7Δ</i>	MAT α <i>his3Δ0 leu2Δ0 met15Δ0 ura3Δ0 coq7::KanMX4</i>	69
BY4742 <i>coq8Δ</i>	MAT α <i>his3Δ0 leu2Δ0 met15Δ0 ura3Δ0 coq8::KanMX4</i>	69
BY4742 <i>coq9Δ</i>	MAT α <i>his3Δ0 leu2Δ0 met15Δ0 ura3Δ0 coq9::KanMX4</i>	69
BY4742 <i>coq10Δ</i>	MAT α <i>his3Δ0 leu2Δ0 met15Δ0 ura3Δ0 coq10::KanMX4</i>	69
BY4742 <i>coq11Δ</i>	MAT α <i>his3Δ0 leu2Δ0 met15Δ0 ura3Δ0 coq11::LEU2</i>	This work
BY4742 <i>coq10Δcoq11Δ</i>	MAT α <i>his3Δ0 leu2Δ0 met15Δ0 ura3Δ0 coq10::HIS3 coq11::LEU2</i>	This work
W303 <i>coq10Δ</i>	MAT α <i>ade2-1 his3-1,15 leu2-3,112trp1-1 ura3-1 coq10::HIS3</i>	18
W303 <i>coq10Δrev</i>	MAT α <i>ade2-1 his3-1,15 leu2-3,112trp1-1 ura3-1 coq10::HIS3</i>	18
W303 <i>coq10rev</i>	MAT α <i>ade2-1 his3-1,15 leu2-3,112trp1-1 ura3-1 coq10::HIS3 sup</i>	This work
MB-10	Diploid produced from W303 <i>coq10Δ</i> x W303 <i>coq10Δrev</i>	This work
W303 <i>coq11Δ</i>	MAT α <i>ade2-1 his3-1,15 leu2-3,112trp1-1 ura3-1 coq11::LEU2</i>	This work
W303 <i>coq10Δcoq11Δ</i>	MAT α <i>ade2-1 his3-1,15 leu2-3,112trp1-1 ura3-1 coq10::HIS3 coq11::LEU2</i>	This work
BY4741 <i>cor1Δ</i>	MAT α <i>his3Δ0 leu2Δ0 met15Δ0 ura3Δ0 cor1::KanMX4</i>	69

^a Gift from Dr. Rodney Rothstein Department of Human Genetics, Columbia University.

coq10 Δ respiratory defect is alleviated by deletion of COQ11

Based on similar mitochondria localization and genetic evolutionary evidence, a putative functional relationship between Coq10 and Coq11 was further probed using a series of *coq10* and *coq11* single- and double-knockout mutants. Strain descriptions are listed in Table 1. The Coq10 polypeptide is required for respiration in yeast, and mutants lacking *coq10* have poor growth on nonfermentable carbon sources, including YPGlycerol, hereafter referred to as “YPG” (18). Unlike deletion of *COQ10*, *coq11 Δ* mutants are respiratory-capable and have comparable growth to WT on nonfermentable carbon sources (14). When *COQ11* was deleted in a *coq10 Δ* mutant in two different yeast genetic backgrounds, the sickly growth of *coq10 Δ* on nonfermentable YPG was rescued (Fig. 2A).

Quantitative respiratory capacity of each mutant was evaluated with an XF96 Extracellular Flux Analyzer (Fig. 2, B and C). Representative and normalized traces of oxygen consumption rates (OCR) of four independent experiments performed in nonrepressive medium (YPGal) are shown in Fig. 2B. Basal rates of OCR were measured prior to the addition of any small molecule inhibitors. Consistent with its slow growth on nonfermentable medium, the *coq10 Δ* mutant had a low rate of basal oxygen consumption compared with WT ($p = 0.052$) (Fig. 2C). Basal OCR was rescued in the *coq10 Δ coq11 Δ* double mutant (Fig. 2C). Following the addition of two sequential injections of FCCP, a mitochondrial oxidative phosphorylation uncoupler, maximal respiration was also quantified. The maximal respiration of *coq10 Δ coq11 Δ* was rescued to that of WT (Fig. 2C). These results show that the deletion of *COQ11* in a *coq10 Δ* mutant confers a beneficial effect, such that both growth on respiratory medium and OCR are rescued to WT.

Deletion of COQ11 rescues PUFA sensitivity of the *coq10 Δ* mutant

PUFA autoxidation is initiated by the radical-mediated abstraction of vulnerable hydrogen atoms at bis-allylic posi-

tions (31). The ensuing carbon-centered radical adds to molecular oxygen to form a lipid peroxy radical that propagates lipid peroxidation, with the resulting lipid hydroperoxides ultimately driving cellular toxicity (32). The *coq10 Δ* mutant is sensitive to treatment with exogenous PUFAs (Fig. 2D) (17, 19), likely because the Q₆ chaperone function of Coq10 is required for the antioxidant function of Q₆. Attenuated respiration in *coq10 Δ* is rescued in the *coq10 Δ coq11 Δ* double knockout (Fig. 2, A–C), presumably through regained function of Q₆ in the electron transport chain. To test whether the antioxidant capability of Q₆ is also restored in the *coq10 Δ coq11 Δ* mutant, yeast strains were evaluated for sensitivity to added PUFAs (Fig. 2D). As anticipated, all strains were resistant to treatment with the monounsaturated oleic acid (Fig. 2D). Q₆-less *coq9 Δ* was sensitive to α -linolenic acid due to the lack of Q₆ antioxidant protection (Fig. 2D). Conversely, the Q₆-replete yet respiratory-deficient *cor1 Δ* remained resistant to α -linolenic acid (Fig. 2D). Deletion of *COQ11* rescued the α -linolenic acid sensitivity of the *coq10 Δ* mutant, suggesting that the double knockout has restored Q₆ antioxidant protection (Fig. 2D) despite the absence of Coq10 as a Q₆ chaperone.

Independent *coq10* revertant with rescued growth on respiratory medium harbors a mutation within COQ11

Although the *coq10 Δ* mutant is unable to grow robustly on nonfermentable medium, an earlier study identified a spontaneous *coq10* revertant (*coq10rev*) that arose when *coq10 Δ* yeast was cultured for several weeks on nonfermentable medium containing ethanol and glycerol as carbon sources (18). Characterization of this revertant revealed a suppressor mutation within the *COQ11* ORE, resulting in a truncated Coq11 protein that is predicted to be nonfunctional (Fig. 3A). This mutation was further assessed for dominance to determine whether it was sufficient to explain the respiratory competence of *coq10rev*. A haploid *coq10 Δ* mutant crossed with haploid *coq10rev* produced diploid MB-10 (Table 1), which was capable of growth on respiratory medium (Fig. 3B). Illustrated growth

Coq10 knockout phenotypes are rescued by deletion of COQ11

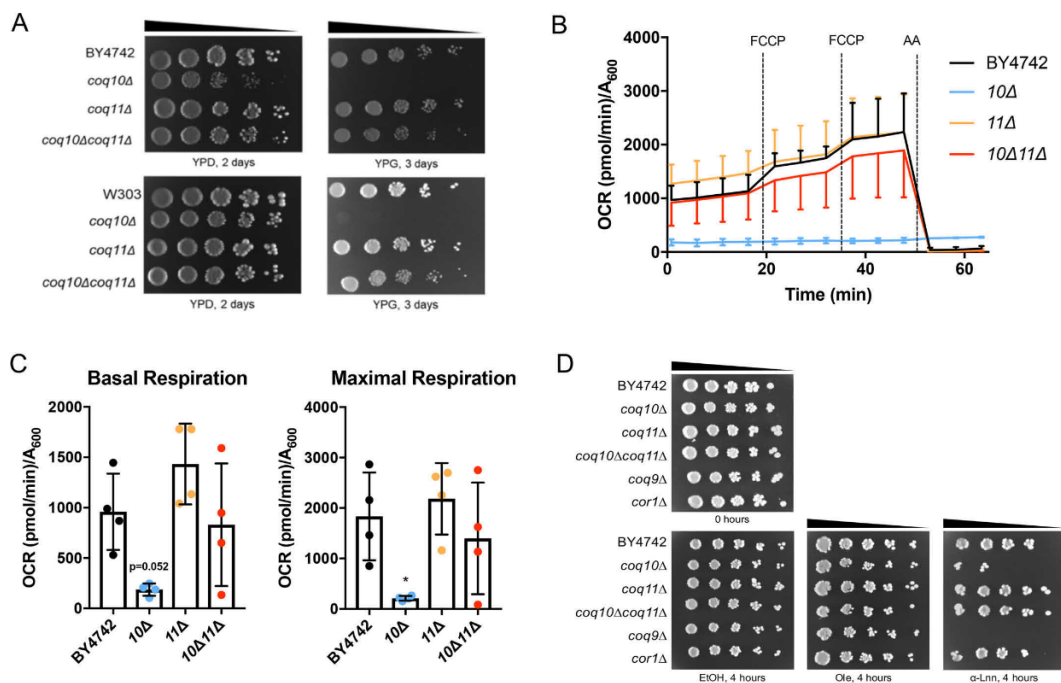


Figure 2. *COQ11* deletion rescues the lack of growth on YPG, low-oxygen consumption rates, and lost Q₆ antioxidant protection in the *coq10Δ* mutant. **A**, strains were grown overnight in 5 ml of YPD, diluted to an A₆₀₀ = 0.2 with sterile PBS, and 2 μl of 5-fold serial dilutions were spotted onto fermentable (YPDextrose, YPD) or respiratory (YPGlycerol, YPG) medium, corresponding to a final A₆₀₀ = 0.2, 0.04, 0.008, 0.0016, and 0.00032. Plates were incubated at 30 °C, and growth was captured after 2 or 3 days. **B** and **C**, quadruplicates of 25-ml cultures of WT, *coq10Δ*, *coq11Δ*, and *coq10Δcoq11Δ* yeast were grown in YPGal until they reached A₆₀₀ ~4. Yeast were diluted to an A₆₀₀ = 0.1 in fresh YPGal and collected by centrifugation on poly-D-lysine-coated Seahorse XF96 microplates to assess oxygen consumption. **B**, representative traces of OCR of yeast strains with the XF96 extracellular flux analyzer. FCCP and antimycin A (AA) were sequentially added to evaluate mitochondrial respiratory states. Measurements were taken approximately every 4 min, as represented by points and their respective error bars. Four independent experiments were performed (Fig. S1), and each group of average traces represents 8–10 technical replicates. **C**, quantification of basal and maximal (maximal electron transport activity induced by the uncoupler FCCP) OCR as obtained from four independent experiments (Fig. S1). The data show the mean ± S.D., and the statistical significance as compared with WT is represented by *, *p* < 0.05. **D**, deletion of *COQ11* in the *coq10Δ* rescues PUFA sensitivity. Results are representative of three experiments.

patterns suggest that the *coq11* truncated allele present in *coq10rev* is a dominant-negative mutation. Because the dominant mutation in *coq10rev* restores growth on respiratory medium via a functionally suppressive Coq11 truncation mutation, this mutant effectively validates the *coq10Δcoq11Δ* phenotype in an independent system.

Deletion of COQ11 fails to fully restore *coq10Δ* Q₆ biosynthesis in whole cells

When a *coq* mutant displays anemic growth on respiratory medium, it is often indicative of inefficient Q₆ biosynthesis (7, 9); yeast lacking *COQ10* exhibit both poor growth on respiratory medium and decreased Q₆ biosynthesis in log phase whole cells (17, 19). Although the *coq11Δ* mutant retains the ability to grow on nonfermentable medium, it is also characterized by impaired Q₆ biosynthesis (14). Only a small amount of Q₆ is required for growth on respiratory medium, ~0.2–3% of the total Q₆ found in WT (9, 33, 34). Because the *coq10Δcoq11Δ* double mutant has rescued respiration, we wanted to assess whether recovered growth was accompanied by increased Q₆ biosynthesis. Whole-cell *de novo*-synthesized [¹³C₆]Q₆ and

[¹²C]Q₆ were measured in yeast by feeding the quinone ring-labeled precursor, [¹³C₆]4HB, or EtOH vehicle control (Fig. 4). These analyses were performed in the fermentable, nonrepressive YPGal medium (35) to match the conditions of experiments involving purified mitochondria.

Consistent with previous results (14, 17), *coq10Δ* and *coq11Δ* had significantly decreased *de novo*-synthesized [¹³C₆]Q₆ and [¹²C]Q₆ compared with WT (Fig. 4A). The *coq10Δ* mutant had a lower total Q₆ content ([¹³C₆]Q₆ + [¹²C]Q₆) than WT and also a lower total Q₆ than *coq11Δ* (Fig. 4B). Deletion of *COQ11* in *coq10Δ* yeast led to a slight increase in *de novo*-synthesized [¹³C₆]Q₆ and unchanged [¹²C]Q₆ compared with *coq10Δ* (Fig. 4A). Therefore, the *coq10Δcoq11Δ* double mutant presented total Q₆ contents that were significantly lower than either WT or *coq11Δ* (Fig. 4B). Given the robust growth of the *coq10Δcoq11Δ* double mutant on YPG, restored respiration, and resistance to PUFA treatment, the low Q₆ concentrations observed are surprising.

Next, we quantified the concentrations of key Q₆-intermediates in the same whole-cell yeast pellets. As shown previously

Coq10 knockout phenotypes are rescued by deletion of COQ11

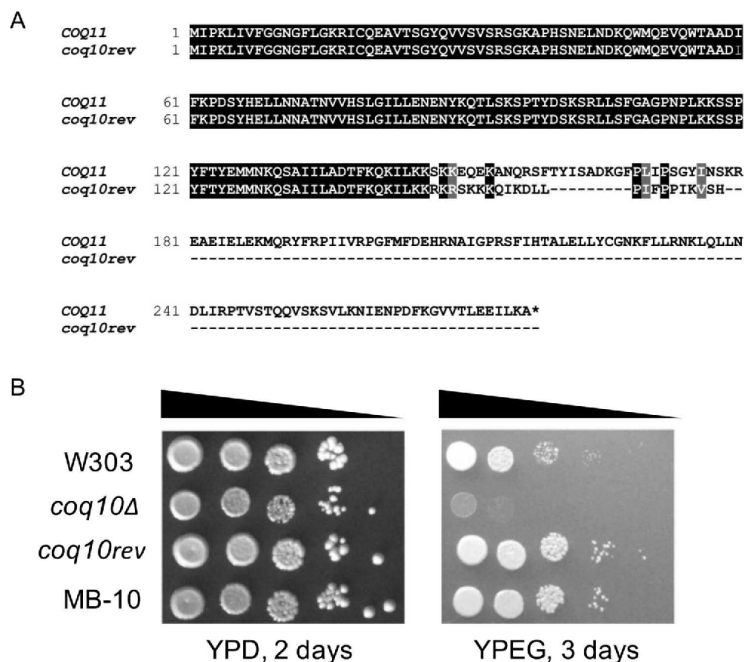


Figure 3. Spontaneous *coq10* revertant with rescued respiratory capacity was identified to possess a base-pair deletion in *COQ11*, encoding a truncated Coq11 protein. **A**, alignment of the amino acid sequence of WT *COQ11* ORF with the *coq11* allele (*coq10rev*) present in the *coq10* revertant. **B**, growth properties of WT were compared with *coq10* mutants and diploid MB-10 (defined in Table 1). Strains were grown overnight in 8 ml of YPDextrose (YPD), diluted to an $A_{600} = 0.2$ with sterile PBS, and 2 μ l of 5-fold serial dilutions were spotted onto fermentable YPD or respiratory (YPEGlycerol (YPEG)) medium, corresponding to a final $A_{600} = 0.2, 0.04, 0.008, 0.0016,$ and 0.00032 . Plates were incubated at 30 °C, and growth was captured after 2 or 3 days. Results are representative of three experiments.

(17, 19), the *coq10*Δ mutant contained lower amounts of the late-stage intermediate [¹³C₆]DMQ₆ and [¹²C]DMQ₆ (Fig. 4C) than WT, and it accumulated the early-stage intermediate [¹³C₆]HHB and [¹²C]HHB (Fig. 4D). In contrast to *coq10*Δ, the *coq11*Δ mutant mirrored WT production of both *de novo*-synthesized and unlabeled early- and late-stage intermediates (Fig. 4, C and D), as shown previously (14). Q₆-intermediate trends in *coq10*Δ*coq11*Δ matched those of the *coq10*Δ mutant rather than *coq11*Δ (Fig. 4, C and D). The low Q₆ content and accumulation of early-stage Q₆-intermediates in the *coq10*Δ*coq11*Δ double knockout suggest the absence of *COQ10* still produces a notable effect on Q₆ biosynthesis, although respiratory capacity is rescued.

*coq10*Δ*coq11*Δ double mutant has increased mitochondrial Q₆ compared with the *coq10*Δ single mutant

Although Q₆ biosynthesis solely occurs within mitochondria, it is found in all cellular membranes (9). Therefore, Q₆ was quantified in both whole cells and purified mitochondria from mutant and WT cells cultured under the same conditions (36). Whole-cell Q₆ determined under mitochondrial purification conditions matched those determined in Figs. 4 and 5A. The *coq10*Δ*coq11*Δ double mutant made slightly more Q₆ than the *coq10*Δ single mutant, but overall less Q₆ compared with the

*coq11*Δ single mutant. All mutants had lower whole-cell Q₆ amounts than WT (Fig. 5A).

Similarly, mitochondrial Q₆ content per microgram of mitochondrial protein was lower in *coq11*Δ than WT (Fig. 5B). However, deletion of *COQ11* in the *coq10*Δ mutant increased the mitochondrial Q₆ 5-fold (Fig. 5B). Despite these profound differences in mitochondrial Q₆ content, mitochondrial mass was consistent between strains as determined by three distinct assays (Fig. 5, C–E). Increased mitochondrial Q₆ in the *coq10*Δ*coq11*Δ double mutant compared with *coq10*Δ indicates that the absence of *COQ11* in part rescues defective Q₆ synthesis in the *coq10*Δ mutant.

Low Coq protein content and destabilized CoQ synthome of the *coq10*Δ mutant are restored in the *coq10*Δ*coq11*Δ double mutant

Proper formation of the CoQ synthome from component Coq polypeptides is required for efficient Q₆ biosynthesis in yeast (9, 12, 13). Deletion of *COQ10* causes a decrease in several other Coq polypeptides, including Coq3–Coq7, Coq9, as well as overall CoQ synthome destabilization (12, 13, 19). These results were confirmed when purified mitochondria from *coq10*Δ yeast were analyzed for each Coq polypeptide (Fig. 6A). The *coq10*Δ mutant had significantly decreased amounts of Coq3,

Coq10 knockout phenotypes are rescued by deletion of COQ11

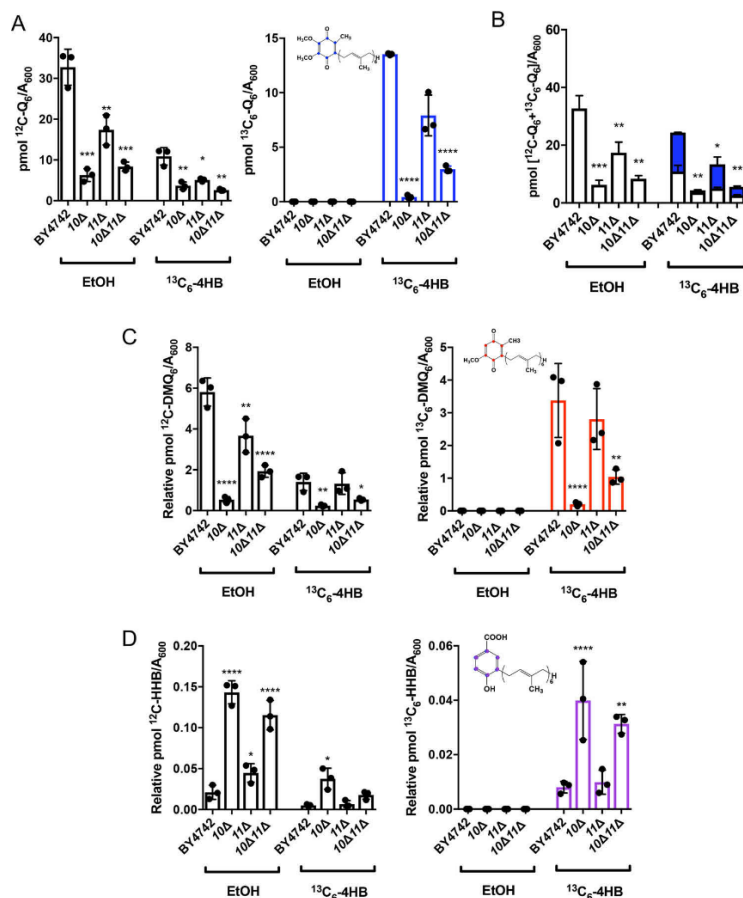


Figure 4. Low amounts of *de novo* [¹³C₆]Q₆ in whole-cell lipid extracts of the *coq10Δ* mutant are only partially restored by deletion of *COQ11*. Triplicates of 6-ml cultures in YPGal were labeled at A₆₀₀ ~1 with 5 μg/ml [¹³C₆]4HB or EtOH vehicle control, and 5 ml of each culture were collected after 4 h, lipid-extracted, and analyzed by LC-MS/MS. A, unlabeled [¹²C]Q₆ and *de novo*-synthesized [¹³C₆]Q₆ (blue); B, total amount of Q₆ determined from the sum of [¹²C]Q₆ and [¹²C]Q₆; C, [¹²C]DMQ₆ and [¹³C₆]DMQ₆ (red); and D, [¹²C]HHB and [¹³C₆]HHB (purple) were measured from the whole-cell lipid extracts of WT and the *coq10Δ*, *coq11Δ*, and *coq10Δcoq11Δ* mutants. Values are the mean of three replicates. The data show mean ± S.D., and the statistical significance as compared with WT is represented by *, *p* < 0.05; ***, *p* < 0.001; and ****, *p* < 0.0001.

Coq4, Coq7, and Coq9 compared to and plotted as a percentage of WT (Fig. 6B).

In contrast to *coq10Δ*, the *coq11Δ* single mutant had elevated Coq4, Coq6, Coq7, and Coq9 (Fig. 6A), with protein quantification shown in Fig. 6B. Furthermore, the *coq10Δcoq11Δ* double mutant also had raised amounts of Coq4, Coq7, and Coq9 polypeptides compared with WT (Fig. 6, A and B). This increase in Coq proteins could not be explained by enhanced *COQ* transcription as there was no corresponding change in the concentration of the respective mRNAs, (Fig. 6C), although *COQ4* mRNA was not detected.

CoQ synthome formation was probed using two-dimensional blue native/SDS-PAGE (2D-BN/SDS-PAGE) with Coq4 and Coq9 serving as sensitive indicators of a high-molecular-weight complex (13). As expected, the CoQ synthome in WT

yeast presented as a heterogeneous high-molecular-weight complex, spanning a range of ~140 kDa to >1 MDa for Coq4 (Fig. 7A) and from ~100 kDa to >1 MDa for Coq9 (Fig. 7B). Consistent with prior results (13, 19), the *coq10Δ* mutant displayed a highly-destabilized CoQ synthome, with a disappearance of large complexes that were replaced by lower-molecular-weight subcomplexes less than ~440 kDa for Coq4 (Fig. 7A) and less than ~232 kDa for Coq9 (Fig. 7B). The *coq11Δ* mutant had a stabilized CoQ synthome compared with WT, with high-molecular-weight complexes shifting to the left and collapsing into a more homogeneous complex spanning ~900 kDa to >1 MDa for both Coq4 (Fig. 7A) and Coq9 (Fig. 7B). When *COQ11* was deleted in combination with *COQ10*, there was a substantial rescue of high-molecular-weight complex formation compared with the *coq10Δ* single mutant (Fig. 7, A and B). The CoQ

Coq10 knockout phenotypes are rescued by deletion of COQ11

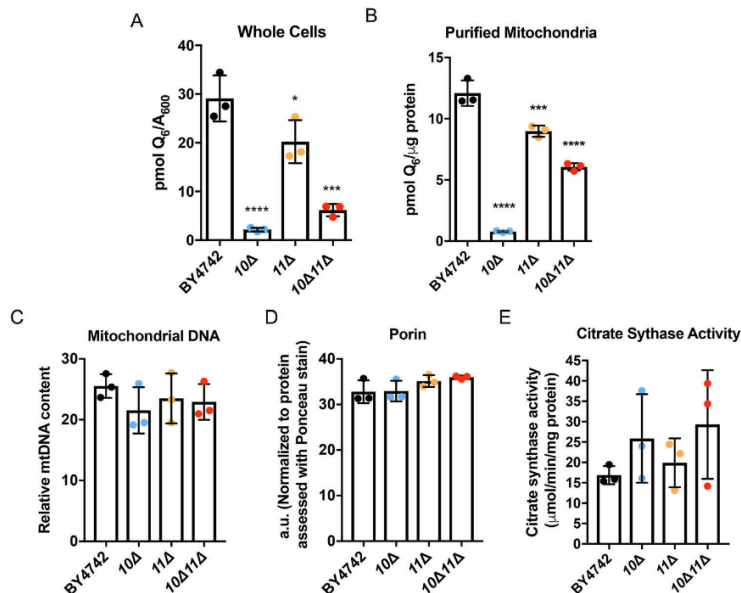


Figure 5. Deletion of COQ11 in the *coq10Δ* mutant enhances mitochondrial Q₆ content. Triplicates of 30-ml cultures of WT, *coq10Δ*, *coq11Δ*, and *coq10Δcoq11Δ* yeast were grown in YPGal until they reached $A_{600} \sim 4$. A, 5 ml of whole cells from each culture were harvested, lipid-extracted, and analyzed by LC-MS/MS for Q₆ content. Alternatively, WT, *coq10Δ*, *coq11Δ*, and *coq10Δcoq11Δ* yeasts were grown in YPGal until they reached $A_{600} \sim 4$ and were subjected to mitochondrial preparation. B, lipids from triplicates of purified mitochondria (100 μg) were analyzed by LC-MS/MS for Q₆ content. C–E, mitochondrial mass was estimated using three distinct methods. C, relative mitochondrial DNA to actin was quantified by qPCR. D, porin protein amounts were quantified by hand using ImageStudioLite following immunoblot and normalized to total protein levels evaluated by Ponceau stain. E, citrate synthase activity was determined using a colorimetric assay as outlined under "Experimental procedures." Values are the mean of three replicates. The data show the mean ± S.D., and the statistical significance as compared with WT is represented by *, $p < 0.05$; ***, $p < 0.001$; and ****, $p < 0.0001$.

synthome of the *coq10Δcoq11Δ* double mutant appeared similar to that of *coq11Δ* complexes spanning ~66 kDa to > 1 MDa for Coq4 (Fig. 7A) and from ~66 kDa to > 1 MDa for Coq9 (Fig. 7B). However, the deletion of COQ11 in *coq10Δ* does not negate the effect from the COQ10 deletion, as it does not restore small subcomplexes <140 kDa to higher molecular weights (Fig. 7, A and B). These CoQ synthome signals for *coq11* mutants were complementary to the observed increased Coq polypeptides, indicating that the absence of COQ11 enhanced the Q₆ biosynthetic machinery.

High-copy COQ8 does not restore Q₆ content in the *coq10Δcoq11Δ* single mutant

The Coq8 polypeptide is a member of an ancient atypical kinase family (37), with several conserved kinase motifs that are essential for Q biosynthesis (13, 38). Prior studies have demonstrated that overexpression of Coq8 in a *coq10Δ* mutant increased the otherwise low amounts of several key Coq polypeptides and stabilized CoQ synthome formation (13). This is similar to the phenotype observed when COQ11 was deleted in the *coq10Δ* mutant. Furthermore, Coq8 overexpression has also been shown to influence Q₆ biosynthesis, including the restoration of late-stage Q₆-intermediates in *coq5–coq9* null mutants (39). Although the CoQ synthome of the *coq10Δ* mutant was stabilized by deletion of COQ11, Q₆ and late-stage Q₆-intermediates remained lower compared with WT and the

coq11Δ single mutant (Fig. 4C). We hypothesized that the overexpression of Coq8 in the *coq10Δ* and *coq10Δcoq11Δ* mutant may restore Q₆ content in both mutants.

WT, *coq10Δ*, *coq11Δ*, and *coq10Δcoq11Δ* were analyzed for growth on nonfermentable medium and Q₆ biosynthesis upon transformation with high-copy COQ8 (hcCOQ8, Table 2) or empty vector control (Fig. 8). Similar to previous observations in a different yeast genetic background (18), *coq10Δ*-expressing hcCOQ8 regained the ability to grow on respiratory medium (Fig. 8A). This growth phenotype may be explained by a stabilized CoQ synthome in the *coq10Δ* mutant harboring hcCOQ8 (13). However, hcCOQ8 had no material effect on the growth properties of WT, *coq11Δ*, or *coq10Δcoq11Δ* strains on YPG (Fig. 8A).

Each strain was grown in minimal selection medium to maintain plasmid expression and was analyzed for Q₆ biosynthesis following metabolic labeling with the ring-labeled Q₆ precursor, [¹³C₆]HB (Fig. 8, B and C). Changing the growth medium from rich (*i.e.* YPGal) to minimal synthetic (*i.e.* SD and drop-out dextrose media (DOD)) changed the relative amounts of Q₆ content among the mutants (Figs. 4B versus 8C). Although WT [¹³C₆]Q₆ and total Q₆ content is similar in Figs. 4B and 8C, the values for *coq11Δ* and the double mutant are quite different. When grown in YPGal, *coq10Δ* had the lowest Q₆ content, followed by the double mutant *coq10Δcoq11Δ*, with *coq11Δ* hav-

Coq10 knockout phenotypes are rescued by deletion of COQ11

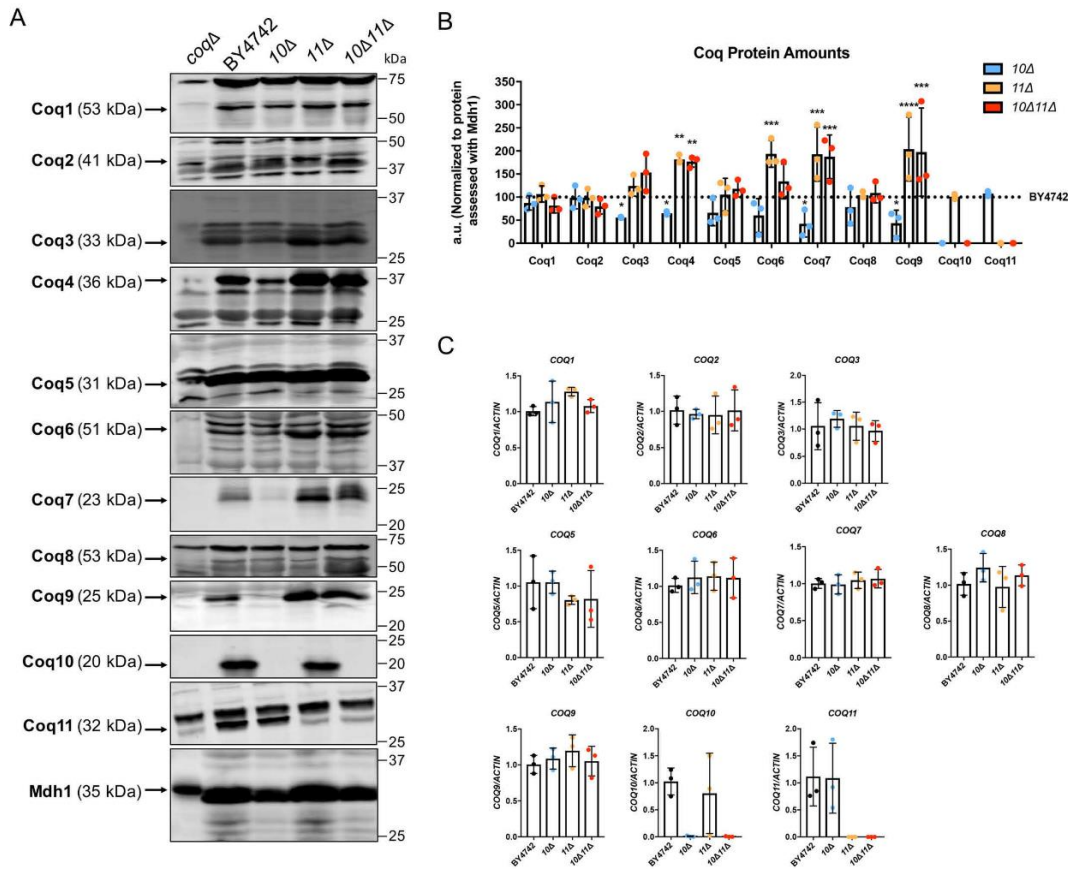


Figure 6. Several Coq polypeptides have increased abundance in *coq11Δ* and *coq10Δcoq11Δ* mutants compared with WT. A, aliquots of purified mitochondria (25 μg) from WT, *coq10Δ*, *coq11Δ*, and *coq10Δcoq11Δ* yeasts were subjected to 10 or 12% Tris-glycine SDS-PAGE. Mitochondrial malate dehydrogenase (Mdh1) was included as a loading control, with a representative blot shown. The Coq5 protein also serves as a qualitative loading control, because the Coq5 polypeptide amounts remain unchanged across the panel of *coq1-coq4* and *coq6-coq10* deletion mutants (12). Aliquots of purified *coqΔ* mitochondria (*coq1Δ-coq11Δ*) were included as negative controls for immunoblotting with antisera to each of the Coq polypeptides. Black arrows highlight the location of each protein on the membrane. B, ImageStudioLite was used to quantify triplicates of each Coq protein band's intensity by hand, which were normalized to Mdh1 and plotted as a percentage of WT. The data show mean ± S.D., and the statistical significance as compared with WT is represented by *, $p < 0.05$; **, $p < 0.01$; ***, $p < 0.001$; and ****, $p < 0.0001$. C, qPCR was used to determine COQ gene expression from whole-cell cultures of WT, *coq10Δ*, *coq11Δ*, or *coq10Δcoq11Δ* mutants as compared with WT.

ing the closest Q_6 content to WT (Figs. 4, A and B, and 5A and Fig. S2, A and B). In contrast, when these strains are cultured in SD-Ura (Fig. 8, B and C), the double mutant *coq10Δcoq11Δ* had the lowest Q_6 content, as compared with either the *coq10Δ* or *coq11Δ* single mutant strains. Growth on minimal dextrose medium in the absence of plasmid selection produced similar trends (Fig. S2, C and D, and Fig. S3, A and B).

Upon Coq8 overexpression, *coq10Δ* had increased *de novo*-synthesized [$^{13}C_6$] Q_6 and [^{12}C] Q_6 (Fig. 8B), and total Q_6 concentrations ([$^{13}C_6$] Q_6 + [^{12}C] Q_6) were restored to those of WT (Fig. 8C). This finding is consistent with previous results, which also indicated that hcCOQ8 restored Q biosynthesis and amounts of Coq polypeptides and the CoQ synthome in the *coq10Δ* mutant (13, 17, 18). Intriguingly, expression of hcCOQ8

had no effect on *de novo* or unlabeled Q_6 content in either the *coq11Δ* single mutant or the *coq10Δcoq11Δ* double mutant (Fig. 8B). Total Q_6 contents of both *coq11Δ* and *coq10Δcoq11Δ* remained significantly decreased compared with WT (Fig. 8C). Together, these results show that the rescue of the *coq10Δ* mutant mediated by Coq8 overexpression requires Coq11.

Expression of low-copy COQ11 rescues only some of the phenotypes of the *coq10Δcoq11Δ* mutant

The functional complementation of *coq11Δ* single and *coq10Δcoq11Δ* double mutants with low-copy COQ11 was assessed (lcCOQ11, Table 2). As expected, the *coq10Δ* mutant, *coq10Δ* with empty vector, and *coq10Δ* complemented with lcCOQ11 showed slow growth on the nonfermentable carbon

Coq10 knockout phenotypes are rescued by deletion of COQ11

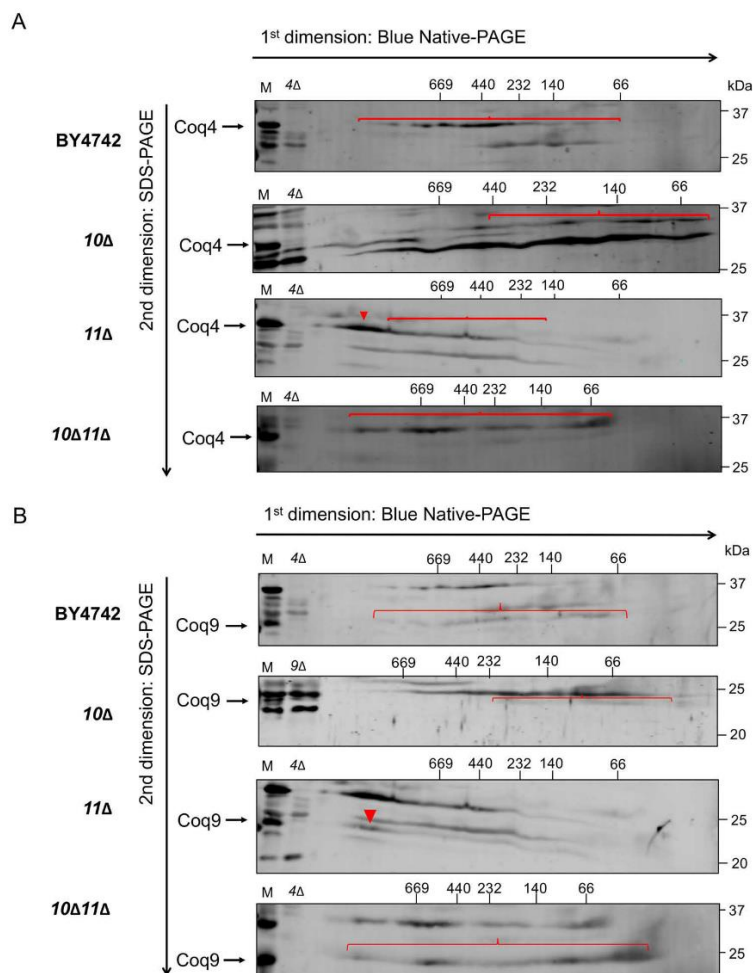


Figure 7. Deletion of *COQ11* in the *coq10Δ* mutant restores the CoQ synthome. Aliquots (100 μ g) of purified mitochondria from WT, *coq10Δ*, *coq11Δ*, and *coq10Δcoq11Δ* yeasts cultured in YPGal were solubilized with digitonin and separated with two-dimensional BN/SDS-PAGE. Following transfer of proteins to membranes, the CoQ synthome was visualized as a heterogeneous signal from ~66 to ~669 kDa in WT control with antibodies to A, Coq4, or B, Coq9. Intact mitochondria (25 μ g) from each designated strain was included as a loading control (M). Aliquots of *coq4Δ*- or *coq9Δ*-purified mitochondria (25 μ g) were included as a negative control for the antisera to Coq4 and Coq9, as the Coq9 polypeptide is absent from the *coq4Δ* mutant. Red arrowheads and brackets indicate distinct complexes.

Table 2
Yeast expression vectors

Plasmid	Relevant genes/markers	Source
pRS305	Yeast vector with <i>LEU2</i> marker	70
pRS313	Yeast vector with <i>HIS3</i> marker	70
pRS316	Yeast shuttle vector; low-copy	70
lcCOQ11	pRS316 with yeast <i>COQ11</i> ; low-copy	This work
pRS426	Yeast shuttle vector; multi-copy	71
p4HN4	pRS426 with yeast <i>COQ8</i> ; multi-copy	12

source YPGlycerol (Fig. 9A). Because yeast lacking *COQ11* retain respiratory capacity (Fig. 2) (14), *coq11Δ* complemented with lcCOQ11 had no detectable change in growth phenotype compared with either the *coq11Δ* mutant or *coq11Δ* with empty

vector (Fig. 9A). Intriguingly, when lcCOQ11 was expressed in the *coq10Δcoq11Δ* double mutant, there was no repression of growth on YPG compared with that of the *coq10Δ* mutant (Fig. 9A).

This observation suggests that Q₆ biosynthesis in *coq10Δcoq11Δ* may not be affected by lcCOQ11. To determine the effect of lcCOQ11 expression on mutant Q₆ biosynthesis, yeast was grown in selection medium to maintain plasmid expression. We tested whether lcCOQ11 expression rescued Q₆ content in the *coq11Δ* mutant. Expression of lcCOQ11 in *coq11Δ* efficiently rescued total Q₆ (¹³C₆Q₆ + ¹²CQ₆) to WT amounts (Fig. 9B).

Coq10 knockout phenotypes are rescued by deletion of COQ11

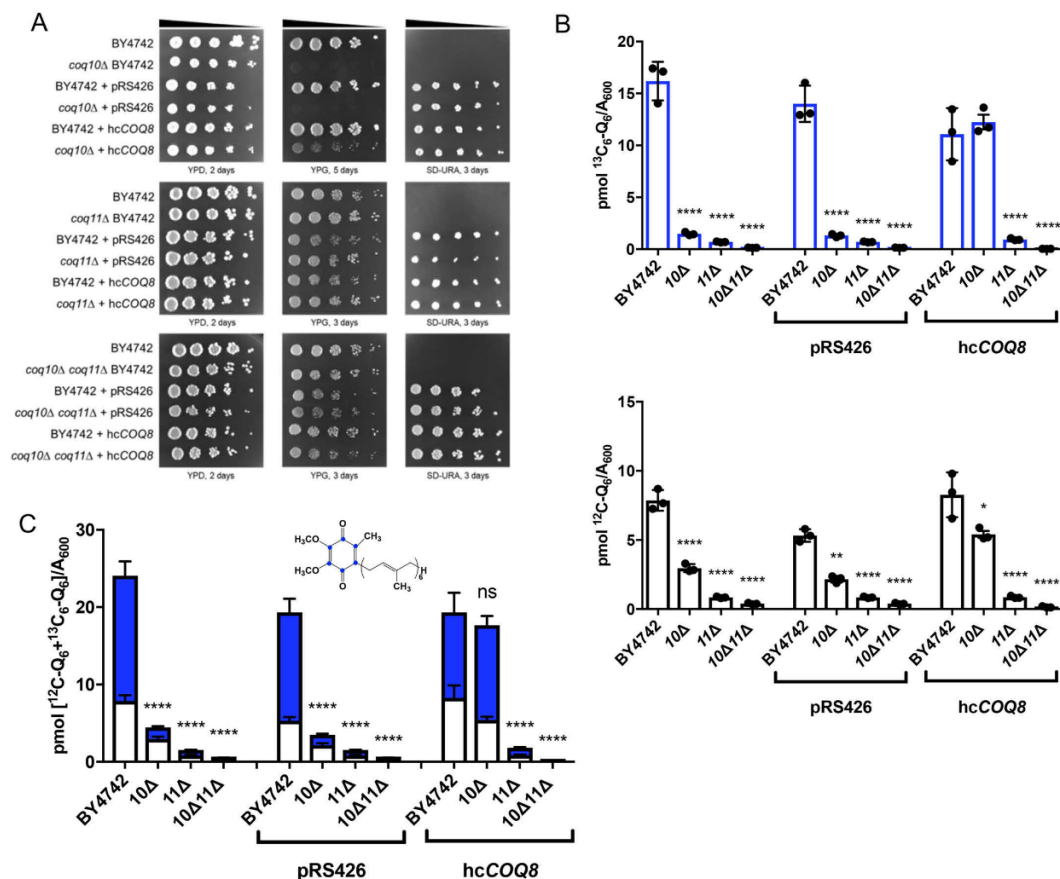


Figure 8. Overexpression of the CoQ synthome stabilizer, COQ8, has no effect on Q₆ synthesis in the *coq10Δcoq11Δ* mutant. WT, *coq10Δ*, *coq11Δ*, and *coq10Δcoq11Δ* mutants were transformed with high-copy COQ8 (hcCOQ8) or empty vector (pRS426) plasmids. **A**, strains were grown overnight in 5 ml of selection medium, diluted to an $A_{600} = 0.2$ with sterile PBS, and 2 μl of 5-fold serial dilutions were spotted onto YPD, YPG, or selection medium (SD-Ura), corresponding to a final $A_{600} = 0.2, 0.04, 0.008, 0.0016,$ and 0.00032 . Plates were incubated at 30 °C, and growth was captured after 2 or 3 days. Triplicates of 5 ml of culture in selection medium were labeled with 5 $\mu\text{g}/\text{ml}$ [$^{13}\text{C}_6$]4HB, collected after 4 h, lipid-extracted, and analyzed by LC-MS/MS. **B**, [^{12}C]Q₆ (white) and *de novo* [$^{13}\text{C}_6$]Q₆ (blue). **C**, total amount of Q₆ was also plotted from the sum of [$^{13}\text{C}_6$]Q₆ and [^{12}C]Q₆. The values are the means of three replicates. The data show mean \pm S.D., and the statistical significance as compared with WT is represented by *, $p < 0.05$; **, $p < 0.01$; ***, $p < 0.001$; ****, $p < 0.0001$. The ns signifies that values are not significantly different from WT.

Finally, whole-cell steady-state Q₆ concentrations were evaluated in all mutants. Even though lcCOQ11 complementation did not suppress *coq10Δcoq11Δ* growth on YPGlycerol (Fig. 9A), Q₆ concentrations were increased in *coq10Δcoq11Δ* to a level comparable with that of *coq10Δ* (Fig. 9C). This implies that Coq11's role in Q₆ biosynthesis is not effective when the COQ11 ORF is expressed on a single-copy plasmid in the absence of COQ10. Perhaps Coq11 expression from a plasmid does not account for multiple levels of regulation that occur through endogenous expression. Alternatively, the *coq10Δcoq11Δ* double mutant may have slightly lower amounts of the Coq11 polypeptide compared with *coq11Δ* when both are complemented by lcCOQ11 (Fig. 9D), and these lower levels may not be sufficient to suppress respiration (Fig. 9A).

Discussion

This work investigated a putative functional relationship between Coq10 and Coq11 within the *S. cerevisiae* Q₆ biosynthetic pathway. The presence of Coq10–Coq11 fusions in several Ustilaginaceae species suggests that these proteins may directly interact or participate in the same biological pathway in yeast (Fig. 1A) (14). Yeast Coq10 and its orthologs were previously shown to be required for efficient *de novo* Q biosynthesis and respiration (17, 18). We were surprised to discover that the yeast *coq10Δ* growth defect on nonfermentable medium and oxygen consumption rates were rescued upon deletion of COQ11 (Fig. 2). Moreover, spontaneous revertants isolated from *coq10Δ* yeast were previously found to exhibit growth on

Coq10 knockout phenotypes are rescued by deletion of COQ11

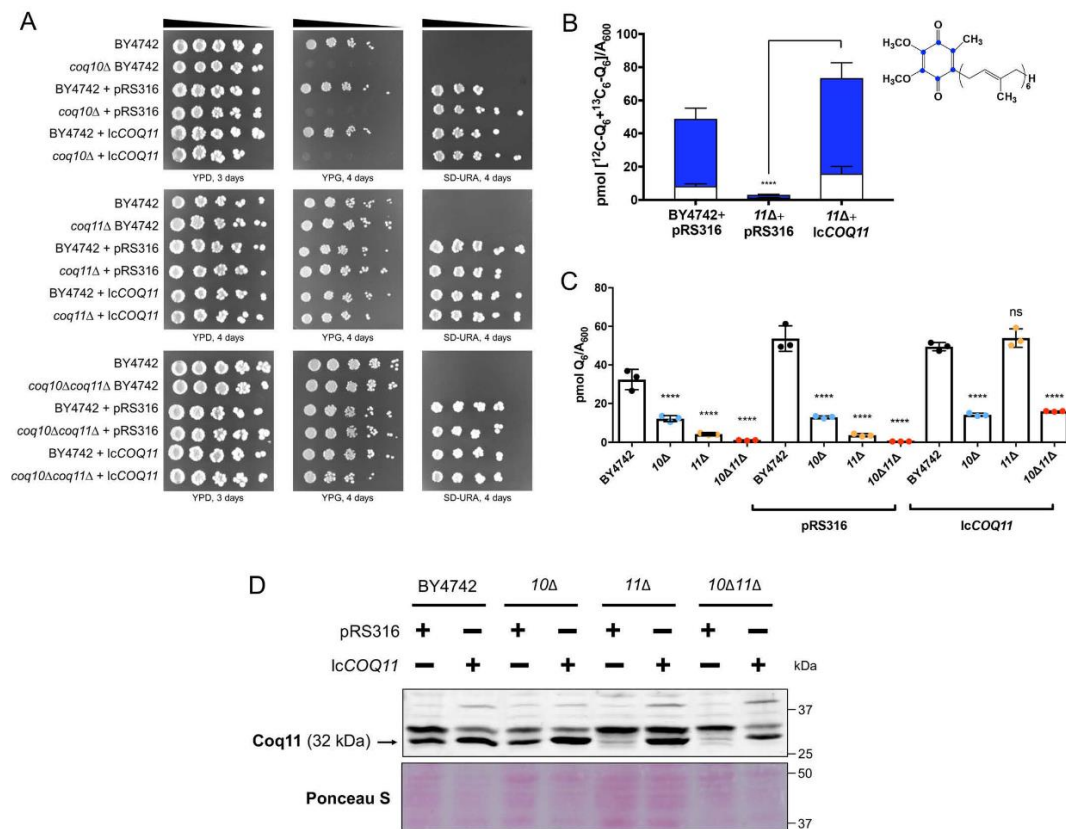


Figure 9. Low-copy *COQ11* rescues only some of the phenotypes of the *coq10Δcoq11Δ* double mutant. A low-copy plasmid expressing *COQ11* (*lcCOQ11*) and an empty vector control (pRS316) were transformed into WT, *coq10Δ*, *coq11Δ*, and *coq10Δcoq11Δ*. A, strains were grown overnight in 5 ml of YPDextrose (YPD) and diluted to an $A_{600} = 0.2$ with sterile PBS, and 2 μ l of 5-fold serial dilutions were spotted onto YPDextrose, YPGlycerol (YPG), or selection medium (SD-Ura), corresponding to a final $A_{600} = 0.2, 0.04, 0.008, 0.0016, \text{ and } 0.00032$. Plates were incubated at 30 °C, and growth was captured after 3 or 4 days. B, rescue of mutant *de novo* and unlabeled Q₆ production was initially demonstrated in *coq11Δ*. Triplicates of 6-ml cultures in selection medium were labeled with 5 μ g/ml [¹³C₆]H₈, and 5 ml of each culture was collected after 4 h, lipid-extracted, and analyzed by LC-MS/MS. Total amount of Q₆ was plotted from the sum of *de novo* [¹³C₆]Q₆ (blue) and unlabeled [¹²C]Q₆. Values are the mean of three replicates. C, rescue of mutant Q₆ content was evaluated in each mutant strain. Triplicates of 6-ml cultures in selection medium were grown until $A_{600} \sim 4$. Lipid extracts from 5 ml of each culture were analyzed by LC-MS/MS. The data show the means \pm S.D., and the statistical significance as compared with WT is represented by *, $p < 0.05$; **, $p < 0.01$; ***, $p < 0.001$; and ****, $p < 0.0001$. ns signifies that values are not significantly different from WT. D, aliquots of purified mitochondria (25 μ g) from WT and mutant yeast containing empty vector or *lcCOQ11* were isolated in YPGal medium and were separated on 10% Tris-glycine SDS-polyacrylamide gels to determine Coq11 protein expression. Proteins stained with Ponceau stain were used as loading control.

nonfermentable medium (18). We have shown that this reversion is due to a dominant base pair deletion within the *COQ11* gene, likely resulting in a nonfunctional, truncated Coq11 protein (Fig. 3). Mutants lacking both *COQ10* and *COQ11* when cultured on YPGal have increased *de novo* Q₆ production (Fig. 4A) in addition to a 5-fold increase in mitochondrial Q₆ content compared with the *coq10Δ* single knockout (Fig. 5B). Therefore, we have demonstrated that deletion of the Coq11 polypeptide in a *coq10Δ* mutant confers a beneficial effect on both respiration and Q₆ biosynthesis (Fig. 10).

Enhanced Q₆ content in the *coq10Δcoq11Δ* double mutant compared with the *coq10Δ* single mutant may be partially due to increased amounts of several key Coq polypeptides (Fig. 6) and Coq synthome stabilization (Fig. 7). The ring-modifying

enzymes within the Q₆ biosynthetic pathway colocalize to numerous distinct "CoQ domains" *in vivo*, and proper assembly of the CoQ synthome components is required for the presence of these CoQ domains (23). Two recent studies demonstrated that mitochondria isolated from yeast lacking *COQ10* have a reduced number of CoQ domain puncta (23, 24). This is likely due to lower levels of certain Coq polypeptides and partial CoQ synthome destabilization in the *coq10Δ* mutant (17, 19), which was confirmed in this work (Figs. 6 and 7). In contrast, *coq11Δ* yeast displayed significantly higher amounts of Coq4, Coq6, Coq7, and Coq9 polypeptides (Fig. 6). The CoQ synthome was likewise shifted to a higher molecular weight in *coq11Δ* mitochondria compared with WT (Fig. 7). When Coq9-yEGFP was used as a marker for CoQ domains, *coq11Δ* had increased CoQ

Coq10 knockout phenotypes are rescued by deletion of COQ11

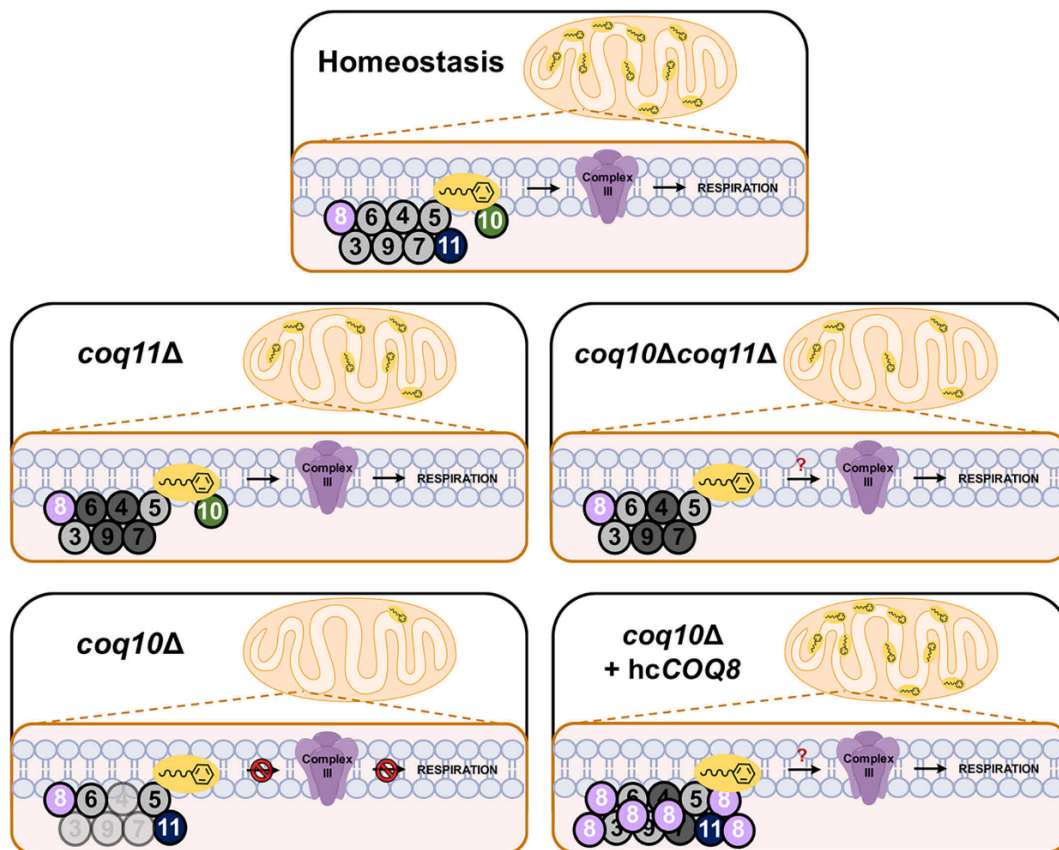


Figure 10. Scheme postulating Coq11 as a modulator of Q_6 synthesis in mitochondria. Under homeostasis, Coq11 associates with the CoQ synthome and acts as a modest negative regulator of Q_6 synthesis via Coq10. In the absence of *COQ11*, several Coq polypeptides are increased (dark shading), and the CoQ synthome is stabilized compared with WT cells, despite a slight decrease in Q_6 content. In contrast, the *coq10Δ* mutant is missing the Q_6 chaperone protein, resulting in a decreased amount (light shading) of Coq3, Coq4, Coq7, and Coq9, a destabilized CoQ synthome, substantially decreased Q_6 concentrations, and a lack of respiration. The deletion of *COQ11* in the *coq10Δ* mutant counterbalances the destabilized CoQ synthome and decreased Q_6 content phenotype of the *coq10Δ* mutant, allowing the *coq10Δcoq11Δ* double mutant to grow on YPG and respire. Expression of hcCOQ8 in the *coq10Δ* mutant produces many similar phenotypes to *COQ11* deletion in *coq10Δ* cells, including increased Coq polypeptides and a stabilized CoQ synthome (13), resulting in restored growth on YPG. Unlike the *coq10Δcoq11Δ* double mutant, *coq10Δ* + hcCOQ8 has rescued Q_6 content pointing to an additional role of Coq11 in Q_6 biosynthesis, redox regulation, or transportation.

domain intensity that stemmed from amplified expression of Coq9–yEGFP, although the number of domains was similar to WT. Mutants lacking essential Coq polypeptides *coq1–coq9*, or *coq10*, displayed significantly less Coq9-labeled domains (24). The CoQ synthome stabilization seen in *coq11Δ* via 2D-BN/SDS-PAGE analyses performed in this work (Fig. 7) agrees with the observation of increased CoQ domains and argues that the CoQ synthome is truly stabilized upon deletion of *COQ11*, as opposed to inducing a greater number of domains.

These observations are consistent with the biochemical data that led to the notion of a CoQ synthome whose formation relies on the presence of prenylated Q-intermediates (13, 40, 41). The *coq10Δ* mutant produced more early-stage intermediates (HHB) and had less late-stage intermediates (DMQ_6) compared with WT (Fig. 4, C and D), resulting in less CoQ syn-

thome formation (Fig. 7). Because *coq11Δ* yeast displayed comparable amounts of early- and late-stage Q_6 -intermediates to WT (Fig. 4, C and D), this mutant retained the ability to fully form the CoQ synthome (Fig. 7). The double knockout synthesized varying amounts of early- and late-stage Q_6 -intermediates that were largely in-between those of the single knockouts (Fig. 4, C and D). The CoQ synthome is thus able to form in *coq10Δcoq11Δ* yeast, albeit not to the efficiency of the *coq11Δ* single mutant (Fig. 7). We suspect that the accumulation of Coq polypeptides and restoration of the CoQ synthome in the *coq10Δcoq11Δ* double mutant are sufficient to allow for Q_6 to escape its site of synthesis and reach the respiratory complexes, despite an absence of the Coq10 Q_6 chaperone protein and lower Q_6 in this strain (Fig. 10). How this occurs is presently not known. One possible explanation could be that Coq11 inhibits

Coq10 knockout phenotypes are rescued by deletion of COQ11

a currently unidentified Q₆ chaperone with lower efficiency than Coq10 that is able to rescue respiration only in the absence of both Coq10 and Coq11.

Overexpression of the Q₆-biosynthetic protein Coq8 also rescued *coq10Δ* mutant growth on nonfermentable medium (Fig. 8A) and *de novo* Q₆ biosynthesis (Fig. 8, B and C) (17). Coq8 has been implicated in the partial extraction of Q₆-intermediates out of the mitochondrial inner membrane for enzymatic modification by other Coq proteins, allowing for appropriate Q₆ biosynthesis (25). Prior investigations also revealed that Coq8 overexpression in *coq10Δ* yeast increased Coq4 and Coq9 polypeptides and stabilized the CoQ synthome (13, 24). Despite the substantial benefit of Coq8 overexpression in a *coq10Δ* single mutant, Coq8 overexpression failed to enhance Q₆ biosynthesis in the *coq10Δcoq11Δ* double knockout (Figs. 8, B and C, and 10). The absence of *COQ11* in the double mutant is sufficient to restore Coq polypeptides and CoQ synthome formation (Figs. 6, A and B, 7, and 10). Coq11 and Coq8 may therefore work by different mechanisms to serve opposing functions for CoQ synthome and Coq polypeptide stabilization. Furthermore, it is clear that Coq11 is required to perform an additional function to Coq8, as *hcCOQ8* requires the presence of Coq11 to restore Q₆ biosynthesis (Figs. 8, B and C, and 10).

Proper CoQ synthome formation is not only required for efficient Q₆ biosynthesis, but it is also vital for the establishment of ER-mitochondrial contact sites mediated by the ER-mitochondrial encounter structure (ERMES) complex (23, 24). The ERMES complex is essential for lipid exchange between the ER and mitochondria (42). Specifically, *ERMES* null mutants have irregular Q₆ cellular distribution and a destabilized CoQ synthome (23). When *COQ10* was deleted in yeast expressing Coq6–GFP, there was a significant decrease in Coq6–GFP puncta colocalization with Mdm34–mCherry, a component of the ERMES complex (23). These results indicate that CoQ synthome positioning next to the ERMES complex, and subsequent Q₆ distribution from the mitochondria, depends on Coq10. Because *COQ11* deletion stabilizes the CoQ synthome (Figs. 6, A and B, and 7), it is possible that *coq11Δ* mutants have more ER-mitochondrial contacts through the ERMES complex and improved transfer of lipids between these organelles. Therefore, one possible role of Coq11 may be an auxiliary protein mediating lipid transport between the ER and mitochondria.

In a recent study, Coq11 was named Mrx2, as part of the mitochondrial organization of gene expression (MIOREX) complex involved in the mitochondrial genetic expression system (43). Considering the proposed regulatory function of Coq11 in CoQ synthome assembly, it is tempting to speculate that Coq11 offers a mechanism to couple Q₆ synthesis with the assembly of the respiratory complexes. When the synthesis of the respiratory complexes is more active, Coq11 is associated to the MIOREX complex, and Q₆ synthesis at ER junctions is stimulated. Coq11 dual localization in the mitochondrial inner membrane, to the MIOREX complex and the CoQ synthome, would also explain the sensitivity of yeast cells to the number of *COQ11* copies, as well as present another example of a loop system control for balanced expression of mitochondrial products (44).

Another potential explanation for the phenotypes induced by the knockout of Coq11 relates to its structural connection with the short-chain dehydrogenase/reductase (SDR) superfamily of NAD(P)(H)-dependent oxidoreductases (14, 45). These enzymes catalyze an assortment of reactions, including isomerization, decarboxylation, epimerization, imine reduction, and carbonyl–alcohol oxidoreduction (45). SDR superfamily proteins contain a conserved protein structural motif known as a Rossmann fold, a feature used in the binding of nucleotide cofactors such as FAD, FMN, and NAD(P) (46). The crystal structure of the *Pseudomonas aeruginosa* gene UbiX, which catalyzes the decarboxylation step in Q₆ biosynthesis, revealed a Rossmann fold with a bound FMN (47). Thus, Coq11 may use its Rossmann fold in conjunction with a nucleotide cofactor to perform similar redox chemistry in *S. cerevisiae* Q₆ biosynthesis. The ratio of QH₂/Q serves as a metabolic sensor for electron transport chain efficiency (48). High QH₂/Q ratios induce respiratory complex I-mediated reverse electron transport (RET) under physiological conditions in both *Drosophila* and mammalian cell lines (48, 49). Superoxide and secondary reactive species produced specifically through complex I RET extended *Drosophila* lifespan and improved mitochondrial function in a model of Parkinson's disease (49). RET induced by over-reduction of the Q pool presumably generates a superoxide-dependent signal essential for homeostasis, such that manipulation of the Q redox state is beneficial for mitochondrial function (48, 49). Mitochondrial phenotypes in the absence of *COQ11*, including restored respiration in *coq10Δcoq11Δ* and up-regulated Q₆ machinery (Figs. 2, A–C, 6, and 7), seem to correlate well with the aforementioned effects of Q₆H₂ accumulation. Yeast *coq11Δ* and *coq10Δcoq11Δ* mutants retain antioxidant protection by Q₆H₂, demonstrated by their resistance to treatment with exogenously-added PUFAs (Fig. 2D). Because cells lacking the Coq11 polypeptide maintain Q₆H₂ as an antioxidant, it follows that Coq11 could be involved in the oxidation of Q₆H₂ to Q₆.

The phenotypes of Coq10 and Coq11 seen in this work are similar to those in both fungi and mammalian hosts. Several fungi use Coq11 or Coq11-like proteins as NAD-dependent epimerases/dehydratases, NADH-ubiquinone oxidoreductases, and NADH dehydrogenase subunits (14). Coq11 orthologs are commonly found in plant and algae genomes, including the chloroplast-localized flavin reductase protein At1g32220 from the land plant *Arabidopsis thaliana*, which is thought to be involved in plastoquinone biosynthesis and storage (14, 50). The closest but distinct higher eukaryotic Coq11-like protein is the SDR subfamily protein NDUFA9 (14), an auxiliary subunit of complex I in humans (51). Patients with decreased NDUFA9 expression are unable to properly assemble complex I and may develop a degenerative infancy respiratory disorder known as Leigh syndrome (52). Although yeast cells do not possess complex I, this evidence indicates that Coq11 may play a crucial role in respiratory regulation or function, supporting the observations of this study.

The function of Coq10 is widely conserved across different organisms. Expression of the Coq10 homolog from *C. crescentus* (CC1736) rescues the impaired respiration and antioxidant function of Q₆ in *coq10* yeast mutants (17). The NMR structure

Coq10 knockout phenotypes are rescued by deletion of COQ11

of CC1736 reveals a START domain, which is known to bind lipids via a hydrophobic tunnel (20). Studies of *S. pombe* Coq10 demonstrate that it is able to bind Q₁₀ (21). One proposed function of Q binding by CC1736 and Coq10 from *S. pombe* may be to regulate Q delivery to its proper sites in the respiratory complexes. Humans have two distinct homologs of yeast Coq10: COQ10A and COQ10B. Expression of either human protein rescues the *coq10Δ* respiratory deficiency and sensitivity to oxidative stress, and it restores the amounts of Coq polypeptides to WT (19). The conserved function of yeast Coq10 with human COQ10A and COQ10B suggests that the findings of this work will shed light on the role of Coq10 as a chaperone in humans, leading to a better understanding of the pathobiology of Q₁₀ diseases.

In summary, this work reveals that Coq11 plays a regulatory role to maintain Q₆ homeostasis in concert with Coq10 in *S. cerevisiae* (Fig. 10). The absence of *COQ11* caused an augmentation of Q₆ production and respiration in the *coq10Δ* mutant, indicating that Coq11 confers a negative effect on the CoQ synthome. Coq11 may be crucial for Q₆ function in addition to Q₆ biosynthesis, as total whole-cell and mitochondrial Q₆ content remained lower than WT in *coq11Δ* and *coq10Δcoq11Δ* mutants.

Experimental procedures

All reagents were obtained commercially from Thermo Fisher Scientific unless otherwise specified

Yeast strains and growth medium

S. cerevisiae strains used in this study are described in Table 1. Yeast strains were derived from S288C (BY4742 (53)) or W303 (54). Growth media were prepared as described previously (55), and plate medium contained 2% bacto-agar. Growth media included the following: YPD (2% glucose, 1% yeast extract, and 2% peptone), YPGal (2% galactose, 1% yeast extract, 2% peptone, and 0.1% dextrose), YPG (3% glycerol, 1% yeast extract, and 2% peptone), and YPEG (3% glycerol, 2% ethanol, 1% yeast extract, and 2% peptone). Synthetic dextrose/selection media (SD–Complete, SD–Ura, SD–Leu, SD–His, SD–His–Leu, SD–Ura–Leu) were prepared as described previously (55) and consisted of all components minus uracil, leucine, histidine, or both uracil and leucine. Drop-out dextrose (DOD) medium was prepared as described previously (14).

COQ11 was disrupted by the one-step gene replacement method (56). The *LEU2* gene from pRS305 was amplified by polymerase chain reaction (PCR), with *COQ11* upstream and downstream flanking sequences 5'-GGGAAATATGTATCGTATACAAAAATACAGCTAAAGCTTGAAGCTG and 3'-GTACTTAAGTATATACAGCTTGGTATAATTTAAAA-TGGTAATAAC. Transformations of PCR products into yeast cells were performed using the Li-acetate method (57). The double *coq10Δcoq11Δ* mutant was constructed via disruption of *COQ10* within the *coq11Δ* strain. The *HIS3* gene from pRS313 was amplified by PCR with *COQ10* upstream and downstream flanking sequences 5'-GGATAAGGAGCCAAACAATAAACGGCTAAAGATACCGTGG and 3'-CAGATA-ACAAAGATCATGCCATCCAGGATAAGCGTATGCA, and transformation was performed as for the *COQ11* disruption.

Primers were designed using SnapGene (GSL Biotech, LLC, Chicago, IL).

Mitochondria isolation from BY4742 WT and mutant yeast

Yeast cultures of BY4742, *coq10Δ*, *coq11Δ*, and *coq10Δcoq11Δ* were grown overnight in 5 ml of YPD. Yeast-containing plasmids were grown overnight in 5 ml of selection medium (SD–Ura). All pre-cultures were back-diluted with YPGal and grown overnight with shaking (30 °C, 250 rpm) until cell density reached an A₆₀₀ ~4. Spheroplasts were prepared with Zymolyase-20T (MP Biomedicals) and fractionated as described previously (36), in the presence of cComplete™ EDTA-free protease inhibitor mixture tablets (Roche Applied Science), phosphatase inhibitor mixture set I (Sigma-Aldrich), phosphatase inhibitor mixture set II (Sigma-Aldrich), and phenylmethylsulfonyl fluoride (Thermo Fisher Scientific). Nycodenz (Sigma-Aldrich) density gradient purified mitochondria were frozen in liquid nitrogen, aliquoted, and stored at –80 °C until further use. Protein concentration of mitochondria was measured by the bicinchoninic acid (BCA) assay (Thermo Fisher Scientific).

Submitochondrial localization of Coq10 and Coq11 polypeptides

Purified mitochondria from BY4742 yeast (3 mg of protein, 150 μl) were subfractionated, as described previously (13). Proteinase K treatment of purified BY4742 mitochondria was also performed as described previously (13). Proteinase K-treated mitoplasts and control samples were resuspended in SDS sample buffer (50 mM Tris, pH 6.8, 10% glycerol, 2% SDS, 0.1% bromophenol blue, and 1.33% β-mercaptoethanol); equal aliquots were separated by SDS-gel electrophoresis on 10 or 12% Tris-glycine polyacrylamide gels as detailed below. Several mitochondrial compartment markers and proteins of interest, Coq10 and Coq11, were detected with rabbit polyclonal antibodies prepared in blocking buffer at dilutions listed in Table S1.

Oxygen consumption evaluation by Seahorse

Mitochondrial function was assessed using the XF96 extracellular flux analyzer (Seahorse Bioscience, Agilent Technologies). Seahorse plates were coated with 50 μg/ml poly-D-lysine (Sigma-Aldrich), diluted 1:1 in UltraPure distilled water (Thermo Fisher Scientific). Volumes of 25 μl were added to each well for 30 min at room temperature and then aspirated before plates were dried overnight at room temperature. The Seahorse XF96 sensor cartridge was hydrated with Seahorse XF calibrant solution (Agilent) and was incubated overnight at room temperature.

Yeast cultures of BY4742, *coq10Δ*, *coq11Δ*, and *coq10Δcoq11Δ* were grown overnight in 25 ml of YPGal medium. On the day of measurement, all cultures were diluted to seed an A₆₀₀ = 0.1 cells/well of BY4742, *coq10Δ*, *coq11Δ*, and *coq10Δcoq11Δ* into a Seahorse XF96 microplate in a total volume of 175 μl YPGal. Four wells containing only medium were included for background measurement. The loaded plate was centrifuged at 500 × g for 3 min at room temperature (with no brakes). Following centrifugation, the loaded plate was incubated for 30

Coq10 knockout phenotypes are rescued by deletion of COQ11

min at 37 °C with no CO₂ to aid in the transitioning of the plate into the Seahorse machine's temperature. Cells were stimulated sequentially with two injections of 4 μM FCCP in ports A and B (optimized for maximum oxygen consumption rate) (Enzo Life Sciences) and 2.5 μM antimycin A in port C (Enzo Life Sciences), delivered in YPGal. Mix, wait, and measure times were 2 min, 30 s, and 2 min, respectively. Basal respiration included four measurements, and then following each injection three measurements were made. All OCR were subtracted for nonmitochondrial respiration and normalized to $A_{600} = 0.1$. Basal respiration was calculated as an average of OCR prior to the first FCCP addition. Maximal respiration was calculated as an average of OCR following the second FCCP addition. Non-mitochondrial respiration was measured as average OCR following antimycin A addition.

Fatty acid sensitivity assay

Sensitivity of yeast cells to PUFA-induced oxidative stress was performed as described previously (19, 58, 59), with some modifications. Briefly, BY4742 WT, *cor1Δ*, *coq9Δ*, *coq10Δ*, *coq11Δ*, and *coq10Δcoq11Δ* were inoculated in 5 ml of YPD medium and incubated overnight at 30 °C, 250 rpm. Cultures were subinoculated to an $A_{600} = 0.25$ in 15 ml of fresh YPD medium and incubated at 30 °C, 250 rpm until they reached an $A_{600} \sim 1$. Cells were harvested, washed twice with 10 ml of sterile H₂O, and diluted in 0.1 M phosphate buffer with 0.2% dextrose, pH 6.2, to an $A_{600} = 0.2$. This cell suspension was divided into 5-ml aliquots and treated with an ethanol vehicle control (final concentration 0.1% v/v), ethanol-diluted oleic acid (Nu-Check Prep), or α -linolenic acid (Nu-Check Prep) to a final concentration of 200 μM. Fatty acid-treated cultures were incubated for 4 h at 30 °C, 250 rpm, after which cell viability was assessed via plate dilutions. Cell viability prior to the addition of fatty acids was determined via plate dilutions, represented in the 0-h plate.

Analysis of Q₆ and Q₆-intermediates

Standards of Q₆ were obtained from Avanti Polar Lipids, and Q₄ was from Sigma-Aldrich. Yeast cultures were grown overnight in 30 ml of YPGal, or selection medium (SD-complete or SD-Ura) for strains harboring plasmids. Cultures were diluted into triplicates of 6 ml of fresh medium to $A_{600} = 0.5$, and 5 ml of medium was harvested by centrifugation once they reached $A_{600} \sim 4$. Cell pellets were stored at -20 °C. Following collection, frozen cell pellets were lipid-extracted in the presence of internal standard Q₄ and analyzed for Q₆ and Q₆-intermediates by LC-MS/MS as described previously (19).

Stable isotope labeling for determination of de novo Q₆ and Q₆-intermediates

Yeast cultures were grown overnight in 30 ml of YPGal and diluted in triplicates of 6 ml of fresh medium to an $A_{600} = 0.1$. Cultures were incubated until they reached an $A_{600} \sim 1$, at which point ethanol vehicle control (0.1% v/v) or 5 μg/ml of the stable isotope [¹³C₆]4HB (Cambridge Isotope Laboratories, Inc.) was added. Cultures were allowed to grow for an additional 4 h when 5 ml of each culture was harvested by centrifur-

gation and stored at -20 °C. Cell pellets were lipid extracted and analyzed by LC-MS/MS as described previously (19).

Mitochondrial DNA determination by qPCR analysis

DNA was extracted from yeast cells as follows. Yeast pellets (10 ml) grown in YPGal were collected at an $A_{600} \sim 4$ by centrifugation at 3000 × *g* for 5 min, washed with 5 ml of H₂O, and transferred to 2-ml screw-cap tubes. Pellets were frozen at -80 °C until DNA extraction was carried out. Cell pellets were resuspended in 200 μl of lysis buffer (10 mM Tris-Cl, pH 8.0, 2% (v/v) Triton X-100, 1 mM EDTA, 100 mM NaCl, 1% SDS), and 200 μl of acid-washed glass beads with 200 μl of phenol/chloroform/isoamyl alcohol (25:24:1) were added to the cell suspension. Cells were lysed using a bead-beater (Precellys 24; Bertin Technologies) three times for 10 s at 6500 rpm with a 45-s break between rounds at 4 °C. Tris-EDTA (TE, 200 μl) was added, and the cell suspension was centrifuged at 13,000 × *g* for 5 min at room temperature. The aqueous layer was removed to a new tube containing 200 μl of chloroform, mixed by inversion, and centrifuged at 13,000 × *g* for 5 min at room temperature. This was repeated once more. The aqueous layer was then transferred to a 2-ml screw-cap tube containing 1 ml of 95% EtOH, mixed by inversion, and centrifuged at 13,000 × *g* for 2 min at room temperature. The resulting pellet was resuspended in 400 μl of TE containing 30 μg of RNase A and incubated at 37 °C for 30 min. Then, 10 μl of 3 M sodium acetate and 1 ml of 95% EtOH was added, mixed by inversion, and incubated at -20 °C for 1 h. After 1 h at -20 °C, the suspension was centrifuged at 13,000 × *g* for 5 min, and the pellet was washed twice with 70% EtOH and air-dried. The dried pellet was resuspended in 25 μl of TE; concentration was measured by Nanodrop (Thermo Fisher Scientific), and the pellet was stored at -20 °C until use.

qPCR was performed on a CFX384 instrument (Bio-Rad) using the SensiFAST™ SYBR® NO ROX kit (Bioline) as per the manufacturer's instructions. Each sample was run in duplicate with 150 ng of total DNA used per reaction using the following thermocycling protocol (95 °C for 2 min, 95 °C for 5 s, 60 °C for 10 s, and 72 °C for 20 s, plate read and cycle repeated ×40, melt curve 40–92 °C with plate read and 40 °C for 10 s). Melting-curve analysis confirmed that all PCRs produced a single product. mtDNA-specific primers (forward (13,999), 5'-GTG CGT ATA TTT CGT TGA TGC GT-3'; reverse (14,297), 5'-TTC ACA CTG CCT GTG CTA TCT AA-3' (60) and actin-specific primers (forward, 5'-GAA TTG AGA GTT GCC CCA GA-3'; reverse, 5'-ATC ACC GGA ATC CAA AAC AA-3) were used. The relative level of gene expression of mitochondrial DNA was normalized to the expression level of actin as described previously (61).

Citrate synthase activity

The measurement of citrate synthase activity in cells was carried out as described previously (62). Briefly, yeast pellets (10 ml) grown in YPGal were collected at an $A_{600} \sim 4$ by centrifugation at 3000 × *g* for 5 min, washed with 5 ml of H₂O, and transferred to 2-ml screw-cap tubes. Cell pellets were resuspended in 200 μl of lysis buffer (100 mM Tris-Cl, pH 7.4, 1% (v/v) Triton X-100, 1 mM EDTA, 1 mM phenylmethylsulfonyl fluoride, 1× cComplete™ Protease Inhibitor Mixture (Roche

Coq10 knockout phenotypes are rescued by deletion of COQ11

Applied Science)), and then 200 μl of acid-washed glass beads were added. Cells were lysed using a bead-beater (Precellys 24; Bertin Technologies) three times for 10 s at 6500 rpm with a 45-s break between rounds at 4 °C. The clarified cell lysate was collected after centrifugation at $16,000 \times g$ for 10 min at 4 °C. The concentration of protein was determined with the BCA assay (Thermo Fisher Scientific). Cell lysates were normalized to 0.05 $\mu\text{g}/\mu\text{l}$ protein. The colorimetric citrate synthase assay was carried out using a VersaMax plate reader (Molecular Devices) and a flat-bottom 96-well plate. First, 40 μl of 500 mM Tris-Cl, pH 7.4, 2 μl of 30 mM acetyl-CoA, 8 μl of 2.5 mM 5,5'-dithiobis(2-nitrobenzoic acid), 90 μl of H_2O , and 50 μl cell lysate (2.5 μg total protein) were added into each well. Then, 10 μl of 10 mM oxaloacetic acid were added per well and mixed by pipetting up and down. A_{412} was measured every 30 s at 25 °C. The initial slope was calculated by using data from the first 10 min and used to determine the enzyme reaction rate using the extinction coefficient for 2-nitro-5-thiobenzoate of $14.15 \text{ mM}^{-1} \text{ cm}^{-1}$ (63).

Porin quantification

Porin content was quantified via immunoblot of yeast WT and mutant whole cells. Protein extraction from whole cells was performed (64), and 25 μg of each sample was separated by SDS-gel electrophoresis as described below. Three replicates of the immunoblots were performed and quantified by hand using ImageStudioLite software normalized to Ponceau total protein staining.

Quantitative real-time PCR (qRT-PCR)

Total RNA was isolated from yeast cells using TRIzol reagent (Invitrogen). DNA contamination from the resulting RNA was removed using the DNase TURBO kit as per the manufacturer's instructions (Invitrogen). RNA concentration was measured by Nanodrop (Thermo Fisher Scientific), and RNA was stored at -20 °C. Reverse transcription was carried out using the Superscript III first strand synthesis system using random hexamer primers (Invitrogen). cDNA was stored at -20 °C until qPCR analyses were carried out. Quantitative real-time PCR was performed on a CFX384 instrument (Bio-Rad) using the SensiFASTTMSYBR[®] NO-ROX kit (Bioline) in duplicate. The relative levels of gene expression were normalized to the expression level of actin. Melting curve analysis confirmed that all PCRs produced a single product. The primers (forward/reverse) used in real-time PCR were designed using Primer3 on line (RRID: SCR_003139). Primers used are given in Table S2.

SDS-PAGE and immunoblot analysis

Purified mitochondria (25 μg) were resuspended in SDS sample buffer and separated by SDS-gel electrophoresis on 10 or 12% Tris-glycine polyacrylamide gels. Proteins were transferred to a 0.45- μm polyvinylidene difluoride membrane (Millipore) and blocked with blocking buffer (0.5% BSA, 0.1% Tween 20, 0.02% SDS in PBS). Representative Coq polypeptides and loading control mitochondrial malate dehydrogenase (Mdh1) were probed with rabbit polyclonal antibodies prepared in blocking buffer at dilutions listed in Table S1. IRDye 680LT goat anti-rabbit IgG secondary antibody (LiCOR) was

used at a dilution of 1:10,000. Proteins were visualized using a LiCOR Odyssey IR Scanner (LiCOR). Immunoblots are representative of three replicates and were quantified by hand using ImageStudioLite software normalized to Mdh1.

Two-dimensional Blue Native/SDS-PAGE immunoblot analysis of high-molecular-weight complexes

2D-BN/SDS-PAGE was performed as described previously (13, 65, 66). Briefly, 200 μg of purified mitochondria were solubilized at 4 mg/ml for 1 h on ice with 16 mg/ml digitonin (Biosynth) in the presence of the protease and phosphatase inhibitors used during mitochondrial isolation. Protein concentration of solubilized mitochondria was determined by BCA assay. NativePAGE 5% G-250 sample additive (Thermo Fisher Scientific) was added to a final concentration of 0.25%. Solubilized mitochondria (100 μg) were separated on NativePAGE 4–16% BisTris gels (Thermo Fisher Scientific) in the first dimension, and native gel slices were further separated on 12% Tris-glycine polyacrylamide gel in the second dimension. Following the second-dimension separation, immunoblot analyses were performed as described above, using antibodies against Coq4 and Coq9 at the dilutions indicated in Table S1. Molecular weight standards for BN gel electrophoresis and SDS gel electrophoresis were obtained from GE Healthcare (Sigma-Aldrich) and Bio-Rad, respectively.

Construction of low-copy COQ11 yeast expression vectors

Plasmids used in this study are described in Table 2. A low-copy COQ11-containing plasmid was constructed using the pRS316 low-copy empty vector. The COQ11 ORF and regions corresponding to 842 bp upstream and 256 bp downstream were cloned into pRS316 using Gibson Assembly (New England Biolabs). Clones were sequenced by Laragen, and successful clones were transformed into WT and mutant yeast, along with the corresponding empty vector (pRS316) control as described above.

Revertant isolation

As reported previously, *coq10* mutant growth deficiency on nonfermentable carbon sources (YPEG) spontaneously revert due to nuclear suppression mutations (18). Here, W303 *coq10 Δ* yeast was grown on glucose to stationary phase, and ~ 10 million cells were plated on YPEG. After several weeks, a colony began to appear on this medium. The colony was purified, and its genome was sequenced.

Genome sequencing

The Wizard[®] genomic purification kit (Promega) was used to extract total DNA from the parental respiratory-deficient mutant W303 *coq10 Δ* and from the spontaneous revertant W303 *coq10rev*. The DNA was quantified using the QUBIT DNATM high-sensitivity assay, and 1 ng of the normalized DNA was tagged by the Nextera XTTM (Illumina) protocol. The libraries were amplified and pooled as described (67). The pooled libraries were subjected to sequencing with the NextSeqTM (Illumina) equipment in the Genome Investigation and Analysis Laboratory of the Institute of Biomedical Sciences at the University of Sao Paulo. The BWA Aligner tool,

Coq10 knockout phenotypes are rescued by deletion of COQ11

version 1.1.4 (Base Space Labs-Illumina), was used to align ~23,000,000 reads obtained from each strain with the reference genomes of *S. cerevisiae*. The alignments were compared using the Integrative Genomics Viewer (Base Space Labs Illumina).

Statistical analyses

All data sets were tested for normality using GraphPad Prism 7 with the Shapiro-Wilk normality test. Because a majority of sets passed the normality test ($\alpha = 0.5$), statistical analyses were performed using GraphPad Prism 7 with parametric one-way analysis of variance correcting for multiple comparisons using Tukey's test, comparing the mean of each sample to the mean of its corresponding WT or empty vector control. The data show the means \pm S.D., and the statistical significance as compared with WT or empty vector control is represented by the following: *, $p < 0.05$; **, $p < 0.01$; ***, $p < 0.001$; and ****, $p < 0.0001$. The denotation *ns* indicates values with "not significant" differences from the corresponding control.

Data availability

The MS source data for determination of Q₆ and Q₆ intermediates will be shared upon request. Please contact Catherine Clarke at cathy@chem.ucla.edu. All remaining data are contained within the article.

Author contributions—M. C. B., M. H. B., and C. F. C. conceptualization; M. C. B., J. N., A. A., H. S. T., O. S. S., M. H. B., and C. F. C. resources; M. C. B., K. Y., L. F.-dR., J. N., A. A., H. S. T., N. A. N., M. H. B., and C. F. C. data curation; M. C. B., J. N., A. A., and M. H. B. software; M. C. B., K. Y., L. F.-dR., J. N., A. A., H. S. T., N. A. N., R. S., M. H. B., and C. F. C. formal analysis; M. C. B., R. S., O. S. S., M. H. B., and C. F. C. supervision; M. C. B., J. N., H. S. T., M. H. B., and C. F. C. funding acquisition; M. C. B., K. Y., L. F.-dR., J. N., A. A., H. S. T., R. S., and M. H. B. validation; M. C. B., K. Y., L. F.-dR., J. N., A. A., H. S. T., N. A. N., R. S., M. H. B., and C. F. C. investigation; M. C. B., K. Y., L. F.-dR., J. N., A. A., H. S. T., N. A. N., M. H. B., and C. F. C. visualization; M. C. B., K. Y., L. F.-dR., J. N., A. A., H. S. T., N. A. N., R. S., M. H. B., and C. F. C. methodology; M. C. B. and C. F. C. writing—original draft; M. C. B., R. S., M. H. B., and C. F. C. project administration; M. C. B., K. Y., L. F.-dR., J. N., A. A., H. S. T., N. A. N., R. S., O. S. S., M. H. B., and C. F. C. writing—review and editing.

Acknowledgments—We thank the UCLA Molecular Instrumentation Core proteomics facility and Dr. Yu Chen for the use of the QTRAP4000 for lipid analysis. We thank undergraduate UCLA researcher Hope Ibarra for her contributions in assisting with experiments.

References

1. Turunen, M., Olsson, J., and Dallner, G. (2004) Metabolism and function of coenzyme Q. *Biochim. Biophys. Acta* **1660**, 171–199 [CrossRef Medline](#)
2. Alcázar-Fabra, M., Trevisson, E., and Brea-Calvo, G. (2018) Clinical syndromes associated with coenzyme Q₁₀ deficiency. *Essays Biochem.* **62**, 377–398 [CrossRef Medline](#)
3. Desbats, M. A., Lunardi, G., Doimo, M., Trevisson, E., and Salvati, L. (2015) Genetic bases and clinical manifestations of coenzyme Q₁₀ (CoQ10) deficiency. *J. Inher. Metab. Dis.* **38**, 145–156 [CrossRef Medline](#)
4. Frei, B., Kim, M. C., and Ames, B. N. (1990) Ubiquinol-10 is an effective lipid-soluble antioxidant at physiological concentrations. *Proc. Natl. Acad. Sci. U.S.A.* **87**, 4879–4883 [CrossRef Medline](#)
5. Okada, K., Suzuki, K., Kamiya, Y., Zhu, X., Fujisaki, S., Nishimura, Y., Nishino, T., Nakagawa, T., Kawamukai, M., and Matsuda, H. (1996) Poly-prenyl diphosphate synthase essentially defines the length of the side chain of ubiquinone. *Biochim. Biophys. Acta* **1302**, 217–223 [CrossRef Medline](#)
6. Kawamukai, M. (2016) Biosynthesis of coenzyme Q in eukaryotes. *Biosci. Biotechnol. Biochem.* **80**, 23–33 [CrossRef Medline](#)
7. Stefely, J. A., and Pagliarini, D. J. (2017) Biochemistry of mitochondrial coenzyme Q biosynthesis. *Trends Biochem. Sci.* **42**, 824–843 [CrossRef Medline](#)
8. Montini, G., Malaventura, C., and Salvati, L. (2008) Early coenzyme Q₁₀ supplementation in primary coenzyme Q₁₀ deficiency. *N. Engl. J. Med.* **358**, 2849–2850 [CrossRef Medline](#)
9. Awad, A. M., Bradley, M. C., Fernández-Del-Río, L., Nag, A., Tsui, H. S., and Clarke, C. F. (2018) Coenzyme Q₁₀ deficiencies: pathways in yeast and humans. *Essays Biochem.* **62**, 361–376 [CrossRef Medline](#)
10. Tran, U. C., Marbois, B., Gin, P., Gulmezian, M., Jonassen, T., and Clarke, C. F. (2006) Complementation of *Saccharomyces cerevisiae* coq7 mutants by mitochondrial targeting of the *Escherichia coli* UbiF polypeptide: two functions of yeast Coq7 polypeptide in coenzyme Q biosynthesis. *J. Biol. Chem.* **281**, 16401–16409 [CrossRef Medline](#)
11. Marbois, B., Gin, P., Faull, K. F., Poon, W. W., Lee, P. T., Strahan, J., Shepherd, J. N., and Clarke, C. F. (2005) Coq3 and Coq4 define a polypeptide complex in yeast mitochondria for the biosynthesis of coenzyme Q. *J. Biol. Chem.* **280**, 20231–20238 [CrossRef Medline](#)
12. Hsieh, E. J., Gin, P., Gulmezian, M., Tran, U. C., Saiki, R., Marbois, B. N., and Clarke, C. F. (2007) *Saccharomyces cerevisiae* Coq9 polypeptide is a subunit of the mitochondrial coenzyme Q biosynthetic complex. *Arch. Biochem. Biophys.* **463**, 19–26 [CrossRef Medline](#)
13. He, C. H., Xie, L. X., Allan, C. M., Tran, U. C., and Clarke, C. F. (2014) Coenzyme Q supplementation or overexpression of the yeast Coq8 putative kinase stabilizes multi-subunit Coq polypeptide complexes in yeast coq null mutants. *Biochim. Biophys. Acta* **1841**, 630–644 [CrossRef Medline](#)
14. Allan, C. M., Awad, A. M., Johnson, J. S., Shirasaki, D. I., Wang, C., Blaby-Haas, C. E., Merchant, S. S., Loo, J. A., and Clarke, C. F. (2015) Identification of Coq11, a new coenzyme Q biosynthetic protein in the CoQ-synthome in *Saccharomyces cerevisiae*. *J. Biol. Chem.* **290**, 7517–7534 [CrossRef Medline](#)
15. Marcotte, E. M., Pellegrini, M., Ng, H. L., Rice, D. W., Yeates, T. O., and Eisenberg, D. (1999) Detecting protein function and protein–protein interactions from genome sequences. *Science* **285**, 751–753 [CrossRef Medline](#)
16. Perocchi, F., Jensen, L. J., Gagneur, J., Ahting, U., von Mering, C., Bork, P., Prokisch, H., and Steinmetz, L. M. (2006) Assessing systems properties of yeast mitochondria through an interaction map of the organelle. *PLoS Genet.* **2**, e170 [CrossRef Medline](#)
17. Allan, C. M., Hill, S., Morvaridi, S., Saiki, R., Johnson, J. S., Liau, W. S., Hirano, K., Kawashima, T., Ji, Z., Loo, J. A., Shepherd, J. N., and Clarke, C. F. (2013) A conserved START domain coenzyme Q-binding polypeptide is required for efficient Q biosynthesis, respiratory electron transport, and antioxidant function in *Saccharomyces cerevisiae*. *Biochim. Biophys. Acta* **1831**, 776–791 [CrossRef Medline](#)
18. Barros, M. H., Johnson, A., Gin, P., Marbois, B. N., Clarke, C. F., and Tzagoloff, A. (2005) The *Saccharomyces cerevisiae* COQ10 gene encodes a START domain protein required for function of coenzyme Q in respiration. *J. Biol. Chem.* **280**, 42627–42635 [CrossRef Medline](#)
19. Tsui, H. S., Pham, N. V. B., Amer, B. R., Bradley, M. C., Gosschalk, J. E., Gallagher-Jones, M., Ibarra, H., Clubb, R. T., Blaby-Haas, C. E., and Clarke, C. F. (2019) Human COQ10A and COQ10B are distinct lipid-binding START domain proteins required for coenzyme Q function. *J. Lipid Res.* **60**, 1293–1310 [CrossRef Medline](#)
20. Shen, Y., Goldsmith-Fischman, S., Atreya, H. S., Acton, T., Ma, L., Xiao, R., Honig, B., Montelione, G. T., and Szyperski, T. (2005) NMR structure of the 18 kDa protein CCI736 from *Caulobacter crescentus* identifies a member of the START domain superfamily and suggests residues mediating substrate specificity. *Proteins* **58**, 747–750 [CrossRef Medline](#)

Coq10 knockout phenotypes are rescued by deletion of COQ11

21. Cui, T. Z., and Kawamukai, M. (2009) Coq10, a mitochondrial coenzyme Q binding protein, is required for proper respiration in *Schizosaccharomyces pombe*. *FEBS J.* **276**, 748–759 [CrossRef Medline](#)
22. Stoldt, S., Wenzel, D., Kehrein, K., Riedel, D., Ott, M., and Jakobs, S. (2018) Spatial orchestration of mitochondrial translation and OXPHOS complex assembly. *Nat. Cell Biol.* **20**, 528–534 [CrossRef Medline](#)
23. Eisenberg-Bord, M., Tsui, H. S., Antunes, D., Fernández-Del-Río, L., Bradley, M. C., Dunn, C. D., Nguyen, T. P. T., Rapaport, D., Clarke, C. F., and Schuldiner, M. (2019) The endoplasmic reticulum-mitochondria encounter structure complex coordinates coenzyme Q biosynthesis. *Contact* **2**, 2515256418825409 [CrossRef Medline](#)
24. Subramanian, K., Jochem, A., Le Vasseur, M., Lewis, S., Paulson, B. R., Reddy, T. R., Russell, J. D., Coon, J. J., Pagliarini, D. J., and Nunnari, J. (2019) Coenzyme Q biosynthetic proteins assemble in a substrate-dependent manner into domains at ER-mitochondria contacts. *J. Cell Biol.* **218**, 1353–1369 [CrossRef Medline](#)
25. Reidenbach, A. G., Kemmerer, Z. A., Aydin, D., Jochem, A., McDevitt, M. T., Hutchins, P. D., Stark, J. L., Stefely, J. A., Reddy, T., Hebert, A. S., Wilkerson, E. M., Johnson, I. E., Bingman, C. A., Markley, J. L., Coon, J. J., et al. (2018) Conserved lipid and small-molecule modulation of COQ8 reveals regulation of the ancient kinase-like UbiB family. *Cell Chem. Biol.* **25**, 154–165.e11 [CrossRef Medline](#)
26. Reading, D. S., Hallberg, R. L., and Myers, A. M. (1989) Characterization of the yeast *HSP60* gene coding for a mitochondrial assembly factor. *Nature* **337**, 655–659 [CrossRef Medline](#)
27. Fujiki, Y., Hubbard, A. L., Fowler, S., and Lazarow, P. B. (1982) Isolation of intracellular membranes by means of sodium carbonate treatment: application to endoplasmic reticulum. *J. Cell Biol.* **93**, 97–102 [CrossRef Medline](#)
28. Chen, W. J., and Douglas, M. G. (1987) Phosphodiester bond cleavage outside mitochondria is required for the completion of protein import into the mitochondrial matrix. *Cell* **49**, 651–658 [CrossRef Medline](#)
29. Ohashi, A., Gibson, J., Gregor, L., and Schatz, G. (1982) Import of proteins into mitochondria. The precursor of cytochrome c_1 is processed in two steps, one of them heme-dependent. *J. Biol. Chem.* **257**, 13042–13047 [Medline](#)
30. Vögtle, F. N., Burkhart, J. M., Gonczarowska-Jorge, H., Kücüköse, C., Taskin, A. A., Kopczyński, D., Ahrends, R., Mossmann, D., Sickmann, A., Zahedi, R. P., and Meisinger, C. (2017) Landscape of submitochondrial protein distribution. *Nat. Commun.* **8**, 290 [CrossRef Medline](#)
31. Yin, H., Xu, L., and Porter, N. A. (2011) Free radical lipid peroxidation: mechanisms and analysis. *Chem. Rev.* **111**, 5944–5972 [CrossRef Medline](#)
32. Pryor, W. A., and Porter, N. A. (1990) Suggested mechanisms for the production of 4-hydroxy-2-nonenal from the autooxidation of polyunsaturated fatty acids. *Free Radic. Biol. Med.* **8**, 541–543 [CrossRef Medline](#)
33. Heeringa, S. F., Chernin, G., Chaki, M., Zhou, W., Sloan, A. J., Ji, Z., Xie, L. X., Salviati, L., Hurd, T. W., Vega-Warner, V., Killen, P. D., Raphael, Y., Ashraf, S., Ovunc, B., Schoeb, D. S., et al. (2011) COQ6 mutations in human patients produce nephrotic syndrome with sensorineural deafness. *J. Clin. Invest.* **121**, 2013–2024 [CrossRef Medline](#)
34. Nguyen, T. P., Casarin, A., Desbats, M. A., Doimo, M., Trevisson, E., Santos-Ocaña, C., Navas, P., Clarke, C. F., and Salviati, L. (2014) Molecular characterization of the human COQ5 C-methyltransferase in coenzyme Q₁₀ biosynthesis. *Biochim. Biophys. Acta* **1841**, 1628–1638 [CrossRef Medline](#)
35. Conrad, M., Schothorst, J., Kankipati, H. N., Van Zeebroeck, G., Rubio-Teixeira, M., and Thevelein, J. M. (2014) Nutrient sensing and signaling in the yeast *Saccharomyces cerevisiae*. *FEMS Microbiol. Rev.* **38**, 254–299 [CrossRef Medline](#)
36. Glick, B. S., and Pon, L. A. (1995) Isolation of highly purified mitochondria from *Saccharomyces cerevisiae*. *Methods Enzymol.* **260**, 213–223 [CrossRef Medline](#)
37. Stefely, J. A., Reidenbach, A. G., Ulbrich, A., Oruganty, K., Floyd, B. J., Jochem, A., Saunders, J. M., Johnson, I. E., Minogue, C. E., Wrobel, R. L., Barber, G. E., Lee, D., Li, S., Kannan, N., Coon, J. J., et al. (2015) Mitochondrial ADCK3 employs an atypical protein kinase-like fold to enable coenzyme Q biosynthesis. *Mol. Cell* **57**, 83–94 [CrossRef Medline](#)
38. Xie, L. X., Hsieh, E. J., Watanabe, S., Allan, C. M., Chen, J. Y., Tran, U. C., and Clarke, C. F. (2011) Expression of the human atypical kinase ADCK3 rescues coenzyme Q biosynthesis and phosphorylation of Coq polypeptides in yeast *coq8* mutants. *Biochim. Biophys. Acta* **1811**, 348–360 [CrossRef Medline](#)
39. Xie, L. X., Ozeir, M., Tang, J. Y., Chen, J. Y., Jaquinod, S. K., Fontecave, M., Clarke, C. F., and Pierrel, F. (2012) Overexpression of the Coq8 kinase in *Saccharomyces cerevisiae coq* null mutants allows for accumulation of diagnostic intermediates of the coenzyme Q₆ biosynthetic pathway. *J. Biol. Chem.* **287**, 23571–23581 [CrossRef Medline](#)
40. Tran, U. C., and Clarke, C. F. (2007) Endogenous synthesis of coenzyme Q in eukaryotes. *Mitochondrion* **7**, Suppl., S62–S71 [CrossRef Medline](#)
41. Wang, Y., and Hekimi, S. (2019) The complexity of making ubiquinone. *Trends Endocrinol. Metab.* **30**, 929–943 [CrossRef Medline](#)
42. Murley, A., and Nunnari, J. (2016) The emerging network of mitochondria-organelle contacts. *Mol. Cell* **61**, 648–653 [CrossRef Medline](#)
43. Kehrein, K., Möller-Hergt, B. V., and Ott, M. (2015) The MIOREX complex—lean management of mitochondrial gene expression. *Oncotarget* **6**, 16806–16807 [CrossRef Medline](#)
44. Fontanesi, F. (2013) Mechanisms of mitochondrial translational regulation. *IUBMB Life* **65**, 397–408 [CrossRef Medline](#)
45. Marchler-Bauer, A., Zheng, C., Chitsaz, F., Derbyshire, M. K., Geer, L. Y., Geer, R. C., Gonzales, N. R., Gwadz, M., Hurwitz, D. I., Lanczycki, C. J., Lu, F., Lu, S., Marchler, G. H., Song, J. S., Thanki, N., et al. (2013) CDD: conserved domains and protein three-dimensional structure. *Nucleic Acids Res.* **41**, D348–D352 [CrossRef Medline](#)
46. Rossmann, M. G., Moras, D., and Olsen, K. W. (1974) Chemical and biological evolution of nucleotide-binding protein. *Nature* **250**, 194–199 [CrossRef Medline](#)
47. Kopec, J., Schnell, R., and Schneider, G. (2011) Structure of PA4019, a putative aromatic acid decarboxylase from *Pseudomonas aeruginosa*. *Acta Crystallogr. Sect. F Struct. Biol. Cryst. Commun.* **67**, 1184–1188 [CrossRef Medline](#)
48. Guarás, A., Perales-Clemente, E., Calvo, E., Acín-Pérez, R., Loureiro-Lopez, M., Pujol, C., Martínez-Carrascoso, I., Nuñez, E., García-Marqués, F., Rodríguez-Hernández, M. A., Cortés, A., Díaz, F., Pérez-Martos, A., Moraes, C. T., Fernández-Silva, P., et al. (2016) The CoQH₂/CoQ ratio serves as a sensor of respiratory chain efficiency. *Cell Rep.* **15**, 197–209 [CrossRef Medline](#)
49. Scialò, F., Sriram, A., Fernández-Ayala, D., Gubina, N., Löhms, M., Nelson, G., Logan, A., Cooper, H. M., Navas, P., Enriquez, J. A., Murphy, M. P., and Sanz, A. (2016) Mitochondrial ROS produced via reverse electron transport extend animal lifespan. *Cell Metab.* **23**, 725–734 [CrossRef Medline](#)
50. UniProt Consortium (2018) UniProt: the universal protein knowledgebase. *Nucleic Acids Res.* **46**, 2699 [CrossRef Medline](#)
51. Pagliarini, D. J., Calvo, S. E., Chang, B., Sheth, S. A., Vafai, S. B., Ong, S. E., Walford, G. A., Sugiana, C., Boneh, A., Chen, W. K., Hill, D. E., Vidal, M., Evans, J. G., Thorburn, D. R., Carr, S. A., and Mootha, V. K. (2008) A mitochondrial protein compendium elucidates complex I disease biology. *Cell* **134**, 112–123 [CrossRef Medline](#)
52. van den Bosch, B. J., Gerards, M., Sluiter, W., Stegmann, A. P., Jongen, E. L., Hellebrekers, D. M., Oegema, R., Lambrichs, E. H., Prokisch, H., Danhauser, K., Schoonderwoerd, K., de Coo, I. F., and Smeets, H. J. (2012) Defective NDUFA9 as a novel cause of neonatally fatal complex I disease. *J. Med. Genet.* **49**, 10–15 [CrossRef Medline](#)
53. Brachmann, C. B., Davies, A., Cost, G. J., Caputo, E., Li, J., Hieter, P., and Boeke, J. D. (1998) Designer deletion strains derived from *Saccharomyces cerevisiae* S288C: a useful set of strains and plasmids for PCR-mediated gene disruption and other applications. *Yeast* **14**, 115–132 [CrossRef Medline](#)
54. Thomas, B. J., and Rothstein, R. (1989) Elevated recombination rates in transcriptionally active DNA. *Cell* **56**, 619–630 [CrossRef Medline](#)
55. Barkovich, R. J., Shtanko, A., Shepherd, J. A., Lee, P. T., Myles, D. C., Tzagoloff, A., and Clarke, C. F. (1997) Characterization of the COQ5 gene from *Saccharomyces cerevisiae*. Evidence for a C-methyltransferase in ubiquinone biosynthesis. *J. Biol. Chem.* **272**, 9182–9188 [CrossRef Medline](#)

Coq10 knockout phenotypes are rescued by deletion of COQ11

56. Rothstein, R. J. (1983) One-step gene disruption in yeast. *Methods Enzymol.* **101**, 202–211 [CrossRef Medline](#)
57. Gietz, R. D., and Woods, R. A. (2002) Transformation of yeast by lithium acetate/single-stranded carrier DNA/polyethylene glycol method. *Methods Enzymol.* **350**, 87–96 [CrossRef Medline](#)
58. Hill, S., Hirano, K., Shmanai, V. V., Marbois, B. N., Vidovic, D., Bekish, A. V., Kay, B., Tse, V., Fine, J., Clarke, C. F., and Shchepinov, M. S. (2011) Isotope-reinforced polyunsaturated fatty acids protect yeast cells from oxidative stress. *Free Radic. Biol. Med.* **50**, 130–138 [CrossRef Medline](#)
59. Hill, S., Lamberson, C. R., Xu, L., To, R., Tsui, H. S., Shmanai, V. V., Bekish, A. V., Awad, A. M., Marbois, B. N., Cantor, C. R., Porter, N. A., Clarke, C. F., and Shchepinov, M. S. (2012) Small amounts of isotope-reinforced polyunsaturated fatty acids suppress lipid autoxidation. *Free Radic. Biol. Med.* **53**, 893–906 [CrossRef Medline](#)
60. Santos, J. H., Mandavilli, B. S., and Van Houten, B. (2002) Measuring oxidative mtDNA damage and repair using quantitative PCR. *Methods Mol. Biol.* **197**, 159–176 [CrossRef Medline](#)
61. Gonzalez-Hunt, C. P., Rooney, J. P., Ryde, I. T., Anbalagan, C., Joglekar, R., and Meyer, J. N. (2016) PCR-based analysis of mitochondrial DNA copy number, mitochondrial DNA damage, and nuclear DNA damage. *Curr. Protoc. Toxicol.* **67**, 20.11.1–20.11.25 [CrossRef Medline](#)
62. Guo, X., Niemi, N. M., Hutchins, P. D., Condon, S. G. F., Jochem, A., Ulbrich, A., Higbee, A. J., Russell, J. D., Senes, A., Coon, J. J., and Pagliarini, D. J. (2017) Ptc7p dephosphorylates select mitochondrial proteins to enhance metabolic function. *Cell Rep.* **18**, 307–313 [CrossRef Medline](#)
63. Eyer, P., Worek, F., Kiderlen, D., Sinko, G., Stuglin, A., Simeon-Rudolf, V., and Reiner, E. (2003) Molar absorption coefficients for the reduced Ellman reagent: reassessment. *Anal. Biochem.* **312**, 224–227 [CrossRef Medline](#)
64. Zhang, T., Lei, J., Yang, H., Xu, K., Wang, R., and Zhang, Z. (2011) An improved method for whole protein extraction from yeast *Saccharomyces cerevisiae*. *Yeast* **28**, 795–798 [CrossRef Medline](#)
65. Schagger, H., Cramer, W. A., and von Jagow, G. (1994) Analysis of molecular masses and oligomeric states of protein complexes by blue native electrophoresis and isolation of membrane protein complexes by two-dimensional native electrophoresis. *Anal. Biochem.* **217**, 220–230 [CrossRef Medline](#)
66. Wittig, I., Braun, H. P., and Schagger, H. (2006) Blue NativePAGE. *Nat. Protoc.* **1**, 418–428 [CrossRef Medline](#)
67. Barros, M. H., and Tzagoloff, A. (2017) Aep3p-dependent translation of yeast mitochondrial ATP8. *Mol. Biol. Cell* **28**, 1426–1434 [CrossRef Medline](#)
68. Santos-Ocaña, C., Do, T. Q., Padilla, S., Navas, P., and Clarke, C. F. (2002) Uptake of exogenous coenzyme Q and transport to mitochondria is required for bc₁ complex stability in yeast *coq* mutants. *J. Biol. Chem.* **277**, 10973–10981 [CrossRef Medline](#)
69. Winzeler, E. A., Shoemaker, D. D., Astromoff, A., Liang, H., Anderson, K., Andre, B., Bangham, R., Benito, R., Boeke, J. D., Bussey, H., Chu, A. M., Connelly, C., Davis, K., Dietrich, F., Dow, S. W., et al. (1999) Functional characterization of the *S. cerevisiae* genome by gene deletion and parallel analysis. *Science* **285**, 901–906 [CrossRef Medline](#)
70. Sikorski, R. S., and Hieter, P. (1989) A system of shuttle vectors and yeast host strains designed for efficient manipulation of DNA in *Saccharomyces cerevisiae*. *Genetics* **122**, 19–27 [Medline](#)
71. Christianson, T. W., Sikorski, R. S., Dante, M., Shero, J. H., and Hieter, P. (1992) Multifunctional yeast high-copy-number shuttle vectors. *Gene* **110**, 119–122 [CrossRef Medline](#)

Coq10 knockout phenotypes are rescued by deletion of COQ11

Respiratory deficiency caused by mutations in the coenzyme Q chaperone protein Coq10 is mitigated by deletion of *COQ11*

Michelle C. Bradley, Krista Yang¹, Lucía Fernández-del-Río¹, Jennifer Ngo^{1,2}, Anita Ayer^{3,4}, Hui S. Tsui¹, Noelle Alexa Novales¹, Roland Stocker^{3,4}, Orian S. Shirihai², Mario H. Barros⁵, Catherine F. Clarke^{1*}

Contents of Supporting Information

Tables S1 and S2
Figures S1, S2, and S3
References

SUPPORTING INFORMATION

Table S1. Description and source of antibodies.

<i>Antibody</i>	<i>Working dilution</i>	<i>Source</i>
Coq1	1:10,000	(1)
Coq2	1:1,000	(2)
Coq3	1:200	(3)
Coq4	1:2,000	(4)
Coq5	1:5,000	(5)
Coq6	1:200	(6)
Coq7	1:1,000	(7)
Coq8	Affinity purified, 1:30	(2)
Coq9	1:1,000	(2)
Coq10	Affinity purified, 1:400	(8)
Coq11	1:500	(8)
Mdh1	1:10,000	Lee McAlister-Henn ^b
Atp2	1:1,000	Carla M. Koehler ^c
Cyt ₁	1:1,000	Carla M. Koehler ^c
Cyb ₂	1:1,000	Carla M. Koehler ^c
Hsp60	1:5,000	Carla M. Koehler ^c
Porin	1:5,000	Carla M. Koehler ^c

^bDr. Lee McAlister-Henn, Department of Molecular Biophysics and Biochemistry, University of Texas Health Sciences Center, San Antonio, TX

^cDr. Carla M. Koehler, Department of Chemistry and Biochemistry, University of California, Los Angeles, Los Angeles, CA

Coq10 knockout phenotypes are rescued by deletion of COQ11

Table S2. Quantitative real-time PCR primers.

Gene	Forward primer (5'-3')	Reverse primer (5'-3')
<i>COQ1</i>	CCCGAAGTCGTAGAACTAATG	GGAACCGGAAGTAGCTTATG
<i>COQ2</i>	CAGCTGGTATGTTGGGTATTT	GACGGACCTGATAACTCTTTG
<i>COQ3</i>	CATGCTGGAGGGAAAGATAAA	TCGACCAACAATGCCTTAAA
<i>COQ4</i>	GTGGTATCCTTGACCTTTAC	CCAGCATTTCCTCCCAATAC
<i>COQ5</i>	TGCTTAAAGAAGGTGAGAAGAG	TACCGAAGGAGACTGTGTAG
<i>COQ6</i>	TGAAGGACGAGTCGGATATT	CCAACAAGGGCAACTCTATC
<i>COQ7</i>	GCTCCCAAGTGTGAGAATTTA	CTGGTCCCATATGTGCTTTAG
<i>COQ8</i>	CGTATGGAGGGAACTGAAATAA	GAGGCACCGAAATCCAATAA
<i>COQ9</i>	CGCTGTCATGGAAGTATAAA	GAGAAAGGCGCTTGAATAG
<i>COQ10</i>	GCGGTACCAATCACACTATTA	GAGAGGCTTGTTATCCACAG
<i>COQ11</i>	GCAGAGATATTTGAGGCCTATTA	CTGCTGAGTGGATACTGTTG
<i>ACT1</i>	TATGTTCTAGCGCTTGACCA	CCAAAGCAGCAACCTCTAAA

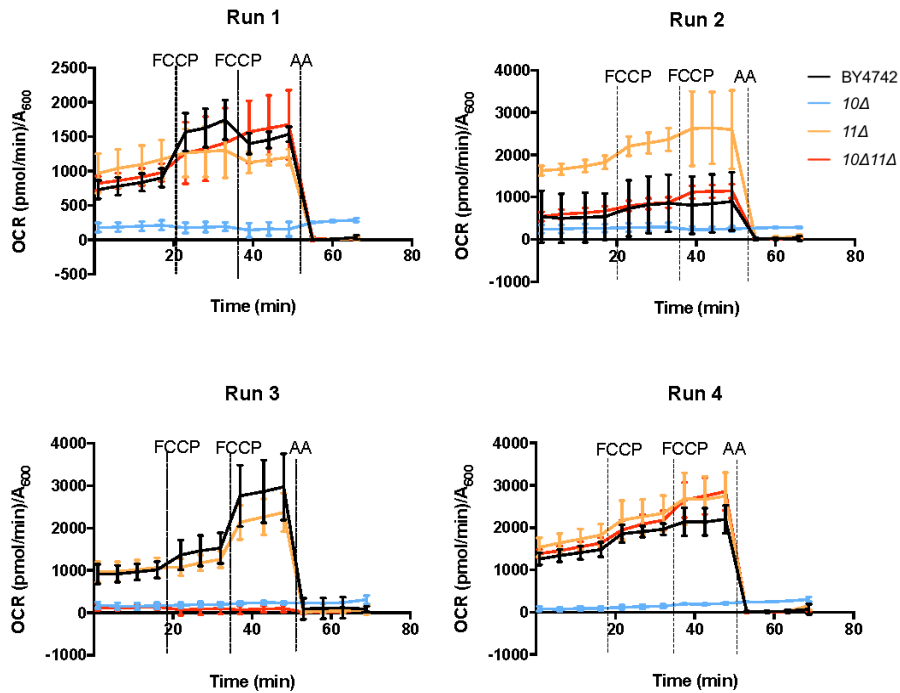


Figure S1. Oxygen consumption rates (OCRs) of yeast strains were determined with the XF96 Extracellular Flux Analyzer. The graphs depict traces from four independent experiments (Run 1 – Run 4). FCCP and Antimycin A (AA) were sequentially added to evaluate mitochondrial respiratory states. Each graph represents an individual experiment from the representative average traces (Fig. 2B), and each group represents 8–10 technical replicates.

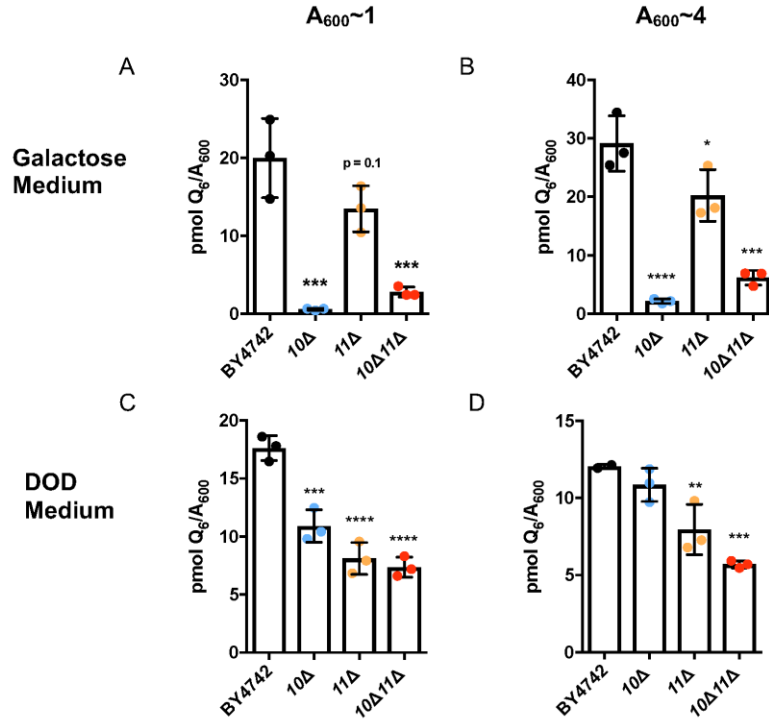


Figure S2. Q₆ content of whole cells have similar trends based on type of growth medium, rather than A₆₀₀ at time of harvest. Triplicates of 30 mL yeast cultures of wild type, *coq10*Δ, *coq11*Δ, and *coq10*Δ*coq11*Δ were grown in *A-B*, YPGal or *C-D*, dextrose-containing synthetic, minimal-medium (DOD) until they reached *A,C*, A₆₀₀~1 or *B,D*, A₆₀₀~4. Lipids from 10 mL of each culture were analyzed by LC-MS/MS. The data show mean ± SD, and the statistical significance as compared to wild type is represented by *p < 0.05, **p < 0.01, ***p < 0.001 and ****p < 0.0001. Panel B is a re-print from Fig. 5A in the main text.

Coq10 knockout phenotypes are rescued by deletion of COQ11

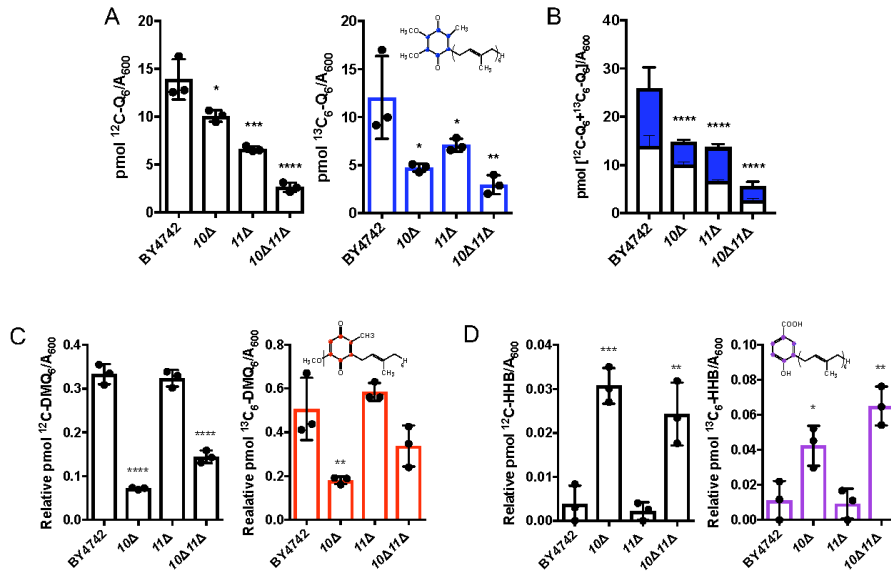


Figure S3. The *coq10Δcoq11Δ* double mutant the lowest total Q_6 compared to the single mutants and wild type in minimal medium. Triplicates of 6 mL cultures in DOD minimal medium were labeled with 5 $\mu\text{g/mL}$ $^{13}\text{C}_6\text{-4HHB}$. After 4 h, lipid extracts from 5 mL of each were analyzed by LC-MS/MS. *A*, Amount of $^{12}\text{C}_6\text{-Q}_6$ and $^{13}\text{C}_6\text{-Q}_6$ (blue); *B*, Total amount of Q_6 , from the sum of $^{13}\text{C}_6\text{-Q}_6$ and $^{12}\text{C}_6\text{-Q}_6$; *C*, $^{12}\text{C}_6\text{-DMQ}_6$ and $^{13}\text{C}_6\text{-DMQ}_6$ (red); and *D*, $^{12}\text{C}_6\text{-HHB}$ and $^{13}\text{C}_6\text{-HHB}$ (purple), were measured from the whole cell lipid extracts of wild type, *coq10Δ*, *coq11Δ*, and *coq10Δcoq11Δ* mutants. The data show mean \pm SD, and the statistical significance as compared to wild type is represented by * $p < 0.05$, ** $p < 0.01$, *** $p < 0.001$ and **** $p < 0.0001$.

SUPPORTING REFERENCES

1. Gin, P., and Clarke, C. F. (2005) Genetic evidence for a multi-subunit complex in coenzyme Q biosynthesis in yeast and the role of the Coq1 hexaprenyl diphosphate synthase. *J Biol Chem* **280**, 2676-2681
2. Hsieh, E. J., Gin, P., Gulmezian, M., Tran, U. C., Saiki, R., Marbois, B. N., and Clarke, C. F. (2007) *Saccharomyces cerevisiae* Coq9 polypeptide is a subunit of the mitochondrial coenzyme Q biosynthetic complex. *Arch Biochem Biophys* **463**, 19-26
3. Poon, W. W., Barkovich, R. J., Hsu, A. Y., Frankel, A., Lee, P. T., Shepherd, J. N., Myles, D. C., and Clarke, C. F. (1999) Yeast and rat Coq3 and *Escherichia coli* UbiG polypeptides catalyze both O-methyltransferase steps in coenzyme Q biosynthesis. *J Biol Chem* **274**, 21665-21672
4. Belogradov, G. I., Lee, P. T., Jonassen, T., Hsu, A. Y., Gin, P., and Clarke, C. F. (2001) Yeast *COQ4* encodes a mitochondrial protein required for coenzyme Q synthesis. *Arch Biochem Biophys* **392**, 48-58
5. Baba, S. W., Belogradov, G. I., Lee, J. C., Lee, P. T., Strahan, J., Shepherd, J. N., and Clarke, C. F. (2004) Yeast Coq5 C-methyltransferase is required for stability of other polypeptides involved in coenzyme Q biosynthesis. *J Biol Chem* **279**, 10052-10059
6. Gin, P., Hsu, A. Y., Rothman, S. C., Jonassen, T., Lee, P. T., Tzagoloff, A., and Clarke, C. F. (2003) The *Saccharomyces cerevisiae* *COQ6* gene encodes a mitochondrial flavin-dependent monooxygenase required for coenzyme Q biosynthesis. *J Biol Chem* **278**, 25308-25316
7. Tran, U. C., Marbois, B., Gin, P., Gulmezian, M., Jonassen, T., and Clarke, C. F. (2006) Complementation of *Saccharomyces cerevisiae* *coq7* mutants by mitochondrial targeting of the *Escherichia coli* UbiF polypeptide: two functions of yeast Coq7 polypeptide in coenzyme Q biosynthesis. *J Biol Chem* **281**, 16401-16409
8. Tsui, H. S., Pham, N. V. B., Amer, B. R., Bradley, M. C., Gosschalk, J. E., Gallagher-Jones, M., Ibarra, H., Clubb, R. T., Blaby-Haas, C. E., and Clarke, C. F. (2019) Human COQ10A and COQ10B are distinct lipid-binding START domain proteins required for coenzyme Q function. *J Lipid Res* **60**, 1293-1310

Appendix VI

Atomic structure of a toxic, oligomeric segment of SOD1 linked to amyotrophic lateral sclerosis (ALS).

The work described in this chapter has been reproduced from:

Sangwan S., Zhao A., Adams K.L., Jayson C.K., Sawaya M.K., Guenther E., Pan A.C., Ngo J., Moore D., Soriaga A.B., Panchal A., Do T.D., Goldschmidt L., Nelson R., Bowers M.T., Geisberg M., Koehler C.M., Shaw D.E., Novitch B.G., Eisenberg D.S. Atomic structure of a toxic, oligomeric segment of SOD1 linked to amyotrophic lateral sclerosis (ALS). PNAS. 2017.

114 (33) 8770-8775. doi.org/10.1073/pnas.1705091114.

Copyright 2017

Smriti Sangwan, Anni Zhao, Katrina L. Adams, Christina K. Jayson, Michael R. Sawaya, Elizabeth L. Guenther, Albert C. Pan, Jennifer Ngo, Destaye M. Moore, Angela B. Soriaga, Thanh D. Do, Lukasz Goldschmidt, Rebecca Nelson, Michael T. Bowers, Carla M. Koehler, David E. Shaw, Bennett G. Novitch, and David S. Eisenberg.



Atomic structure of a toxic, oligomeric segment of SOD1 linked to amyotrophic lateral sclerosis (ALS)

Smriti Sangwan^a, Anni Zhao^a, Katrina L. Adams^b, Christina K. Jayson^c, Michael R. Sawaya^a, Elizabeth L. Guenther^a, Albert C. Pan^d, Jennifer Ngo^c, Destaye M. Moore^b, Angela B. Soriaga^a, Thanh D. Do^e, Lukasz Goldschmidt^a, Rebecca Nelson^a, Michael T. Bowers^c, Carla M. Koehler^c, David E. Shaw^{d,f}, Bennett G. Novitch^b, and David S. Eisenberg^{a,1}

^aHoward Hughes Medical Institute, UCLA-DOE and Molecular Biology Institutes, Department of Biological Chemistry, University of California, Los Angeles, CA 90095; ^bDepartment of Neurobiology, Eli and Edythe Broad Center of Regenerative Medicine and Stem Cell Research, David Geffen School of Medicine at UCLA, Los Angeles, CA 90095; ^cDepartment of Chemistry & Biochemistry, University of California, Los Angeles, CA 90095; ^dD. E. Shaw Research, New York, NY 10036; ^eDepartment of Chemistry and Biochemistry, University of California, Santa Barbara, CA 93106; and ^fDepartment of Biochemistry and Molecular Biophysics, Columbia University, New York, NY 10032

Contributed by David S. Eisenberg, June 27, 2017 (sent for review March 28, 2017; reviewed by J. Paul Taylor and Peter Walter)

Fibrils and oligomers are the aggregated protein agents of neuronal dysfunction in ALS diseases. Whereas we now know much about fibril architecture, atomic structures of disease-related oligomers have eluded determination. Here, we determine the corkscrew-like structure of a cytotoxic segment of superoxide dismutase 1 (SOD1) in its oligomeric state. Mutations that prevent formation of this structure eliminate cytotoxicity of the segment in isolation as well as cytotoxicity of the ALS-linked mutants of SOD1 in primary motor neurons and in a *Danio rerio* (zebrafish) model of ALS. Cytotoxicity assays suggest that toxicity is a property of soluble oligomers, and not large insoluble aggregates. Our work adds to evidence that the toxic oligomeric entities in protein aggregation diseases contain antiparallel, out-of-register β -sheet structures and identifies a target for structure-based therapeutics in ALS.

oligomer | SOD1 | ALS

Since Alzheimer's pioneering report in 1906 (1), fibrillar protein deposits have been linked to neurodegenerative diseases. More recently, this link has been challenged by findings that transient soluble oligomers formed by these proteins are cytotoxic (2, 3). Whereas atomic-resolution structures of the spines of amyloid fibrils have shown tightly packed β -sheets with interdigitated side chains (4–6), atomic-level details of toxic oligomers remain elusive. Various reports suggest that toxic intermediates formed by amyloid-forming proteins consist of antiparallel β -sheet-rich structures (7–9). These reports used chemical cross-linking, analytical size exclusion, EM, and FTIR, but no atomic structure of toxic amyloid oligomers has been reported.

ALS is a debilitating disease, destroying spinal motor neurons and often leading to death within a few years of symptom onset. More than 170 different mutations in superoxide dismutase 1 (SOD1), a metal-binding, homodimeric protein of 153 residues, are found in familial cases of ALS (10, 11). Most of these SOD1 mutants show little change in enzymatic function, suggesting that toxicity derives not from a loss of native function but from a gain of toxic function (12–14). Transgenic mouse models of the familial mutants show motor neuron degeneration and stain positive for SOD1-containing inclusions, suggesting that protein aggregation is a mode of toxicity (14–16). Enrichment of oligomers has also been observed in cell culture and in transgenic mice (17–19). However, a causal relationship between the appearance of aggregates and neuronal death has not been conclusively supported, and no atomic structure has been described for toxic oligomers of SOD1 or any other neurodegenerative disease-related protein. Here, we propose a structure for toxic oligomers formed by SOD1.

Results

Crystal Structure of SOD1 Residues 28–38 Reveals an Antiparallel β -Sheet Oligomer. We identified residues 28–38 of SOD1 (with the sequence PVK/VGSIKGL) as having the potential to form a toxic amyloid oligomer based on mutational studies of others

(19–23) and our own (discussed below) (*SI Appendix*, Figs. S1–S3). To increase solubility for crystallization, we engineered a single-residue substitution: P28K. Rod-like crystals measuring 5 μ m in the shortest dimension appeared overnight, and upon further optimization, they diffracted X-rays to 2.0-Å resolution. We determined the phases by single isomorphous replacement with anomalous scattering using crystals soaked in potassium iodide (*SI Appendix*, Table S1).

The crystal structure shows a twisted β -sheet built of antiparallel, out-of-register β -strands. Describing its shape, we term it the “corkscrew” (Fig. 1A). Each β -strand in the sheet contains eight residues, from Lys28 to Ile35. The three C-terminal residues, Lys36, Gly37, and Leu38, adopt a β -hairpin conformation, positioning the C-terminal carboxylate to hydrogen-bond with the N-terminal residue of an adjacent strand. The twist of the sheet is left-handed, as is commonly observed for β -sheets. The sheet undergoes a full turn every 16 strands, with a helical pitch of 71 Å corresponding to the unit cell “c” dimension. Unit cell repeats extend the corkscrew throughout the length of the crystal. Examination of Lys28 reveals that the P28K substitution made to facilitate crystallization affects only crystal lattice contacts (*SI Appendix*, Fig. S4), and suggests that the native sequence would adopt the corkscrew structure seen here. Indeed, SOD1 residues 28–38 assembled preferentially into a corkscrew in our molecular dynamics (MD) simulations (Fig. 1F and *SI Appendix*, Fig. S5B).

The corkscrew architecture differs markedly from amyloid fibrils. Sheets from adjacent corkscrews do not mate together tightly as

Significance

More than 170 mutations in superoxide dismutase 1 (SOD1) are linked to inherited forms of ALS, and aggregates of this protein are a pathological feature associated with this disease. Although it is accepted that SOD1 gains a toxic function in the disease state, a molecular understanding of the toxic species is lacking. Here, we identify a short segment of SOD1 that is both necessary and sufficient for toxicity to motor neurons. The crystal structure of the segment reveals an out-of-register β -sheet oligomer, providing a structural rationale for the toxic effects of mutant SOD1 in ALS.

Author contributions: S.S., A.Z., B.G.N., and D.S.E. designed research; S.S., A.Z., C.K.J., M.R.S., E.L.G., A.C.P., J.N., D.M.M., and T.D.D. performed research; K.L.A., A.B.S., L.G., and R.N. contributed new reagents/analytic tools; D.E.S. supervised the simulation work; S.S., M.R.S., E.L.G., A.C.P., M.T.B., C.M.K., and B.G.N. analyzed data; and S.S. and D.S.E. wrote the paper.

Reviewers: J.P.T., St. Jude Children's Medical Hospital; and P.W., University of California, San Francisco.

The authors declare no conflict of interest.

Data deposition: The atomic coordinates and structure factors have been deposited in the Protein Data Bank, www.pdb.org (PDB ID codes [SDLI](https://doi.org/10.1073/pnas.1705091114) and [SIIW](https://doi.org/10.1073/pnas.1705091114)).

¹To whom correspondence should be addressed. Email: david@mbi.ucla.edu.

This article contains supporting information online at www.pnas.org/lookup/suppl/doi/10.1073/pnas.1705091114/-DCSupplemental.

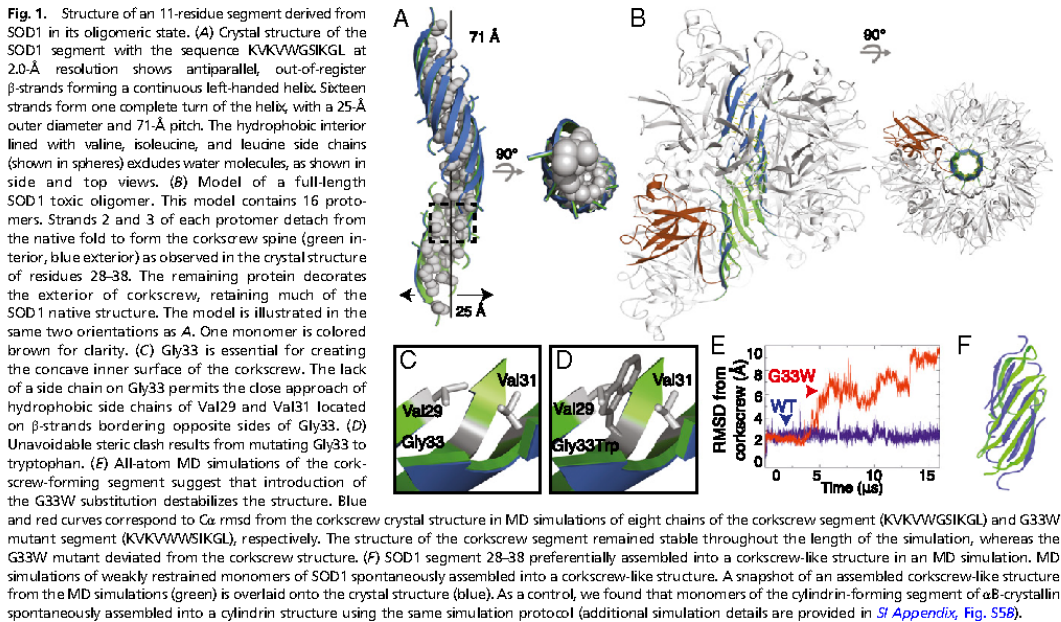


Fig. 1. Structure of an 11-residue segment derived from SOD1 in its oligomeric state. (A) Crystal structure of the SOD1 segment with the sequence KVKVWGSIKGL at 2.0-Å resolution shows antiparallel, out-of-register β -strands forming a continuous left-handed helix. Sixteen strands form one complete turn of the helix, with a 25-Å outer diameter and 71-Å pitch. The hydrophobic interior lined with valine, isoleucine, and leucine side chains (shown in spheres) excludes water molecules, as shown in side and top views. (B) Model of a full-length SOD1 toxic oligomer. This model contains 16 protomers. Strands 2 and 3 of each protomer detach from the native fold to form the corkscrew spine (green interior, blue exterior) as observed in the crystal structure of residues 28–38. The remaining protein decorates the exterior of corkscrew, retaining much of the SOD1 native structure. The model is illustrated in the same two orientations as A. One monomer is colored brown for clarity. (C) Gly33 is essential for creating the concave inner surface of the corkscrew. The lack of a side chain on Gly33 permits the close approach of hydrophobic side chains of Val29 and Val31 located on β -strands bordering opposite sides of Gly33. (D) Unavoidable steric clash results from mutating Gly33 to tryptophan. (E) All-atom MD simulations of the corkscrew-forming segment suggest that introduction of the G33W substitution destabilizes the structure. Blue and red curves correspond to Ca rmsd from the corkscrew crystal structure in MD simulations of eight chains of the corkscrew segment (KVKVWGSIKGL) and G33W mutant segment (KVKVWWSIKGL), respectively. The structure of the corkscrew segment remained stable throughout the length of the simulation, whereas the G33W mutant deviated from the corkscrew structure. (F) SOD1 segment 28–38 preferentially assembled into a corkscrew-like structure in an MD simulation. MD simulations of weakly restrained monomers of SOD1 spontaneously assembled into a corkscrew-like structure. A snapshot of an assembled corkscrew-like structure from the MD simulations (green) is overlaid onto the crystal structure (blue). As a control, we found that monomers of the cylinder-forming segment of αB -crystallin spontaneously assembled into a cylinder structure using the same simulation protocol (additional simulation details are provided in *SI Appendix*, Fig. S5B).

sheets do in amyloid fibrils, but instead contact weakly through polar and charged side chains scattered over the exterior of the corkscrew (Lys28, Lys30, Ser34, and Lys36), Trp32, and water-mediated contacts. Hence, unlike amyloid fibrils, the corkscrew has no dry interface between sheets to stabilize its assembly. Instead, the corkscrew assembly is stabilized by weaker hydrophobic forces arising from the concave interior filled with aliphatic side chains of Val29, Val31, Ile35, and Leu38 (Fig. 1A and *SI Appendix*, Fig. S3).

The absence of a stable, amyloid-like, dry sheet-sheet interface suggests that fragmentation of the corkscrew could be relatively facile and that its subsets of various sizes could fit the definition of soluble oligomers. Indeed, ion mobility MS experiments confirm that this SOD1 segment 28–38 forms low-molecular-weight oligomers in solution similar in cross-section to the crystal structure of the corkscrew (*SI Appendix*, Fig. S6), supporting our hypothesis that the corkscrew represents the structure of a soluble oligomer. Furthermore, the β -sheet-rich nature of the corkscrew is a property shared in common with other amyloid-related oligomers, such as α -synuclein, amyloid- β , and HET-s (8, 9, 24). In fact, several amyloid oligomers have been reported to share antiparallel, out-of-register β -strand architecture (24–26).

The corkscrew shares several structural features with another soluble oligomer, cylindrin, from the nonpathogenic amyloid-forming protein, αB -crystallin (27). Both oligomers are composed of antiparallel β -strands, shifted out-of-register by two residues. Both sheets are highly curved, and opposite faces of the sheet display different sets of side chains not related by symmetry (28). In both oligomers, individual strands hydrogen-bond to neighboring strands through alternating weak and strong interfaces (*SI Appendix*, Fig. S5A). The strong interface of the corkscrew is composed of nine interchain hydrogen bonds, and the weak interface is composed of seven hydrogen bonds: one intramain chain and six intermain chain hydrogen bonds. The β -strands in both oligomers have similar values of buried surface area (984 Å² vs. 943 Å²) and shape complementarity (0.79 vs. 0.74) (*SI Appendix*, Table S2). The primary difference between the two architectures is that cylindrin is a closed barrel of defined stoichiometry (six strands), whereas the corkscrew, although

highly curved, is not entirely closed and is likely to exist in a range of oligomeric sizes.

The role of the corkscrew in ALS is supported by a model accommodating full-length SOD1. We modeled the remainder of SOD1 around the corkscrew scaffold, keeping the tertiary structure of SOD1 intact everywhere except near the corkscrew and avoiding steric conflict (Fig. 1B). In our model, strands 2 and 3 detach from the native fold, exposing the corkscrew-forming residues 28–38. This local unfolding may be triggered by dissociation of the SOD1 dimer and metal depletion. Biochemical studies have noted that metal-depleted monomer is prevalent in patient tissues (29, 30) as well as in mouse models, and is an intermediate in the conversion of native holo-SOD1 to pathological aggregates (31). This model agrees with H/D exchange and with MD and MS studies showing that most familial SOD1 mutants have minimal change in their secondary structure and contain a partially unfolded β -barrel at physiological temperature with local unfolding in β -strand 3 (20, 31).

We probed the role of the corkscrew in SOD1-associated cytotoxicity by introducing mutations to disrupt corkscrew architecture. The absence of a bulky side chain at position 33 appears essential to form the concave inner surface of the corkscrew (Fig. 1C). Mutation of Gly33 to a larger residue, such as tryptophan (Fig. 1D) or valine, would introduce severe steric clashes with Val29 and Val31, destabilizing the corkscrew structure. Consistent with this observation, our all-atom MD simulations revealed that the corkscrew was less stable for W33 than for G33, regardless of whether the N terminus was proline or lysine (Fig. 1E and *SI Appendix*, Fig. S4C). Thus, if the corkscrew were a cytotoxic motif, we would expect G33 mutants to alleviate toxicity of SOD1 familial mutants.

Segment 28–38 Is Necessary and Sufficient for Toxicity. Corkscrew-disruptive mutations alleviated toxicity of segment 28–38. We assayed cytotoxicity by 3-(4,5-dimethylthiazol-2-yl)-2,5-diphenyltetrazolium bromide (MTT) reduction in embryonic stem-cell-derived motor neurons expressing GFP to facilitate visualization of neuron morphology (32). The corkscrew-forming segment was aggregated, applied to motor neurons, and incubated overnight. We found that

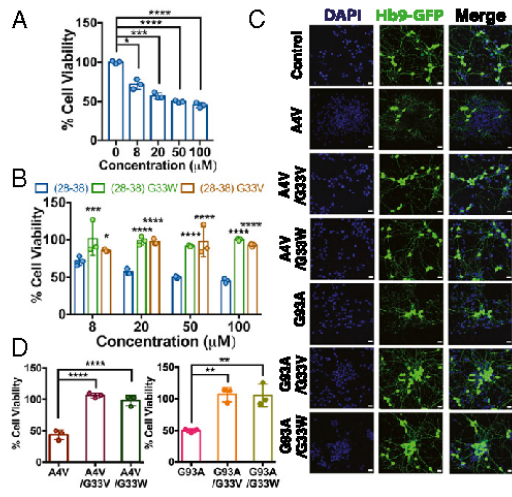


Fig. 2. Corkscrew-forming segment 28–38 is necessary and sufficient for cytotoxicity. (A) Cell viability of motor neurons measured by an MTT reduction assay shows that the corkscrew segment (KVKVW/GSIKGL) is toxic to primary motor neurons in a dose-dependent manner. Results are shown as mean \pm SD ($n = 3$). Symbols represent individual values of triplicates, and bars represent average values. Statistical significance was analyzed using two-tailed t tests with Welch's correction. (B) Corkscrew-forming segment (28–38) harboring single-point substitutions at Gly33 (G33V and G33W) is nontoxic to motor neurons. All peptide segments were prepared identically, and motor neurons were treated with different final concentrations. The statistical significance of G33V and G33W mutants was compared with segment 28–38 by two-way ANOVA. (C) Hb9-GFP-labeled motor neurons treated with 8 μ M aggregated full-length familial mutants (A4V and G93A) lose neurites, but the corresponding corkscrew-disrupting mutants (G93A/G33V, G93A/G33W, A4V/G33V, and A4V/G33W) are nontoxic and neurons look healthy. (Scale bars, 20 μ m.) (D) Cell viability measured by an MTT reduction assay confirming that the familial mutants A4V and G93A are toxic and that substitution of Gly33 with valine or tryptophan renders the protein nontoxic. Results are shown as mean \pm SD ($n = 3$). Symbols represent individual values of triplicates, and bars represent average values. Statistical significance was analyzed by one-way ANOVA (* $P < 0.05$, ** $P < 0.01$, *** $P < 0.001$, **** $P < 0.0001$).

viability was reduced by 60% compared with buffer-treated cells at physiological concentrations of 8–100 μ M in a dose-dependent manner (Fig. 2A). In contrast, neither the segment harboring the corkscrew-disruptive G33W mutation (Fig. 2B) nor the less bulky G33V mutant (Fig. 2B) induced toxicity in cells at any concentration tested. The same trends were observed with the native 28–38 segment (P28) and the corresponding G33W and G33V mutations (SI Appendix, Fig. S7).

Corkscrew-disruptive mutations also alleviated toxicity of full-length SOD1 familial mutants A4V and G93A. These proteins were recombinantly expressed, purified, and aggregated by demetallation and agitation at 37 $^{\circ}$ C for 12 h, which produced a mixture of fibrils and oligomers. Motor neurons were treated with aggregated proteins overnight and then assayed for cellular viability. A4V and G93A mutants were toxic to the cells at 8 μ M, which looked drastically degenerated compared with buffer-treated cells (Fig. 2C) and demonstrated reduced viability (Fig. 2D). In contrast, A4V/G33V, A4V/G33W, G93A/G33V, and G93A/G33W proteins were nontoxic at the same concentration, and cellular morphologies were indistinguishable from the cellular morphologies of the buffer-treated cells. Together, these data suggest that the segment 28–38 is both necessary and sufficient for motor neuron toxicity.

Toxicity of Full-Length SOD1 Derives from Soluble Oligomers. We asked if toxicity of full-length SOD1 derives from soluble oligomers or

insoluble fibrils. We tested the cytotoxic effects of the non-fibril-forming mutant (I104P) (33). Even though it did not form any mature fibrils (Fig. 3A), it was toxic to motor neurons, and addition of the corkscrew-disrupting substitution, G33W, alleviated the cytotoxicity (Fig. 3B and C). These results suggest that fibril formation is not essential for cytotoxicity.

To identify which species of SOD1 aggregate is toxic, we monitored the toxicity of various SOD1 mutants as their aggregates

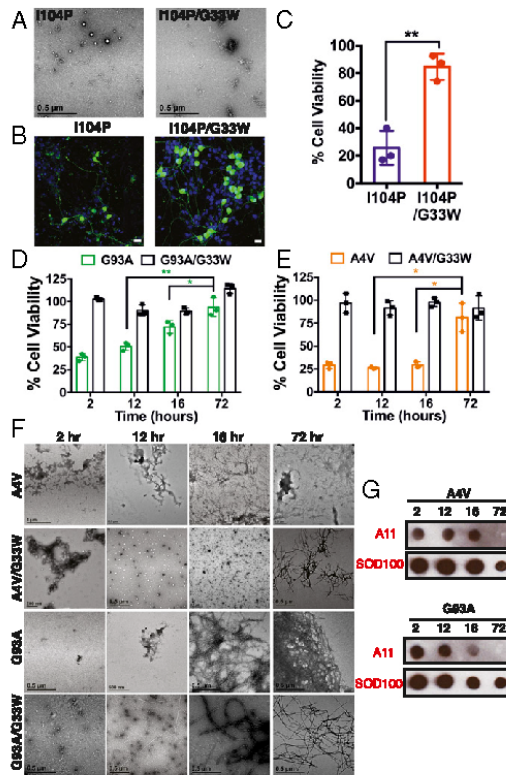
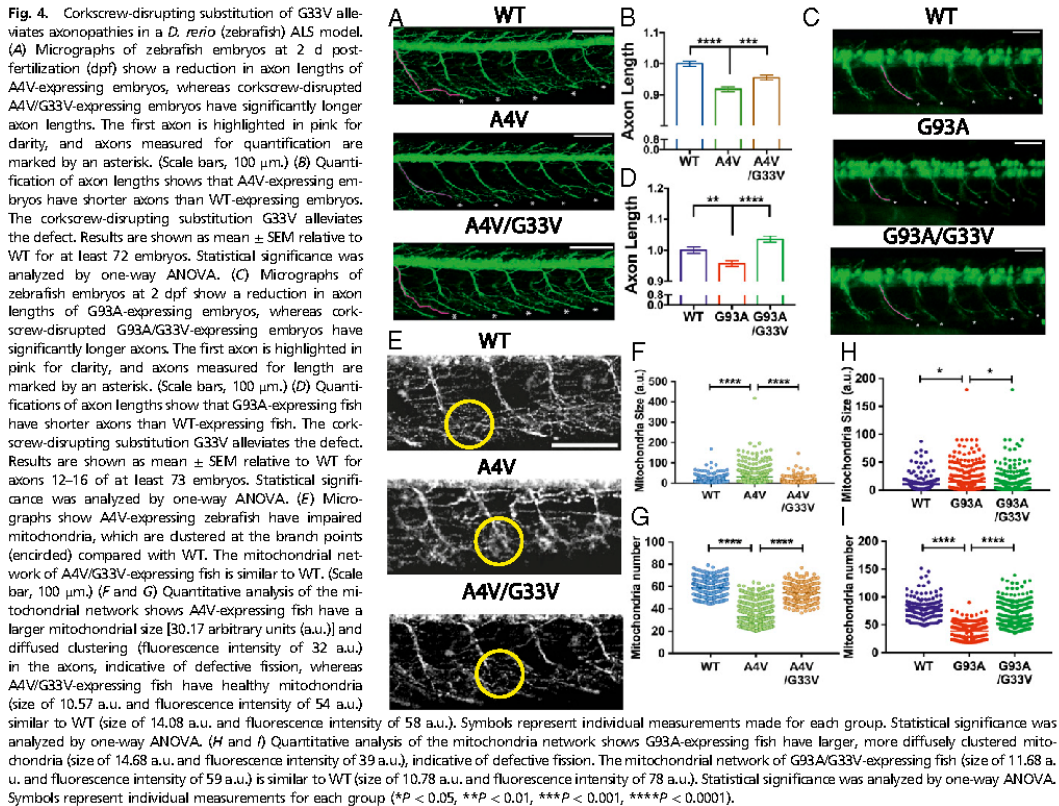


Fig. 3. Toxicity of full-length SOD1 derives from soluble oligomers. (A) Electron micrographs of a non-fibril-forming SOD1 mutant (I104P) and the corresponding double mutant (I104P/G33W) show some aggregates but no large fibrils. (B) Motor neurons treated with I104P lose neurites and have shrunken cell bodies (left), but I104P/G33W-treated cells look healthy (right). (Scale bars, 20 μ m.) (C) Cell viability measured by an MTT reduction assay confirmed that I104P is toxic and I104P/G33W is nontoxic. Statistical significance was analyzed using a two-tailed t test with Welch's correction. (D and E) Toxic properties of SOD1 mutants depend on the duration of aggregation. The A4V and G93A mutants aggregated for 12–16 h are toxic to motor neurons, whereas extended agitation for 72 h renders the proteins nontoxic. The corkscrew-disrupting proteins (A4V/G33V and G93A/G33W) are nontoxic irrespective of the duration of aggregation. Results are shown as mean \pm SD ($n = 3$). Symbols represent individual values of triplicates, and bars represent average values. Statistical significance was analyzed by two-tailed t tests with Welch's correction (* $P < 0.05$, ** $P < 0.01$). (F) Representative electron micrographs of various preparations of the familial mutants A4V and G93A and the double mutants A4V/G33W and G93A/G33W. Some large aggregates can be seen at 2- to 16-h time points, but no fibrils can be seen, whereas all constructs show large fibril loads at 72 h. (G) Immunoblots of the familial mutants aggregated for different time points. Samples aggregated for 12–16 h are A11-positive, and both proteins lose A11 reactivity when aggregated for 72 h. SOD100 was used as a loading control.



evolved over time. We found that both familial mutants (A4V and G93A) were toxic to cultured neurons when aggregated for 12–16 h but that extended aggregation for 72 h rendered the protein nontoxic (Fig. 3 D and E). A4V/G33W and G93A/G33W were nontoxic irrespective of the duration of aggregation. Negative-stain EM showed abundant fibrils in the samples aggregated for 72 h (Fig. 3F), and immunoblotting with the conformational oligomer-specific antibody (A11) suggested that samples aggregated for 72 h contained no oligomers (Fig. 3G). These results suggest that toxicity of aggregated SOD1 mutants derives from oligomers.

Whereas the relevance of our work to SOD1-related ALS seems clear, the relevance to non-SOD1-related ALS is less clear. A few reports suggest that wild-type SOD1 (WT) aggregates in sporadic ALS (34–36) analogous to mutant SOD1 aggregates in familial ALS; however, it is unknown if WT and mutant SOD1 aggregate by the same mechanism or have the same toxicity. We compared the aggregation and cytotoxic properties of WT and mutant SOD1. We used Thioflavin T, a dye that fluoresces upon binding to fibrils. We found that the fibril-forming behavior of WT, G93A, and G33W constructs was similar (SI Appendix, Fig. S8). We then performed a motor neuron cytotoxicity assay with protein aggregates from several time points. WT or G93A protein samples that were allowed to aggregate for up to 12 h were toxic, whereas the same protein preparations that were aggregated for 16 h or longer exhibited no toxicity (SI Appendix, Fig. S8 A and B). G33W, which cannot form the corkscrew, was nontoxic regardless of the extent of fibril formation (SI Appendix, Fig. S8C). Although there is limited evidence

of WT aggregation in non-SOD1-linked ALS cases, our results suggest that WT and mutant SOD1 share similar mechanisms of cytotoxicity that depend on self-assembly of residues 28–38; this exposure may be enhanced by structural perturbations induced by familial mutations.

Corkscrew Disruption Alleviates Defects in a *Danio rerio* (Zebrafish) ALS Model.

To determine whether corkscrew-disrupting mutations alleviate axonopathies caused by familial SOD1 mutants in vivo, we conducted experiments using a zebrafish model of ALS (37–40). We expressed A4V SOD1 with and without the corkscrew-disrupting substitution at Gly33 in a zebrafish TDL6 line in which the primary motor neurons are labeled with GFP and the mitochondria are labeled with dsRed (41). We analyzed the axons at 2 d postfertilization. The A4V mutation caused an 8% reduction in axon length (Fig. 4 A and B), as has been previously shown (39), but axon lengths of A4V/G33V-injected fish were significantly longer (Fig. 4 A and B). Additionally, we observed that 30% of A4V-injected fish were severely deformed and could not be imaged, suggesting that an acute phenotype is lethal (SI Appendix, Fig. S9C). In contrast, the WT and double-mutant-expressing fish did not display large mortality. We observed a similar phenotype upon expression of the G93A familial mutant; G93A-expressing zebrafish have 5% reduction in axon lengths, whereas axon lengths of G93A/G33V-expressing zebrafish were significantly longer (Fig. 4 C and D).

Defects in mitochondrial assembly and trafficking, along with vacuolation (42, 43) and abnormal clustering in neuronal processes (44–46), are established pathological phenotypes observed

in transgenic mice, patient-derived cells, and other models. However, they have not been reported in any zebrafish model of ALS thus far. Therefore, we analyzed the mitochondrial morphology upon expression of SOD1 familial mutants. Expression of A4V mutant protein caused remarkable mitochondrial pathology characterized by abnormal diffused clustering at the branch points indicative of defective mitochondria (Fig. 4E), whereas A4V/G33V-expressing fish had a mitochondrial network similar to WT fish. These defects were quantified by measuring the size and fluorescence intensity of the mitochondria, confirming that A4V-expressing fish displayed enlarged mitochondria (Fig. 4F and *SI Appendix*, Fig. S9), which were fewer in number (Fig. 4G and *SI Appendix*, Fig. S9). We also observed similar defects in the G93A-expressing zebrafish (Fig. 4H and *I* and *SI Appendix*, Fig. S9). Thus, disrupting the corkscrew segment alleviates ALS-linked axonopathies and mitochondrial defects in this *in vivo* model.

Discussion

Our experiments suggest that segment 28–38 of SOD1 is important for SOD1-mediated toxicity. The crystal structure of this segment revealed an oligomer composed of antiparallel, out-of-register β -strands, which assemble into a corkscrew-like structure. The G33V and G33W point mutants, which were designed to disrupt the observed oligomer, alleviated toxicity of both the isolated peptide and full-length SOD1. In a zebrafish model of ALS, G33V prevented axonopathies and mitochondrial defects, two characteristic features of ALS-linked pathology. Taken together, these results suggest that the corkscrew structure is critical for SOD1-mediated cytotoxicity.

The corkscrew structure explains its oligomeric state and suggests the identity of its potential interacting partners in the cell. The corkscrew is composed of a single twisted sheet rather than pairs of tightly mated sheets, as observed in 88 steric zipper structures published thus far. A clue about the identity of the corkscrew's interacting partners in the cell is offered by examining the functions of its structural homologs. A search for corkscrew homologs in the Protein Data Bank using the DALI server (47) yielded matches with other highly twisted β -sheet proteins, such as membrane receptor proteins, enzymes, and bactericidal-permeability increasing (BPI) protein (*SI Appendix*, Fig. S10). The twisted sheet seen in the crystal structure of BPI has been shown to bind lipids and destabilize membranes (48). It is conceivable that the cleft seen in the corkscrew structure is important for cytotoxicity, potentially as a binding site for lipids. The cleft of corkscrew is accessible to lipids and small molecules. In contrast, cytochrome *c* has no accessible cleft, which could explain its lower cytotoxicity relative to corkscrew.

Our results demonstrate that toxicity derives from the corkscrew oligomers rather than from fibrils (*SI Appendix*, Fig. S11). Previously, we have shown that out-of-register oligomers are likely off-pathway from in-register fibril formation due to the large energetic cost of rearrangement of out-of-register oligomers into in-register fibrils (49). Although we cannot ascertain whether the fibrils observed in our experiments are in-register, our results are consistent with this hypothesis. The corkscrew-disrupting mutations of G33V/G33W attenuate cytotoxicity but do not attenuate fibril formation.

Cytotoxicity assays of the non-fibril-forming mutant (I104P) and the time-course assays with the familial mutants (A4V and G93A) suggest that toxicity is a property of soluble oligomers, and not of large insoluble fibrils. These findings for SOD1 align with the hypotheses proposed by others for amyloid- β and huntingtin that large insoluble aggregates are relatively inert deposits (50–53).

From a molecular perspective, it would be unlikely to find ALS-linked mutations in the 28–38 segment of SOD1, given its structural importance for mediating toxicity. Indeed, compared with other regions of SOD1, this segment contains few familial mutations, and no mutations are found in the core of this segment spanning residues 32–36 (19). Notably, familial mutants, including G37R and the rare mutants V29A and V31A, are found near the ends of this segment. From our crystal structure, we infer that all these mutations are compatible with the corkscrew structure, although it is unclear if they actively promote oligomer assembly.

In summary, we have identified an 11-residue segment in ALS-associated SOD1 that is necessary for its cytotoxicity. Our data support the hypothesis that SOD1 forms toxic oligomers composed of antiparallel, out-of-register β -sheet structures involving residues 28–38. This cytotoxic segment may be a target for developing structure-based ALS therapeutics.

Materials and Methods

Crystals of SOD1(28–38) with P28K substitution were grown by hanging drop vapor diffusion using VDX plates (Hampton Research). Lyophilized peptide at 98% purity (Genscript, Inc.) was dissolved to 50 mg/mL in 50 mM Tris-base buffer. The reservoir solution contained 0.2 M sodium citrate (pH 5) and 13% PEG 6000. All SOD1 constructs were expressed recombinantly in *Escherichia coli*. Hb9:eGFP mouse embryonic stem cells were maintained and differentiated into motor neurons as previously described (32). Aggregated protein preparations were added to cultured neurons at the given final concentration, and viability was measured by MTT reduction assay. Details are provided in *SI Appendix*, *Materials and Methods*.

All zebrafish (*Danio rerio*) were maintained in accordance with standard laboratory conditions (23). The University of California, Los Angeles Chancellor's Animal Research Committee approved all experiments performed on zebrafish.

ACKNOWLEDGMENTS. We thank Lisa Johnson, David Borchelt, and Joan Valentine for discussions; Hamilton Trinh, Michael Collazo, Dullio Cascio, and staff at Argonne Photon Source, Northeastern Collaborative Access Team beamline 24-ID-E. We thank Hynek Wichterle (Columbia University) for the gift of Hb9:eGFP embryonic stem cells. We are grateful for the support to D.S.E. from the Howard Hughes Medical Institute, Department of Energy, and a grant from the National Institutes of Health (NIH) (AG029430). B.G.N. was supported by the University of California, Los Angeles (UCLA) Broad Center of Regenerative Medicine and Stem Cell Research, the Rose Hills Foundation, and grants from the National Institute of Neurological Disorders and Stroke (NS072804), Muscular Dystrophy Association (92901), and the California Institute for Regenerative Medicine (CIRM) (R61-01367 and R65-07480). C.M.K. was supported by grants from CIRM (RT307678) and the National Institute of General Medical Sciences (GM61721). M.T.B. was supported by grants from the NIH (AG047116) and the National Science Foundation (CHE-1301032 and CHE-1565941). S.S. was supported by a Whitcome Pre-Doctoral fellowship; K.L.A. was supported by the UCLA Cellular and Molecular Biology Training program (Ruth L. Kirschstein NIH Grant GM007185), a UCLA-California Institute for Regenerative Medicine Training Grant, and a UCLA Graduate Division Dissertation Year Fellowship; R.N. supported by a Larry L. Hillblom Foundation Fellowship; and C.K.J. was supported by a Beckman Research Scholarship.

- Alzheimer A (1906) Über einen eigenartigen schweren Erkrankungsprozeß der Hirnrinde. *Neurol Central* 25:1134. German.
- Baglioni S, et al. (2006) Prefibrillar amyloid aggregates could be generic toxins in higher organisms. *J Neurosci* 26:8160–8167.
- Eisele YS, et al. (2015) Targeting protein aggregation for the treatment of degenerative diseases. *Nat Rev Drug Discov* 14:759–780.
- Sawaya MR, et al. (2007) Atomic structures of amyloid cross- β spines reveal varied steric zippers. *Nature* 447:453–457.
- Tuttle MD, et al. (2015) Solid-state NMR structure of a pathogenic fibril of full-length human α -synuclein. *Nat Struct Mol Biol* 23:409–415.
- Walsh MA, et al. (2016) Atomic-resolution structure of a disease-relevant A β (1–42) amyloid fibril. *Proc Natl Acad Sci USA* 113:E4976–E4984.
- Berthelot K, Ts HP, Géan J, Lecomte S, Cullin C (2011) *In vivo* and *in vitro* analyses of toxic mutants of HET-s: FTIR antiparallel signature correlates with amyloid toxicity. *J Mol Biol* 412:137–152.
- Celaj MS, et al. (2012) Toxic prefibrillar α -synuclein amyloid oligomers adopt a distinctive antiparallel β -sheet structure. *Biochem J* 443:719–726.
- Sandberg A, et al. (2010) Stabilization of neurotoxic Alzheimer amyloid-beta oligomers by protein engineering. *Proc Natl Acad Sci USA* 107:15595–15600.
- Rosen DR, et al. (1993) Mutations in Cu/Zn superoxide dismutase gene are associated with familial amyotrophic lateral sclerosis. *Nature* 362:59–62.
- Sangwan S, Eisenberg DS (2016) Perspective on SOD1 mediated toxicity in amyotrophic lateral sclerosis. *Postepy Biochem* 62:362–369.
- Gurney ME, et al. (1994) Motor neuron degeneration in mice that express a human Cu, Zn superoxide dismutase mutation. *Science* 264:1772–1775, and erratum (1995) 269:149.
- Taylor JP, Brown RH Jr, Cleveland DW (2016) Decoding ALS: From genes to mechanism. *Nature* 539:197–206.
- Bruijn LI, et al. (1998) Aggregation and motor neuron toxicity of an ALS-linked SOD1 mutant independent from wild-type SOD1. *Science* 281:1851–1854.

15. Bruijn LJ, et al. (1997) ALS-linked SOD1 mutant G85R mediates damage to astrocytes and promotes rapidly progressive disease with SOD1-containing inclusions. *Neuron* 18:327–338.
16. Oztug Durer ZA, et al. (2009) Loss of metal ions, disulfide reduction and mutations related to familial ALS promote formation of amyloid-like aggregates from superoxide dismutase. *PLoS One* 4:e5004.
17. Zetterstrom P, et al. (2007) Soluble misfolded subfractions of mutant superoxide dismutase-1s are enriched in spinal cords throughout life in murine ALS models. *Proc Natl Acad Sci USA* 104:14157–14162.
18. Park Y-N, et al. (2012) Huntingtin fragments and SOD1 mutants form soluble oligomers in the cell. *PLoS One* 7:e40329.
19. Wright GSA, Antonyuk SV, Kershaw NM, Strange RW, Samar Hasnain S (2013) Ligand binding and aggregation of pathogenic SOD1. *Nat Commun* 4:1758.
20. Durazo A, et al. (2009) Metal-free superoxide dismutase-1 and three different amyotrophic lateral sclerosis variants share a similar partially unfolded beta-barrel at physiological temperature. *J Biol Chem* 284:34382–34389.
21. Shaw BF, et al. (2006) Local unfolding in a destabilized, pathogenic variant of superoxide dismutase 1 observed with HD exchange and mass spectrometry. *J Biol Chem* 281:18167–18176.
22. Taylor DM, et al. (2007) Tryptophan 32 potentiates aggregation and cytotoxicity of a copper/zinc superoxide dismutase mutant associated with familial amyotrophic lateral sclerosis. *J Biol Chem* 282:16329–16335.
23. Do TD, et al. (2016) Amyloid β -protein C-terminal fragments: Formation of cylinders and β -barrels. *J Am Chem Soc* 138:549–557.
24. Liu P, et al. (2015) Quaternary structure defines a large class of amyloid- β oligomers neutralized by sequestration. *Cell Rep* 11:1760–1771.
25. Cerf E, et al. (2009) Antiparallel β -sheet: A signature structure of the oligomeric amyloid β -peptide. *Biochem J* 421:415–423.
26. Hoyer W, Grönwall C, Jonsson A, Ståhl S, Härd T (2008) Stabilization of a beta-hairpin in monomeric Alzheimer's amyloid-beta peptide inhibits amyloid formation. *Proc Natl Acad Sci USA* 105:5099–5104.
27. Laganowsky A, et al. (2012) Atomic view of a toxic amyloid small oligomer. *Science* 335:1228–1231.
28. Eisenberg DS, Sawaya MR (2017) Structural studies of amyloid proteins at the molecular level. *Annu Rev Biochem* 86:69–95.
29. Rakhit R, et al. (2007) An immunological epitope selective for pathological monomer-misfolded SOD1 in ALS. *Nat Med* 13:754–759.
30. Liu H-N, et al. (2012) Targeting of monomer/misfolded SOD1 as a therapeutic strategy for amyotrophic lateral sclerosis. *J Neurosci* 32:8791–8799.
31. Valentine JS, Hart PJ (2003) Misfolded CuZnSOD and amyotrophic lateral sclerosis. *Proc Natl Acad Sci USA* 100:3617–3622.
32. Wichterle H, Lieberam I, Porter JA, Jessell TM (2002) Directed differentiation of embryonic stem cells into motor neurons. *Cell* 110:385–397.
33. Ivanova MI, et al. (2014) Aggregation-triggering segments of SOD1 fibril formation support a common pathway for familial and sporadic ALS. *Proc Natl Acad Sci USA* 111:197–201.
34. Gruzman A, et al. (2007) Common molecular signature in SOD1 for both sporadic and familial amyotrophic lateral sclerosis. *Proc Natl Acad Sci USA* 104:12524–12529.
35. Forsberg K, et al. (2010) Novel antibodies reveal inclusions containing non-native SOD1 in sporadic ALS patients. *PLoS One* 5:e11552.
36. Guareschi S, et al. (2012) An over-oxidized form of superoxide dismutase found in sporadic amyotrophic lateral sclerosis with bulbar onset shares a toxic mechanism with mutant SOD1. *Proc Natl Acad Sci USA* 109:5074–5079.
37. Ramesh T, et al. (2010) A genetic model of amyotrophic lateral sclerosis in zebrafish displays phenotypic hallmarks of motoneuron disease. *Dis Model Mech* 3:652–662.
38. Sakowski SA, et al. (2012) Neuromuscular effects of G93A-SOD1 expression in zebrafish. *Mol Neurodegener* 7:44.
39. Van Hoecke A, et al. (2012) EPHA4 is a disease modifier of amyotrophic lateral sclerosis in animal models and in humans. *Nat Med* 18:1418–1422.
40. Lemmens R, et al. (2007) Overexpression of mutant superoxide dismutase 1 causes a motor axonopathy in the zebrafish. *Hum Mol Genet* 16:2359–2365.
41. Levesque MP, Krauss J, Koehler C, Boden C, Harris MP (2013) New tools for the identification of developmentally regulated enhancer regions in embryonic and adult zebrafish. *Zebrafish* 10:21–29.
42. Wong PC, et al. (1995) An adverse property of a familial ALS-linked SOD1 mutation causes motor neuron disease characterized by vacuolar degeneration of mitochondria. *Neuron* 14:1105–1116.
43. Shi P, Gal J, Kwintar DM, Liu X, Zhu H (2010) Mitochondrial dysfunction in amyotrophic lateral sclerosis. *Biochim Biophys Acta* 1802:45–51.
44. Kiskinis E, et al. (2014) Pathways disrupted in human ALS motor neurons identified through genetic correction of mutant SOD1. *Cell Stem Cell* 14:781–795.
45. Vande Velde C, et al. (2011) Misfolded SOD1 associated with motor neuron mitochondria alters mitochondrial shape and distribution prior to clinical onset. *PLoS One* 6:e22031.
46. Magrané J, Cortez C, Gan W-B, Manfredi G (2014) Abnormal mitochondrial transport and morphology are common pathological denominators in SOD1 and TDP43 ALS mouse models. *Hum Mol Genet* 23:1413–1424.
47. Holm L, Rosenstrom P (2010) DALI server: Conservation mapping in 3D. *Nucleic Acids Res* 38:W545–W549.
48. Beamer LJ, Carroll SF, Eisenberg D (1997) Crystal structure of human BPI and two bound phospholipids at 2.4 angstrom resolution. *Science* 276:1861–1864.
49. Liu C, et al. (2012) Out-of-register β -sheets suggest a pathway to toxic amyloid aggregates. *Proc Natl Acad Sci USA* 109:20913–20918.
50. Treusch S, Cyr DM, Lindquist S (2009) Amyloid deposits: Protection against toxic protein species? *Cell Cycle* 8:1668–1674.
51. Arrasate M, Mitra S, Schweitzer ES, Segal MR, Finkbeiner S (2004) Inclusion body formation reduces levels of mutant huntingtin and the risk of neuronal death. *Nature* 431:805–810.
52. Kuperstein I, et al. (2010) Neurotoxicity of Alzheimer's disease A β peptides is induced by small changes in the A β 42 to A β 40 ratio. *EMBO J* 29:3408–3420.
53. Martins IC, et al. (2008) Lipids revert inert A β 25–233 oligomers to neurotoxic protofibrils that affect learning in mice. *EMBO J* 27:224–233.

Supporting Information:

Materials and Methods

SOD1(28-38) structure determination

Crystals of SOD1(28-38) with P28K substitution were grown by hanging drop vapor diffusion using VDX plates (Hampton Research, Aliso, Viejo, CA). Lyophilized peptide at 98% purity (Genscript Inc.) was dissolved to 50 mg/ml in 50 mM Tris-base buffer. The reservoir solution contained 0.2 M sodium citrate pH 5 and 13% PEG 6000. Crystallization drops were prepared by mixing peptide with reservoir in a 2:1 ratio, in a total volume of 2 μ L. Thick needle-like crystals appeared overnight and harvested after 2-3 days growth at ambient temperature. For isomorphous replacement, the crystals were soaked for 30 seconds in a solution composed of approximately 60% KI stock solution (prepared by dissolving solid KI to 0.5 M in reservoir), 30% reservoir solution, and 10% glycerol stock for cryoprotection. The crystals were subsequently flash frozen in liquid nitrogen. Single crystals were mounted with CrystalCap HT Cryoloops (Hampton Research, Aliso Viejo, CA). All data were collected at the Advanced Photon Source (Chicago, IL) on beamline 24-ID-E, which has a 5 μ m microfocus beam suitable for the crystals. All data were processed using DENZO and SCALEPACK or XDS (1). SIRAS phasing produced an interpretable map and the structure was built using COOT (2). Model refinement was performed using REFMAC (3) and BUSTER (4). Figures were generated using PyMol (5). Unless stated otherwise, SOD1(28-38) refers to KVKVWWSIKGL.

Molecular Dynamics simulations

We performed all-atom MD simulations of SOD1 and α B crystallin on Anton (6, 7), a special-purpose computer designed to accelerate standard molecular dynamics simulations by orders of magnitude. Protein, water, and ions were represented explicitly, using the AMBER 99SB*-ILDN (8–10) force field and the TIP3P water model (11). Simulations of the SOD1 corkscrew were initiated from the crystal structure comprised of an eight-stranded corkscrew with either a wild-type (KVKVWWSIKGL and PVKVWWSIKGL) or G33W mutant (KVKVWWSIKGL and PVKVWWSIKGL) monomer sequence. Initial structures were placed in a cubic box 76 \AA on each side and solvated with approximately 13,000 water molecules and 150 mM NaCl. The systems were minimized and then equilibrated in the NPT ensemble at 1 bar and 300 K for 50 ns with 5 kcal mol⁻¹ \AA ⁻² harmonic position restraints applied to all non-hydrogen atoms of the protein; these restraints were tapered off linearly over 50 ns. Production runs were initiated from the final snapshot of the equilibration run and performed in the NVT ensemble using a 2.5 fs time step. Non-bonded interactions were truncated at 12 \AA . The wild-type (KVKVWWSIKGL and PVKVWWSIKGL) and G33W mutant (KVKVWWSIKGL and PVKVWWSIKGL) corkscrew simulations were run for 16.4 μ s, 13.8 μ s, 16.6 μ s and 15.2 μ s, respectively. RMSDs in Figs. 1E and S4C were calculated on the hydrophobic core of the corkscrew (C α atoms of residues 3 to 9, excluding the chains at the end).

SOD1 oligomer assembly simulations were initiated from three monomers of a tandem repeat structure (KVKVWWSIKGL--GG--KVKVWWSIKGL) built in homology to a monomer of the tandem repeat structure of α B crystallin cylindrin (PDB ID 3SGR (12)). These monomers were separated in space by at least 30 \AA ,

placed in a box 62 Å on each side, and solvated with approximately 7,600 water molecules and 150 mM NaCl. System preparation and simulations then proceeded as described above for the SOD1 corkscrew simulations. Each monomer was weakly restrained such that its C α root-mean-square deviation (RMSD) was within approximately 2 Å of the starting structure. In particular, a flat-bottom harmonic restraint, U , was applied to each monomer such that $U(R) = \frac{1}{2}k(R - R_0)^2$ for $R > R_0$, and $U(R) = 0$ otherwise. Here, R is the RMSD from the initial structure, $R_0 = 2$ Å, and $k = 50$ kcal mol $^{-1}$ Å $^{-2}$. The flat-bottom RMSD restraints limit the monomers' sampling of very collapsed structures and structures that have significantly reduced β -sheet content, and allow simulations to focus on discovering possible amyloid-like oligomers. We ran 20 assembly simulations beginning from the same starting conformation with different initial velocities drawn from a Maxwell-Boltzmann distribution. Of the twenty simulations, four were run for 4 μ s and the rest were run for 1 μ s.

The α B crystallin assembly simulations were initiated from three monomers of the tandem repeat structure of α B crystallin (GKLKVLGDVIEV--GG--KLKVLGDVIEV, PDB ID 3SGR). System preparation and simulation protocol were as above, except that we ran 10 assembly simulations in this case. Of these 10 simulations, two were run for 5 μ s, two were run for 2 μ s, and the rest were run for 1 μ s.

Full-length model of corkscrew oligomers

We tested the hypothesis that full-length SOD1 is compatible with a corkscrew oligomer assembly by constructing a model. We aimed to achieve the following three goals: (i) maintain residues 28-38 in the exact corkscrew conformation as observed in the crystal structure of this segment; (ii) maintain the tertiary structure of native SOD1 intact for all remaining residues; (iii) maintain good stereochemistry and avoid steric overlap throughout. Coordinates of the native SOD1 fold were obtained from PDB ID code 2C9S, the 1.24 Å resolution structure of Zn-Zn human superoxide dismutase (13).

It was obvious by inspection that residues 28-38 must detach from the native SOD1 fold to expose its main chain for hydrogen bonding with the identical segment of other protomers and thereby form the twisted β -sheet that constitutes the corkscrew spine. Residues 28-38 encompass the third β -strand (β 3) of the native SOD1 8-stranded β -barrel fold. This strand is hydrogen-bonded on both edges with its neighboring strands in the barrel, β 2 and β 6. The least disruptive way that we could find to expose β 3 was to detach both β 2 and β 3 from the native barrel. This pair of strands is connected by only a short hairpin, so β 3 would not be able to fully detach from the barrel without the co-detachment of β 2. The alternative possibility, which is to detach strands 3 and 4 from the native fold, would disrupt more hydrogen bonds and van der Waals contacts.

We positioned and oriented the native SOD1 barrels in close proximity to the fixed coordinates of the corkscrew crystal structure (residues 28-38). The degrees of freedom for positioning and orienting the SOD1 barrels were limited by the constraints that barrel residues 27 and 39 be placed within a covalent bond length of residues 28 and 38 of the corkscrew, and that there be no steric clashes between

neighboring protomers. To aid in the positioning and orienting of the SOD1 barrels, we defined the helical symmetry operations of the corkscrew structure (pitch 71 Å, 16 strands per turn, two-fold symmetry axes perpendicular to helix axis), and applied these operations to a single SOD1 barrel. We interactively manipulated a single SOD1 barrel in the graphics program “O” (14), which simultaneously propagated each manipulation to the helical symmetry-related copies. Thus we were able to visually explore the orientations and positions of the SOD1 barrel that met the constraints of close proximity and steric clash avoidance while maintaining the helical symmetry of the corkscrew.

After suitably positioning and orienting the SOD1 barrel around the corkscrew spine, we covalently linked barrel residues 27 and 39 to corkscrew residues 28 and 38, respectively, using the graphics program Coot (15). At the N-terminal connection (residue 27 to 28), we note that we reoriented $\beta 2$ (residues 15-22) to disrupt its main chain hydrogen bonds with $\beta 3$, as was necessary to permit copies of $\beta 3$ to self-associate as a corkscrew. To recover some of the main chain hydrogen bonds that were lost when $\beta 2$ was separated from $\beta 3$, we positioned pairs of $\beta 2$ strands from neighboring protomers to form main chain hydrogen bonds. To make the connections stereochemically plausible, it was necessary to slightly perturb the conformation of the three hairpin forming residues at the C-terminus of the corkscrew β -strand (residues 36-38). One full turn, 16 protomers, were energy minimized with the program CNS (16), with hydrogen bond potentials included (17).

Expression and purification of SOD1 constructs

All SOD1 constructs were expressed recombinantly in *E. coli*. All recombinant proteins are based on a SOD1 background strain that carries a C6A, C111S double mutation to simplify the purification. The SOD1 gene was inserted into the pET22b vector from Novagen with NcoI and Sall restriction enzyme digestion sites (gift from Professor Joan Valentine’s lab at UCLA). Mutations in the SOD1 gene were made using the QuickChange Site-Directed mutagenesis Kit (Stratagene). The plasmid was transformed into the BL21(DE3)Gold (Agilent Technologies) expression strain. For expression, 10 ml LB + Amp (100 $\mu\text{g}/\text{mL}$) was inoculated from frozen stock and grown overnight. 10 ml of starting culture was added to a 2 L flask of 1 L LB + Amp (100 $\mu\text{g}/\text{mL}$) and grown for 3 hours at 37 °C to $\text{OD}_{600} = 0.6$. IPTG was then added to 1 mM and Zn^{2+} was added to 0.05 mM to induce protein expression, which continued for an additional 3 hours. The bacterial pellet was collected by centrifugation at 4000 rpm for 10 mins.

To purify SOD1 from the bacteria, osmotic shock was used to release proteins including SOD1 from the periplasm. First, the cell pellet was resuspended in 30 mL of 30 mM Tris-HCl pH 8 with 20% sucrose and stirred slowly for 20 mins. The cells were collected by centrifugation at $10,000 \times g$ at 4 °C for 10 mins. The pellet was then resuspended in 30 mL of ice-cold water and stirred slowly for 20 mins on ice to release periplasmic proteins. Next, cell debris was removed by centrifugation at 4 °C for 10 mins at $10,000 \times g$. The contaminant proteins were then removed by precipitation with ammonium sulfate. 0.326 g/ml $(\text{NH}_4)_2\text{SO}_4$ was added to the supernatant, and the solution was stirred at 4 °C for 45 mins. The protein was purified out of ammonium sulfate by separation over a phenyl sepharose column. The column was equilibrated with buffer A (2 M $(\text{NH}_4)_2\text{SO}_4$, 0.15 M NaCl, 0.05 M NaH_2PO_4 , pH 7.0) and buffer B (0.15 M NaCl, 0.05 M NaH_2PO_4 , pH 7.0). The protein eluted at 6-

30% buffer B. The protein was then concentrated and further purified by size exclusion chromatography on a silica G3000 column (Tosoh Bioscience). The column buffer comprised 0.1 M sodium sulfate, 25 mM sodium phosphate, and 1 mM sodium azide, pH 6.5.

SOD1 demetallation (required for aggregation)

The protein constructs purified by size exclusion chromatography were dialyzed in four buffers at 4°C to remove the bound metals. Protein preparations were put in a dialysis cassette (10 kDa molecular weight cutoff) and exchanged with buffer 1 twice (100 mM Na Acetate pH 3.8, 10 mM EDTA pH 8.0), followed by exchange with buffer 2 (100 mM Na Acetate pH 3.8, 100 mM NaCl, 1 mM EDTA pH 8.0), buffer 3 (100 mM Na Acetate pH 5.5, 100 mM NaCl, 1 mM EDTA pH 8.0), and finally buffer 4 (20 mM K Phosphate pH 7.0, 1 mM EDTA pH 8.0). Each exchange lasted 12 hours. To avoid metal contamination, all stock solutions (except for EDTA) were treated with Chelex 100 resin (Bio-Rad) to remove trace metals and all beakers were rinsed with metal-free water.

Protein and peptide aggregation

Full-length SOD1: Following metal removal, proteins were concentrated using a centrifugal concentrator (10 kDa molecular weight cutoff) to 800 μ M (monomer) stock concentration and stored at -80 °C in 50 μ L aliquots until further use. Aggregation assays were carried out in 1.5 mL microcentrifuge tubes (Fisher Scientific) under acidic conditions with 80 μ M SOD1, 50 mM sodium acetate, 1 mM EDTA and 1 mM TCEP, pH 3.5. Preparations were agitated at 900 rpm (in Torrey Pine Shakers) at 37 °C for indicated times. These samples were then dialysed with 10 mM potassium phosphate and 1 mM EDTA, pH 7.0 for 4 hours at 4 °C.

Peptide: Peptide segments were aggregated by incubation at 37 °C for 12 hours with agitation in 50 mM tris-base buffer and added to cultured neurons.

Differentiation of mESCs to motor neurons

Hb9:eGFP mESCs were maintained and differentiated into motor neurons as previously described (18). Briefly, mESCs were first plated on gelatin to remove mouse embryonic fibroblasts (MEFs) prior to differentiation, and then plated in 60 mm bacterial petri dishes in core motor neuron medium (DMEM/F12, Neurobasal, 10% Knockout Serum Replacement, Pen-Strep, Glutamax) to induce embryoid body (EB) formation. Two days later, N2 supplement (1x), retinoic acid (1 μ M; Sigma), and SAG (1 μ M; Calbiochem) were added to the EBs. Media was changed every two days. After five days post-retinoic acid and SAG addition, Hb9:GFP EBs were dissociated using ice-cold 0.25% Trypsin-EDTA for 6 minutes at room temperature, followed by trituration in L-15 medium (Hyclone). Dissociated motor neurons were plated in core motor neuron medium with GDNF, BDNF, CNTF (all 10 ng/ml; Peprotech) on 96-well plates that were previously coated with poly-L-ornithine (0.01%; Sigma) and laminin (5 μ g/ml; BD Biosciences) and incubated for 12-16 hrs before treatment with the SOD1 peptides or proteins. Approximately 80,000 cells were plated per well. All reagents are from Invitrogen, unless otherwise noted.

Cytotoxicity Assays

Aggregated protein preparations were added to cultured neurons at the given final concentration. Unless stated otherwise, all full-length proteins were aggregated for 12 hours before adding to motor neurons at 8 μ M final concentration. Motor neurons were incubated for 12-16 hrs and imaged (Axio Observer.D1 microscope, Zeiss), followed by cell viability assay. Cell viability was measured using the commercially available MTT assay (Promega Cat#G4100) according to the manufacturer's protocol with 4 hour incubation with the MTT reagent. All data were normalized using buffer as 100% viability and 0.2% SDS as 0% viability. Experiments were performed in triplicates and repeated a minimum of three times.

Electron Microscopy

Each 3-5 μ L sample was spotted directly on freshly glow-discharged carbon-coated electron microscopy grids (Ted Pella, Redding, CA). After 4 min incubation, grids were rinsed twice with 5 μ L distilled water and stained with 5 μ L of 2% uranyl acetate for 1 min. Excess uranyl acetate was removed by blotting and specimens were examined on a T-12 electron microscope at an accelerating voltage of 80 kV. Images were recorded digitally by wide angle (top mount) BioScan 600W 1 \times 1K digital camera (Gatan, Pleasanton, CA).

Dot Blot Assay

3-5 μ L sample was spotted on a nitrocellulose membrane (Trans-Blot, Bio-Rad) followed by blocking with 10% fat-free milk in 1X TBST buffer (50 mM Tris, 150 mM NaCl, 0.05% Tween20) for 30 mins. Membranes were incubated with primary antibody – SOD100 (Enzo Life Sciences) at 1:1000 dilution, A11 (EMD Millipore) at 1:500 diluted in 5% fat free milk in TBST buffer at room temperature for 1 hour. The membranes were washed three times in TBST buffer before incubating with HRP-linked secondary antibody - anti-mouse HRP secondary antibody (Life Technologies) at 1:10000 dilution, or anti-rabbit HRP secondary antibody (Life Technologies) at 1:10000 diluted in 5% fat-free milk in TBST buffer at room temperature for 1 hour. Pierce ECL Western Blotting Substrate, (Thermo Scientific, #32209), a chemiluminescent substrate was used for the detection of horseradish peroxidase (HRP) on the immunoblots following the manufacturer's instructions. A detailed protocol can be found at the following URL, https://tools.thermofisher.com/content/sfs/manuals/MAN0011536_Pierce_ECL_West_Blot_Substr_UG.pdf

Thioflavin-T (ThT) Assay

Fibril formation assays were performed with 80 μ M protein concentration in 50 mM sodium acetate buffer, 1 mM EDTA, 1 mM TCEP, pH 3.5 and 10 μ M ThT – conditions identical to those used for aggregating proteins for the cytotoxicity assays, but with the addition of ThT. All assays were carried out in black Nunc 96-well optical bottom plates (Thermo Scientific). Plates were agitated at 300 rpm in 3-mm rotation diameter in a Varioskan microplate reader (Thermo) at 37 $^{\circ}$ C. Fluorescence measurements were recorded every 30 mins using $\lambda_{\text{ex}} = 444$ nm, $\lambda_{\text{em}} = 482$ nm, with an integration time of 200 μ s.

Mass Spectrometry

Peptide segments were dissolved in 20 mM ammonium acetate buffer (pH = 7) to a final concentration of 200 μ M and incubated at room temperature without agitation.

Experiments were carried out at time t_0 and every day for a week and ion mobility was used to calculate the cross sections of oligomers. The peptide samples were nano-electrosprayed on a home-built, high-resolution ion mobility mass spectrometer (19) consisting of a source ion-funnel, a two-meter long drift cell, an exit funnel, a quadrupole mass analyzer and detectors. The ions were stored and focused in the source funnel and subsequently pulsed into the drift cell filled with helium gas at high pressure. A drift voltage was applied across the cell to create a weak electrical field. The ions moved forward under the influence of the electrical field, and at the same time experienced the drag force due to multiple collisions with helium buffer gas. An ion traveled with a constant velocity that reflected its size and shape. At the end of the drift cell, the ions were collected by an exit funnel where they were steered and focused into a quadrupole mass analyzer and detected as a function of arrival time in the arrival time distributions (ATDs). By measuring ATDs at different pressure to voltage (P/V) ratios, the absolute mobility of the ion of interest could be measured:

$$t_A = \frac{l^2}{K_0} \frac{273.16 K}{760 \text{ torr} \cdot T} \cdot \frac{P}{V} + t_0 \text{ (Eq. 1)}$$

In Eq. 1, l is the length of the drift cell, P is the gas pressure in torr, V is the voltage across the cell, and t_0 is the time the ions spend outside the drift cell before reaching the detector. The collision cross section σ can then be approximated from K_0 (20)

$$\sigma \approx \frac{3q}{16N} \left(\frac{2\pi}{\mu k_B T} \right)^{\frac{1}{2}} \frac{1}{K_0} \text{ (Eq. 2)}$$

Here, N is the buffer gas density, μ is the reduced mass of the collision system (He^+ ion) and k_B is Boltzmann's constant. The cross section contains information about the three dimensional structure of the ion. In the ATDs shown in Fig. S6, underneath each experimental peak is a dotted line representing the peak shape expected for a single conformer (21).

Zebrafish

All zebrafish (*Danio rerio*) were maintained in accordance with standard laboratory conditions (22). The University of California, Los Angeles (UCLA) Chancellor's Animal Research Committee approved all experiments performed on zebrafish. The TDL6 (Tübingen driver line) zebrafish used in all experiments were identified in a screen for developmentally regulated enhancers that drive tissue-specific expression. Gal4-driven GFP expression marks primary motor neurons. Mitochondria were marked by a TOL2-mediated insertion of a Gal4-UAS-MLSsRed construct (23).

RNA production and injections

SOD1 constructs used for zebrafish expressions were the full-length sequence with Cys6 and Cys111 intact. The constructs (WT, G93A, G93A/G33V, A4V, A4V/G33V) were subcloned into pcGlobin2 vector and the constructs were linearized using XbaI to generate RNA. The Translation efficiency of the RNA of all constructs was tested by ThT® Quick Coupled Transcription/Translation System (Promega) using the manufacturer's instructions. Construct G93A/G33V has an additional mutation of I18G designed to prevent steric clashes due to the presence of G33V in the native SOD1 barrel. As a control, we also tested the cytotoxicity of this construct in cell culture and found that it was non-toxic similar to G33V construct (Fig. S9B). RNA was transcribed using the mMessage Machine T7 kit (Ambion) and the mRNA was diluted to 500 ng/ μL and 1000 ng/ μL aliquots and stored at -80°C . 1 μL mRNA at 500 ng/ μL (WT, G93A, G93A/G33V) and at 1000 ng/ μL (WT, A4V, A4V/G33V) was

injected into TDL6 embryos from timed mating at the 1-4 cell stage. Embryos were incubated in 1x E3 buffer at 28.5 °C.

Analysis of axonopathy

At 2 dpf (days post fertilization) zebrafish larvae microinjected with SOD1 constructs were anesthetized in 0.01% tricaine and imaged using a Leica MZ16F fluorescent stereoscope at 11.5X magnification. Observers were blinded and the length from the exit point of the spinal cord to the tip of the motor axon was measured for 5 axons per embryo corresponding to axons 12-16 - using Fiji Simple Neurite Tracer. Experiments were repeated multiple times and a minimum of 72 embryos were assessed for each construct.

Analysis of Mitochondrial defects

The mitochondrial network from the base of the spinal cord to the tip of the motor axon was imaged on a Leica TCS SP8 confocal microscope at 10X magnification with a 1.5X optical zoom. Images were processed with the Leica AF software and mitochondria size was measured for 5 axons per embryo using Fiji Image J Particle Analysis with the described algorithm (24). Before quantification, fluorescence from the spinal cord and regions outside of the larvae body were excluded. The program allowed automatic detection of isolated fluorescent spots by threshold and watershedding of binary formatted images without introducing user-bias. Spots with a circularity of 0.5-1 were selected to have their intensity and area quantified, where 1 is a complete circle. Intensity was quantified for each spot via overlapping gray levels.

Protein expression in zebrafish

Protein expression was confirmed by western blotting (Fig. S9). Zebrafish embryos were pooled from each group at 2 dpf and washed twice in Ringer's buffer (NaCl 135 mM, KCl 5 mM, MgSO₄ 1mM, K₂HPO₄ 0.4 mM, Glucose 5.5 mM, HEPES 20 mM pH 7.4). They were subsequently deyolked and dechorionated and lysed in RIPA buffer (Sigma) (volume equals twice the number of embryos in μ L) with Halt protease inhibitor cocktail EDTA-free (Thermo Scientific) added. Lysates were homogenized by sonication and protein concentration was determined using the BCA protein assay kit (Thermo Fisher Cat #23252). Equal amounts of protein were loaded on 12% Tris-glycine PAGE gels and transferred onto a PVDF membrane using an iBlot dry blotting system (Thermo Fisher) at 20 V for 6 mins. Membranes were washed with methanol followed by water and then blocked with 10% fat free milk in TBST for 1 hr at room temperature and washed three times with TBST buffer. Membranes were incubated with primary antibodies – SOD100 (Enzo Life sciences) at 1:500 dilution in 5% milk in TBST and incubated for 1hr at room temperature or anti β -actin (Abcam) at 1:1000 diluted in 5% milk in TBST and incubated overnight at 4°C. Membranes were first probed with SOD100 and then stripped using Restore PLUS Western Blot stripping buffer (Thermo Scientific) and subsequently probed with anti β -actin. Blots were washed thrice with 1X TBST and subsequently incubated with the secondary anti-rabbit HRP secondary antibody (Sigma) at a 1:10000 dilution in 5% milk in TBST for 1hr at room temperature. Pierce ECL Western Blotting Substrate, (Thermo Scientific, #32209), a chemiluminescent substrate was used for the detection of horseradish peroxidase (HRP) on the immunoblots following the manufacturer's instructions.

Statistical Significance

All statistical analyses were done using GraphPad Prism 7.0.

Antibodies used

The following antibodies were used in this study. SOD100 (EnzoLife sciences) at 1:1000 dilution, A11 (EMD Millipore) at 1:500 dilution, anti β -actin (Abcam) at 1:1000, anti-mouse HRP secondary antibody (Life technologies) 1:10000 dilution, anti-rabbit HRP secondary antibody (Life technologies) 1:10000 dilution.

Supporting Text

Prediction of oligomer forming segments in SOD1

Several reports have suggested that oligomers formed by amyloid proteins have a pore or barrel shape and are composed of antiparallel β -strands (25, 26). To investigate segments in SOD1 that may be critical for oligomer formation, we applied a combination of 3D-profiling and manual sequence fitting using a model of antiparallel β -sheet structure that we had previously discovered, termed cylindrin (12) (Fig. S1). In order to predict which 11-residue segments of SOD1 might form a cylindrin-like structure, we analyzed the cylindrin structure by visual inspection and computational modeling. We examined the structural features of the native cylindrin, and compared these with cylindrin models of segments from other proteins. Our analysis followed three stages:

1. Computational prediction of cylindrin-compatible segments by 3D profiling

Using a process analogous to our 3D profile method for predicting steric-zipper-forming segments (27), we used the Rosetta modeling suite (28) for high-throughput computational modeling and prediction of cylindrin-forming segments (Fig. S1A). Starting from the 6-stranded cylindrin barrel structure (from PDB 3SGO), we stripped off all side-chain atoms, then threaded on each 11-residue sequence segment of several amyloid proteins (The same 11-residue sequence segment was threaded onto each of the six strands of the cylindrin.). Side chains matching the amino acid sequence of the segment being threaded were attached to the backbone and repacked; this selects an energetically favorable rotamer at each position. The backbone was then randomly perturbed by small sub-Angstrom moves, followed by repacking for up to 1000 iterations, or until energetic convergence. We then used the final, minimized Rosetta energy scores to rank the threaded protein segments—those with the lowest energy show the best compatibility with the cylindrin structure. The default Rosetta energy function (Talaris2013) was used.

2. Analysis of computational predictions and visual comparison with the native cylindrin

Among the lowest-energy computational predictions, one sequence feature immediately stood out – glycine at position 6. A closer look at the native cylindrin structure revealed why: glycine's lack of side chain provides room for the adjacent, inward-facing valine side chains (at position 4) to pack. As shown in Figure S1C, unrolling the cylindrin barrel to view the interior surface reveals a series of 'knobs' (valine 4 side chains, cyan) that can pack into 'holes' (green) provided by glycine. Without these glycine 'holes', the interior of the barrel would be too full, forcing the β -strands apart. A swap in the positions of knobs and holes (that is, moving glycine to position 4, and valine to position 6) might also be expected to allow the barrel to close. However, the computational modeling never gave low scores to segments with swapped knobs and holes. The reason we found is that the cylindrin backbone torsion angles at position 6 favor glycine.

Our analysis of the cylindrin's interior packing also highlighted the importance of the other inward-facing side chains, which pack in symmetric layers (Fig. S1B). From

the center, and moving outward, these are valine 4, valine 8, and valine 2. The valines form a hydrophobic core, which together with hydrophilic side chains on the exterior likely promote assembly of the cylindrin. Based on these observations, our expectation was that good candidates for cylindrin formation would have three features: (1) a glycine at either position 4 or 6; (2) segregated hydrophobic and hydrophilic residues, in inward- and outward-facing positions, respectively; and (3) appropriately sized inward-facing residues, to optimize packing in the narrow interior of the barrel.

We therefore went on to analyze the predicted structures of the lowest-energy models, to see whether our expectations matched the computational predictions. As mentioned above, all of the lowest-energy segments had glycine at position 6. Regarding segregation of hydrophobic and hydrophilic residues, there was no clear pattern. Some low-energy segments were nearly completely hydrophobic. Others had polar, or even charged, residues positioned in the interior. Some of these polar residues, such as asparagine, were positioned to largely fulfill potential hydrogen bonds. Others, such as serine and histidine, were generally not able to hydrogen bond with adjacent side chains, suggesting their segments are unlikely to form a cylindrin. We concluded that while Rosetta seemed well-able to handle steric considerations when packing side chains, it had more difficulty handling charge and hydrogen-bonding considerations.

The sizes and shapes of interior side chains in low-energy models fit better with our expectations. Valine, and similarly sized side chains like threonine and isoleucine, packed quite well (Fig. S1D). Slightly larger side chains of methionine and histidine also fit (Fig. S1E, S1F). Even larger side chains, such as phenylalanine, tyrosine, and tryptophan, were absent in top-scoring segments. Side chains smaller than valine, such as alanine, serine, and even glycine, also came out in top-scoring segments (Fig. S1G, S1H). Although these did not give rise to steric clashes, they did leave visible gaps in the interior, which we hypothesized would be less favorable than if the holes were filled (similar to the original cylindrin).

3. Manual selection of cylindrin-compatible segments

Although the 3D profile method provided a number of reasonable predictions, there were enough deviations from our expectations that we also performed a manual search for cylindrin-compatible segments (Fig. S1I). We began by casting a wide net, using a sequence-based search to pull out any segments that matched either a basic pattern found in the cylindrin core sequence or in variations that we predicted were possible (for example, swapped ‘knob’ and ‘hole’ positions). Adjacent to the glycine ‘hole’, we restricted possible ‘knob’ residues to five: valine, isoleucine, leucine, methionine, and threonine. Sequences matching at least one of these basic patterns were then screened for clearly unfavorable features at other positions, and removed accordingly.

From an initial group of 143, 11-residue segments spanning the full sequence of SOD1, our screen yielded 4 overlapping sequences from the N-terminal region: segments 28-38, 30-40, 32-42, and 34-44. One of these, 32-42, was also predicted by our computational threading. A re-examination of the 28-38 segment showed that the small backbone movements allowed in our computational threading could not relieve

a clash between the proline at position 1 and the position 11 leucine of the neighboring strand, without breaking apart the structure.

As mentioned above inward facing glycines are critical for the hydrophobic packing. Among the 4 segments, 28-38 was the only segment with glycine at position 6 that is conserved in ALS patients and contains a central stretch of amino acids that are conserved in ALS patients (Fig. S2). Interestingly, the segment has also been found to be prone to local unfolding by H/D exchange and mass spectrometry studies and small molecule inhibitors of aggregation are found to bind this segment (29–31). Keeping these reports in mind, the segment 28-38 was chosen for further characterization.

Mass assignment by ion-mobility mass spectrometry (IM-MS)

A detailed experimental workflow for IM-MS experiments has been described elsewhere (32, 33). In this experiment, the ions were generated by n-ESI, stored in an ion-funnel, and subsequently pulsed into a drift cell filled with helium gas at $P = 13$ torr. The ions move through the drift cell toward the quadrupole mass analyzer under the influence of both a weak electrical field and a drag force caused by collisions with buffer gas. For the same oligomer with different conformations, those that are more extended will experience more collisions with the buffer gas, thus travel slower than those that are more compact. For oligomers with different sizes, species with higher charges are affected more by the electrical field ('drift' voltage) and travel faster than species with smaller charges. For example, a dimer with $z = +2$ charge will travel faster than a monomer with $z = +1$ charge, and the ATD (arrival time distribution) feature corresponding to the dimer will have a shorter arrival time than that of the monomer (34). By measuring the arrival times at different pressure to drift-voltage ratios, experimental collision cross sections can be measured for all features in the ATDs. The values can be compared to the cross sections obtained from theoretical modeling and x-ray crystallography.

The mass spectra of the cylindrin and corkscrew forming peptides are shown in Figure S6, panels A and B. Despite the difference in charge states in solution, major peaks with $n/z = +1/2, +2/3, +1/1$ and $+5/4$ were observed in the mass spectra for both peptides. SOD1(28-38) has additional peaks of $n/z = +1/3$ and $+3/4$. In addition, since SOD1(28-38) is highly charged, salt-adduct peaks are also observed, which are not observed in the mass spectra of the cylindrin segment.

We focused our analysis on the $n/z = 1/1$ mass spectral peaks of both segments since they contain multiple features that may correspond to large oligomers. First, we analyzed the ATD of the cylindrin segment, which has been shown to form hexamers by x-ray crystallography. The ATD shows multiple features (Fig. S6A), and we can unambiguously identify the monomer ($\sigma = 268 \text{ \AA}^2$) and dimer ($\sigma = 440 \text{ \AA}^2$) at 108.95 and 90.40 ms, respectively. The $z = +1$ monomer observed at this ATD has a similar cross section to $z = +2$ monomer at 599 m/z ($\sigma = 263 - 274 \text{ \AA}^2$, data not shown). Similarly, the cross section of $z = +2$ dimer is similar to $z = +3$ dimer at 799 m/z ($\sigma = 442 - 452 \text{ \AA}^2$, data not shown). The next peak at 85.5 ms is assigned a trimer with $\sigma = 625 \text{ \AA}^2$, as it does not fit a dimer. The spacing between the 75.75 ms peak and its adjacent peak at 85.5 ms (10.2 ms) is much larger than the spacing between dimer and trimer (4.85 ms). Thus, it cannot be classified as a tetramer and fits a hexamer with a cross section of 1122 \AA^2 . To resolve the size of the peak at 69.65 ms, we compared the mass spectra at different time points. The ATD of cylindrin after 24 hours shows a rearrangement in the peaks (Fig. S6D). The dimer and trimer peaks are essentially gone, while the hexamer peak at 75.75 ms is relatively unchanged. The peak at 69.65 ms increased in intensity, and no further peaks at shorter times have appeared. Hence the 69.65 ms peak is most likely the terminal stable soluble oligomer. The best assignment for the 69.95 ms peak is a compact hexamer with a cross section of $1020 - 1023 \text{ \AA}^2$. If we use the X-ray coordinates of the cylindrin, we obtain a cross section of $\sigma_{av} = 1029 \text{ \AA}^2$ (σ_{av} is the average cross section obtained from the trajectory and projected superposition approximation methods) (33, 35, 36), in excellent agreement with this assignment. Thus, it appears there are two stable hexamers of cylindrin, one open and one compact.

Next, we analyzed the mass spectra of SOD1(28-38). In this case, the $n/z = 1/1$ mass spectral peak initially appears to have a single, broad feature as its ATD (Fig S6E). After 24 hours, a more intense ATD is observed and now two features are resolved (Fig. S6F). Given our results for the cylindrin segment discussed above, the arrival times of these two features correspond to open (1189 \AA^2) and compact (1113 \AA^2) hexamers. The X-ray coordinates of SOD1(28-38) yield a cross section of $\sigma_{av} = 1182 \text{ \AA}^2$ that increases to 1226 \AA^2 after 20-ns of MD relaxation, in good agreement with experiment. Similar to the cylindrin segment, the terminal species appears to be a hexamer for SOD1(28-38). In addition, the compact feature in the ATD is broad suggesting numerous “cylindrin-like” structures. If we thread the sequence of SOD1(28-38) on the backbone of the cylindrin structure, we obtain a cross section of 1107 \AA^2 , which is near the $\sigma_{av} = 1113 \text{ \AA}^2$ experimental cross section calculated above. This calculation supports our assignment of the broad peak centered near 74 ms as a compact, cylindrin-like hexamer. Thus, in solution, SOD1(28-38) segment forms oligomers similar in cross section to the observed crystal structure of the corkscrew and a more closed, cylindrin-like structure.

References:

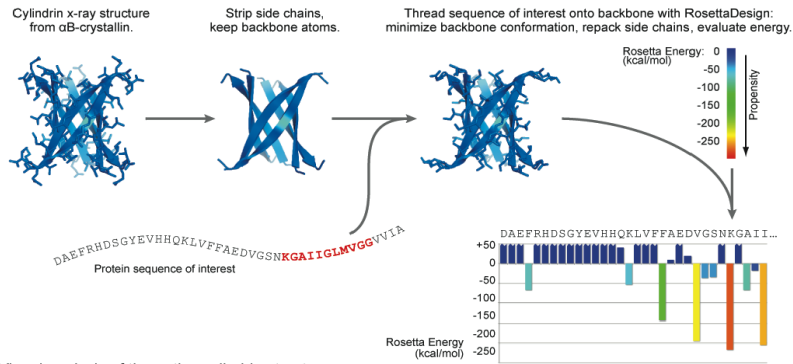
1. Kabsch W (1993) Automatic processing of rotation diffraction data from crystals of initially unknown symmetry and cell constants. *J Appl Crystallogr* 26(6):795–800.
2. Emsley P, Cowtan K (2004) *Coot*: model-building tools for molecular graphics. *Acta Crystallogr D Biol Crystallogr* 60(12):2126–2132.
3. Vagin AA, et al. (2004) *REFMAC 5* dictionary: organization of prior chemical knowledge and guidelines for its use. *Acta Crystallogr D Biol Crystallogr* 60(12):2184–2195.
4. Bricogne G, et al. BUSTER version 1.10.0. Cambridge, United Kingdom: Global Phasing Ltd.
5. Delano W The PyMOL Molecular Graphics System. (2002).
6. Shaw DE, et al. (2009) Millisecond-scale molecular dynamics simulations on Anton (ACM Press), p 1.
7. Shaw DE, et al. (2014) Anton 2: Raising the Bar for Performance and Programmability in a Special-Purpose Molecular Dynamics Supercomputer (IEEE), pp 41–53.
8. Hornak V, et al. (2006) Comparison of multiple Amber force fields and development of improved protein backbone parameters. *Proteins Struct Funct Bioinforma* 65(3):712–725.
9. Best RB, Hummer G (2009) Optimized Molecular Dynamics Force Fields Applied to the Helix–Coil Transition of Polypeptides. *J Phys Chem B* 113(26):9004–9015.
10. Lindorff-Larsen K, et al. (2010) Improved side-chain torsion potentials for the Amber ff99SB protein force field. *Proteins Struct Funct Bioinforma*:NA-NA.
11. Jorgensen WL, Chandrasekhar J, Madura JD, Impey RW, Klein ML (1983) Comparison of simple potential functions for simulating liquid water. *J Chem Phys* 79(2):926.
12. Laganowsky A, et al. (2012) Atomic View of a Toxic Amyloid Small Oligomer. *Science* 335(6073):1228–1231.
13. Strange RW, et al. (2006) Variable Metallation of Human Superoxide Dismutase: Atomic Resolution Crystal Structures of Cu–Zn, Zn–Zn and As-isolated Wild-type Enzymes. *J Mol Biol* 356(5):1152–1162.
14. Jones TA, Zou JY, Cowan SW, Kjeldgaard M (1991) Improved methods for building protein models in electron density maps and the location of errors in these models. *Acta Crystallogr A* 47(2):110–119.

15. Emsley P, Lohkamp B, Scott WG, Cowtan K (2010) Features and development of *Coot*. *Acta Crystallogr D Biol Crystallogr* 66(4):486–501.
16. Brünger AT, et al. (1998) Crystallography & NMR system: A new software suite for macromolecular structure determination. *Acta Crystallogr D Biol Crystallogr* 54(Pt 5):905–921.
17. Fabiola F, Bertram R, Korostelev A, Chapman MS (2002) An improved hydrogen bond potential: Impact on medium resolution protein structures. *Protein Sci* 11(6):1415–1423.
18. Wichterle H, Lieberam I, Porter JA, Jessell TM (2002) Directed Differentiation of Embryonic Stem Cells into Motor Neurons. *Cell* 110(3):385–397.
19. Kemper PR, Dupuis NF, Bowers MT (2009) A new, higher resolution, ion mobility mass spectrometer. *Int J Mass Spectrom* 287(1–3):46–57.
20. Mason EA, McDaniel EW (1988) *Transport Properties of Ions in Gases: MASON: TRANSPORT PROPERTIES O-BK* (Wiley-VCH Verlag GmbH & Co. KGaA, Weinheim, FRG).
21. Gidden J, Ferzoco A, Baker ES, Bowers MT (2004) Duplex Formation and the Onset of Helicity in Poly d(CG)_n Oligonucleotides in a Solvent-Free Environment. (126 (46), 15132-15140).
22. Westerfield, M. *The Zebrafish Book*. The University of Oregon Press, Eugene, Oregon. (2003).
23. Levesque MP, Krauss J, Koehler C, Boden C, Harris MP (2013) New Tools for the Identification of Developmentally Regulated Enhancer Regions in Embryonic and Adult Zebrafish. *Zebrafish* 10(1):21–29.
24. Sankur B (2004) Survey over image thresholding techniques and quantitative performance evaluation. *J Electron Imaging* 13(1):146.
25. Kaye R (2003) Common Structure of Soluble Amyloid Oligomers Implies Common Mechanism of Pathogenesis. *Science* 300(5618):486–489.
26. Sandberg A, et al. (2010) Stabilization of neurotoxic Alzheimer amyloid-oligomers by protein engineering. *Proc Natl Acad Sci* 107(35):15595–15600.
27. Thompson MJ, et al. (2006) The 3D profile method for identifying fibril-forming segments of proteins. *Proc Natl Acad Sci* 103(11):4074–4078.
28. Leaver-Fay A, et al. (2011) Rosetta3. *Methods in Enzymology* (Elsevier), pp 545–574.
29. Banci L, et al. (2007) Metal-free superoxide dismutase forms soluble oligomers under physiological conditions: A possible general mechanism for familial ALS. *Proc Natl Acad Sci* 104(27):11263–11267.

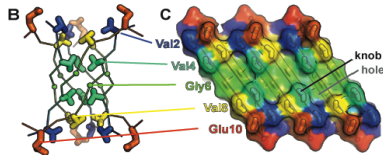
30. Durazo A, et al. (2009) Metal-free Superoxide Dismutase-1 and Three Different Amyotrophic Lateral Sclerosis Variants Share a Similar Partially Unfolded - Barrel at Physiological Temperature. *J Biol Chem* 284(49):34382–34389.
31. Wright GSA, Antonyuk SV, Kershaw NM, Strange RW, Samar Hasnain S (2013) Ligand binding and aggregation of pathogenic SOD1. *Nat Commun* 4:1758.
32. Bernstein SL, et al. (2009) Amyloid- β protein oligomerization and the importance of tetramers and dodecamers in the aetiology of Alzheimer's disease. *Nat Chem* 1(4):326–331.
33. Bleiholder C, Dupuis NF, Wytttenbach T, Bowers MT (2011) Ion mobility–mass spectrometry reveals a conformational conversion from random assembly to β -sheet in amyloid fibril formation. *Nat Chem* 3(2):172–177.
34. Bernstein SL, et al. (2005) Amyloid β -Protein: Monomer Structure and Early Aggregation States of A β 42 and Its Pro¹⁹ Alloform. *J Am Chem Soc* 127(7):2075–2084.
35. Mesleh MF, Hunter JM, Shvartsburg AA, Schatz GC, Jarrold MF (1996) Structural Information from Ion Mobility Measurements: Effects of the Long-Range Potential. *J Phys Chem* 100(40):16082–16086.
36. Bleiholder C, Contreras S, Do TD, Bowers MT (2013) A novel projection approximation algorithm for the fast and accurate computation of molecular collision cross sections (II). Model parameterization and definition of empirical shape factors for proteins. *Int J Mass Spectrom* 345–347:89–96.

Supplemental figures:

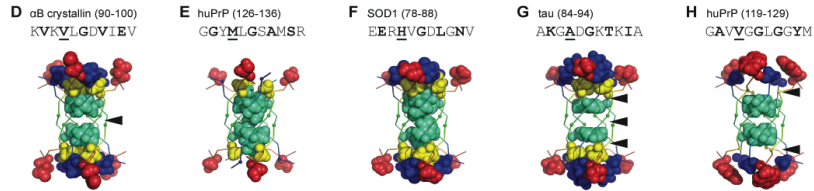
A Computational prediction of cylindrin-compatible segments by 3D profiling



Visual analysis of the native cylindrin structure



Analysis of computational cylindrin predictions



I Manual selection of cylindrin-compatible segments of SOD1

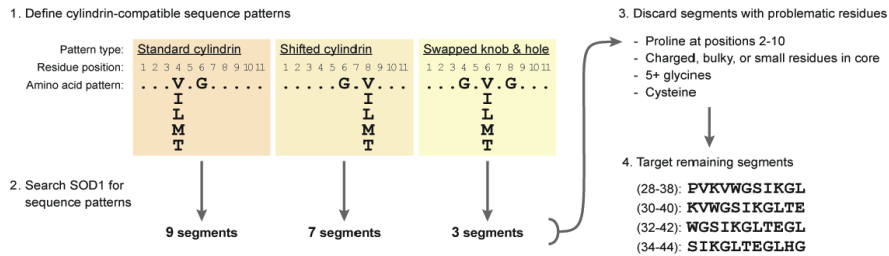


Fig. S1. Prediction of cylindrin-compatible segments.

(A) 3D profile method for predicting cylindrin-compatible segments in amyloid proteins. An example of threading with the amyloid- β peptide is shown.

(B,C) Visual analysis of the cylindrin structure revealed a layering of side chains in the core (b; backbone trace with even-numbered, 'inward-facing' side chains shown as sticks, and glycine C α shown as a small sphere), and a 'knob in hole' packing of valine and glycine residues (c; surface rendering) that allows for the small circumference of the barrel.

(D-H) Structures resulting from the 3D profile predictions were analyzed for packing in the barrel core. Representation is similar to panel B, but side-chain atoms are shown as spheres with van der Waals radii. The protein of origin and segment sequence are given, with even-numbered, 'inward-facing' residues in bold, and the critical position 4 residue underlined. (D) The original cylindrin structure, after Rosetta-based side-chain repacking and energy minimization. Notice the packing of valine 4, cyan, near the center. Although there is a gap between the two layers (arrowhead), it is small. (E) In this model of a segment from the human prion protein, methionine (cyan) occupies the central position 4, filling the space more completely than valine of the cylindrin sequence. (F) A histidine side chain at position 4 can also fill the central space, but is not able to satisfy hydrogen bonding groups. (G) Alanine at position 4 does not fill the core as well, leaving gaps (arrowheads). (H) Adjacent alanine and glycine, at positions 2 and 8 respectively, leave large gaps in outer layers of the cylindrin model core (arrowheads), in spite of a native valine packing in the middle at position 4.

(I) Manual selection of cylindrin-compatible segments. First, three sequence-based criteria, which define the glycine position and the position of an adjacent, appropriate side chain (with cylindrin-compatible size and charge) in the core, were used in the initial selection of segments. The resulting sequences were further culled based on the presence of undesirable amino acids in specific positions. Prolines were avoided because of their tendency to disrupt β -structure. Charged and bulky inward-facing residues were avoided because of likely disruption to the packing. Small inward-facing residues were avoided because of gaps in packing, *e.g.* as in panel H. Large numbers of glycines were avoided because of the tendency for these sequences to be flexible rather than adopt a fixed conformation. Cysteines were avoided for experimental purposes. Four overlapping segments of SOD1 resulted from this manual selection.

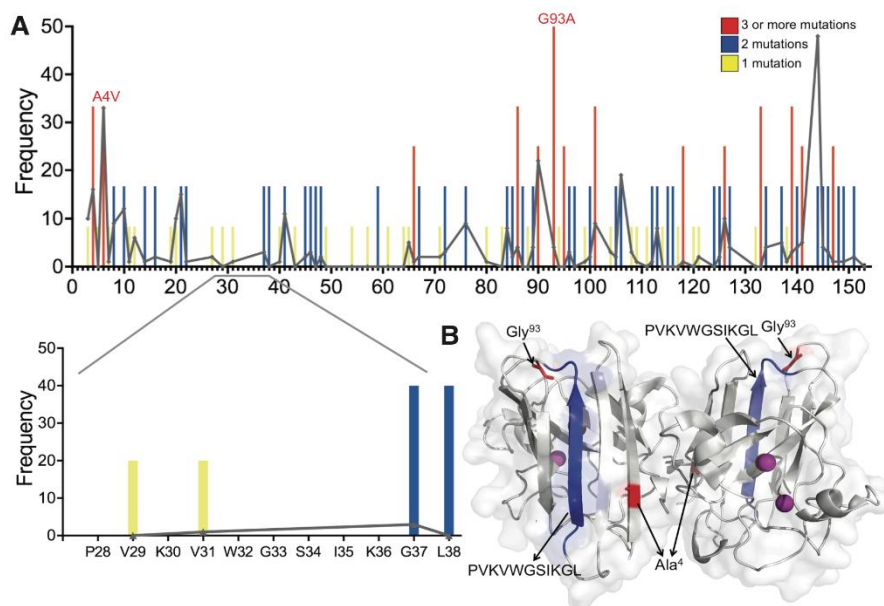


Fig. S2. Frequency distribution of ALS-related mutations in SOD1. (A) Histogram representation of the number of familial-disease mutations found at each residue position. Gray connected line refers to the total number of patients known to carry mutations at that residue. The segment 28-38 is expanded. Val29 and Val31 each have one known familial mutation and Gly37 and Leu38 have two known familial mutations. Notice that the segment 28-38 has low frequency of individuals with ALS linked mutations with none in residues 32-36. A total of 4 individuals are known to carry mutations in this region. Data were obtained from <http://alsod.iop.kcl.ac.uk> (B) Ribbon diagram of dimeric SOD1 (PDB ID: 2C9S) with the segment 28-38 highlighted in blue. Zinc and copper atoms are shown as magenta spheres, and the familial mutation residues, A4V and G93A are colored red.

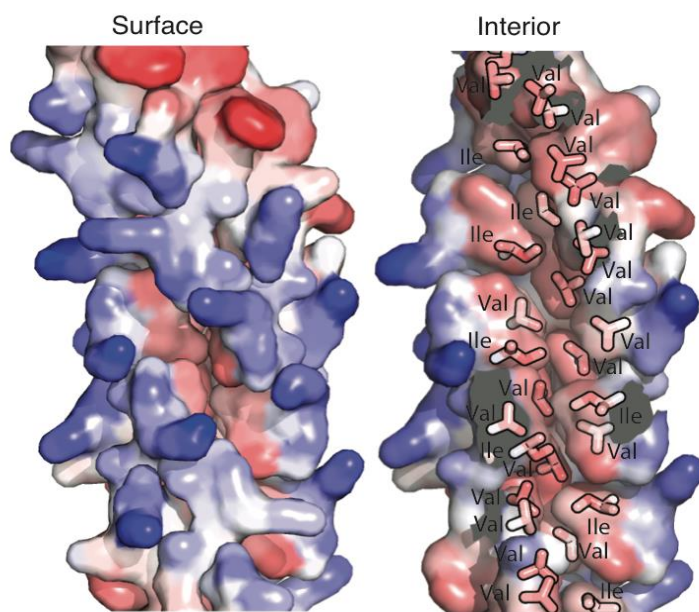


Fig. S3. Hydrophobicity mapped on the surface of the corkscrew crystal structure (left), and a lengthwise cross-section (right). The cleft interior is strongly hydrophobic (red) made up of valine and isoleucine side chains of Val29, Val31, and Ile35, whereas the exterior is strongly hydrophilic (blue) arising from Lys28, Lys30, Ser34, and Lys36.

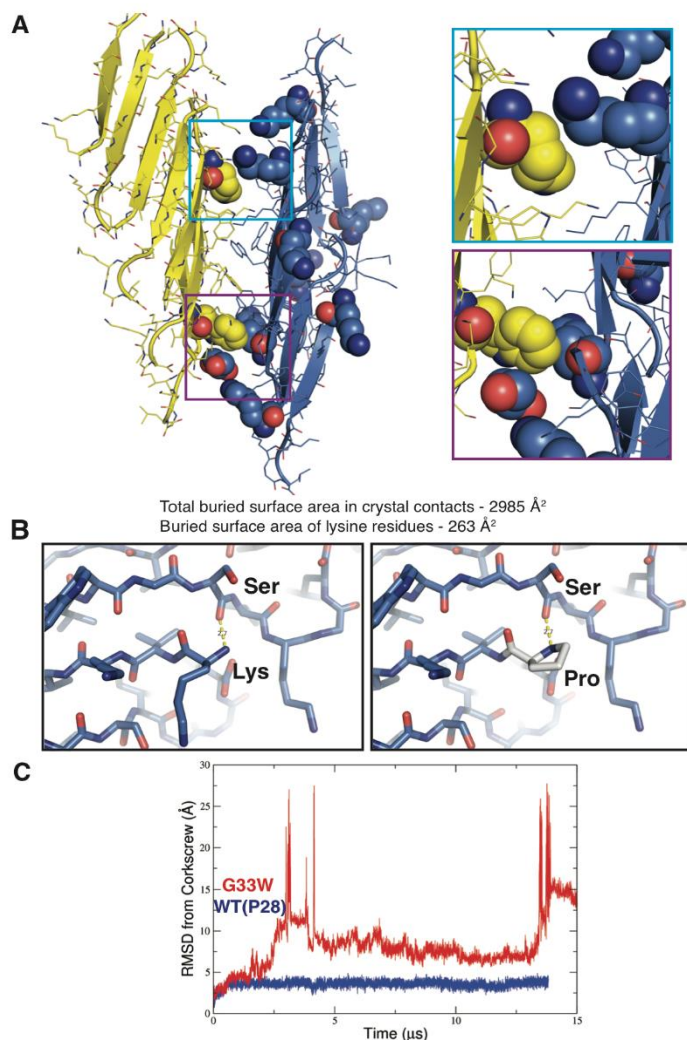


Fig. S4. Lysine substitution at position 28 contributes weakly to the crystal packing and not to the stability of the corkscrew structure. (A) Crystal packing of the corkscrew structure. Two asymmetric units forming crystal contacts are shown in blue and yellow from neighboring corkscrews and N-terminal lysines are shown in sphere representation. Among the eight N-terminal lysines in each asymmetric unit, 5 form weak van der Waals interactions with a lysine residue and a tryptophan residue of the neighboring corkscrew. These interactions contribute weakly (~9%) of the total buried surface area in the crystal contacts. Buried surface area in the crystal contacts was calculated by AREAIMOL. (B) Lysine at position 28 is not essential for corkscrew

formation and replacing it with the native proline residue does not disrupt the potential for hydrogen bonding. The N-terminal lysine forms a hydrogen bond with the carbonyl oxygen of Ser34 in an adjacent β -strand (left). Substituting the N-terminal lysine with the native proline residue (gray) maintains the hydrogen bond (right). (C) The blue and red curves correspond to $C\alpha$ root-mean-square deviations (RMSD) from the corkscrew crystal structure in MD simulations of the 8-chain wild-type (PVKVVWGSIKGL) and G33W mutant (PVKVVWSIKGL) corkscrews, respectively. The G33W mutant deviates from the corkscrew structure, whereas the wild-type structure remains stable throughout the length of the simulation. The simulations suggest that the dynamics of the backbone at residue 33 may contribute to the instability of the G33W mutant. The G33 residue in the corkscrew structure occupies a region of Ramachandran space different from the allowable region for tryptophan and other non-glycine amino acids. In the wild-type simulations, the backbone dihedral angles of G33 tend to remain in the lower right quadrant of a Ramachandran plot, whereas those of W33 in the mutant quickly relax to the β -sheet/ α -helix regions, leading to deviations from the corkscrew structure. The extra hydrophobicity of G33W may also have an effect, making the mutant corkscrew more likely to collapse.

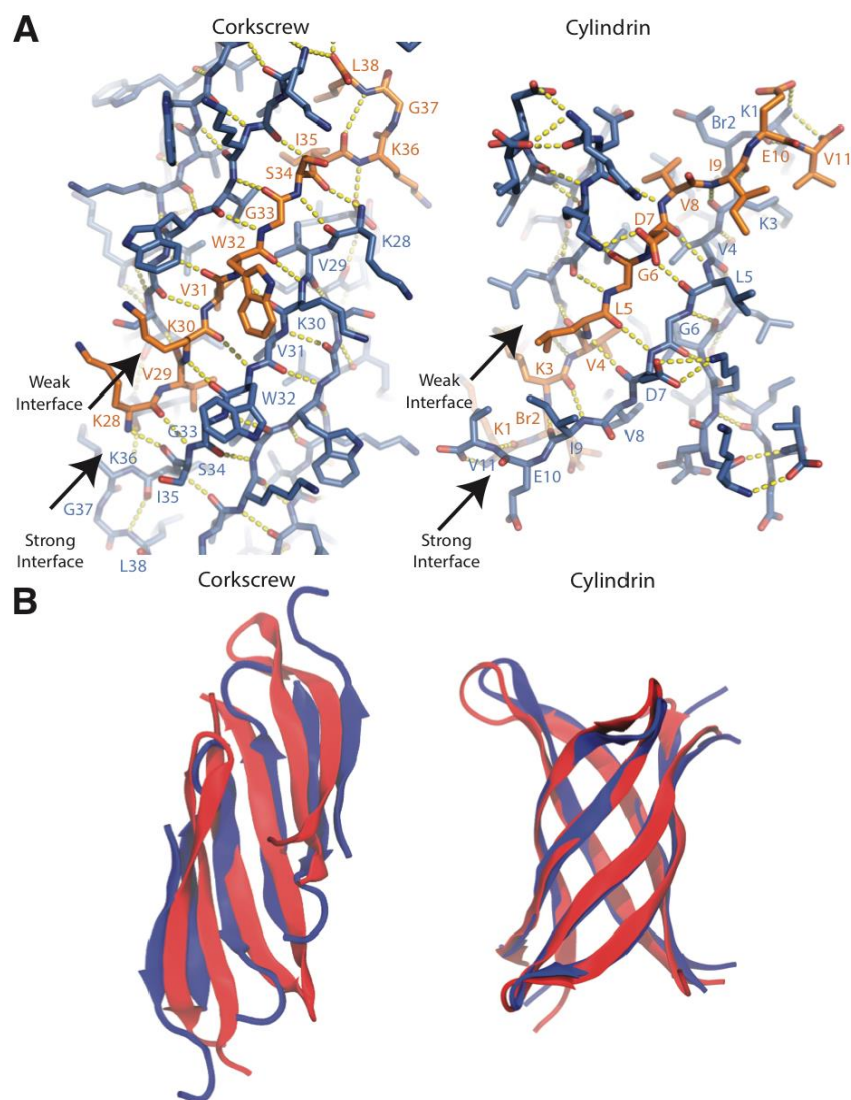


Fig. S5. Structural comparison of corkscrew and cylindrin. (A) Hydrogen bonding network of the corkscrew structure (left). Shown here the orange β -strand has a strong interface with the β -strand below composed of 9 hydrogen bonds and a weak interface with the β -strand above composed of 7 hydrogen bonds. Hydrogen bonding network in the cylindrin structure (Right, PDB ID: 3SGO) shares a similar architecture where the orange strand has a stronger interface with the β -strand below composed of 12 hydrogen

bonds and a weak interface with the β -strand above composed of 8 hydrogen bonds. Br2 refers to the non-natural amino acid 2-bromoallyl-glycine that was used for phasing. **(B)** MD simulations of weakly restrained monomers of SOD1 spontaneously assembled into a corkscrew-like structure. A snapshot of an assembled corkscrew-like structure from the MD simulations (red) is overlaid onto the crystal structure (blue). Out of 20 simulations, three successfully assembled to a corkscrew-like structure. Interestingly, in trajectories where a corkscrew did not form, individual monomers often formed interfaces composed of out-of-register β -sheets. As a control, we found that monomers of α B crystallin spontaneously assembled into a cylindrin structure using the same simulation protocol. A snapshot of an assembled cylindrin from the MD simulation (red) is overlaid onto the crystal structure (blue, PDB ID 3SGR). Out of 10 simulations, one successful assembly to cylindrin was obtained. As in the SOD1 assembly runs, in α B crystallin assembly trajectories where a cylindrin did not form, we often observed dimers composed of out-of-register β -sheet interfaces.

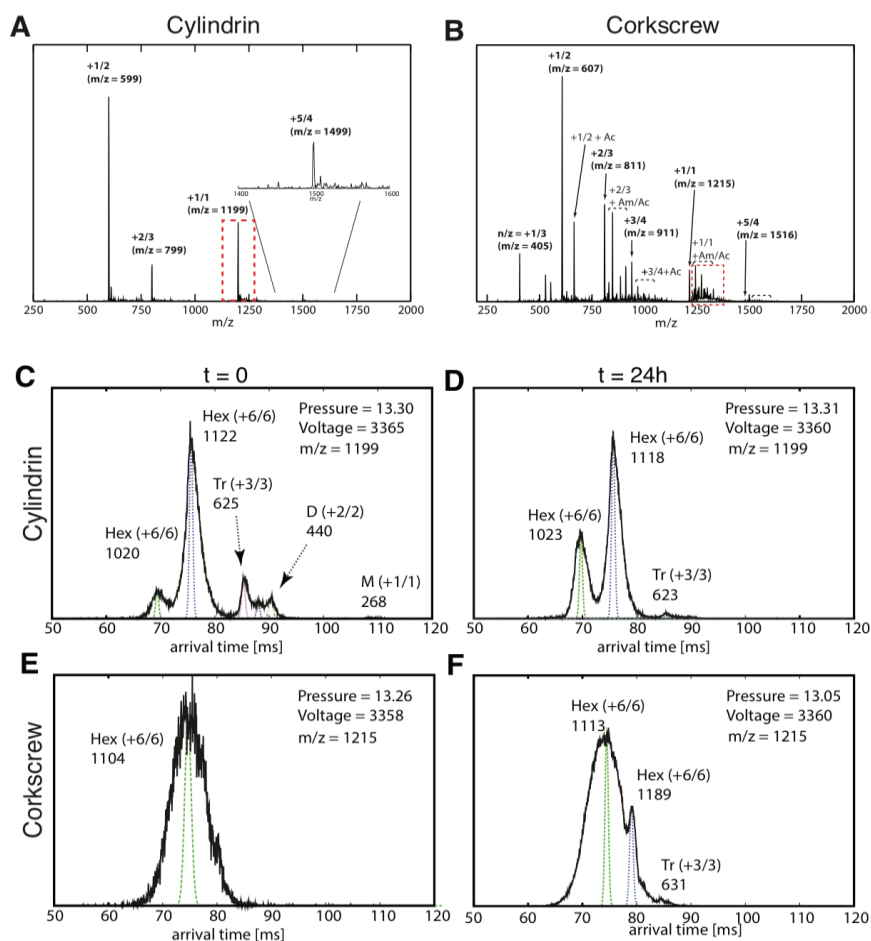


Fig. S6. The corkscrew-forming segment, SOD1(28-38) forms oligomers in solution with cross section similar to the crystal structure. (A, B) n-ESI-q mass spectrum of 200 μ M cylindrin and corkscrew peptides in 20 mM ammonium acetate buffer (pH = 7.0), respectively. Each mass spectral peak is annotated with n/z where n is the oligomer number and z is the charge. (C-F) Representative ATDs of $n/z = 1/1$ peaks of the cylindrin and corkscrew peptides incubated for $t = 0$ and 24 hours. Each ATD feature is annotated with n/z and an experimental collision cross section (M = monomer, D = dimer, Tr = trimer, Hex = hexamer). The narrow dashed lines are the peak shapes predicted for a single conformer of the cross sections given.

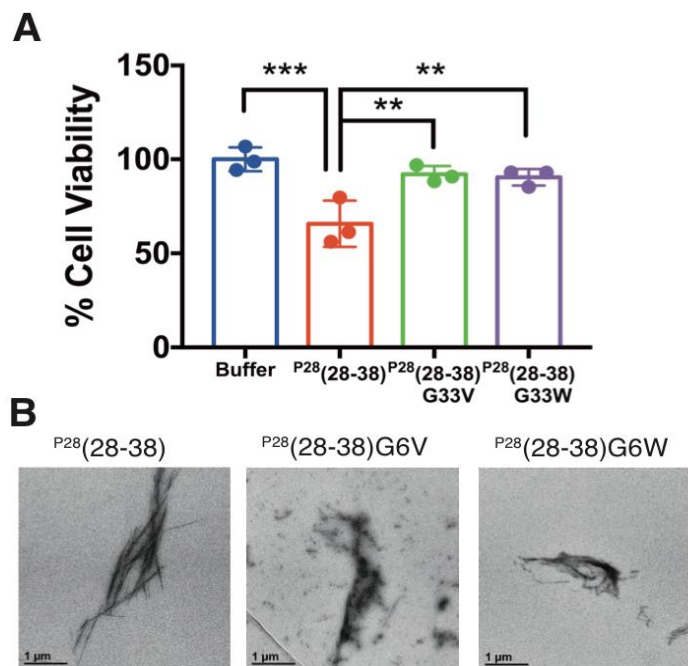


Fig. S7. Segment (28-38) with native proline is toxic and substitution at Gly33 renders it non-toxic. (A) Peptides were prepared identically by solubilizing in 50 mM tris-base buffer and overnight incubation at 37 °C with agitation and ES-derived motor neurons were treated with 100 μM final concentration. P²⁸(28-38) is toxic while the peptides with substitutions G33V and G33W are non-toxic. Symbols represent individual values and bars represent average values. Statistical significance was measured by ANOVA. (**p < 0.01, ***p < 0.001). (B) Electron micrographs of all three peptides showed similar fibrils suggesting that substitution at Gly33 does not change the fibrillation propensity.

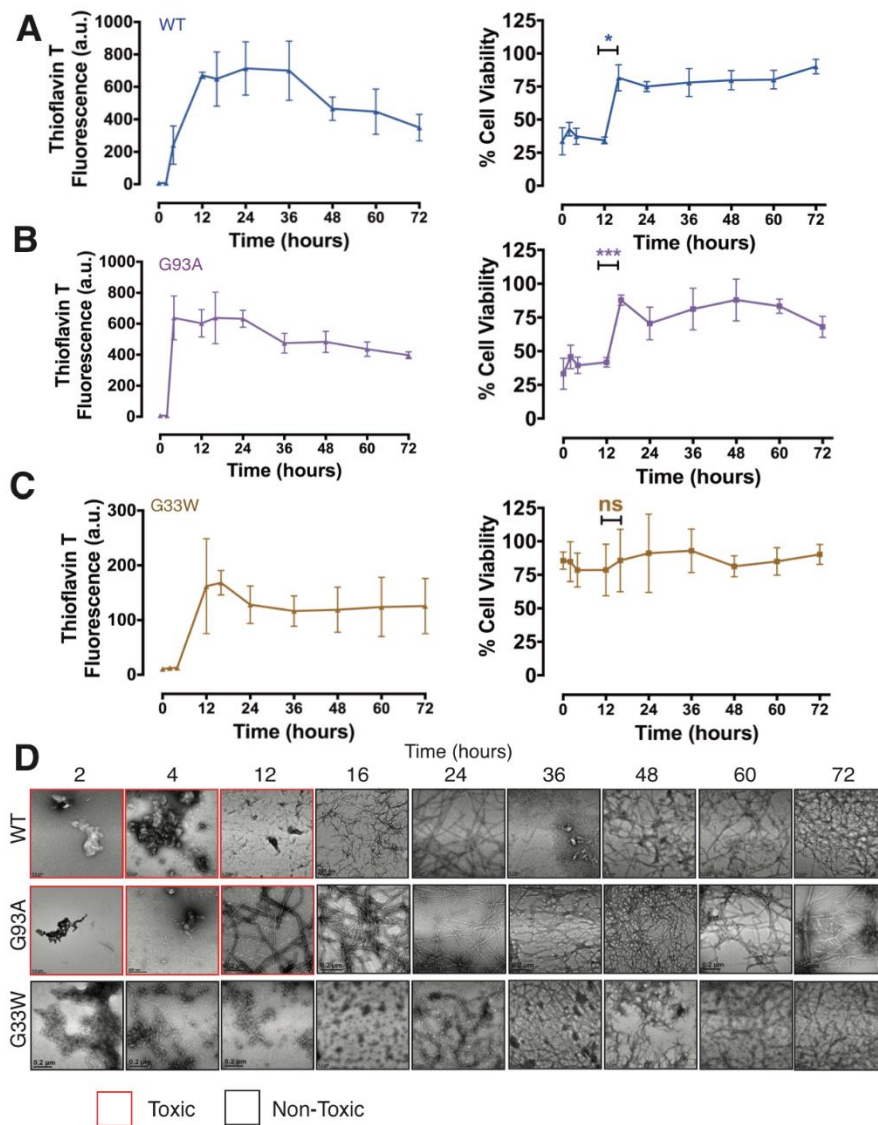


Fig. S8. WT and mutant SOD1 show similar kinetics of aggregation and cytotoxicity. (A) Thioflavin T assay of 80 μ M WT protein shows a lag time of 2-4 hours

before fibrils first appear (left). Cell viability (right) of ES-derived primary motor neurons incubated with protein aggregated for indicated times shows WT is only toxic when shaken up to 12 hours, when abundant fibrils first appear. **(B)** Similar to WT, the mutant G93A shows a lag time of 2-4 hours in a thioflavin T assay (left). Cell viability (right) of ES-derived primary motor neurons incubated with protein aggregated for indicated times shows G93A is also toxic when shaken up to 12 hours, when abundant fibrils first appear. **(C)** Thioflavin T assay (left) shows G33W, the corkscrew-disrupted mutant protein behaves similar to WT and G93A with a lag phase of 2-4 hours. However, it is non-toxic at all time points (right). Results shown as Mean±SD (n=3). Statistical significance was analyzed using a two-tailed T-test with Welch's correction (*p < 0.05, ***p < 0.001, ns not significant). **(D)** Electron micrographs of SOD1 constructs aggregated for different lengths of time. Samples aggregated up to 12 hours tend to show some aggregates and sparse fibrils while samples aggregated for 16 hours or more show a large fibril load. Scale bar 200 nm.

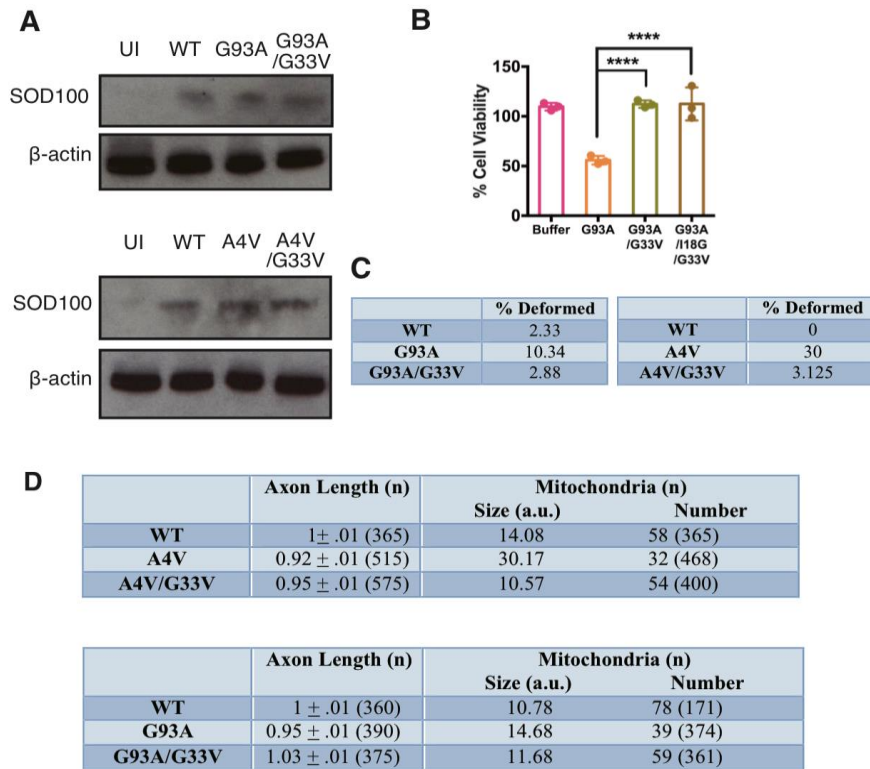


Fig. S9. Expression of A4V and G93A mutant proteins causes axon shortening and abnormal mitochondrial clustering in zebrafish model. (A) Western blotting of zebrafish embryos to confirm expression of the mRNA injected. SOD100 was used to detect SOD1 and β -actin was used as loading control. UI refers to uninjected zebrafish. (B) Construct G93A/G33V/I18G is non-toxic in cell culture model similar to the G93A/G33V mutant. (C) Zebrafish at 2 dpf were imaged and higher percentage of A4V (30%) and G93A (10%) injected zebrafish displayed significant deformation compared to WT and the G33V expressing fish. (D) Average axon length (normalized to WT construct) and mitochondrial size of the different constructs. n refers to the total number of measurements made for each construct.

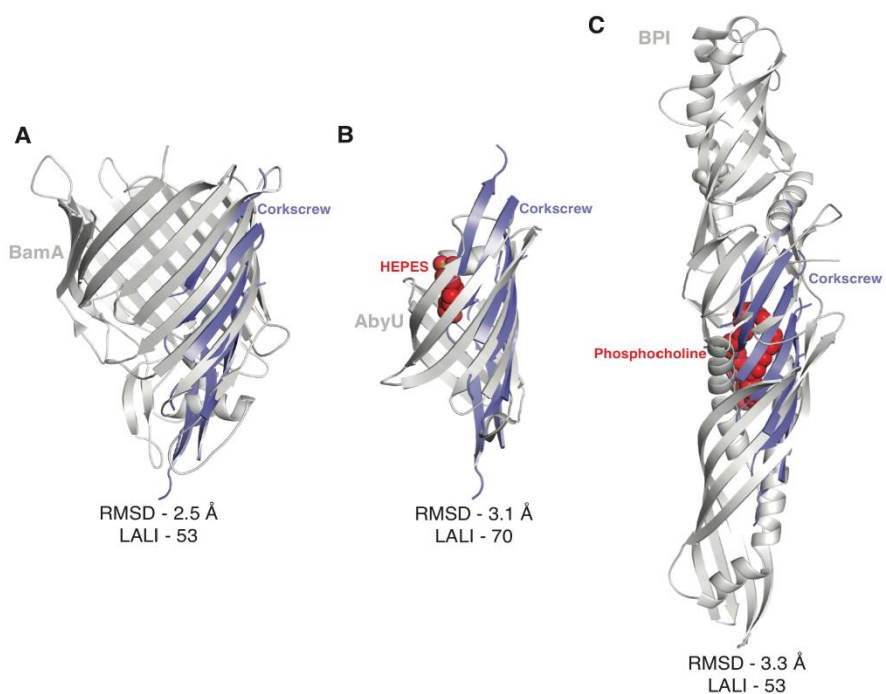


Fig. S10. Structural comparison of corkscrew with other β -sheet proteins. The DALI server was used to search the Protein Data Bank for proteins with a similar structural fold. Three main categories of proteins were found – big barrel proteins, small β -sheet proteins that bind ligands and open twisted β -sheet proteins that bind ligands. **(A)** Overlay of corkscrew (purple) with the structure of BamA (PDB: 4K3C), a β -barrel membrane protein (gray). **(B)** Overlay of corkscrew (purple) with the structure of AbyU (PDB: 5DYV), a diels alderase (gray) with HEPES (red) bound in the barrel. **(C)** Overlay of corkscrew (purple) with BPI (PDB: 1BP1), a bactericidal protein with phosphocholine bound. Notice that the twisted sheet creates a groove for binding phosphocholine (red). RMSD – root mean square deviation of $C\alpha$, LALI – length of aligned residues.

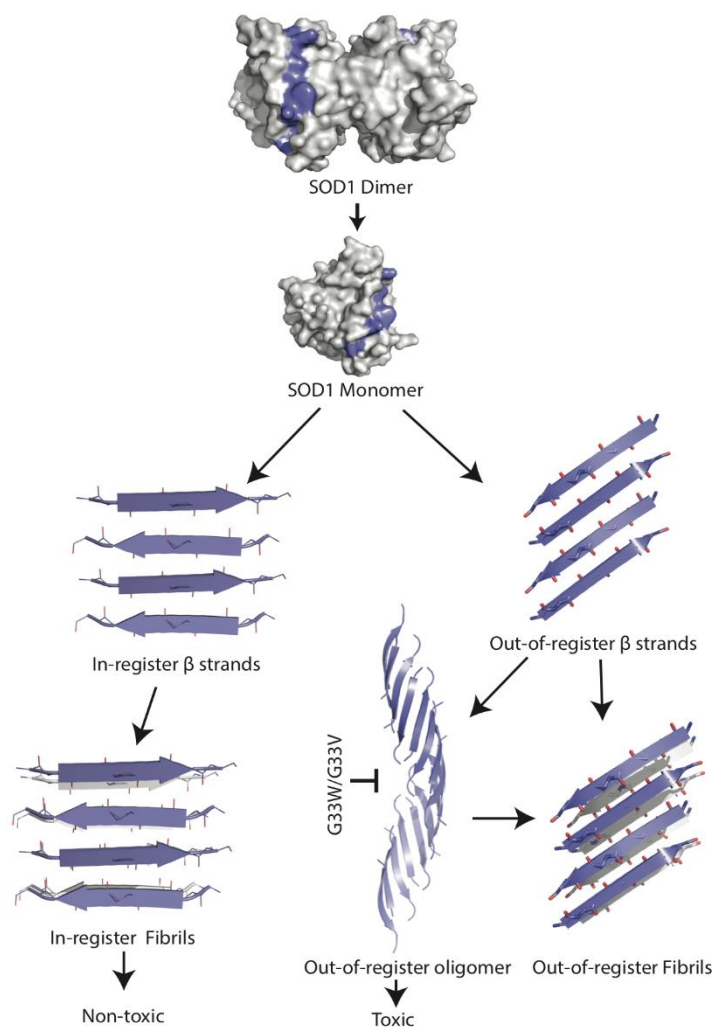


Fig. S11. Model of SOD1 aggregation pathway. SOD1 forms a stable dimer that is resistant to aggregation. Its destabilization into monomers renders it prone to aggregation into β -sheet rich fibrils. The corkscrew structure of segment 28-38 (purple) determined here, suggests that there is an off-pathway for oligomer formation independent of the in-register fibrils. The mutations, G33W/G33V specifically prevent corkscrew formation, an out-of-register oligomer. Fibril formation assays suggest that G33W/G33V do not affect the in-register fibril formation pathway and large fibrils are non-toxic.

Table S1. X-Ray Data Collection and Refinement Statistics

	KVKVWGSIKGL	KVKVWGSIKGL (iodide)
Beamline	APS 24-ID-E	APS 24-ID-E
Resolution Å	1.9	2.1
Total unique reflections	8378	11489
Total reflections observed	47323	43500
Unit cell dimensions		
a, b, c (Å)	33.2, 44.4, 71.2	33.1, 44.4, 71.4
α , β , γ (°)	90.0, 90.0, 90.0	90.0, 90.0, 90.0
Space group	P2 ₁ 2 ₁ 2 ₁	P2 ₁ 2 ₁ 2 ₁
R _{merge}	16.5% (48.4%)	9.5% (41.8%)
I/ σ	8.4 (4.3)	11.1 (3.6)
Completeness	95.5 %	96.7%
Wavelength (Å)	0.9791	0.9791
Refinement		
Resolution (Å)	35.5-2.0	19.3-2.0
Reflections for refinement (after merging Friedel Pairs)	6690	6249
R _{free} /R _{work} (%)	25.08/21.09	26.2/21.2
Molecules per asymmetric unit	8	8
Solvent content (%)	54.6	54.6
Matthews coefficient (Å ³ /Da)	2.71	2.71
Total water molecules	34	52
Total iodide atoms	0	2
Glycerol molecule	0	1
Rmsd bond length (Å)	0.010	0.010
Rmsd angles (°)	1.022	0.88
Ramachandran plot		
Allowed	100	100
Generous	0	0
Disallowed	0	0

Table S2. Comparison of shape complementarity (Sc) and buried surface area (A_b) of corkscrew with cylindrin and steric zippers.

	Corkscrew	Cylindrin*	Steric Zipper**
Sc	0.79	0.74	0.68
A_b (\AA^2)	984	943	1034
$A_b/\text{Residue}$	89	86	94

* PDB ID: 3SGO

** PDB ID: 4RIL

For the Sc calculation, we examined the interface between one chain and the remaining chains of the assembly.

A_b values were calculated using AREAIMOL. The area buried was calculated by subtracting the solvent accessible surface area of one chain of the assembly from the total solvent accessible surface area of an isolated chain.